Title

Understanding the Galactic Black Hole Population with Gravitational Microlensing

Author

Lam, Casey

Publication Date

2023

Understanding the Galactic Black Hole Population with Gravitational Microlensing

by

Casey Y. Lam

A dissertation submitted in partial satisfaction of the

requirements for the degree of

Doctor of Philosophy

in

Astrophysics

in the

Graduate Division

of the

University of California, Berkeley

Committee in charge:

Professor Jessica R. Lu, Chair
Professor Joshua S. Bloom
Professor Liang Dai
Professor Daniel R. Weisz

Summer 2023

Understanding the Galactic Black Hole Population with Gravitational Microlensing

Abstract

Understanding the Galactic Black Hole Population with Gravitational Microlensing

by

Casey Y. Lam

Doctor of Philosophy in Astrophysics

University of California, Berkeley

Professor Jessica R. Lu, Chair

This thesis addresses the problem of finding and characterizing isolated Galactic stellar-mass BHs via the technique of gravitational microlensing. We present work on both the theoretical and simulation front as well as an observational and modeling perspective.

Prior to 2019, most estimates for the number of BHs in the Milky Way were highly uncertain and dated. This limited our ability to accurately predict and interpret the number of BHs detectable with microlensing. To address this shortcoming, we develop a Milky Way microlensing simulation called `PopSyCLE` (Population Synthesis for Compact object Lensing Events). Using `PopSyCLE`, we identify an improved strategy for finding and identifying BHs photometrically, advancing our ability to identify good BH candidates and enable statistical constraints on the BH population to be made.

Although photometric microlensing can statistically characterize BHs, it cannot disentangle the lensing system's relative proper motion from the lens's mass. Astrometric microlensing is required to break this fundamental photometric degeneracy to definitively measure a lens's mass and confirm its BH nature. We analyze 5 archival BH candidate microlensing events by jointly modeling ground-based microlensing survey photometry and Hubble Space Telescope (*HST*) astrometric observations. We identify one candidate, OB110462, to be a neutron star or low-mass BH ($1.6 - 4.4 M_\odot$), making it the first dark isolated compact object confirmed with a mass measurement. In addition, using the full sample of five objects including non-BH detections and quantifying selection effects, we find this sample to be consistent with 100 million isolated BHs in the Milky Way.

The exact nature of OB110462 was disputed; another group independently found its mass to be $7 M_\odot$, firmly establishing it as a higher-mass BH. We re-analyze OB110462 using new and re-reduced data, along with updated analysis software. We find that OB110462 is a $6 M_\odot$ BH, making it a solid BH detection. The main reason for finding a higher mass in this work is that the software used in previous work underestimated a positional bias correction,

resulting in different astrometric measurements and hence a different mass.

Presently, microlensing is a small and relatively obscure subfield of astronomy. However, this will change with the launch of NASA's next flagship mission, the Nancy Grace Roman Space Telescope. *Roman* will conduct a microlensing survey of the Galactic Bulge. In addition, other public time-domain surveys will enable searches for microlensing events. In order to enable broader participation and newcomers to the field, we provide some examples of important considerations to take into account when modeling microlensing light curves. We also document, explain, and provide examples of some microlensing notations and conventions not easily found in the literature.

Contents

Acknowledgments

First and foremost, a huge thanks to my advisor, Jessica Lu. When I started grad school, I knew nothing about observational astronomy, and possibly even worse, had no computer skills. This thesis would not exist without Jessica's incredible mentorship and significant investment in my development as a scientist over the last six years. To this end, she has done more than can be possibly listed in one paragraph, or even one page. So to summarize, I am most grateful for Jessica's encouragement and generosity with her time, and teaching me the many technical and non-technical skills needed to do research and pursue a career in science. This has not only allowed me to complete the work presented here, but also enabled me to start charting my own research directions and have the opportunity to pursue them. Thank you, Jessica, for everything.

Thanks to the members of Jessica's research group over the years for both science and fun, in particular: Matt Hosek for his friendliness, enthusiasm, and patience, even when I wreaked havoc on some of his code with `git rm -rf`; Nicholas Rui and Nijaid Arredondo, exceptional undergrads that helped me figure out things when I joined the group; Dongwon Kim for the office shenanigans, including excessive sugar/gummy bear consumption and being a "bad influence postdoc"; Siyao Jia for being a great conference travel buddy, office-mate, and friend (we still need to reschedule our Chinese New Year 2020 hotpot); and the OB110462 crew that put in a 16-hour workday on a moment's notice. In addition, Panda thanks Kat and Oukiey for their friendship.

Thanks to Dan Weisz, Josh Bloom, and Liang Dai for serving on my qual and thesis committees. Thanks also to Dan for being a great Head Grad Advisor, Josh for letting me into Berkeley despite missing his first call for my interview, and Liang for interesting discussions at arXiv.

Thanks to the other faculty whom I've had the pleasure of learning from, in particular: Eugene Chiang for letting me GSI for 7B (a great class from which some examples in Chapter 1 were drawn) and saving me from having to GSI radio lab instead, and a fun semester of OOM physics; Courtney Dressing for being a wonderful academic advisor; Mariska Kriek for exceptional patience and encouragement in Galaxies; Chung-Pei Ma for a fun semester of black holes; and Raffaella Margutti for being a great HGA.

Thanks to the department staff past and present, who navigate university bureaucracy, handle reimbursements, fix computers, deal with ants, keep the department functioning, and always handle endless requests and problems graciously and with a smile.

Thanks to the co-authors on the papers I have written during graduate school for their contributions, feedback, and insights; they are acknowledged at the beginning of each chapter. Thanks also to collaborators Scott Gaudi and Jay Anderson.

Thanks to my undergrad advisors that gave me my first opportunity to do research: Joe Lauer, Tracy Slatyer, Alan Guth, and Jolyon Bloomfield. Having now supervised students, I am even more appreciative of your patience and mentorship.

Last but certainly not least, thanks to my family, and especially my parents, for everything else. I love you even more than black holes.

Funding acknowledgements: I am grateful for financial support provided through the NSF, NASA, the Heising-Simons foundation, the H2H8 foundation, and the UC Berkeley astronomy department. In particular, I acknowledge support from NASA FINESST grant No. 80NSSC21K2043.

Acknowledgements for Chapter 2: We thank the PALS collaboration and Will Clarkson for helpful conversations. We also thank the anonymous referee for comments that improved this paper. C. Y. L. and J. R. L. acknowledge support by the National Aeronautics and Space Administration (NASA) under Contract No. NNG16PJ26C issued through the WFIRST Science Investigation Teams Program. Portions of this work were performed under the auspices of the U.S. Department of Energy by Lawrence Livermore National Laboratory under Contract DE-AC52-07NA27344 and supported by the LLNL-LDRD Program under Project No. 17-ERD-120.

Acknowledgements for Chapter 3: We thank Dan Foreman-Mackey, Tharindu Jayasinghe, Tom Loredo, Greg Martinez, and Jeff Andrews for helpful and interesting conversations. In addition, we thank the referee for feedback that improved this paper. We also thank Kailash Sahu, Howard Bond, Jay Anderson, Martin Dominik, Philip Yock, and Annalisa Calamida for proposing and taking the archival HST observations used in this work.

C.Y.L. and J.R.L. acknowledge support by the National Science Foundation under Grant No. 1909641 and the National Aeronautics and Space Administration (NASA) under contract No. NNG16PJ26C issued through the WFIRST (now Roman) Science Investigation Teams Program. C.Y.L. also acknowledges support from NASA FINESST grant No. 80NSSC21K2043. D.P.B. was supported by NASA grants NASA-80NSSC18K0274 and 80GSFC17M0002. Ł.W. acknowledges support from the Polish National Science Centre (NCN) grants Harmonia No. 2018/30/M/ST9/00311 and Daina No. 2017/27/L/ST9/03221 as well as the European Union's Horizon 2020 research and innovation programme under grant agreement No 101004719 (OPTICON-RadioNet Pilot, ORP) and MNiSW grant DIR/WK/2018/12.

Based on observations made with the NASA/ESA Hubble Space Telescope, obtained from the data archive at the Space Telescope Science Institute (STSci) operated by the Association of Universities for Research in Astronomy, Inc. under NASA contract NAS 5-26555, and obtained from the the Hubble Legacy Archive, a collaboration between STScI/NASA, the Space Telescope European Coordinating Facility (ST-ECF/ESA) and the Canadian Astronomy Data Centre (CADC/NRC/CSA).

This paper makes use of data obtained by the MOA collaboration with the 1.8 metre MOA-II telescope at the University of Canterbury Mount John Observatory, Lake Tekapo, New Zealand. The MOA collaboration is supported by JSPS KAKENHI (Grant Number JSPS24253004, JSPS26247023, JSPS23340064, JSPS15H00781, JP16H06287, and JP17H02871) and the Royal Society of New Zealand Marsden Fund. The MOA project has received funding from the Royal Society of New Zealand, grant MAU1901 to IB.

This work presents results from the European Space Agency (ESA) space mission Gaia. Gaia data are being processed by the Gaia Data Processing and Analysis Consortium

(DPAC). Funding for the DPAC is provided by national institutions, in particular the institutions participating in the Gaia MultiLateral Agreement (MLA).

This research has made use of data obtained from the Chandra Source Catalog, provided by the Chandra X-ray Center (CXC) as part of the Chandra Data Archive.

Acknowledgements for Chapter 4: C.Y.L. and J.R.L. acknowledge support from the National Science Foundation under grant No. 1909641 and the Heising-Simons Foundation under grant No. 2022- 3542. C.Y.L. also acknowledges support from NASA FINESST grant No. 80NSSC21K2043 and a research grant from the H2H8 Foundation.

We thank Kailash Sahu, Howard Bond, and Jay Anderson for proposing and taking the HST SNAP observation used in this work.

This research has made use of NASA's Astrophysics Data System.

Chapter 1

Background: Black holes, microlensing, and finding black holes with microlensing

1.1 Black holes

A black hole (BH) is an object so dense that light cannot escape from it. The concept of a BH had been articulated as far back as the late 1700s (Laplace 1799; Michell 1784), but was not rigorously introduced to physics until 1916 when Schwarzschild found a solution to the Einstein field equations of general relativity that characterized a BH (Schwarzschild 1916). It would take another several decades after Schwarzschild's solution for BHs to become an active area of astrophysics research (Bardeen and Petterson 1975; Bardeen, Press, et al. 1972; Bolton 1972; Kerr 1963; Lynden-Bell 1969; Peebles 1972; Trimble et al. 1969; Webster et al. 1972; Wolfe et al. 1970).

Presently, BHs have been observed in a range of masses spanning 10 orders of magnitude: from $3M_\odot$ (Thompson et al. 2019) up to $7 \times 10^{10} M_\odot$ (Shemmer et al. 2004). BHs with masses $M \lesssim 10^2 M_\odot$ are called *stellar-mass*, those with $M \gtrsim 10^6 M_\odot$ are called *supermassive*, and those in between are called *intermediate-mass*. This thesis is concerned with stellar-mass BHs, specifically isolated stellar-mass BHs.

1.1.1 The formation of stellar-mass black holes and the uncertainty in their progenitors

Astrophysical stellar-mass BHs form from the death of stars. This can occur via the core collapse of a massive star, the accretion-induced collapse of neutron stars (NSs), or the merger of two NSs. Here, we focus on the massive star channel.

Stars produce energy to support themselves through fusion; as the lighter elements are burned up, heavier and heavier elements must be subsequently burned. For stars with zero-age main sequence (ZAMS) masses $\gtrsim 10 M_\odot$, this process continues until it becomes energetically unfavorable to continue burning heavier elements. Nickel-56 is most stable, and thus an iron-nickel core builds up within the star. Eventually, when even electron degeneracy pressure cannot hold up this iron-nickel core, the star collapses, sometimes accompanied by a supernova explosion. The stellar remnant left behind from the collapse can either be a NS or a BH.

It was previously assumed that upon their deaths the lighter massive stars with ZAMS masses $10M_\odot \lesssim M \lesssim 25M_\odot$ would produce NSs, and the most massive stars with ZAMS masses $M \gtrsim 25M_\odot$ would produce BHs, with some additional dependence on the metallicity of the star where the ZAMS mass boundary for NS vs. BH formation moves to higher masses with increasing metallicity (Heger et al. 2003). Another way to state this is that the initial-final mass relation (IFMR), which maps the ZAMS mass of a star to its final compact object type and remnant mass, is monotonic and simply connected.

Over the last decade, theoretical and simulation work has shown that the NS and BH IFMR is more complex than the simplistic picture presented in the previous paragraph. Using a large suite of 1-D neutrino driven simulations, Sukhbold, Ertl, et al. (2016) showed that the landscape of explosions and compact object remnants is neither monotonic nor simply connected. Different diagnostics have been devised to characterize whether a star will explode or not, ranging in complexity and predictive power. This includes the compactness of the core (O'Connor et al. 2011), the entropy per nucleon and mass derivative as a proxy for mass infall rate and neutrino luminosity (Ertl et al. 2016), the silicon-oxygen interface, and even features extracted from machine learning (Tsang et al. 2022).

On the observational side, there are two ways to understand the connection between a massive progenitor star and its compact remnant. If archival imaging exists at the location at which a supernova went off, the progenitor star can be characterized (for a review, see Smartt 2009). Conversely, the *disappearance* of a star from a series of images can indicate core collapse and a "failed" supernovae, which led to the formation of a BH (Kochanek et al. 2008).

All this theoretical and observational work ultimately connects back to understanding the IFMR. Quantifying the IFMR is important, as it determines the number and mass distribution of compact objects, and explosions (or lack thereof) of massive stars affects the chemical enrichment of the galaxy, as well as the amount of feedback that influences galactic evolution.

However, the observational methods mentioned have some difficulties. First, converting observations into stellar luminosities and masses is fraught with complications—systematics such as extinction from dusty circumstellar material, calculation of bolometric corrections from single-band observations, and adopted mass-luminosity relations can significantly change the results (Davies et al. 2018). Second, failed supernovae are difficult to confirm—they are red, dim, and rare, and ruling out any surviving non-BH remnant hidden behind dust is almost impossible (Byrne et al. 2022). Third, coincidentally having sufficient archival imaging of rare events requires some luck, limiting the sample size and hindering statistical studies. The "red supergiant problem" coined in Smartt et al. (2009) regarding an apparent dearth of high-mass red supergiants progenitors to Type IIP core-collapse supernovae, its significance, and its possible interpretation that these massive stars form BHs is still actively debated (Davies et al. 2020a,b; Kochanek 2020). We need additional and more direct observational probes to study BH populations and the IFMR (Chapter 1.3).

Finally, we briefly mention here that there has been a recent resurgence of interest in *primordial BHs*. In contrast to the astrophysical stellar-mass BHs described at the beginning of this section that form from dying stars, primordial BHs are predicted to form from the collapse of $\mathcal{O}(1)$ quantum fluctuations in inflationary fields in the early universe (Hawking 1971; Zel'dovich et al. 1966). In other words, the density of light itself was so high it gravitationally collapsed to form a BH. Primordial BHs have been invoked to explain the masses of BHs found by gravitational wave detectors (Bird et al. 2016). Primordial BHs have also been a long-time dark matter candidate; although most mass ranges of have been ruled out as making up a significant fraction of dark matter, several windows remain open and constraints are often revisited (Carr and Kühnel 2020).

1.1.2 Expectations of the Galactic stellar-mass black hole population

Our lack of understanding of the formation of BHs is directly related to the lack of BH observations. The number of BHs in our own Galaxy is uncertain to orders of magnitude; most estimates suggest $10^7 - 10^9$ (Agol, Kamionkowski, et al. 2002; Samland 1998; Sartore et al. 2010; Timmes et al. 1996). There are different methods using different observational probes to infer this number; here, we consider a back-of-the-envelope estimate presented in Shapiro et al. (1983). The Salpeter initial mass function (IMF)

$$\xi(M) = \xi_0 \left(\frac{M}{M_\odot}\right)^{-2.35} \tag{1.1}$$

describes the number of stars per (linear) mass M bin formed per volume per time; ξ_0 is a normalization constant. By assuming a constant star formation rate and assuming BHs form from stars with initial masses M_1 to M_2, the number of BHs in the Milky Way is

$$\begin{aligned} N_{BH} &= V_{MW} T_{MW} \int_{M_1/M_\odot}^{M_2/M_\odot} \xi(M) d\left(\frac{M}{M_\odot}\right) \\ &= V_{MW} T_{MW} \xi_0 \int_{M_1/M_\odot}^{M_2/M_\odot} \left(\frac{M}{M_\odot}\right)^{-2.35} d\left(\frac{M}{M_\odot}\right) \\ &= -\frac{1}{1.35} V_{MW} T_{MW} \xi_0 \left(\frac{M}{M_\odot}\right)^{-1.35} \Bigg|_{M_1/M_\odot}^{M_2/M_\odot} \end{aligned} \tag{1.2}$$

where V_{MW} and T_{MW} are the volume and age of the Milky Way. Taking $V_{MW} = 200$ kpc^3, $T_{MW} = 13.6 \times 10^9$ yr, $\xi_0 = 2 \times 10^{-3}$ star kpc^{-3} yr^{-1}, and assuming $M_1 = 25 M_\odot$, $M_2 = 120 M_\odot$ for BHs, this gives $N_{BH} \sim 5 \times 10^7$.

BHs can exist in binary systems, or be isolated and free-floating without a companion. The majority of BHs are expected to be isolated, although massive stars are typically born in binaries. This counterintuitive claim can be argued from several considerations. Around $20-30\%$ of O-stars are expected to merge with their companion (Sana et al. 2012). Of those that initially remain in binary systems, the majority are expected to be disrupted during the formation of the BH and/or NS. This can be due to sudden and/or significant mass loss that disrupts the binary system (Blaauw 1961), anisotropic neutrino emission (for a review, see Janka 2012), or asymmetric mass loss during the supernova explosion (Janka 2013).

1.1.3 The Galactic black hole census

The existence of BHs was observationally established in the 1970s with the discovery of the BH X-ray binary Cygnus X-1 (Bolton 1972; Webster et al. 1972). In an X-ray binary, the BH accretes material from a close stellar companion; this accretion produces an X-ray transient that signals the presence of the BH. For nearly a half century, this was the only method by which stellar-mass BHs were detected.

It was suggested that compact objects could be hiding in single-lined spectroscopic binaries. The invisible BH would induce a wobbling motion on the visible star it orbited, allowing the BH's presence to be inferred. The first searches of this kind were attempted in the late 1960s by Zeldovich et al. (1966) and Trimble et al. (1969), but it was the advent of large spectroscopic (e.g., the Sloan Digital Sky Survey) and astrometric surveys (e.g., *Gaia*) nearly a half-century later that finally enabled these searches to come to fruition. To date, the masses of three BHs in detached binaries in the Milky Way have been measured (El-Badry, Rix, Cendes, et al. 2023; El-Badry, Rix, Quataert, et al. 2023; Chakrabarti et al. 2022; Thompson et al. 2019).

In total, there are now about two dozen Galactic BHs in binary systems with mass measurements, and many more candidates that have yet to be dynamically confirmed. Attempts to do statistics on the masses of BHs in X-ray binaries began with Bailyn et al. (1998) using just 7 systems, and was later updated by Farr et al. (2011) and Özel, Psaltis, et al. (2010) using $15-16$ systems. These works suggested that most BHs in the Galaxy are around $8M_\odot$, and that there was a "lower mass gap" between the most massive NSs ($\sim 2M_\odot$) and least massive BHs ($\sim 5M_\odot$). However, it has been called into question whether the BH X-ray binaries with mass measurements are a representative sample, due to a bias in the types of systems that are followed up that could preferentially lead to more lower-mass systems having mass measurements (Jonker et al. 2021). However, there is an even more glaring bias in trying to draw conclusions about BHs from this small subset: all the mass measurements are of systems in (X-ray) binaries. X-ray binaries are expected to comprise only a fraction of a percent the Galactic BH population; BHs in detached binaries are expected to contribute a few percent, and the remainder of BHs are isolated (Figure 1.1).

Thus, although isolated BHs are expected to be the most numerous types of BHs in the Galaxy, they are the hardest to find because they have no companion to interact with in order to produce an electromagnetic signal. However, without detecting and characterizing them,

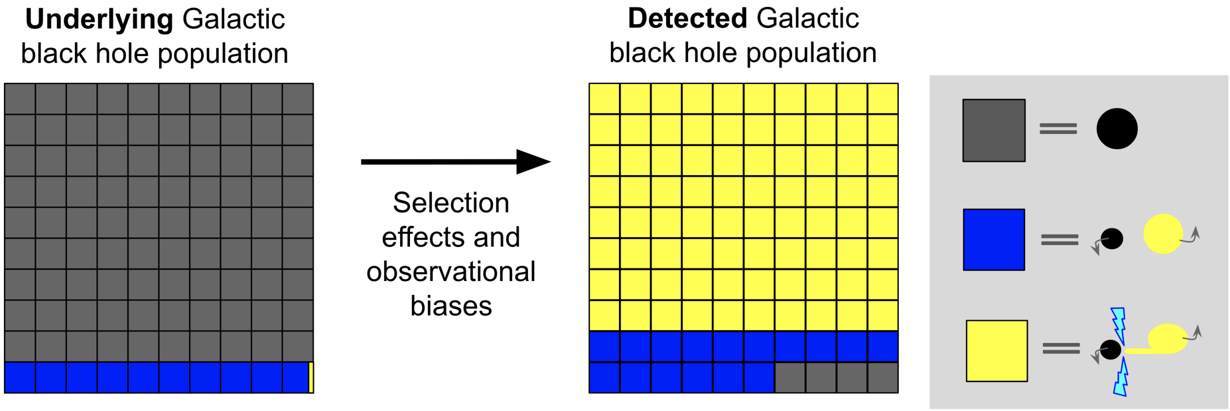

Figure 1.1: Detected Galactic BHs are not a representative sample of the underlying astrophysical population. The colored boxes represent the fractional contribution of each type of BH system to the underlying or detected population (gray = isolated, blue = wide non-interacting binary, yellow = X-ray binary). To infer the underlying population from the detected population requires quantifying the selection effects and observational biases of the detected sample.

we cannot understand the full Galactic BH population, and in turn, questions about BHs, their formation, and their effect on the Galaxy will remain unanswered. What is needed is a search technique that only depends on the mass, and not the luminosity, of the object being probed. This requirement makes gravitational lensing the ideal way to find these elusive isolated BHs.

1.2 Gravitational microlensing

1.2.1 The gravitational lens equation

According to general relativity, the deflection angle of light by a mass M with impact parameter b is

$$\alpha = \frac{4GM}{bc^2}, \tag{1.3}$$

where G is the gravitational constant, and c is the speed of light. Note that this deflection is larger by a factor of 2 than what Newtonian classical mechanics might suggest the answer to be.[1]

Suppose there is a massive object (i.e. a gravitational lens) an angular diameter distance D_L away along an observer's line of sight, and a background source of light an angular diameter distance D_S away and angular separation θ_S along the lens-observer line. The lens

---

[1] "After years of hard labor and low pay, you get... 4." –Eugene Chiang

and source are separated an angular diameter distance D_{LS} apart. The impact parameter between the light ray and the lens is b. Due to the deflection of the gravitational lens, where does the background source of light appear on the sky to the observer (i.e. the lensed image)?

Figure 1.2 sketches the geometry of the problem. The light from the background source is deflected by angle α (Equation 1.3) in the lens plane, and the lensed image is at an angular separation θ from the lens-observer line. The angular diameter distance between the background source of light and the lensed image in the source plane is h. The angular diameter distance between the lens and source along the observer-lens line is D_{LS}. The lens is assumed to be a point mass, which is valid for lenses whose size r_L is small relative to the distance scales in the problem $r_L \ll D_L, D_S, D_{LS}$.

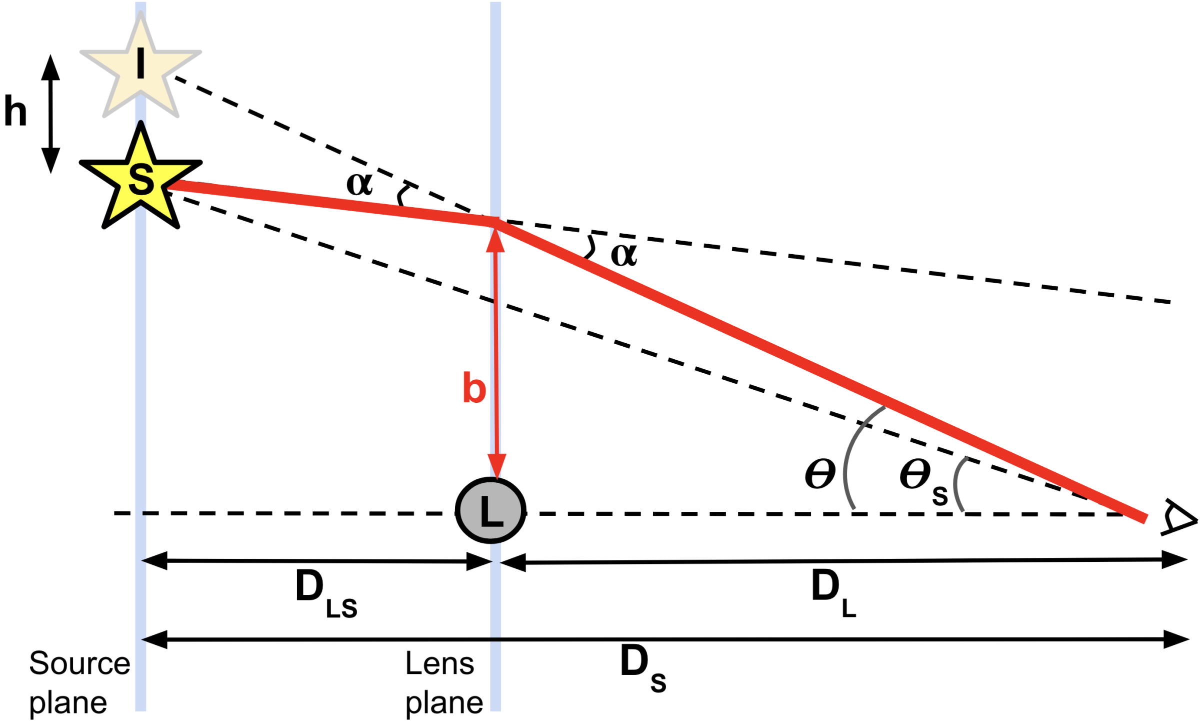

Figure 1.2: Gravitational lensing geometry. The solid yellow star (labeled S) is the background source of light. The light from this star is deflected by a lens of mass M (gray circle labeled L) on its way to the observer; the path of the light is traced by the solid red line; it is deflected by an angle α. The transparent yellow star (labeled I) is the location of the image of the star. h is the distance between the source and the image. b is the impact parameter between the light ray and the lens. θ_S and θ are angular positions of the source and image, respectively. D_L, D_S, and and D_{LS} are the observer-lens, observer-source, and source-lens distances, respectively. The source and lens plane are shown in the light blue vertical lines.

We are working in the small angle regime, so all angles α, θ_S, $\theta \ll 1$. By using the small angle assumption, the following three relations relating ratios of distances to various angles can be obtained from Figure 1.2:

$$b = D_L\theta \tag{1.4}$$

$$h = \alpha D_{LS} \tag{1.5}$$

$$h = (\theta - \theta_S)D_S. \tag{1.6}$$

Define the *Einstein radius*

$$\theta_E = \sqrt{\frac{4GM}{c^2}\frac{1}{D}}, \tag{1.7}$$

where D is defined as

$$D = \frac{D_L D_S}{D_{LS}}. \tag{1.8}$$

Combining Equations 1.3 – 1.6 and substituting the definition of the Einstein radius (Equation 1.7) yields the *lens equation*

$$\theta^2 - \theta\theta_S - \theta_E^2 = 0. \tag{1.9}$$

Solving the lens equation for the position of the image θ using the quadratic formula yields

$$\theta = \frac{\theta_S \pm \sqrt{\theta_S^2 + 4\theta_E^2}}{2}. \tag{1.10}$$

First, consider where the images θ are located for the following three values of θ_S:

1. $\theta_S = 0 \implies \theta = \theta_E$. This corresponds to the case where there is a perfect alignment of the source, lens, and observer. Instead of two separate images, a single image of a ring of angular radius θ_E is produced.

2. $\theta_S \ll \theta_E \implies \theta \approx \frac{\theta_S}{2} \pm \theta_E$. This corresponds to the case where the source is slightly off from being perfectly aligned with the lens-observer line of sight. In this case, two images are produced, one outside the Einstein radius ($\frac{\theta_S}{2} + \theta_E$), and one inside the Einstein radius ($\frac{\theta_S}{2} - \theta_E$).

3. $\theta_S \gg \theta_E \implies \theta \approx 0, \theta_S$. This corresponds to the source being a very large angular separation away from the lens-observer line of sight. The light from the source is barely deflected at all. The observer therefore only sees the unlensed source, as expected.

Next, consider the setup illustrated in the left panel of Figure 1.3: four identical background sources (*colored dots*) are being lensed by some foreground mass (*black dot*). The Einstein radius is outline in the *dashed circle*. Although the sources are the same physical distance behind the lens, they are located at different angular positions, so their lensed images will lie in different places. The images of the different sources (middle panel of Figure 1.3, *thick outline*) are color-coded the same as their respective source. There is always one image inside the Einstein ring, and always one image outside, as can be seen from Equation

1.10. Here we label the images outside the Einstein ring the "1" images, and the ones inside the Einstein ring "2". By connecting the dots on the sources to form an arc (e.g., red to orange to green to blue back to red, right panel of Figure 1.3), and repeating for the two images in the same manner, the orientation of the images can be seen. For the Sources, the orientation is counterclockwise. For Images 1, the orientation is also counterclockwise. However, for Images 2, the orientation is counterclockwise—it is inverted with respect to the Sources.

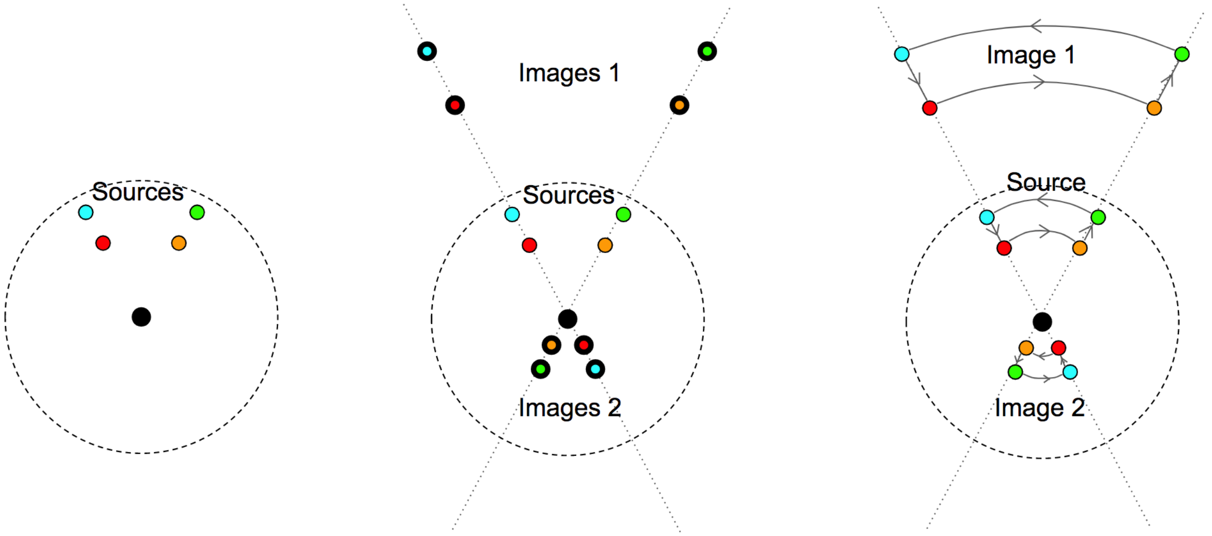

Figure 1.3: Exploring the orientation of lensed images with respect to the source. *Left panel*: four identical sources (*colored points*) that will be lensed by a foreground lens (*black point*). *Middle panel*: the images of the sources (*black outlined colored points*), color-coded by their corresponding source. Images outside the Einstein radius are labeled "1" and images inside the Einstein radius are labeled "2". *Right panel*: Connecting the set of sources to illustrate their orientation. The lensed images outside the Einstein radius ("1") have the same orientation as the source. However, the lensed images inside the Einstein radius ("2") are oriented in thee opposite direction as the source.

So far, we have assumed that the source is a point of light. However, physical sources of light, like stars, are not infinitely small, but rather subtend a finite area on the sky. To understand how such a physical finite source would be lensed, imagine dividing up a disk of light into a grid of much smaller sources. By making the grid sufficiently small, each grid cell can be regarded as a single point of light. Based on an argument about the continuity of the source to image mapping, each individual grid cell can be treated as a single point source, and the superposition of the lensed images of the individual grid cells is equivalent to the lensed images of the finite source. Thus, one can plausibly imagine that if the arc-shaped source labeled “Source” was lensed, it would produce two image arcs, like those labeled “Image 1” and “Image 2” in the right panel of Figure 1.3.

Consider such a situation now, as illustrated in Figure 1.4. The source is at an angular separation $\vec{\theta_S}$ from the lens, and Image 1 and 2 are angular separations $\vec{\theta_1}$ and $\vec{\theta_2}$ from the lens, respectively. The thickness of the Source arc is $d\theta_S$, and the thicknesses of Image 1 and 2 arcs are $d\theta_1$ and $d\theta_2$, respectively. The ratio of the area of Image 1 to the area of Source A_1 is

$$A_1 = \frac{\theta_1 \, d\theta_1}{\theta_S \, d\theta_S} \tag{1.11}$$

and the ratio of the area of Image 2 to the area of Source A_2 is

$$A_2 = \frac{\theta_2 \, d\theta_2}{\theta_S \, d\theta_S}. \tag{1.12}$$

Surface brightness is conserved in gravitational lensing. In other words, the brightness per area of the images is the same as that of the source. This is known as Louiville’s Theorem. Suppose a little square of the source dA has brightness B. Then a little square of the same area dA from one of the lensed images would also have the same brightness B.[2] However, the total area of the lensed images are different than the total area of the source, so the *total* brightness will be different. In other words, the ratio of the image to source area A_1 and A_2 are the magnifications of the images. As a final note, the proper mathematical way these magnifications are derived is by calculating the inverse of the determinant of the Jacobian of the lens mapping, but derivation by picture gives us the same answer.

Define the dimensionless source position $u \equiv \frac{\theta_S}{\theta_E}$. The magnification factors A_1 and A_2 from Equations 1.11 and 1.12 can be written in terms of u. Dividing θ (Equation 1.10) by θ_S yields

$$\begin{aligned} \frac{\theta_{1,2}}{\theta_S} &= \frac{1}{2}\left(1 \pm \sqrt{1 + 4\frac{\theta_E}{\theta_S}^2}\right) \\ &= \frac{1}{2}\left(1 \pm \frac{\sqrt{u^2+4}}{u}\right). \end{aligned} \tag{1.13}$$

---

[2] One way to understand this is when you look at something through a magnifying glass, the object does not change its brightness.

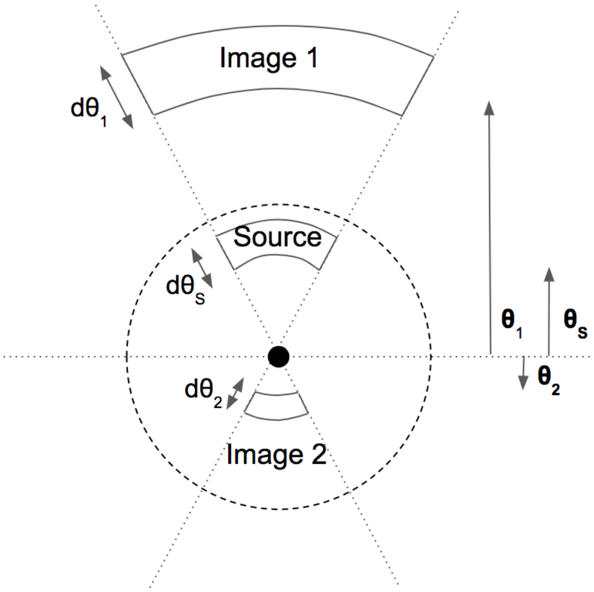

Figure 1.4: Geometry illustrating an arc-shaped source lensed into two arc-shaped images.

Differentiating θ (Equation 1.10) with respect to θ_S yields

$$\begin{aligned}\frac{d\theta_{1,2}}{d\theta_S} &= \frac{1}{2}\left(1 \pm \frac{1}{2}(\theta_S^2 + 4\theta_E^2)^{-1/2} \cdot 2\theta_S\right) \\ &= \frac{1}{2}\left(1 \pm \frac{\theta_S}{\sqrt{\theta_S^2 + 4\theta_E^2}}\right) \\ &= \frac{1}{2}\left(1 \pm \frac{u}{\sqrt{u^2+4}}\right).\end{aligned} \tag{1.14}$$

Putting Equations 1.13 and 1.14 together, we can compute $A_{1,2}$:

$$\begin{aligned}
A_{1,2} &= \frac{\theta_{1,2}}{\theta_S}\frac{d\theta_{1,2}}{d\theta_S} \\
&= \frac{1}{2}\left(1 \pm \frac{\sqrt{u^2+4}}{u}\right)\cdot\frac{1}{2}\left(1 \pm \frac{u}{\sqrt{u^2+4}}\right) \\
&= \frac{1}{4}\left(1 \pm \frac{u}{\sqrt{u^2+4}} \pm \frac{\sqrt{u^2+4}}{u} + 1\right) \\
&= \frac{1}{4}\left(2 \pm \frac{2u^2+4}{u\sqrt{u^2+4}}\right) \\
&= \frac{1}{2}\left(1 \pm \frac{u^2+2}{u\sqrt{u^2+4}}\right).
\end{aligned} \tag{1.15}$$

As is the convention in optics[3], $|A| > 1$ is magnification and $|A| < 1$ is demagnification; $A > 0$ is an image "right side up" and $A < 0$ is an inverted image.

Figure 1.5 shows the quantity $\frac{u^2+2}{u\sqrt{u^2+4}}$ vs. u. For $u > 0$, $\frac{u^2+2}{u\sqrt{u^2+4}} > 1$ and for $u < 0$, $\frac{u^2+2}{u\sqrt{u^2+4}} < -1$. Hence for $u > 0$, $A_1 > 1$ and $A_2 < 0$, while for $u < 0$, $A_1 < 0$ and $A_2 > 1$. Thus, the signs of A_1 and A_2 are always opposite each other. In other words, one image is "right side up" and the other is inverted, as we showed earlier. The "right side up" image is always magnified, and the inverted image can be either magnified or demagnified.

We pause here to make three comments:

1. Gravitational lensing is a purely geometric effect, dependent on the position and velocity of the observer (see Figure 1.6). This dependence on the observer will be considered in detail in Chapter 6.

2. Although the source and images are simultaneously illustrated in Figures 1.2 – 1.4, the observer never sees the source itself, only the images.

3. Gravitational lensing is achromatic—the deflection angle α is not dependent on the wavelength of light. This leads to the phrase "there are no rainbows in gravitational lensing". However, there can be wavelength-dependent effects due to the observational setup, which will be described later in Chapter 1.2.2.

Finally, we note there are three different "regimes" of gravitational lensing.

- *Strong* gravitational lensing is the regime where the individual images or Einstein rings can be resolved. This is seen most spectacularly when a galaxy or galaxy cluster lenses another galaxy. More formally, strong lensing is the regime where both the convergence and shear are $\mathcal{O}(1)$ (see Schneider et al. 1992, for more details).

---

[3] Our lenses are stars and BHs instead of glass and mirrors!

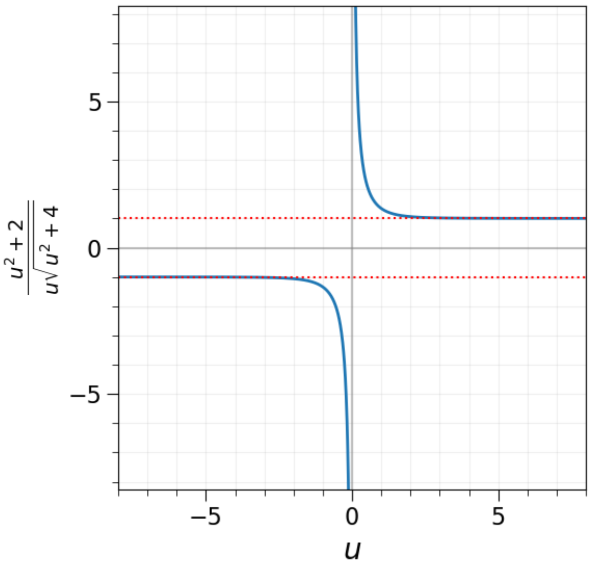

Figure 1.5: Illustrating the u dependence of the magnification factor. The red dashed lines illustrate the asymptotic values of -1 and 1.

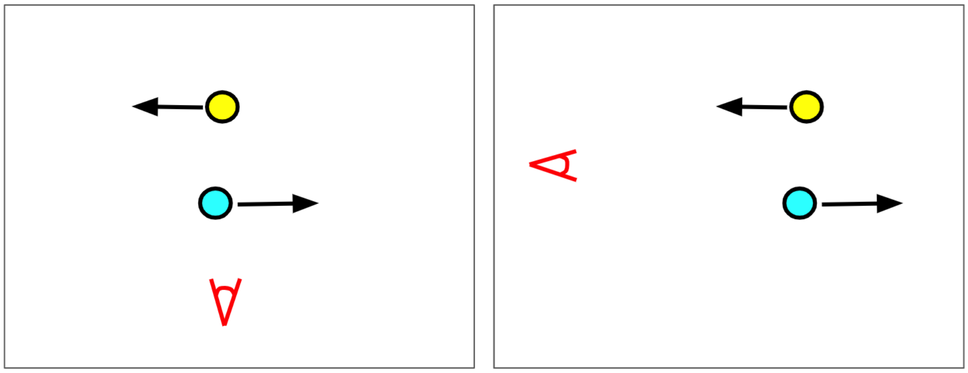

Figure 1.6: A schematic illustrating how gravitational lensing depends on the observer's perspective. The observer is shown in *red*. *Left*: From the observer's perspective, the lens *(blue)* passes in front of the source *(yellow)*. The observer would see a strong lensing event in this case. *Right*: Same geometry as before, but the observer is in a different position this time, and from this perspective, the blue object is not passing in front of the yellow object. In this case, the observer would not see a strong lensing event.

- *Weak* gravitational lensing occurs in the $\theta_S \gg \theta_E$ regime. Instead of multiple images, only a single image that looks like a minor stretching/squashing of the source is seen.

By assuming knowledge of the distribution of shapes of unlensed galaxies, the observed shapes of weakly lensed galaxies can be used to statistically study the distribution of intervening mass between the galaxies and observer. More formally, weak lensing is the regime where both the convergence and shear are $\ll 1$ (see Schneider et al. 1992, for more details).

- *Microlensing* is the limit of strong gravitational lensing, where the images or Einstein rings cannot be resolved. Microlensing can occur when a stellar-mass lens object bends the light of a background star in the Milky Way. Microlensing toward nearby galaxies like the Magellanic Clouds (Alcock, Akerlof, et al. 1993; Alcock, Allsman, Alves, Axelrod, Becker, Bennett, Cook, Freeman, Griest, Guern, et al. 1997; Alcock, Allsman, Alves, Axelrod, Becker, Bennett, Cook, Freeman, Griest, Keane, et al. 1997; Palanque-Delabrouille et al. 1998) and M31 (de Jong et al. 2004; Paulin-Henriksson et al. 2003; Uglesich et al. 2004) has also been observed.

Consider the mass and length scales that would occur in a "typical" Milky Way gravitational scenario: a Bulge star background source at 8 kpc, and a 0.5 $M_\odot$ Disk star lens at 4 kpc. In the Milky Way, where we do not have to consider redshift affecting our distance measures, the distance between lens and source D_{LS} is simply equal to $D_S - D_L$. This yields $\theta_E = 3.46 \times 10^{-9}\,\mathrm{rad} = 0.71\,\mathrm{mas}$. For comparison, assuming the diffraction limit is achievable on a 10-m class telescope (e.g., *Keck*), observing at K-band (2.2 micron) can still only resolve at a scale of $\sim 1.22\lambda/D = 55\,\mathrm{mas}$. This is why microlensing is the relevant regime of gravitational lensing for Milky Way distance and timescales when considering single telescopes[4]. For the remainder of this thesis, we stay in the Milky Way regime, and write the Einstein radius as

$$\theta_E = \sqrt{\frac{4GM}{c^2}\Big(\frac{1}{D_L} - \frac{1}{D_S}\Big)}. \tag{1.16}$$

There are two different flavors of microlensing—*photometric* microlensing and *astrometric* microlensing. Since the lensed images have a total area greater than the source and surface brightness is conserved, the net effect is the apparent brightening of the source; this is the photometric signal. In addition, the centroid ("center of light") of the lensed images (image*s*, because there are 2) changes as the lens and source move relative to each other, where the net effect is an apparent positional deflection of the source; this is the astrometric signal. We will now derive and explore these two signals in more detail.

1.2.2 Photometric microlensing

The total magnification is just the sum of the magnifications of the images. In this case, the parity of the image is irrelevant—an upside down image is the same brightness as its

---

[4] Interferometry is another story, which we do not consider here.

noninverted version. Equation 1.15 can be used to calculate the total magnification A:

$$\begin{aligned} A(u) &= |A_1| + |A_2| \\ &= \frac{u^2+2}{u\sqrt{u^2+4}}. \end{aligned} \tag{1.17}$$

Thus, as a star is lensed, because the unresolved images get larger and the surface brightness is conserved, the observer will see the star brighten.

The relative separation of the source and the lens changes as a function of time. Thus, the total magnification will also change as a function of time. This time dependence is given by

$$u(t) = \left[u_0^2 + \left(\frac{t-t_0}{t_E}\right)^2\right]^{1/2} \tag{1.18}$$

where u_0 is the minimum lens-source separation (i.e. the impact parameter), t_0 is the time of maximum magnification (which is the time at which $u = u_0$), and

$$t_E = \frac{\theta_E}{\mu_{rel}} \tag{1.19}$$

is the Einstein crossing time, where μ_{rel} is the relative proper motion of the source and lens.

A microlensing light curve is the magnification as a function of time, which can be determined by substituting $u(t)$ into $A(u)$ to get the light curve $A(t)$. Figure 1.7 illustrates a couple of lightcurves for varying values of u_0 and t_E.

We can also consider how the magnification scales in the regime of very close lens-source separation ($u \ll 1$) and very far lens-source separation ($u \gg 1$). In the limit $u \ll 1$:

$$\begin{aligned} A(u) &= \frac{u^2+2}{u\sqrt{u^2+4}} \\ &= \frac{u^2+2}{2u\sqrt{1+u^2/4}} \\ &= \frac{u^2+2}{2u}\left(1 - \frac{u^2}{8} + ...\right) \\ &= \frac{1}{u} + \frac{3u}{8} - ... \\ &\approx \frac{1}{u}. \end{aligned} \tag{1.20}$$

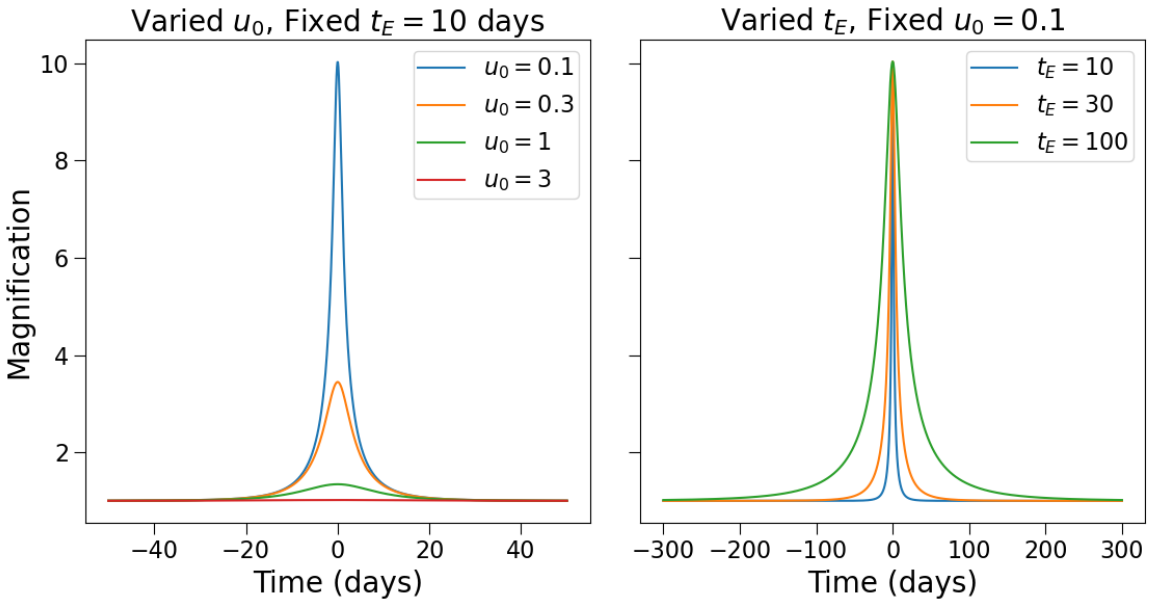

Figure 1.7: Microlensing lightcurves. The left panel shows how the magnification varies by changing the impact parameter u_0, while the right panel shows how the duration of the event varies by changing the Einstein crossing time t_E. Smaller impact parameters lead to higher maximum magnification, and longer Einstein crossing times lead to wider lightcurves. In both panels, $t_0 = 0$ days. Note the x-range in the two panels are different.

In the limit $u \gg 1$:

$$\begin{aligned} A(u) &= \frac{u^2+2}{u\sqrt{u^2+4}} \\ &= \frac{u^2+2}{u^2\sqrt{1+4/u^2}} \\ &= \frac{u^2+2}{u^2}\left(1 - \frac{2}{u^2} + \frac{6}{u^4} - \frac{20}{u^6} + ...\right) \\ &= 1 + \frac{2}{u^4} - \frac{8}{u^6} + ... \\ &\approx 1 + \frac{2}{u^4}. \end{aligned} \tag{1.21}$$

Thus, as the lens and source separate from each other, the magnification drops off extremely quickly.

One final effect that must be considered in photometric microlensing is called *blending*. Suppose the (unlensed) source has flux F_S. Any light in the aperture of the telescope unrelated to the source is called *blended* light, and suppose it contributes flux F_B. The blended light can come from the lens itself, or from stars completely unrelated to the lensing event that just happen to fall in the aperture of the telescope. This blended light is not lensed, so the observed flux as a function of time $F(t)$ during the microlnsing event will be

$$F(t) = A(t)F_S + F_B. \tag{1.22}$$

The effect of blending on the observed lightcurve is illustrated in Figure 1.8.

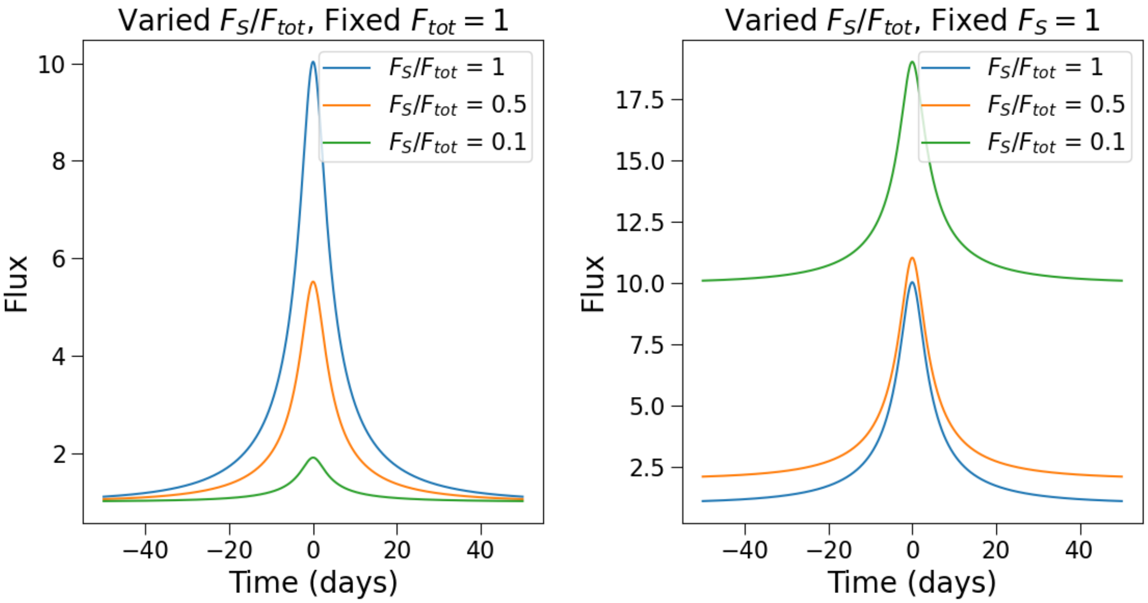

Figure 1.8: Blended microlensing lightcurves. All lightcurves have $t_E = 30$ days, $u = 0.1$, and $t_0 = 0$ days. The left panel shows how the flux varies over time by changing the ratio of source flux F_S to total flux $F_{tot} = F_S + F_B$, while keeping the total flux fixed. The right panel shows the same, but for source flux fixed. Note the y-range in the two panels are different.

1.2.3 Astrometric microlensing

Analogous to the center of mass of two objects, we can calculate a center of light of the two lensed images. The position of the center of light, or centroid $\vec{\theta}_c$, is equal to

$$\vec{\theta}_c = \frac{|A_1|\vec{\theta}_1 + |A_2|\vec{\theta}_2}{|A_1| + |A_2|}. \tag{1.23}$$

The difference between the position of the centroid of the lensed images with respect to the source, the astrometric shift $\vec{\delta}_c$, is equal to

$$\vec{\delta}_c = \vec{\theta}_c - \vec{\theta}_S. \tag{1.24}$$

As with the photometric magnification, we can calculate the magnitude of the astrometric shift in terms of the dimensionless source position $u \equiv \frac{\theta_S}{\theta_E}$.

First, the position of the centroid is a vector quantity. Things are easily simplified because $\vec{\theta}_S \parallel \vec{\theta}_1$ and $\vec{\theta}_S \parallel -\vec{\theta}_2$:

$$\begin{aligned}\vec{\delta}_c &= \frac{|A_1|\vec{\theta}_1 + |A_2|\vec{\theta}_2}{|A_1| + |A_2|} \\ &= \left(\frac{|A_1|\theta_1 - |A_2|\theta_2}{|A_1| + |A_2|} - \theta_S\right)\hat{\theta}_S.\end{aligned} \tag{1.25}$$

From the derivation of the magnification, an expression for A_1 and A_2 is given from Equation 1.15. With some rearranging of Equation 1.13, an expression for θ_1 and θ_2 in terms of u and θ_E can be obtained:

$$\theta_{1,2} = \frac{\theta_E}{2}(u \pm \sqrt{u^2+4}). \tag{1.26}$$

To calculate an expression for $|A_1|\theta_1 - |A_2|\theta_2$, note that it is of the form

$$(A+B)(C+D)E - (A-B)(C-D)E = 2E(AD+BC),$$

where $A = 1$, $B = \frac{u^2+2}{u\sqrt{u^2+4}}$, $C = u$, $D = \sqrt{u^2+4}$, $E = \frac{\theta_E}{4}$. Hence,

$$\begin{aligned}|A_1|\theta_1 - |A_2|\theta_2 &= \frac{\theta_E}{2}\left(\sqrt{u^2+4} + \frac{u^2+2}{\sqrt{u^2+4}}\right) \\ &= \frac{u^2+3}{\sqrt{u^2+4}}\theta_E.\end{aligned} \tag{1.27}$$

$|A_1| + |A_2| = \frac{u^2+2}{u\sqrt{u^2+4}}$ was derived in Equation 1.15. Combined with the definition of u rearranged as $\theta_S = u\theta_E$, $\vec{\delta}_c$ is equal to

$$\begin{aligned}\vec{\delta}_c(u, \theta_E) &= \left(\frac{\frac{\theta_E(u^2+3)}{\sqrt{u^2+4}}}{\frac{u^2+2}{u\sqrt{u^2+4}}} - u\theta_E\right)\hat{\theta}_S \\ &= \left(\frac{u}{u^2+2}\theta_E\right)\hat{\theta}_S.\end{aligned} \tag{1.28}$$

We can consider how the magnitude of the astrometric shift scales in the regime of very close lens-source separation ($u \ll 1$) and very far lens-source separation ($u \gg 1$). In the limit $u \ll 1$:

$$\begin{aligned} \delta(u) &= \frac{u}{u^2+2}\theta_E \\ &= \frac{u}{2(1+u^2/2)}\theta_E \\ &\approx \frac{u}{2}\Big(1-\frac{u^2}{2}\Big)\theta_E \\ &\approx \frac{u}{2}\theta_E \end{aligned} \tag{1.29}$$

In the limit $u \gg 1$:

$$\begin{aligned} \delta(u) &= \frac{u}{u^2+2}\theta_E \\ &= \frac{u}{u^2(1+2/u^2)}\theta_E \\ &\approx \frac{1}{u}\Big(1-\frac{2}{u^2}\Big)\theta_E \\ &\approx \frac{1}{u}\theta_E \end{aligned} \tag{1.30}$$

Note how the astrometric signal decays slowly as u^{-1}, in contrast to the photometric signal, which decays rapidly as u^{-4} for $u \gg 1$.

The $u = u_{max}$ where $d\delta_c(u_{max})/du = 0$ and $d^2\delta_c(u_{max})/du^2 < 0$ corresponds to the source-lens separation of the maximum astrometric shift. A quick calculation shows $u_{max} = \sqrt{2}$, and thus the magnitude of the maximum astrometric shift is $\delta_{c,max} = \theta_E/\sqrt{8}$. This is in contrast to the photometric magnification A, since as $u \to 0^+$, $A \to \infty$: the maximum magnification will always occur at the closest source-lens separation, which is by definition the impact parameter u_0. Figure 1.9 shows the magnitude of the astrometric shift normalized to the Einstein radius $\delta_c/\theta_E = \frac{u}{u^2+2}$ as a function of time, for several different values of u_0.

We pause here to make two comments:

1. If $u_0 < \sqrt{2}$, then the maximum astrometric shift does not temporally coincide with the maximum photometric amplification: it will be maximized before and after.
2. The photometric magnification A is solely a function of u. On the other hand, the astrometric shift $\vec{\delta_c}$ has dependence on not only u, but θ_E.

These two facts are crucial in using microlensing to find isolated BHs (Chapter 1.3).

1.2.4 Acceleration and microlensing parallax

Thus far, microlensing lightcurves and the magnitude of the astrometric shift are completely symmetric in time, as it is assumed the observer is in an inertial, or rectilinear, reference frame with respect to the lens and source. However, for Earthly observers this assumption is invalid

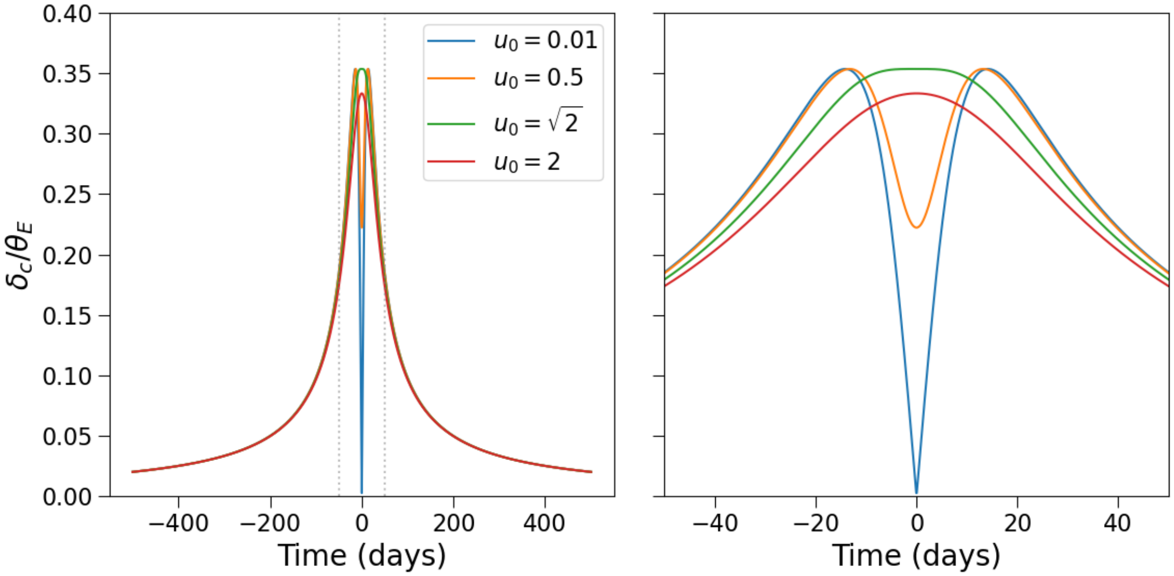

Figure 1.9: Astrometric shift. The *right* panel is a zoomed-in version of the *left* panel (gray dashed lines), to see the region where the astrometric shift is changing most rapidly. Note the very slow fall-off with time (in contrast to the photometric microlensing signal).

as Earth orbits around the Sun, rendering Earth a non-rectilinear reference frame. The effect Earth's orbit imparts on observations of microlensing is called *annual microlensing parallax*. Note that there are other types of microlensing parallax (e.g., terrestrial, satellite) due to other kinds of perspective differences. In this thesis we only consider annual microlensing parallax due to Earth's orbital motion around the Sun.

The *microlensing parallax* is a dimensionless quantity defined as the relative parallax of the lens and source $\pi_{rel} = \mathrm{AU}(D_L^{-1} - D_S^{-1})$ normalized by the Einstein radius θ_E,

$$\pi_E = \frac{\pi_{rel}}{\theta_E}. \tag{1.31}$$

The *microlensing parallax vector* is a vector defined to have the same magnitude as π_E, in the direction of the source-lens relative proper motion,

$$\vec{\pi}_E = \pi_E \hat{\mu}_{rel}. \tag{1.32}$$

The direction of the relative proper motion with respect to the ecliptic plane determines the effect on the lightcurve. The component of relative proper motion parallel to the ecliptic plane manifests as an asymmetry in the lightcurve about the time of maximum brightness. The component of relative proper motion perpendicular to the ecliptic plane manifests as a symmetric change in the lightcurve about the time of maximum brightness. Figure 1.10 shows two examples of lightcurves with parallax signals.

A more in-depth discussion of microlensing parallax is presented in Chapter 6.

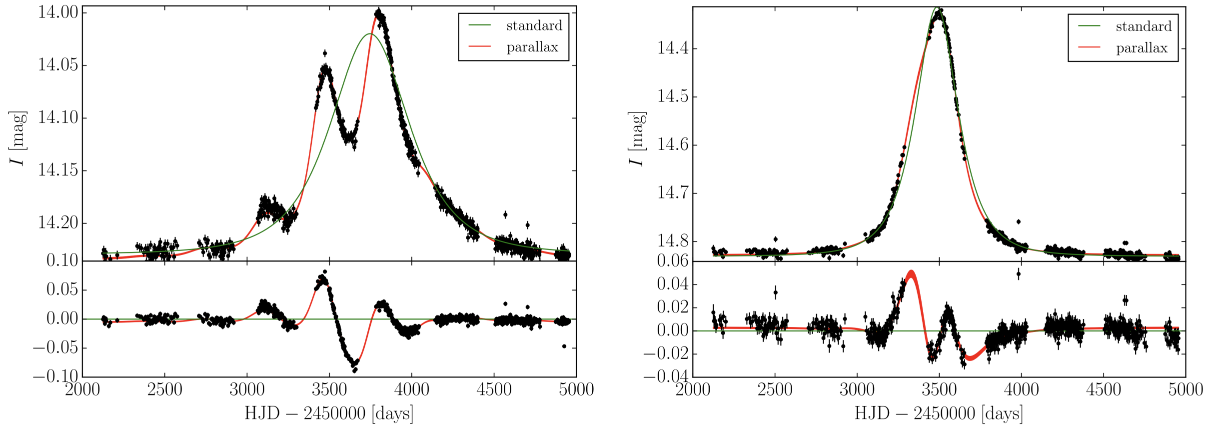

Figure 1.10: Two examples of microlensing parallax in observed lightcurves. The top panels show data from the OGLE microlensing survey (*black points*), along with the best-fit model neglecting microlensing parallax (*green line*) and the best-fit model including microlensing parallax (*red line*). The bottom panel shows the residuals to the fits. The lightcurve on the left is an extreme example of microlensing parallax inducing multiple "wiggles" into the light curve, and is likely due to a very nearby lens. The lightcurve on the right is a much more typical example of microlensing parallax, which shows just a mild asymmetry in the lightcurve. *The plots above are reproduced from Figures 6 and 10 of "Black hole, neutron star and white dwarf candidates from microlensing with OGLE-III" by Wyrzykowski et al. published in Monthly Notices of the Royal Astronomical Society, Volume 458, Issue 3 (Wyrzykowski, Kostrzewa-Rutkowska, et al. 2016).*

1.2.5 Photometric microlensing surveys

Photometric microlensing surveys were initially conceived as a method to detect the dark matter candidate MAssive Compact Halo Objects (MACHOs) in the Galactic Halo (Paczynski 1986b), but their utility to also detect stars and exoplanets toward the Galactic Bulge was quickly realized (Mao and Paczynski 1991; Paczynski 1991). Given the mass and velocity distribution of objects along the line of sight to the Bulge, only about one in a million stars will be lensed. However, by monitoring billions of stars, many events should be seen. In addition, a typical microlensing event toward the Bulge has a duration of $t_E \sim 20$ days, so they are transient events; thus, the sky must be constantly monitored.

As a historical note, it was fortunate that at the time these ideas were proposed, the confluence of detector technology and computing power became available to implement the first modern time domain survey. Thirty years later, time domain and transient astronomy is a large and significant subfield of astrophysics, with many upcoming surveys and projects both big and small, spanning a variety of astrophysical phenomenon and science cases; microlensing was where it all started.

At present, there are several different ground-based microlensing surveys: Microlensing Observations for Astrophysics (MOA), Optical Gravitational Microlensing Experiment (OGLE), and KMTNet (Korean Microlensing Telescope Network). These surveys are dedicated to continuously observing the Galactic Bulge and detect roughly one to two thousand photometric microlensing events each year. These surveys publish public alert streams online of possible ongoing microlensing events.

1.3 Finding black holes with microlensing

If BHs contribute $\sim 0.1\%$ to the number of the Galaxy's possible lenses, they should comprise roughly $\sim 1\%$ of microlensing events seen in photometric surveys of the Galactic Bulge; since the lensing cross sectional area is proportional to the lens mass $\theta_E^2 \propto M$, massive objects are more likely to be microlenses. In addition, since the Einstein crossing time is proportional to the square root of the lens mass $t_E \propto \sqrt{M}$, longer duration microlensing events are more likely to be BHs, which are on average much more massive than stellar lenses.

Several notable BH candidates have been identified by virtue of having very long $t_E >$ 300 days (MACHO-96-BLG-5, MACHO-98-BLG-6, MACHO-99-BLG-22/OGLE-1999-BUL-32; Bennett, Becker, et al. 2002; Mao, Smith, et al. 2002). However, these events remain BH *candidates* because photometric microlensing cannot disentangle the lens mass from the relative source-lens proper motion. One way to see this is by rewriting the definition of the Einstein radius (Equation 1.16) in the form

$$M = \frac{\theta_E}{\kappa \pi_E} \tag{1.33}$$

where $\kappa = 4G/(1\text{AU} \cdot c^2) = 8.144\,\text{mas}/M_\odot$ is a constant. Photometric microlensing cannot provide a measure of θ_E,[5] as the observables (t_E, Equation 1.19 and π_E, Equation 1.31)) are normalized by θ_E. This is because the photometric amplification A (Equation 1.17) is expressed solely in terms of u, the dimensionless impact parameter.

Astrometric microlensing is needed to break this fundamental photometric degeneracy (Miyamoto et al. 1995). As can be seen in Equation 1.28, the astrometric shift provides a way to directly measure θ_E, and in turn, lens masses. Howver, unlike photometric microlensing, it is presently not possible to perform a blind astrometric microlensing survey of the Galactic Bulge. As calculated in Chapter 1.2.1, typically $\theta_E \lesssim 1$ mas in the Milky Way. Only two[6] specialized facilities can achieve ~ 0.3 mas astrometric precision in the optical-infrared in crowded regimes: the Hubble Space Telescope (*HST*), and the *Keck* telescopes equipped with laser guide star adaptive optics. Thus, astrometry cannot be obtained for all photometric microlensing events.

---

[5] This can be possible in very special cases, such as where finite source effects are detected, or with optical interferometry; we do not consider those here.

[6] In addition, *JWST* (launched in the final days of 2021) has been demonstrated to have excellent astrometric precision (Libralato et al. 2023).

However, not all hope is lost for using astrometric microlensing to measure BH masses. Because the astrometric signal is maximized both before and after the photometric signal, it is possible to search through photometric microlensing alerts, estimate which are the longest duration (and thus the best BH candidates), and then subsequently perform astrometric follow-up measurements of those candidates with *HST* or *Keck* (Lu et al. 2016). By understanding the candidate selection function as well as the selection effects of microlensing, a sample of BHs can be built up, and used to infer the number and velocity of isolated Galactic BHs.

1.4 Thesis outline

The rest of this thesis is outlined as follows. Chapter 2 presents the development of a new compact object population synthesis and microlensing code called `PopSyCLE`, and describes an improved way to identify BH candidates via photometric microlensing. Chapter 3 presents the analysis of five archival BH candidates, the identification of the first dark compact object detected with astrometric microlensing, and observational constraints on the Galactic BH population. Chapter 4 presents an updated re-analysis of OGLE-2011-BLG-0462/MOA-2011-BLG-191, the disputed isolated BH candidate. Chapter 5 presents a series of examples and methods related to modeling microlensing lightcurves. Chapter 6 presents formulae and examples for converting between several different microlensing reference frame conventions. Chapter 7 presents conclusions and future directions.

Chapter 2

PopSyCLE: A New Population Synthesis Code for Compact Object Microlensing Events

A version of this chapter was originally published in the Astrophysical Journal, Volume 889, Issue 1 (2020), and was co-authored with Jessica R. Lu, Matthew W. Hosek Jr., William A. Dawson, and Nathan R. Golovich.

We present a new Milky Way microlensing simulation code, dubbed `PopSyCLE` (Population Synthesis for Compact object Lensing Events). `PopSyCLE` is the first resolved microlensing simulation to include a compact object distribution derived from numerical supernovae explosion models and both astrometric and photometric microlensing effects. We demonstrate the capabilities of `PopSyCLE` by investigating the optimal way to find black holes (BHs) with microlensing. Candidate BHs have typically been selected from wide-field photometric microlensing surveys, such as OGLE, by selecting events with long Einstein crossing times ($t_E > 120$ days). These events can be selected at closest approach and monitored astrometrically in order to constrain the mass of each lens; `PopSyCLE` predicts a BH detection rate of $\sim$40% for such a program. We find that the detection rate can be enhanced to $\sim 85\%$ by selecting events with both $t_E > 120$ days and a microlensing parallax of $\pi_E < 0.08$. Unfortunately, such a selection criterion cannot be applied during the event as π_E requires both pre- and post-peak photometry. However, historical microlensing events from photometric surveys can be revisited using this new selection criteria in order to statistically constrain the abundance of BHs in the Milky Way. The future *WFIRST* microlensing survey provides both precise photometry and astrometry and will yield individual masses of $\mathcal{O}(100 - 1000)$ black holes, which is at least an order of magnitude more than is possible with individual candidate follow-up with current facilities. The resulting sample of BH masses from *WFIRST* will begin to constrain the shape of the black hole present-day mass function, BH multiplicity, and BH kick velocity distributions.

2.1 Introduction

The Milky Way is predicted to contain 10^8-10^9 stellar mass black holes (Agol, Kamionkowski, et al. 2002); however, the exact number is still very uncertain. Only a few dozen black holes (BHs) have been detected to date in X-ray binaries or BH-BH mergers (Abbott, Abbott, Abbott, Abernathy, et al. 2016; Remillard et al. 2006); no *isolated* stellar mass BHs have yet been definitively and unambiguously detected. Although BHs likely form after the death of a massive star, uncertainties in the final stages of massive star evolution have made quantitative predictions of BH masses and numbers difficult (Heger et al. 2003). Whether a massive star will form a BH, neutron star, or compact remnant at all is not only a function of the initial stellar mass, but other factors such as metallicity, stellar winds and the core structure at time of collapse. Additionally, it is still unknown whether BH binary systems form directly from stellar binaries, dynamically from two isolated BHs, or if there are multiple formation channels.

Detecting and characterizing a sample of isolated stellar mass BHs would provide insight into these unsolved problems by constraining the number of BHs in the Milky Way and the present-day mass function, binary fraction, and spatial and velocity distributions. This in turn will place constraints on stellar evolution models and improve understanding of supernova physics (Janka 2012). It would also allow better interpretation of recent LIGO results. For example, is the "mass gap" between the heaviest neutron stars and the lightest BHs real, or is it an artifact of the observational bias resulting from only having detected binary BHs (from an observational perspective, see Abbott, Abbott, Abbott, Abraham, Acernese, Ackley, Adams, Adhikari, Adya, Affeldt, Agathos, Agatsuma, Aggarwal, Aguiar, Aiello, Ain, Ajith, Allen, Allocca, Aloy, Altin, Amato, Ananyeva, et al. (2019), Farr et al. (2011), and Özel, Psaltis, et al. (2010); from a theoretical perspective, see Belczynski, Wiktorowicz, et al. (2012) and Fryer et al. (2012))?

Gravitational microlensing is a technique particularly well suited for detecting dark isolated objects in the Milky Way such as BHs, as properties of the lens can be inferred from changes in the source image, without having to directly observe the lens itself (Paczynski 1986b). For example, the MACHO (Alcock, Akerlof, et al. 1993), EROS (Aubourg et al. 1993), and OGLE (Udalski, Szymanski, Kaluzny, Kubiak, Mateo, et al. 1994) collaborations used gravitational microlensing to determine that the majority of dark matter in the Galactic halo is not due to ordinary baryonic matter (Alcock, Allsman, Alves, Axelrod, Becker, Bennett, Cook, Dalal, et al. 2000; Tisserand et al. 2007; Wyrzykowski, Skowron, et al. 2011). However, after the LIGO BH-BH merger detection, there has been a major resurgence in interest in BHs (and in particular primordial BHs) as a viable dark matter candidate (Bird et al. 2016; Sasaki et al. 2016). Additionally, for the past 15 years microlensing has been used to detect extrasolar planets; for a review see Gaudi (2012). Currently, microlensing is being used to search for isolated BHs by combining information from the photometric brightening and parallax signal and the astrometric shift of the source image to constrain the mass of the lens (Lu et al. 2016; Rybicki et al. 2018). As all current microlensing surveys are ground-based photometric surveys, a substantial development is space-based survey telescopes such as *Gaia* and *WFIRST*, which will provide astrometric measurements for microlensing events (Gaia Collaboration, Prusti, et al. 2016; Penny, Gaudi, et al. 2019; Rybicki et al. 2018; Spergel et al. 2015).

Previous theoretical work modeled microlensing in the Milky Way due to a population of stars, brown dwarfs, and stellar remnants (Han and Gould 2003; Wood et al. 2005). However, these models use a heavily simplified model for compact object population synthesis. Osłowski et al. (2008) investigated compact object lensing by using the `StarTrack` population code (Belczynski, Kalogera, et al. 2008) to generate isolated BHs and neutron stars via two different formation channels. However, in all these models a realistic extinction map, which varies significantly across the sky and affects both the optical depth and events rates, was lacking. Dai et al. (2015) followed Wood et al. (2005) to specifically investigate lensing by neutron stars, but incorporated updated kinematic information and extinction via a variable luminosity function, showing that most neutron star lensing events occur on much shorter timescales than previously thought, and that the steepness of the luminosity function has a strong effect on the timescale distribution. However, they did not have updated modeling for BHs. Several new simulations have been recently developed to investigate optical depths and event rates of Galactic microlensing involving more sophisticated Galactic models and realistic extinction (Awiphan et al. 2016; Penny, Kerins, et al. 2013). However, the population synthesis in these models lack high-mass stellar remnants as they are primarily focused on lower mass stars and exoplanets.

In this chapter, we will describe new a code we have developed called Population Synthesis for Compact object Lensing Events (`PopSyCLE`).[1] White dwarfs, neutron stars, and BHs are synthesized and injected into a stellar model of the Milky Way using stellar evolution models and an initial-final mass relation. Each individual object is then propagated in time to perform a synthetic microlensing survey. Cuts are then made on observational quantities. Since the simulation is resolved, all microlensing parameters are known for each individual event. We can then begin to investigate microlensing events due to BH lenses.

The rest of the chapter is organized as follows. In Chapter 2.2, the input models used to perform both stellar and compact object population synthesis in `PopSyCLE` are described. The details of the compact object population synthesis are given in Chapter 2.3, and the procedure for selecting microlensing events is given in Chapter 2.4. Simulation parameters are presented in Chapter 2.5, then synthetic `PopSyCLE` surveys are compared to observations and theory in Chapter 2.6. In Chapter 2.7 we consider strategies for BH microlensing candidate selection, search, and verification, both from the ground and with the upcoming *WFIRST* mission. A discussion of `PopSyCLE` compared to other work is presented in Chapter 2.8, along with comments on further developments to be made to the code. Lastly, in Chapter 2.9 we present our conclusions.

---

[1] https://github.com/jluastro/PopSyCLE

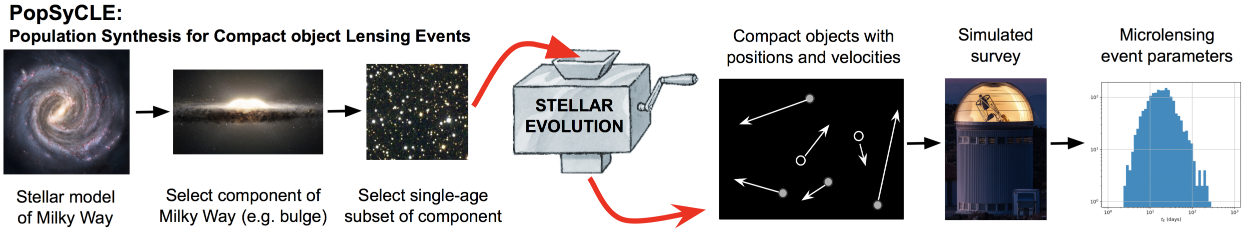

Figure 2.1: A schematic of the `PopSyCLE` pipeline. The first three panels are described in Chapter 2.2.1. The next two panels are described in Chapter 2.2.2 and 2.3. The last two panels are described in Chapter 2.4. Image credits: Universe Today (Panel 1), ESO/NASA/JPL-Caltech/M. Kornmesser/R. Hurt (Panel 2), NOAO/AURA/NSF (Panel 3), Simply scheme: introducing computer science, Harvey and Wright (Panel 4), OGLE survey (Panel 6).

2.2 PopSyCLE Ingredients

To calculate microlensing event rates and parameters, knowledge of the masses, positions, and velocities of stars and compact objects in the Milky Way is required. Photometric information to estimate quantities such as blending and survey depth limits is also required. We utilize existing models of the Milky Way to describe the stars (Chapter 2.2.1) and inject compact objects according to our own population synthesis estimates and an initial-final mass relation for BHs, neutron stars, and white dwarfs (Chapter 2.2.2).

2.2.1 Generating Stars with `Galaxia`

`Galaxia` is a synthetic stellar survey of the Milky Way (Sharma et al. 2011). Given a survey area and location, `Galaxia` will generate a stellar model of the Milky Way for a circular field of sky, which corresponds to a 3-D conical volume. `Galaxia` is a resolved simulation; that is, for every single star in the field, it will return a position, velocity, age, mass, photometry in several filters, 3-D extinction, metallicity, surface gravity, and more.[2] `Galaxia` implements the Besançon analytic model for the Milky Way (Robin, Reylé, et al. 2003), with a modified version of the disk kinematics that adjusts the velocity in the azimuthal direction (Shu 1969). For a detailed description of the implementation and galactic model parameters see Sharma et al. (2011) and references therein; for a summary of the model, see Tables 1–3 in Sharma et al. (2011). We also perform additional modifications to `Galaxia`'s bulge kinematics, as they are known to produce some inconsistencies with observations. This is described in more detail in Chapter 2.10. In the rest of the main text, whenever reference is made to `Galaxia`, we specifically mean `Galaxia` with the modified bulge, unless otherwise mentioned. Additionally, there is also an option to implement the N-body stellar halo model of Bullock et al. (2005) instead of the smooth analytic stellar halo model from the Besançon

---

[2] http://galaxia.sourceforge.net/Galaxia3pub.html

model. We choose to use the smooth analytic model instead of the N-body model as we are primarily considering lensing in the disk and bulge; stellar halo substructure is not a significant concern.

`Galaxia` includes a 3-D extinction map; however, the built-in extinction law from Schlegel et al. (1998) is not well suited to the high-extinction regions towards the inner Galactic bulge. Unfortunately, the newest 3-D extinction maps (e.g., Green (2018)) do not cover significant fractions of the Galactic Bulge region. Similarly, the extinction maps of Nataf et al. (2013), which were constructed using OGLE, VVV, and 2MASS data, only cover the OGLE-III bulge fields. Instead, we modify the Galaxia output in order to adopt the reddening law of Damineli et al. (2016a) as described in Chapter 2.11.

2.2.2 Generating Compact Objects

`PyPopStar` is a software package that generates single-age, single-metallicity populations (i.e. star clusters) using adjustable initial mass functions (IMFs), multiplicity distributions, stellar evolution and atmosphere grids, and extinction laws; for a more detailed description see Chapter 4 of Hosek, Lu, Anderson, Najarro, et al. (2019).[3] In summary, IMFs are parametrized as piecewise functions consisting of multiple power-laws and generated according to the prescription from Pflamm-Altenburg et al. (2006). We adopt the MESA Isochrones and Stellar Tracks (MIST) v1.2 stellar evolution models (Choi et al. 2016; Dotter 2016), which are calculated using the Modules for Experiments in Stellar Astrophysics (MESA) code (Paxton, Bildsten, et al. 2011; Paxton, Cantiello, et al. 2013; Paxton, Marchant, et al. 2015). These models provide theoretical isochrones with stellar temperatures and surface gravities as a function of mass at a given stellar age. Model atmosphere grids are then used to assign an atmosphere to each star. The stellar temperature determines which grid is used; an ATLAS9 grid is used for stars with $T_{eff} > 5500$ K (Castelli et al. 2004), a PHOENIX grid is used for $3800 \text{ K} < T_{eff} < 5000$ K (version 16; Husser et al. 2013), and a BTSettl grid is used for $1200 \text{ K} < T_{eff} < 3200$ K (Baraffe et al. 2015). For temperatures at a transition region between grids (e.g., 5000 K − 5500 K), an average atmosphere between the two model grids is used. For all models, solar metallicity is assumed. This assumption will not have a large effect on the BH population synthesis; see Chapter 2.8.4.2 for justification. Although the MIST stellar evolution models do not evolve stars all the way down to neutron stars and BHs, it does have some partial support for white dwarfs; a full discussion of stellar evolution with white dwarfs is presented in Chapter 2.2.2.2.

The `PyPopStar` software as described in §4 of Hosek, Lu, Anderson, Najarro, et al. (2019) would discard stars that had evolved into compact objects. To be able to perform population synthesis, we have updated `PyPopStar` with an initial-final mass relation (IFMR) that will properly account for compact objects. Given the zero-age main sequence (ZAMS) mass of a star, the IFMR describes the type and mass of compact object formed. The IFMR is an active area of research, as the ZAMS mass does not solely determine the evolutionary path

---

[3] https://github.com/astropy/PyPopStar

of a star. Factors such as rotation (which induces mixing in the star) and mass loss due to stellar winds (which are a function of metallicity) are important in the final stages of stellar evolution. In particular, the pre-supernova core structure of the star strongly determines whether there is an explosion or not, which in turn affects the type of compact remnant formed (Sukhbold, Woosley, et al. (2018) and references therein). We modify `PyPopStar` to implement a combination of IFMRs taken from recent simulations to build a population of white dwarfs, black holes, and neutron stars as described in more detail below.

Note that `PyPopStar` has support for stellar multiplicity. However, as `Galaxia` only has a treatment of single stars, this functionality was not used. A discussion of this is presented in Chapter 2.8.4.1.

2.2.2.1 Neutron Stars and Black Holes

For neutron stars (NSs) and BHs, we have adopted the IFMR presented in Raithel et al. (2018), hereafter R18, which is calculated by combining observational data of BH and NS masses along with 1-D neutrino-driven supernova simulations (Sukhbold, Ertl, et al. 2016). We have made several minor modifications, described in Chapter 2.12. The IFMR of R18 is only a function of the ZAMS mass; other factors that influence a BH or NS outcome such as small differences in core structure are taken into account by making the IFMR probabilistic. For a given ZAMS mass, the probability of forming a BH or a NS is given in Table 2.1; the values come from R18. There are then two separate IFMRs for BHs and NSs. The BH IFMR is a piecewise function (Figure 2.7.1), while we make the assumption that the NS IFMR is a constant (justification in Chapter 2.12.) Thus, because of the probabilistic nature of the total IFMR, one ZAMS mass can be mapped to two remnant masses, of either a BH or NS.

The maximum BH mass generated by the BH IFMR is about $16 M_\odot$. This appears to run contrary to the recent results from gravitational wave astronomy experiments, which has found 15 out of 20 pre-merger black holes with masses above $16 M_\odot$ (The LIGO Scientific Collaboration et al. 2018). As discussed in detail in Chapter 6 of R18, the models of Sukhbold, Ertl, et al. (2016) are all solar metallicity, while the formation of LIGO-mass BHs from single-star evolution requires lower metallicity. Additionally, the models are of single stars, and do not consider formation of BHs via dynamical assembly in dense stellar clusters nor strong magnetic fields (Groh et al. 2020; Petit et al. 2017), other proposed mechanism for obtaining LIGO-mass BHs. See Chapter 2.8.4.2 and Chapter 2.8.4.1 for a further discussion.

2.2.2.2 White Dwarfs

One complicating factor in white dwarf (WD) population synthesis is that the MIST models do not include the late stages of WD cooling. Thus not all WDs are generated, in particular the oldest and faintest ones. This means a WD IFMR is also required. For all white dwarfs not included in a set of evolutionary models, we use the empirically determined IFMR of Kalirai et al. (2008), hereafter K08, given by

$$M_{WD} = (0.109\ M_{ZAMS} + 0.394)\ M_\odot. \tag{2.1}$$

The data in K08 range in initial mass from $1.16M_\odot < M_{ZAMS} < 6.5M_\odot$. However, to have continuous coverage in M_{ZAMS} for the IFMR, we extend the domain to M_{ZAMS} to $0.5M_\odot < M_{ZAMS} < 9M_\odot$, where the lower mass limit was chosen the match the MIST models' lower mass limit, and the upper mass limit was chosen to match where the IFMR for NSs and BHs begin. The low-mass extrapolation covers all possible WDs formed within the age of the Universe. The high-mass extrapolation ensures that that there is an IFMR for all stellar masses and the maximum WD mass would then be

$$M_{WD}(M_{ZAMS} = 9M_\odot) = 1.375M_\odot \lesssim M_{ch}$$

where $M_{ch} = 1.4M_\odot$ is the Chandrasehkar mass.

In particular for the MIST models, WDs are tracked only so far down the cooling curve and the coolest/oldest WDs are usually dropped. For these objects, the WD IFMR (Equation 2.1) is used to produce *dark* WDs and their luminosity is neglected. This is justified as these old WDs have absolute magnitudes of M∼18 in red-optical filters and they contribute negligible flux at typical distances for lenses and sources (e.g., Campos et al. 2016). Thus a `PopSyCLE` population will contain both luminous WDs from the MIST models and dark WDs from the K08 IFMR.

Mass Range ($M_\odot$)	P_{WD}	P_{NS}	P_{BH}
0.5 < M < 9	1.000	0	0
9 < M < 15	0	1.000	0
15 < M < 17.8	0	0.679	0.321
17.8 < M < 18.5	0	0.833	0.167
18.5 < M < 21.7	0	0.500	0.500
21.7 < M < 25.2	0	0	1.000
25.2 < M < 27.5	0	0.652	0.348
27.5 < M < 60	0	0	1.000
60 < M < 120	0	0.400	0.600

Table 2.1: *Compact Object Formation Probabilities.* Given the ZAMS mass (the first column), what are the probabilities of forming a white dwarf, neutron star, or black hole. The NS and BH columns come from Table 3 of R18.

2.3 Population synthesis

First, `Galaxia` is used to generate a synthetic stellar survey of a circular area on the sky. Only stars that are within a distance of 20 kpc to Earth are kept, as these are the ones most likely to be observable lenses and sources. In addition to mass, age, 6-D kinematics, and photometry, `Galaxia` also tags each star by its population type (thin disk, thick disk, bulge, stellar halo.) The stars generated are sorted by population to preserve age and kinematic information. The thin disk is a multi-age population ranging from less than 0.15 Gyr up to 10 Gyr; we split the thin disk population into sub-populations of 29 finer age bins. The thick disk, bulge, and halo are all single-age populations of 11, 10, and 14 Gyr, respectively. Some of the youngest stars in the thin disk need to have their ages reassigned because the youngest age available for the MIST isochrones is 10^5 years. This is only necessary for a very small number of stars; for example, in a survey pointed toward the Galactic center, less than 0.001 percent of stars were younger than 10^5 years. Additionally, the age of the 14 Gyr halo star population are reassigned to be 13.8 Gyr, to be within the age of the universe.

Each of these (sub)-populations is then approximated as a group of single-age stars. If necessary, these age groups are further broken up into smaller sub-groups of 2 million stars each, to keep the population synthesis calculation manageable.

Knowledge of the initial mass of each age group of stars is needed to perform the compact object population synthesis. The present-day mass of the age group can be calculated with knowledge of the ZAMS mass of each star. The initial age group mass can be found by multiplying the present-day group mass by an initial-current mass ratio factor; the calculation of this ratio is described in Chapter 2.13. With the initial mass of the age group of stars in hand, we can then generate a similar group of stars of the correct mass and age with `PyPopStar`.

Next, compact objects are generated to inject back into the stellar population using `PyPopStar`. A Kroupa IMF $\xi(m) = dN/dm \propto m^{-\alpha}$,

$$\alpha = \begin{cases} -1.3, & 0.1\ M_\odot < m \leq 0.5\ M_\odot \\ -2.3, & 0.5\ M_\odot < m \leq 120\ M_\odot \end{cases} \tag{2.2}$$

is assumed with the lower mass limit set to match the MIST models' lower mass limit, and the upper mass limit set to match the IFMR's upper mass limit (Kroupa 2001). Any object that evolves off the isochrone becomes a compact object. As described in Chapter 2.2.2, the IFMRs of R18 and K08 are used to obtain masses for BHs, NSs, and WDs.

We assume the positions and velocities of the compact objects follows that of the stellar population in `Galaxia`; they are assigned using kernel density estimation (KDE). The 6-D kinematic data is simultaneously fit using a Gaussian kernel and Euclidean metric with a bandwidth of 0.0001. The bandwidth is a smoothing parameter, where a bandwidth of zero results in no smoothing, and a bandwidth approaching infinity results in complete smoothing, i.e. a mean equal to that of the original data that has the shape of the kernel. Here, using such a small bandwidth means the data is extremely unsmoothed. However, this is desired as we want to randomly draw from the existing distribution. For the BHs and NSs, a tuneable birth kick is also applied in a random direction in addition to the stellar velocity assigned from KDE. NSs have been observed to have birth velocities of $\sim 200 - 500\,\text{km/s}$, and up to $1000\,\text{km/s}$; it is thought that the initial kick velocity is due to asymmetry in the supernova explosion (Janka 2012; Lai 2001). BHs should also receive kicks; by conservation of momentum, BH kicks should be smaller than NS kicks (although see Janka (2013) and Repetto, Davies, et al. (2012) which suggests they will be of similar magnitude).

All the compact objects produced with the IFMRs are assumed to be dark, while luminous WDs produced with the MIST models are assigned the same color excess $E(B-V)$ as the star nearest to them in 3-D space.

For easier processing and parallelization, the stars from `Galaxia` and the compact objects generated from `PyPopStar` are sorted into a grid of Galactic latitude and longitude bins as seen from the solar system barycenter. The size of these latitude and longitude bins $\Delta\theta_{bin}$ must be sufficiently large such that most stars do not cross over multiple bins during the survey duration, but not so large that finding source-lens pairs is computationally infeasible (described in Chapter 2.4.3). Assuming that typical microlensing surveys are of ~ 5 years, and proper motions of >5 arcsec/year are rare, this gives a lower limit on $\Delta\theta_{bin}$ of $25''$. We have chosen the default bin sizes to be roughly $30'' \times 30''$; however, the bin size is adjustable by the user.

The above process of generating compact objects and sorting them into bins for each (sub)-population group is then repeated. Thus, the generated compact objects preserve the correlations between population age, structure, and dynamics that are present in the stellar population, with the addition of tunable birth kicks.

2.4 Identifying Microlensing Events

Microlensing occurs when a foreground star or compact object (the lens) passes near a background star (the source) as projected on the sky. However, not all close approaches may produce detectable or significant microlensing events. Therefore, microlensing event candidates are first identified, then detailed properties of the lensing event are calculated and used to decide whether the candidate is significant enough to classify as a microlensing event. In Chapter 2.4.1 and 2.4.2, basic definitions for microlensing event parameters are presented. The process by which candidates are identified and converted into a final microlensing list is described in Chapter 2.4.3 and 2.4.4. Going forward, the point source point lens (PSPL) regime of microlensing is assumed.

2.4.1 Candidate Selection Parameters

The scale of the microlensing event is set by the the angular *Einstein radius*

$$\theta_E = \sqrt{\frac{4GM}{c^2}\left(\frac{1}{d_L} - \frac{1}{d_S}\right)}, \tag{2.3}$$

where d_S is the observer-source distance, d_L is the observer-lens distance, and M is the mass of the lens. Note that in microlensing, θ_E is unresolved, unlike in strong lensing. For a "typical" microlensing event consisting of a stellar bulge source at $d_S = 8\,\mathrm{kpc}$ and a stellar disk lens at $d_L = 4\,\text{kpc}$ with a mass $M = 0.5M_\odot$, the Einstein radius is $\theta_E = 0.71\,\text{mas}$. For context, the highest-resolution images from the largest ground-based or space-based telescopes (with a filled aperture) is 50 mas in the optical or infrared. However, in some cases Einstein radii of this scale are interferometrically resolvable (Dong et al. 2019), moving from the regime of microlensing to strong lensing.

The *Einstein crossing time* t_E, the time it takes for the lens to traverse the Einstein radius, can be inferred from the photometric light curve. The magnitude of the relative source-lens proper motion μ_{rel} relates the Einstein crossing time and Einstein radius via

$$\theta_E = \mu_{rel} t_E. \tag{2.4}$$

The dimensionless source-lens separation vector normalized in units of the Einstein radius is

$$\vec{u} = \frac{\vec{\theta}_S - \vec{\theta}_L}{\theta_E}, \tag{2.5}$$

where $\vec{\theta}_L$ and $\vec{\theta}_S$ denote the angular position of the lens and source on the sky, respectively. The magnitude of the separation $|\vec{u}| = u$ as a function of time, neglecting higher-order effects such as parallax, can be written as

$$u(t) = \sqrt{u_0^2 + \left(\frac{t - t_0}{t_E}\right)^2}, \tag{2.6}$$

where t_0 is the time of closest approach and u_0 is the separation at t_0; u_0 is also known as the *impact parameter*.

The *photometric amplification* of the source is given by

$$A(u) = \frac{u^2 + 2}{u\sqrt{u^2 + 4}}, \tag{2.7}$$

and is maximized at $u = u_0$. It can be seen from this formula that a smaller u_0 produces a larger amplification. Most microlensing surveys define a “microlensing event” as an event that has u_0 less than 1 or 2.

The *source flux fraction*, which is sometimes called the blend parameter, or confusingly, the blend fraction, is the fraction of source flux over total flux in the telescope's photometric extraction aperture

$$b_{SFF} = \frac{F_S}{F_S + F_L + F_N}, \tag{2.8}$$

where F_S, F_L, and F_N are the fluxes due to the (unlensed) source, lens, and any neighboring stars. From this definition, a highly blended event will have a source flux fraction of $b_{SFF} \approx 0$ and an event with no blending (i.e. only flux from the source) will have $b_{SFF} = 1$.

The photometric extraction aperture is typically proportional to the spatial resolution of the images; we adopt an aperture diameter of the full-width half-maximum (FWHM), which is set by seeing for ground-based surveys like OGLE and the diffraction limit for space-based surveys such as *WFIRST* (these surveys are described in Chapter 2.5). To give concrete numbers, the median seeing for the OGLE survey is roughly 1.3", which we take to be the FWHM. *WFIRST*, a planned 2.4 meter space telescope observing at 1630 nm (H-band), will have FWHM $\sim 0.17''$. These FWHM values for OGLE and *WFIRST* would correspond to aperture radii of roughly $0.65''$ and $0.09''$, respectively.

The *bump magnitude*, Δm, is the difference between the baseline magnitude m_{base} and the peak magnitude m_{peak}

$$\Delta m = -2.5\log_{10}\left(\frac{A(u_0)F_S + F_L + F_N}{F_S + F_L + F_N}\right). \tag{2.9}$$

Note that although the magnification of the source flux is achromatic, the bump magnitude and the source flux fraction are dependent on wavelength and the photometric extraction aperture (Di Stefano et al. 1995). Thus, when events are selected on Δm or b_{SFF}, we explicitly note the filter and aperture used.

2.4.2 Other Selection Parameters

In addition to the selection parameters described in Chapter 2.4.1, there are a number of other measureable microlensing quantities. In particular, the astrometric and microlensing parallax signals are useful for identifying possible black hole microlensing events.

The *astrometric shift* $\vec{\delta}_c$ of the source image centroid, assuming no blending, is given by

$$\vec{\delta}_c = \frac{\theta_E}{u^2+2}\vec{u}. \tag{2.10}$$

In contrast to the photometric amplification, the maximum astrometric shift occurs at $u = \pm\sqrt{2}$. Thus, if $u_0 < \sqrt{2}$, the maximum astrometric shift will occur before and after the maximum photometric amplification. However, if $u_0 \geq \sqrt{2}$, the time at which maximum astrometric shift and photometric amplification occur will coincide. It should be noted that δ_c is the maximum possible astrometric shift for a given geometry (i.e. for given M, d_L, d_S), as it does not include blending.

Blending due to a luminous lens modifies the astrometric signal to

$$\vec{\delta}_{c,LL} = \frac{\theta_E}{1+g}\frac{1+g(u^2 - u\sqrt{u^2+4}+3)}{u^2+2+gu\sqrt{u^2+4}}\vec{u}, \tag{2.11}$$

where $g = F_L/F_S$ (Dominik and Sahu 2000). Blending due to the lens and other neighboring stars dilutes the astrometric signal further to

$$\vec{\delta}_{c,LLN} = \frac{\tilde{A}(u)F_S\vec{\theta}_S + F_N\vec{\theta}_N}{A(u)F_S + F_L + F_N} - \frac{F_S\vec{\theta}_S + F_N\vec{\theta}_N}{F_S + F_L + F_N}, \tag{2.12}$$

where $\vec{\theta}_S$ and $\vec{\theta}_N$ are the angular positions of the source and the centroid of all the on-sky neighbors contributing to blending, relative to the lens position; $A(u)$ is given by Equation 2.7 and $\tilde{A}(u)$ is defined

$$\tilde{A}(u) = \frac{u^2 + 3}{u\sqrt{u^2 + 4}}. \tag{2.13}$$

For long-duration events ($t_E \gtrsim 3$ months), the motion of Earth orbiting the Sun will modify the otherwise symmetric light curve. This signal is called the *microlensing parallax* π_E and is given by

$$\pi_E = \frac{\pi_{rel}}{\theta_E}, \tag{2.14}$$

where π_{rel} is the *relative parallax*

$$\pi_{rel} = 1\mathrm{AU}\left(\frac{1}{d_L} - \frac{1}{d_S}\right). \tag{2.15}$$

Combining Equations 2.3 and 2.15 and solving for the lens mass M yields

$$M = \frac{\theta_E}{\kappa \pi_E}, \tag{2.16}$$

where $\kappa \equiv \frac{4G}{1\,AU \cdot c^2}$. If both the photometric magnification $A(u)$ and the astrometric shift $\delta_c(u, \theta_E)$ can be measured, the Einstein radius θ_E can be deduced. Along with a measurement of the microlensing parallax π_E, the mass of the lens M can then be derived using Equation 2.16. Thus, by having both astrometric and photometric measurements, the degeneracies between lens mass, lens distance, and source distance can be broken. [4] The lens mass can then be constrained without having to resort to assumptions about the lens and source distances. Many microlensing studies only measure the photometric signal and use a Galactic model to weight different source distances in order to derive the lens mass; however, this is a significant assumption. By combining both the photometric and astrometric microlensing signal, the lens mass can be determined without having to resort to modeling distances. Additionally, the astrometric signal peaks after the photometric signal when $u_0 < \sqrt{2}$.

The method just described can be used to measure the masses of BHs. Since long-duration microlensing events are more likely to be BHs, probable BH microlensing events can be selected from ground-based photometry, then followed up astrometrically (Lu et al. 2016).

---

[4] In the case of more complicated microlensing scenarios (e.g., binary sources or lenses that may also be rotating), additional information might be needed to break new degeneracies introduced, such as incorporating e.g., spectroscopic measurements (Smith, Mao, Woźniak, et al. 2002). Fitting and extracting masses from these types of events is beyond the scope of this chapter , although we do discuss binary effects in Chapter 2.8.4.1.

2.4.3 Event Selection Algorithm

With population synthesis complete, we can specify a duration and sampling cadence to perform a synthetic microlensing survey. Typical microlensing survey lengths are on the order of years, over which celestial motions are linear for nearly all lenses and sources. Thus, with an initial position and velocity, the position of any object at some later time in the survey can be calculated.

First, a grid of latitude and longitude bins is overlaid across the entire survey area. Next, four adjacent latitude and longitude bins of objects generated from population synthesis are read in and combined to make one large bin over which microlensing events are searched for at the sampled times within the survey window. This combination ensures that microlensing events that occur across the edges of two smaller bins are not missed. The algorithm for finding event candidates has four "cuts" as follows:

1. Find the nearest *on-sky* neighbor for each object and calculate the separation $\Delta\theta$. Pairs with separations of $\Delta\theta > \theta_{cut}$ are rejected, where θ_{cut} is a user-specified separation. Analogous to the bin size selection, choosing too small a value for θ_{cut} will mean some events are missed. Choosing too large a value for θ_{cut} is less problematic; it will merely slow down subsequent calculations by considering pairs that will not produce a detectable microlensing signal.

2. Calculate the Einstein radius θ_E of the lenses from these initial microlensing candidate pairs. Only keep the pairs where $\Delta\theta/\theta_E < u_{cut}$, where u_{cut} is another user-specified value that sets the maximum impact parameter. For this further refined list of candidates, record all the stars that fall within the seeing disk radius θ_{blend}, which will be used to calculate blending later on. The seeing disk radius is also a user-specified parameter.

3. From the new list of microlensing candidate pairs, calculate the time of closest approach t_0 when $u = u_0$. Events are kept if $t_0 \in [t_i, t_f]$ where t_i and t_f are the start and end times for the survey.

4. Remove unphysical "events" where the source is a dark object.

This yields the list of microlensing event candidates. The procedure is then repeated for all the bins. This algorithm will generate many repeats, due to the multiple overlaps in the bins, and also the multiple evaluation times. Only unique events are counted, that is, a lens-source pair is only counted once; the event parameters that get recorded are the ones corresponding to when the source and lens are closest to each other. A cartoon schematic of this entire process is shown in Figure 2.4.3.

With complete information about the 6-D kinematics, masses, and photometry, any microlensing parameters of interest can be calculated for all event candidates.

It should also be noted that the choice of sampling cadence t_{obs}, defined as the time between consecutive observations, will change the number of event candidates. For example,

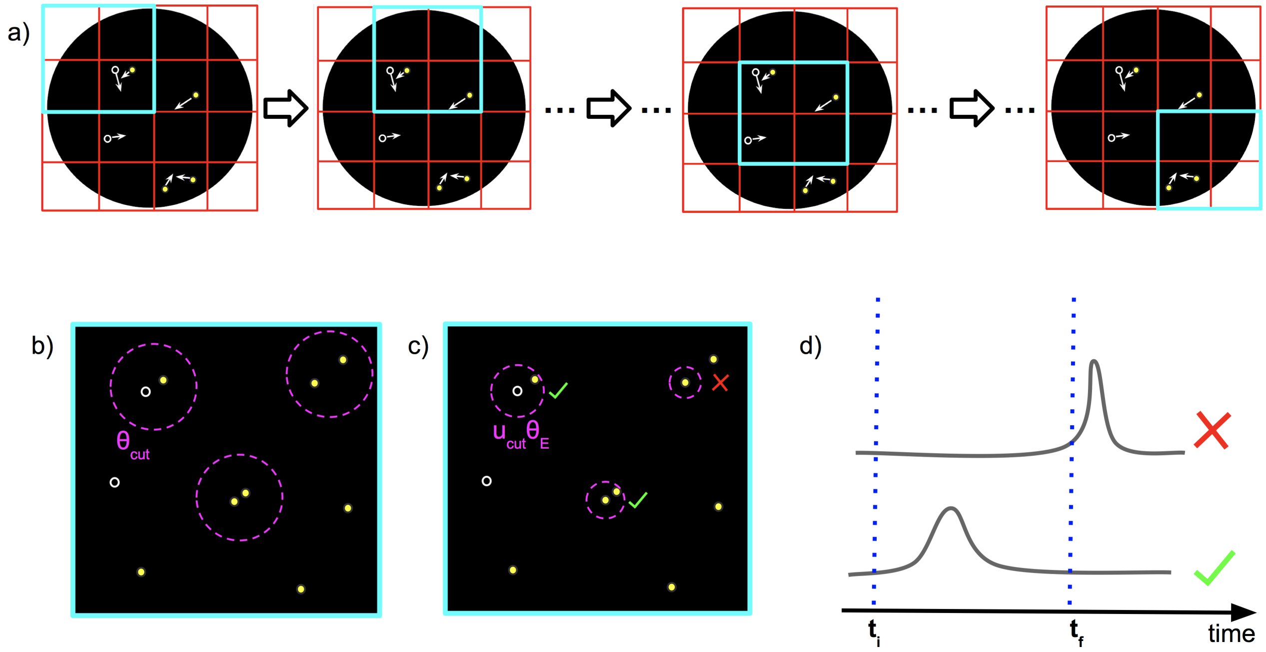

Figure 2.2: a) A schematic of the binning algorithm described in the second paragraph of Chapter 2.4.3. Each field is divided into a grid (*red lines*) and then the four adjacent boxes at each grid vertex are binned (*blue square*) to search for candidate microlensing events and contaminating neighbor stars. Within each blue bin, event selection criteria are applied (subfigures b through d). The process is then repeated on the next blue bin until the entire grid has been covered. Finally, results are aggregated and duplicates are removed. b) A schematic of Cut 1, which selects all object pairs within some on-sky separation of $\Delta\theta < \theta_{cut}$. Microlensing parameters are computed for all of these object pairs. c) A schematic of Cut 2, which selects all of the objects pairs left after Cut 1 that satisfy the condition $\Delta\theta/\theta_E < u_{cut}$. Note that unlike in Cut 1, the circles have different radii, as θ_E depends on the lens mass and the source and lens distances. The pairs that pass this selection have green checks next to them, while those that do not pass the selection have a red “x”. d) A schematic of Cut 3, which selects the source-lens pairs whose point of closest approach on-sky occurs within the survey window. This is equivalent to selecting light curves that peak photometrically within the survey window. Note: none of these cartoons are to scale.

$t_{obs} = 1$ day corresponds to a very dense sampling, while $t_{obs} = 100$ days corresponds to a very sparse sampling. There will be a loss of sensitivity to events with $t_E < t_{obs}$ since shorter events will fall between observations. It should also be emphasized that the sampling cadence of `PopSyCLE` has no relation to the observational survey cadence of real microlensing surveys. For example, as shown in Figure 2.4.3, `PopSyCLE` run with a sampling cadence of 100 days finds nearly all events with $t_E \gtrsim 30$ days since objects only have to approach each other

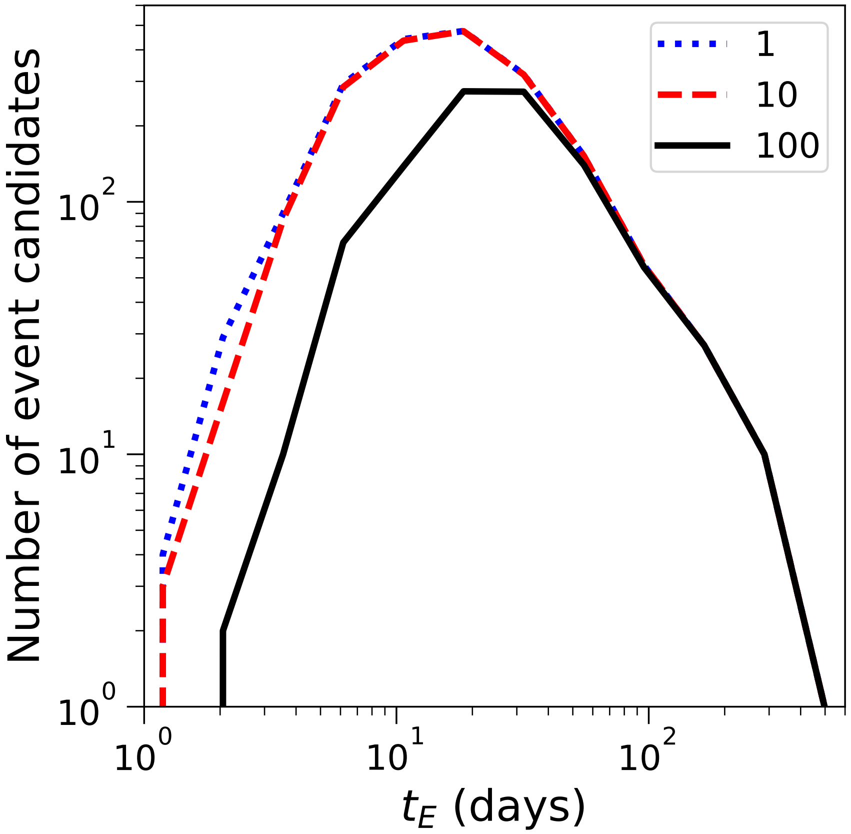

Figure 2.3: The t_E distribution for all event candidates (i.e. no observational cuts) from field F01, but with three different survey cadences. The number in the legend corresponds to the sampling cadence, in days. The long timescale end above 30 days is insensitive to the sampling cadence. Cadences of 10 days or less provide an accurate description of the peak of the t_E distribution.

within $u_{cut}\theta_E$ to be detected.

2.4.4 Survey Implementation

Many of the microlensing events reported by `PopSyCLE` as described in Chapter 2.4.3 would be undetectable by a real survey. For example, there will be events too faint to be observed. Thus, we consider the list of events generated in Chapter 2.4.3 to be event candidates. The user can select from this list of event candidates those which satisfy some observational criteria to generate a final list of microlensing events.

2.5 PopSyCLE Simulations

All the event candidates generated by `PopSyCLE` are microlensing events, as there are no other types of transient phenomena (e.g., variable stars, telescope artifacts) in the simulation. Nonetheless, observational cuts are applied to replicate what a real survey would see. As different microlensing surveys use different telescopes, selection criteria, reduction pipelines and methods, etc. the cuts are different for each survey. We simulate several current and future microlensing surveys, as described below.

Parameter	Value
NS kick velocity	350 km/s
BH kick velocity	100 km/s
Duration	1000 days
Cadence	10 days
θ_{cut}	$2''$
u_{cut}	2
Extinction Law	Damineli et al. (2016a)
Area Per Field	0.34 deg^2

Table 2.2: *Common Simulation Parameters.* As described in Chapter 2.3, a birth kick is added to the progenitor star's velocity in a random direction for black holes and neutron stars. As described in Chapter 2.4.3, duration describes the length of synthetic survey, and cadence specifies the sampling frequency. θ_{cut} is used to set the maximum separation between potential microlensing event candidates. Considering relatively extreme values to maximize θ_E, such as $d_L = 10\,\text{pc}$, $d_S = 20\,\text{kpc}$, and $M = 15 M_\odot$ correspond to $\theta_E = 0.11''$; thus, the choice of $2''$ will capture all observable microlensing events in the simulation. u_{cut} defines the maximum allowed u_0.

First, we provide background information on current surveys we will emulate. The Optical Gravitational Lensing Experiment (OGLE) (Udalski, Szymanski, Kaluzny, Kubiak, and Mateo 1992) and the Microlensing Observations in Astrophysics (MOA) (Muraki et al. 1999) collaborations run dedicated long-term photometric surveys monitoring the Milky Way bulge (and other targets) for microlensing events from small ground-based, seeing-limited telescopes. For instance, OGLE-IV regularly observes $\gtrsim 150\ \text{deg}^2$ of the Galactic bulge for 8 to 9 months out of the year, from February to October. The observing cadence typically ranges from 20 min to 2 days, depending on the sky location, and events are detected at $I \lesssim 22$ and the median seeing ranges from 1.25" to 1.35" (Udalski, Szymański, et al. 2015). OGLE also posts alerts about phometric microlensing events through the Early Warning System (EWS). The OGLE EWS reduces photometry in real time, providing information about potential microlensing candidates. With the advent of OGLE-IV, roughly 2000 microlensing events

Name	l (deg)	b (deg)	Alt. Name
F00	$-0.93°$	$-7.70°$	OGLE-IV-BLG547
F01	$8.81°$	$-3.64°$	OGLE-IV-BLG527
F02	$-2.75°$	$-3.32°$	OGLE-2017-BLG-0019[a]
F03	$3.51°$	$-3.17°$	MOA-II-gb14
F04	$9.62°$	$-2.93°$	MOA-II-gb21
F05	$1.83°$	$-2.52°$	OGLE-2015-BLG-0029[a]
F06	$0.65°$	$-1.86°$	MOA-II-gb5
F07	$-7.91°$	$-1.85°$	OGLE-IV-BLG672
F08	$1.25°$	$-1.38°$	OGLE-2014-BLG-0613[a]
F09	$1.00°$	$-1.03°$	OGLE-IV-BLG500
F10	$-3.61°$	$1.86°$	OGLE-2015-BLG-0211[a]
F11	$0.33°$	$2.82°$	OGLE-IV-BLG611
F12	$7.81°$	$4.81°$	OGLE-IV-BLG629
F13	$-4.21°$	$4.96°$	OGLE-IV-BLG617

Table 2.3: ***PopSyCLE** Fields.* Fields labeled with [a] are centered on individual microlensing events from the OGLE EWS.

are published each season on the EWS website.[5]

We compare `PopSyCLE` simulation results to three different papers that use data gathered from these two surveys: Sumi and Penny (2016), hereafter S16, which used MOA-II data, and Mróz, Udalski, Skowron, Szymański, et al. (2019a) and Mróz, Udalski, Skowron, Poleski, et al. (2017), hereafter M19 and M17, which used OGLE-IV data. Note that S16 is an updated version of Sumi, Bennett, et al. (2013) with corrected event rates, due to a correction in the stellar number count. Observational surveys must correct for the ability to detect a given microlensing event. This is quantified by the efficiency correction ε which is a function of a multitude of parameters, such as the Einstein crossing time, source flux fraction, unlensed source magnitude, survey duration and cadence, and stellar confusion. These three papers calculate efficiency corrections to convert the directly observed distribution of microlensing events to efficiency corrected event rates and t_E distributions; we compare our `PopSyCLE` simulations to these efficiency corrected quantities.

We also run `PopSyCLE` simulations to explore the possibilities of future microlensing surveys. The Wide Field Infrared Survey Telescope (*WFIRST*) is a 2.4 meter space telescope scheduled to launch in 2025. As part of the program, a microlensing survey searching for exoplanets will observe 1.97 deg^2 of the Galactic bulge down to $H < 26$ every 15 minutes over 6 observing seasons, where each season is 72 days long (Penny, Gaudi, et al. 2019, hereafter P19). However, the exact way in which the 6 seasons will be distributed across the survey lifetime of $4.5-5$ years is not yet determined.

---

[5] http://ogle.astrouw.edu.pl/ogle4/ews/ews.html

Parameter/Criteria	Mock Sumi	Mock EWS	Mock Mróz19	Mock Mróz17	Mock WFIRST
Filter	I	I	I	I	H
Seeing disk radius, θ_{blend}	–[a]	$0.65''$	–[b]	$0.65''$	$0.09''$
Minimum source magnitude, m_S [mag]	≤ 20	–	≤ 21	≤ 22	–
Minimum baseline magnitude, m_{base} [mag]	–	≤ 21	–	–	≤ 26
Maximum impact parameter, u_0	≤ 1	≤ 2	≤ 1	≤ 1	≤ 2
Removal of highly-blended events, $b_{SFF,m}$	–	–	–	≥ 0.1	–
Einstein crossing time range, t_E [days]	$[0.3, 200]$	–	$[0.5, 300]$	$[0.1, 316]$	–
Removal of low-amplitude events, Δm [mag]	–	≥ 0.1	–	–	≥ 0.1

Table 2.4: *Simulation Parameters.* The selection parameters for Mock Sumi, Mróz19, and Mróz17 come from S16, M19, M17 respectively. For Mock EWS, we choose values based on numbers reported on the OGLE EWS website for the 2016-2018 seasons (described in more detail in Chapter 2.7.2.1). For Mock WFIRST, the minimum baseline magnitude comes from P19, and the remaining parameter cuts are based on Mock EWS.

[a] There is no cut involving a parameter dependent on θ_{blend} (such as b_{SFF} or Δm) in the Mock Sumi simulation; however, the median seeing at the MOA site is approximately $2.0''$ (S16), which would roughly correspond to $\theta_{blend} = 1.0''$.

[b] Similarly to [a], there is no cut involving a parameter dependent on θ_{blend}; however, the seeing is the same as for M17.

`PopSyCLE` simulations are run in two parts. We define a *field* as the projected area on the sky over which `PopSyCLE` is run, and a *simulation* is defined to be the particular parameters used and observational criteria imposed on the `PopSyCLE` run for some field. Table 2.2 lists the parameters common to all simulations presented in this chapter . In summary, for the population synthesis portion of the simulation, we assume that NSs and BHs receive birth kicks of 350 km/s and 100 km/s in a random direction, respectively. Microlensing events with an impact parameter $u_0 < 2$ are then selected from a 0.34 deg^2 area survey of 1000 days in length with observations made every 10 days. Table 2.3 contains a list of all fields run in all simulations. These fields were selected from the OGLE and MOA surveys' Galactic bulge fields, and picked to sample a variety of latitude and longitudes. For *WFIRST*, only three of these fields are utilized (F06, F08, F09) from the `PopSyCLE` simulations, as they are representative samples of the *WFIRST* Cycle 7 design field of view (see Figure 7 of P19).

Note that a survey duration of 1000 continuous days is used in the simulations (Table 2.2), which does not match those of any of the surveys described above. Survey duration and structure have an effect on the types of events detectable. For example, having gaps between observing seasons can cause a lack of data from one side of the light curve, making it difficult to fit for event parameters. Additionally, some events will be undetectable, simply because they are too long to be observed in a particular observing window, or fall entirely within an observational gap. We assume that for published event rates and t_E distributions (e.g., S16, M17, M19) efficiency corrections take these effects into account. However, this statement does not apply to results from the OGLE EWS, as it is only used for alerting events in real time and does not have any type of correction. Similarly for *WFIRST*, when trying to determine how many BHs are detectable over the duration of the survey, we assume no efficiency correction. The effect that the season spacing will have on the number of detectable BH events is not so obvious, as the exact details of the season distribution have not been set. The effect this has on our estimate of the number of BH masses that *WFIRST* can measure will be discussed further in Chapter 2.7.5.

Five different simulations are run, named Mock Sumi, Mock Mróz19, Mock Mróz17, Mock EWS, and Mock WFIRST. The first three attempt to mimic the microlensing event selection criteria of S16, M19, and M17 respectively, after taking into account detection efficiency. These criteria are selected to match the particular magnitude limit, impact parameter, and t_E range of the survey's efficiency correction. Mock EWS is designed to mimic the detection capabilities of the OGLE EWS, while Mock WFIRST is designed to mimic *WFIRST*'s microlensing survey based on "reasonable" criteria expected for the mission.

Table 2.4 lists the corresponding selection criteria for these five simulations.

2.6 PopSyCLE Comparison

2.6.1 Number of black holes and neutron stars in the Milky Way

We first use our population synthesis model to calculate the number of BHs and NSs in the Milky Way. First, `Galaxia` generates a random fraction of the entire Milky Way. We then perform a simplified version of the compact object population synthesis described in Chapter 2.3 by ignoring the spatial distribution and kinematics of the compact objects, instead only returning the masses of the compact objects. We then scale the number of compact objects in accordance to the fraction of stars generated to obtain the actual number.

With this method, we estimate that there are 2.2×10^8 black holes and 4.4×10^8 neutron stars in the entire Milky Way. Our findings compare well with previous theoretical estimates that predict around 10^8 to 10^9 stellar-mass black holes in the Milky Way, with a similar estimate for neutron stars, using methods based on the number of microlensing events toward the Galactic Bulge (Agol, Kamionkowski, et al. 2002) and supernova explosion and Galactic chemical evolution models (Timmes et al. 1996).

Of the 2.2×10^8 black holes produced by `PopSyCLE`, 8.5×10^7 have masses greater than $10M_\odot$. This is comparable the findings of Elbert et al. (2018), where they estimate there should be around 10^8 black holes with $M > 10M_\odot$ in a galaxy with a stellar mass equal to that of the Milky Way ($M_{*,MW} \approx 6 \times 10^{10} M_\odot$). Note that the models of Elbert et al. (2018) include metallicity and BH-BH mergers, which `PopSyCLE` currently does not include. The mass distribution of BHs is shown in Figure 2.7.1 and a discussion of the distribution is presented in Chapter 2.7.1.

2.6.2 Microlensing event rate

Field	n_s (10^6/deg^2)		Γ (10^{-6}/star/yr)		$\langle t_E \rangle$ (days)	
	Obs.	Mock	Obs.	Mock	Obs.	Mock
F00^{M19}	2.62	2.52	1.3 ± 0.8	5.97	32.6	20.4
F01^{M19}	4.54	2.92	5.5 ± 0.9	8.09	39.5	25.0
F03^{S}	3.64	3.97	$14.0^{+2.9}_{-2.4}$	22.74	25.5	18.5
F04^{S}	1.11	1.12	$3.5^{+2.6}_{-1.7}$	7.66	17.0	28.5
F06^{S}	2.80	5.77	$36.6^{+4.9}_{-4.4}$	50.67	17.4	18.4
F07^{M19}	1.75	2.09	5.6 ± 1.4	4.11	51.8	39.5
F09^{M19}	4.84	4.75	23.9 ± 2.0	43.69	18.8	17.4
F11^{M19}	4.95	5.7	16.2 ± 1.3	32.2	21.8	17.0
F12^{M19}	3.26	2.07	3.4 ± 1.1	7.25	36.7	16.7
F13^{M19}	4.51	3.44	5.2 ± 1.1	11.25	30.8	21.9

Table 2.5: *Comparing `PopSyCLE` to surveys.* Fields with ^{M19} indicate the observed values come from M19, while those with ^{S} are from S16.

We next compare stellar densities, event rates, and Einstein crossing times from `PopSyCLE` simulations with those from M19 and S16. A summary is presented in Table 2.5.

For each field listed in Table 2.3, we apply the observational cuts from Tables 2.2 and 2.4 to generate a final list of detectable events as described in Chapter 2.5. In order to convert to an event rate in units of [events star^{-1} year^{-1}], we also calculate the total number of detectable stars within the magnitude limits for the corresponding survey. The microlensing event rate, Γ, varies between different observational surveys and different fields. The rates for Mock Sumi and Mock Mróz19 are presented in Table 2.6.

The event rates from S16 for fields F03, F04, and F06 (corresponding to MOA-II-gb14, gb21, and gb5) are 14.0, 3.5, and 36.6 events star^{-1} year^{-1}, respectively. For those same fields, the Mock Sumi `PopSyCLE` simulation gives event rates of 22.74, 7.66, and 50.67 events star^{-1} year^{-1}. The event rates from `PopSyCLE` are roughly between 1.4 to 2.2 times higher than the ones reported in S16.

The event rates from M19 for fields F00, F01, F07, F09, F11, F12, and F13 (corresponding to OGLE-IV-BLG547, 527, 672, 500, 611, 629, and 617) are 1.3, 5.5, 5.6, 23.9, 16.2, 3.4, and 5.2 events star^{-1} year^{-1}, respectively. For those same fields, the Mock Mróz19 `PopSyCLE` simulation gives event rates of 5.97, 8.09, 4.11, 43.69, 32.2, 7.25, 11.25 events star^{-1} year^{-1}. The event rates from `PopSyCLE` are generally a factor of 2 times higher than the ones reported in M19, although for one field it is nearly 5 times higher and in one field it is only 0.7 of the observed rate.

Our event rate estimates from `PopSyCLE` use a total number of stars that is 100% complete down to the selected magnitude, as we have not imposed any confusion due to the finite beam size of a real telescope. We assume that the reported event rates in Mróz, Udalski, Skowron, Poleski, et al. (2017), Mróz, Udalski, Skowron, Szymański, et al. (2019a), and Sumi and Penny (2016) use completeness-corrected stellar number counts.

Field	Sim	n_s (10^6) (deg^{-2})	Γ (10^{-6}) (star^{-1} yr^{-1})	$\langle t_E \rangle$ (days)	Med(t_E) (days)
F00	S	1.46	5.87	17.3	11.2
	M19	2.52	5.97	20.4	14.4
F01	S	1.52	6.37	25.1	14.8
	M19	2.92	8.09	25.0	15.5
F02	S	2.70	19.09	20.2	14.2
	M19	6.11	25.66	19.5	13.9
F03	S	3.97	22.74	18.5	13.2
	M19	7.92	30.80	19.7	14.5
F04	S	1.12	7.66	28.5	21.6
	M19	2.37	9.96	19.6	17.3
F05	S	5.38	38.57	17.5	13.4
	M19	11.05	43.65	19.5	13.9
F06	S	5.77	50.67	18.4	12.4
	M19	12.53	59.68	18.9	12.8
F07	S	0.99	4.33	40.9	28.1
	M19	2.09	4.11	39.5	22.9
F08	S	2.07	33.68	20.1	16.0
	M19	5.02	40.04	18.1	13.1
F09	S	2.06	33.84	20.5	16.0
	M19	4.75	43.69	17.4	12.7
F10	S	0.33	19.69	13.4	13.0
	M19	0.64	33.32	24.5	15.1
F11	S	2.05	21.53	16.6	10.1
	M19	5.70	32.20	17.0	11.4
F12	S	1.11	5.80	18.1	10.1
	M19	2.07	7.25	16.7	9.1
F13	S	1.68	6.40	12.3	7.9
	M19	3.44	11.25	21.9	13.1

Table 2.6: *Mock Simulations.* For each field simulation (S = Mock Sumi, M19 = Mock Mróz19) we list the density of stars n_s brighter than the survey magnitude limit (no correction for blending or confusion), the event rate Γ, average Einstein crossing time $\langle t_E \rangle$, and the median Einstein crossing time Med(t_E).

2.6.3 Einstein Crossing Time Distribution

The average Einstein crossing time $\langle t_E \rangle$ is a commonly reported parameter for microlensing distributions. Most authors refer to both the raw $\langle t_E \rangle$ derived from the uncorrected distribution obtained directly after making all observational cuts, and an efficiency corrected $\langle t_E \rangle_\varepsilon$, obtained after correcting for the detection efficiency. In this section, we compare the reported $\langle t_E \rangle_\varepsilon$ from S16 and M19 to those obtained from `PopSyCLE` simulations. For brevity, whenever the notation $\langle t_E \rangle$ is used, it is understood to be efficiency corrected, unless otherwise stated.

The $\langle t_E \rangle$ from S16 for fields F03, F04, and F06 are 25.5, 17.0, and 17.4 days, respectively. For these same fields, the Mock Sumi `PopSyCLE` simulation gives $\langle t_E \rangle$ of 18.5, 28.5, 18.4 days; these values range between factors of 0.7 to 1.7 times the observed timescales.

The $\langle t_E \rangle$ from M19 for fields F00, F01, F07, F09, F11, F12, and F13 are 32.6, 39.5, 51.8, 18.8, 21.8, 36.7, and 30.8 days, respectively. For these same fields, the Mock Mróz19 simulation gives $\langle t_E \rangle$ of 20.4, 25.0, 39.5, 17.4, 17.0, 16.7, and 21.9 days; these values are all shorter than the observed timescales by factors of 0.5 to 0.9.

Values for $\langle t_E \rangle$ for the events in M17 cannot be calculated as they do not report nor present individual event parameters (only the values binned into the histogram are given). Thus we compare the entire t_E distribution to `PopSyCLE`, and in particular the "peak" of the t_E distribution ($t_{E,peak}$), defined as the location of the maximum of the t_E distribution when the individual timescales are binned *logarithmically*. The peak of a logarithmically binned distribution is not the best quantity to compare, and we advocate performing a fit to the t_E distribution instead. However, for the moment we use $t_{E,peak}$ as a proxy for some measure of central tendency (note that $t_{E,peak}$ does not correspond to the mean, median, nor mode of the t_E values).

From the efficiency-corrected t_E distributions presented in several papers, $t_{E,peak}$ is located around $15-20$ days (see Figure 13 of Sumi, Bennett, et al. (2013), Figure 17 of Wyrzykowski, Rynkiewicz, et al. (2015), and Figure 2 of M17). As can be seen in Figure 2.6.3, $t_{E,peak}$ from `PopSyCLE` falls in the lower end of that range.

2.7 Results

2.7.1 Milky Way Present-Day BH Mass Function

The BH present-day mass function (PDMF) encodes information about the BH IFMR and stellar IMF, and to a lesser degree the star formation history (SFH). It also provides information about BH binaries and their formation channel(s). With a sufficiently large sample of BH mass measurements from both LIGO (extragalactic) and microlensing (Galactic), the BH PDMF can be measured and the IFMR can be constrained.

We use `PopSyCLE` to generate the Milky Way BH PDMF which is shown in Figure 2.7.1. The R18 IFMR clearly shows the "mass gap", as the lowest mass BH is around $5M_\odot$, which is greater than the largest possible NS mass $M_{NS,max} \sim 2-3M_\odot$ (Özel and Freire (2016), but also see Margalit et al. (2017) which suggests an upper limit closer to $\sim 2.2M_\odot$). As

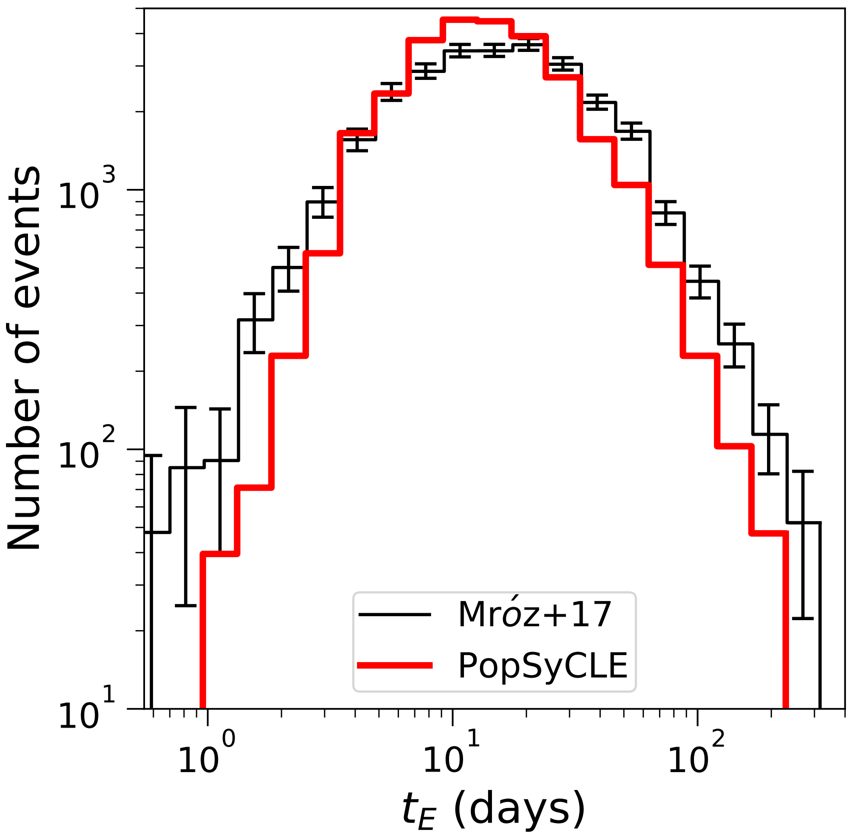

Figure 2.4: The t_E distribution in black comes from Figure 2 of M17. Overplotted in red is the Mock Mróz17 `PopSyCLE` simulation, scaled such that the number of events are the same.

discussed in Chapter 2.2.2.1, there are no $\gtrsim 30 M_\odot$ black holes as the R18 IFMR assumes only solar metallicity progenitor stars and `PopSyCLE` currently implements only single BHs. For the Milky Way, the SFH (according to the Besançon model) does not influence the BH PDMF very much, as most stars are over 10^9 years old. The minimum ZAMS mass for a star to form a black hole is $\sim 15 M_\odot$, and the corresponding main-sequence lifetime of such a star is $\sim 10^7$ years. Thus, the vast majority of BHs produced when their progenitor star dies will have already been formed.

The R18 IFMR also produces structures such as peaks and gaps in the BH PDMF. The spike around $6 M_\odot$ is due to a combination of stars with ZAMS masses between $15 - 20 M_\odot$ and $70 - 120 M_\odot$. Although there are more stars of lower ZAMS masses due to the IMF, only 34% of stars within $15 - 20 M_\odot$ form BHs, while 60% of the $> 70 M_\odot$ stars form BHs. The paucity around $10 M_\odot$ is due to the fact that most stars between $25 - 27 M_\odot$ form NS

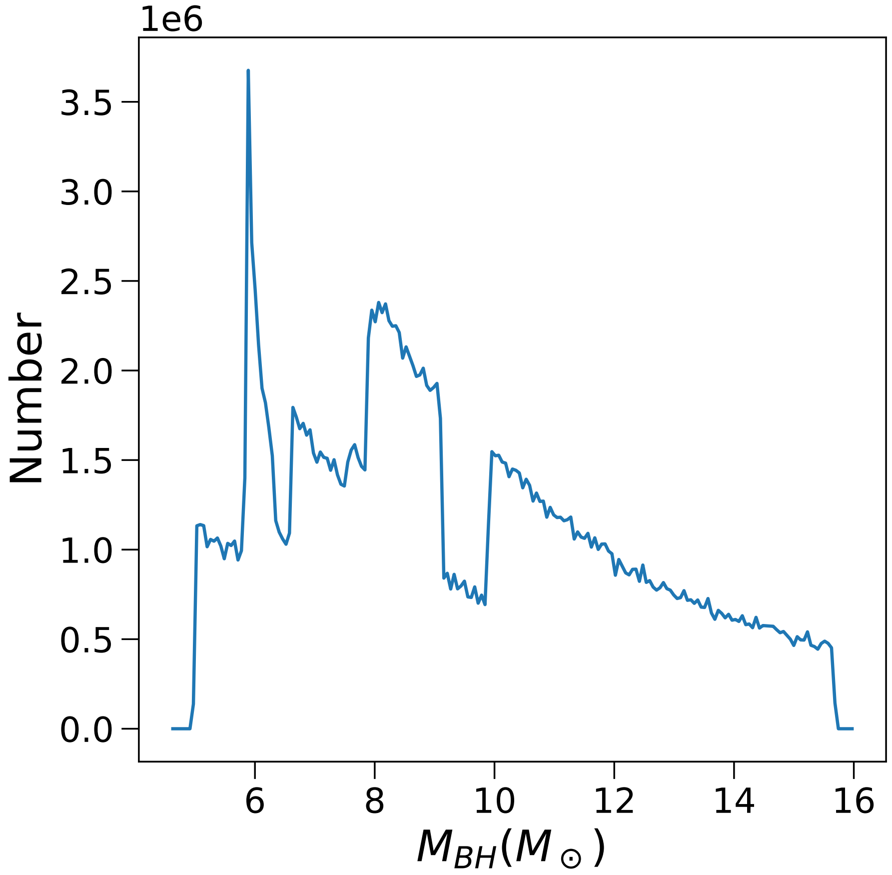

Figure 2.5: The Milky Way BH present-day mass function. The description of BH population synthesis used to produce this distribution is described in Chapter 2.6.1. Note that this is the theoretical underlying distribution for the *entire* Milky Way, not just those observable via microlensing; no observational constraints or limitations have been taken into account. The BH IFMR comes from R18.

and not BHs. The general decrease in number of BHs greater than $8M_\odot$ is simply due to the IMF; high mass stars are rarer. These trends are shown visually in Figure 2.7.1, which combines the IFMR with the IMF and SFH. We re-emphasize that this structure is specific to the R18 IFMR; a different IFMR will produce a different BH PDMF. However, with this assumption, the structure in the BH PDMF may be detectable with a sample of ~100 BHs. This will become a possiblity with *WFIRST*, as discussed in Chapter 2.7.5.

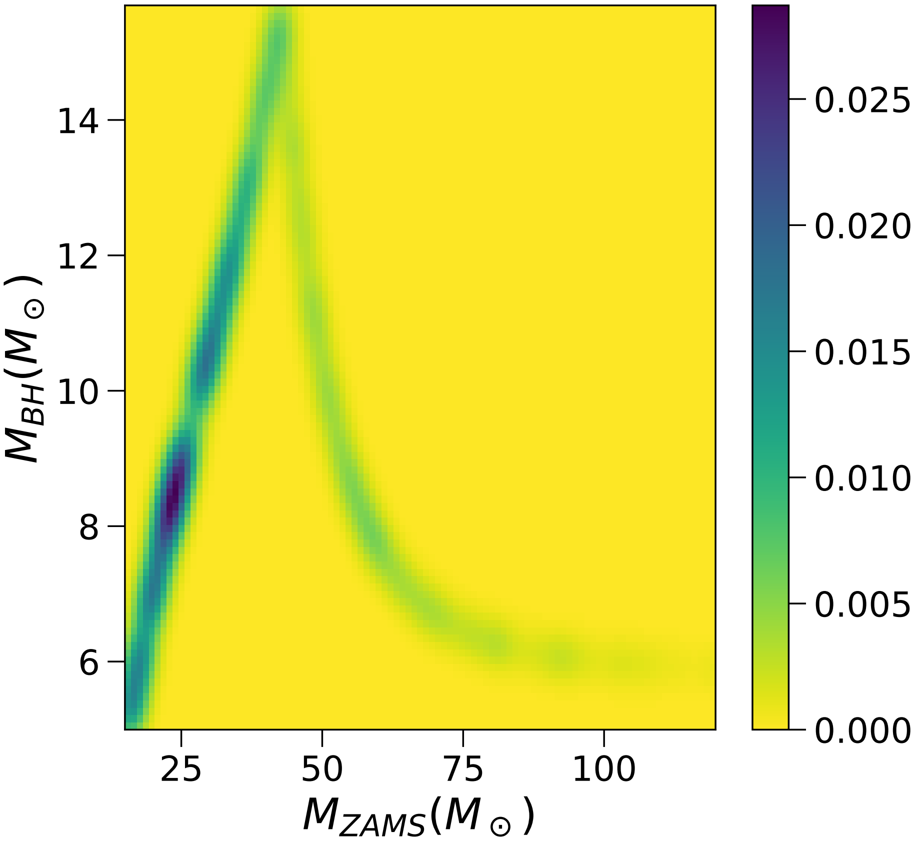

Figure 2.6: The black hole initial-final mass relation (BH IFMR), with the colorbar indicating the density of Milky Way stars at that part of the IFMR. For example, there is an overall trend where there are many more lower mass progenitors; this is mainly due to the IMF. However within that overall framework, there is more structure, which comes from the fact that some of the progenitor stars will form NSs and not BHs. The BH IFMR provides a mapping between the ZAMS mass of a star and the mass of the BH it forms, assuming it forms a BH and not a neutron star. It is described by a piecewise function (Equation 2.19, with ejection fraction $f_{ej} = 0.9$). This value of f_{ej} was selected as it most closely reproduced the observed distribution of black hole masses (R18).

2.7.2 Measuring Black Holes Masses with Individual Astrometric Follow-up

Identifying a BH with microlensing requires showing that the lens mass exceeds $5M_\odot$ and is not luminous. Since $5M_\odot$ stars are extremely bright, it is relatively easy to rule out massive stellar lenses once a lens mass is in hand. However, as described in Chapter 2.4.2, photometric microlensing alone is not sufficient to determine the mass of the lens in a microlensing event; astrometry is also needed to break degeneracies between lens mass and source and lens distances. Thus, data from a photometric survey must be combined with astrometric follow-up of a smaller set of BH candidates. As an example, we investigate the strategy of Lu et al. (2016) of selecting astrometric follow-up candidates with long Einstein crossing times $t_E \gtrsim 120$ days, high magnification $A_{max} \gtrsim 10 \equiv u_0 \lesssim 0.1$, and high source flux fraction $b_{SFF} \approx 1$ from photometric surveys updates such as the OGLE EWS (described in Chapter 2.5).

2.7.2.1 Selecting BH Candidates with OGLE

Out of all the Mock EWS events, ∼1% of them have a BH lens. This is consistent with the fraction of BH lensing events in the unfiltered `PopSyCLE` event candidates list as well. While BHs make up $\lesssim$0.1% of objects in the Milky Way by number, their lensing rate is enhanced by their ∼10× larger Einstein radius. Thus, the observational selection criteria of the OGLE survey does not dramatically change the probability of detecting BH lensing events. In Figure 2.7, the various types of lenses contributing to the t_E distribution is shown, which is comparable to the efficiency-corrected t_E curves produced by surveys. Figure 2.7.2.1 shows roughly the number of candidates that can be followed up based on EWS photometry per season. Although there usually are nearly 100 events with $t_E > 120$ days, often only 10 or so of those have sufficiently high SNR data and good coverage of the event, which are necessary later when trying to fit the event and extract the microlensing parameters t_E and π_E.

Selecting Mock EWS events with $t_E > 120$ days increases the probability of the lens being a BH to 40% (Figure 2.9). Note that a different Galactic model can increased this fraction by up to a factor of two (see Chapter 2.10). We then explored two additional selection criteria in addition to long events.

First, we tried selecting on events from `PopSyCLE` simulations with $b_{SFF} \approx 1$. Intuitively, one would expect a source to be less blended with a BH lens than with a stellar lens, as the BH does not contribute any flux. However, for ground based surveys the seeing disk is so large that many background stars fall within the disk, and whether the lens is luminous or not does not significantly change b_{SFF}. In principle, additional high-resolution imaging from space or ground-based telescopes with adaptive optics provides a much smaller seeing disk, reducing contamination from neighboring stars. This would then circumvent the aforementioned problem, meaning BH lensing events would truly have a high b_{SFF}. However, this strategy fails, as OGLE microlensing events are observationally biased toward brighter sources and the average lens is quite faint ($I \sim 26$). Thus, the distribution of b_{SFF} for BH and stellar lenses are similar in a sample limited to I$\lesssim$ 21.

Similarly, selecting events with small u_0 does not increase the probability of finding a BH lens. Although the average BH is more massive than the average star and thus has a larger θ_E, it does not have a correspondingly smaller u_0, as u_0 is independent of mass.

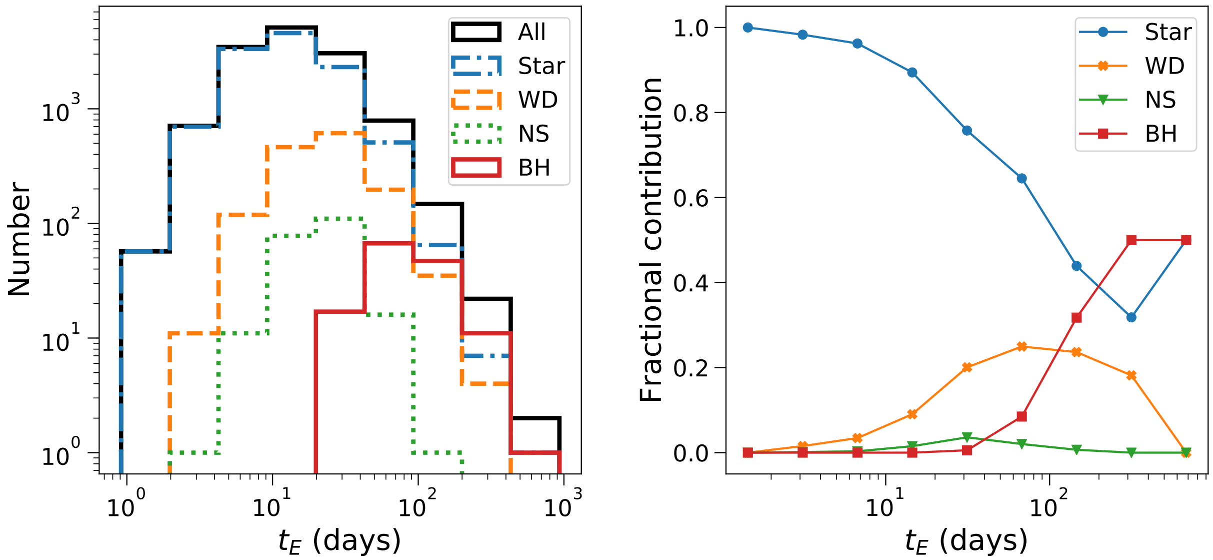

Figure 2.7: *Left:* t_E distribution from the Mock EWS simulation, showing the different contributions due to different components. *Right:* The fractional contribution from each type of object type at different t_E times. Note that the NS and BH contributions can be shifted to different t_E depending on the adopted kick velocities. Also note that many of these events would be difficult to detect as they have parameters with low detection efficiency; however, it serves to illustrate the underlying contributions to the t_E distribution.

2.7.2.2 Individual Candidate Follow-up

As our ultimate goal is to measure the number of BHs in the Milky Way, we now consider how many BHs can be expected to be detected via astrometric follow-up. We estimate that ∼12 BH candidates (corresponding to 5 expected BH detections) are required to constrain the total number of BHs in the Milky Way to 50 percent, assuming Poisson statistics (Figure 2.7.2.2). With an astrometric follow-up program, due to practicalities such as limited telescope time on facilities able to perform such measurements, $3-4$ candidates can be observed each year and the probability of the candidate being a BH is ∼40%; thus about $1-2$ BHs per year can be expected to be detected. Over 5 years, this would result in a total of $5-10$ BHs. However, the BH PDMF would be difficult to constrain based on current sample sizes and sporadic astrometric follow-up, due to the inefficiency of the process. Dedicated astrometric surveys are needed to place useful constraints on the BH PDMF.

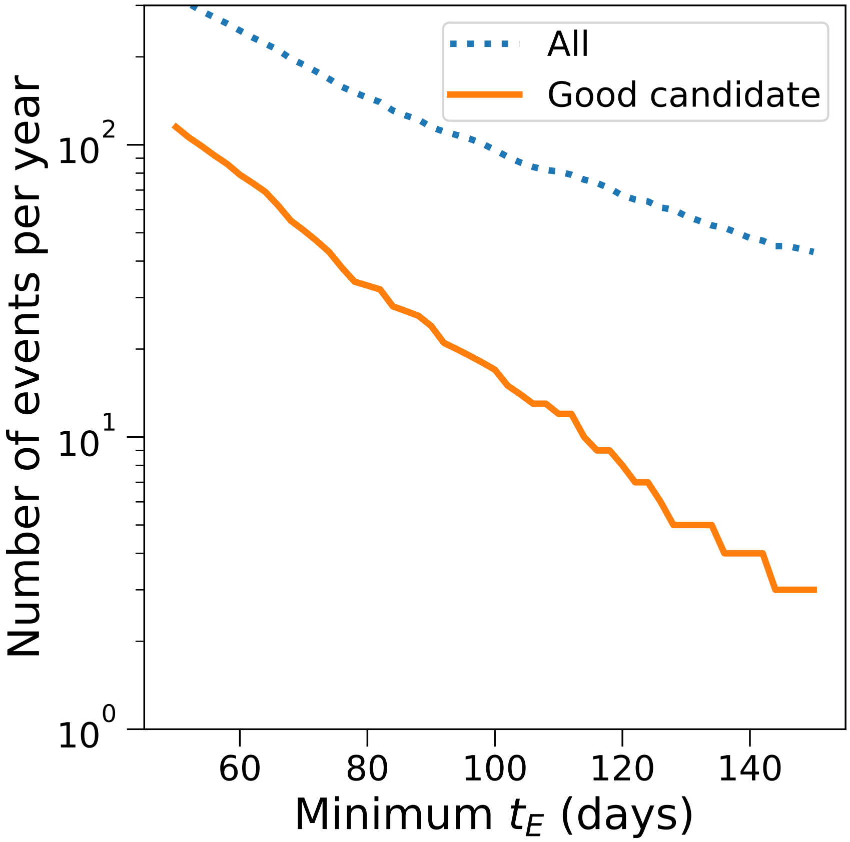

Figure 2.8: Number of events per season from the OGLE Early Warning System that have t_E larger than some minimum value (dotted blue line). However, even events with $t_E > 120$ days are not necessarily good follow-up candidates, as they may not have sufficient coverage of the photometric peak or insufficient SNR. Thus, good candidates have 1) $\pm 0.5 t_E$ coverage of the peak, 2) $I_{base} < 19.5$ mag, 3) $\Delta I > 0.5$ mag (orange line). The numbers plotted are the averages over the 2016, 2017, and 2018 seasons reported on the OGLE EWS website.

2.7.3 Confirming BH Lenses with Astrometry and Microlensing Parallax

BH candidates identified from photometric microlensing surveys can be followed up with high-precision astrometric measurements in order to measure the astrometric microlensing shift, $\delta_{c,max}$. When combined with t_E, π_E, and u_0 from the photometric light-curve, the astrometric shift yields a constraint on the lens mass. In Figures 2.7.3 and 2.7.3, microlensing events are plotted in $\delta_{c,max} - \pi_E$ space. In Figures 2.7.3 and 2.7.3 the microlensing events are plotted in $\pi_E - t_E$ and $\delta_{c,max} - t_E$ space, respectively. We note that blending due to

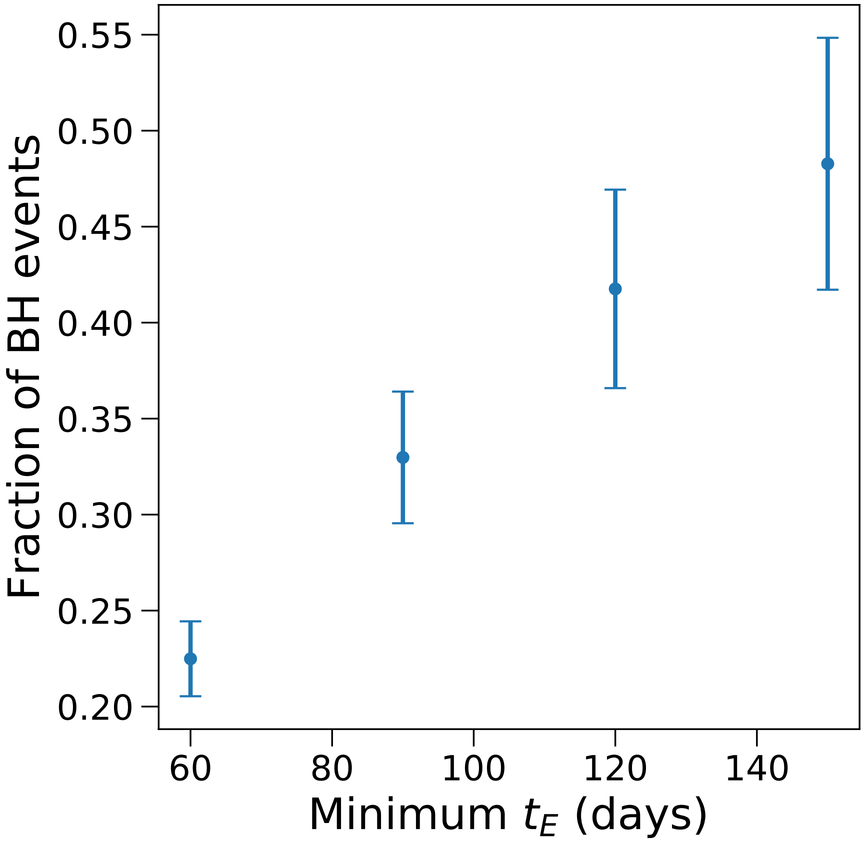

Figure 2.9: Fraction of long-duration Mock EWS events from `PopSyCLE` that have BH lenses. $t_E > 120$ day selections are still recommended for maximizing the probability of finding a BH lens.

the lens (if it is luminous) is incorporated into the astrometric shift calculations, assuming a $\sim$100 mas aperture size that is roughly equivalent to infrared imaging with JWST or with an $8-10$ meter telescope and an adaptive optics system. BHs occupy a very particular region in $\delta_{c,max} - \pi_E$ space (large $\delta_{c,max}$ and small π_E) as they are massive. Although both a massive luminous stellar lens and equally massive black hole will have equal Einstein radii, all else equal, the astrometric shift will be larger for the BH, as it do not blend with the source images (see Equation 2.10 vs. Equation 2.11).

The very sharp delineation between the stars, WDs, NSs, and BHs in Figure 2.7.3 can be simply explained. Consider a lens of mass M. Using Equations 2.3, 2.14, 2.15, and the

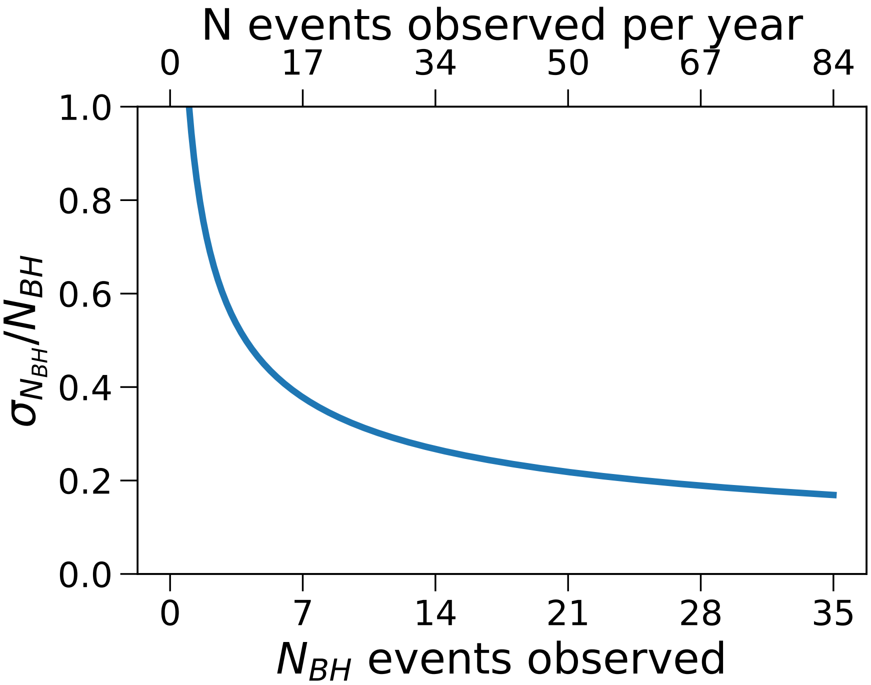

Figure 2.10: Number of BH candidates needed to constrain the total number of BHs in the Milky Way to some uncertainty (top horizontal axis), assuming Poisson uncertainty. The number of actual BHs resulting from the sample of candidates is the bottom horizontal axis. This assumes we have selected candidates from long-duration ($t_E > 120$ days) OGLE EWS following the strategy outlined in Chapter 2.7.2.1.

definition of κ given in Chapter 2.4.2, the microlens parallax will simply be

$$\pi_E = \sqrt{\frac{\pi_{rel}}{\kappa M}}. \tag{2.17}$$

Assuming an impact parameter of $u_0 \leq \sqrt{2}$, the maximum astrometric shift, assuming no blending, can be then written

$$\delta_{c,max} = \sqrt{\frac{\kappa M \pi_{rel}}{8}} \tag{2.18}$$

by combining Equations 2.3, 2.10, and 2.15. Thus, for a given mass M, both π_E and $\delta_{c,max}$ scale as $\sqrt{\pi_{rel}}$. Hence, when plotting $\delta_{c,max}$ against π_E for a given mass lens, the slope is 1. Since `PopSyCLE` currently assumes that all NSs are of the same mass, they lie artificially on a straight line. Similarly, as there exists a minimum mass for BHs, WDs, and stars, there is a hard edge on the right diagonal side of those populations. There is some downward scatter

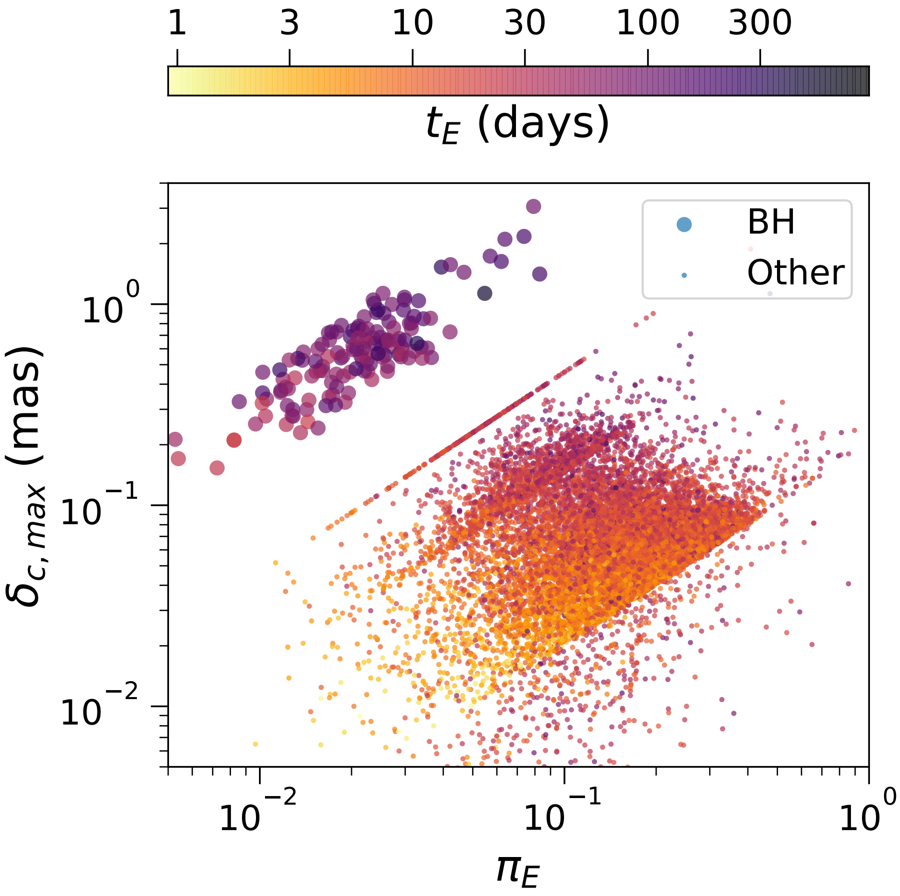

Figure 2.11: The maximum astrometric shift $\delta_{c,max}$ vs. the microlensing parallax π_E, with the color of the point indicating the Einstein crossing time t_E of the event. We include blending between the lens and source when calculating $\delta_{c,max}$. The BHs (*large points*) are easily seperable in this space. The points correspond to microlensing events from the Mock EWS simulation.

in $\delta_{c,max}$ due to some events with $\sqrt{2} < u_0 < 2$, as the maximum astrometric shift is less than what would be given in Equation 2.18. Additionally when blending is included, $\delta_{c,max}$ scatters lower for some stars, depending on the lens luminosity. The larger scatter from the slope of 1 in the BH, WD, and stellar populations are simply due to the fact that there are a range of masses.

Equations 2.17 and 2.18 can also be used to understand the t_E gradient stretching from the bottom right (large π_E, small $\delta_{c,max}$) to the top left (small π_E, large $\delta_{c,max}$) shown in Figure 2.7.3. Since t_E scales with the square root of the lens mass, heavier lenses will have smaller π_E, larger $\delta_{c,max}$, and longer t_E, on average. Scatter in this relation is due to the

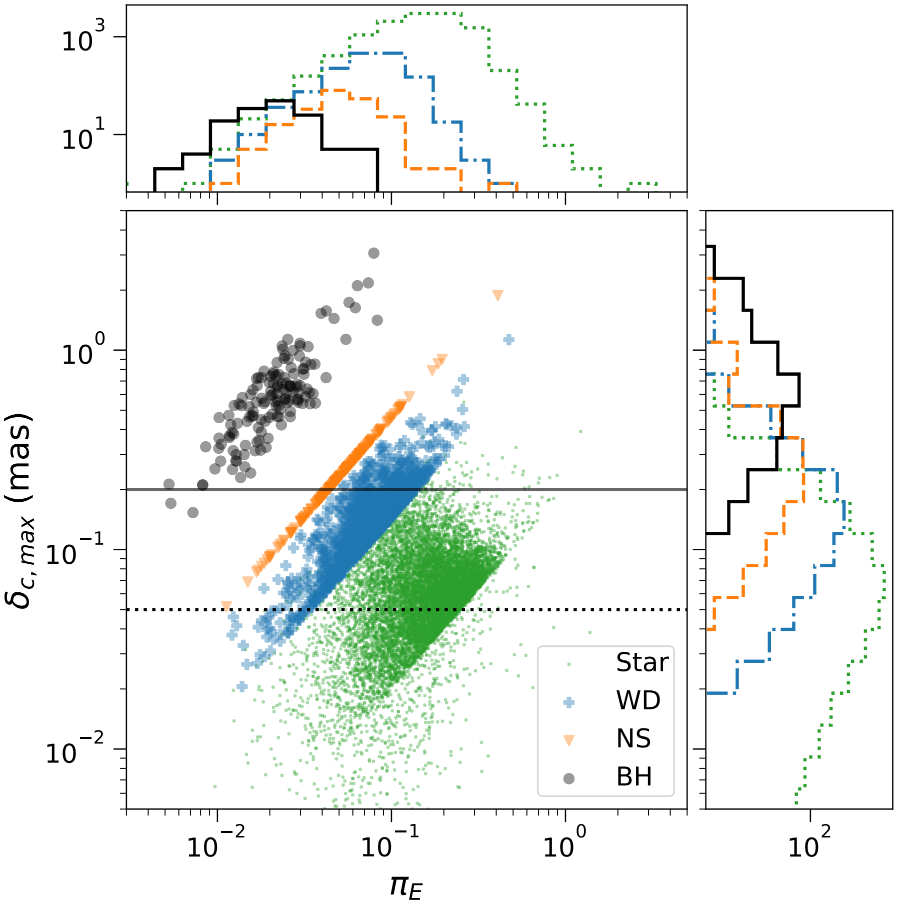

Figure 2.12: The maximum astrometric shift $\delta_{c,max}$ vs. the microlensing parallax π_E for different lens types. Blending between the lens and source is included when calculating $\delta_{c,max}$. The solid line denotes the current astrometric precision (~ 0.2 mas, using the Keck laser guide star adaptive optics system). The dotted line denotes anticipated astrometric precision achievable in the next decade (~ 0.05 mas, using *WFIRST* or the Thirty Meter Telescope). The points correspond to microlensing events in the Mock EWS simulation.

fact that t_E is also degenerate with the relative source-lens proper motion μ_{rel}.

2.7.4 Statistical Samples of Black Holes from Photometry Alone

The microlensing parallax π_E combined with a measurement of the Einstein crossing time t_E appears to be a powerful means of picking out BHs (Figure 2.7.3). Unfortunately, π_E can only be observed significantly after the photometric peak, and thus cannot be used as a BH-candidate selection criteria for astrometric follow-up. However, the combination of π_E

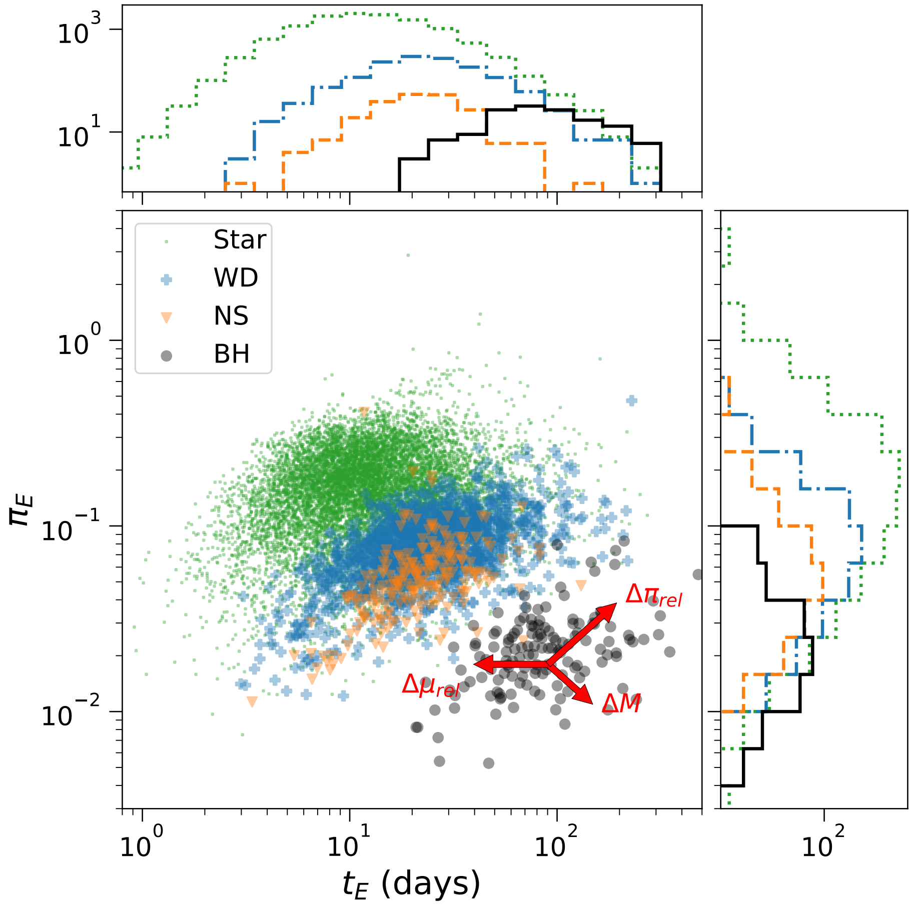

Figure 2.13: The microlensing parallax π_E vs. the Einstein crossing time t_E. The points correspond to microlensing events in the Mock EWS simulation. The red arrows correspond to the effects of changing π_{rel}, μ_{rel}, and M. Consider the fiducial parameters $d_L = 6.89\,\text{kpc}$, $d_S = 8.62\,\text{kpc}$, $\mu_{rel} = 6.55\,\text{mas/yr}$, and $M = 11.12 M_\odot$; this corresponds to $t_E = 90.50$ days and $\pi_E = 0.018$. If the lens mass M is increased to $30 M_\odot$ and all other parameters are held fixed, then $t_E = 148.64\,\text{days}$ and $\pi_E = 0.011$. If the relative proper motion μ_{rel} is increased to 15 mas/yr and all other parameters are held fixed, then $t_E = 39.53\,\text{days}$ and π_E does not change. If the relative parallax π_{rel} is increased from $0.029\,\text{mas}$ to $0.13\,\text{mas}$ by changing d_L to $4\,\text{kpc}$ and all other parameters are held fixed, then $t_E = 193.93\,\text{days}$ and $\pi_E = 0.039$.

and t_E can still be used to obtain a sample of microlensing events with a very high fraction of BH lenses, as compared to looking at t_E alone. By selecting events with both $t_E > 120\,\text{days}$ and a microlensing parallax of $\pi_E < 0.08$, the detection rate of BHs is $\sim 85\%$; by using an even lower value of π_E, the minimum value of t_E could be shifted to lower values and still preserve the high fraction of BHs. This has the additional advantage that t_E and π_E

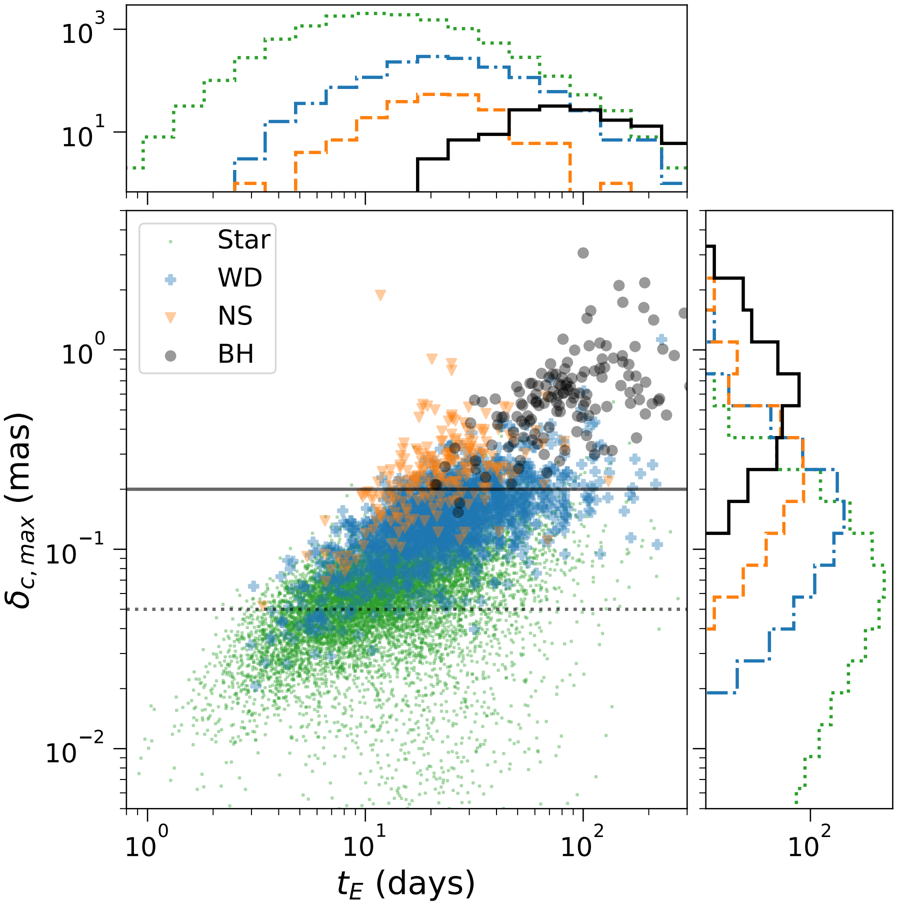

Figure 2.14: The maximum astrometric shift $\delta_{c,max}$ vs. the Einstein crossing time t_E. We assume blending between the lens and source when calculating $\delta_{c,max}$. The solid line denotes the achievable astrometric precision of ~ 0.2 mas using the Keck laser guide star adaptive optics system (Lu et al. 2016). The dotted line denotes anticipated astrometric precision achievable in the next decade (e.g., ~ 0.05 mas, using *WFIRST* or the Thirty Meter Telescope). The points correspond to microlensing events in the Mock EWS simulation.

are quantities that can be fit from photometry alone. Thus, with a set of photometric light curves, events can be sorted into BH and non-BH lenses with high statistical confidence.

This method is only useful if the π_E distribution does not vary dramatically as the Galactic model changes. It is not entirely clear how distinct this separation will be if different assumptions are made about the underlying distributions of M, d_L, d_S, and μ_{rel}. We evaluate the impact on the $\pi_E - t_E$ space by using the scaling relations,

$$t_E \propto \frac{\sqrt{\pi_{rel} M}}{\mu_{rel}}$$
$$\pi_E \propto \sqrt{\frac{\pi_{rel}}{M}}.$$

as illustrated in the arrows on Figure 2.7.3.

Of all the populations in `PopSyCLE`, the most uncertainty lies in the BH spatial positions, velocities, and masses. We consider the effects of changing these parameters. The following trends are illustrated with specific values in Figure 2.7.3.

- Our BH mass distribution ranges from $5M_\odot$ to 16 $M_\odot$; by including more high-mass BHs such as the ones discovered by LIGO into the distribution, the BH population would shift toward longer t_E and smaller π_E.
- The kick velocities of BHs at birth, if there are any, is unknown. Changes in kick velocity are manifested in changes in μ_{rel}. If μ_{rel} increases (holding d_L and d_S fixed) t_E becomes shorter.
- The spatial distribution of BHs is also not known. Two extremes could be considered: a centrally concentrated population of BHs in the bulge, or a distribution spread throughout the stellar or dark matter halo. Bulge lenses have smaller π_{rel}, while disk lenses have a larger π_{rel}. Thus, having only BH bulge lenses would cause the average π_{rel} to decrease, causing both π_E and t_E to decrease. On the other hand, with a non-centrally concentrated distribution of BHs, this would cause more lenses to fall closer to Earth, meaning the average d_L to decrease and thus π_{rel} would increase, causing π_E and t_E to increase.

Although this method of selecting BH lenses does not allow for direct confirmation nor mass measurement, it does allow for a statistical analysis of BH lensing events. For example, the number of BHs in the Milky Way could be constrained; their masses could also be estimated by invoking some type of Galactic model, as is commonly done. It's strength is that no additional data is necessary and the improved BH selection process can still lead to improved physical constraints.

The challenge associated with this method is constraining π_E accurately down to the level which is necessary for this measurement. However, with high cadence observations and high photometric precision this is possible.

2.7.5 BH Hunting with *WFIRST*

Lastly, we consider future microlensing surveys and the prospects they hold for measuring BH masses. As described in Chapter 2.5, the *WFIRST* mission includes a microlensing survey designed for exoplanet detections. Some primary differences between the OGLE and

WFIRST surveys will be their filters, sensitivity, and resolution (seeing limited $I \lesssim 22$ vs. diffraction limited $H \lesssim 26$, respectively). An additional important difference is that with *WFIRST*, the astrometry will be obtained at the same time as the photometry. Thus, it is not necessary to do individual follow-up of candidate BH events; all the information will be contained within the *WFIRST* survey data. Simultaneous astrometry also has the advantage that it is possible to go "back in time" to look at astrometric data from before the photometric peak (i.e. before the microlensing event is recognized photometrically).

P19 presents thorough simulations and a detailed analysis to calculate the expected yield of bound planet detections with *WFIRST* microlensing. We present here a complementary analysis with `PopSyCLE` to determine the number of BHs we may expect a *WFIRST*-like survey to find. Detailed simulations of different season distributions and understanding how the BH yield changes is beyond the scope of this chapter and is left as future work. However our continuous 1000 day survey simulation with Mock WFIRST parameters (Table 2.4) is a good order-of-magnitude estimation, considering the other uncertainties in the `PopSyCLE` simulation and the *WFIRST* survey design itself.

To normalize the Mock WFIRST survey area to that of the actual *WFIRST* microlensing survey, the number of events is multiplied by the ratio of the areas (a factor of 1.93). Microlensing events from the Mock WFIRST simulation with BH lenses and an Einstein crossing time of $90 < t_E < 300$ days are defined to have "measureable" BH masses. Note that there will certainly be many BH microlensing events with t_E that fall above or below this range; however, we do not consider those to have measureable masses, for the following reason. As described in Chapter 2.4.2, in addition to the photometric brightening, it is necessary to measure the astrometric shift and microlensing parallax to constrain the lens mass. The choice for the lower bound on t_E takes into the consideration that an event needs to have a somewhat long duration ($t_E \gtrsim 3$ months) to have a potentially measureable microlensing parallax π_E. The choice for the upper bound on t_E takes into consideration that the astrometric signal falls off much more slowly than the photometric signal; a rough guess is that to measure $\delta_{c,max}$ requires astrometric data for $\sim 5 - 10 t_E$. Note the amount of astrometric data required also is dependent on when the astrometric measurements occur. To properly determine this requires detailed simulation (e.g., Chapter 8 of Lu et al. (2016)) and is beyond the scope of this chapter .

With this definition, the `PopSyCLE` Mock WFIRST survey produces ~ 1000 BH lensing events with measureable masses, nearly 100 times more than with an individual astrometric follow-up program, as estimated in Chapter 2.7.2.2. With this number of mass measurements, we can constrain the present-day BH mass function (Figure 2.7.5) and the results of supernova simulations.

A major source of uncertainty in this estimate is due to the Galactic model, in both the stellar and compact object components. As described in Chapter 2.10, we consider two different angles ($\alpha = 11.1^\circ$ and $\alpha = 28^\circ$) for the Galactic bar/bulge; this modification significantly changes the number of stars along a given line of sight. The more tilted bar with $\alpha = 11.1^\circ$ produces $4-5$ times less microlensing event candidates than the less tilted bar with $\alpha = 28^\circ$. By applying the Mock WFIRST criterion to the six fields in Table 2.7, the

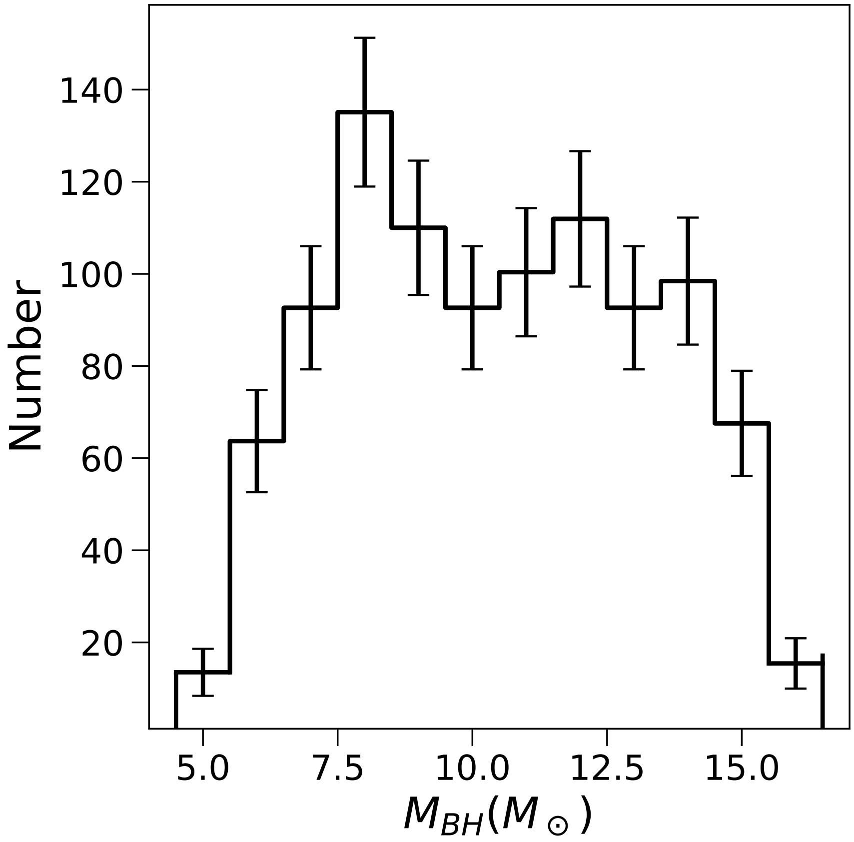

Figure 2.15: Histogram of the BH masses that are measurable from the Mock WFIRST BH simulation, scaled to match the area of the actual *WFIRST* survey. To infer the underlying BH PDMF, an observational completeness correction will be required in order to account for the astrometric bias towards heavier lenses. `PopSyCLE` is ideally suited for forward modeling populations, including completeness corrections.

number of events with measureable BH masses is decreased by a factor of about 4. To take into account these uncertainties, we estimate the number of BHs with measureable masses is $\mathcal{O}(100 - 1000)$.

2.8 Discussion

2.8.1 Comparison with other simulations

2.8.1.1 Microlensing Simulations

Here we discuss several other recent microlensing simulations and compare them to `PopSyCLE`. Kerins et al. (2009) generated synthetic maps of the microlensing optical depth, event rate, and average Einstein crossing time of the Galactic bulge, incorporating a 3-D extinction map. The `GULLS` code of Penny, Kerins, et al. (2013) and Penny, Gaudi, et al. (2019) improved upon this work by taking into account the effects of blending, while the MaBμLS code of Awiphan et al. (2016) also included low-mass stars and brown dwarfs. All three of these simulations follow a similar method, as summarized in P19, of drawing sources and lenses from a distribution described by the Besançon model, then assigning weights proportional that source-lens pair's contribution to the total event rate along that sight line. A constant correction factor to adjust for the number of sources and optical depth of the Galactic bulge as derived from the Besançon model is also included to adjust the normalization of the event rate. The Besançon models used includes white dwarfs; however, neutron stars and black holes are not part of the models.

In particular, the `GULLS` code has been applied toward exoplanet microlensing survey designs for the *Euclid* and *WFIRST* missions. Toward this end, it models single planets orbiting a single host star. Properties of the detector and filters are included in the simulation, and `GULLS` can also generate images and light curves which includes Gaussian noise. Planetary detections were then evaluated on a $\Delta\chi^2$ criterion as is commonly done in other exoplanetary microlensing surveys and simulations. However, there are discrepancies between the simulation and observed event rates, as there is substantial uncertainty in the Galactic models used. As one of the purposes of `GULLS` is to estimate yields for microlensing survey missions, the results are rescaled by a factor to match observed star counts and optical depth (Penny, Kerins, et al. 2013) or star counts and event rates (P19).

In comparison, `PopSyCLE` is designed to understand how changes in the stellar and compact object population and imposition of observational selection criteria modify the underlying and observed microlensing event distribution. It is modular in design to allow different initial-final mass relations, dust maps, observational cuts, etc. to be used. `PopSyCLE` is also unique in its emphasis for studying lensing by massive compact objects, specifically black holes, and its calculation of not just photometric, but also astrometric microlensing quantities. The current version of `PopSyCLE` is not designed to generate light curves including complexities such as detector noise or atmospheric seeing, nor is it designed/optimized to probe the short-t_E end of the distribution, as we are interested in the long-t_E events. Like `GULLS`, `PopSyCLE` also has a discrepancy in the event rates as compared to observations. However, we choose to not rescale our event rates to match observation. Although this might limit `PopSyCLE`'s predictive power, we consider the discrepancies to clearly indicate limitations in our understanding of the physics of the simulations, corrections to our data, or both (e.g., Section 5.1 of Awiphan et al. (2016)). For this reason we present our *WFIRST* BH yield as an order-of-magnitude estimate. However, the `PopSyCLE` simulation results are available for download and can be rescaled as desired for survey yield predictions.

2.8.1.2 Compact Object Population Synthesis

There are several other compact object population synthesis packages. For example, a widely used package is the Stellar EVolution N-body (`SEVN`) code[6], which combines a single stellar evolution code along with several core-collapse supernovae models, pair-instability and pair-instability pulsational supernovae, along with many different binary evolution recipes (Spera et al. 2015). We note `SEVN` is purely a population synthesis model, that can (and has) been interfaced with N-body stellar dynamics codes, to study interactions in star clusters, for instance. It does not include a full model of the Milky Way, nor microlensing. One thing to note is that the IFMRs in `SEVN` are heavily simplified analytic models that do not incorporate explosion physics. Ultimately, it would still be worth adding support for `SEVN` inside `PopSyCLE` in addition to the current `PyPopStar` stellar evolution code; however, we chose `PyPopStar` initially due to its support for a larger range of models, flexibility, and Python implementation.

2.8.2 Comparison with on-sky microlensing surveys

We advocate for defining a microlensing event using quantities that are directly observable/measured rather than fit. This is described in Dominik (2009) as a reparametrization when fitting microlensing events. For example, in the survey papers discussed, cuts were made on events whose source magnitude, m_S is fainter than some value, where m_S is generally set by the magnitude limit of the telescope and camera. However, the more easily observed quantity is the baseline magnitude m_{base} since m_S is generally a parameter derived from fitting and is subject to degeneracy with other parameters (Dominik 2009). When fitting light curves, blending is degenerate with the observed timescale and peak magnification of the event, and if blending is not taken into account correctly the microlensing parameters derived will be incorrect; masses and timescales will be systematically underestimated (Di Stefano et al. 1995; Han 1999; Woźniak et al. 1997). In other words, events with small t_E, large u_0, and large b_{SFF} are degenerate with events with large t_E, small u_0, and small b_{SFF} (Sumi, Kamiya, et al. 2011). In order to facilitate easier comparison between simulations and observations and explore this degeneracy, we recommend that future microlensing analyses adopt cuts using observable quantities, as advocated for in Dominik (2009). However, we also suggest that such observational cuts be applied for sample selection, as these are more easily reproduced and are less dependent on differences in fitting codes and prior assumptions.

Additionally, although the mean Einstein crossing time $\langle t_E \rangle$ is the most commonly reported parameter by surveys, the t_E distribution is asymmetric in linear t_E bins[7]; thus, the

---

[6] http://web.pd.astro.it/mapelli/group.html

[7] t_E is often plotted in bins of $\log t_E$ which makes the distribution look more symmetric.

mean is easily skewed and depends on the range of t_E used to estimate the mean. For future comparisons across observational surveys and simulations, the median is a better choice and is less impacted by particular cuts. It is also important to note the range of t_E over which the distribution is made (e.g., as in Sumi, Bennett, et al. (2013)).

2.8.3 Hunting for BHs

Over the years, many types of follow-up observations have been proposed and used to constrain lens properties. Agol, Kamionkowski, et al. (2002) proposed to constrain lens masses of BH microlensing candidates by searching for their X-ray emission due to accretion from the interstellar medium or stellar winds. Nucita, De Paolis, Ingrosso, Elia, et al. (2006) and Maeda et al. (2005) used *XMM-Newton* and *Chandra* observations, respectively, to search for X-rays from the extremely long-duration BH candidates MACHO-96-BLG-5 (Mao, Smith, et al. 2002); however, no significant detections were made.

HST high-resolution imaging follow-up of BH candidates has also been used to measure the degree of blending (Bennett, Becker, et al. 2002). As discussed in Chapter 2.7.2.1, this is not particularly useful for selecting photometric candidates for astrometric follow-up; however, it still may be a useful means of confirming that the lens is not a massive star. Poindexter et al. (2005) also suggested that *HST* observations could be used to measure the source proper motion; however they note that many degeneracies remain even with this measurement. High-resolution images can be taken many years after an event, when it may be possible to resolve the source and lens (Alcock, Allsman, Alves, Axelrod, Becker, Bennett, Cook, Drake, et al. 2001; Batista et al. 2015; Bennett, Bhattacharya, et al. 2015, Abdurrahman et al. in prep.) and the absence of a lens may provide additional confirmation of a BH.

For nearby sources, it is sometimes also possible to measure the source distance via parallax, which would give complete event parameters. The combination of photometry and astrometry is powerful not only for BH lenses, but also for obtaining precise mass measurements of any type of lens, as was shown with the first astrometric microlensing signal detected outside our Solar System (Sahu, Anderson, Casertano, Bond, Bergeron, et al. 2017). Another method of breaking degeneracies is to have the ability to resolve the images themselves, which is possible for stellar-mass lenses using interferometric techniques (Dong et al. 2019).

We have not yet considered the number of BHs detectable with the *Gaia* satellite, an astrometric space mission which has been operating since 2013 (Gaia Collaboration, Prusti, et al. 2016). Although *Gaia* has incredible astrometric precision for parallax measurement (down to ~ 10 μas for some stars by the end of the mission), it does not perform as well for single-epoch astrometric measurements in the bulge due to the decreased observing cadence as well as significant stellar crowding ($> 1\,$mas, Rybicki et al. (2018)). Additionally, *Gaia* observes at green optical wavelengths, which cannot probe dusty, high extinction regions like the bulge. However, there are estimates of the number of BHs that *Gaia* will be able to detect over it's lifetime. Mashian et al. (2017) estimated that $\sim 2 \times 10^5$ BHs in astrometric binary systems can be detected over *Gaia*'s 5 year mission; however, this is a severe overestimate, as this calculation has neglected extinction and crowding effects. Rybicki et al. (2018) estimated that a few isolated stellar mass BHs should be detectable astrometrically at the end of the *Gaia* mission. Wyrzykowski and Mandel (2019) used *Gaia* DR2 data to calculate distances and proper motions for sources in OGLE-III microlensing events from 2001 to 2009, providing additional information to perform a more careful reanalysis of the lens masses to determine whether they could be BHs.

In Chapter 2.7, two different methods to better understand BHs in the Milky Way are discussed. The first involves using a combination of astrometry and photometry to measure t_E, π_E, and $\delta_{c,max}$, which allows lens masses to be measured for *individual* microlensing events. The second involves photometry only to measure t_E and π_E, enabling statistical constraints on a *population* of BHs. Although the BH nature of individual lenses cannot be confirmed, ensemble information can still be gleaned. To obtain masses with the second method would involve assuming some type of Galactic model or spatial distribution. It is interesting to note that searching for a small/undetectable parallax signal to identify BHs is the opposite of previous approaches in the literature (Drlica-Wagner et al. 2019; Poindexter et al. 2005; Wyrzykowski, Kostrzewa-Rutkowska, et al. 2016).

2.8.4 Future Work

In the next version of `PopSyCLE`, we plan to add support for stellar and compact object binary systems, compact object mergers, metallicity-dependent IFMRs, different compact object spatial distributions, and primordial BHs. This will allow for a more realistic simulation and a larger exploration of parameter space. The lack of these features at the present put some caveats on this work, which we discuss.

2.8.4.1 Binarity and Mergers

Although all of the comprehensive catalogs of microlensing events in the literature from which event rates and optical depths are calculated are only for events which can be fit by point source point lens (PSPL) models (Mróz, Udalski, Skowron, Poleski, et al. 2017; Sumi and Penny 2016; Wyrzykowski, Rynkiewicz, et al. 2015), it is estimated that that binary lenses will consist of around 10% of Galactic bulge stars lensing events (Mao and Paczynski 1991). It is difficult to ascertain the binary fraction from the observed distribution of microlensing events because binary lenses can produce light curves that resemble single lens events. For a widely separated binary, only one of the lenses might be lensing the source star, while for a closely separated binary, both lenses act as a single more massive lens. Moreover, the addition of another lens greatly increases the complexity and variety of light curve shapes, depending on how the source approaches and/or crosses the caustics, making binary lens events difficult to identify. Additionally there is the issue of binary source stars. Similar to binary lens events, binary source events can produce light curves that appear quite similar to PSPL events (Dominik 1998; Han and Jeong 1998), although these degeneracies can be broken by the addition of astrometric information (Nucita, De Paolis, Ingrosso, Giordano, et al. 2016).

`Galaxia` does not have support for binaries; however, most massive stars are in binary systems (Duchêne et al. 2013). Additionally, our current population synthesis method does not include compact object binaries (either compact-compact or compact-stellar). `PyPopStar` currently has a heuristic prescription for stellar multiplicity, where stars are taken from single-stellar evolution models and combined into multiple systems based on multiplicity fraction. However, this does not take into account the effect that mass exchange has on the evolution of stars in multiple systems. For main sequence stars, such effects are likely negligible; however, in the later stages of stellar evolution, binary evolution cannot be neglected. For a more rigorous treatment of stellar multiplicity, binary evolution models will be incorporated into `PyPopStar`. Additionally, future work on binary IFMRs will also be added to `PyPopStar`.

Adding support for binaries (stellar-stellar, compact-stellar, and compact-compact) into `PopSyCLE` would help us put further constraints on the number of BHs in the Milky Way and understand BH formation channels. For example, both single and binary BHs may form from binary star systems; single star systems can be formed when the stellar binary is disrupted or merges. If the binary is disrupted, this could impart large kick velocities to the BHs; the frequency at which disruption occurs depends on the assumptions made about the kicks (Wiktorowicz, Wyrzykowski, et al. (2019) and references therein). The spatial distribution will also be affected by disrupted binaries and the associated kicks; the scale height distribution of X-ray binaries can act as a proxy for different compact object formation mechanisms (Repetto, Igoshev, et al. 2017).

Another possibility for forming more massive stellar mass BHs is through the mergers of less massive BHs. By adjusting the merger rate and fraction, we can adjust the mass spectrum and fraction of BHs in single and binary systems. Adding support for compact-object mergers would allow us determine our ability to set constraints on the merger rate and fraction, which would again improve our understanding of BH formation channels and LIGO merger events.

2.8.4.2 Metallicity

When performing population synthesis, metallicity has not been taken into account. Although `Galaxia` and `PyPopStar` have metallicity support, the R18 IFMR does not. With the IFMR, metallicity can have a significant effect on the mass and type of the compact remnant. In particular, having $[Fe/H] > [Fe/H]_\odot$ will not particularly change the IFMR, while having $[Fe/H] < [Fe/H]_\odot$ will produce more high-mass black holes. New models to be used in the IFMR have been run to include a metallicity dependence (T. Sukhbold, private communication.) A non-mutually exclusive option would be to add other IFMRs that have a dependence on both the progenitor mass and metallicity, such as the one in Appendix C of Spera et al. (2015).

In `Galaxia`, the metallicity of the bulge population is centered at solar metallicity with a spread $\sigma_{[Fe/H]} = 0.4$ (Table 2, Sharma et al. (2011)), and with respect to the current iteration of `PopSyCLE`, about 80% of stars within 10 kpc of Earth in the bulge direction have $-0.5 <$ [Fe/H] < 0.5, where the IFMR likely does not change significantly. Thus, the solar-metallicity approximation is reasonable for the bulk statistics; the largest effect would be a slight deficit of higher-mass BHs.

2.8.4.3 Compact object distributions and kinematics

In `PopSyCLE`, it is assumed that the positions of the compact objects followed the stellar spatial distribution. Additionally, the velocity of the object is assumed to be the stellar progenitor velocity and kick velocity added together; however, this is only true at the time the compact object is born. This choice is roughly justified given that the number of objects leaving a region is the same as the number of objects entering that region, since the direction of the kick velocity is random. However, effects like dynamical friction might cause black holes to settle toward the Galactic Center. Conversely, supernovae may provide large enough kicks to unbind neutron stars from the Galactic disk. In future iterations of `PopSyCLE`, we will allow for different compact-object spatial distributions. Currently, the kick velocities for both NSs and BHs is tunable; however, it is only allowed to be a single value. In the future, support for kick velocity distributions will be added.

The additions above are necessary to provide support for primordial black holes (PBHs) in `PopSyCLE`. Ultimately, we plan to implement a PBH mass spectrum such that PBHs can be injected with their own position, velocity, and mass distributions that differ from the underlying stellar halo (Carr, Kühnel, and Sandstad 2016; Chapline et al. 2018). Similar to the IFMR, a variety of different mass spectra could be implemented.

2.9 Conclusions

We have developed a Milky Way microlensing simulation, dubbed `PopSyCLE`, which is the first to consider both photometric and astrometric microlensing effects and perform compact object population synthesis in a realistic manner. With `PopSyCLE`, we investigate different strategies to hunt for isolated stellar mass BHs in the Milky Way and measure their masses. We highlight the following results:

- Assuming a state-of-the-art initial-final mass relations, the BH present-day mass function has structure (peaks and gaps) that can be measured with samples of $\mathcal{O}(100)$ BH mass measurements from both LIGO detections and BH microlensing surveys.

- The optimal isolated BH candidates to follow up astrometrically are long-duration microlensing events with Einstein crossing times $t_E \gtrsim 90 - 120\,\text{days}$; additional selection criteria based on the source flux fraction b_{SFF} or the impact parameter u_0 or obtaining high-resolution imaging does not significantly improve the outcome. Current photometric surveys and astrometric follow-up campaigns should yield a 40% success rate for measuring BH masses.

- From photometry alone, BHs can be identified in a statistical manner with a combined measurement of t_E and the microlensing parallax π_E. The BH detection rate can be raised to $\sim 85\%$ by selecting events with both $t_E > 120\,\text{days}$ and $\pi_E < 0.08$.
- BH lenses are easily distinguished from stellar lenses with a combined measurement of the microlensing parallax π_E and the maximum astrometric shift $\delta_{c,max}$, providing a useful method for confirming the BH nature of the lens and measuring its mass. In particular, we note that BH lenses nearly always have $\pi_E < 0.1$.
- The *WFIRST* microlensing survey will be able to measure the masses of $\mathcal{O}(100-1000)$ isolated BHs over it's 5 year lifetime, which is at least an order of magnitude more than is possible with individual astrometric follow-up. This is sufficient to constrain the BH IFMR, binary fraction, and kick velocity distribution.

`PopSyCLE` can also be used to forward model microlensing survey results and constrain the properties of compact objects, the initial-final mass relation, Galactic structure, the existence of primordial black holes, and more. `PopSyCLE` can be downloaded from `https://github.com/jluastro/PopSyCLE` and community contributions are welcome. We also provide the simulation files used for this work at `https://drive.google.com/open?id=12ALPCqMVOBN54fy1YhHfiJjI9Y1bnlQj`.

2.10 Appendix: `Galaxia` Galactic Model

There are several known issues in the Besançon model, and by extension `Galaxia`, particularly with the bulge. Many of these are discussed in Chapter 6.2 of P19, albeit for a slightly different version of the Besançon model than that implemented in `Galaxia`. We modify the bulge kinematics of `Galaxia`, specifically the pattern speed and velocity dispersions, in an attempt to ameliorate these issues. We also validate these changes by performing some comparisons to star counts and event rates from Mróz, Udalski, Skowron, Szymański, et al. (2019a) and Sumi and Penny (2016).

2.10.1 Galactic Models Comparison

There are three specific properties of the bulge we consider modifying:

- *Pattern speed*: `Galaxia` implements a pattern speed of $\Omega = 71.62\,\text{km/s/kpc}$ (see Chapter 3.3 in Sharma et al. (2011)). However, this is nearly twice as fast as the most recent values reported in the literature, which range from around 36 to 44 km/s/kpc (Bovy et al. 2019; Clarke et al. 2019; Sanders et al. 2019), determined using combinations of Gaia DR2, VVV, and APOGEE.

- *Velocity dispersion*: `Galaxia` implements velocity dispersions of $\sigma_R = \sigma_\phi = 110\,\mathrm{km/s}$. However, this produces microlensing events with timescales that are too short, which suggests smaller velocity dispersions might be more appropriate.[8] In reality, σ_R and σ_ϕ should vary with latitude and longitude (Howard, Rich, Clarkson, et al. 2009; Howard, Rich, Reitzel, et al. 2008), but to implement this in `Galaxia` would require significant rewriting of the code, which is far beyond the scope of this current work.

- *Bar angle and length*: `Galaxia` implements a bar angle of $\alpha = 11.1°$, where α is the angle from the Sun-Galactic Center line-of-sight, and a major axis scale length of $x_0 = 1.59\,\mathrm{kpc}$. It is suggested that the angle should be closer to $\alpha = 28°$ (Wegg and Gerhard 2013; Wegg, Gerhard, and Portail 2015), with a shorter scale length of 0.7 kpc. In fact, Portail et al. (2017) performed dynamical modeling using $\alpha = 28°$ to find a bar pattern speed of around 40 km/s/kpc. However, there is still considerable debate in the literature about the value of α and the scale length, with values for α ranging from $10° - 45°$ (see Robin, Marshall, et al. (2012) for a summary and references).

We create two new variations of the original Galactic model implemented in `Galaxia`. We dub "v2" to be the version of `Galaxia` with a pattern speed $\Omega = 40\,\mathrm{km/s/kpc}$ and bulge velocity dispersions $\sigma_R = \sigma_\phi = 100\,\mathrm{km/s}$. We dub "v3" to be the version where the bar is short and tilted, with $\Omega = 40\,\mathrm{km/s/kpc}$, bulge velocity dispersions $\sigma_R = \sigma_\phi = 100\,\mathrm{km/s}$, bar angle $\alpha = 28°$ and major axis scale length $x_0 = 0.7\,\mathrm{kpc}$.

Tables 2.5 and 2.7 compare `PopSyCLE` stellar densities, event rates, and Einstein crossing times to results from S16 and M19 for v2 and v3, respectively. Figure 2.10.1 summarizes the results of the two tables together. The stellar densities of v2 match reasonably well with the observed number counts; v3 is consistently too low. Note that although in projection the length of the bar is the same, as $\sin(11.1°) \cdot 1.59\,\mathrm{kpc} \approx \sin(28°) \cdot 0.7\,\mathrm{kpc}$ (P19), the number counts are quite different, due to extinction. The event rates for v3 match reasonably well with the observed rates; v2 is consistently too high. With respect to the average Einstein crossing time, it is not as clear whether v2 or v3 matches the observed values better.

Based on this analysis we chose to use v2 instead of v3 for the analysis in the main text of this chapter . Stellar density is the more fundamental observational quantity, hence we prefer the simulation reproduce this aspect accurately. The event rate is microlensing-specific and dependent on many more factors (e.g., the detection efficiency correction). However, it is curious in and of itself that the tilted bar creates agreement in one regime but not the other. Additional modifications (such as the 3-D $E(B-V)$ map) may be necessary to bring the models into better agreement with observation. We do not explore this further here, and leave detailed Galactic modeling to the investigation of future work. However, it is worth

---

[8] This issue of too short microlensing events is also a problem described in Chapter 6.2.2 of Penny, Gaudi, et al. (2019), who implement the Besançon model to study microlensing, although it should be noted that the versions of the Besançon model in Penny, Gaudi, et al. (2019) and `Galaxia` are slightly different.

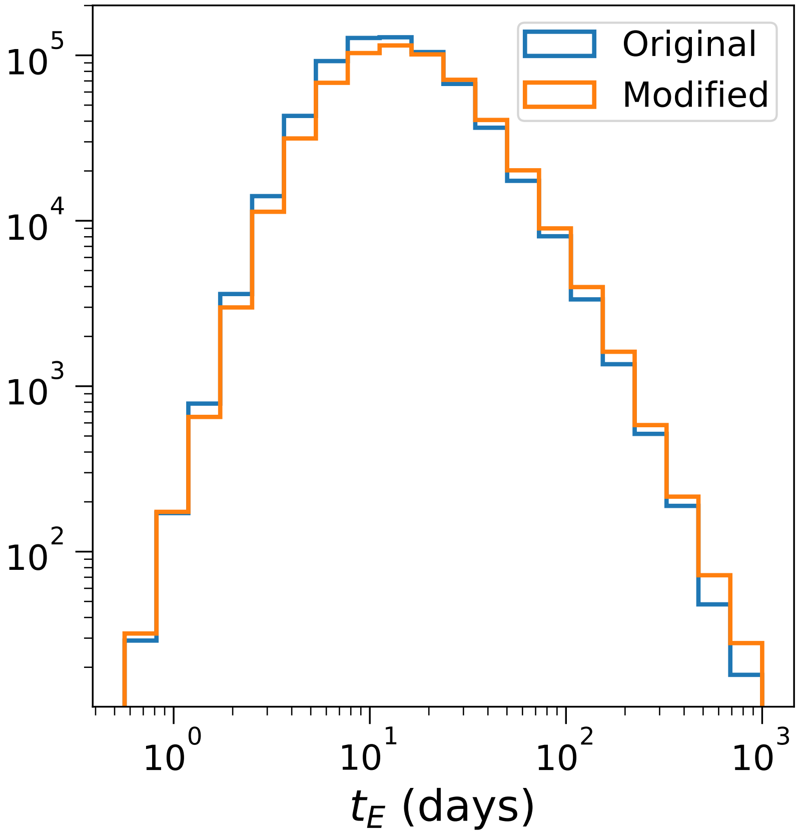

Figure 2.16: t_E distribution of microlensing event candidates (i.e. without any selection cuts applied). The "Original" curve was generated using `Galaxia` unmodified. The "Modified" curve was generated using `Galaxia` v2 with $\Omega = 71.62\,\text{km/s/kpc}$ and $\sigma_R = \sigma_\phi = 110\,\text{km/s}$. It can be seen that the modified `Galaxia` has more long t_E events and fewer short t_E events.

noting how this uncertainty affects some of the results of this chapter . In Chapter 2.7.2.1, the fraction of BH events at long times can be up to a factor of 2 higher for v3 than for v2. In Chapter 2.7.5 we consider the number of BH masses *WFIRST* can measure; the number is about a factor of 4 higher for v2 than for v3.

The rest of the analysis and validation performed in this chapter is also using v2.

2.10.2 Bulge Kinematics

Following Chapter 6.2.2 of P19, we compare the results of our simulation to observational studies of bulge kinematics. In Clarkson, Sahu, et al. (2008), a study of proper motions

Field	n_s (10^6/deg^2)		Γ (10^{-6}/star/yr)		$\langle t_E \rangle$(days)	
	Obs.	Mock	Obs.	Mock	Obs.	Mock
F00^{M19}	2.62	1.48	1.3 ± 0.8	4.35	32.6	14.8
F01^{M19}	4.54	2.04	5.5 ± 0.9	3.69	39.5	46.2
F03^{S}	3.64	2.47	$14.0^{+2.9}_{-2.4}$	8.26	25.5	20.3
F11^{M19}	4.95	3.66	16.2 ± 1.3	17.88	21.8	19.7
F12^{M19}	3.26	1.49	3.4 ± 1.1	2.88	36.7	51.1
F13^{M19}	4.51	2.19	5.2 ± 1.1	4.9	30.8	28.2

Table 2.7: *Comparing* `PopSyCLE` *to surveys (*`Galaxia` *v3).* Identical analysis as presented in Table 2.5, but using `Galaxia` v3 (with the tilted shorter bar) instead of v2. Fields with ^{M19} indicate the observed values come from M19, while those with ^{S} are from S16.

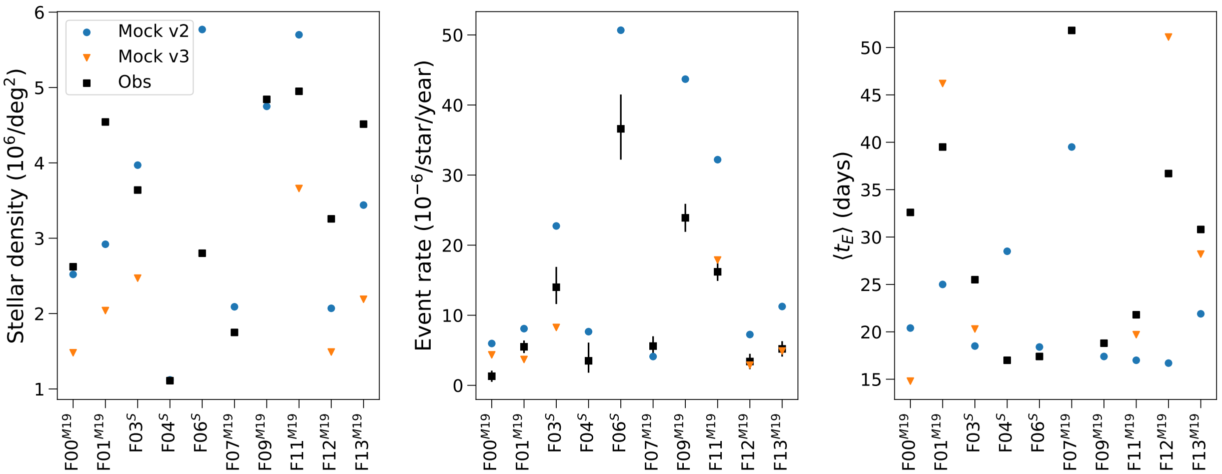

Figure 2.17: Comparison of the stellar density, event rate, and average Einstein crossing times for several fields. The labels FXX correspond to the field used (see Table 2.3), and the superscript correspond to the paper from which observed values and selection criteria for the mock values were drawn (S from Sumi and Penny (2016), M19 from Mróz, Udalski, Skowron, Szymański, et al. (2019a)). Note that only a handful of fields were initially tested, which is why there are certain fields for v3 that have no points.

in the Galactic Bulge is performed using observations of the *HST* SWEEPS field (centered at $(l, b) = (1.25, -2.65)$ covering an area of 11 arcmin^2) in the *HST* F606W and F814W bands. To compare, we created a synthetic survey in the same direction of the same area using `Galaxia`; we use I and R band as these have the closest effective wavelength as the *HST* F606W and F814W bands. First, we select stars in `Galaxia` photometrically (Figure 2.10.2) similarly to Clarkson, Sahu, et al. (2008) to obtain a red population (bulge proxy) and a blue population (disk proxy). We obtain 347 blue stars and 699 red stars (c.f. P19 37 blue stars and 105 red stars, drawing from an area of 1.44 arcmin^2).

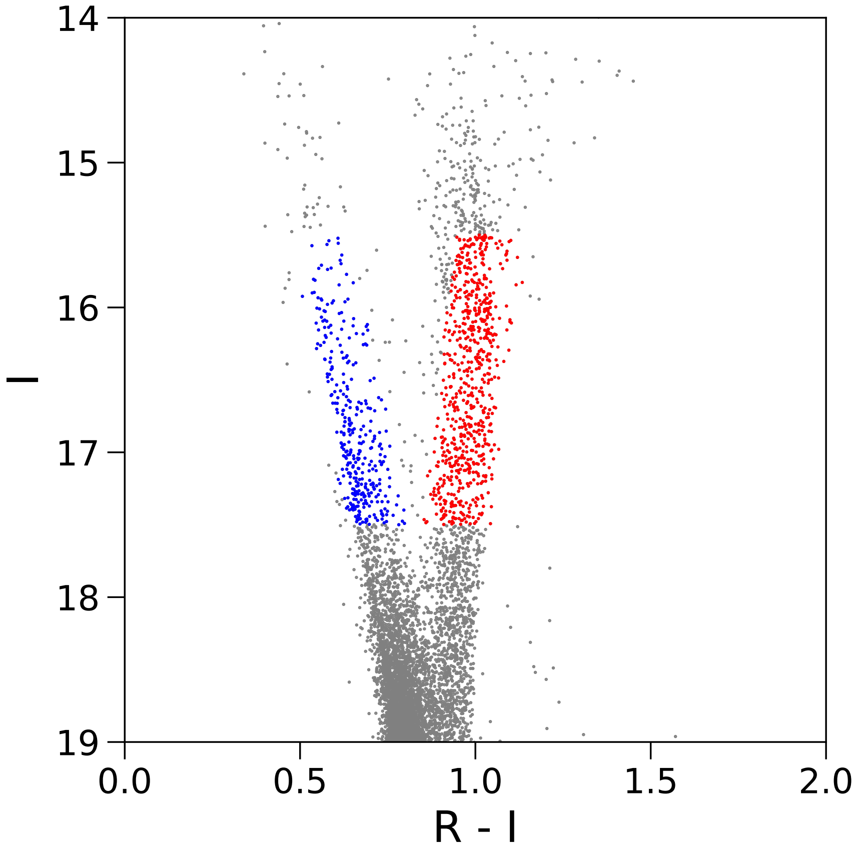

Figure 2.18: Photometrically selected red and blue populations, c.f. Clarkson, Sahu, et al. (2008) Figures 8 and 9. The gray points correspond to all stars, while the red points correspond to the proxy bulge population and the blue points correspond to the proxy disk population.

We then compare our results to those of Clarkson, Sahu, et al. (2008) and P19, who use a different version of the Besançon model, named BGM1106 for short. The results are summarized in Table 2.8, and illustrated in Figures 2.10.2 and 2.10.2. In particular, the match between Clarkson, Sahu, et al. (2008) is improved in $\sigma_{l,*}$ for the red population.

2.11 Appendix: Extinction

The amount of extinction given in `Galaxia`, which uses the Schlegel et al. (1998) dust map overestimates the extinction towards the Galactic Bulge. Thus, in `PopSyCLE` we have instead

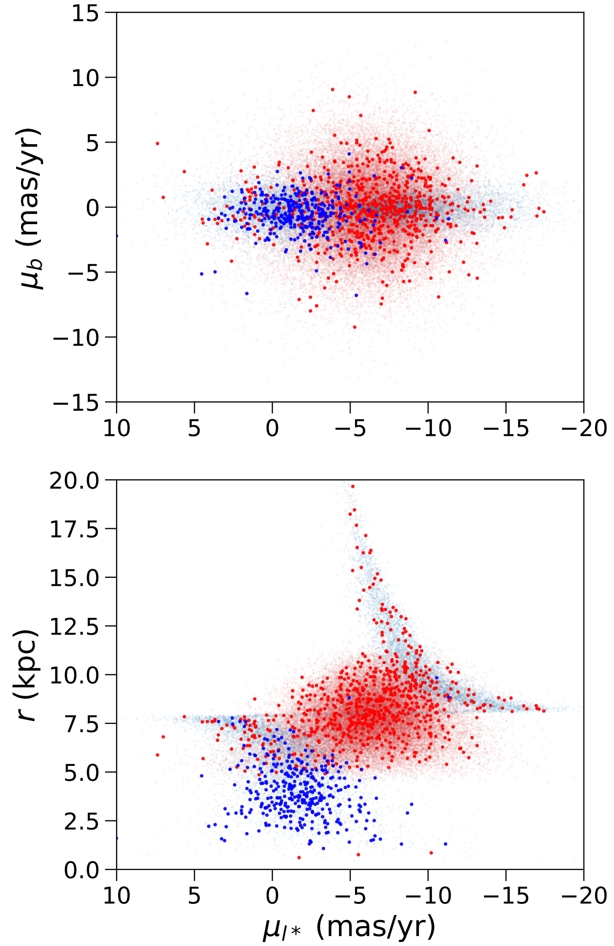

Figure 2.19: Large red points are the photometrically selected bulge stars ("red"/bulge proxy) while large blue points are the photometrically selected disk stars ("blue"/disk proxy). Small red points are the bulge stars and small blue points are the disk stars in `Galaxia`. *Top*: Proper motion vector point diagram for the red and blue populations, c.f. P19 Figure 20. *Bottom*: Distance vs. longitudinal proper motion diagram for the red and blue populations, c.f. P19 Figure 20.

chosen to implement the reddening law of Damineli et al. (2016a), which is tailored for the direction toward the Galactic Plane. We continue to use the color excess values $E(B-V)$ from Schlegel et al. (1998), which is not strictly correct; however, this is satisfactory, as we show below.

We compare the `Galaxia` model using the $E(B-V)$ from Schlegel et al. (1998) with either the Schlegel et al. (1998) or Damineli et al. (2016a) reddening laws, to the data from

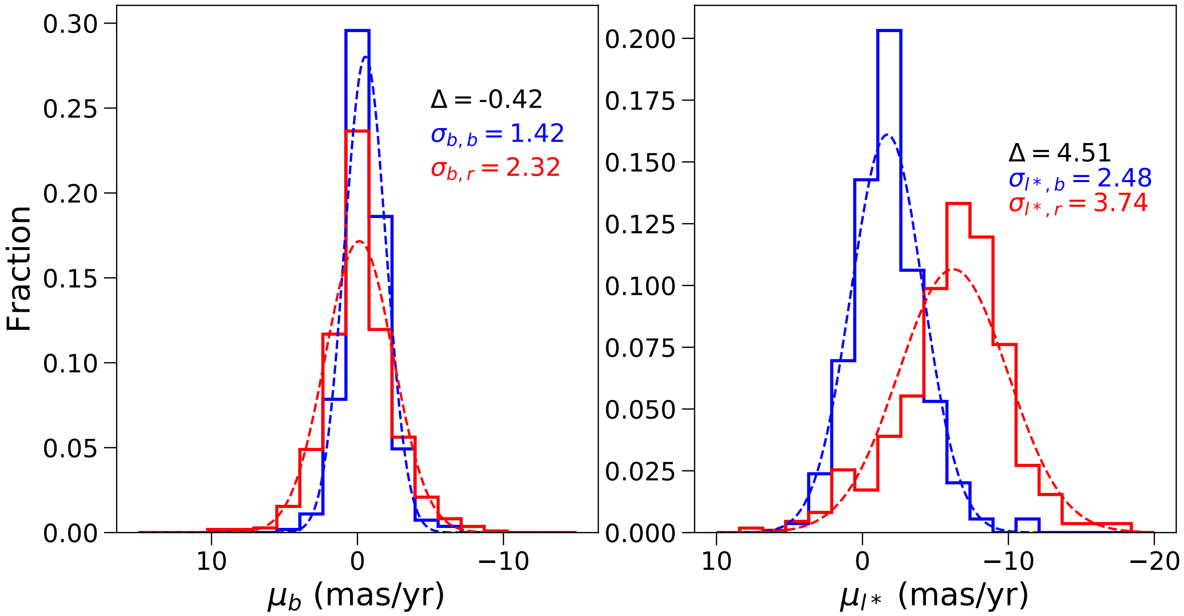

Figure 2.20: Histograms of proper motion for the red (bulge-proxy) and blue (disk-proxy) populations from Galaxia, with the dotted line being a Gaussian of the mean and standard deviation of each respective population. The Δ listed gives the differences between the means of the populations (blue − red). Units of all inset numbers are mas/yr.

Model/Data	$\Delta\mu_{l*}$	$\Delta\mu_b$	σ_{l*}, blue	σ_b, blue	σ_{l*}, red	σ_b, red
Clarkson, Sahu, et al. (2008)	3.24 ± 0.15	−0.81 ± 0.12	2.2	1.3	3.0	2.8
BGM1106 (P19)	3.53 ± 0.65	−0.12 ± 0.32	2.47 ± 0.29	1.11 ± 0.13	5.19 ± 0.36	2.64 ± 0.18
`Galaxia`	4.51	−0.42	2.48	1.42	3.74	2.32

Table 2.8: *Clarkson, Calamida, et al. (2018), BGM1106,* `Galaxia` *Proper Motion Comparison.* All units are (mas/yr). Δ is defined as blue − red.

the OGLE Early Warning System (EWS). From the OGLE 2017 EWS, 4 different events were selected: OGLE-2017-BLG-0001 at (l,b) = (0.92, −1.63); OGLE-2017-BLG-0100 at (−2.07, 0.98); OGLE-2017-BLG-0150 at (1.74, −4.46); OGLE-2017-BLG-0921 at (−0.71, −1.79). These 4 particular events were selected because their finding charts had different CMDs. For these events, the I and V magnitudes of stars in a $2' \times 2'$ area centered on the event are provided. With `Galaxia`, fields in those directions are generated with that equivalent area ($0.0011\,\mathrm{deg}^2$). Since `Galaxia` returns the distance and absolute magnitude of the stars in various filters, along with and the Schlegel $E(B-V)$ color excess, the apparent magnitude of these stars using either the Schlegel or Damineli reddening can be calculated and used to produce synthetic CMDs and luminosity and color functions. The comparisons are plotted in Figure 2.11.

In general, `Galaxia` captures the various structures in the OGLE CMDs. Although there is still some underestimation in the number of stars, the Damineli et al. (2016a) reddening law does a significantly better job than Schlegel et al. (1998) at capturing the total number of stars in the field. The Damineli et al. (2016a) law also does slightly better at replicating the CMD shape and luminosity and color functions.

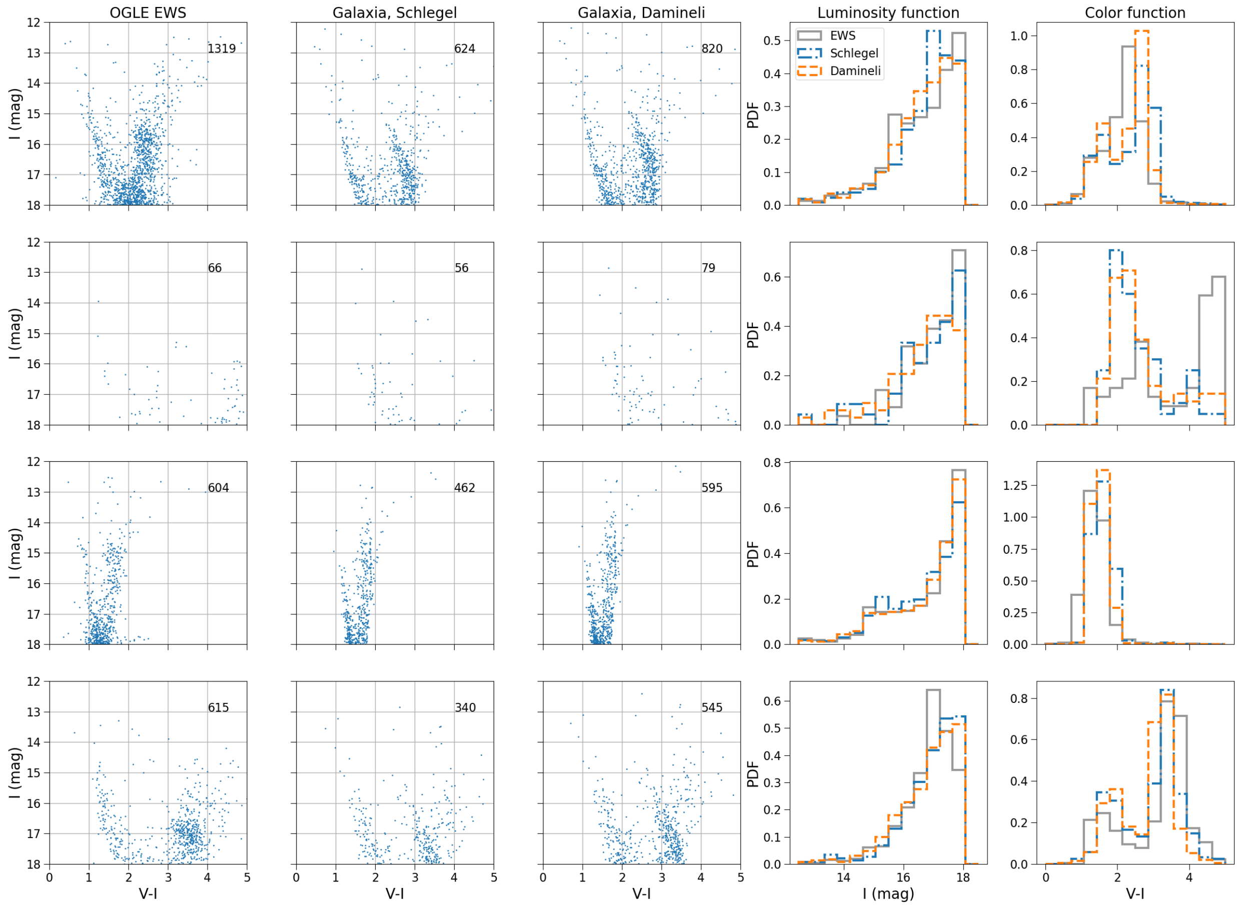

Figure 2.21: Comparison of CMDs, luminosity, and color functions for different fields and extinction laws. The rows, from top to bottom, correspond to the fields OGLE-2017-BLG-0001 at (l,b) = (0.92, −1.63), OGLE-2017-BLG-0100 at (l,b) = (−2.07, 0.98), OGLE-2017-BLG-0150 at (l,b) = (1.74, −4.46), and OGLE-2017-BLG-0921 at (l,b) = (−0.71, −1.79). The numbers in the corners of the CMDs correpond to the number of stars in that CMD.

We also consider an extinction map produced by Nataf et al. (2013) using data from the OGLE-III, VVV, and 2MASS surveys. However, for the fields available, the differences are random and small, hence they do not consistently skew our number counts in one direction.

2.12 Appendix: Initial-Final Mass Relation

As defined in R18 Equations (1) through (4), the black hole initial-final mass relation (IFMR) is a piecewise function, where the two pieces are dubbed Branches I and II. Branch I, which covers $15 \leq M_{ZAMS} \leq 40 M_{\odot}$, the remnant BH mass is given by

$$M_{BH}(M_{ZAMS}; f_{ej}) = f_{ej} M_{BH,core}(M_{ZAMS}) + (1 - f_{ej}) M_{BH,all}(M_{ZAMS}) \tag{2.19}$$

where f_{ej} is the ejection fraction describing how much of the envelope is ejected in a supernova explosion ($f_{ej} = 0$ is where the entire star collapses, $f_{ej} = 1$ is where only the star's He-core collapses), and $M_{BH,core}$ and $M_{BH,all}$ are defined as

$$\begin{aligned} M_{BH,core}(M_{ZAMS}) &= -2.049 + 0.4140\ M_{ZAMS} \\ M_{BH,all}(M_{ZAMS}) &= 15.52 - 0.3294(M_{ZAMS} - 25.97) \\ &\quad - 0.02121(M_{ZAMS} - 25.97)^2 + 0.003120(M_{ZAMS} - 25.97)^3. \end{aligned}$$

In `PopSyCLE` we use $f_{ej} = 0.9$ as this is the value reported by R18 that most closely reproduces the observed distribution of BH masses. The $M_{BH,core}$ term describes the BH IFMR where only the star's He-core collapses, while the $M_{BH,all}$ term describes the BH IFMR where the entire star collapses; f_{ej} interpolates between the two. The black hole IFMR for Branch II, which covers $45 \leq M_{ZAMS} \leq 120 M_{\odot}$, is

$$M_{BH,core}(M_{ZAMS}) = 5.697 + 7.8598 \times 10^8 (M_{ZAMS})^{-4.858}. \tag{2.20}$$

Similarly, there is a piecewise defined neutron star initial-final mass relation. Overall, there are seven branches, Branches I through VII, described in R18 Equations (11) through (16). Each branch of the IFMR is defined over a particular range of ZAMS masses. Five of these branches are described by third order polynomials, and two are described by Gaussian distributions.

We have made the following modifications to the original initial-final mass function/relation:

1. Since the gap between $40 \leq M \leq 45 M_{\odot}$ between Branches I and II is due to the discrete sampling of the simulations from Sukhbold, Ertl, et al. (2016), we extend Branches I and II such that there isn't a gap. Specifically, we find where the function describing Branch I intersects Branch II, assuming $f_{ej} = 0.9$; this point is $M_{ZAMS} = 42.21 M_{\odot}$. So for our purposes, Branch I goes from $15 \leq M_{ZAMS} \leq 42.21 M_{\odot}$ and Branch II goes from $42.21 \leq M_{ZAMS} \leq 120 M_{\odot}$.

2. A distinction is made between black holes made by fallback, and those made by direct collapse. As described by Equation (8), black holes only form from direct collapse immediately after the SNe. However, for our purposes, a black hole formed by fallback vs. direct collapse is not relevant. We modify the fraction of black holes to then be

$$X_{BH} = \frac{N_{BH} + N_{fb}}{N_{BH} + N_{NS} + N_{fb}} = 1 - X_{NS} \tag{2.21}$$

We do this for completeness; however N_{fb} is quite small compared to N_{BH} and this will not substantially change the results.

3. Since all the neutron stars fall in such a small mass range (between 1.3 and 1.9 $M_\odot$), for simplicity, we just assume the neutron star initial-final mass function is a constant, that is,
$$M_{NS}(M_{ZAMS}) = 1.6 M_\odot \tag{2.22}$$
where $1.6 M_\odot$ was selected since is the mean of this mass range. In future versions, we plan to release a more realistic NS IFMR.

2.13 Appendix: Initial-Final Group Mass Ratio

`Galaxia` simulation output is divided into groups of stars with a similar age in order to determine the appropriate number, types, and masses of compact objects for that group. Each group is treated as a simple stellar population of a fixed age and solar metallicity. Currently, differences in metallicity within each group are ignored since the R18 IFMR only has solar metallicity. The total stellar mass of the age group from `Galaxia` is the present-day group mass; however, the initial group mass is needed in order to determine how many black holes and other compact objects should be added to `Galaxia`. As each group ages, the present-day mass decreases in a non-linear fashion and the conversion from present-day to the initial group mass must be derived through simulations. Ultimately, during `PopSyCLE` simulations, this relation between the initial-final group mass ratio and age is used to estimate the total initial group mass, generate a `PyPopStar` cluster of that mass and age, and insert the resulting white dwarfs, neutron stars, and compact objects back into `PopSyCLE`.

The relationship between the initial-final group mass ratio and age is calibrated using `PyPopStar` by simulating groups of stars of mass $10^7 M_\odot$ over a wide range of ages (Figure 2.13). The group mass is chosen to be large, to ensure that stochasticity does not dominate the result of the initial-final group mass ratio. For all age groups, we adopt the same Kroupa IMF and MIST evolutionary models described in Section 2.3. The process is as follows:

A $10^7 M_\odot$ group of stars is generated using `PyPopStar` and evolved to the desired age. As the MIST isochrones include some white dwarfs, while `Galaxia` does not include any white dwarfs, all stars beyond the main sequence (post-AGB and Wolf-Rayet stars) are discarded from the group. The mass of the remaining stars constitute that age group's current stellar mass. The current age group's stellar mass is then divided by the initial group's stellar mass ($10^7 M_\odot$) to obtain the initial-final group mass ratio.

Implicit in this process, it is assumed that the IMF shape and mass limits used to calculate the initial-current group mass ratio with `PyPopStar` are the same as the IMF used in `Galaxia`.

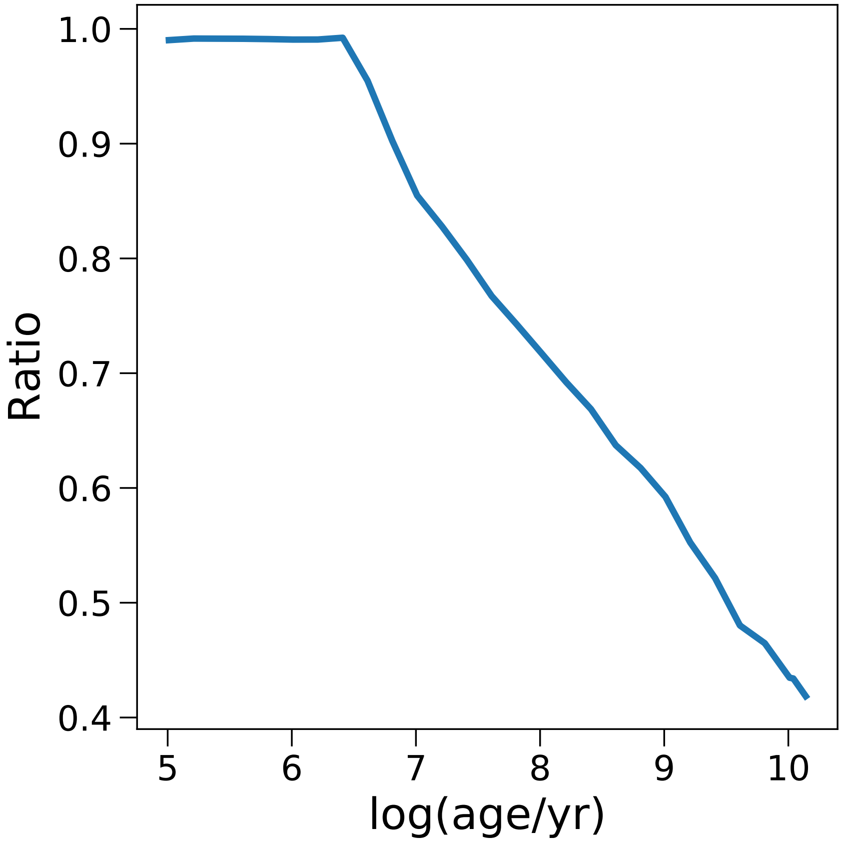

Figure 2.22: Ratio of current group mass to initial group mass as a function of group age. Most stars do not begin to evolve off the main sequence until after 10^6 years. After that, stellar mass is converted to remnant mass in a roughly linear fashion as a function of log age.

Chapter 3

An Isolated Mass-gap Black Hole or Neutron Star Detected with Astrometric Microlensing

A version of this chapter was originally published in The Astrophysical Journal Letters, Volume 933, Issue 1 (2022) and The Astrophysical Journal Supplement Series, Volume 260, Issue 2 (2022), and was coauthored with Jessica R. Lu, Andrzej Udalski, Ian Bond, David P. Bennett, Jan Skowron, Przemek Mróz, Radek Poleski, Takahiro Sumi, Michał K. Szymański, Szymon Kozłowski, Paweł Pietrukowicz, Igor Soszyński, Krzysztof Ulaczyk, Łukasz Wyrzykowski, Shota Miyazaki, Daisuke Suzuki, Naoki Koshimoto, Nicholas J. Rattenbury, Matthew W. Hosek, Fumio Abe, Richard Barry, Aparna Bhattacharya, Akihiko Fukui, Hirosane Fujii, Yuki Hirao, Yoshitaka Itow, Rintaro Kirikawa, Iona Kondo, Yutaka Matsubara, Sho Matsumoto, Yasushi Muraki, Greg Olmschenk, Clément Ranc, Arisa Okamura, Yuki Satoh, Stela Ishitani Silva, Taiga Toda, Paul J. Tristram, Aikaterini Vandorou, Hibiki Yama, Natasha S. Abrams, Shrihan Agarwal, Sam Rose, and Sean K. Terry.

We present the analysis of five black hole candidates identified from gravitational microlensing surveys. Hubble Space Telescope astrometric data and densely sampled light curves from ground-based microlensing surveys are fit with a single-source, single-lens microlensing model in order to measure the mass and luminosity of each lens and determine if it is a black hole. One of the five targets (OGLE-2011-BLG-0462/MOA-2011-BLG-191 or OB110462 for short) shows a significant > 1 mas coherent astrometric shift, little to no lens flux, and has an inferred lens mass of $1.6 - 4.4$ $M_{\odot}$. This makes OB110462 the first definitive discovery of a compact object through astrometric microlensing and it is most likely either a neutron star or a low-mass black hole. This compact object lens is relatively nearby ($0.70 - 1.92$ kpc) and has a slow transverse motion of <30 km/s. OB110462 shows significant tension between models well-fit to photometry vs. astrometry, making it currently difficult to distinguish between a neutron star and a black hole. Additional observations and modeling with more complex system geometries, such as binary sources are needed to resolve the puzzling nature of this object. For the remaining four candidates, the lens masses are

$< 2M_\odot$ and they are unlikely to be black holes; two of the four are likely white dwarfs or neutron stars. We compare the full sample of five candidates to theoretical expectations on the number of black holes in the Milky Way ($\sim 10^8$) and find reasonable agreement given the small sample size.

3.1 Introduction

Stellar-mass black holes are produced when massive stars collapse under their own gravity. Observations of black holes (BHs) are a key ingredient for understanding outstanding questions in massive stellar evolution, such as which stars explode, which stars produce neutron stars vs. BHs, and whether there is a gap between the heaviest neutron stars (NSs) and the lightest BHs.

Back-of-the-envelope calculations predict $\sim 10^8$ BHs in the Milky Way (Shapiro et al. 1983). Other estimates using supernovae and galactic chemical evolution models (Samland 1998; Timmes et al. 1996) or photometric microlensing (Agol, Kamionkowski, et al. 2002; Sartore et al. 2010) also predict $\sim 10^7 - 10^9$ BHs. Despite the large predicted number of BHs, only about two dozen have dynamical mass measurements (Corral-Santana et al. 2016; Thompson et al. 2019). These BHs are not a representative sample of the Galactic BH population, as they are all in binary systems.

While most massive stars exist in binary or multiple systems (Sana 2017), the majority of the BH population is expected to be isolated due to the disruption of the progenitor systems (Belczynski, Sadowski, et al. 2004; Fender et al. 2013; Wiktorowicz, Wyrzykowski, et al. 2019). However, to date there are no confirmed isolated BH detections. Attempts have been made to detect X-rays from interstellar medium (ISM) accretion onto a BH, but they have been unsuccessful and even future X-ray missions may not be sensitive enough to make such a detection (Tsuna et al. 2018). As almost all other BH detection methods require a companion (e.g., X-ray binaries, astrometric binaries, gravitational waves), microlensing is the ideal way to detect and measure the masses of isolated BHs.

Paczynski (1986a) first proposed monitoring the Galactic halo to search for the characteristic brightening of microlensing events to constrain the properties of dark massive compact halo objects (MACHOs). Several years later Paczynski (1991) and Griest et al. (1991) proposed monitoring the Galactic bulge for microlensing events, calculating a lensing rate of $\sim 10^{-6}$/star/year. Presently, thirty years later, ground-based microlensing surveys such as the Optical Gravitational Lensing Experiment (OGLE) (Udalski, Szymanski, Kaluzny, Kubiak, Mateo, et al. 1994), Microlensing Observations in Astrophysics (MOA) (Bond, Abe, et al. 2001), and Korea Microlensing Telescope Network (KMTNet) (Kim et al. 2016) monitor hundreds of millions of stars toward the Galactic bulge, identifying thousands of photometric microlensing events each year.

The advent of ground-based microlensing surveys provided a new avenue to search for isolated black holes (BHs). Notable BH candidates identified with photometric microlensing include MACHO-96-BLG-5, MACHO-98-BLG-6 (Bennett, Becker, et al. 2002), and MACHO-

99-BLG-22/OGLE-1999-BUL-32 (Mao, Smith, et al. 2002). Poindexter et al. (2005) found that MACHO-99-BLG-22 is likely a BH, MACHO-96-BLG-5 is possibly a BH, and MACHO-98-BLG-6 is most likely not a BH, with BH lens probabilities of 78%, 37%, and 2%, respectively. On the other hand, Abdurrahman et al. (2021) found that MACHO-96-BLG-5 and MACHO-98-BLG-6 are still good BH candidates, ruling out non-BH lenses for source-lens relative proper motions larger than 2.5 mas/yr. However, mass estimates for these lensing events cannot be made without invoking a Galactic model. These candidates only had photometric microlensing observations, which alone cannot constrain the mass of the lens, unless rare higher-order effects such as finite-source effects are detected.

As mentioned briefly at the end of Paczynski (1986a), microlensing also has an astrometric signature, in which the centroid of the image is displaced from the source's true position (Hog et al. 1995; Miyamoto et al. 1995; Walker 1995). In contrast to the now-routine measurements of photometric microlensing, detections of astrometric microlensing are still at the forefront of our technical capabilities. Typical astrometric shifts toward the Bulge are $O(0.01-1)$ mas, and few existing facilities are currently capable of the astrometric precision to perform this measurement. Only a handful of astrometric measurements of the gravitational deflection of light have ever been made, all for nearby ($<$ 10 pc) lenses that were astrometrically anticipated (Eddington 1919; Sahu, Anderson, Casertano, Bond, Bergeron, et al. 2017; Zurlo et al. 2018). However, a combination of photometric and astrometric microlensing together can determine the mass of the lensing object, making detection of astrometric microlensing important for BH searches.

To date, there have been two endeavors to measure lens masses by combining photometric and astrometric microlensing. Lu et al. (2016) attempted a measurement with *Keck* laser guide star adaptive optics (LGS AO), but no detections of astrometric microlensing were made. Kains et al. (2017) reported a detection of astrometric microlensing made with the Hubble Space Telescope (*HST*), but the signal was very weak and no lens masses were well constrained. The currently operating *Gaia* mission is also anticipated to make measurements of astrometric microlensing, which can be searched for once per-epoch astrometry is released (McGill et al. (2020) and references therein). A handful of these deflections should be due to BHs (Rybicki et al. 2018).

If there are 10^8 BHs in the Milky Way, they should contribute only about 0.1% to the number of lenses of the Milky Way. In contrast, they would make up around 1% of the Milky Way's microlensing events due to their larger lensing cross section. Thus, of the thousands of microlensing events detected each year, a few tens should be due to BHs (Gould 2000; Lam, Lu, Hosek, et al. 2020). However, a 1% detection rate is akin to looking for BH needles in a Galactic haystack. By limiting to long duration microlensing events with $t_E > 120$ days, the probability of a microlensing event being a BH rises to $\sim 40\%$ (Lam, Lu, Hosek, et al. 2020).

In this paper, we present an analysis of five BH candidates, which constitute a sufficient sample to place early constraints on the number of isolated black holes in the Milky Way. All five BH candidates were identified in ground-based microlensing surveys and followed up astrometrically with *HST*. The *HST* data is used to perform an astrometric analysis and then combined with MOA and OGLE photometry to fit the events and produce mass constraints on the lenses. By combining the mass, distance, and photometry constraints on the lenses with stellar evolution and Galactic models, we determine the probability that the lenses are stars, white dwarfs, neutron stars, or black holes. This is used to determine whether the number of BHs from this sample is consistent with a population of 10^8 Galactic BHs.

This chapter is organized as follows. In Chapter 3.2, the datasets and reduction processes for our BH search are described, and in Chapter 3.3 the photometric and astrometric analysis of the *HST* data is explained. In Chapter 3.4, the microlensing modeling and fitting procedure are described, while Chapter 3.5 describes how to combine the high-resolution imaging and results of the microlensing modeling to constrain the lens' luminosity. Chapter 3.6 presents the results of the modeling for the five candidates, in particular the inferred lens masses. Constraints on the Milky Way BH population and future BH microlensing searches are discussed in Chapter 3.7. Conclusions are presented in Chapter 3.8.

3.2 Observations

3.2.1 Targets and Selection Criteria

Short Name	OGLE Alert Name	MOA Alert Name	RA (J2000.0)	Dec (J2000.0)
MB09260	–	MOA-2009-BLG-260	17:58:28.561	-26:50:20.88
MB10364	–	MOA-2010-BLG-364	17:57:05.401	-34:27:05.01
OB110037	OGLE-2011-BLG-0037	MOA-2011-BLG-039	17:55:55.83	-30:33:39.7
OB110310	OGLE-2011-BLG-0310	MOA-2011-BLG-332	17:51:25.39	-30:24:35.0
OB110462	OGLE-2011-BLG-0462	MOA-2011-BLG-191	17:51:40.19	-29:53:26.3

Table 3.1: *Target Summary.*

Five BH candidate microlensing events[1] were selected from the OGLE Early Warning System[2] (Udalski, Szymański, et al. 2015) and MOA Alerts[3] to be imaged with *HST*. These targets were selected to have long ($t_E > 200$ days) duration, no light contribution from the lens, and high magnifications to allow detection of parallax signals, making them good isolated BH candidates (Sahu 2009). Preliminary results by Sahu, Anderson, Casertano, Bond, Bergeron, et al. (2017) reported that all five candidates were low-mass ($< 0.5M_\odot$) stars, with no BH detections in the sample. We chose to re-analyze these targets in order to

---

[1] Three additional other targets were initially observed with *HST*, but dropped from the target list after a year (Sahu 2012).

[2] http://ogle.astrouw.edu.pl/ogle4/ews/ews.html

[3] https://www.massey.ac.nz/∼iabond/moa/alerts/

use both BH detections and non-detections in the sample to constrain the total number of BHs in the Milky Way.

Three of the targets, OGLE-2011-BLG-0037/MOA-2011-BLG-039, OGLE-2011-0310/MOA-2011-BLG-332, and OGLE-2011-BLG-0462/MOA-2011-BLG-191 (hereafter OB110037, OB110310, and OB110462), were alerted by both OGLE and MOA. The other two targets, MOA-2009-BLG-260 and MOA-2010-BLG-364 (hereafter MB09260 and MB10364), were only alerted by MOA. Table 3.1 lists their coordinates. Figures 3.3 – 3.8 show the light curves of the targets.

3.2.2 MOA

The MOA-II survey is carried out with a 1.8-m telescope at Mt. John University Observatory in New Zealand (Hearnshaw et al. 2006; Sumi 2008). The seeing at the site ranges from $\sim 1.8'' - 3.5''$, with the median seeing being $\sim 2.5''$. The telescope has a 2.2 deg^2 FOV, with a 10-chip CCD camera with a plate scale $0.57''$/pixel. The main observations are taken using the MOA-Red (630 – 1000 nm) filter (Bond, Abe, et al. 2001).

MOA data for MB09260 and MB10364 were reduced as described in Bond, Bennett, et al. (2017).[4] The MOA light curves are photometrically calibrated to the OGLE-III I-band.

3.2.3 OGLE

The OGLE-IV survey is carried out at the 1.3-m Warsaw telescope at Las Campanas Observatory in Chile (Udalski, Szymański, et al. 2015). The seeing at the site ranges from $\sim 1.0'' - 2.0''$, with the median seeing being $\sim 1.3''$. The telescope has a 1.4 deg^2 FOV, with a 32-chip CCD camera with a plate scale of $0.26''$/pixel. The main observations are taken using the OGLE-I filter, which is similar to Cousins I-band. The data was reduced using the Difference Image Analysis technique as implemented by Wozniak (2000). In addition, we rescaled the photometric uncertainties of OB110462 according to the method described in Skowron, Udalski, Kozłowski, et al. (2016).

OGLE data is only available for OB110037, OB110310, and OB110462. The magnification of MB09260 was not observed by OGLE as it occurred during the OGLE-III to OGLE-IV upgrade. MB10364 is located in a gap in the detectors of the OGLE camera.

3.2.4 *HST*

Target	Epoch (UT) (yyyy-mm-dd)	PA (deg)	Filter	T_{exp} (sec)	N_{im}

---

[4] OB110037, OB110310, and OB110462 also have MOA light curves. For simplicity we only present the OGLE light curve fits for those events, since the seeing at OGLE is better.

MB09260	2009-10-01	275.0	F606W	10.0	4*
				100.0	2
			F814W	20.0	1*
	2009-10-19	275.0	F606W	310.0	1*
			F814W	72.0	6
	2010-03-22	95.0	F606W	300.0	1*
			F814W	280.0	5
	2010-06-14	95.0	F606W	200.0	1*
			F814W	275.0	5
	2010-10-20	270.0	F606W	275.0	2*
			F814W	275.0	4
	2011-04-19	90.0	F606W	275.0	2
			F814W	275.0	4
	2011-10-24	270.0	F606W	275.0	2
			F814W	275.0	4
	2012-09-25	270.0	F606W	275.0	2
			F814W	275.0	4
	2013-06-17	105.5	F606W	275.0	2
			F814W	275.0	4
MB10364	2010-09-13	270.0	F606W	1.0	1
				2.0	1
			F814W	3.0	5
				1.0	1*
	2010-10-26	277.4	F606W	12.0	2
			F814W	12.0	6
	2011-04-13	90.0	F606W	260.0	2*
			F814W	120.0	4*
	2011-07-22	260.5	F606W	160.0	4*
			F814W	90.0	4*
	2011-10-31	278.8	F606W	30.0	5
			F814W	30.0	6
	2012-09-25	270.9	F606W	30.0	5
			F814W	30.0	6
	2013-10-24	277.0	F606W	40.0	5
			F814W	40.0	6
OB110037	2011-08-15	245.0	F606W	30.0	4
			F814W	40.0	4
				20.0	3*
	2011-09-26	270.8	F606W	30.0	5
			F814W	20.0	6
	2011-11-01	276.1	F606W	50.0	5

			F814W	30.0	5
	2012-05-07	98.1	F606W	80.0	4
			F814W	60.0	5
	2012-09-25	270.8	F606W	80.0	4
			F814W	60.0	5
	2013-10-21	274.3	F606W	80.0	4
			F814W	60.0	6
	2014-10-26	275.1	F606W	60.0	4
			F814W	55.0	6
	2017-03-13	90.0	F606W	60.0	3
			F814W	55.0	6
	2017-09-04	256.9	F606W	60.0	3
			F814W	55.0	6
OB110310	2011-09-21	270.0	F606W	75.0	4
			F814W	75.0	5
	2011-10-31	276.5	F606W	280.0	3
			F814W	200.0	4
	2012-04-24	96.0	F606W	280.0	3
			F814W	230.0	4
	2012-09-24	271.3	F606W	280.0	3
			F814W	230.0	4
	2013-10-21	274.8	F606W	280.0	3
			F814W	68.0	1*
				230.0	4
	2017-03-14	90.4	F606W	270.0	3
			F814W	230.0	4
	2017-09-01	268.4	F606W	270.0	3
			F814W	230.0	4
OB110462	2011-08-08	270.0	F606W	60.0	1*
				75.0	3
			F814W	120.0	1*
				60.0	1*
				75.0	3
	2011-10-31	276.1	F606W	280.0	3
			F814W	200.0	4
	2012-09-09	269.5	F606W	290.0	3
			F814W	190.0	4
	2012-09-25	271.3	F606W	280.0	3
			F814W	200.0	4
	2013-05-13	99.9	F606W	280.0	3*
			F814W	200.0	4*

2013-10-22	274.6	F606W	285.0	3
		F814W	285.0	4
2014-10-26	275.2	F606W	265.0	3
		F814W	265.0	4
2017-08-11	255.2	F606W	250.0	3^*
		F814W	250.0	4^*
2017-08-29	268.3	F606W	250.0	3
		F814W	250.0	4
2021-10-01	272.0	F606W	407.0	5
		F814W	307.0	6

Table 3.2: *HST WFC3-UVIS Observations.* Asterisk (*) denotes observations excluded from analysis.

HST observations come from a multi-year campaign following up these five targets (GO-11707, GO-12322, GO-12670, GO-12986, GO-13458, GO-14783; PI: K. C. Sahu). Observations were taken with the UVIS channel on the Wide Field Camera 3 (WFC3) in two different wide-band filters, F606W (V-band) and F814W (I-band). Table 3.2 summarizes the *HST* observations.

The WFC3 UVIS channel is composed of two 2k×4k CCDs and has a $162'' \times 162''$ field of view with a plate scale $0.04''$/pixel. WFC3 UVIS supports sub-arraying, in which only a portion of the entire detector is read out, which can reduce data volume or exposure time and increase observational efficiency. All observations prior to 2011-07-22 were taken with the UVIS1-2K4-SUB subarray mode. Beginning *HST* Cycle 18, more subarray sizes were made available, and observations after 2011-07-22 were taken with the UVIS2-2K2C-SUB subarray mode, a 2k×2k subarray.

Additional observations of OB110462 commenced in Cycle 29 (GO-16760; PI: C. Lam). These were taken in as similar a configuration as possible to the later epochs of the archival program, using WFC3 UVIS in UVIS2-2K2C-SUB subarraying mode, with observations in F606W and F814W filters. The first set of observations from this program was taken October 2021 and is presented here; an additional set of observations is anticipated to be taken Fall 2022 (Lam and Lu 2021).

3.2.5 *Gaia*

Gaia is an all-sky scanning astrometric space mission (Gaia Collaboration, Prusti, et al. 2016). All of the targets, with the exception of OB110462, are found in *Gaia* Early Data Release 3 (EDR3, Table 3.3). *Gaia* EDR3 covers the period from 25 July 2014 to 28 May 2017 (Gaia Collaboration, Brown, et al. 2021). MB10364, OB110037, and OB110310 have proper motions and parallaxes, while MB09260 does not. OB110462 was not in *Gaia* as it is too faint. We note that there is a *Gaia* source located $\sim 0.35''$ away from OB110462 (*Gaia*

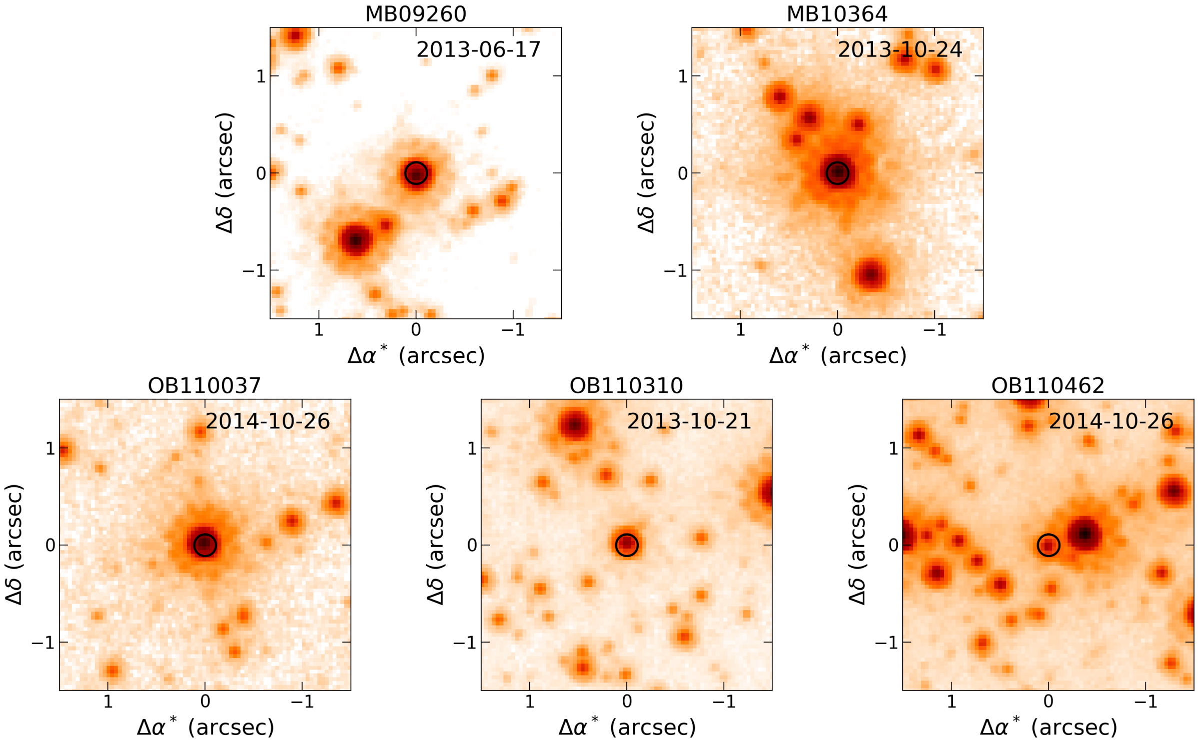

Figure 3.1: Central 3″ × 3″ of *HST* WFC3-UVIS F814W combined images of the observed fields, centered on the target (circled). These images are of the target at or near baseline, i.e. unmagnified. The color stretch is logarithmic. Note that the color scale is not the same across panels.

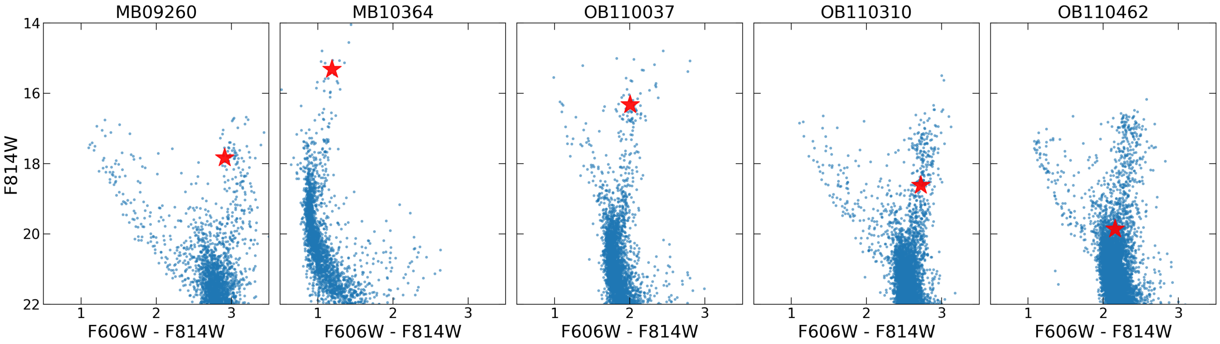

Figure 3.2: CMDs for each field. The target at baseline magnitude and color is marked as a red star.

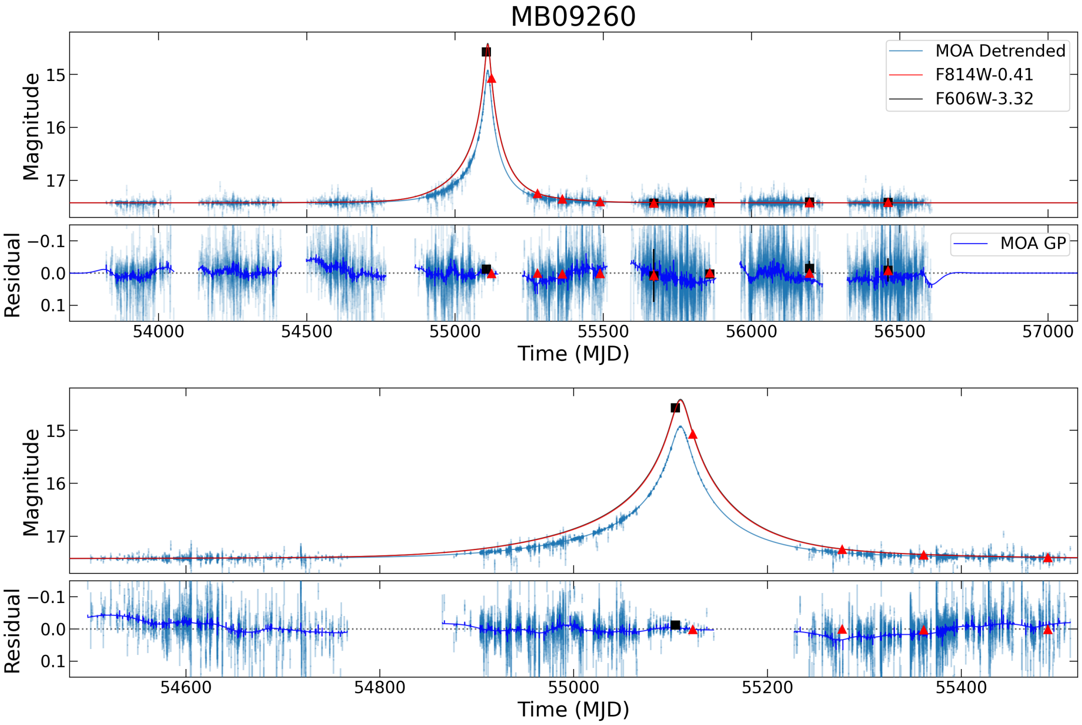

Figure 3.3: *Top panel*: Detrended MB09260 light curve, as seen by MOA and *HST* F814W and F606W. The maximum likelihood model (MLE, described in Chapter 3.6) is plotted over the data. *Second from top panel*: The residuals to the MLE model. The Gaussian Process (GP) model is plotted on top of the residual. We emphasize the residual is not independently fit by the GP, but is simultaneously fit with the model parameters; this is purely to visualize the data (also see Golovich et al. (2022)). See Chapter 3.4 for more details about the fitting procedure. *Second from bottom panel*: Same as top panel, but zoomed into the three most magnified years. *Bottom panel*: Same as second from top panel, but zoomed into the three most magnified years.

EDR3 Source ID 4056442477683080960), which coincides with the bright star directly west of the target seen in the *HST* images (Figure 3.1).

3.3 *HST* Data Analysis

3.3.1 Reduction

The *HST* archival data was accessed from the Mikulski Archive for Space Telescopes[5] (MAST) in June 2021. The Cycle 29 data was accessed October 2021. For the following

---

[5] `https://archive.stsci.edu/hst/`

Parameter	MB09260	MB10364	OB110037	OB110310
Source ID	4064007633015639552	4042290560398692096	4056117808133831936	4056344036933003264
RA (deg)	269.619073405 ± 7.3e-07	269.272538687 ± 1.9e-08	268.982636391± 3.0e-08	267.855757518 ± 2.3e-07
Dec (deg)	-26.839323825 ± 5.9e-07	-34.451415987 ± 1.5e-08	-30.561059419± 2.5e-08	-30.409776355 ± 1.7e-07
$\mu_{\alpha*}$ (mas/yr)	–	-7.43 ± 0.08	2.40 ± 0.13	-2.08 ± 1.12
μ_δ (mas/yr)	–	-6.80 ± 0.05	-3.91 ± 0.09	-6.75 ± 0.58
π (mas)	–	0.40 ± 0.08	0.15 ± 0.13	0.54 ± 1.16
ZP-corrected π (mas)	–	0.43	0.19	0.53*
G (mag)	19.216 ± 0.004	16.086 ± 0.002	17.477 ± 0.001	20.051 ± 0.010
RP (mag)	–	14.929 ± 0.009	16.323 ± 0.010	–
BP (mag)	–	16.557 ± 0.011	19.049 ± 0.032	–
ipd_gof_harmonic_amplitude	0.089	0.064	0.036	0.042
ipd_frac_multi_peak	0	15	0	0
ipd_frac_odd_win	18	0	0	55
ruwe	–	1.388	0.971	0.981
astrometric_excess_noise (mas)	1.241	0.406	0.000	0.894
astrometric_excess_noise_sig	2.657	12.020	0.000	0.332
astrometric_params_solved	3	95	31	95
phot_bp_rp_excess_factor	–	1.69	1.39	–

Table 3.3: *Gaia EDR3 Values.* Magnitude uncertainties are estimated from the *Gaia* reported flux errors. Zero-point (ZP) correction comes from Lindegren, Bastian, et al. (2021), * denotes values that are extrapolations. For full descriptions we refer the reader to *Gaia* EDR3 documentation (van Leeuwen et al. 2021), Section 13.1.1 gaia_source. OB110462 is not in *Gaia*.

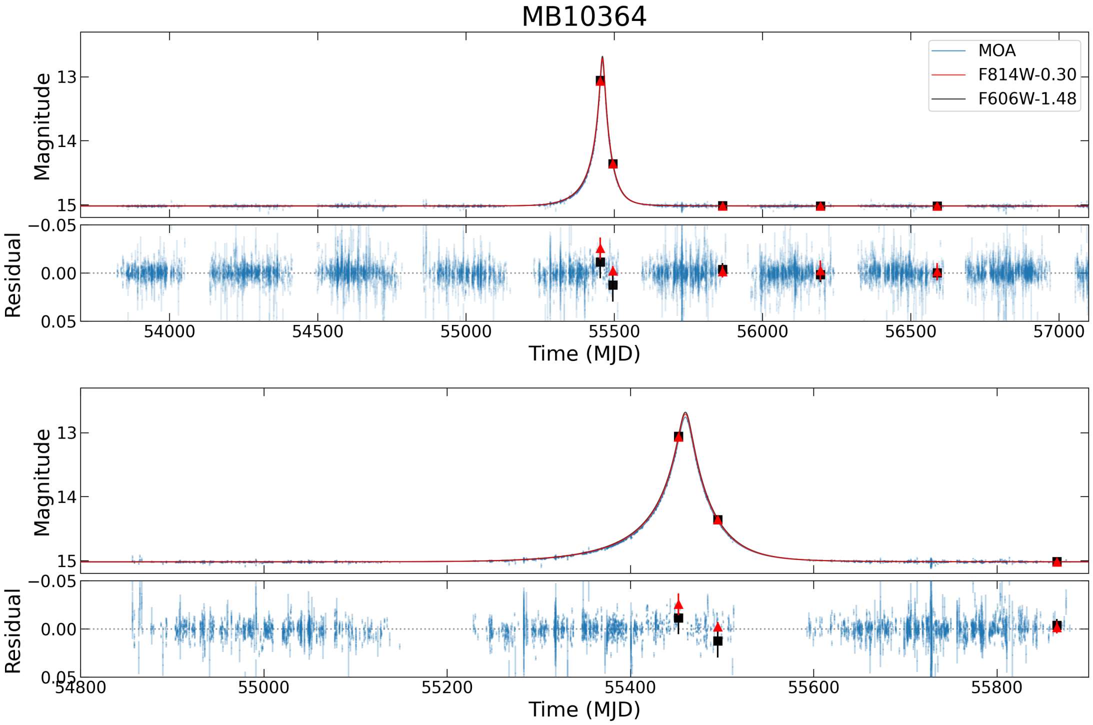

Figure 3.4: Same as Figure 3.3, but for MB10364. Note we do not include GP in the MB10364 fit.

analysis, we employed the calibrated, flat-fielded, individual exposures corrected for charge transfer efficiency (CTE, *HST* files with suffix `_flc`[6]). The archival data was processed with Version 3.6.0 (Dec-31-2020) of the `calwf3` pipeline, using Version 2.0 of the CTE correction algorithm.

CTE can alter astrometry at the milliarcsecond level, hence it is important to use `_flc` files. However, even the `_flc` files do not necessarily fix all problems associated with CTE (Kuhn et al. 2021). Exploration of other methods of CTE correction will be explored in future work. At the present we mitigate CTE effects via other methods (Chapter 3.3.2.2) and validate our astrometry to ensure it is not distorted by CTE.

Images were converted into calibrated star lists via the following steps.

1. *Star list extraction from individual frames.* Star lists were extracted from the individual `_flc` exposures by modeling the PSFs of sources with `hst1pass`, an updated version of the software described in Anderson and King (2006). Empirical filter-dependent PSF models as described in Anderson (2016) and geometric distortion solutions as described in Bellini, Anderson, and Bedin (2011) were used when performing source extraction with `hst1pass`.

---

[6] See Gennaro (2018) for a full description of the different file name suffixes.

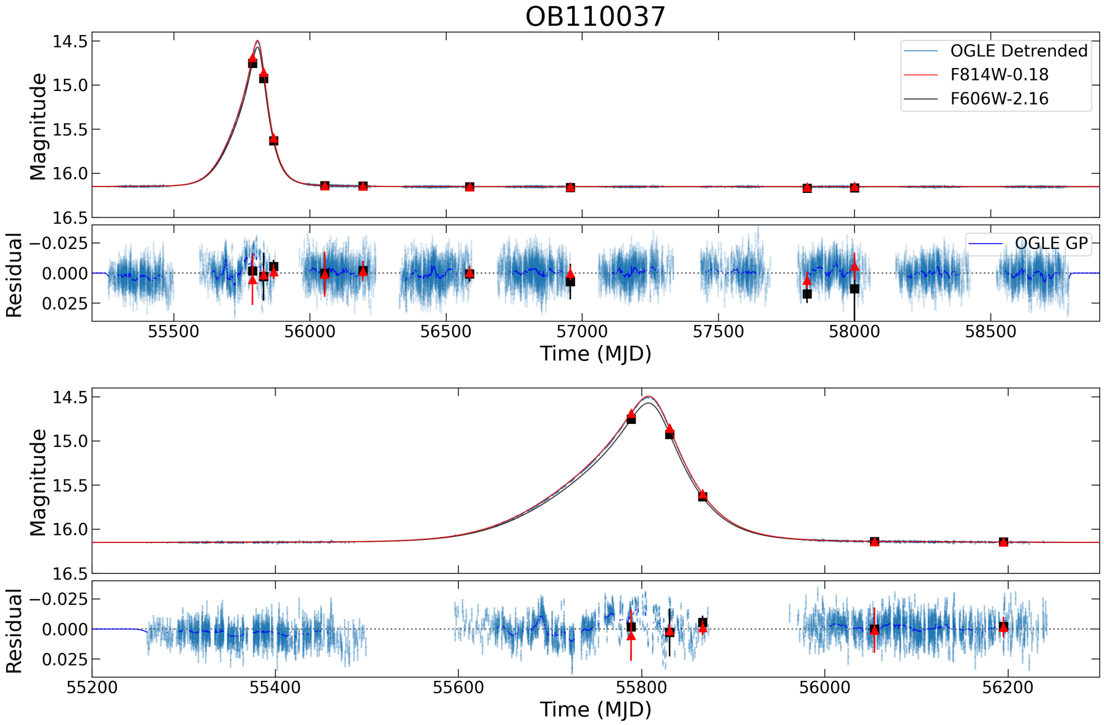

Figure 3.5: Same as Figure 3.3, but for OB110037. Instead of MOA data, the blue data are OGLE data.

2. *Combined star list for one epoch.* Within a single epoch and filter, multiple star lists were aligned to a common coordinate system in an iterative manner using `xym2mat` and `xym2bar` (Anderson and King 2006), which include the distortion solution for the WFC3 camera and filters (Bellini, Anderson, and Bedin 2011) to produce a single matched star list.

3. *Photometric calibration.* Lastly, a zero-point is applied to the star lists to convert from instrumental to Vega magnitudes. Star lists were calibrated against photometrically calibrated star lists on the Hubble Legacy Archive, Data Release 10 (HLA DR10). A magnitude offset is applied later during the astrometric alignment (Chapter 3.3.3) to obtain more precise relative photometry.

Note that data taken in F606W and F814W filters are treated as independent measurements. That is, observations taken on the same date are treated as distinct epochs, and are not combined into a single star list, as the importance of filter dependence in astrometry is not well established. See Chapter 3.3.2.5 and Chapter 3.16 for further details.

Certain epochs were excluded from the analysis; these are marked with an asterisk in Table 3.2. The reason for their exclusion is detailed as follows.

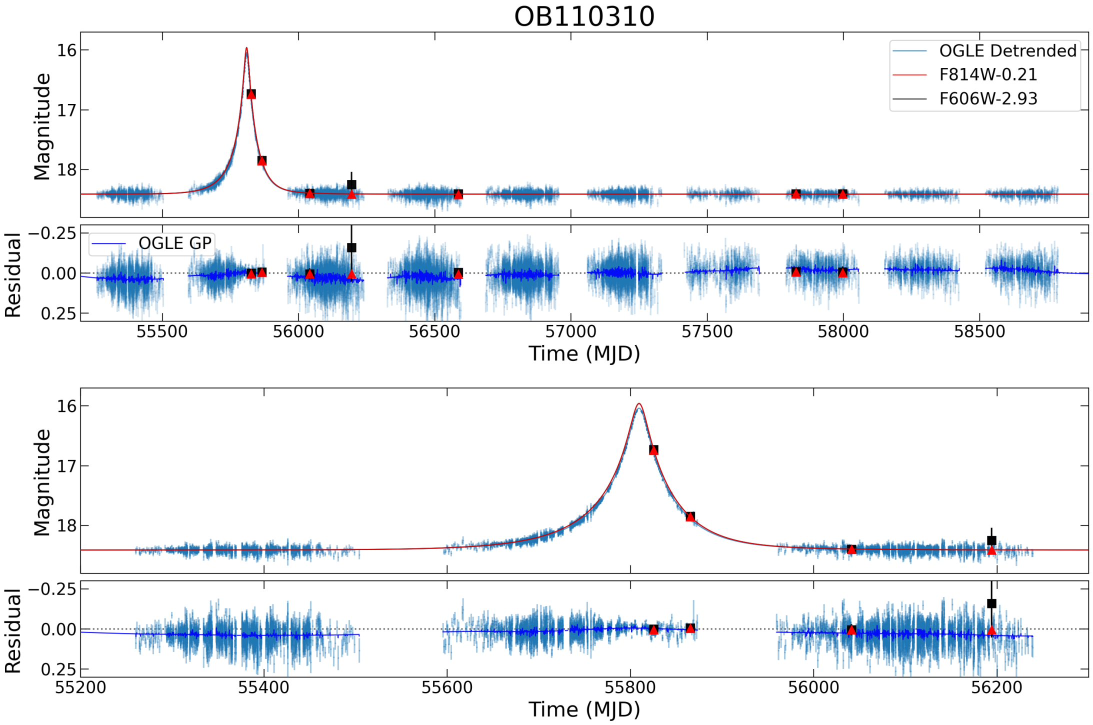

Figure 3.6: Same as Figure 3.5, but for OB110310.

- *Epochs with only a single frame.* Observations with only a single frame per filter cannot produce any useful photometric or astrometric constraints using `hst1pass`. This is the case for the MB09260 2009-10-01 F814W and 2009-10-19, 2010-03-22, and 2010-06-14 F606W epochs. In the MB09260 2010-10-20 F606W epoch, a cosmic ray in one of the exposures interfered with the extraction of the target, effectively leaving only a single usable frame.

- *Multiple exposure times.* Although in principle mixing multiple exposure times in a single epoch is possible, in practice most of the data was obtained with several long exposures and only a single frame with a shorter exposure. Rather than analyze the few short frames with different detection thresholds, PSF reference stars, and astrometric reference stars, which can lead to systematic errors, we choose to only use frames with the same exposure times within an epoch. For this reason, some frames from the MB09260 2009-10-01 F606W, MB10364 2010-09-13 F814W, OB110037 2011-08-15 F814W, OB110310 2013-10-21 F814W, and OB110462 2011-08-08 F606W and F814W epochs were not used.

- *Saturation of target.* No useful astrometric limits can be placed when the target is saturated. The target is saturated in both filters in the MB10364 2011-04-13 and

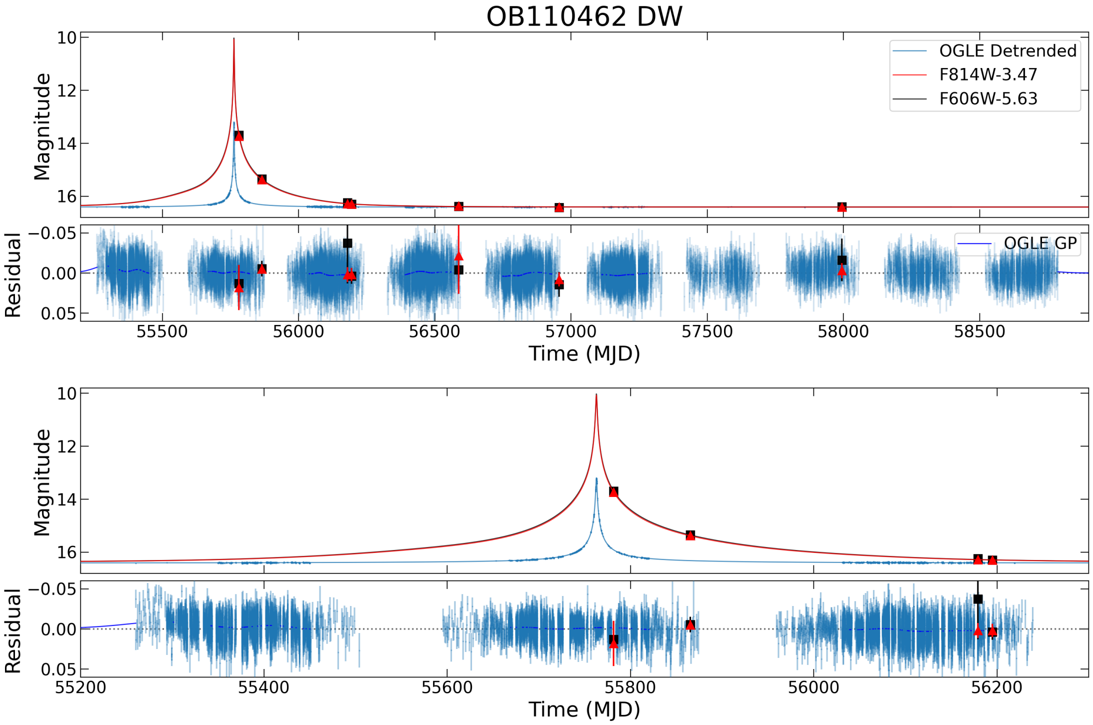

Figure 3.7: Same as Figure 3.5, but for OB110462. This maximum likelihood model was calculated using the default weighted likelihood described in Chapter 3.4.3.

2011-07-22 epochs.

- *Telescope pointing issues.* The observations of OB110462 on 2017-08-11 suffered a telescope drifting issue, resulting in streaked images.

- *Astrometric alignment systematics.* Although there are no standalone issues with the observations of OB110462 on 2013-05-13, astrometric systematics are apparent in the reference stars when this epoch is astrometrically aligned along with the other epochs using the methodology described in Chapter 3.3.2. This is due to the difference in position angle of the observations taken, as the 2013-05-13 epoch was taken at PA = 99.9 deg, while all the other epochs were taken with a PA different by ~ 180 deg, with PA = 255.2 - 276.1 deg. Thus, the 2013-05-13 epoch is left out of the analysis.

  The other targets (MB09260, OB110037, OB110310) with ~ 180 deg differences in PA across observations do not suffer this same problem, as there are multiple observations at each PA. This allows the systematics due to the ~ 180 deg PA flip to be calibrated out during the astrometric alignment.

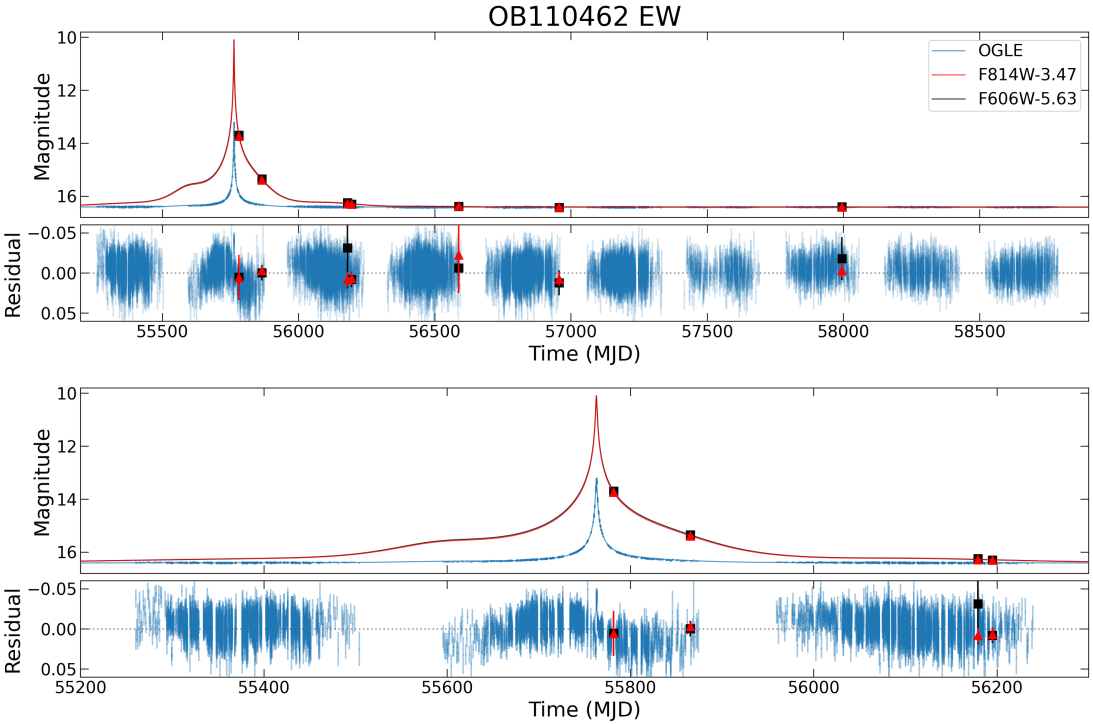

Figure 3.8: Same as Figure 3.5, but for OB110462. This maximum likelihood model was calculated using the equal weight likelihood described in Chapter 3.4.3.

3.3.2 *HST* Astrometric Analysis

The positional measurements extracted from the different epochs of *HST* data (Chapter 3.3.1) must be transformed into a common reference frame in order to derive the motion of the target. This is an iterative process, with multiple “passes” at refining the reference frame, allowing for the best relative astrometry possible to be extracted. We follow a similar procedure as described in §4.2 of Lu et al. (2016). The final positions and magnitudes of the targets resulting from the analysis in this section is presented in Table 3.6. The photometry is shown in Figures 3.3 − 3.8 and the astrometry is shown in Figures 3.14 − 3.19.

3.3.2.1 Alignment procedure

Following standard image processing techniques, a 2-D polynomial transformation of the form

$$x' = a_0 + a_1 x + a_2 y + a_3 x^2 + a_4 xy + a_5 y^2 + ... \tag{3.1}$$

$$y' = b_0 + b_1 x + b_2 y + b_3 x^2 + b_4 xy + b_5 y^2 + ... \tag{3.2}$$

is applied to the images in order to match them to a reference image. A first order 2-D polynomial transformation ($x' = a_0 + a_1 x + a_2 y$; $y' = b_0 + b_1 x + b_2 y$) is an affine transformation[7], which can be used to model translation, rotation, scaling, and shearing introduced by the camera. A higher-order polynomial can correct for additional distortions, but going beyond second order generally does not improve results as the number of free parameters quickly increases and results in overfitting.

In the first pass, the *HST* images are aligned to the absolute reference frame of *Gaia* with a first order 2-D polynomial transformation to roughly establish the transformation. The *Gaia* EDR3 catalog is matched to the *HST* catalog using the pattern matching algorithm of Groth (1986).

In subsequent passes, the *HST* images are aligned to themselves, using a 2-D polynomial transformation going up to second order. It is empirically determined that $3-4$ passes gives optimal results. In each successive pass, the *HST* images are aligned to the reference frame derived in the previous pass, which continually refines the reference frame and derived proper motions.

To calculate the optimal transformation, a set of reference stars $r^R_{ref}(t_0)$ are selected from the stars in reference frame $R(t_0)$ observed at time t_0. The reference stars $r^R_{ref}(t_0)$ are matched to corresponding stars $u^U_{ref}(t)$ in the untransformed $U(t)$ frame observed at time t. The transformation $T : U(t) \rightarrow R(t)$ is found by least-squares minimization of the x and y position residuals from the alignment

$$x_{res} = \sum_i w_{x,i}(x^R_{r,i}(t) - T(x^U_{u,i}(t)))^2 \tag{3.3}$$

$$y_{res} = \sum_i w_{y,i}(y^R_{r,i}(t) - T(y^U_{u,i}(t)))^2 \tag{3.4}$$

where $w_{(x,y),i}$ is the weight for the i-th reference star, $(x^R(t)_{r,i}, y^R(t)_{r,i})$ and $(x^U_{u,i}(t), y^U_{u,i}(t))$ are the positions of the stars in the reference $R(t)$ and untransformed $U(t)$ frames at time t. The positions of the reference stars $r^R_{ref}(t)$ in the reference frame R at time t are propagated from time t_0 using the proper motions

$$x^R_{r,i}(t) = x^R_{r,i}(t_0) + v^R_{x,r,i}(t - t_0) \tag{3.5}$$

$$y^R_{r,i}(t) = y^R_{r,i}(t_0) + v^R_{y,r,i}(t - t_0) \tag{3.6}$$

where $v^R_{(x,y),r,i}$ are the proper motions of the i-th reference stars in reference frame R. After the transformation T is derived, it is applied to all the stars u^U in the U frame to obtain a transformed star list $u^R(t) = T(u^U(t))$, where the stars $u^R(t)$ are now in the frame R. This

---

[7] An affine transformation maps points to points, lines to lines, planes to planes, and so on. Affine tranformations preserve collinearity and ratios of distances. Parallel lines also remain parallel after an affine transformation.

yields starlists for all N epochs $u^R_1(t_1)$, ..., $u^R_N(t_N)$, where the positions of all the stars are now in the same reference frame R. For each star j, a proper motion is derived by finding the best-fit straight line via non-linear least squares through the $n \leq N$ observations.[8]

Lu et al. (2016) examined several different weighting schemes and showed that the resulting astrometry is not affected. We choose to use weights $w_{(x,y),i} = 1/\sigma_{(x,y),i}$, where $\sigma_{(x,y),i}$ are the positional uncertainties of the stars in the untransformed frame. For the positional uncertainties, instead of using the root mean square values σ_{RMS} directly returned by `hst1pass`, we follow Hosek, Lu, Anderson, Ghez, et al. (2015) and use the error on the mean $\sigma_{RMS}/\sqrt{N}$ where N is the number of frames the source is detected in, with an additional empirical additive error. The uncertainties, as well as the procedure used to determine them, are detailed in Chapter 3.9. The additive error term dominates over the $\sigma_{RMS}/\sqrt{N}$ term for bright stars, which makes the positional errors more uniform across epochs and magnitude as would be expected for systematic errors.

As we are interested in the astrometry of the target, the target itself is not used to establish the transformation into a common reference frame (Chapter 3.3.2.2) nor to judge the quality of the final transformation (Figure 3.9).

3.3.2.2 Reference star selection

Reference stars are stars assumed to have linear proper motions, which are used to derive the reference frame transformation and the motions of the other stars. The selection of reference stars depends on multiple considerations, such as the stellar density, amount of geometric distortion, instrumental systematics, and number and brightness of targets of interest, to name a few. The goal is to balance having enough stars to establish the reference frame, while excluding stars which would produce a non-stable reference frame. The criteria for reference star selection for each target is summarized in Table 3.4. We choose reference stars with brightness similar to the target, relatively large radial separations from our target of interest, and exclude likely foreground stars. The target itself is also excluded from being a reference star. We detail the reasoning for these choices below.

Brightness range: Due to the nature of CTE, there are strong magnitude-dependent astrometric residuals, even when using the latest CTE-corrected `_flc` images. However, this is not unexpected (Kuhn et al. 2021). For this reason, stars are chosen to be in a brightness range similar to the one spanned by the target as narrow as possible. For OB110310 and OB110462, which are relatively faint and where there are many stars of similar brightness, all stars falling within ±0.1 mag of the target's brightest and faintest in the *HST* data are used. MB09260, on the other hand, is brighter, with less stars of similar brightness, so the range is larger, with all stars falling within ±1 mag of the target's brightest and faintest in the *HST* data are used. MB10364 is so bright that many stars of comparable brightness are saturated in the longer exposures. Because of this, only bright (F814W < 18.0, F606W

---

[8] Some stars are not detected in all epochs, which is why it is possible to have $n < N$ observations.

< 19.2) and unsaturated stars were selected; the bright limit on the magnitude range differs between epochs because of the different exposure times.

Spatial separation: Only reference stars within $30''$, or $20''$ for the denser field around OB110462, are used as reference stars. This minimizes the impact of geometric distortion residuals and spatially dependent PSF variations.

Foreground stars: A key assumption in the astrometric alignment process is that reference stars have linear proper motions, and parallax effects are ignored. For a typical bulge star 8 kpc from Earth, this is a reasonable assumption as the parallax will be 1/8000 arcsec = 0.125 mas, below our achievable astrometric precision. However, for nearby stars, ignoring parallax is an issue when trying to derive an accurate transformation. As all the target fields are toward the highly extincted Galactic bulge, bright blue stars as identified on a CMD (Figure 3.2) are likely to be nearby and have a non-negligible parallax, and are excluded from the set of reference stars. The color-magnitude exclusion criteria are listed in the last column of Table 3.4. For MB10364, no bright blue stars were removed as reference stars, as all the observations came from within 6 weeks of the same time of year. Hence, any type of yearly parallax signal would be negligible within this time span.

Number of detections: We require reference stars to be detected in most, if not all, epochs. If there are $N_{\rm ep}$ total epochs, we require reference stars to be detected in $N_{\rm ep,detect} = N_{\rm ep} - 2$ epochs.

Lastly, as the motion of the target is the quantity we are interested in, we do not use it as a reference star.

3.3.2.3 Derived stellar proper motions

To evaluate the goodness of the fits of the derived stellar proper motions, we consider the χ^2 distributions of the position residuals

$$\chi^2_x = \sum_t \left(\frac{x_t - x_{t,fit}}{\sigma_{x_t}}\right)^2 \tag{3.7}$$

$$\chi^2_y = \sum_t \left(\frac{y_t - y_{t,fit}}{\sigma_{y_t}}\right)^2 \tag{3.8}$$

where $x \equiv$ RA, $y \equiv$ Dec, $(x, y)_t$ are the positions in the data, $(x, y)_{t,fit}$ are the positions as derived from the linear motion fit, and $\sigma_{(x,y),t}$ are the positional uncertainties at time t. The distributions of χ^2_x and χ^2_y for the reference stars detected in all epochs N_{ep} are shown in Figure 3.9, with the expected χ^2 distribution overplotted on top. The distributions for the positions in F814W and F606W are shown separately. The expected residual distribution has $N_{ep,detect} - 2$ degrees of freedom, as there are two free parameters in the linear motion fit (initial position and proper motion). Note that unlike *Gaia*, this linear model fit does not include parallax. Parallax is only included when modeling the microlensing event.

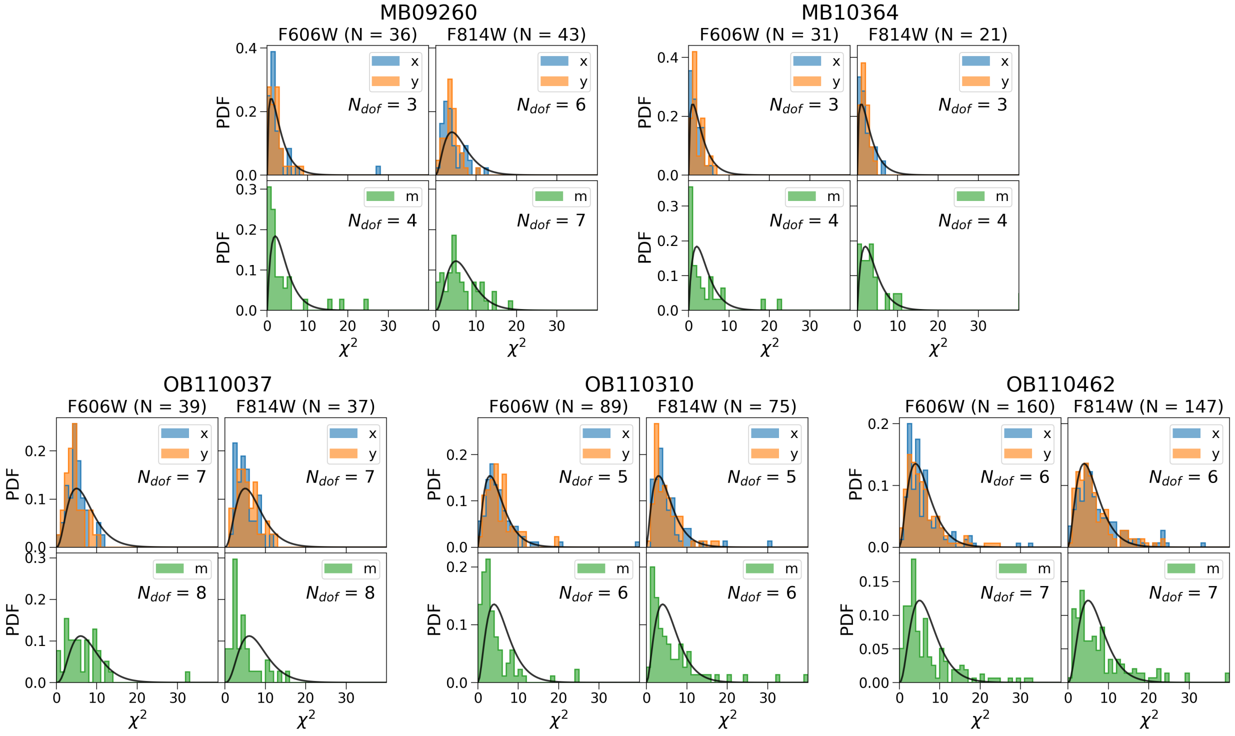

Figure 3.9: Histogram of χ^2 residual values to the linear fits with no parallax for the reference stars of each target (Table 3.4). In each panel, the left column shows the distributions for reference stars in F606W, while the right column shows F814W. The number of reference stars is listed as N. In each panel, the top row shows the χ^2 distribution of residuals of a linear fit to positions vs. time in $x \equiv$ RA and $y \equiv$ Dec. The bottom row shows the χ^2 distribution of residuals of a constant fit to magnitude vs. time. The expected χ^2 distributions are shown in black, with the number of degrees of freedom listed as N_{dof}.

3.3.2.4 OB110462 bias correction

There is a bright star ("the neighbor") ∼10 pixels (∼0.4 arcsec) west of OB110462. The neighbor is ∼3 magnitudes brighter than OB110462 at baseline (F814W = 16.7 mag, F606W = 19.0 mag). Because of its proximity and high contrast, the neighbor's PSF might "leak" onto OB110462 and alter its astrometry and photometry. We perform injection and recovery tests to ascertain the reliability of faint source extraction near a bright source, in order to determine whether the astrometry and photometry of OB110462 as determined in Chapter 3.3.2 and Chapter 3.3.3 is biased by the bright neighbor.

The methodology and results of the injection and recovery analysis are detailed in Chapter 3.10. In summary, the positional bias is negligible when the target is highly magnified and of similar brightness to the neighbor. However, in epochs where the target is no longer magnified, the bright star biases the position of the target. In F814W, where the resolution

Target	Magnitude range	Radius	$N_{\mathrm{ep,detect}}$	EXCLUDED bright blue stars
MB09260	Target range ± 1 mag: 14.5 < F814W < 18.8 16.9 < F606W < 21.7	30”	11	F606W-F814W < 2.6 & F814W < 20.6
MB10364	2010-09-13: 12.5 < F814W < 18.0 11.5 < F606W < 19.2 2010-10-26: 15.1 < F814W < 18.0 13.4 < F606W < 19.2 2011-10-31: 15.8 < F814W < 18.0 14.4 < F606W < 19.2 2012-09-25: 16.0 < F814W < 18.0 14.5 < F606W < 19.2 2013-10-24: 16.1 < F814W < 18.0 14.7 < F606W < 19.2	30”	8	None excluded
OB110037	Target range ± 0.5 mag: 14.4 < F814W < 16.9 16.4 < F814W < 18.8	30”	12	F606W-F814W < 1.75 & F814W < 19.6
OB110310	Target range ± 0.1 mag: 16.9 < F814W < 18.7 19.6 < F606W < 21.4	30”	12	F606W-F814W < 2.4 & F814W < 21.0
OB110462	Target range ± 0.1 mag: 17.1 < F814W < 20.0 19.2 < F606W < 22.1	20”	14	F606W-F814W < 1.9 & F814W < 20.6

Table 3.4: *Reference star criteria.* These are the criteria for the last pass.

is lower, the measured position of the target is biased toward the neighbor by $\sim 0.4\,\mathrm{mas}$ along the target-neighbor separation vector. In F606W, where the resolution is higher, the bias is less ($\sim 0.25\,\mathrm{mas}$) with the direction of bias more randomly oriented. Similarly, the photometric bias is larger when the contrast is large, with the bright neighbor causing the extracted photometry of OB110462 to be brighter than the injected values. The effect is again more severe in F814W than F606W because of the lower resolution.

Using the results of the injection and recovery analysis, we calculate a bias correction to apply to OB110462 astrometry and photometry (Table 3.18). The values in Table 3.18 are added in quadrature to the uncertainties of the astrometry and photometry derived in Chapter 3.3.2 and Chapter 3.3.3.

We only perform this analysis for OB110462, as it is the only faint target near a bright companion. All the other targets are either bright with faint companions, isolated, or both bright and isolated.

3.3.2.5 Astrometric color offset

As mentioned in Chapter 3.3.1 the data taken in F606W and F814W filters are treated as independent measurements. For OB110037 and OB110462, the astrometric measurements in F606W and F814W do not agree within the uncertainties.

For OB110037, although the 2011 and 2012 epochs show good agreement, the 2013 to 2017 epochs become increasingly discrepant as time goes on. We attribute this difference to binarity (Chapter 3.6.4).

In contrast, for OB110462 the astrometry in the F606W and F814W are discrepant in all datasets, but the difference appears to be a relatively constant offset with time. This is true both before and after applying the bias correction in Chapter 3.3.2.4. Because the nature of the color difference appears to be a constant offset, we apply a constant shift to the OB110462 F606W astrometry

$$\Delta_x = \frac{\sum_t w_{x,t}(x_{F814W,t} - x_{F606W,t})}{\sum_t w_{x,t}} \tag{3.9}$$

$$\Delta_y = \frac{\sum_t w_{y,t}(y_{F814W,t} - y_{F606W,t})}{\sum_t w_{y,t}} \tag{3.10}$$

where

$$w_{x,t} = (\sigma^2_{x,F814W,t} + \sigma^2_{x,F606W,t})^{-1/2} \tag{3.11}$$

$$w_{y,t} = (\sigma^2_{y,F814W,t} + \sigma^2_{y,F606W,t})^{-1/2}. \tag{3.12}$$

and t indexes the observation times. Thus the modified astrometry for F606W is

$$x'_{F606W,t} = x_{F606W,t} + \Delta_x \tag{3.13}$$

$$y'_{F606W,t} = y_{F606W,t} + \Delta_y. \tag{3.14}$$

The values of the offset are $\Delta_x = -0.57$ mas and $\Delta_y = 0.39$ mas. Note that these offsets are calculated using the bias-corrected astrometry.[9] See Chapter 3.16 for further details and justification.

We also investigate stars nearby to determine whether any of them show similar behavior. For the 70 stars within $3''$ of OB110462, we calculate the average positional offset between F814W and F606W in RA and Dec using Eqs. 3.9 and 3.10. We then search for stars where the average positional uncertainty in F814W and F606W (whichever is larger) is smaller than

---

[9] Note that even before the bias correction of Chapter 3.3.2.4 is applied, this color offset is still present. In fact, it is slightly larger, with $\Delta_x = -0.79$ mas and $\Delta_y = 0.52$ mas. The bias correction is not the source of the color dependent astrometric offset; rather, it helps to slightly decrease the offset.

the average positional offset to determine which differences are significant. There are 4 stars where the average positional offset is greater than the average positional uncertainty in RA, and an additional 4 stars the average offset is greater than the average positional uncertainty in Dec. Hence, a total of 8 out of the 70 stars near the target also show these significant offsets. Thus, this effect is seen for roughly 10% of the stars, and so is not very unusual. Although we currently have no explanation for its significance, it appears random, and thus include the astrometric offset when analyzing the data, although it may be attributed to binarity (see Chapter 3.6.4 and Chapter 3.6.1). See Chapter 3.16 for additional details.

3.3.2.6 Comparison to *Gaia* proper motions and parallaxes

Target	$\mu_{HST,L}$ (mas/yr)	$\mu_{HST,S}$ (mas/yr)	μ_{Gaia} (mas/yr)
MB10364	$(-5.11^{+1.62}_{-1.10}, -7.78^{+0.58}_{-0.89})$	$(-7.56^{+0.12}_{-0.12}, -6.49^{+0.11}_{-0.11})$	$(-7.43 \pm 0.08, -6.80 \pm 0.05)$
OB110037	$(6.27^{+1.27}_{-1.20}, -6.56^{+0.77}_{-0.81})$	$(2.19^{+0.24}_{-0.24}, -3.87^{+0.20}_{-0.20})$	$(2.40 \pm 0.13, -3.91 \pm 0.09)$
OB110310	$(-0.02^{+1.93}_{-1.16}, -4.68^{+2.39}_{-2.13})$	$(-2.41^{+0.12}_{-0.12}, -7.26^{+0.08}_{-0.08})$	$(-2.08 \pm 1.12, -6.75 \pm 0.58)$

Table 3.5: *Gaia vs. HST Proper Motions.* The source and lens proper motions here have been transformed into the absolute *Gaia* proper motion frame, which is offset to the *HST* proper motion frame as described in Chapter 3.11. The uncertainties on μ_L and μ_S also reflect the uncertainty in the *Gaia* to *HST* proper motion transformation; the standard error on the mean of that transformation was added in quadrature to the uncertainties from the proper motion fits. For this reason, the uncertainties for μ_L and μ_S in this table do not match those in Tables 3.12 – 3.14.

For the three targets with astrometric solutions in *Gaia* EDR3 (MB10364, OB110037, and OB110310; Table 3.3), the *Gaia* proper motions and parallaxes are compared to the fit proper motions and parallaxes presented in Chapter 3.6 and Tables 3.12 – 3.14. Direct comparisons are made in Table 3.5 and Figures 3.10 and 3.11. Note that we fit a proper motion and parallax to the source and lens along with an astrometric microlensing model. On the other hand, *Gaia* fits a proper motion and parallax to the source and lens (the "target") as they are unresolved, and assumes the target is a single star with parallax. The effect of astrometric lensing in *Gaia* on the proper motions is negligible (Chapter 3.12). Additional details about the various *Gaia* metrics discussed are in Chapter 3.13 and Lindegren, Bastian, et al. (2021).

To make proper motion comparisons between *Gaia* and *HST*, the proper motions from the *HST* frame in which the fitting was performed need to be transformed into the absolute *Gaia* frame, as the iterative astrometric alignment procedure described in Chapter 3.3.2 produces a reference frame that is at rest with the average proper motion of the aligned stars (Lu et al. 2016). See Chapter 3.11 on how the proper motion offset between the *HST* and *Gaia* frames is calculated. The source and lens proper motion in the *Gaia* frame, as well as the *Gaia* target proper motions, are listed in Table 3.5 for MB10364, OB110037, and

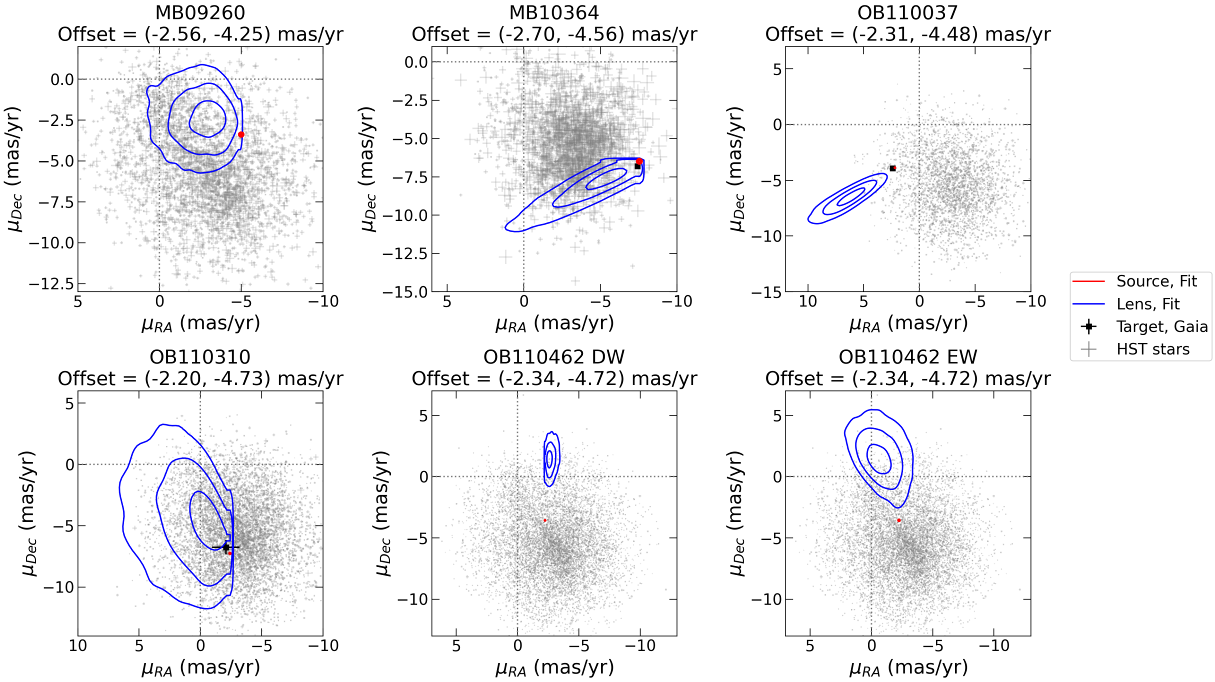

Figure 3.10: Proper motions for stars in the field of the target. The proper motions derived from F814W *HST* observations for stars within 30″ of the target are shown in gray with 1σ uncertainties. Only stars with F814W < 23 for MB09260, OB110310, OB110462 and F814W < 22 for MB10364, OB110037 are shown. For OB110462 there are two models depending on the likelihood used (default weighted "DW" or equal weighted "EW", see Chapter 3.4.3 for details). As the alignment procedure places the stars in a reference frame where the relative motion is zero, a constant offset must be added to obtain proper motions in the original *Gaia* absolute reference frame. This offset is calculated by matching the stellar positions in *HST* to those in *Gaia* with `astrometric_excess_noise_sig`< 2, and then calculating the 3σ clipped average weighted by the uncertainty in their difference. The offset value is given in the title for each field. For targets in *Gaia* where a single-star proper motion is estimated (MB10364, OB11037, OB110310), they are plotted as black squares. The lens and source proper motion as determined from fitting the *HST* data with a microlensing model is shown in blue and red $1-2-3\sigma$ contours, respectively. Note that the red contours are extremely small.

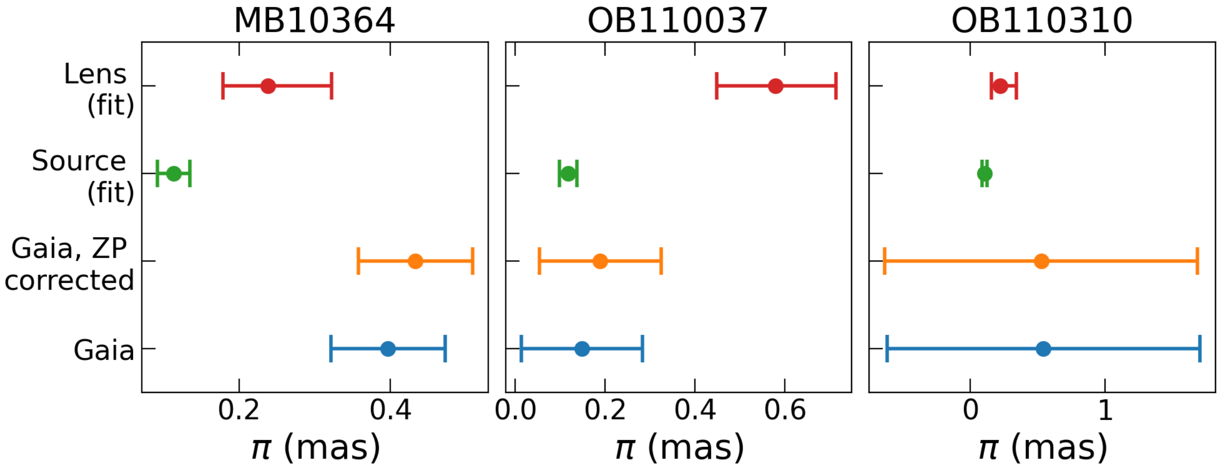

Figure 3.11: Comparison of *Gaia* parallaxes with the fit lens and source parallax.

OB110310. The vector point diagram for all stars from the *HST* observations transformed to the *Gaia* frame, along with the $1-2-3\sigma$ contours from the source and lens fit, are shown in Figure 3.10. For MB10364, OB110037, and OB110310 the target proper motion from *Gaia* is also included.

MB10364 MB10364's proper motion in *Gaia* is $(-7.43 \pm 0.08, -6.80 \pm 0.05)$ mas/yr. The fit from *HST* for the lens is $(-5.11^{+1.62}_{-1.10}, -7.78^{+0.58}_{-0.89})$ mas/yr, inconsistent with *Gaia* in RA and Dec at $\sim 2\sigma$. The fit from *HST* for the source is $(-7.56^{+0.12}_{-0.12}, -6.49^{+0.11}_{-0.11})$ mas/yr, inconsistent with *Gaia* in Dec at $\sim 2\sigma$. MB10364 has parallax $\pi = 0.43 \pm 0.08$ in *Gaia*. The source and lens parallax from the MB10364 fits are $\pi_S = 0.11^{+0.02}_{-0.02}$, $\pi_L = 0.24^{+0.08}_{-0.06}$, neither of which are consistent with the *Gaia* value. The *Gaia* fit for MB10364 has a large renormalized unit weight error (RUWE = 1.388), and a large astrometric excess noise ($\epsilon = 0.406$ mas) with high significance ($D = 12.020$), indicating the single star model is not providing a good fit. This mismatch is not due to astrometric microlensing (Chapter 3.12). The most likely explanation for the discrepancies are crowding—there are several stars close to MB10364 that would cause confusion (Figures 3.1 and 3.12). As the source and lens are not resolvable, the fact that 15% of the Image Parameters Determination (IPD) algorithm has identified a double peak is likely due to confusion. This means the *Gaia* measurement is not reliable. See Chapter 3.13 for further discussion.

OB110037 OB110037's proper motion in *Gaia* is $(2.40 \pm 0.13, -3.91 \pm 0.09)$ mas/yr. The fit from *HST* for the lens is $(6.27^{+1.27}_{-1.20}, -6.56^{+0.77}_{-0.81})$ mas/yr, inconsistent with *Gaia* in both RA and Dec at $\sim 3\sigma$. The fit from *HST* for the source is $(2.19^{+0.24}_{-0.24}, -3.87^{+0.20}_{-0.20})$ mas/yr, consistent with *Gaia*. The caveat to this is that the fit to the *HST* F606W astrometry is poor

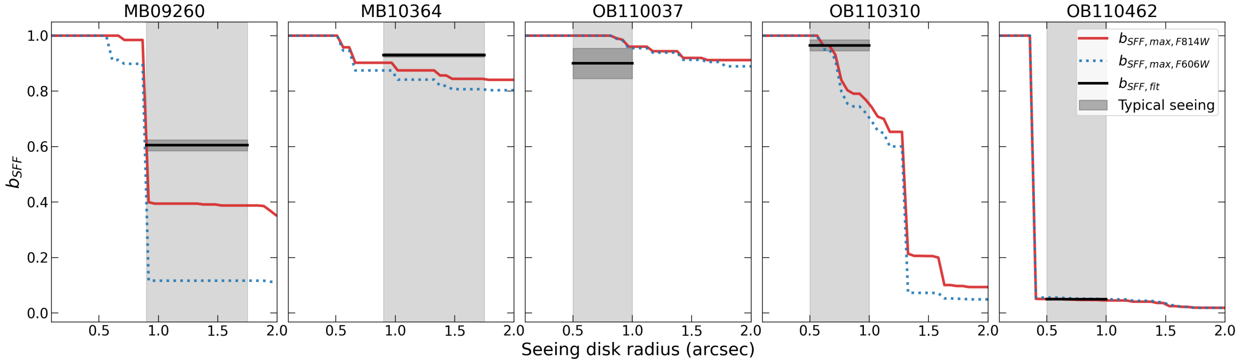

Figure 3.12: Comparison of b_{SFF} inferred from fitting microlensing events, as compared to upper limits inferred from the high-resolution *HST* images. The typical seeing disk *radius* ranges are shown in light gray for MOA (MB09260, MB10364) and OGLE (OB110037, OB110310, OB110462). The inferred value of b_{SFF} from fitting each microlensing event is shown as a black line, with uncertainties in dark gray. The upper limits on blending $b_{SFF,max}$ as a function of aperture radius, as estimated using the method described in Chapter 3.6.7, are shown as the solid red line (*F814W*) and the dotted blue line (*F606W*). For the three OGLE targets, at the relevant seeing disk radii, the inferred value of b_{SFF} from the fit are at or below $b_{SFF,max}$ as inferred from the *HST* images. For the two MOA targets, the inferred values of b_{SFF} are higher than the maximum value as inferred from the *HST* images. In the case of MB09260, this is likely due to the bright star around $1.0''$ from the target which causes an abrupt change in b_{SFF} around that radius; proper convolution with a PSF would likely resolve the difference. In the case of MB10364, the difference is minimal, and likely just due to the imperfect nature of the comparison (for example, lack of proper PSF convolution, and F814W not exactly matching the red filter in MOA/OGLE).

(Figure 3.18). However, the astrometric lensing model is mostly independent of the proper motion model, hence the proper motion value can still be believed. OB110037 is very well measured and behaved in *Gaia* (it is the only target with a 5-parameter solution, see Table 3.3). Additionally from the image (Figures 3.1 and 3.12) OB110037 is relatively bright and isolated. The fact that the fit source and *Gaia* proper motions are consistent would indicate that the lens is dim in comparison to the star in *Gaia G* band. This makes sense as the astrometric shift for OB110037 is undetectable by the time *Gaia* begins observing.

OB110037 is well modeled in *Gaia* by a single source with parallax. Although the microlensing model is a poor fit to the astrometry due to a time-dependent color-offset, the proper motions from our model are in good agreement with *Gaia*. OB110037 has parallax $\pi = 0.19 \pm 0.13$ in *Gaia*. The source and lens parallax from the OB110037 fits are $\pi_S = 0.12^{+0.02}_{-0.02}$, $\pi_L = 0.58^{+0.14}_{-0.13}$. The source parallax is consistent with the *Gaia* value. We note that the source may appear well-behaved in *Gaia* because the astrometry is in a single filter. The multi-band *HST* astrometry may be useful in identifying binary companions. See

Chapter 3.13 for further discussion.

OB110310 OB110310's proper motion in *Gaia* is $(-2.08 \pm 1.12,\ -6.75 \pm 0.58)$ mas/yr. The fit from *HST* for the lens is $(-0.02^{+1.93}_{-1.16},\ -4.68^{+2.39}_{-2.13})$ mas/yr, consistent with *Gaia* due to large uncertainties in both *Gaia* and the fit. The fit from *HST* for the source is $(-2.41^{+0.12}_{-0.12},\ -7.26^{+0.08}_{-0.08})$ mas/yr, consistent with *Gaia*. OB110310 has parallax $\pi = 0.53 \pm 1.16$ in *Gaia* (note the OB110310 zero point correction is an extrapolation), consistent with non-detection of parallax. The source and lens parallax from the OB110310 fit are $\pi_S = 0.10^{+0.02}_{-0.02}$, $\pi_L = 0.22^{+0.12}_{-0.07}$, which are both consistent within the very wide uncertainties of *Gaia*. The fact that the source and *Gaia* proper motions are consistent would indicate that the lens is dim in comparison to the star in *Gaia* G band; blending in F814W and F606W also suggest a dark lens (Table 3.14). The fact that in the IPD 55% of transits have either truncation or multiple gates flagged in one or more windows indicates likely contamination. OB110310 is not very bright and in a somewhat crowded region (Figures 3.1 and 3.12). The astrometric noise is large ($\epsilon = 0.894\,\text{mas}$) but the value is insignificant ($D = 0.332$). Together these explain why the *Gaia* measurement does not produce very good constraints. See Chapter 3.13 for further discussion.

3.3.3 *HST* Photometric Analysis

To obtain precise relative photometry, for each epoch a small constant magnitude offset is applied to the stars. The offset is calculated by assuming the reference stars have constant brightness in time, which we define as the 3σ clipped mean. As with the positional uncertainties, for the magnitude uncertainties we used the error on the mean, with an additional additive error empirically determined during the astrometric alignment process; details are in Chapter 3.9.

Analogous to the positional transformation, we evaluate the magnitude transformation by checking how well a constant magnitude describes the stars

$$\chi^2_m = \sum_i \left(\frac{m_i - m_0}{\sigma_{m_i}} \right)^2 \tag{3.15}$$

where m_i are the calibrated magnitudes, m_0 is the constant magnitude fit, and σ_{m_i} is the uncertainty on the calibrated magnitude. The χ^2 distributions for the magnitude residuals of the reference stars detected in all N_{ep} epochs are shown in the bottom panels of Figure 3.9. The expected residual distribution has $N_{ep,detect} - 1$ degrees of freedom, as there is one free parameter in the constant magnitude fit.

Target	Filter	Date	RA (mas)	Dec (mas)	Mag (Vega)
MB09260	F814W	2009-10-19	7.80 ± 0.15	5.15 ± 0.14	15.484 ± 0.005
		2010-03-22	5.31 ± 0.14	3.80 ± 0.14	17.656 ± 0.005
		2010-06-14	4.31 ± 0.18	2.97 ± 0.18	17.760 ± 0.007

		2010-10-20	2.54 ± 0.14	1.60 ± 0.14	17.812 ± 0.014
		2011-04-19	0.12 ± 0.15	0.01 ± 0.15	17.838 ± 0.018
		2011-10-24	-2.44 ± 0.21	-1.71 ± 0.21	17.833 ± 0.005
		2012-09-25	-7.07 ± 0.15	-4.80 ± 0.15	17.836 ± 0.007
		2013-06-17	-10.57 ± 0.26	-7.02 ± 0.22	17.829 ± 0.011
	F606W	2009-10-01	8.15 ± 0.22	5.57 ± 0.22	17.899 ± 0.013
		2011-04-19	0.13 ± 0.57	0.17 ± 0.57	20.750 ± 0.083
		2011-10-24	-2.17 ± 0.52	-1.59 ± 0.52	20.748 ± 0.007
		2012-09-25	-6.23 ± 1.31	-4.41 ± 1.32	20.733 ± 0.023
		2013-06-17	-10.10 ± 0.49	-7.21 ± 0.54	20.738 ± 0.036
MB10364	F814W	2010-09-13	9.61 ± 0.16	8.24 ± 0.16	13.366 ± 0.011
		2010-10-26	8.76 ± 0.16	7.72 ± 0.15	14.657 ± 0.005
		2011-10-31	1.23 ± 0.19	0.81 ± 0.18	15.315 ± 0.006
		2012-09-25	-5.70 ± 0.19	-4.89 ± 0.19	15.315 ± 0.010
		2013-10-24	-13.90 ± 0.18	-11.89 ± 0.18	15.316 ± 0.009
	F606W	2010-09-13	8.81 ± 1.70	8.81 ± 1.70	14.538 ± 0.017
		2010-10-26	8.46 ± 0.50	7.59 ± 0.50	15.842 ± 0.017
		2011-10-31	1.47 ± 0.28	1.13 ± 0.28	16.498 ± 0.006
		2012-09-25	-5.66 ± 0.31	-4.99 ± 0.31	16.504 ± 0.008
		2013-10-24	-13.89 ± 0.25	-11.79 ± 0.25	16.502 ± 0.008
OB110037	F814W	2011-08-15	-4.35 ± 0.11	8.24 ± 0.14	14.864 ± 0.021
		2011-09-26	-4.33 ± 0.12	7.82 ± 0.12	15.029 ± 0.005
		2011-11-01	-4.34 ± 0.12	7.52 ± 0.12	15.774 ± 0.006
		2012-05-07	-3.10 ± 0.13	5.40 ± 0.12	16.315 ± 0.019
		2012-09-25	-2.22 ± 0.14	3.86 ± 0.14	16.321 ± 0.009
		2013-10-21	0.10 ± 0.12	-0.36 ± 0.12	16.327 ± 0.005
		2014-10-26	2.45 ± 0.14	-4.36 ± 0.13	16.328 ± 0.006
		2017-03-13	7.74 ± 0.12	-13.21 ± 0.12	16.334 ± 0.007
		2017-09-04	8.05 ± 0.14	-14.90 ± 0.13	16.322 ± 0.011
	F606W	2011-08-15	-4.02 ± 0.25	8.15 ± 0.24	16.916 ± 0.011
		2011-09-26	-4.23 ± 0.20	7.79 ± 0.20	17.086 ± 0.020
		2011-11-01	-4.39 ± 0.24	7.36 ± 0.23	17.794 ± 0.005
		2012-05-07	-2.69 ± 0.31	5.34 ± 0.33	18.301 ± 0.016
		2012-09-25	-2.34 ± 0.26	3.81 ± 0.26	18.306 ± 0.006
		2013-10-21	0.65 ± 0.24	-0.76 ± 0.24	18.314 ± 0.006
		2014-10-26	3.73 ± 0.22	-5.29 ± 0.22	18.320 ± 0.015
		2017-03-13	9.48 ± 0.26	-14.04 ± 0.26	18.331 ± 0.008
		2017-09-04	9.80 ± 0.27	-16.84 ± 0.24	18.326 ± 0.027
OB110310	F814W	2011-09-21	5.20 ± 0.14	15.95 ± 0.14	16.945 ± 0.013
		2011-10-31	4.86 ± 0.17	14.85 ± 0.17	18.058 ± 0.004
		2012-04-24	3.79 ± 0.13	11.35 ± 0.13	18.602 ± 0.013

		2012-09-24	2.82 ± 0.17	8.47 ± 0.17	18.616 ± 0.011
		2013-10-21	0.14 ± 0.13	0.59 ± 0.14	18.621 ± 0.005
		2017-03-14	-7.92 ± 0.18	-23.84 ± 0.18	18.608 ± 0.005
		2017-09-01	-8.88 ± 0.16	-27.36 ± 0.16	18.613 ± 0.012
	F606W	2011-09-21	5.43 ± 0.22	15.98 ± 0.22	19.663 ± 0.018
		2011-10-31	4.73 ± 0.34	15.06 ± 0.34	20.780 ± 0.007
		2012-04-24	3.55 ± 0.38	11.44 ± 0.37	21.329 ± 0.034
		2012-09-24	2.79 ± 0.49	8.02 ± 0.49	21.180 ± 0.212
		2013-10-21	0.56 ± 0.30	0.87 ± 0.30	21.339 ± 0.007
		2017-03-14	-7.81 ± 0.31	-23.78 ± 0.31	21.333 ± 0.022
		2017-09-01	-9.31 ± 0.34	-27.08 ± 0.35	21.335 ± 0.034
OB110462	F814W	2011-08-08	7.53 ± 0.15	11.45 ± 0.15	17.209 ± 0.028
		2011-10-31	6.44 ± 0.23	9.71 ± 0.22	18.849 ± 0.006
		2012-09-09	4.08 ± 0.23	6.55 ± 0.23	19.756 ± 0.009
		2012-09-25	4.25 ± 0.37	6.42 ± 0.37	19.767 ± 0.008
		2013-10-22	1.43 ± 0.33	2.40 ± 0.34	19.839 ± 0.048
		2014-10-26	-0.87 ± 0.29	-1.00 ± 0.30	19.881 ± 0.009
		2017-08-29	-7.18 ± 0.27	-10.61 ± 0.26	19.874 ± 0.009
		2021-10-01	-15.67 ± 0.19	-24.93 ± 0.19	19.865 ± 0.020
	F606W	2011-08-08	6.76 ± 0.43	11.77 ± 0.43	19.313 ± 0.023
		2011-10-31	6.25 ± 0.50	10.54 ± 0.52	20.974 ± 0.010
		2012-09-09	4.60 ± 0.37	5.57 ± 0.37	21.867 ± 0.050
		2012-09-25	4.38 ± 0.59	6.40 ± 0.59	21.920 ± 0.010
		2013-10-22	1.76 ± 0.37	2.45 ± 0.36	22.011 ± 0.015
		2014-10-26	-1.22 ± 0.46	-0.83 ± 0.44	22.042 ± 0.015
		2017-08-29	-7.10 ± 0.41	-10.62 ± 0.41	22.017 ± 0.027
		2021-10-01	-15.44 ± 0.44	-25.06 ± 0.44	22.021 ± 0.017

Table 3.6: *HST Calibrated Data for Each Target.* Relative positions and magnitude of the target by epoch and filter.

3.4 Microlensing Modeling

The mass of the lens M_L in a microlensing event is given by

$$M_L = \frac{\theta_E}{\kappa \pi_E}, \tag{3.16}$$

where θ_E is the angular Einstein radius (Equation 3.17), π_E is the microlensing parallax (Equation 3.21), and $\kappa = 4G/(1AU \cdot c^2) = 8.14\,mas/M_\odot$ is a constant. Densely sampled photometric microlensing observations constrain π_E, while astrometric microlensing observations constrain θ_E.[10]

To measure these quantities of interest, we simultaneously fit the ground-based photometry and *HST* photometry and astrometry with a point-source point-lens (PSPL) microlensing model with parallax. We do not consider models involving either binary lenses or sources, nor higher-order effects beyond parallax; these are beyond the scope of this work. Discussion of the need for models more complex than PSPL with parallax are discussed in Chapter 3.6.

Throughout this section and the remainder of the paper, we report vector quantities decomposed into their RA and Dec components, subscripted by "$\alpha*$" and "δ". Because we work solely in the Equatorial coordinate system, we also equivalently refer to RA as East and Dec as North, subscripted by "E" or "N", where RA increases to the East and Dec increases to the North.

3.4.1 Microlensing Definitions

All microlensing quantities defined in the following section are in the heliocentric reference frame.

By rearranging the terms in Equation 3.16, the Einstein radius, which sets the angular scale of the microlensing event, can be written

$$\theta_E = \sqrt{\kappa \pi_{rel} M_L} \tag{3.17}$$

where $\pi_{rel} = \pi_L - \pi_S$ is the relative parallax of the lens and source.

The Einstein crossing time t_E, the time it takes for the source to traverse the angular radius of the lens and sets the timescale of the events, is given by

$$t_E = \frac{\theta_E}{\mu_{rel}} \tag{3.18}$$

where μ_{rel} is the lens-source proper motion $|\boldsymbol{\mu}_S - \boldsymbol{\mu}_L|$.

The source-lens separation on sky $\boldsymbol{\theta}_S - \boldsymbol{\theta}_L$ normalized by the Einstein radius is denoted $\boldsymbol{u}(t)$. The minimum separation is denoted $\boldsymbol{u}(t_0) = \boldsymbol{u}_0$. The impact parameter u_0 is the scalar quantity associated with $\boldsymbol{u}_0$. We follow the convention of Gould (2004) where if $u_{0,E} > 0$, the source is to the East of the lens, and $u_0 > 0$; if $u_{0,E} < 0$, the source is to the West of the lens, and $u_0 < 0$.[11] If rectilinear motion is assumed, the lens-source separation is given by

$$\boldsymbol{u}(t) = \boldsymbol{u}_0 + \frac{t - t_0}{t_E} \hat{\boldsymbol{\mu}}_{rel}. \tag{3.19}$$

---

[10] Theoretically, astrometric microlensing observations should also be able to constrain π_E, but due to the cadence of observations, this is currently unachievable.

[11] Note that we define our coordinate system differently than Gould (2004). Gould (2004) works in a system where the position of the source relative to the lens is defined in a coordinate system that is right-handed in the relative proper motion and minimum separation vector. However, we work in a system where the coordinate system is consistent on the sky; this means a coordinate system based on the relative proper motion and minimum separation vector does not always preserve handedness.

However, an Earthly observer's perspective of the lensing event is modulated by the Earth's motion around the Sun. For events with long duration ($t_E \gtrsim 3$ months), the Earth's orbital motion violates this rectilinear assumption and must be taken into account. This modifies $\boldsymbol{u}(t)$ to

$$\boldsymbol{u}(t) = \boldsymbol{u}_0 + \frac{t - t_0}{t_E}\hat{\boldsymbol{\mu}}_{rel} - \pi_E \boldsymbol{P}(t) \tag{3.20}$$

where

$$\pi_E = \frac{\pi_{rel}}{\theta_E} \tag{3.21}$$

is the microlensing parallax and $\boldsymbol{P}(t)$ is the parallax vector, defined to be the Sun-Earth separation vector normalized by 1 AU. The microlensing parallax vector $\boldsymbol{\pi}_E$ (not to be confused with the parallax vector $\boldsymbol{P}(t)$) encodes the magnitude of the microlensing parallax and the direction of the relative source-lens proper motion:

$$\boldsymbol{\pi}_E = \pi_E \hat{\boldsymbol{\mu}}_{rel}. \tag{3.22}$$

The photometric brightening of the source is given by

$$A(u) = \frac{u^2 + 2}{u\sqrt{u^2 + 4}}. \tag{3.23}$$

where the total flux $F(t)$ in the telescope aperture is

$$F(t) = A(t)F_S + F_L + F_N \tag{3.24}$$

where F_S, F_L, and F_N are the fluxes of the source, lens, and neighboring un-lensed stars in the aperture of the telescope, respectively. The source flux fraction is

$$b_{SFF} = \frac{F_S}{F_S + F_L + F_N} \tag{3.25}$$

and quantifies the fraction of light lensed in an observed microlensing event. Note that b_{SFF} depends on the observing wavelength and seeing/aperture. The non-source flux $F_L + F_N$ is also called blend flux. Blend flux decreases b_{SFF} and dilutes the magnitude of both the photometric amplification and astrometric shift.

A PSPL photometric microlensing event is characterized by five geometric parameters: t_0, u_0, t_E, and $\boldsymbol{\pi}_E$. For each telescope that observes this event, two additional parameters, m_{base} and b_{SFF}, are needed to describe each light curve; these depend on the seeing and camera filter. As all photometric microlensing observable quantities are normalized by θ_E, the lens mass cannot be determined.

In contrast, astrometric microlensing provides a direct measurement of θ_E. The apparent position of the source, i.e. the centroid of the lensed source images $\boldsymbol{\theta}_{S,c}$, is given by

$$\boldsymbol{\theta}_{S,c}(u, \theta_E) = \frac{(u^2 + 3)\boldsymbol{u}\theta_E}{u^2 + 2}. \tag{3.26}$$

Assuming no blended light, the difference between the source's apparent and true positions, i.e. the astrometric shift, is given by

$$\boldsymbol{\delta}_c(u, \theta_E) = \frac{\boldsymbol{u}\theta_E}{u^2 + 2}. \tag{3.27}$$

The astrometric shift δ_c is maximized at $u = \sqrt{2}$. This corresponds to the value of the maximum astrometric shift

$$\delta_{c,max} = \frac{\theta_E}{\sqrt{8}}, \tag{3.28}$$

which is directly proportional to the Einstein radius.

Note that Equation 3.27 is for an unblended event, i.e. $b_{SFF} = 1$. If an event has $b_{SFF} < 1$, the non-source light would dilute the astrometric shift (see Equations 11 and 12 in Lam, Lu, Hosek, et al. (2020)). For the five candidates analyzed here, $b_{SFF} \sim 1$ in the *HST* filters, so assuming that the astrometry is unblended in *HST* is valid.

3.4.2 Modeling framework

We perform parameter estimation using a Bayesian framework. Bayes' theorem

$$\pi(\boldsymbol{\Theta})\mathcal{L}(\boldsymbol{y}|\boldsymbol{\Theta}) = \mathcal{Z}(\boldsymbol{y})\mathcal{P}(\boldsymbol{\Theta}|\boldsymbol{y}) \tag{3.29}$$

relates the prior π and likelihood $\mathcal{L}$ to the evidence $\mathcal{Z}$ and posterior $\mathcal{P}$. The goal of parameter estimation is to calculate $\mathcal{P}$. The likelihood $\mathcal{L}(\boldsymbol{y}|\boldsymbol{\Theta})$ is presented in Chapter 3.14, and the priors $\pi(\boldsymbol{\Theta})$ are discussed in Chapter 3.15.

The data is fit using `MultiNest` (Feroz et al. 2009), an implementation of the nested sampling algorithm (Skilling 2004). Nested sampling produces an estimate of the evidence $\mathcal{Z} = \int \pi(\boldsymbol{\Theta})\mathcal{L}(\boldsymbol{\Theta})\, d\boldsymbol{\Theta}$, and as a by-product, the posterior $\mathcal{P}$. In contrast to methods such as MCMC, nested sampling is designed to better explore multimodal likelihood spaces; however, care must still be taken to ensure that all local minima are explored.

3.4.3 Likelihood weighting

There is a question of how best to combine the photometry and astrometry data sets, as they represent two different types of measurements. In particular, the question is how much weight each dataset should receive given that there are several orders of magnitude more ground-based data points than *HST* data points. Thus, the ground-based photometry has an outsize effect on the likelihood. It can be argued that each data point should contribute equally to the likelihood. We consider this to be "default weight" (hereafter abbreviated as DW) likelihood, i.e.

$$\log \mathcal{L}_{tot} = \log \mathcal{L}_{O,phot} + \log \mathcal{L}_{H,phot} + \log \mathcal{L}_{H,ast} \tag{3.30}$$

where $\mathcal{L}_{O,phot}$, $\mathcal{L}_{H,phot}$, and $\mathcal{L}_{H,ast}$ are the likelihoods of the OGLE or MOA photometry, *HST* photometry, and *HST* astrometry respectively.

However, it could also be argued that each dataset is independent, and so should each contribute equally to the likelihood. We call this the "equal weight" (hereafter abbreviated as EW) likelihood, i.e.

$$\log \mathcal{L}_{tot} = \frac{\log \mathcal{L}_{O,phot}}{n_{O,phot}} + \frac{\log \mathcal{L}_{H,phot}}{n_{H,phot}} + \frac{\log \mathcal{L}_{H,ast}}{n_{H,ast}} \tag{3.31}$$

where $n_{O,phot}$, $n_{H,phot}$, and $n_{H,ast}$ are the number of data points in in the OGLE photometry, *HST* photometry, and *HST* astrometry.

These different likelihoods are essentially giving the different datasets different weights, in the case that they are inconsistent with each other. For all targets, we fit using the default weight likelihood; for OB110462 we additionally fit using the equal weight likelihood.

3.5 Constraining the nature of the lens

By modeling photometric and astrometric microlensing data as described in Chapter 3.4, the lens' mass can be measured. However, a mass measurement alone cannot distinguish the difference between a $5M_\odot$ stellar lens and a $5M_\odot$ BH. Additional information about the lens' brightness is needed, which can be estimated using the source flux fractions in the high-resolution *HST* filters. By calculating the brightest star allowed by the inferred source flux fractions, we can determine whether a luminous lens (i.e. stellar lens) or dark lens (i.e. compact object lens) scenario is more likely.

We follow a procedure similar to Wyrzykowski, Kostrzewa-Rutkowska, et al. (2016) in order to calculate the probability of a dark lens. The two main differences between the analysis of Wyrzykowski, Kostrzewa-Rutkowska, et al. (2016) and ours is that they work with photometric data only and must invoke a Galactic model to obtain lens masses and distances, while in our case astrometric data allows us to fit lens mass and distances. This greatly simplifies the analysis as we do not need to calculate the Jacobian to transform the PDFs between different variables. In addition, we use realistic stellar and Galactic models to determine the lens luminosities, instead of relying on simple mass-luminosity scaling relations.

From fitting the microlensing data, we have posterior distributions for the lens mass M_L, distance d_L, baseline magnitude m_{base}, and source flux fraction b_{SFF}. In the following analysis we reassign any fit values with $b_{SFF} \geq 1$ to instead be equal to 0.999999. This is because values of $b_{SFF} \geq 1$ would result in an infinite lens magnitude (Equation 3.32).[12]

---

[12] One might worry this could bias the results. However, a visual check comparing the posteriors (both individual and joint) for lens mass and distance don't show a change when excluding fits with $b_{SFF} > 1$. In particular, the lens mass and distances are nearly independent of the lens magnitude. In addition, if the true value of b_{SFF} is 1, we would expect some scatter around that value, including unphysical > 1 values.

We draw a random sample of 1000 stars from our posterior. For each star we calculate 1) the brightest lens allowed by b_{SFF} and m_{base}, and 2) the brightest star allowed by M_L and d_L.

To calculate 1), by assuming there are no contaminating neighbor stars, $b_{SFF} = F_S/(F_S + F_L)$, an upper limit can be placed on the brightness of the lens:

$$m_L = m_{base} - 2.5 \log_{10}(1 - b_{SFF}). \tag{3.32}$$

We denote this $m_L(b_{SFF}, m_{base})$.

To calculate 2), we use the simple stellar population synthesis code `SPISEA` (Hosek, Lu, Lam, et al. 2020) to generate a suite of simple stellar populations (SSPs) to simulate the possible lens population. We use the `MISTv1.2` solar metallicity isochrones (Choi et al. 2016), `get_merged_atmosphere` atmosphere model[13], Damineli et al. (2016b) reddening law, and Kroupa (2001) initial mass function (IMF) over the mass range $0.1M_\odot < M < 120M_\odot$. Each cluster is $10^4 M_\odot$, in order to reduce stochastic effects in the sampling of the IMF.

SSPs are generated at the distances spanned by each target's lens distance posteriors, sampled every 0.25 kpc. SSPs of ages 7.0 to 10.0 $\log_{10}$ years in increments of 0.5 $\log_{10}$ years are simulated at each sampled distance in order to cover the age range of disk and bulge stars. The stellar age distribution as a function of distance is drawn from the `Galaxia` Milky Way stellar simulation (Sharma et al. 2011), which implements a version of the Besançon Galactic model of Robin, Reylé, et al. (2003). As our target sight lines are toward the bulge, most of the stars are old, with $\gtrsim 85\%$ of stars being at least 9.0 $\log_{10}$ years old, although younger stars tend to be at closer distances as disk stars dominate. To calculate the simulated stars' apparent magnitudes, we use the 3-D extinction map of Marshall et al. (2006), accessed via the `dustmaps` software package (Green 2018), to obtain an A_{K_s} value for each distance.

For each sample from the posterior, we sample one of the SSPs at the corresponding distance at a particular stellar age from the Galactic distribution. All stars in the simulated SSP with masses within 10% of the sampled posterior mass are identified, and the brightest apparent magnitude of the star in this group is denoted $m_L(M_L, D_L, \bigstar)$. If no stars are found within 10% of the sampled posterior mass, this indicates that stars of that mass have all died and formed compact objects.

If $m_L(M_L, D_L, \bigstar) < m_L(b_{SFF}, m_{base})$, a star with the inferred stellar mass from stellar evolution models would be too bright to be hidden in the blended light allowed by the fit. This means that the lens is not a star. We take this to mean the lens is a compact object, and hence a dark lens. Thus the lower limit on the probability of a dark lens in the observed filter is the fraction of samples where $m_L(M_L, D_L, \bigstar) < m_L(b_{SFF}, m_{base})$ or no mass match is found.

Objects with $m_L(M_L, D_L, \bigstar) > m_L(b_{SFF}, m_{base})$ are samples where a luminous stellar lens is consistent with the inferred amount of blending. Note that $m_L(b_{SFF}, m_{base})$ is an

---

[13] This is a combination of the ATLAS9 (Castelli et al. 2004), PHOENIX v16 (Husser et al. 2013), BTSettl (Baraffe et al. 2015), abd Koester10 (Koester 2010) models. For further details see Appendix B of Hosek, Lu, Lam, et al. (2020).

upper limit on the brightness of the lens, as we assumed all the blended flux in Equation 3.32 is due to the lens; it could be due to unresolved unrelated neighbor stars. Thus the upper limit on the probability of a stellar lens in the observed filter is thus the fraction of samples where $m_L(M_L, D_L, \bigstar) > m_L(b_{SFF}, m_{base})$.

For dark lenses (i.e. any objects where $m_L(M_L, D_L, \bigstar) < m_L(b_{SFF}, m_{base})$ or no star of the same mass was found in the simulated SSP), we categorize them as brown dwarfs (BD), white dwarfs (WD), neutron stars (NS), or BHs by simplistically sorting them by their masses:

- Brown dwarfs: $M < 0.2M_\odot$
- White dwarfs: $0.2M_\odot < M < 1.2M_\odot$
- Neutron stars: $1.2M_\odot < M < 2.2M_\odot$
- Black holes: $M > 2.2M_\odot$.

In reality there is overlap between white dwarf and neutron star masses, and the overlap between neutron star and BH masses (if they overlap at all) is unknown. In addition, the maximum brown dwarf mass set by stellar physics is $0.08M_\odot$, but we extend this up to $0.2M_\odot$ to have continuity between the lowest mass WDs of around $0.2M_\odot$. Hence these values are only approximate.

The above analysis is performed for both the *HST* F606W and F814W filters. The reported probabilities are the joint constraint. A lens is dark if no masses consistent with a stellar lens are found in either filter. A lens is also dark if the maximum inferred lens flux is insufficient to hide a star (i.e. $m_L(M_L, D_L, \bigstar) < m_L(b_{SFF}, m_{base})$) in either filter. A lens is luminous if the maximum inferred lens flux is sufficient to hide a star (i.e. $m_L(M_L, D_L, \bigstar) > m_L(b_{SFF}, m_{base})$) in both filters. We do not perform this analysis for the OGLE or MOA photometry parameters as the high resolution *HST* images show the seeing-limited apertures have unrelated neighbor stars in the blend, and hence the limits will all be weaker than using *HST*.

3.6 Results

A large (> 1 mas) astrometric microlensing signal is detected in OB110462 (Chapter 3.6.1). A filter-dependent astrometric signal is also detected in OB110037 (Chapter 3.6.4); averaging the astrometry across the F814W and F606W filters shows a small but significant 0.4 mas signal. The remaining three targets MB09260 (Chapter 3.6.2), MB10364 (Chapter 3.6.3), and OB110310 (Chapter 3.6.5) have astrometric signals that are below *HST*'s detection threshold. Table 3.7 reports the lens masses, Einstein radii, maximum astrometric shifts, and microlensing parallaxes either as measured values or upper limits.

In Chapter 3.6.1 – Chapter 3.6.5, the posteriors of the joint photometry and astrometry microlensing fits for the individual targets are presented. Tables 3.9 – 3.14 list the median

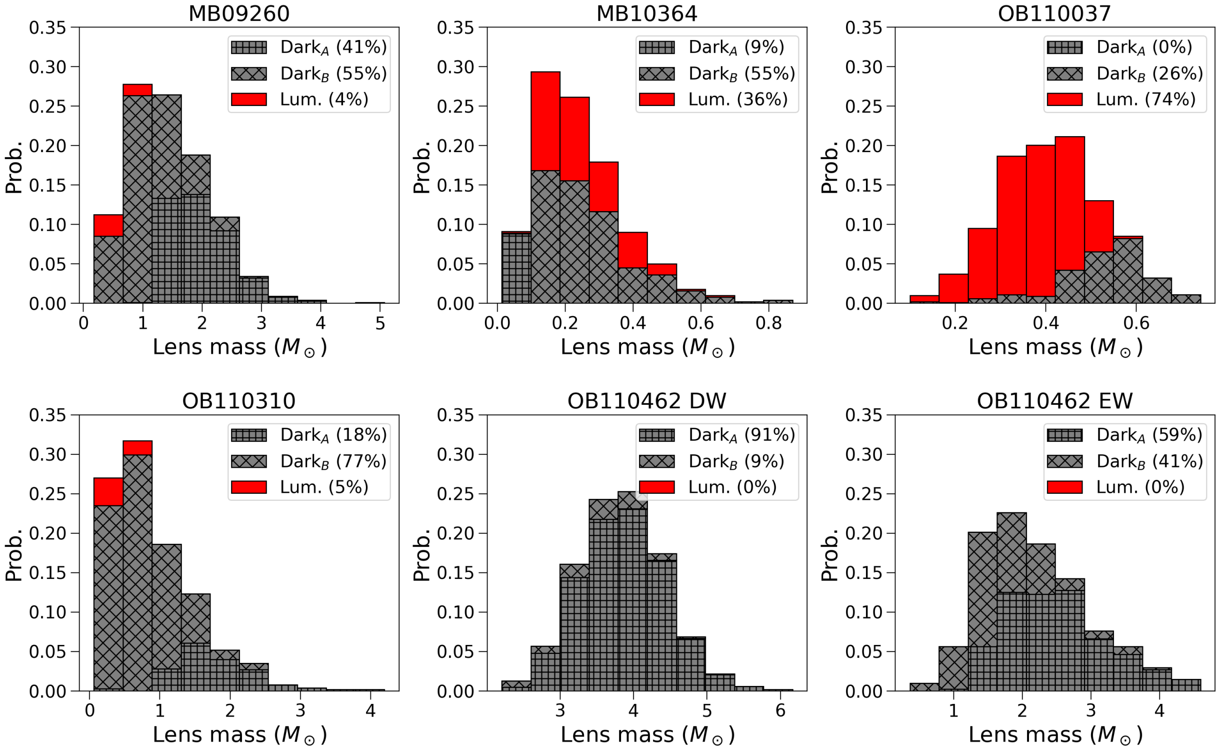

Figure 3.13: Probabilities for dark (*gray*) and luminous lenses (*red*) , as a function of lens mass for each target. Lenses that are dark because all stars of that mass have already evolved and died (implying they are compact objects) are subscripted with A (*square hatch*), while lenses that are dark because a star would be too bright to be hidden in the allowed lens flux are subscripted with B (*diamond hatch*). The probabilities for the luminous lenses are upper limits, while the probabilities for the dark lenses are lower limits, since the method described in Chapter 3.5 only places an upper limit on the brightness of the lens. Note that there are two fits for OB110462, one with equal weighting to the astrometry and photometry data (OB110462 EW) and one with the default weighting of the astrometry and photometry data (OB110462 DW). See Chapter 3.4.3 for details.

and 1σ (68%) credible intervals for each parameter, in addition to the maximum a posteriori (MAP) and maximum likelihood (MLE)[14] solution.

Using the methodology described in Chapter 3.5, constraints are placed on the lens types of each target. We report the relative probabilities of Star:BD:WD:NS:BH in Table 3.8. Figure 3.13 shows the distribution of dark vs. luminous lens probability as a function of mass for each target. Table 3.8 lists the upper limit on the probability of a stellar lens and

---

[14] For most of the targets, the MAP solution is equal to the MLE solution, i.e. values of the parameters for the mode of the posterior distribution are the same as those where the likelihood function is maximized.

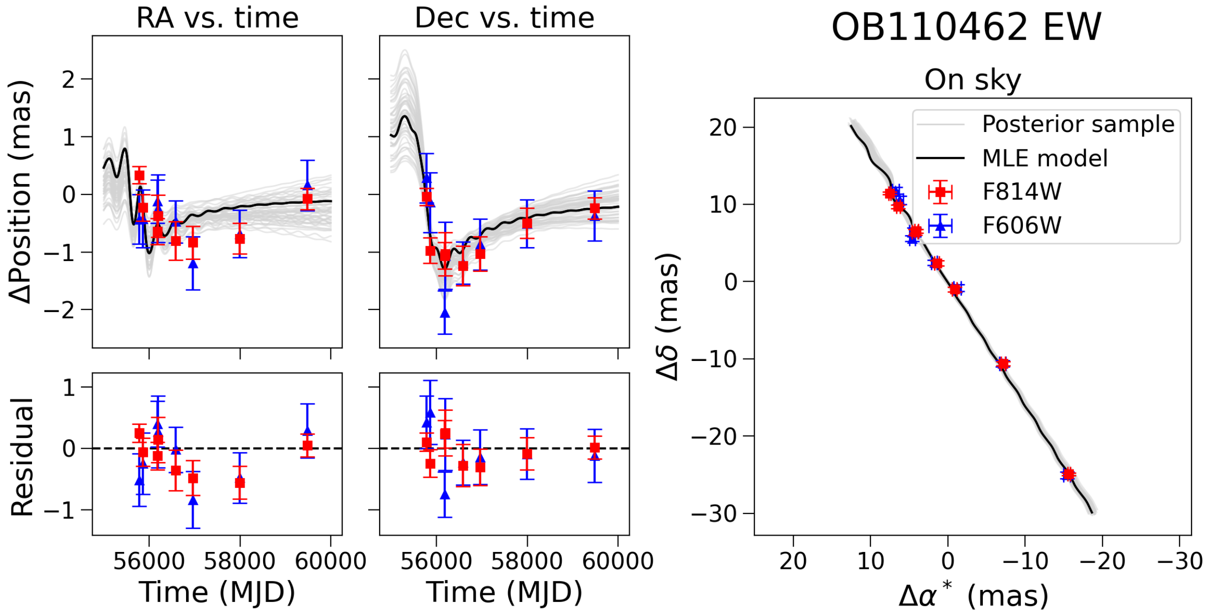

Figure 3.14: OB110462 astrometry, using the equally weighted likelihood. *Left column, top to bottom*: RA vs. time with maximum likelihood (MLE) unlensed source motion model subtracted; residuals to the MLE model for RA vs. time fit. *HST* F814W astrometry data is shown in red; *HST* F606W astrometry data is shown in blue. The MLE model is shown in black. Fifty random draws from the posterior distribution are shown in light gray. *Middle column, top to bottom*: Same as left column, except Dec instead of RA. *Right panel*: astrometry as seen on-sky, in the barycentric frame. OB110462 shows a strong > 1 mas astrometric microlensing signal.

Parameter	θ_E (mas)	$\delta_{c,max}$ (mas)	$M_L(M_\odot)$	π_E
MB09260	< 2.42	< 0.85	$1.37^{+2.72}_{-1.16}$	$0.09^{+0.13}_{-0.03}$
MB10364	< 1.76	< 0.62	$0.21^{+0.61}_{-0.18}$	$0.27^{+0.02}_{-0.01}$
OB110037	$1.24^{+1.10}_{-0.90}$	$0.44^{+0.39}_{-0.32}$	$0.41^{+0.37}_{-0.30}$	$0.37^{+0.02}_{-0.02}$
OB110310	< 2.75	< 0.97	$0.78^{+2.98}_{-0.68}$	$0.13^{+0.20}_{-0.08}$
OB110462 (EW)	$4.13^{+2.98}_{-3.02}$	$1.46^{+1.05}_{-1.07}$	$2.15^{+3.50}_{-1.43}$	$0.24^{+0.11}_{-0.16}$
OB110462 (DW)	$3.89^{+1.69}_{-1.61}$	$1.37^{+0.60}_{-0.57}$	$3.79^{+2.17}_{-1.64}$	$0.12^{+0.03}_{-0.04}$

Table 3.7: *99.73% credible intervals/upper limits.* There are two entries for OB110462, one based on a fit with "default weighting" (OB110462 DW) and one based on a fit with "equal weighting" (OB110462 EW). See Chapter 3.4.3 for details.

lower limits on the probabilities of different dark lenses for each target. In Chapter 3.7.2, we compare the yield of BHs from our search to that expected from simulations assuming there

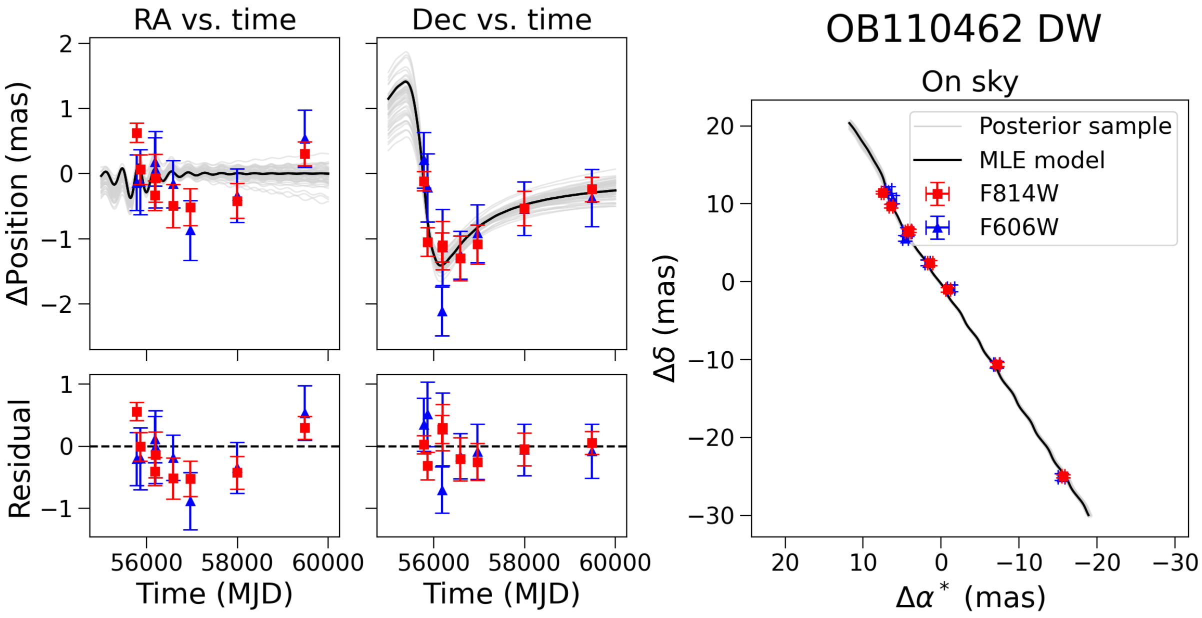

Figure 3.15: Same as Figure 3.14, but using the default weighted likelihood for OB110462.

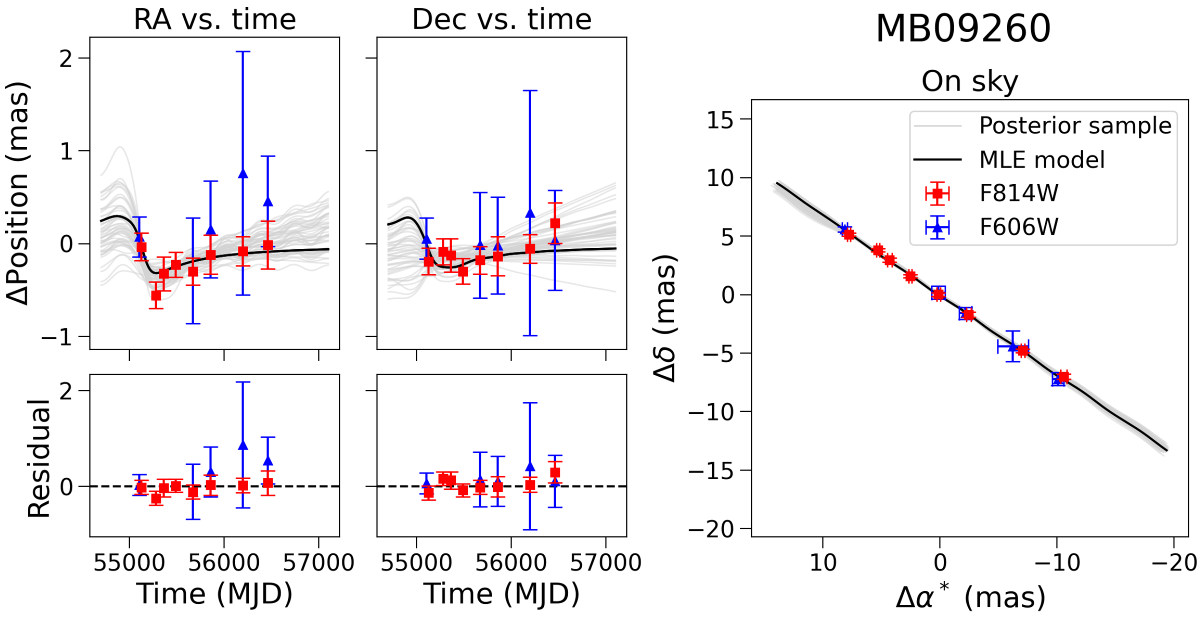

Figure 3.16: MB09260 astrometry. Same as Figure 3.14, but for MB09260. The astrometric signal is small, and around the limit of the precision of the F814W measurements.

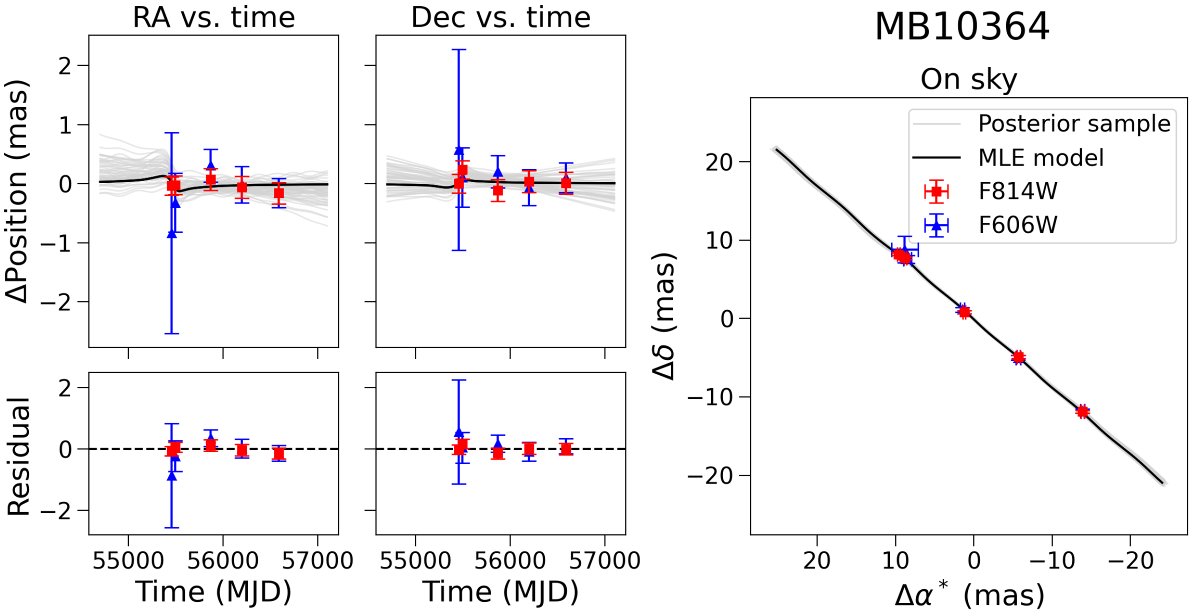

Figure 3.17: Same as Figure 3.14, but for MB10364. The astrometric signal is small, at or below the limit of the precision of the F814W measurements.

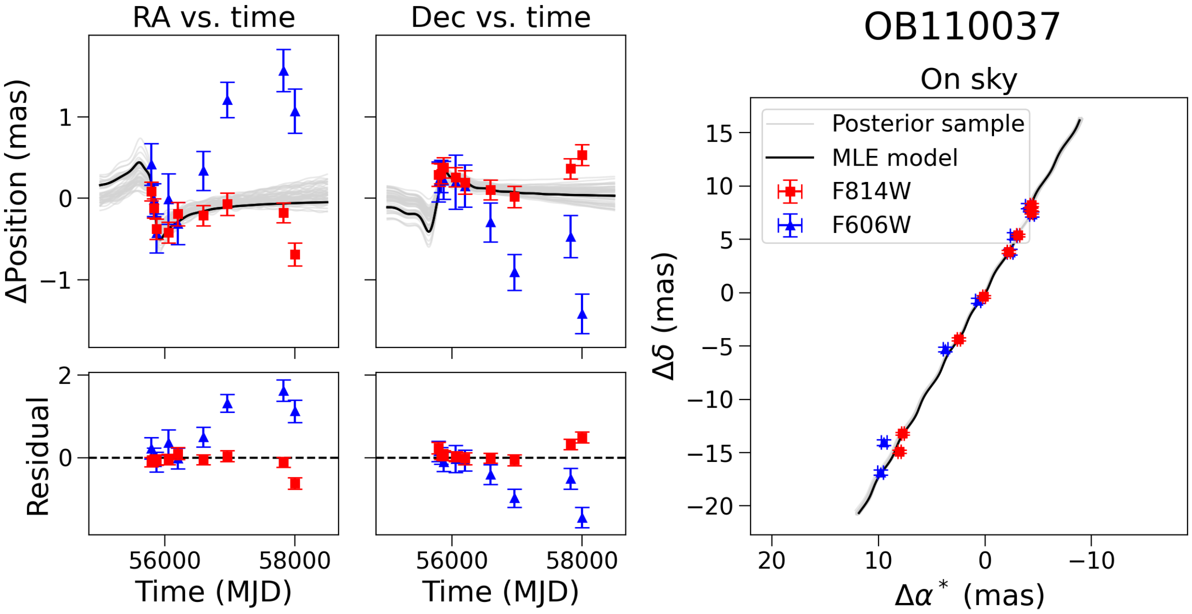

Figure 3.18: Same as Figure 3.14, but for OB110037. The photometry and astrometry seem to indicate this object is a binary.

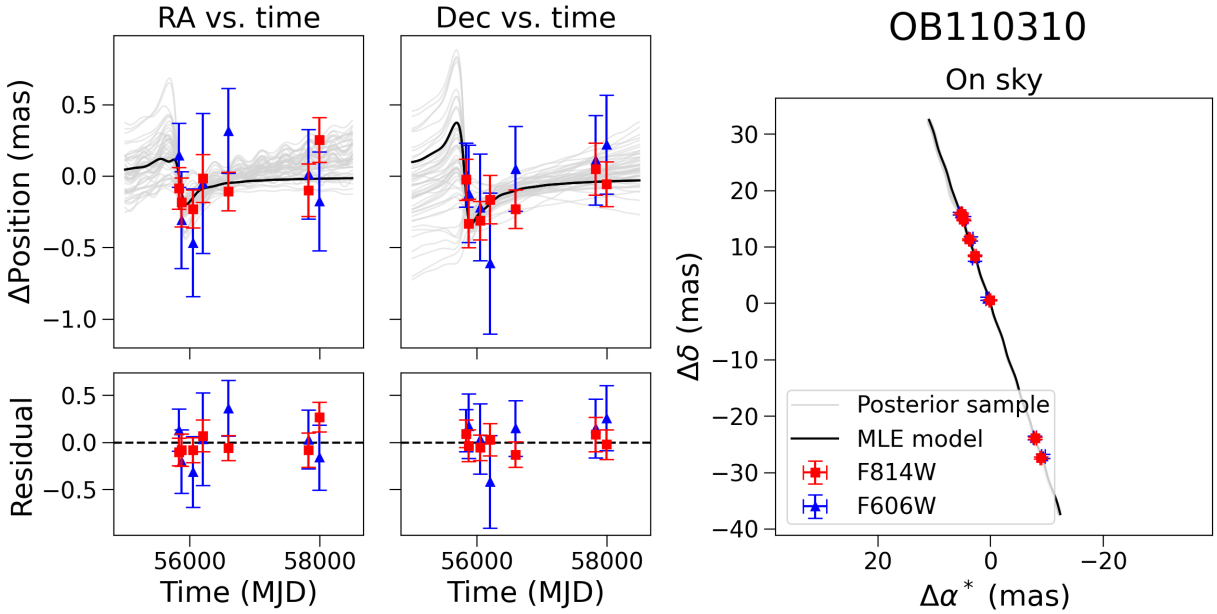

Figure 3.19: Same as Figure 3.14, but for OB110310. The astrometric signal is small, and around the limit of the precision of the F814W measurements.

Target	Star	BD	WD	NS	BH
MB09260	4	0	38	44	14
MB10364	36	29	35	0	0
OB110037	74	0	26	0	0
OB110310	5	3	65	22	5
OB110462 DW	0	0	0	0	100
OB110462 EW	0	0	6	50	44

Table 3.8: *Lens type probabilities (%).* The Star probabilities are upper limits, while the brown dwarf (BD), white dwarf (WD), neutron star (NS), and BH probabilities are lower limits. This is because the luminous lens probabilities are upper limits, and the dark lens probabilities are lower limits; see Chapter 3.5 for details. Note that there are two entries for OB110462, one based on a fit with "default weighting" (OB110462 DW) and one based on a fit with "equal weighting" (OB110462 EW). See Chapter 3.4.3 for details.

are $\sim 10^8$ BHs in the Milky Way.

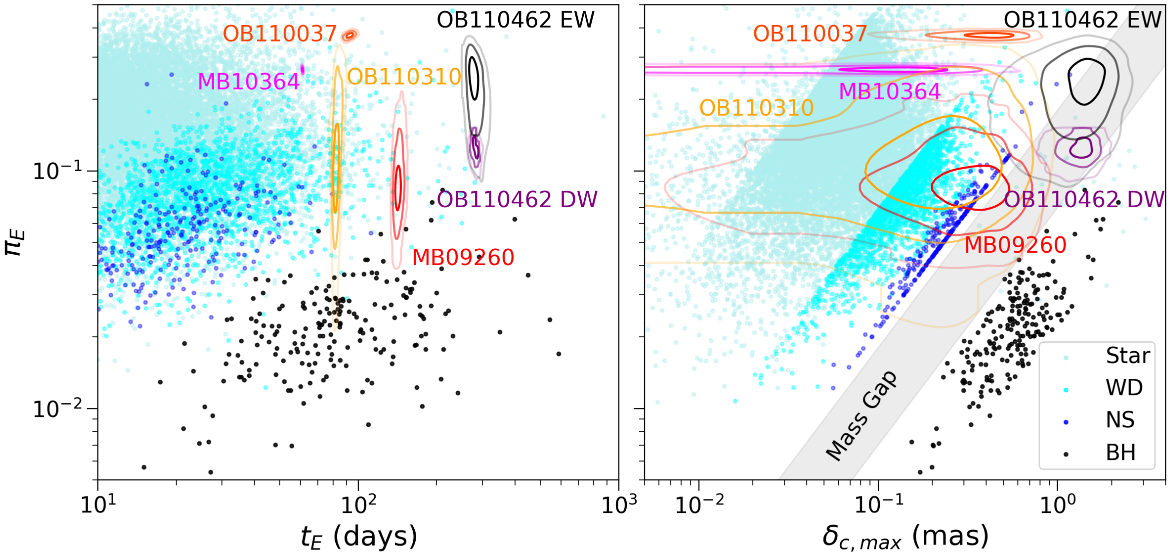

Figure 3.20: Microlensing parallax π_E vs. Einstein crossing time t_E *(left)* and maximum astrometric shift $\delta_{c,max}$ *(right)*. Points are from the `PopSyCLE` simulation. Contours are $1-2-3\sigma$ (39.3-86.5-98.9%) credible regions from the microlensing model fits to the five BH candidates. There are two fits for OB110462 (default weight (DW) and equal weight (EW); see Chapter 3.4.3 for details). The OB110462 DW solution has a smaller π_E than the OB110462 EW solution, and has a correspondingly more massive lens mass. Both solutions fall solidly in the NS-BH mass gap, making OB110462 the best BH-candidate. MB09260 and OB110310 are most likely white dwarfs or neutron stars, although due to uncertainty in π_E and $\delta_{c,max}$ higher and lower mass lenses cannot be definitively ruled out. OB110037 and MB10364 are not BHs as they have very large π_E, as well as relatively short t_E and small $\delta_{c,max}$.

3.6.1 OB110462

From the microlensing fit, we infer that OB110462 is a NS or a mass gap BH, depending on the likelihood function adopted (see Chapter 3.4.3). The data and model for OB110462 with the default weight (DW) likelihood are shown in Figures 3.7 (photometry) and 3.15 (astrometry), and the fit posteriors are summarized in Table 3.9. The mass posteriors of the lens are shown in Figure 3.21. The inferred Einstein crossing time t_E is $280.87^{+6.54}_{-5.96}$ days, the microlensing parallax π_E is $0.12^{+0.01}_{-0.01}$, the Einstein radius θ_E is $3.89^{+1.12}_{-1.16}$, and the lens mass M_L is $3.79^{+0.62}_{-0.57} M_\odot$. The data and model for OB110462 with the equal weight (EW) likelihood are shown in Figures 3.8 (photometry) and 3.14 (astrometry), and the fit posteriors are summarized in Table 3.10. The inferred Einstein crossing time t_E is $278.56^{+12.52}_{-9.16}$ days, the microlensing parallax π_E is $0.24^{+0.05}_{-0.05}$, the Einstein radius θ_E is $4.13^{+0.96}_{-0.91}$, and the lens mass M_L is $2.15^{+0.67}_{-0.54} M_\odot$. Further, we find that the object is located relatively nearby at

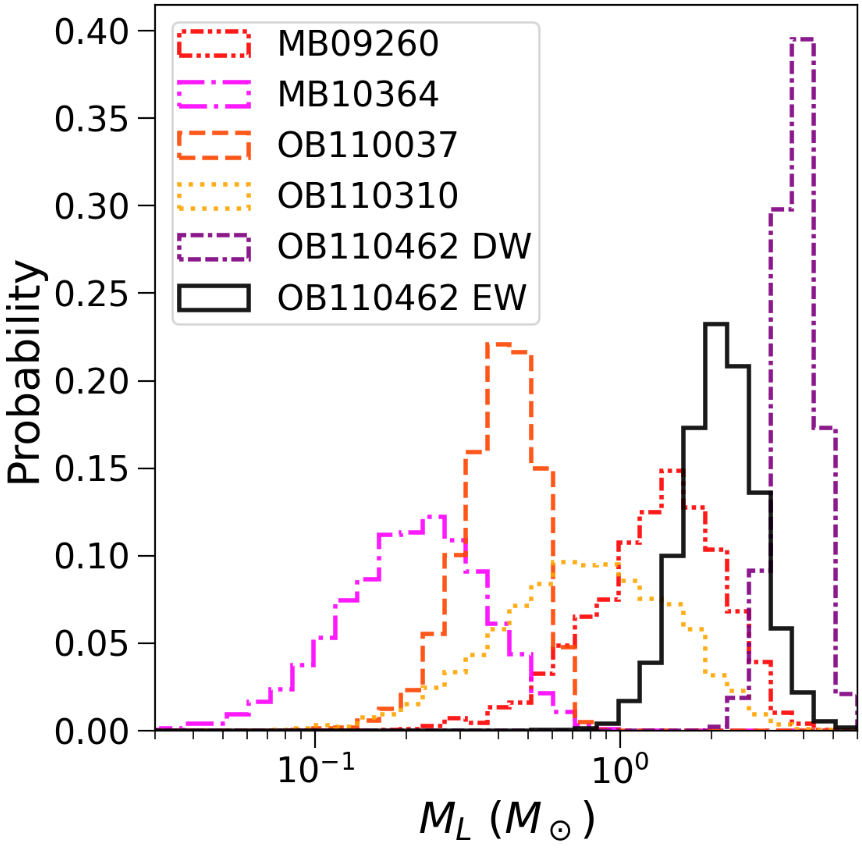

Figure 3.21: Lens mass posterior probabilities for the five microlensing BH candidates. Two mass posteriors are shown for OB110462, one for each model (default weight (DW) and equal weight (EW)). See Chapter 3.4.3 for details on the two models.

0.70 − 1.92 kpc in the direction of the Galactic bulge and has a small transverse velocity of < 30 km/s. Figure 3.22 shows the on-sky lensing geometry of OB110462 inferred from the DW and EW likelihood models, showing the relative motions of the source and lens with respect to each other.

The probability that OB110462 is a dark lens is 100%, ruling out the possibility of a stellar lens and making OB110462 the first detection of a compact object with astrometric microlensing. Assuming there is a transition from white dwarfs to neutron stars at $1.2 M_\odot$ and neutron stars to BHs at $2.2 M_\odot$, the relative probabilities of WD:NS:BH are 0:0:100 for the default weighted (DW) fit and 6:50:44 for the equally weighted (EW) fit.

The microlensing fit also yields information about the distance and transverse velocity of the lens. The lens is relatively nearby at a distance of 1.47 - 1.92 kpc or 0.70 - 1.30 kpc for the DW and EW solutions, respectively. The inferred lens velocity is < 30 km/s for both solutions with a slower velocity 2 - 12 km/s from the EW solution and a faster velocity of 21 - 27 km/s from the DW solution. In both cases, the velocities appear consistent with the compact object receiving little to no kick, although the line-of-sight velocity is not measurable from these observations.

A point-source, point-lens (PSPL) model is not the end of the story for OB110462. There is no PSPL model which can simultaneously fit both the photometry and the astrometry. Specifically, the direction of μ_{rel} preferred by the photometry and astrometry are different. The best fit PSPL model for the default weight (DW) likelihood fits the photometry very well, but leaves a significant $\sim 0.5\,\mathrm{mas}$ coherent astrometric residual in RA (Figure 3.15). The best fit PSPL model for the equal weight (EW) likelihood leaves a significant and coherent ~ 0.03 mag residual in the photometry, but fits the astrometry in RA better than the DW likelihood model, although some unexplained astrometric residuals still remain (Figure 3.14). More complex microlensing geometry models, such as those involving a binary source or lens, should be explored. As mentioned in Chapter 3.3.2.5, we apply a constant positional offset to the F606W data in order to make it match up with the F814W data. However, this filter dependent positional difference may actually be astrophysical and consistent with a small contribution from a faint companion to the source. Either way, both solutions indicate a NS or BH detection.

The alternative explanation to the tension between the photometry and astrometry of OB110462 is some type of systematic error in one or both sets observations. This possibility is discussed in Chapter 3.7.5.

3.6.2 MB09260

The data and model for MB09260 are shown in Figures 3.3 (photometry) and 3.16 (astrometry), and the fit posteriors are summarized in Table 3.11. The inferred Einstein crossing time t_E is $142.64^{+3.49}_{-2.87}$ days, the microlensing parallax π_E is $0.09^{+0.03}_{-0.01}$, the Einstein radius θ_E is $1.04^{+0.42}_{-0.39}$, and the lens mass is $1.37^{+0.74}_{-0.60} M_\odot$.[15]

The probability that MB09260 has a dark lens is at least 96%, and the probability of a stellar lens is at most 4%. The relative probabilities of Star:BD:WD:NS:BH are 4:0:38:44:14. Stellar lenses are only allowed below $1 M_\odot$. A white dwarf or neutron star is the most probable type of lens, with black holes possible but less likely.

3.6.3 MB10364

The data and model for MB10364 are shown in Figures 3.4 (photometry) and 3.17 (astrometry), and the fit posteriors are summarized in Table 3.12. The inferred Einstein crossing

---

[15] These are the values for the posteriors before they are split into modes, which is why the values differ from what is reported in Table 3.11. However, since these parameters are all globally unimodal, their distributions nearly identical across modes within the uncertainties, and neither mode is strongly favored, the values are not very different and we report the global median and uncertainties.

Parameter	$\mathrm{Med}^{+1\sigma}_{-1\sigma}$	MAP	MLE
t_0 (MJD)	$55761.07^{+0.99}_{-0.96}$	55760.65	55759.15
u_0	$-0.06^{+0.006}_{-0.009}$	-0.06	-0.07
t_E (days)	$280.87^{+6.54}_{-5.96}$	284.94	277.47
$\log_{10}(\theta_E/\mathrm{mas})$	$0.59^{+0.05}_{-0.07}$	0.47	0.60
π_S (mas)	$0.11^{+0.02}_{-0.02}$	0.12	0.12
$\pi_{E,E}$	$0.010^{+0.005}_{-0.004}$	0.009	0.0007
$\pi_{E,N}$	$-0.12^{+0.01}_{-0.01}$	-0.12	-0.14
$x_{S0,E}$ (mas)	$229.75^{+0.07}_{-0.08}$	229.82	229.80
$x_{S0,N}$ (mas)	$-214.28^{+0.11}_{-0.13}$	-214.58	-214.22
$\mu_{S,E}$ (mas/yr)	$-2.25^{+0.02}_{-0.02}$	-2.25	-2.25
$\mu_{S,N}$ (mas/yr)	$-3.57^{+0.02}_{-0.02}$	-3.55	-3.57
$b_{SFF,O}$	$0.05^{+0.0004}_{-0.0004}$	0.05	0.05
$m_{base,O}$ (mag)	$16.41^{+0.0001}_{-0.0001}$	16.41	16.41
$b_{SFF,H8}$	$0.90^{+0.02}_{-0.02}$	0.89	0.91
$m_{base,H8}$ (mag)	$19.86^{+0.006}_{-0.006}$	19.86	19.87
$b_{SFF,H6}$	$0.94^{+0.02}_{-0.02}$	0.95	0.94
$m_{base,H6}$ (mag)	$22.04^{+0.009}_{-0.009}$	22.05	22.04
M_L ($M_\odot$)	$3.79^{+0.62}_{-0.57}$	3.01	3.58
π_L (mas)	$0.60^{+0.08}_{-0.08}$	0.48	0.67
π_{rel} (mas)	$0.48^{+0.08}_{-0.08}$	0.36	0.55
$\mu_{L,E}$ (mas/yr)	$-2.64^{+0.18}_{-0.24}$	-2.54	-2.28
$\mu_{L,N}$ (mas/yr)	$1.46^{+0.63}_{-0.71}$	0.26	1.69
$\mu_{rel,E}$ (mas/yr)	$0.40^{+0.23}_{-0.19}$	0.28	0.03
$\mu_{rel,N}$ (mas/yr)	$-5.02^{+0.71}_{-0.64}$	-3.81	-5.26
θ_E (mas)	$3.89^{+1.12}_{-1.16}$	2.98	4.00
π_E	$0.12^{+0.01}_{-0.01}$	0.14	0.13
$\delta_{c,max}$ (mas)	$1.37^{+0.40}_{-0.41}$	1.05	1.41

Table 3.9: *OB110462 DW Fit Values.* The columns list the median $\pm 1\sigma$ (68%) credible intervals, maximum a posteriori (MAP) solution, and and maximum likelihood estimator (MLE) solution.

time t_E is $61.11^{+0.24}_{-0.24}$ days, the microlensing parallax π_E is $0.27^{+0.01}_{+0.01}$, the Einstein radius θ_E is $0.46^{+0.31}_{-0.21}$, and the lens mass is $0.21^{+0.14}_{-0.10} M_\odot$.

MB10364 is a low mass object, with the possibility of a neutron star or BH lens ruled out. The relative probabilities of Star:BD:WD are 36:29:35.

Parameter	$\mathrm{Med}^{+1\sigma}_{-1\sigma}$	MAP	MLE
t_0 (MJD)	$55747.17^{+7.36}_{-7.55}$	55735.10	55735.10
u_0	$-0.11^{+0.02}_{-0.01}$	-0.13	-0.13
t_E (days)	$278.56^{+12.52}_{-9.16}$	267.37	267.37
$\log_{10}(\theta_E/\mathrm{mas})$	$0.62^{+0.09}_{-0.11}$	0.60	0.60
π_S (mas)	$0.11^{+0.02}_{-0.02}$	0.10	0.10
$\pi_{E,E}$	$-0.07^{+0.05}_{-0.05}$	-0.15	-0.15
$\pi_{E,N}$	$-0.23^{+0.05}_{-0.03}$	-0.29	-0.29
$x_{S0,E}$ (mas)	$229.97^{+0.16}_{-0.17}$	230.07	230.07
$x_{S0,N}$ (mas)	$-214.31^{+0.21}_{-0.21}$	-214.37	-214.37
$\mu_{S,E}$ (mas/yr)	$-2.25^{+0.03}_{-0.03}$	-2.24	-2.24
$\mu_{S,N}$ (mas/yr)	$-3.56^{+0.03}_{-0.03}$	-3.57	-3.57
$b_{SFF,O}$	$0.05^{+0.003}_{-0.004}$	0.06	0.06
$m_{base,O}$ (mag)	$16.41^{+0.007}_{-0.007}$	16.41	16.41
$b_{SFF,H8}$	$0.95^{+0.05}_{-0.06}$	0.99	0.99
$m_{base,H8}$ (mag)	$19.88^{+0.008}_{-0.007}$	19.88	19.88
$b_{SFF,H6}$	$0.99^{+0.04}_{-0.06}$	1.04	1.04
$m_{base,H6}$ (mag)	$22.04^{+0.01}_{-0.01}$	22.03	22.03
M_L ($M_\odot$)	$2.15^{+0.67}_{-0.54}$	1.51	1.51
π_L (mas)	$1.09^{+0.34}_{-0.32}$	1.38	1.38
π_{rel} (mas)	$0.98^{+0.34}_{-0.32}$	1.27	1.27
$\mu_{L,E}$ (mas/yr)	$-0.69^{+0.91}_{-0.94}$	0.25	0.25
$\mu_{L,N}$ (mas/yr)	$1.53^{+1.21}_{-1.12}$	1.22	1.22
$\mu_{rel,E}$ (mas/yr)	$-1.56^{+0.95}_{-0.91}$	-2.49	-2.49
$\mu_{rel,N}$ (mas/yr)	$-5.08^{+1.13}_{-1.22}$	-4.79	-4.79
θ_E (mas)	$4.13^{+0.96}_{-0.91}$	3.95	3.95
π_E	$0.24^{+0.05}_{-0.05}$	0.32	0.32
$\delta_{c,max}$ (mas)	$1.46^{+0.34}_{-0.32}$	1.40	1.40

Table 3.10: *OB110462 EW Fit Values.*

3.6.4 OB110037

The data and model for OB110037 are shown in Figures 3.5 (photometry) and 3.18 (astrometry), the fit posteriors are summarized in Table 3.13. The inferred Einstein crossing time t_E is $92.78^{+2.63}_{-2.60}$ days, the microlensing parallax π_E is π_E is $0.37^{+0.01}_{-0.01}$, the Einstein radius θ_E is $1.24^{+0.36}_{-0.35}$, and the lens mass is $0.41^{+0.12}_{-0.12} M_\odot$.

The probability that OB110037 has a dark lens is at least 26%, and the probability of a stellar lens is at most 74%. The relative probabilities of Star:BD:WD:NS:BH are 74:0:26:0:0. Stellar lenses are only allowed below $0.6 M_\odot$, and white dwarfs are the only type of compact objects allowed.

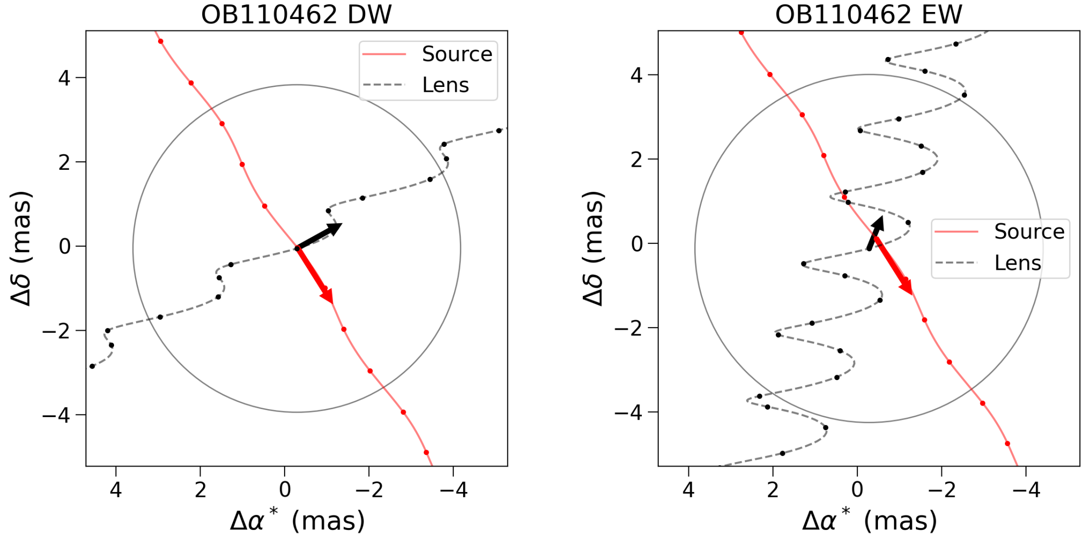

Figure 3.22: On-sky lensing geometry of OB110462 showing the resolved motion of the lens and source, as inferred from the default weight (DW) model (*left*) and the equal weight (EW) model (*right*); see Chapter 3.4.3 for details about the different models. The Einstein ring is shown as a gray circle of radius θ_E. The solid red line shows the trajectory of the source, while the dashed black line shows the trajectory of the lens. Note that the red line shows the *unlensed* position or the source, and not the centroid of the source's lensed images. The dots on top of the trajectories are spaced at intervals of 100 days. The red and black arrows indicate the proper motion of the source and lens, respectively. The tail of the arrow is at the location of the source and lens at time t_0; the length of the arrows are proportional to the magnitude of the source and lens proper motions.

The light curve of OB110037 appears to have some type of perturbation at MJD $\sim$ 55690. This feature is also apparent in the MOA light curve, raising our confidence that the light curve feature is real. This perturbation may be attributed to a binary lens.

In addition, the astrometry fit, in particular for the F606W filter, is quite poor (Figure 3.18). Although the first 5 observations from 2011−2012 seem to agree between the two filters, a drastic difference that increases as time goes on begins in 2013−2017. This may be attributed to a binary source.

It is curious that the photometry may be better explained by a binary lens model, while the astrometry is likely better explained by a binary source model. Re-analysis of this event with both types of binary models would be a worthwhile and interesting pursuit, but is beyond the current scope of this paper.

Parameter	Mode 1			Mode 2		
	Med$^{+1\sigma}_{-1\sigma}$	MAP	MLE	Med$^{+1\sigma}_{-1\sigma}$	MAP	MLE
t_0 (MJD)	$55099.19^{+1.40}_{-1.37}$	55099.27	55099.27	$55099.33^{+1.26}_{-1.25}$	55099.99	55099.99
u_0	$-0.09^{+0.02}_{-0.04}$	-0.07	-0.07	$0.02^{+0.03}_{-0.06}$	-0.0002	-0.0002
t_E (days)	$143.16^{+3.35}_{-2.95}$	141.71	141.71	$142.37^{+3.43}_{-2.89}$	141.64	141.64
$\log_{10}(\theta_E/\text{mas})$	$0.03^{+0.14}_{-0.20}$	0.24	0.24	$0.008^{+0.15}_{-0.21}$	0.06	0.06
π_S (mas)	$0.10^{+0.02}_{-0.02}$	0.12	0.12	$0.10^{+0.02}_{-0.02}$	0.09	0.09
$\pi_{E,E}$	$-0.08^{+0.010}_{-0.009}$	-0.08	-0.08	$-0.08^{+0.009}_{-0.009}$	-0.07	-0.07
$\pi_{E,N}$	$-0.02^{+0.03}_{-0.04}$	-0.005	-0.005	$-0.04^{+0.04}_{-0.06}$	-0.06	-0.06
$x_{S0,E}$ (mas)	$236.25^{+0.13}_{-0.12}$	236.43	236.43	$236.20^{+0.13}_{-0.11}$	236.30	236.30
$x_{S0,N}$ (mas)	$-692.07^{+0.11}_{-0.10}$	-692.15	-692.15	$-692.01^{+0.12}_{-0.13}$	-691.91	-691.91
$\mu_{S,E}$ (mas/yr)	$-5.00^{+0.05}_{-0.05}$	-5.07	-5.07	$-4.99^{+0.05}_{-0.05}$	-5.05	-5.05
$\mu_{S,N}$ (mas/yr)	$-3.38^{+0.04}_{-0.05}$	-3.34	-3.34	$-3.39^{+0.05}_{-0.05}$	-3.44	-3.44
$b_{SFF,M}$	$0.61^{+0.02}_{-0.02}$	0.60	0.60	$0.60^{+0.02}_{-0.02}$	0.61	0.61
$m_{base,M}$ (mag)	$17.43^{+0.003}_{-0.003}$	17.43	17.43	$17.43^{+0.003}_{-0.003}$	17.42	17.42
$b_{SFF,H8}$	$1.00^{+0.02}_{-0.03}$	0.99	0.99	$0.99^{+0.02}_{-0.03}$	1.00	1.00
$m_{base,H8}$ (mag)	$17.84^{+0.003}_{-0.004}$	17.83	17.83	$17.84^{+0.003}_{-0.003}$	17.84	17.84
$b_{SFF,H6}$	$1.03^{+0.02}_{-0.03}$	1.02	1.02	$1.02^{+0.02}_{-0.03}$	1.02	1.02
$m_{base,H6}$ (mag)	$20.75^{+0.007}_{-0.007}$	20.75	20.75	$20.75^{+0.006}_{-0.007}$	20.75	20.75
M_L ($M_\odot$)	$1.44^{+0.74}_{-0.59}$	2.70	2.70	$1.30^{+0.74}_{-0.58}$	1.44	1.44
π_L (mas)	$0.20^{+0.05}_{-0.04}$	0.25	0.25	$0.20^{+0.06}_{-0.04}$	0.20	0.20
π_{rel} (mas)	$0.09^{+0.04}_{-0.04}$	0.14	0.14	$0.10^{+0.05}_{-0.04}$	0.11	0.11
$\mu_{L,E}$ (mas/yr)	$-2.62^{+1.18}_{-0.93}$	-0.61	-0.61	$-2.88^{+1.15}_{-0.94}$	-2.82	-2.82
$\mu_{L,N}$ (mas/yr)	$-2.63^{+0.98}_{-0.91}$	-3.04	-3.04	$-2.40^{+1.09}_{-1.12}$	-1.49	-1.49
$\mu_{rel,E}$ (mas/yr)	$-2.40^{+0.95}_{-1.17}$	-4.46	-4.46	$-2.11^{+0.94}_{-1.16}$	-2.23	-2.23
$\mu_{rel,N}$ (mas/yr)	$-0.73^{+0.89}_{-1.01}$	-0.31	-0.31	$-1.01^{+1.15}_{-1.09}$	-1.95	-1.95
θ_E (mas)	$1.07^{+0.41}_{-0.40}$	1.73	1.73	$1.02^{+0.41}_{-0.39}$	1.15	1.15
π_E	$0.09^{+0.02}_{-0.01}$	0.08	0.08	$0.09^{+0.04}_{-0.01}$	0.10	0.10
$\delta_{c,max}$ (mas)	$0.38^{+0.15}_{-0.14}$	0.61	0.61	$0.36^{+0.15}_{-0.14}$	0.41	0.41
$\sum w_i$	0.42			0.58		
$log\mathcal{Z}$	31613.22			31613.55		

Table 3.11: *MB09260 Fit Values, Modes.* The columns list the median $\pm 1\sigma$ (68%) credible intervals, maximum a posteriori (MAP) solution, and and maximum likelihood estimator (MLE) solution for the microlensing parameters of MB09260. The posterior is multimodal (primarily in u_0); it has been split and the parameters for each mode reported separately. The fraction that each mode contributes to the whole posterior (Σw_i) and log evidence ($\log \mathcal{Z}$) are listed for each mode at the end of the table.

3.6.5 OB110310

The data and model for OB110310 are shown in Figures 3.6 (photometry) and 3.19 (astrometry), and the fit posteriors are summarized in Table 3.14. The inferred Einstein crossing

Parameter	Med$^{+1\sigma}_{-1\sigma}$	MAP	MLE
t_0 (MJD)	$55445.13^{+0.12}_{-0.12}$	55445.06	55445.06
u_0	$-0.008^{+0.01}_{-0.01}$	-0.004	-0.004
t_E (days)	$61.11^{+0.24}_{-0.24}$	61.06	61.06
$\log_{10}(\theta_E/\text{mas})$	$-0.33^{+0.22}_{-0.25}$	-0.40	-0.40
π_S (mas)	$0.11^{+0.02}_{-0.02}$	0.11	0.11
$\pi_{E,E}$	$-0.24^{+0.003}_{-0.003}$	-0.24	-0.24
$\pi_{E,N}$	$0.12^{+0.01}_{-0.01}$	0.12	0.12
$x_{S0,E}$ (mas)	$130.18^{+0.11}_{-0.10}$	130.13	130.13
$x_{S0,N}$ (mas)	$-78.98^{+0.11}_{-0.10}$	-79.02	-79.02
$\mu_{S,E}$ (mas/yr)	$-7.56^{+0.06}_{-0.06}$	-7.52	-7.52
$\mu_{S,N}$ (mas/yr)	$-6.49^{+0.06}_{-0.06}$	-6.47	-6.47
$b_{SFF,M}$	$0.93^{+0.007}_{-0.007}$	0.93	0.93
$m_{base,M}$ (mag)	$15.02^{+0.00006}_{-0.00006}$	15.02	15.02
$b_{SFF,H8}$	$0.99^{+0.02}_{-0.02}$	0.98	0.98
$m_{base,H8}$ (mag)	$15.32^{+0.006}_{-0.006}$	15.32	15.32
$b_{SFF,H6}$	$1.00^{+0.02}_{-0.02}$	1.01	1.01
$m_{base,H6}$ (mag)	$16.50^{+0.006}_{-0.006}$	16.50	16.50
M_L ($M_\odot$)	$0.21^{+0.14}_{-0.10}$	0.18	0.18
π_L (mas)	$0.24^{+0.08}_{-0.06}$	0.22	0.22
π_{rel} (mas)	$0.12^{+0.08}_{-0.05}$	0.11	0.11
$\mu_{L,E}$ (mas/yr)	$-5.11^{+1.62}_{-1.09}$	-5.38	-5.38
$\mu_{L,N}$ (mas/yr)	$-7.78^{+0.57}_{-0.89}$	-7.56	-7.56
$\mu_{rel,E}$ (mas/yr)	$-2.46^{+1.09}_{-1.61}$	-2.13	-2.13
$\mu_{rel,N}$ (mas/yr)	$1.29^{+0.88}_{-0.57}$	1.09	1.09
θ_E (mas)	$0.46^{+0.31}_{-0.21}$	0.40	0.40
π_E	$0.27^{+0.005}_{-0.005}$	0.27	0.27
$\delta_{c,max}$ (mas)	$0.16^{+0.11}_{-0.07}$	0.14	0.14

Table 3.12: *MB10364 Fit Values.* Same as Table 3.11, but for MB10364. The solution is unimodal, hence there is only one column and Σw_i and $\log \mathcal{Z}$ are not reported.

time t_E is $82.64^{+2.18}_{-1.50}$ days, the microlensing parallax π_E is $0.13^{+0.08}_{-0.04}$, and Einstein radius θ_E is $0.88^{+0.61}_{-0.42}$, and the lens mass is $0.78^{+0.71}_{-0.39} M_\odot$.[16]

The probability that OB110310 has a dark lens is at least 95%, and the probability of a stellar lens is at most 5%. The relative probabilities of Star:BD:WD:NS:BH are 5:3:65:22:5.

---

[16] These are the values for the posteriors before they are split into modes, which is why the values differ from what is reported in Table 3.14. However, since these parameters are all globally unimodal, their distributions nearly identical across modes within the uncertainties, and neither mode is strongly favored, the values are not very different and we report the global median and uncertainties.

Parameter	Med$^{+1\sigma}_{-1\sigma}$	MAP	MLE
t_0 (MJD)	$55781.53^{+0.28}_{-0.30}$	55781.49	55781.49
u_0	$-0.002^{+0.03}_{-0.02}$	-0.008	-0.008
t_E (days)	$92.78^{+2.63}_{-2.60}$	93.31	93.31
$\log_{10}(\theta_E/\text{mas})$	$0.09^{+0.11}_{-0.14}$	0.22	0.22
π_S (mas)	$0.12^{+0.02}_{-0.02}$	0.11	0.11
$\pi_{E,E}$	$-0.31^{+0.005}_{-0.005}$	-0.31	-0.31
$\pi_{E,N}$	$0.21^{+0.01}_{-0.02}$	0.21	0.21
$x_{S0,E}$ (mas)	$15.21^{+0.06}_{-0.06}$	15.23	15.23
$x_{S0,N}$ (mas)	$-115.53^{+0.07}_{-0.07}$	-115.61	-115.61
$\mu_{S,E}$ (mas/yr)	$2.19^{+0.02}_{-0.02}$	2.18	2.18
$\mu_{S,N}$ (mas/yr)	$-3.87^{+0.02}_{-0.02}$	-3.86	-3.86
$b_{SFF,O}$	$0.90^{+0.06}_{-0.05}$	0.89	0.89
$m_{base,O}$ (mag)	$16.15^{+0.0003}_{-0.0003}$	16.15	16.15
$b_{SFF,H8}$	$0.91^{+0.06}_{-0.05}$	0.90	0.90
$m_{base,H8}$ (mag)	$16.33^{+0.003}_{-0.003}$	16.33	16.33
$b_{SFF,H6}$	$0.84^{+0.06}_{-0.05}$	0.82	0.82
$m_{base,H6}$ (mag)	$18.32^{+0.004}_{-0.003}$	18.31	18.31
M_L ($M_\odot$)	$0.41^{+0.12}_{-0.12}$	0.55	0.55
π_L (mas)	$0.58^{+0.14}_{-0.13}$	0.74	0.74
π_{rel} (mas)	$0.46^{+0.14}_{-0.13}$	0.62	0.62
$\mu_{L,E}$ (mas/yr)	$6.27^{+1.25}_{-1.17}$	7.59	7.59
$\mu_{L,N}$ (mas/yr)	$-6.56^{+0.74}_{-0.78}$	-7.54	-7.54
$\mu_{rel,E}$ (mas/yr)	$-4.07^{+1.17}_{-1.25}$	-5.42	-5.42
$\mu_{rel,N}$ (mas/yr)	$2.69^{+0.78}_{-0.75}$	3.68	3.68
θ_E (mas)	$1.24^{+0.36}_{-0.35}$	1.67	1.67
π_E	$0.37^{+0.008}_{-0.009}$	0.37	0.37
$\delta_{c,max}$ (mas)	$0.44^{+0.13}_{-0.12}$	0.59	0.59

Table 3.13: *OB110037 Fit Values.* Same as Table 3.12, but for OB110037.

Stellar lenses are only allowed below $1M_\odot$. A white dwarf or neutron star is the most probable type of lens, although brown dwarfs and black holes are still allowed at the low and high mass ends, respectively.

3.6.6 Source properties inferred from CMDs

As there is very little blending for all the targets in the high resolution F814W and F606W filters ($b_{SFF} \sim 1$), the difference between the target and source on the CMD does not change much in color nor magnitude space (ΔF814W $\lesssim 0.1$ mag and Δ(F606W $-$ F814W)

Parameter	Mode 1			Mode 2		
	Med$^{+1\sigma}_{-1\sigma}$	MAP	MLE	Med$^{+1\sigma}_{-1\sigma}$	MAP	MLE
t_0 (MJD)	$55802.11^{+1.21}_{-1.57}$	55801.39	55801.39	$55802.66^{+1.15}_{-1.17}$	55801.95	55801.95
u_0	$-0.18^{+0.05}_{-0.07}$	-0.24	-0.24	$-0.005^{+0.07}_{-0.08}$	-0.09	-0.09
t_E (days)	$83.40^{+2.39}_{-1.83}$	83.23	83.23	$82.20^{+1.66}_{-1.33}$	81.47	81.47
$\log_{10}(\theta_E/\text{mas})$	$-0.05^{+0.24}_{-0.28}$	0.04	0.04	$-0.06^{+0.21}_{-0.28}$	0.04	0.04
π_S (mas)	$0.10^{+0.02}_{-0.02}$	0.10	0.10	$0.10^{+0.02}_{-0.02}$	0.09	0.09
$\pi_{E,E}$	$-0.08^{+0.01}_{-0.01}$	-0.09	-0.09	$-0.09^{+0.01}_{-0.02}$	-0.10	-0.10
$\pi_{E,N}$	$-0.08^{+0.06}_{-0.08}$	-0.14	-0.14	$-0.11^{+0.10}_{-0.09}$	-0.21	-0.21
$x_{S0,E}$ (mas)	$-104.56^{+0.12}_{-0.10}$	-104.62	-104.62	$-104.62^{+0.09}_{-0.09}$	-104.58	-104.58
$x_{S0,N}$ (mas)	$-183.61^{+0.13}_{-0.11}$	-183.53	-183.53	$-183.57^{+0.13}_{-0.14}$	-183.49	-183.49
$\mu_{S,E}$ (mas/yr)	$-2.41^{+0.02}_{-0.03}$	-2.39	-2.39	$-2.40^{+0.02}_{-0.02}$	-2.43	-2.43
$\mu_{S,N}$ (mas/yr)	$-7.26^{+0.03}_{-0.03}$	-7.26	-7.26	$-7.26^{+0.03}_{-0.03}$	-7.28	-7.28
$b_{SFF,O}$	$0.97^{+0.02}_{-0.02}$	0.98	0.98	$0.96^{+0.02}_{-0.03}$	0.96	0.96
$m_{base,O}$ (mag)	$18.41^{+0.005}_{-0.005}$	18.41	18.41	$18.41^{+0.005}_{-0.005}$	18.41	18.41
$b_{SFF,H8}$	$1.02^{+0.02}_{-0.03}$	1.04	1.04	$1.02^{+0.02}_{-0.03}$	1.04	1.04
$m_{base,H8}$ (mag)	$18.62^{+0.003}_{-0.003}$	18.61	18.61	$18.62^{+0.003}_{-0.003}$	18.62	18.62
$b_{SFF,H6}$	$1.02^{+0.02}_{-0.03}$	1.04	1.04	$1.02^{+0.02}_{-0.03}$	1.05	1.05
$m_{base,H6}$ (mag)	$21.34^{+0.006}_{-0.006}$	21.34	21.34	$21.34^{+0.006}_{-0.006}$	21.34	21.34
M_L ($M_\odot$)	$0.90^{+0.77}_{-0.47}$	0.83	0.83	$0.71^{+0.62}_{-0.34}$	0.58	0.58
π_L (mas)	$0.21^{+0.11}_{-0.06}$	0.28	0.28	$0.23^{+0.13}_{-0.07}$	0.35	0.35
π_{rel} (mas)	$0.11^{+0.10}_{-0.06}$	0.18	0.18	$0.12^{+0.13}_{-0.07}$	0.25	0.25
$\mu_{L,E}$ (mas/yr)	$0.21^{+2.20}_{-1.30}$	0.22	0.22	$-0.16^{+1.67}_{-1.06}$	-0.30	-0.30
$\mu_{L,N}$ (mas/yr)	$-4.79^{+2.45}_{-1.96}$	-3.22	-3.22	$-4.57^{+2.32}_{-2.31}$	-2.84	-2.84
$\mu_{rel,E}$ (mas/yr)	$-2.61^{+1.30}_{-2.22}$	-2.60	-2.60	$-2.24^{+1.06}_{-1.69}$	-2.13	-2.13
$\mu_{rel,N}$ (mas/yr)	$-2.46^{+1.97}_{-2.48}$	-4.04	-4.04	$-2.69^{+2.33}_{-2.34}$	-4.44	-4.44
θ_E (mas)	$0.90^{+0.66}_{-0.43}$	1.10	1.10	$0.87^{+0.55}_{-0.41}$	1.10	1.10
π_E	$0.12^{+0.06}_{-0.03}$	0.16	0.16	$0.14^{+0.08}_{-0.05}$	0.23	0.23
$\delta_{c,max}$ (mas)	$0.32^{+0.23}_{-0.15}$	0.39	0.39	$0.31^{+0.20}_{-0.14}$	0.39	0.39
$\sum w_i$	0.43			0.57		
$log\mathcal{Z}$	24631.66			24631.92		

Table 3.14: *OB110310 Fit Values, Modes.* Same as Table 3.11, but for OB110310.

$\lesssim 0.1$ mag, Figure 3.2). Based on a CMD analysis, the source stars in MB09260, MB10364, OB110037, and OB110310 are likely red giant stars in the bulge, as is typical for microlensing events in this part of the sky.

The source of OB110462 in the CMD is around the sequence turnoff (MSTO) on the redder and more luminous side of the main sequence, suggesting it is most likely a giant or sub-giant star. However, a main sequence source could still be consistent.

The region of the CMD around the MSTO contains both foreground stars from the disk as well as bulge stars. We compare the proper motions of OB110462's source to stars in the bright blue foreground as well as in the bulge red giant branch to determine which population it most likely belongs to (Figure 3.23). The source is consistent with either population, although it falls within the bulk of the bulge population and more on the edge of the disk population, hence we consider it is most likely a bulge star. This is also consistent with the source parallax $\pi_S = 0.11 \pm 0.02$ inferred from the fit which also indicates the source is likely in the bulge.

MB09260 and OB110310 are in the the most highly reddened field, OB110462 and OB110037 are in intermediately reddened fields, and MB10364 is in the least reddened field. This serves as a reminder that within the bulge the amount of extinction is highly variable, even over relatively small fields.

3.6.7 Verifying fit results with b_{SFF}

The fitting results are validated by comparing the best-fit OGLE or MOA I-band source flux fraction ($b_{SFF,O}$, $b_{SFF,M}$ in Tables 3.9 -3.14) to the high-resolution F814W *HST* images (Figure 3.12). We only compare the F814W images, as it is has a similar effective wavelength to OGLE I-band. Assuming a seeing disk radius of $\sim 0.65''$ for OGLE and $\sim 1.25''$ for MOA, we add up the flux from all stars detected by `hst1pass` within this radius around the target. Next, by assuming all the flux from the microlensing target at baseline as seen by *HST* is due to the source (i.e. no flux from the lens or blended neighbor stars within *HST*'s diffraction limited aperture $\theta_{HST} \sim 0.09''$), we can estimate an upper limit on the source flux fraction for a given seeing disk radius $\theta_{see} > \theta_{HST}$ using

$$b_{SFF,HST-derived} \leq \frac{F_{event}}{\sum_i F_i} \tag{3.33}$$

where F_i are the fluxes of the i stars within θ_{see} and F_{event} is the flux of the event at baseline in *HST*. This estimate on the upper limit of the source flux fraction derived using *HST*, $b_{SFF,O,HST-derived}$ or $b_{SFF,M,HST-derived}$, is compared to the values inferred from the light curve fit, $b_{SFF,O}$ or $b_{SFF,M}$. This approach is sufficient to cross check our results, considering other differences prevent a perfect comparison (e.g., *HST* F814W is not a perfect match to the OGLE I filter).

From the photometry fits, MB10364 has $b_{SFF,M} \sim 0.93$, OB110037 has $b_{SFF,O} \sim 0.90$, OB110310 has $b_{SFF,O} \sim 0.97$, and OB110462 has $b_{SFF,O} \sim 0.05$, which are all below or no more than ~ 0.05 higher than the upper limits inferred from the *HST*-derived values shown in Figure 3.12.

MB09260 has $b_{SFF,M} \sim 0.60$, which is higher than the upper limit of $b_{SFF,HST-derived} \sim 0.4$ in F814W at $1.25''$ estimated from the high resolution *HST* images. However, there is an abrupt transition from $b_{SFF,HST-derived} \sim 1$ to $b_{SFF,HST-derived} \sim 0.4$ (indicating a very bright star) at a radius of 1" from the source. The best-fit $b_{SFF,M} \sim 0.60$ falls within these two values, indicating that properly treating this situation by convolving the *HST* image with a MOA PSF would result in a better match. Hence, MB09260 seems consistent with the high resolution image.

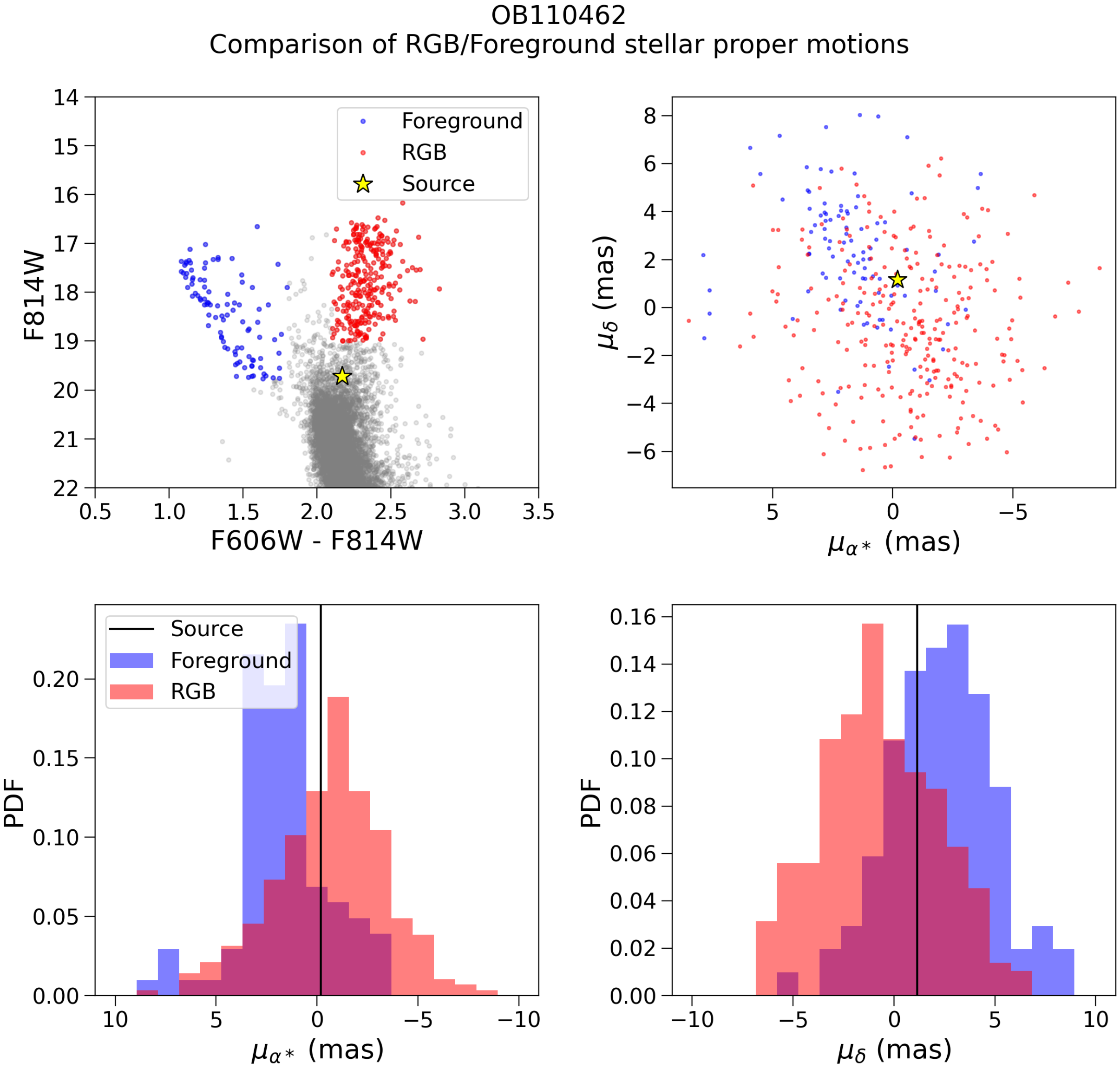

Figure 3.23: *Top left:* CMD with the blue foreground and red giant branch (RGB) stars marked. The source color and magnitude as inferred from the fit are shown as the yellow star. *Top right:* VPD of the foreground and RGB stars. The source proper motion as inferred from the fit is shown as the yellow star. *Bottom left:* Histogram of the foreground and RGB RA proper motions. The proper motion of the source is shown in the black line. *Bottom right:* Same as bottom left, but for Dec. The source proper motion is consistent with either the foreground or RGB bulge population, although it falls closer to the bulk of the RGB population, hence we consider it is most likely a bulge star.

The consistency between the source flux fraction inferred from the fits and the high resolution imaging provides an extra degree of confidence in the inferred fit values.

3.6.8 Prospects for resolving lens and source

By definition, microlensing means the source and lens are not resolvable. However, after many years, the lens and source can separate far enough to be resolved (e.g., Batista et al. (2015) and Bennett, Bhattacharya, et al. (2015)). In the case of dark lenses, such as black holes, non-detections of the lens many years after the event can be used to place constraints on its properties (e.g., Abdurrahman et al. (2021)). For the five targets in this paper, we provide estimates to determine if and when taking late-time follow-up data would enable such analyses.

From the results of the fit, we can estimate the time necessary to resolve the source and lens t_{res} via

$$t_{res} = \theta_{res}/\mu_{rel} \tag{3.34}$$

where the relative proper motion μ_{rel} comes from fitting the data, and the minimum angular separation θ_{res} can be estimated using the Rayleigh criterion. For *HST* with a mirror diameter of 2.4m, θ_{res} corresponds to 63.53 mas in F606W and 85.35 mas in F814W.

Assuming there are no contaminating stars, $b_{SFF} = F_S/(F_S + F_L)$. Then the ratio of lens to source flux, or contrast, is $F_L/F_S = (1 - b_{SFF})/b_{SFF}$. Note that $b_{SFF} > 1$ are allowed by some of the fits which would lead to an unphysical negative contrast. $b_{SFF} > 1$ is often referred to as "negative blending" because it means there is negative non-source flux (see Equation 3.25). Negative blending can occur in ground-based images if the background subtraction is imperfect (Park et al. 2004). For *HST*, where the photometry is not derived from difference imaging but rather PSF fitting, this is unlikely to be the case. However, when fitting a microlensing model to data, negative blending can occur if $b_{SFF} \approx 1$, simply due to normal photometric uncertainties. This is the most likely explanation for *HST*; all fits with negative blending values have posterior probabilities that encompass $b_{SFF} = 1$. Thus, if a contrast value is negative, we cap it at 0.[17] In addition, the fit values for μ_{rel} and b_{SFF} are nearly independent, and so these results for t_{res} and F_L/F_S can be thought of as independent.

The resolving time after photometric peak and maximum contrast in the F814W and F606W *HST* filters for each target are listed in Table 3.15. Currently, only OB110037 could potentially have its source-lens pair resolved in F606W. All the other targets have lens-source resolving times at least 15 years post-photometric peak or very low contrast. In addition, since they all have very high source flux fractions b_{SFF}, their lens-source contrasts are very low, which means even after enough time has passed for the lens and source to separate, a

---

[17] This is technically not correct, analogous to truncating negative parallaxes in *Gaia*; a proper treatment would involve a full Bayesian analysis as explained in Luri et al. (2018). Such a treatment is beyond the scope of this paper. We proceed with capping the contrast at 0, as if $b_{SFF} \sim 1$ then the target is likely very dim or dark, and the contrast unlikely to be detectable.

luminous lens would be difficult to detect. Thus, high resolution imaging of OB110037 in the near future could confirm the results of the fit if the separating source and lens could be detected. For the other targets, the absence of any lens detection would imply consistency with the results presented here, but could not confirm them; however, any detection of a lens would imply the fit results here are incorrect.

	Resolving time t_{res} (yr)		Contrast (F_L/F_S)	
Parameter	F814W	F606W	F814W	F606W
MB09260	$32.08^{+19.38}_{-9.20}$	$23.88^{+14.42}_{-6.85}$	$0.01^{+0.03}_{-0.00}$	$0.00^{+0.01}_{-0.00}$
MB10364	$30.72^{+24.58}_{-12.19}$	$22.87^{+18.29}_{-9.07}$	$0.01^{+0.02}_{-0.00}$	$0.00^{+0.02}_{-0.00}$
OB110037	$17.45^{+6.92}_{-4.01}$	$12.99^{+5.15}_{-2.98}$	$0.10^{+0.07}_{-0.07}$	$0.20^{+0.08}_{-0.07}$
OB110310	$22.03^{+19.49}_{-8.95}$	$16.40^{+14.51}_{-6.66}$	$0.00^{+0.01}_{-0.00}$	$0.00^{+0.01}_{-0.00}$
OB110462 DW	$16.91^{+2.76}_{-1.89}$	$12.59^{+2.05}_{-1.41}$	$0.07^{+0.04}_{-0.04}$	$0.03^{+0.04}_{-0.00}$
OB110462 EW	$15.81^{+4.68}_{-3.06}$	$11.77^{+3.49}_{-2.27}$	$0.06^{+0.07}_{-0.05}$	$0.02^{+0.07}_{-0.00}$

Table 3.15: *Lens/source resolvability.* There are two entries for OB110462, one based on a fit with "default weighting" (OB110462 DW) and one based on a fit with "equal weighting" (OB110462 EW). See Chapter 3.4.3 for details.

3.7 Discussion

OB110462 is the first definitive detection of a compact object discovered with astrometric microlensing. Depending on the fit, it is either a neutron star (50% probability for the EW fit), a black hole (44% probability for the EW fit, 100% probability for the DW fit), or a white dwarf (6% probability for the EW fit). MB09260 and OB110310 are mostly likely white dwarfs or neutron stars, although a NS-BH mass gap object cannot be ruled out. MB10364 and OB110037 are definitively low mass objects; OB110037 is most likely a star or white dwarf, while MB10364 is either a star, brown dwarf, or white dwarf.

Here, we discuss the BH yield as compared to theoretical expectations (Chapter 3.7.1), our sample of BH candidates and the questions it raises about the Galactic BH population (Chapter 3.7.3), additional observations of OB110462 (Chapter 3.7.4), potential sources of systematics in OB110462 observations (Chapter 3.7.5), and the future of BH microlensing searches (Chapter 3.7.6 and Chapter 3.7.7).

3.7.1 Comparison to simulations

3.7.1.1 π_E-t_E-$\delta_{c,max}$

As described in Lam, Lu, Hosek, et al. (2020), BH candidates can be identified photometrically by their long t_E and small π_E, and confirmed astrometrically by measuring the maximum astrometric shift $\delta_{c,max} = \theta_E/\sqrt{8}$ (see Chapter 3.4.1). Figure 3.20 shows the $1-2-3\sigma$ posterior contours of π_E vs. t_E *(left)* and π_E vs. $\delta_{c,max}$ *(right)* of the microlensing models for the 5 targets, compared against simulated microlensing events generated by the `PopSyCLE` software (Lam, Lu, Hosek, et al. 2020). By comparing the $\pi_E - t_E$ and $\pi_E - \delta_{c,max}$ posteriors against simulation, we can gain a more intuitive understanding of the inferred lens types for the targets (Table 3.8).

Both EW and DW models for OB110462 fall solidly within the $2-5M_\odot$ mass gap shown in the $\pi_E - \delta_{c,max}$ parameter space. Because the EW solution leads to a larger and more uncertain value of π_E than the DW solution, a neutron star or even white dwarf lens is a possibility. On the other hand, the DW solution prefers a smaller and more well constrained value of π_E than the EW solution, leading to a much more definitive solution of a mass-gap BH. However, both the EW and DW solution for OB110462 fall in a somewhat unusual part of the $\pi_E - t_E$ parameter space for BHs: typical BH π_E are around 0.02, while for OB110462, π_E is around 0.1. This is because `PopSyCLE` simulations only contain BHs with masses from $\sim 5-16M_\odot$; if OB110462 is truly a mass-gap BH, it would not correspond to any BHs in the simulation.

MB10364 and OB110037 are definitively non-BHs, due to their large π_E ($\gtrsim 0.2$) and small $\delta_{c,max}$ ($\lesssim 0.5$ mas). Although OB110310 and MB09260 are most likely white dwarfs of neutron stars, it is difficult to definitively rule out lower or higher mass lenses due to their large uncertainty in π_E. In particular, only an upper limit on $\delta_{c,max}$ was obtained for OB110310, making it especially difficult to rule out the lower mass possibilities.

3.7.2 Number of detected BHs

Target	t_E range	% BH
MB09260	$135 < t_E < 155$ days	50
MB10364	$60 < t_E < 62$ days	14
OB110037	$87 < t_E < 100$ days	12
OB110310	$78 < t_E < 90$ days	20
OB110462 DW	$266 < t_E < 300$ days	17
OB110462 EW	$256 < t_E < 325$ days	14

Table 3.16: *Fraction of expected BH detections vs. t_E from **`PopSyCLE`** simulation.* For each target, the t_E range is the median $\pm 3\sigma$. For OB110462 there are two entries, one with equal weighting to the astrometry and photometry data (OB110462 EW) and one with the default weighting of astrometry and photometry data (OB110462 DW). See Chapter 3.4.3 for details.

Next, we compare our observed BH yield to the theoretical expectation calculated using the `PopSyCLE` simulations. For a sample of simulated events that would be observable by

OGLE (see Table 4 of Lam, Lu, Hosek, et al. (2020)), we calculate the fraction of those events due to BHs as a function of the Einstein crossing time t_E. Assuming the OGLE observability criterion for the MOA sample is not strictly correct; however, OGLE and MOA often observe an overlapping set of events, so this approximation suffices.

We wish to calculate the probability of detecting k BHs in our sample given n events, where the probability of detecting a BH in the i-th event is p_i. This is described by a Poisson binomial distribution, which characterizes a "success/no success" experiment with n independent trials, where the i-th trial has probability p_i of success (Wang 1993). The probability of k successes is given by

$$P(K = k) = \sum_{A \in F_k} \prod_{i \in A} p_i \prod_{j \in A^c} (1 - p_j) \tag{3.35}$$

where F_k is the set of all subsets of k integers that can be selected from the set $\{1, ..., n\}$, i.e.

$$F_k = \{A : A \subseteq \{1, ..., n\}, |A| = 0, 1, ..., n\}.$$

$|A|$ is the number of elements in A, and A^c is the complement of A. In the limit where all p_i are equal, the Poisson binomial distribution is equivalent to the ordinary binomial distribution.

In our case, there are $n = 5$ independent trials (i.e. microlensing targets). We calculate the probability of success p_i (i.e. BH detection) using `PopSyCLE`. We define the success probability for the i-th target as the fraction of BH lensing events in `PopSyCLE` over the range of t_E inferred from the fit

$$med(t_E) - 3\sigma < t_E < med(t_E) + 3\sigma.$$

The probabilities of BH detection for each target are listed in Table 3.16.[18]

The results of evaluating Eq. 3.35 for $k = 0, ..., 5$ BH detections assuming success probabilities p_i is presented in Figure 3.24. `PopSyCLE`'s Galactic model contains 2×10^8 BHs ranging from $5 - 16 M_\odot$ (Lam, Lu, Hosek, et al. 2020). There are no $2 - 5 M_\odot$ mass gap NSs or BHs in the simulation, and hence no exact OB110462 analogue. Thus, we consider a mass gap detection as falling between 0 to 1 BH detections. The probability of detecting 0 or 1 BHs are ∼25% and ∼40%, respectively. This estimate is consistent with our single detection of a NS-BH mass gap object.

---

[18] The fact that BH probability does not increase monotonically as a function of t_E appears to contradict the claims that events with longer t_E are more likely to have a BH lens. The issue is that the uncertainty in BH probability rapidly increases at longer t_E, as the number of events steeply drops off for $t_E \gtrsim 50$ days (Figure 3.20). For example, for both OB110462 solutions, the estimates are based on < 10 events. Because of the small number of events, the estimate is highly sensitive to the particular t_E range.

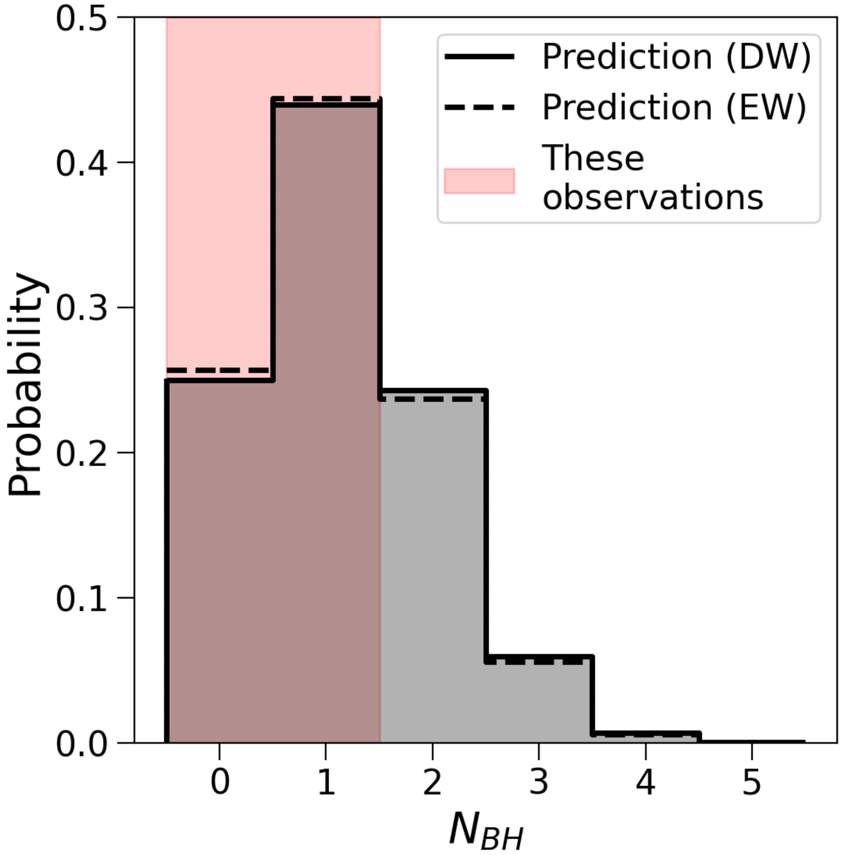

Figure 3.24: Probability of detecting N BHs as calculated from the `PopSyCLE` simulation. Two predictions are shown, depending on the likelihood used for OB110462 (default weight (DW) or equal weight (EW)). See Chapter 3.4.3 for details on the two models. Our observation of 0 or 1 BHs is consistent with either OB110462 model prediction.

3.7.3 OB110462 in comparison to the BH population

3.7.3.1 Low-mass X-ray binaries

Several attempts have been made to determine the Milky Way BH mass function using dynamical mass measurements of BHs in low-mass X-ray binaries (LMXBs). Using a sample of 7 LMXBs, Bailyn et al. (1998) found the BH mass function to be tightly centered around $7M_\odot$ with a dearth of systems between $3 - 5M_\odot$; they argued this dearth was not due to observational selection effects. Later work by Özel, Psaltis, et al. (2010) and Farr et al. (2011) using samples of $15-16$ LMXBs found similar results, providing further support to the idea of the NS-BH mass gap. However, Kreidberg et al. (2012) cautioned that systematic errors in the analysis of LMXB systems could push their inferred masses high, artificially creating the mass gap, and Jonker et al. (2021) identified potential observational biases that prevent measurement of high-mass LXMB systems. Additionally, LXMBs occupy a very small and specific part of BH evolutionary parameter space, and the BHs found in those systems are likely not representative of the Galactic BH population as a whole.

3.7.3.2 Filling the NS-BH mass gap

Measurements of BH masses in non-LMXB systems do not show evidence of a mass gap. Gravitational wave searches have found mass gap objects both as the merger remnant ($\sim 3M_\odot$ in GW170917 (Abbott, Abbott, Abbott, Acernese, et al. 2017) and $\sim 3.4M_\odot$ in GW190425 (Abbott, Abbott, Abbott, Abraham, Acernese, Ackley, Adams, Adhikari, Adya, Affeldt, Agathos, Agatsuma, Aggarwal, Aguiar, Aiello, Ain, Ajith, Allen, Allocca, Aloy, Altin, Amato, Anand, et al. 2020)), and in the merger components ($\sim 2.6M_\odot$ in GW190814 (Abbott, Abbott, Abraham, et al. 2020)). Non-interacting mass gap BHs of $\sim 3M_\odot$ with red giant companions have also been detected in the Milky Way (Thompson et al. 2019). With a mass of $1.6-4.4$ $M_\odot$, the lens of OB110462 is the first measured isolated Galactic NS or mass gap BH. These detections of mass-gap objects will improve our theoretical understanding of compact object formation channels.

3.7.3.3 A lack of higher-mass BH systems?

In order to gain a full understanding of the Galactic BH population, BHs must be uncovered outside of closely interacting X-ray binary systems.

We first consider searches for isolated BHs using microlensing, as discussed in this paper. From our sample of 5 events, we have a single detection of a mass gap object; all other lenses are lower mass non-BH detections. In addition, we have a single detection of a > 1 mas astrometric shift; most of the remaining detections are at the ~ 0.5 mas level, near the limit of *HST*'s precision. As discussed in Chapter 3.7.1, the low yield of BHs in this sample is consistent with predictions by Galactic models. However, this presents tentative evidence that Galactic BHs may be less massive than the $\sim 10M_\odot$ expectation. If the BH mass function truly peaks at $8M_\odot$, then selecting candidates via long duration microlensing events should doubly bias us toward finding these high-mass lenses. First, the lensing cross section $\sigma = \pi\theta_E^2$ is proportional to the mass of the lens M_L, since $\theta_E \propto \sqrt{M_L}$. Thus, more massive objects are more likely to be microlenses. Second, the Einstein crossing time is proportional to the square root of the lens mass, $t_E \propto \sqrt{M_L}$. Thus, long duration events are also more likely to be due to massive microlenses.

Next, we consider searches for BHs in detached/non-interacting binary systems. The mass function f of a single lined spectroscopic binary is given by

$$f = \frac{P_{orb}K^3(1-e^2)^{3/2}}{2\pi G} = \frac{M_2^3 \sin^3 i}{(M_1+M_2)^2} \tag{3.36}$$

where P_{orb} is the orbital period, K is the radial velocity (RV) semi-amplitude, e is the orbital eccentricity, i is the orbital inclination, M_1 is the mass of the visible component, and M_2 is the mass of the unseen component. If measurements of P_{orb}, K, e, and M_1 can be obtained, then a minimum mass on M_2 can be derived. If $M_2 > 5M_\odot$ without evidence of luminosity, the unseen system is inferred to be a BH. Since systems with larger RV semi-amplitudes have larger mass functions, they are most likely to host unseen BH companions. To date, searches for large RV semi-amplitudes in spectroscopic catalogs have detected an object which fall within the mass gap, but no $\sim 10M_\odot$ BHs, which suggest a paucity of higher-mass systems (El-Badry, Seeburger, et al. (2022) and Thompson et al. (2019)). Complementary searches using ellipsoidal variables (Rowan et al. 2021) also suggest that higher-mass systems are rare.

Although both microlensing and RV searches should be biased toward finding $10M_\odot$ objects more easily than $3M_\odot$ objects, only the latter are being detected. It may be that the selection bias for massive objects is cancelled out by the fact that the mass function of stars, WDs, NS, and BHs sharply decreases from low to high mass. Additional work to quantify and compare these two competing effects, combined with larger sample sizes, will be needed to understand the Galactic BH mass function.

Finally, astrometric searches for detached binaries are also eagerly anticipated with *Gaia* (e.g., Wiktorowicz, Lu, et al. (2020), Yalinewich et al. (2018), and Yamaguchi et al. (2018)). It will be very fruitful to compare the results of those searches to the X-ray transient, microlensing, and RV searches.

3.7.4 Auxiliary OB110462 observations

Additional observations of OB110462 may assist in ascertaining its NS or BH nature. Here we describe planned observations of OB110462, as well as data found in searches of archival catalogs.

The 2021 astrometric observations of OB110462 are crucial to the modeling as they extend the temporal baseline of the original archival observations by 50%, from 6 years to 10 years. The remaining data from *HST* Cycle 29 program GO-16760 to be taken in Fall 2022 (Lam and Lu 2021) will further extend the baseline by another year and improve the characterization of the astrometric signal. The astrometric microlensing shift is a deflection with respect to the unlensed position of source (Equation 3.27), and we can only have confidence in our measurement of that shift if we also have confidence in our measurement of the source's unlensed proper motion. The astrometric shift due to lensing when $u \gg 1$ can be approximated as $\delta_c \approx \theta_E t_E/(t - t_0)$ (see Chapter 3.12). For OB110462 ($t_E = 280$ days and $\theta_E = 4\,\text{mas}$), the microlensing astrometric shift did not dip below *HST*'s astrometric precision of $\sim 0.3\,\text{mas}$ until 2021, 10 years after source-lens closest approach. This calculation illustrates the importance of having a long temporal baseline for OB110462 in order to properly measure the source's unlensed proper motion and characterize the astrometric microlensing signal.

Additional follow-up observations in the X-ray can place limits on accretion from the ISM (Agol and Kamionkowski 2002). For example, Maeda et al. (2005) and Nucita, De Paolis, Ingrosso, Elia, et al. (2006) looked for X-rays at the location of BH microlensing candidate MACHO-96-BLG-5 reported in Bennett, Becker, et al. (2002), using ACIS on Chandra and EPIC on XMM-Newton, respectively. Neither detected any X-rays.

We searched several X-ray catalogs that have observed at OB110462's coordinates to determine whether there are any coincident sources. OB110462 was not detected as an X-ray source in any of the following catalogs:

- Chandra Source Catalog 2.0[19] (Evans, Allen, Anderson, Budynkiewicz, Burke, Chen, Civano, D'Abrusco, Doe, Evans, Fabbiano, Gibbs, Glotfelty, Graessle, Grier, Hain, Hall, Harbo, Houck, Lauer, Laurino, Lee, Martinez-Galarza, et al. 2019; Evans, Allen, Anderson, Budynkiewicz, Burke, Chen, Civano, D'Abrusco, Doe, Evans, Fabbiano, Gibbs, Glotfelty, Graessle, Grier, Hain, Hall, Harbo, Houck, Lauer, Laurino, Lee, Martınez-Galarza, et al. 2019). The limiting sensitivity provides an upper limit of 1.91×10^{-14} erg/s/cm^2 at 0.5 – 7.0 keV.

- XMM-Newton Science Archive[20] (Sarmiento et al. 2019). This provides an upper limit of 1.52×10^{-14} erg/s/cm^2 and $< 1.38 \times 10^{-3}$ counts/s at 0.2 - 12.0 keV.

- Swift XRT Point Source Catalogue[21] (Evans, Page, et al. 2020). This provides an upper limit of 2.4×10^{-3} counts/s at 0.3 - 10 keV.

OB110462's coordinates are not in the eROSITA-DE Early Data Release catalog[22].

We also searched the Australia Telescope National Facility Pulsar Catalogue[23] (Manchester et al. 2005) Version 1.65 for any pulsars coincident with the target. There are no coincident pulsars; the nearest pulsar is 0.55 deg away.

As mentioned in Chapter 3.2.5, OB110462 is not in the *Gaia* EDR3 catalog. OB114062's baseline magnitude is F606W ≈ 22, while *Gaia*'s nominal magnitude limit is $G \approx 20.7$, and will be even brighter in crowded regions (Fabricius et al. 2021).

---

[19] https://cxc.harvard.edu/csc/

[20] http://nxsa.esac.esa.int/nxsa-web/#search

[21] https://www.swift.ac.uk/2SXPS/

[22] https://erosita.mpe.mpg.de/edr/

[23] https://www.atnf.csiro.au/research/pulsar/psrcat/

High contrast imaging observations in the next $5-10$ years would also be worthwhile. If the lens is indeed a solitary NS or BH, lack of an optical/infrared lens detection would bolster support of the dark isolated lens interpretation, but be unable to distinguish between NS or BH as the relative proper motion differentiating the DW and EW solutions cannot be measured in the case of a dark lens. In that case, only a deep, targeted X-ray observation could help in differentiating between the NS vs. BH scenarios. On the other hand, optical/infrared detection of a lens separate from the source would point to a binary lens scenario. Binary source or binary lens models can be further explored through precision radial velocity searches.

3.7.5 Potential systematics in OB110462 observations

We briefly discuss whether the tension between the photometry and astrometry could be due to systematics in the data.

First we consider the OGLE photometry. Possible sources of systematic error include differential refraction, proper motion, or low-level stellar variabliliy are possibilities for such a long baseline. However, no trends due to proper motion or stellar variability are seen in the light curve. In addition, the F814W $-$ F606W color of the bright star within ~ 0.3 arcsec of OB110462 that are blended together in the OGLE images are within 0.1 of each other, and hence effects due to differential refraction would be undetectable. We also inspect the light curves of several stars near OB110462 that have similar magnitude to the baseline magnitude of OB110462. No trends can be seen that resemble the residuals in the EW fit. In addition, we explored re-scaling the photometric uncertainties of the OGLE data; however, even inflating all uncertainties by a factor of ~ 2 did not significantly change the structure of the residuals, nor the inferred microlensing parameters, including lens mass.

Potential sources of systematics in the *HST* astrometry are discussed in the next section.

3.7.6 Improving experimental strategy and design

3.7.6.1 Multi-filter astrometry

In contrast to photometric observations, multi-filter astrometry is not routinely obtained, as astrometric observations are expensive and facilities with the requisite precision are rare. This is one of the first projects to explore the impact of different filters on relative astrometry. The nature of the difference between F606W and F814W filter astrometric observations of OB110037 and OB110462 is an open question, whether it be astrophysical (e.g., binaries sources with different color), systematic (e.g., uncorrected CTE), or statistical. However, it demonstrates that multi-filter observations are worth continuing to pursue in future astrometric microlensing studies. For example, it could help break degeneracies between certain types of binaries lenses or sources.

3.7.6.2 CTE correction

As mentioned in Chapter 3.3.1, the CTE correction in the `_flc` files is not perfect. Future pursuits will explore other methods of correction, such as a re-analysis of OB110462 that uses the newer and more accurate tabular correction for CTE (Anderson 2021). In addition, trying to fix CTE via a magnitude-dependent astrometric alignment is another avenue that is being explored.

3.7.6.3 Observational strategy

For these precise astrometric measurements, taking good observations is critical. The lens mass constraints for several of the targets are only upper limits, as the astrometric shifts were so small as to be undetectable at the precision of the measurements. A dominant source of astrometric uncertainty with *HST* WFC3-UVIS observations is the undersampling of the PSF. It has been shown that there is a floor in the astrometric precision that can be achieved, even at high SNR, when only a few exposures are used (Hosek, Lu, Anderson, Ghez, et al. 2015). As the majority of the observations in each filter had 4 or less exposures, this limited the achievable astrometric precision for several of the targets, in particular OB110462. Increasing the number of exposures and implementing small uncorrelated dithers to sample different pixel phases can reduce this floor as $\sqrt{N_{dithers}}$.

In addition, the effects of CTE are worsening with time. Actively mitigating CTE through careful planning of observations rather than trying to correct it afterwards is even more important than before (e.g., as described in §7 of Anderson, Baggett, et al. (2021)).

3.7.6.4 Event selection

Although all events presented in this work were selected to have $t_E > 200$ days (Sahu 2009), the inferred t_E values for 4 of the 5 events did not satisfy this criteria. As a result, the true t_E range probed extended down to $t_E = 60$ days, and did not sample the t_E range that maximizes the expected yield of BHs ($t_E \gtrsim 100$ days). Only MB09260 and OB110462 had $t_E > 100$ days, weakening the constraints on the BH fraction. We are currently attempting to determine whether prediction of t_E before the photometric peak of the event could be improved. If possible, this would enable improved selection of BH candidates for astrometric follow-up.

A secondary concern is the target field itself. A sufficient number of reference stars is needed, hence the field in the immediate vicinity of the target must be sufficiently crowded. However, the magnitude range of those nearby stars must also be similar to the target. Because of the steepness of the luminosity function, bright targets or targets with high magnification are more difficult to analyze as they lack sufficient reference stars to perform relative astrometric alignment. This is in tension with the need to have high photometric precision in order to precisely measure the microlensing parallax. Although bright and highly magnified stars should still be followed up if they are long duration events, special care must be taken when designing observations to ensure good astrometric alignment.

3.7.7 BH searches with the Roman Space Telescope

Although the initial idea and subsequent design requirements for the Roman Space Telescope (hereafter *Roman*) microlensing survey are driven by exoplanet searches (Penny, Gaudi, et al. 2019), it also hails the next generation of astrometric microlensing campaigns searching for BHs. Presently, each event must be followed up individually, with only two facilities (*HST* and *Keck*) capable of the precision in the near-infrared required to make such a measurement. Such measurements are expensive (requiring an ∼orbit of *HST* or ∼hour of *Keck* time per measurement), prohibiting dense astrometric temporal sampling or a large sample of targets.

Roman will change this with its ability to simultaneously obtain precise photometry and astrometry over a wide field of view 100× the area of *HST* and astrometric precision almost an order of magnitude better than *HST* (Spergel et al. 2015; WFIRST Astrometry Working Group et al. 2019). This will also allow the masses of NS-BH mass gap objects to be precisely measured, and allow a sample of 100-1000 BH candidates to be built up over the duration of the survey (Lam, Lu, Hosek, et al. 2020). In addition, *Roman* will probe a large sample of shorter t_E events which will place constraints on BH kicks.

To make *Roman* as effective as possible for finding BHs, there are several considerations that need to be addressed. Due to the placement of the observatory's solar panels, which dictates the available pointings of the telescope, the Galactic Bulge can only be observed twice a year during a 72 day window centered on the vernal and autumnal equinoxes. In addition, for *Roman*'s planned 5 year mission, only 6 of the 10 available Bulge seasons are to be dedicated to the microlensing survey. These large temporal gaps are generally not a concern for exoplanets searches, as the transient portion of the light curve is nearly covered within the 72 day window. However, for long duration events where the transient portion of the light curve is much longer than the window and where a measurement of small microlensing parallax is crucial, incomplete light curve coverage will mean the difference between a confirmed BH mass measurement and only an upper limit. Observations filling in these gap will be crucial. Collaboration with a ground-based telescope to provide imaging during the gaps, or a smaller independent follow-up efforts would be very important.

3.8 Conclusion

We analyze five microlensing events with candidate BH lenses. Combining *HST* astrometry and densely sampled ground-based photometry, we derive masses for these five lenses as well as their probability of being a BH. Of the five targets, we make one definitive $> 1\,\mathrm{mas}$ detection of astrometric microlensing (OB110462). The mass of the lens in OB110462 is in the range $1.6 - 4.4\ M_\odot$, making it the first detection of a compact object through astrometric microlensing.

We use our detection of a mass-gap BH or neutron star and the non-detections of BHs in the rest of the sample to observationally constrain the number of BHs in the Milky Way. Our observational BH yield currently agrees with simulations assuming 2×10^8 BHs in the

Milky Way, albeit with very large uncertainties due to the small sample size. The ability to place more stringent constraints on the number and mass distribution of Galactic BHs will require larger samples, such as those that may be delivered by the Roman Space Telescope's microlensing survey.

Astrometric microlensing holds the key to uncovering the hidden BH population. Further pursuit and refinement of the event selection, observing, and modeling process will fulfill the full promise of this technique and its ability to reveal the properties of Galactic BHs.

Shortly prior to this work being submitted for review, we learned of an independent analysis of OB110462 carried out by Sahu, Anderson, Casertano, Bond, Udalski, et al. (2022). Notably, they reach a different conclusion about the mass of the lens ($7.1 \pm 1.3 M_\odot$). It is not clear whether the discrepancy is due to the use of different datasets (e.g., we include an additional epoch of 2021 *HST* data), performing the analysis differently (e.g., we explore solutions allowed by both photometry and astrometry using different likelihood weights), or a combination of both. In addition, although both analyses make clear detections of an astrometric deflection, the direction of the deflections are in opposing directions in RA. Preliminary work shows that different choice of reference stars across the two teams is not the source of the discrepancy. However, significant further work is required to fully understand the differences between the two analyses.

3.9 Appendix: Rescaling of uncertainties

For each epoch, `hst1pass` returns the RMS error of extracted source positions and magnitudes over multiple frames σ_x, σ_y and σ_m, respectively. Following Hosek, Lu, Anderson, Ghez, et al. (2015), instead of using the RMS errors for our uncertainties, we use the error on the mean $\sigma/\sqrt{N}$ where N is the number of frames the star is detected in, inflated with a empirical additive error. The empirical constant additive error on the positions Δ_{xy} and magnitudes Δ_m is calculated for each epoch and added in quadrature to the error on the mean. This produces the final rescaled uncertainties used in the analysis

$$\sigma'_x = \sqrt{\sigma_x^2/N + \Delta_{xy}^2} \tag{3.37}$$

$$\sigma'_y = \sqrt{\sigma_y^2/N + \Delta_{xy}^2} \tag{3.38}$$

$$\sigma'_m = \sqrt{\sigma_m^2/N + \Delta_m^2}. \tag{3.39}$$

To determine Δ_{xy} and Δ_m, a sample of bright, unsaturated stars are selected. The exact magnitude range constituting "bright" is roughly saturation to $3-5$ magnitudes fainter, with the exact range determined empirically through the astrometric alignment process. In this sample, the additive error is selected such that the χ^2 distribution of the reference stars position and magnitude fits is roughly consistent with the expected distribution (Figure 3.9). The resulting values are listed in Table 3.17. Note that for MB09260 F606W, the same additive magnitude error was used across all epochs.

As mentioned in Chapter 3.3.2.1, for the five microlensing targets, the RMS and rescaled astrometric uncertainties are generally similar. However, adopting an additive error makes the resulting astrometric uncertainties more uniform across the field, particularly for bright stars. This is critical as these uncertainties are used as weights in the astrometric alignment (Chapter 3.3.2.3 and Figure 3.9). The reference stars' uncertainties are used to determine how good the reference frame transformation is, which is ultimately used to measure the astrometry of the target.

Epoch	Pos. error (mas)		Mag. error (mmag)	
(yyyy-mm-dd)	F814W	F606W	F814W	F606W
MB09260				
2009-10-01	–	0.21	–	4.0
2009-10-19	0.12	–	3.2	–
2010-03-22	0.14	–	4.9	–
2010-06-14	0.14	–	6.1	–
2010-10-20	0.13	–	9.2	–
2011-04-19	0.14	0.36	12.8	4.0
2011-10-24	0.15	0.23	4.0	4.0
2012-09-25	0.15	0.27	4.3	4.0
2013-06-17	0.16	0.28	9.8	4.0
MB10364				
2010-09-13	0.14	1.61	8.6	11.6
2010-10-26	0.14	0.49	4.5	8.6
2011-10-31	0.17	0.26	5.9	5.0
2012-09-25	0.18	0.26	8.5	6.1
2013-10-24	0.17	0.25	6.8	5.8
OB110037				
2011-08-15	0.11	0.22	16.0	8.5
2011-09-26	0.11	0.18	4.1	14.0
2011-11-01	0.10	0.21	4.0	3.8
2012-05-07	0.10	0.26	12.9	12.2
2012-09-25	0.10	0.22	6.7	4.3
2013-10-21	0.10	0.23	3.9	4.9
2014-10-26	0.10	0.21	4.2	9.7
2017-03-13	0.10	0.21	4.9	5.1
2017-09-04	0.11	0.21	8.5	19.6
OB110310				
2011-09-21	0.10	0.20	9.3	12.9
2011-10-31	0.12	0.30	4.2	4.9
2012-04-24	0.13	0.30	10.0	24.3
2012-09-24	0.14	0.29	10.2	10.9

2013-10-21	0.13	0.29	4.3	6.3
2017-03-14	0.13	0.31	4.1	18.8
2017-09-01	0.14	0.32	10.0	24.9
OB110462				
2011-08-08	0.13	0.41	18.1	17.0
2011-10-31	0.19	0.37	3.9	5.4
2012-09-09	0.19	0.36	4.7	7.2
2012-09-25	0.19	0.36	6.8	7.2
2013-10-22	0.19	0.36	3.6	4.8
2014-10-26	0.19	0.39	3.8	10.7
2017-08-29	0.20	0.40	5.4	14.7
2021-10-01	0.17	0.36	7.5	12.9

Table 3.17: *Additive errors for HST data.*

3.10 Appendix: Injection and recovery tests

We use the `ks2` software (Anderson, Sarajedini, et al. (2008) and Bellini, Libralato, et al. (2018), see also §3 of Sabbi et al. (2016) for a detailed description) to inject artificial stars into the OB110462 *HST* images to determine how well we can recover the magnitudes and positions of faint sources near bright sources. Injection and recovery tests are performed for all OB110462 epochs in two different manners:

1. Sources are injected radially around the bright neighbor star at the radius of OB110462 at a variety of azimuths excluding the azimuth of OB110462 itself, as we cannot recover a source planted on top of a real star.
2. Sources are injected near a star of similar brightness to the neighbor, in the same radial and azimuthal configuration relative to the star as OB110462 relative to the bright neighbor.

The first test directly probes the region around the neighbor itself but excludes the actual position of the OB110462, while the second test probes a region around a star similar to the neighbor, at the same separation and angle of OB110462 relative to the neighbor.

The star we dub “the neighbor” is ∼10 pixels (∼0.4 arcsec) west of OB110462. The star we dub “the neighbor-like star” in F814W is ∼75 pixels (∼3 arcsec) northeast of OB110462; for F606W the neighbor-like star is ∼40 pixels (∼1.6 arcsec) north of OB110462 (Figure 3.25).

In summary, both methods produce similar results (Figures 3.26 and 3.27). We use the single-azimuth results from injection around the neighbor-like star in order to capture any azimuthal dependence which would be lost by averaging over multiple azimuths (Table 3.18).

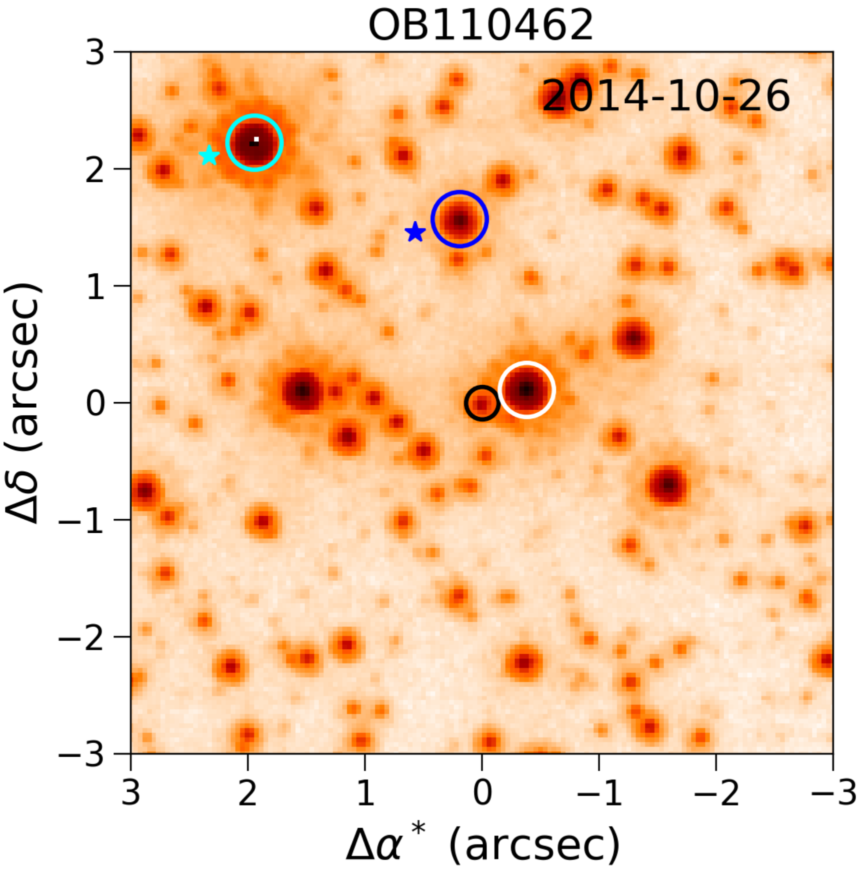

Figure 3.25: Injection and recovery for OB110462. *Black circle, center*: OB110462. *White circle*: the bright neighbor. *Blue circle*: neighbor-like star for F606W. *Cyan circle*: neighbor-like star for F814W. Positions where stars are injected in reference to the neighbor-like star are shown as blue and cyan stars (F606W and F814W, respectively).

In F814W, the bias is negligible in the first epoch, when the target is magnified and is of similar brightness to the neighbor. However, in later epochs once the target is no longer magnified, the measured position of the target is biased by ~ 0.4 mas toward the bright neighbor star along the target-neighbor separation vector. The magnitude and direction of the positional offset are comparable across the two approaches, except in 2014, where the injection around the neighbor-like star leads to a larger difference than when injecting around the neighbor. The uncertainties are larger in the approach of planting around the neighbor, as it averages over more azimuths and results in a larger uncertainty.

In F606W, the bias is smaller than F814W because the shorter wavelength results in higher resolution. Like F814W, the bias is also negligible in the first epoch, and around

$\sim 0.25\,\mathrm{mas}$ in later epochs. The uncertainties are also larger when averaging across many azimuths. Unlike F814W, the bias is mixed between radial and azimuthal components when injecting around the neighbor-like star at a single azimuth.

3.10.1 Injection around the neighbor

For each epoch, we determine the separation r of OB110462 and the bright neighbor. We inject three rings of stars surrounding the bright neighbor, of radii $r - 0.2$, r, and $r + 0.2$ pixels. Each ring consists of 24 evenly spaced stars, resulting in one star every 15 degrees. Because we cannot recover stars injected on top of the target itself, we do not attempt to recover injected stars that fall within 4 pixels of the target itself; this excludes three of the positions. We thus inject a total of $(24 - 3) \times 3 = 63$ stars per epoch.

Epoch	ΔRA (mas)	ΔDec (mas)	ΔMag (mag)
F606W			
2011-08-08	-0.025 ± 0.001	0.012 ± 0.001	-0.001 ± 0.000
2011-10-31	-0.068 ± 0.002	0.168 ± 0.002	-0.001 ± 0.000
2012-09-09	-0.216 ± 0.001	-0.185 ± 0.001	-0.005 ± 0.000
2012-09-25	0.108 ± 0.002	0.136 ± 0.001	-0.003 ± 0.000
2013-10-22	-0.431 ± 0.001	0.070 ± 0.001	-0.007 ± 0.000
2014-10-26	-0.033 ± 0.001	0.298 ± 0.001	-0.004 ± 0.000
2017-08-29	-0.144 ± 0.001	0.032 ± 0.001	-0.011 ± 0.000
2021-10-01	0.124 ± 0.002	-0.014 ± 0.001	-0.007 ± 0.000
F814W			
2011-08-08	-0.049 ± 0.000	-0.014 ± 0.000	-0.001 ± 0.000
2011-10-31	-0.203 ± 0.001	-0.070 ± 0.001	-0.004 ± 0.000
2012-09-09	-0.278 ± 0.001	-0.150 ± 0.001	-0.016 ± 0.000
2012-09-25	-0.292 ± 0.001	0.025 ± 0.002	-0.007 ± 0.000
2013-10-22	-0.490 ± 0.001	-0.081 ± 0.001	-0.011 ± 0.000
2014-10-26	-0.665 ± 0.001	-0.138 ± 0.001	-0.013 ± 0.000
2017-08-29	-0.258 ± 0.001	-0.129 ± 0.001	-0.013 ± 0.000
2021-10-01	-0.315 ± 0.000	-0.001 ± 0.001	-0.007 ± 0.000

Table 3.18: *Bias correction derived from injection and recovery.* Bias correction derived from injection/recovery around a star of comparable brightness at the same separation, azimuth, and magnitude difference as the target to its bright neighbor.

3.10.2 Injection around the neighbor-like star

The neighbor-like star we inject around is different for F814W and F606W, because the surrounding stars do not have the same colors as the neighbor and target. The neighbor-like stars were chosen to have similar magnitude and saturation level to the neighbor. In F814W, the neighbor tended to be saturated; the F814W neighbor-like star is also saturated. On the other hand, in F606W the neighbor was not saturated, and the F606W neighbor-like star is also not saturated. The F814W neighbor-like star is brighter than the neighbor in F814W by ~ 0.6 mag, and the F606W neighbor-like star is fainter than the neighbor in F606W by ~ 0.5 mag.

In each epoch, we inject three arcs of radii $r - 0.2$, r, and $r + 0.2$ pixels centered on the neighbor-like star, where r is the target-neighbor separation (~ 10 pixels). Each arc consists of 15 stars at the azimuth of the target relative to the neighbor $\pm$ 0.2 pixels/(target - neighbor separation in pixels), which corresponds to a subtended angle of approximately 2.2 degrees. This corresponds to a region of $\sim$0.04 pix^2 where $3 \times 3 \times 15 = 135$ stars are injected.

At each position we inject stars of magnitude $m_I - 0.1$, m_I, and $m_I + 0.1$, where m_I is the magnitude that results in the same contrast with the neighbor-like star as OB110462 to the neighbor. That is, if OB110462 has magnitude m_T and the neighbor m_N, and the injected star is m_I around the neighbor-like star m_C, then $m_T - m_N = m_I - m_C$.

3.10.3 Recovery of injected sources

After planting fake stars into the image, we determine how well we can recover the positions and magnitudes. To match the properties of our original dataset, we consider stars to be recovered if they are detected in at least N frames, where N is the number of frames that were used to calculate the position of the source. Iterative 3-sigma clipping is performed to exclude outliers due to confusion, e.g., from the diffraction spike mask. We then use the transformation parameters derived for this epoch (as described in Chapter 3.3.2.1) to convert from (x,y) pixel positions to (RA, Dec) coordinates.

We define a polar coordinate system with the origin located at the neighbor star for the analysis in Chapter 3.10.1 and located at the neighbor-like star for the analysis in Chapter 3.10.2. The azimuthal direction is measured counterclockwise from the origin-OB110462 separation vector. The average offset in the radial and azimuthal directions are r and θ (Figures 3.26 and 3.27).

The color of the neighbor and OB110462 are very similar (F606W - F814W = 2.25 and 2.15, respectively). At baseline, the neighbor is about 3.1 magnitudes brighter than OB110462. During magnification in the first epoch (2011-08-08), the neighbor is only about 0.4 magnitudes brighter. Since the resolution is higher at shorter wavelengths, it is not unexpected that the positional bias is less in F606W than F814W, since the separation is the same in both filters. It is also not surprising that the bias is smallest in the first epoch when the magnitude difference between OB110462 and the neighbor is small, and larger in the remaining epochs when the magnitude difference is large.

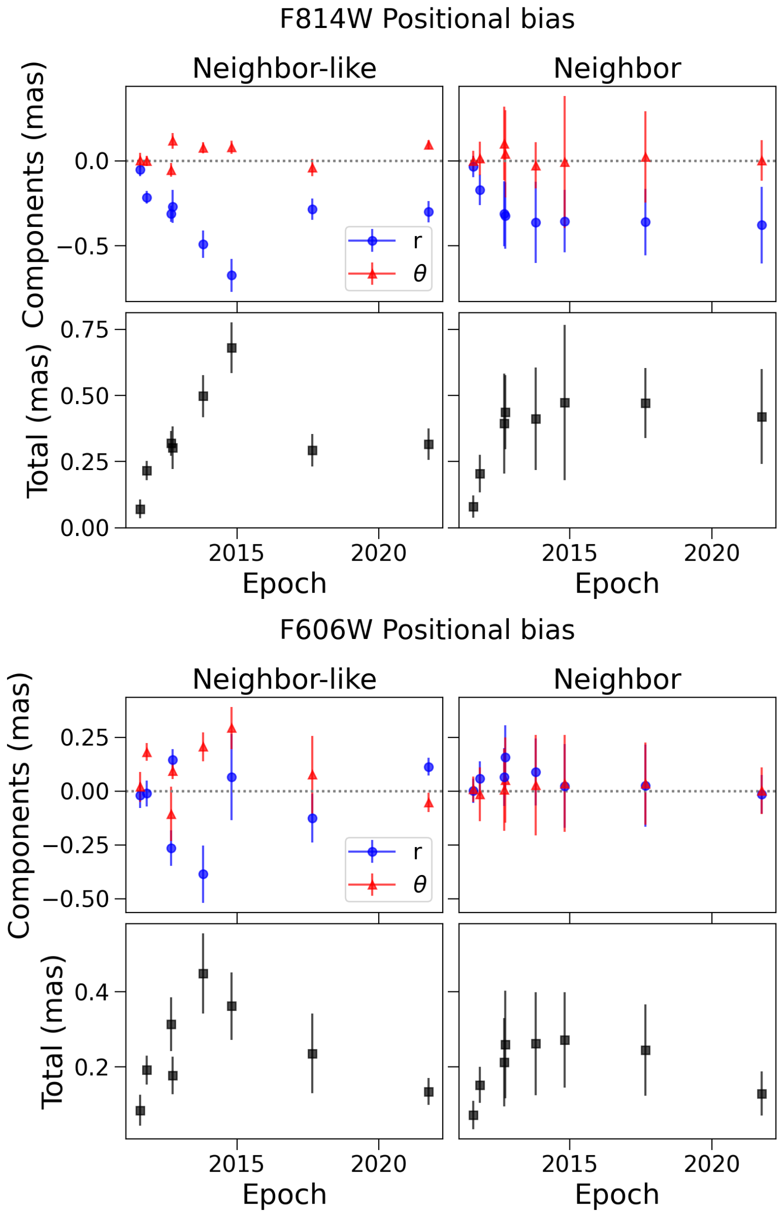

Figure 3.26: Positional bias in F814W (*top panel*) and F606W (*bottom panel*) as calculated from injection and recovery tests, injecting around a neighbor-like star (*left column*) or around the neighbor (*right column*). The positional bias (position recovered minus the true position input) is shown as a function of radial r and azimuthal θ components (*top row*), as well as total positional bias (*bottom row*).

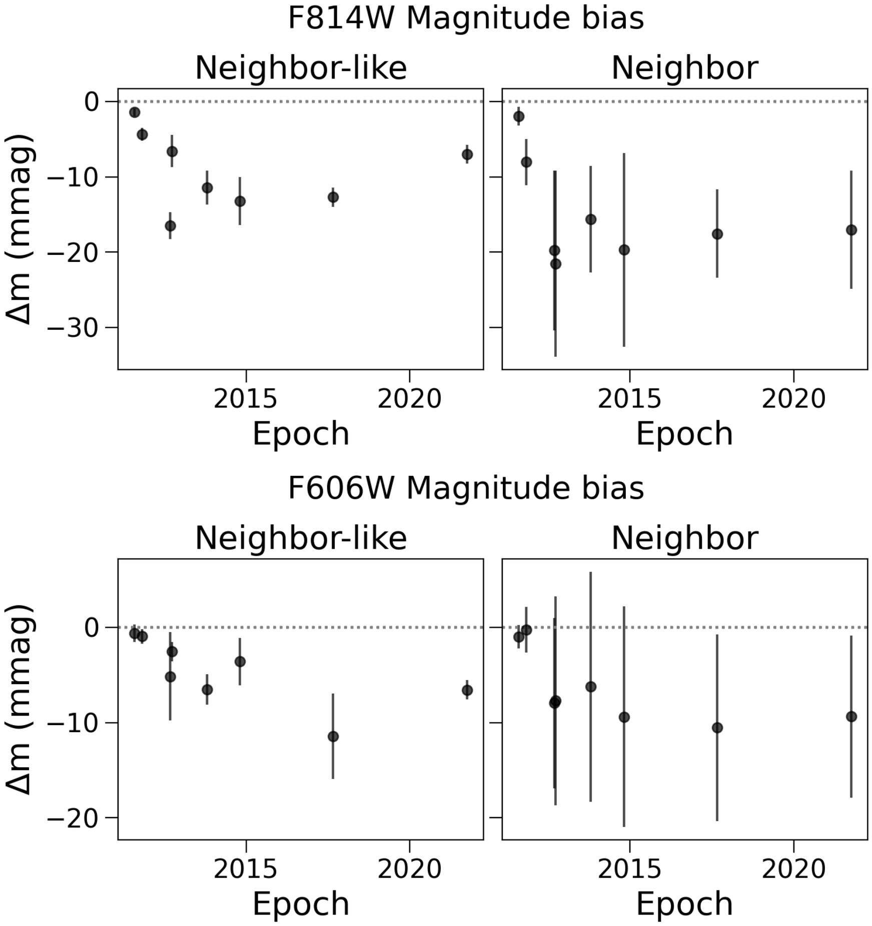

Figure 3.27: Magnitude bias in F814W (*top panel*) and F606W (*bottom panel*) as calculated from injection and recovery tests, injecting around a neighbor-like star (*left column*) or around the neighbor (*right column*). The magnitude bias is defined as the magnitude recovered minus the true magnitude input.

3.11 Appendix: Absolute proper motion reference frame

The *HST* astrometry in Chapter 3.3.2 is derived in a procedure where the average motion of the stars is at rest with respect to the reference frame. To interpret the lens' proper motion or transverse velocity, we must place the relative astrometry into an absolute reference frame. To do this, we calculate the proper motion offset between stars in the relative *HST* frame and the absolute *Gaia* frame. We match all stars in the *Gaia* EDR3 catalog within 1 arcmin of the target that have `astrometric_excess_noise_sig` < 2 and a proper motion measurement (i.e. 5-parameter and 6-parameter solutions) to the bright stars in our *HST* proper motion catalog (F814W < 22 for MB10364 and OB110037; F814W < 23 for MB09260, OB110310, and OB110462). The 1-iteration 3σ-clipped uncertainty-weighted average difference in the proper motion between the cross-matched stars is calculated, then applied to the relative *HST* astrometry to place it into the absolute *Gaia* proper motion frame. The values to convert between the *HST* and *Gaia* frames for each target's field are listed in Table 3.19.

The vector point diagram of proper motion differences between cross-matched sources in the *Gaia* and *HST* F814W catalogs, after applying the proper motion offset to place the *HST* catalog into the *Gaia* reference frame, is shown in Figure 3.28. In general, the proper motions of bright stars in *Gaia* are inconsistent with those derived using *HST*. For fainter stars, the uncertainties are much larger, so there is more consistency between *Gaia* and *HST*; however, there is substantial scatter between the measurements of the two catalogs. The discrepancies between the *HST* and *Gaia* proper motions could indicate that the uncertainties are underestimated in one or both catalogs, or that there are higher-order distortions between the two reference frames that cannot be captured by a constant offset. However, the most likely explanation is that the *Gaia* proper motions are not accurate, as it is clear that the *Gaia* EDR3 astrometry is unreliable in crowded regions like the Galactic Bulge (see Chapter 3.13 and Rybizki et al. (2022)).

Target	$\langle\Delta\mu_{\alpha*}\rangle$ (mas/yr)	$\langle\Delta\mu_{\delta}\rangle$ (mas/yr)
MB09260	-2.56 ± 0.13	-4.25 ± 0.10
MB10364	-2.70 ± 0.10	-4.56 ± 0.10
OB110037	-2.31 ± 0.23	-4.48 ± 0.20
OB110310	-2.20 ± 0.12	-4.73 ± 0.08
OB110462	-2.34 ± 0.15	-4.72 ± 0.11

Table 3.19: *HST to* Gaia *Proper Motion Reference Frame Offset.* $\Delta\mu_{\alpha*} = \mu_{Gaia,\alpha*} - \mu_{HST\ F814W,\alpha*}$ and $\Delta\mu_{\delta} = \mu_{Gaia,\delta} - \mu_{HST\ F814W,\delta}$.

3.12 Appendix: Astrometric lensing in *Gaia*

As discussed in Chapter 3.3.2.6, there are several differences between the proper motion modeling of microlensing targets in this chapter as compared to *Gaia*. First, we simultaneously model the proper motions of the lens and source with parallax within a microlensing model. In contrast, *Gaia* models the proper motion of a single star with parallax. As the source and lens are not resolved by *Gaia* during the observations, if the lens is luminous, the proper motion of the source and lens are being treated as a single object. Depending on the relative source-lens motion and colors, this can produce different inferred proper motions. Second, the temporal baseline of the data used to calculate the proper motions differ. The *HST* time baseline spans 2010 − 2013 for MB10364 and 2011 − 2017 for OB110037 and OB110310, in contrast to 2014 − 2017 in *Gaia*. As the astrometric lensing signal is time dependent, temporal baseline differences can also lead to different inferred proper motions.

With regard to the second point, we estimate the amount by which astrometric microlensing could affect the proper motion measurement. The lens-source separation $\boldsymbol{u}(t)$ (Equation 3.20) sets the time evolution of the astrometric shift $\delta_c(t)$ (Equation 3.27). Three terms contribute to $\boldsymbol{u}(t)$: the impact parameter $\boldsymbol{u}_0$, the source-lens proper motion $(t - t_0)\hat{\boldsymbol{\mu}}_{rel}/t_E$, and the microlensing parallax $\pi_E \boldsymbol{P}(t)$. As the Earth's orbit around the Sun in nearly circular, $|\boldsymbol{P}(t)| \approx 1$ to within 3%. For typical microlensing events like MB10364, OB110037, and OB110310, $|\boldsymbol{u}_0| < 1$ and $\pi_E < 1$. Thus, long after source-lens closest approach, i.e. $(t - t_0)/t_E \gg 1$, the contribution by the impact parameter and microlensing parallax terms to $\boldsymbol{u}(t)$ are subdominant to that of the source-lens relative proper motion, and the source-lens separation can be approximated

$$u(t) \approx \frac{t - t_0}{t_E} \gg 1. \tag{3.40}$$

The astrometric shift for large source-lens separations $u \gg 1$ can be approximated as

$$\delta_c(t) \approx \frac{\theta_E}{u(t)}. \tag{3.41}$$

Putting these two equations together, we can approximate how much a proper motion measurement based on observations made at times t_2 and t_1 will change due to astrometric microlensing as

$$\begin{aligned} \Delta_{PM} &\approx \frac{\delta_c(t_2) - \delta_c(t_1)}{t_2 - t_1} & (3.42)\\ &\approx \frac{\theta_E}{t_2 - t_1}\left(\frac{t_E}{t_2 - t_0} - \frac{t_E}{t_1 - t_0}\right), & (3.43) \end{aligned}$$

where $(t_2 - t_0)/t_E$, $(t_1 - t_0)/t_E \gg 1$. For MB10364, OB110037, and OB110310, for t_1 and t_2 corresponding to the start and end of *Gaia* EDR3 observations, $\Delta_{PM} \approx 0.003$, 0.02, and

0.01 mas/yr, respectively. In other words, the effect of lensing on proper motions should be negligible in *Gaia*. Thus, if the lens is dark, the proper motions of the source as measured by the *HST* data and the proper motion of the target reported by *Gaia* should be the same within the uncertainties.

3.13 Appendix: *Gaia* diagnostics

We would ideally like to incorporate information from *Gaia* EDR3 into our target analysis (e.g., using the reported parallaxes and proper motions to inform the prior on the source parallax in the fit, or to compare to the posteriors as a cross-check to validate the results). However, it is known that there are many as-of-yet-unresolved systematics in the *Gaia* EDR3 astrometry, especially toward the Bulge, and extra care must be taken to verify if a proper motion or parallax for a particular *Gaia* source is reliable. *Gaia* EDR3 is much better than *Gaia* DR2 in terms of photometry, but the astrometry still has issues that need to be worked out (Fabricius et al. 2021). We investigate several different metrics for the *Gaia* solutions for our targets to determine the reliability of the reported parallax and proper motions. A brief summary of the meaning of relevant *Gaia* statistics is presented in Table 3.3; we refer the reader to the *Gaia* Early Data Release 3 documentation (van Leeuwen et al. 2021) for details.

3.13.1 Solution type

Sources in *Gaia* have varying amounts of information available, described by the `astrometric_params_solved` parameter. A value of 3 signifies a 2-parameter solution (position), a value of 31 signifies a 5-parameter solution (position, parallax, proper motion), and a value of 95 signifies a 6-parameter solution (position, parallax, proper motion, astrometrically estimated effective wavenumber). 5-parameter solutions are generally the most accurate, followed by 6-parameter, then 2-parameter solutions. 6-parameter solutions are worse than 5-parameter solutions because it means an assumption had to be made about the source color. This usually indicates an issue with determining the properties of the source, which reduces the accuracy of the solution. This can happen in very crowded regions, like the Bulge. MB09260 has a 2-parameter solution, MB10364 and OB110310 have 6-parameter solutions, and only OB110037 has a 5-parameter solution. Based on the high-resolution *HST* images (Figure 3.1) this is not surprising, as OB110037 is the brightest object in its vicinity, while the other targets are near comparably bright stars.

3.13.2 Image parameter determination parameters

The *Gaia* EDR3 solution assumes each source is a single star. *Gaia*'s image parameter determination parameters (IPD) can be used to determine whether this assumption is valid. Different types of binaries can be identified through large of IPD values:

Parameter	MB09260	MB10364	OB110037	OB110310
N_{stars}	611	1157	1056	884
$f_{D>2}$	0.44	0.51	0.59	0.55
$f_{\epsilon=0}$	0.81	0.77	0.85	0.86
$f_{multi=0}$	0.79	0.41	0.53	0.70
med(multi$_{>0}$)	4.50	14.00	9.00	5.00
multi$_{>0[95\%]}$)	37.55	54.00	42.30	43.00
$f_{odd=0}$	0.76	0.61	0.64	0.64
med(odd$_{>0}$)	25.50	30.00	26.00	27.50
odd$_{>0[95\%]}$)	83.55	78.20	80.00	78.70
$\langle\log_{10}(amp)\rangle$	-1.24	-0.89	-1.03	-1.13
$\sigma_{\log_{10}(amp)}$	0.45	0.39	0.58	0.44
$\langle\log_{10}(ruwe)\rangle$	0.04	0.12	0.08	0.06
$\sigma_{\log_{10}(ruwe)}$	0.10	0.16	0.11	0.11
$\langle\log_{10}(C)\rangle$	0.23	0.22	0.25	0.26
$\sigma_{\log_{10}(C)}$	0.12	0.16	0.15	0.15

Table 3.20: *Distribution of Gaia parameters towards fields of interest.* N_{stars}: Number of *Gaia* sources within 1 deg^2 of the target.
$f_{D>2}$: Fraction of sources with `astrometric_excess_noise_significance`> 2.
$f_{\epsilon=0}$: Fraction of sources with `astrometric_excess_noise`> 2.
$f_{multi=0}$: Fraction of stars with `ipd_frac_multi_peak` $= 0$.
med(multi$_{>0}$): Median of nonzero `ipd_frac_multi_peak` values.
multi$_{>0[95\%]}$): 95th quantile of nonzero `ipd_frac_multi_peak` values.
$f_{odd=0}$: Fraction of stars with `ipd_frac_odd_win`$= 0$.
med(odd$_{>0}$): Median of nonzero `ipd_frac_odd_win`values.
odd$_{>0[95\%]}$): 95th quantile of nonzero `ipd_frac_odd_win` values.
$\langle\log_{10}(amp)\rangle$: Mean of $\log_{10}$(`ipd_gof_harmonic_amplitude`).
$\sigma_{\log_{10}(amp)}$: Standard deviation of $\log_{10}$(`ipd_gof_harmonic_amplitude`).
$\langle\log_{10}(ruwe)\rangle$: Mean of $\log_{10}$(ruwe).
$\sigma_{\log_{10}(ruwe)}$: Standard deviation of $\log_{10}$(ruwe).
$\langle\log_{10}(C)\rangle$: Mean of $\log_{10}$(`phot_bp_rp_excess_factor`).
$\sigma_{\log_{10}(C)}$: Standard deviation of $\log_{10}$(`phot_bp_rp_excess_factor`).

`ipd_gof_harmonic_amplitude` (indicates partially resolved binaries, asymmetric images), `ipd_frac_multi_peak` (indicates resolved, close binaries), `ipd_frac_odd_win` (indicates another bright source, or observation window conflicts for wide pairs) (Lindegren, Klioner, et al. 2021). Given that the targets all have light curves well described by point lenses (although see Chapter 3.6.4 regarding indications of binarity in OB110037), we do not expect any of these parameters to be unusual for our targets; unusual values likely indicates problems with the astrometric solution itself due to crowding or contamination.

The `ipd_gof_harmonic_amplitude` values for MB09260, MB10364, OB110037, and OB11030 (0.089, 0.064, 0.036, 0.042, respectively) are somewhat large compared to the median values reported in Tables 4 – 6 of Lindegren, Klioner, et al. (2021). However, this is to be expected toward the Bulge. Compared to other sources within 1 deg^2 (Table 3.20) of these targets, the values are not unusual.[24]

MB10364 has `ipd_frac_multi_peak` = 15. The high-resolution *HST* images do not indicate MB10364 is a resolved binary. The last *HST* image is from 2014, and *Gaia* EDR3 observations span 2014 – 2017. A possibility is that the lens and source separation after 2014 was large enough to resolve with *Gaia* EDR3. However, this is ruled out by considering the lens-source separation criteria (Table 3.15) and that *Gaia*'s resolution is worse than *HST*'s. The most likely explanation is confusion in *Gaia* due to stars near MB10364 since the crowding within 1 arcsec of MB10364 is high. The other targets have `ipd_frac_multi_peak` = 0.

MB09260 has `ipd_frac_odd_win` = 18 and OB110310 has `ipd_frac_odd_win` = 55. Similar to the case of MB10364 in the previous paragraph, this is likely due to bright stars within 1 arcsec of these targets that led to confusion in *Gaia*. The other targets have `ipd_frac_odd_win` = 0.

3.13.3 Astrometric goodness-of-fit statistics

Gaia also presents several relevant goodness-of-fit (GOF) statistics from the astrometric fit: the renormalized unit weight error (RUWE; ideally 1), the extra noise required per observation to explain the residual in the astrometric fit of the source (`astrometric_excess_noise`; ideally 0), and the significance of this source noise (`astrometric_excess_noise_sig`; insignificant if < 2).

MB09260 does not have a RUWE because it is not calculated for 2-parameter solutions. OB110037 and OB110310 both have RUWE ~ 1 (0.971 and 0.981, respectively). MB10364 has a large RUWE (1.388), although not unusual compared to the sources nearby (Table 3.20).[25]

MB09260 and MB10364 both have significant astrometric excess noise (1.241 mas and 0.406 mas, respectively). OB110037 does not have astrometric excess noise and the noise for OB110310 is not significant.

Table 3.20 lists the distributions of D = astrometric excess noise significance for the stars in *Gaia* within 1 deg^2 of our targets. *Gaia* documentation notes that $D = 0$ for roughly half the sources and $D > 2$ for a few percent of sources with well-behaved astrometric solutions (van Leeuwen et al. 2021). Near MB09260, 84% sources have $D > 0$ and 44% have $D > 2$.

---

[24] Note the values reported in Table 3.20 are the logarithms of `ipd_gof_harmonic_amplitude`. We choose to report the logarithms as they are approximately normally distributed.

[25] Note the values reported in Table 3.20 are the logarithms of RUWE. We choose to report the logarithms as they are approximately normally distributed.

Near MB10364, 79% sources have $D > 0$ and 51% with have $D > 2$. Near OB110037, 86% sources have $D > 0$ and 59% have $D > 2$. Near OB110310, 87% sources have $D > 0$ and 54% have $D > 2$. This indicates the astrometric solution is not well-behaved. This is not surprising, as there still exist many systematics in the astrometry, especially toward the Bulge. Figure 3.29 shows astrometric excess noise significance plotted against astrometric excess noise for systems where astrometric excess noise is nonzero.

3.13.4 Color excess

Fabricius et al. (2021) use $C =$ `phot_bp_rp_excess_factor` as a proxy for contamination due to crowding. Stars with large excess ($C > 5$) tend to have underestimated proper motion uncertainties by a factor of ~ 1.7. All of our targets have $C < 5$; less than 1% of stars within 1 deg^2 of the targets have $C > 5$. This metric does not seem to capture crowding toward the Bulge.

3.13.5 Summary

Compared to the high resolution images from *HST*, the various metrics reported by *Gaia* make sense.

- OB110037 is the brightest source in its vicinity, and hence has a good astrometric solution. Its astrometric solution (parallax and proper motion) are likely to be reliable. The *HST* source proper motion agrees with the *Gaia* proper motion measurement.
- MB10364 is bright but is in a crowded field. OB110310 is somewhat isolated but is faint. Their astrometric solutions are likely to be unreliable.
- MB09260 does not have enough visibility periods to generate an astrometric solution (which requires at least 9 visibility periods, while MB09260 only has 8).

In conclusion, although *Gaia* is a dedicated astrometric mission, it is not optimized for the crowded and extincted Bulge, and the astrometric parameters are likely to be untrustworthy there (Fabricius et al. 2021; Rybizki et al. 2022). Although *Gaia* EDR3 is also an improvement over DR2, those improvements are in the photometry and not the astrometry. Placing too much weight on the Bulge astrometry in analyses (especially the uncertainties) should be done with caution. To make use of *Gaia* data for these targets, we will need to wait for future data releases with improved astrometry in crowded fields as well as per-epoch astrometry.

3.14 Appendix: Gaussian Process

The photometric microlensing survey data contains uncharacterized systematics in the light curves, which may be due to unaccounted correlated noise from astrophysical processes or data acquisition and reduction. Correlated noise can bias the results of parameter estimation. Golovich et al. (2022) fit a set of publicly released OGLE-III and OGLE-IV microlensing light curves using gaussian processes (GPs) to account for correlated noise; we follow that approach here. We use the `celerite` package (Foreman-Mackey et al. 2017) to implement GPs in our microlensing model.

For a thorough reference about GPs and their application to machine learning and inference, the reader may consult sources such as Rasmussen et al. (2006). In short, a GP is composed of two parts: the noise (the stochastic component) and the mean function (the deterministic component). The properties of the stochastic component are governed by the covariance matrix, also known as the kernel, of the GP. The notation

$$y \sim \mathcal{GP}(\mu_{\boldsymbol{\theta}}(t), K_{\boldsymbol{\alpha}}(t, t')) \tag{3.44}$$

indicates a GP with mean function μ with parameters $\boldsymbol{\theta}$ and kernel K with parameters $\boldsymbol{\alpha}$.

When trying to infer some set of parameters $\boldsymbol{\theta}$ from data

$$\boldsymbol{y} = (y_1(t_1) \quad ... \quad y_N(t_N))^T \tag{3.45}$$

the Gaussian log-likelihood is

$$\log\mathcal{L}(\boldsymbol{y}|\boldsymbol{\theta}, \boldsymbol{\alpha}) = -\frac{1}{2}\boldsymbol{r}_{\boldsymbol{\theta}}^T K_{\boldsymbol{\alpha}}^{-1}\boldsymbol{r}_{\boldsymbol{\theta}} - \frac{1}{2}\log|K_{\boldsymbol{\alpha}}| - \frac{N}{2}\log(2\pi), \tag{3.46}$$

where N is the number of data points, and $\boldsymbol{r}_\theta$ is the residual vector

$$\boldsymbol{r}_{\boldsymbol{\theta}} = (y_1 - \mu_{\boldsymbol{\theta}}(t_1) \quad ... \quad y_N - \mu_{\boldsymbol{\theta}}(t_N))^T. \tag{3.47}$$

In the residual vector, $\mu_{\boldsymbol{\theta}}$ is the mean model, which in our case is the microlensing model. The kernel or covariance matrix $K_{\boldsymbol{\alpha}}$ describes the correlated errors. If the errors are not correlated, $K_{\boldsymbol{\alpha}}$ is diagonal and the likelihood reduces to the familiar form

$$\begin{aligned}\log\mathcal{L}(\boldsymbol{y}|\boldsymbol{\theta}) &= -\frac{1}{2}\sum_i\left(\log[2\pi\sigma_i^2] + \frac{(y_i - \mu_{\boldsymbol{\theta}}(t_i))^2}{\sigma_i^2}\right)\\ &= -\frac{1}{2}\sum_i \log[2\pi\sigma_i^2] - \frac{1}{2}\chi^2,\end{aligned} \tag{3.48}$$

where σ_i is the uncertainty on data point y_i and χ^2 is the "goodness of fit".

Following Golovich et al. (2022), a damped driven simple harmonic oscillator (DDSHO) kernel κ_{DDSHO} added to a Matérn-3/2 kernel $\kappa_{M3/2}$ is used to model the correlated noise in the photometric microlensing survey light curves. Both these kernels are stationary, as they are a function of the differences of the times only:

$$\tau_{ij} = |t_i - t_j|. \tag{3.49}$$

The kernel is given by

$$K_{\boldsymbol{\alpha}}(\tau_{ij}) = \kappa_{DDSHO}(\tau_{ij}) + \kappa_{M3/2}(\tau_{ij}) + \delta_{ij}\sigma_i^2. \tag{3.50}$$

Qualitatively, the DDSHO kernel models smooth variations, while the Matérn-3/2 captures more irregular variations.

The DDSHO kernel is given by

$$\kappa_{DDSHO}(\tau_{ij}) = S_0\omega_0 e^{-\omega_0\tau_{ij}/\sqrt{2}} \cos\left(\frac{\omega_0\tau_{ij}}{\sqrt{2}} - \frac{\pi}{4}\right) \tag{3.51}$$

where S_0 controls the amplitude of the deviation from the mean model and ω_0 controls the variation frequency. This kernel has been used in asteroseismic modeling (Li et al. (2019) and references therein).

The Matérn-3/2 kernel is given by

$$\kappa_{M3/2}(\tau_{ij}) = \sigma^2 e^{-\sqrt{3}\tau_{ij}/\rho}\left(1 + \frac{\sqrt{3}\tau_{ij}}{\rho}\right) \tag{3.52}$$

where σ determines the amount of deviation allowed from the mean model, and ρ is the characteristic coherence scale. The Matérn-3/2 kernel has been used to model correlated noise in the light curves of transiting and eclipsing exoplanets (Evans, Aigrain, et al. 2015; Gibson et al. 2013), and in particular is appropriate for modeling non-smooth behaviors (Gilbertson et al. 2020). For numerical reasons (see §4 of Foreman-Mackey et al. 2017), the Matérn-3/2 kernel is approximated

$$\kappa_{M3/2}(\tau_{ij}) = \sigma^2\left[\Big(1 + \frac{1}{\epsilon}\Big)e^{-\sqrt{3}(1-\epsilon)\tau_{ij}/\rho}\Big(1 - \frac{1}{\epsilon}\Big)e^{-\sqrt{3}(1+\epsilon)\tau_{ij}/\rho}\right]. \tag{3.53}$$

In the limit $\epsilon \to 0$, this is exactly the Matérn-3/2 kernel. We implement the approximation with $\epsilon = 0.01$.

The ground-based OGLE and MOA photometry are fit using the Gaussian likelihood with a full covariance matrix (Equation 3.46). The *HST* photometry and astrometry are fit using the Gaussian likelihood assuming a diagonal covariance matrix (Equation 3.48).

Note for MB10364, instead of fitting the MOA light curve using a GP, we instead fit an additive error on the ground-based photometry. During nested sampling, the GP showed some numerical instability.

3.15 Appendix: Priors

The distributions for the priors π are described in this sections. $\mathcal{N}(\mu, \sigma)$ denotes a normal distribution with mean μ and standard deviation σ. $\mathcal{N}_T(\mu, \sigma, l_\sigma, u_\sigma)$ denotes a normal distribution with a low end truncation at $\mu + \sigma l_\sigma$ and a high end truncation at $\mu + \sigma u_\sigma$. $\mathcal{U}(a, b)$

denotes a uniform distribution from a to b. $\Gamma^{-1}(\alpha, \beta)$ is the inverse gamma distribution

$$\Gamma^{-1}(x; \alpha, \beta) = \frac{\beta^\alpha}{\Gamma(\alpha)} x^{-\alpha-1} \exp[-\beta/x]. \tag{3.54}$$

The prior distributions for each target are summarized in Table 3.21.

3.15.1 Photometry priors

The five microlensing parameters in a PSPL with parallax fit are t_0, u_0, t_E, $\pi_{E,E}$, and $\pi_{E,N}$.

The prior on t_0 is a normal distribution centered on the time of peak magnification in the geocentric frame, with a spread of 75 days

$$\pi(t_0) \sim \mathcal{N}(t_{peak,\oplus}, 75 \text{ days}). \tag{3.55}$$

Note that the time at peak magnification in the heliocentric frame t_0 is not necessarily the same as in the geocentric frame $t_{peak,\oplus}$, hence the large amount of spread in the prior.

The prior on u_0 is a Gaussian with mean 0 and standard deviation 0.5

$$\pi(u_0) \sim \mathcal{N}(0, 0.5) \tag{3.56}$$

which takes into account that events with smaller $|u_0|$ are more likely to be detected, and that events with $|u_0| > 1.5$ are not robustly detectable with current ground-based surveys.[26]

The prior on t_E is a Gaussian centered at 200 days with a large spread of $\sigma = 100$ days. The distribution is truncated at -1.8σ and 3σ (20 and 500 days, respectively):

$$\pi(t_E) \sim \mathcal{N}_T(200, 50, -1.8, 10) \text{ days}. \tag{3.57}$$

The priors on the microlensing parallax are estimated from the population of bulge microlensing events from the `PopSyCLE` simulation:

$$\pi(\pi_{E,E}) \sim \mathcal{N}(-0.02, 0.12) \tag{3.58}$$

$$\pi(\pi_{E,N}) \sim \mathcal{N}(-0.03, 0.13). \tag{3.59}$$

For each dataset filter, b_{SFF} and m_{base} are also fit. For the ground-based photometry, we use a prior

$$b_{SFF,ground} \sim \mathcal{U}(0, 1.1) \tag{3.60}$$

where the negative blend flux implied by $b_{SFF} > 1$ allows for some extra noise such as imperfect background subtraction. Similarly for the *HST* astrometry, we use a uniform prior on b_{SFF}

$$b_{SFF,HST} \sim \mathcal{U}(0, 1.05). \tag{3.61}$$

---

[26] $|u_0| = 1.5$ corresponds to a brightening of no more than around 0.1 mag. When selecting microlensing events, those with a brightening less than 0.1 mag are generally excluded in survey samples to prevent contamination from low-amplitude variables (e.g., Mróz, Udalski, Skowron, Szymański, et al. (2019b)).

Parameter	MB09260	MB10364	OB110037	OB110310	OB110462 DW	OB110462 EW
t_0 (MJD)	$\mathcal{N}(55110, 75)$	$\mathcal{N}(55460, 75)$	$\mathcal{N}(55805, 75)$	$\mathcal{N}(55810, 75)$	$\mathcal{N}(55770, 75)$	$\mathcal{N}(55770, 75)$
u_0	$\mathcal{N}(0, 0.5)$	"	"	"	"	"
t_E (days)	$\mathcal{N}_T(200, 100, -1.8, 3)$	"	"	"	"	"
$\pi_{E,E}$	$\mathcal{N}(-0.02, 0.12)$	"	"	"	"	"
$\pi_{E,N}$	$\mathcal{N}(-0.03, 0.13)$	"	"	"	"	"
$m_{base,O/M}$ (mag)	$\mathcal{N}(17.43, 0.2)$	$\mathcal{N}(15.02, 0.2)$	$\mathcal{N}(16.15, 0.1)$	$\mathcal{N}(18.41, 0.1)$	$\mathcal{N}(16.41, 0.1)$	$\mathcal{N}(16.41, 0.1)$
$b_{SFF,O/M}$	$\mathcal{U}(0, 1.1)$	"	"	"	"	"
$m_{base,H8}$ (mag)	$\mathcal{N}(17.83, 0.05)$	$\mathcal{N}(15.32, 0.05)$	$\mathcal{N}(16.33, 0.05)$	$\mathcal{N}(18.61, 0.05)$	$\mathcal{N}(19.85, 0.05)$	$\mathcal{N}(19.85, 0.05)$
$b_{SFF,H8}$	$\mathcal{U}(0, 1.05)$	"	"	"	"	"
$m_{base,H6}$ (mag)	$\mathcal{N}(20.74, 0.05)$	$\mathcal{N}(16.50, 0.05)$	$\mathcal{N}(18.33, 0.05)$	$\mathcal{N}(21.34, 0.05)$	$\mathcal{N}(22.03, 0.05)$	$\mathcal{N}(22.03, 0.05)$
$b_{SFF,H6}$	$\mathcal{U}(0, 1.05)$	"	"	"	"	"
$\log \sigma_{0,O/M}$ (mag)	$\mathcal{N}(0, 5)$	"	"	"	–	–
$\rho_{O/M}$ (days)	$\Gamma^{-1}(0.448, 0.063)$	$\Gamma^{-1}(0.448, 0.113)$	$\Gamma^{-1}(0.473, 0.162)$	$\Gamma^{-1}(0.527, 0.450)$	–	–
$\log \omega^4_{0,O/M} S_{0,O/M}$ (mag^2 days^{-3})	$\mathcal{N}(3.53e-04, 5)$	$\mathcal{N}(8.41e-06, 5)$	$\mathcal{N}(3.60e-05, 5)$	$\mathcal{N}(1.02e-03, 5)$	–	–
$\log \omega_{0,O/M}$ (days^{-1})	$\mathcal{N}(0, 5)$	"	"	"	–	–
$\log_{10}(\theta_E)$ (mas)	$\mathcal{N}(-0.2, 0.3)$	"	"	"	$\mathcal{N}(0.5, 0)$	$\mathcal{N}(0.5, 0)$
π_S (mas)	$\mathcal{N}_T(0.1126, 0.0213, -2.94, 90)$	"	"	"	"	"
$x_{S0,E}$ (arcsec)	$\mathcal{U}(0.213, 0.250)$	$\mathcal{U}(0.086, 0.158)$	$\mathcal{U}(-0.034, 0.091)$	$\mathcal{U}(-0.108, -0.103)$	$\mathcal{U}(0.227, 0.233)$	$\mathcal{U}(0.227, 0.233)$
$x_{S0,N}$ (arcsec	$\mathcal{U}(-0.697, -0.683)$	$\mathcal{U}(-0.096, -0.068)$	$\mathcal{U}(-0.122, -0.104)$	$\mathcal{U}(-0.228, -0.154)$	$\mathcal{U}(-0.235, -0.183)$	$\mathcal{U}(-0.235, -0.183)$
$\mu_{S,E}$ (mas/yr)	$\mathcal{U}(-5.96, 1.12)$	$\mathcal{U}(-7.93, -1.78)$	$\mathcal{U}(0.87, 8.05)$	$\mathcal{U}(-1.30, 0.95)$	$\mathcal{U}(-4.82, 4.99)$	$\mathcal{U}(-4.82, 4.99)$
$\mu_{S,N}$ (mas/yr)	$\mathcal{U}(-2.37, 4.17)$	$\mathcal{U}(-7.28, 3.41)$	$\mathcal{U}(-1.67, 2.94)$	$\mathcal{U}(-4.55, -0.49)$	$\mathcal{U}(-3.49, 5.91)$	$\mathcal{U}(-3.49, 5.91)$

Table 3.21: *Priors.* For definitions of the different variables, see Chapter 3.15. There are two fits for OB110462 depending on the likelihood used, “equal weighting” (OB110462 EW) or “default weighting” (OB110462 DW). See Chapter 3.4.3 for details.

m_{base} is a normal distribution

$$m_{base} \sim \mathcal{N}(\overline{m}_{base}, \sigma_{\overline{m}_{base}}) \tag{3.62}$$

where $\overline{m}_{base}$ is the average magnitude during the un-magnified seasons, weighted by the measurement uncertainties, and $\sigma_{\overline{m}_{base}}$ is 0.1 for OGLE, 0.2 for MOA, and 0.05 for *HST*.

3.15.2 Gaussian Process hyperparameter priors

The ground-based photometry includes correlated noise we fit. We follow a very similar parametrization to Golovich et al. (2022) for the GP priors. The main difference is that fit in magnitude space instead of flux space, and so our priors are also in magnitudes instead of fluxes.

For σ, we use the prior

$$\log(\sigma/\text{mag}) \sim \mathcal{N}(0, 5) \tag{3.63}$$

which allows a wide range of light curve amplitude variability.

For ρ, we use the prior

$$\rho \sim \Gamma^{-1}(a, b) \tag{3.64}$$

where a and b are the constants that satisfy the relation

$$0.01 = \int_0^{\text{med}(\Delta t)} \Gamma^{-1}(x; a, b)\, dx \tag{3.65}$$

$$0.01 = 1 - \int_0^{\Delta T} \Gamma^{-1}(x; a, b)\, dx \tag{3.66}$$

where med(Δt) is the median duration between observations and ΔT is the duration of full dataset. This helps suppress values at extremely short or long timescales that might lead to ill-behaved models.[27]

For S_0 and ω_0 we use the priors

$$\log S_0\omega_0^4 \sim \mathcal{N}(\text{med}(\sigma_m^2), 5) \tag{3.67}$$

$$\log \omega_0 \sim \mathcal{N}(0, 5). \tag{3.68}$$

3.15.3 Astrometry priors

The prior on the Einstein radius θ_E is a lognormal distribution estimated from `PopSyCLE` for events with $t_E > 50$ or $t_E > 120$ days as

$$\pi(\log_{10}(\theta_E/\text{mas})) \sim \mathcal{N}(-0.2, 0.3) \tag{3.69}$$

$$\pi(\log_{10}(\theta_E/\text{mas})) \sim \mathcal{N}(0, 0.5), \tag{3.70}$$

---

[27] See https://betanalpha.github.io/assets/case_studies/gaussian_processes.html.

respectively. We use the prior from $t_E > 120$ days for OB110462 and $t_E > 50$ days for the other 4 targets.

The prior on the source parallax π_S is estimated from the population of bulge microlensing events from the `PopSyCLE` simulation

$$\pi(\pi_S) \sim \mathcal{N}_T(0.1126, 0.0213, -2.9390, 90.0) \text{ mas} \tag{3.71}$$

which corresponds to source distances ranging from 0.5 to 20 kpc.

The prior on the source proper motion $\mu_{S,E}$ and $\mu_{S,N}$ are uniform distributions

$$\pi(\mu_{S,E}) \sim \mathcal{U}(\overline{\mu}_{S,E} - f\sigma_{\overline{\mu}_{S,E}}, \overline{\mu}_{S,E} + f\sigma_{\overline{\mu}_{S,E}}) \tag{3.72}$$

$$\pi(\mu_{S,N}) \sim \mathcal{U}(\overline{\mu}_{S,N} - f\sigma_{\overline{\mu}_{S,N}}, \overline{\mu}_{S,N} + f\sigma_{\overline{\mu}_{S,N}}) \tag{3.73}$$

where $\overline{\mu}_{S,E}$, $\overline{\mu}_{S,N}$ are the proper motions inferred from assuming straight-line motion (no parallax) from the F814W data, $\sigma_{\overline{\mu}_{S,E}}$, $\sigma_{\overline{\mu}_{S,N}}$ are the uncertainties to that fit, and f is an inflation factor. To allow a wide range of proper motions we use $f = 100$.

The prior on the source position at t_0, $x_{0_S,E}$ and $x_{0_S,N}$, is

$$\pi(x_{0_S,E}) \sim \mathcal{U}(\min(x_E) - f\sigma_{x_E}, \max(x_E) + f\sigma_{x_E}) \tag{3.74}$$

$$\pi(x_{0_S,N}) \sim \mathcal{U}(\min(x_N) - f\sigma_{x_N}, \max(x_N) + f\sigma_{x_N}) \tag{3.75}$$

where x_E, x_N are the positions in the F814W data of the target, σ_{x_E}, σ_{x_N} is the standard deviation, and f is an inflation factor. We use $f = 5$.

3.16 Appendix: Astrometric color analysis

For some stars, the astrometric measurements taken in the F814W and F606W filter are discrepant at the level of the reported uncertainties. We explore this discrepancy specifically for OB110462, but this issue is also seen in OB110037 and reference stars for all targets.

First, we must quantify the discrepancy. We consider several ways to measure the total offset between the astrometry of the two filters across all epochs. $\overline{dx}$ is the average of the offsets in RA across all epochs for a particular star, and can be thought of measuring the amount of translation between F814W and F606W. $\overline{|dx|}$ is the average of the magnitude of the offsets in RA across all epochs for a particular star, and can be thought of measuring the absolute amount of translation between F814W and F606W. $|\overline{dx}|$ is the absolute value of the average of the magnitude of the offsets in RA across all epochs for a particular star, and can be thought of as measuring the total amount of deviation between F814W and F606W. Note that $|\overline{dx}|$ is distinct from $\overline{|dx|}$. The definitions for $\overline{dy}$, $\overline{|dy|}$, and $|\overline{dy}|$ are analogous, except they are the offsets in Dec. We also consider these quantities in units of sigma, where the differences in each epoch dx_i and dy_i are normalized by the positional uncertainties $\sigma_{x,i}$ and $\sigma_{y,i}$.

In Figure 3.30, we show the distributions of these quantities as a function of magnitude for stars within $30''$ of OB110462. While not falling in the bulk of the distribution, OB110462 is not an extreme outlier. Considering how large the variation in positional differences is, especially for fainter stars, OB110462 seems well within the other positions. For this reason, we assume the positional differences are a systematic we can correct empirically. We apply a constant positional offset to the F606W OB110462 observations to match the positions of the F814W observations as described in Chapter 3.3.2.5. However, further investigation to determine whether the source of the filter dependent astrometry of OB110462 and other stars may actually be astrophysical is worth pursuing, as are more observational programs to study filter dependence on astrometry.

3.17 Appendix: Directly confronting the photometry and astrometry tension

To try and elucidate the tension between the photometry and astrometry, we fit the OGLE photometry alone, and separately fit the *HST* astrometry alone. The results are shown in Figure 3.31. The *HST* astrometry alone does not have very much constraining power—the uncertainties on parameters such as t_0, t_E, and u_0 are so wide that the fit itself is not useful. However, the results are consistent with those of the EW fit. The OGLE photometry has much more constraining power, but alone cannot constrain the lens mass. The results are consistent with those of the DW fit.

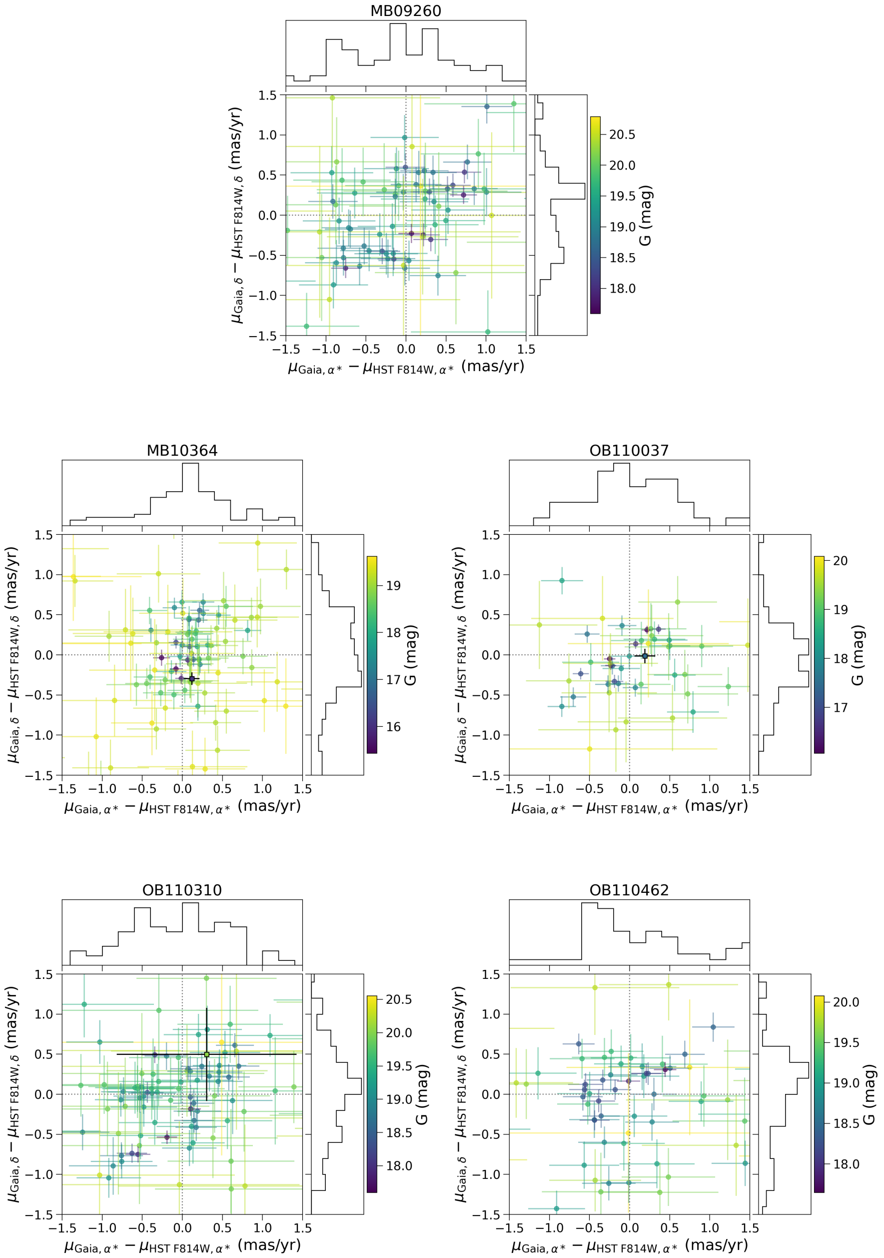

Figure 3.28: Vector point diagram of proper motion differences between cross-matched sources in the *Gaia* and *HST* F814W catalogs within 60″ of the targets, after applying the constant proper motion offset derived in Chapter 3.11 to place the *HST* catalog into the *Gaia* reference frame. The color of the point denotes the cross-matched source's magnitude in *Gaia* G-band. MB10364, OB110037, and OB110310 are sources in *Gaia*; they are shown as the black-outlined squares and error bars.

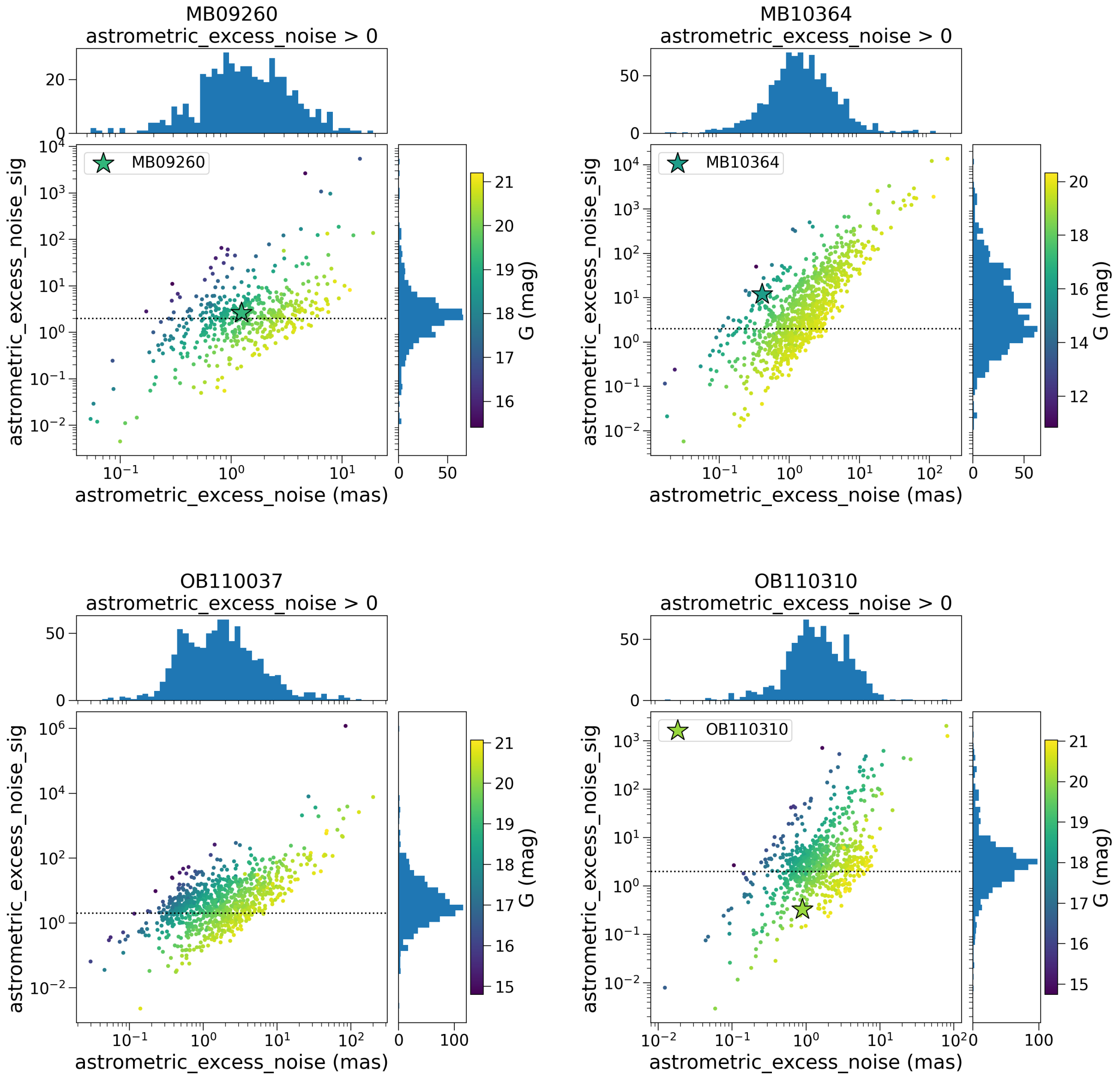

Figure 3.29: Astrometric excess noise vs. astrometric excess noise significance as a function of G magnitude, for sources with non-zero astrometric excess noise in the 1 deg^2 fields surrounding the microlensing targets found in *Gaia*. The targets are marked as stars; OB110037 is not marked as it has astrometric excess noise 0. The dotted horizontal line denotes `astrometric_excess_noise_sig` $= 2$; values < 2 are not significant.

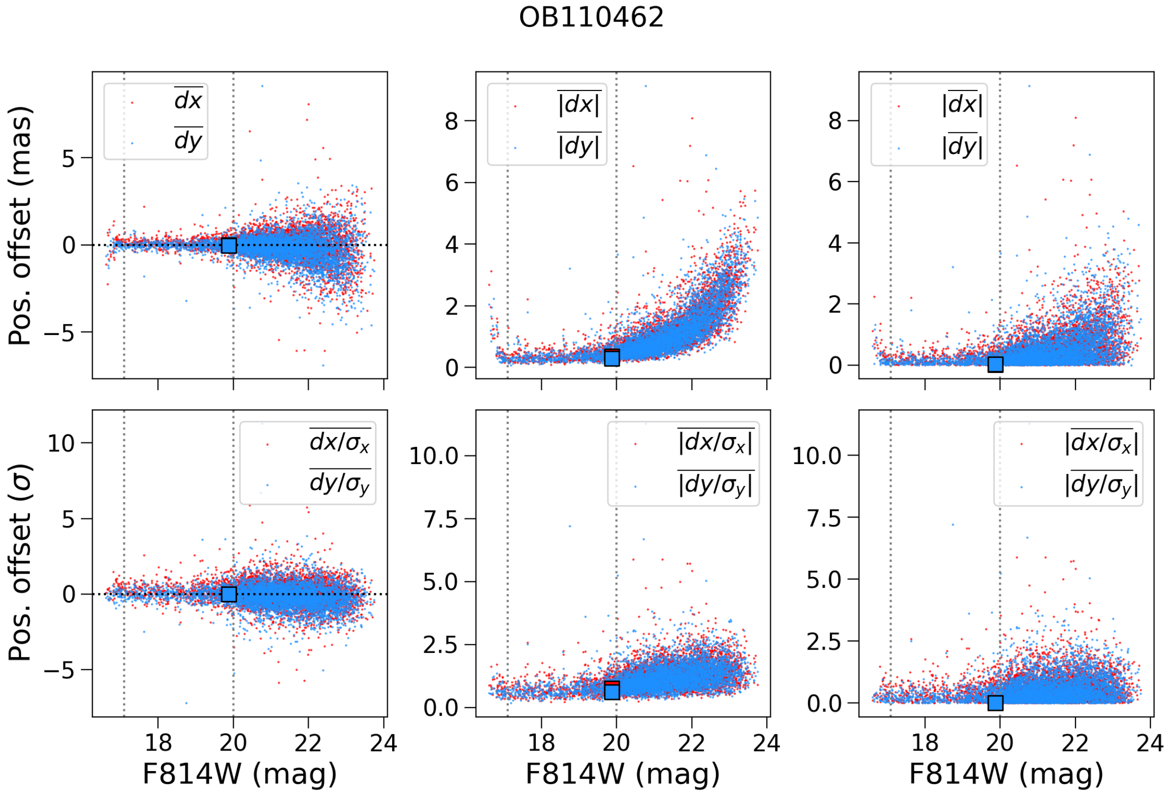

Figure 3.30: Difference in astrometry between observations taken in F814W vs. F606W for stars in the OB110462 images, aggregated across all epochs. Definitions of $\overline{dx}$, $\overline{|dx|}$, and $|\overline{dx}|$ are given in text of Chapter 3.16. The squares mark OB110462. The dashed lines indicate the magnitude range of the reference stars in the OB110462 images.

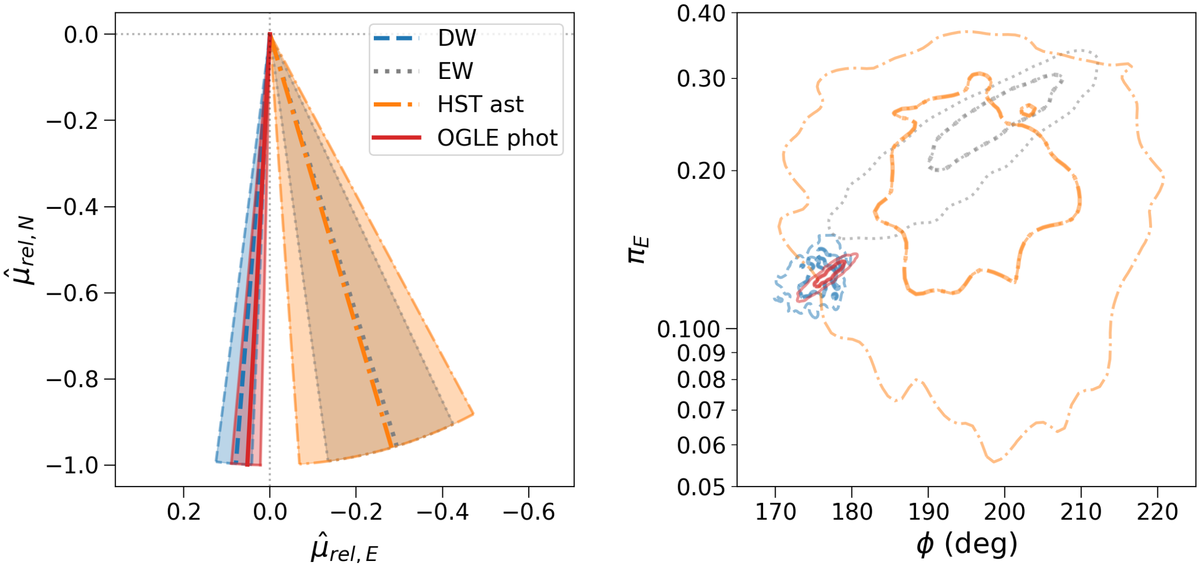

Figure 3.31: *Left:* Comparison of the source-lens relative proper motion inferred from the photometry and astrometry using the default weighted likelihood (DW), the photometry and astrometry using the equal weighted likelihood (EW), from the *HST* astrometry alone (*HST ast*), and from the OGLE photometry alone (*OGLE phot*). The median is shown as the thick line; the shaded region denotes the 1σ uncertainties. *Right*: 1 and 2σ contours of π_E and direction of the source-lens relative proper motion ϕ, for the 4 fits presented in the left panel. the EW fit is consistent with the fit to the *HST* astrometry, although the astrometry alone has very little constraining power. The DW and OGLE phot fits are consistent with each other, as expected.

Chapter 4

A re-analysis of the isolated black hole candidate OGLE-2011-BLG-0462/MOA-2011-BLG-191

A version of this chapter was submitted in May 2023 to the American Astronomical Society Journals to be reviewed for publication and was coauthored with Jessica R. Lu.

There are expected to be $\sim 10^8$ isolated black holes (BHs) in the Milky Way. OGLE-2011-BLG-0462/MOA-2011-BLG-191 (OB110462) is the only such BH with a mass measurement to date. However, its mass is disputed: Lam, Lu, Udalski, et al. (2022a,b) measure a lower mass of $1.6 - 4.4 M_\odot$, while Mróz, Udalski, and Gould (2022) and Sahu, Anderson, Casertano, Bond, Udalski, et al. (2022) measure a higher mass of $5.8 - 8.7 M_\odot$. We re-analyze OB110462, including new data from the Hubble Space Telescope (*HST*) and re-reduced Optical Gravitational Lensing Experiment (OGLE) photometry. We also re-reduce and re-analyze the *HST* dataset with newly available software. We find significantly different ($\sim 1\,\mathrm{mas}$) *HST* astrometry than Lam, Lu, Udalski, et al. (2022a,b) in the de-magnified epochs due to the amount of positional bias induced by a bright star ∼0.4 arcsec from OB110462. After modeling the updated photometric and astrometric datasets, we find the lens of OB110462 is a $6.0^{+1.2}_{-1.0} M_\odot$ BH. Future observations with the Nancy Grace Roman Space Telescope, which will have an astrometric precision comparable or better to HST but a field of view 100× larger, will be able to measure hundreds of isolated BH masses via microlensing. This will enable the measurement of the BH mass distribution and improve understanding of massive stellar evolution and BH formation channels.

4.1 Introduction

Although massive stars, the progenitors of black holes (BHs), are typically born in binaries, the majority of the Milky Way's $10^7 - 10^9$ BHs are expected to be isolated (Fender et al. 2013; Olejak et al. 2020; Wiktorowicz, Wyrzykowski, et al. 2019). Around $20-30\%$ of O-stars are expected to merge and form a single, even more massive star (Sana et al. 2012), and many of the remaining binary systems are disrupted before, during, or after the formation of the BH due to natal kicks or mass loss. Despite this, nearly all known Galactic BHs are in binary systems (El-Badry, Rix, Cendes, et al. 2023; El-Badry, Rix, Quataert, et al. 2023; Chakrabarti et al. 2022; Corral-Santana et al. 2016; Thompson et al. 2019). This detection bias exists because, unlike BH binaries, isolated BHs do not have a companion that can electromagnetically identify their presence, making them particularly elusive. Detecting and characterizing isolated BHs is a critical first step needed to understand the full Galactic BH population.

Gravitational lensing is the most practical way to detect isolated BHs, as the observational signature depends only on the mass of the lens, and not its luminosity. In particular, *microlensing*, the regime of gravitational lensing where the images are unresolved, provides a way to find and measure the masses of dark objects. As a foreground lens (e.g., a BH) aligns in front of a background source of light (e.g., a Bulge star), this causes the background source to temporarily brighten and change its apparent position; the transient brightening is called *photometric microlensing* and the transient change in position is called *astrometric microlensing*. The combination of the photometric and astrometric signals can be used to measure the mass, distance, and proper motion of the lens (Hog et al. 1995; Miyamoto et al. 1995; Walker 1995). For more details on astrometric microlensing, see Dominik and Sahu (2000).

4.1.1 An isolated dark compact object found with microlensing

OGLE-2011-BLG-0462/MOA-2011-BLG-191 (hereafter OB110462) is the first isolated, dark compact object to have its mass measured with astrometric microlensing. It was identified as a microlensing event toward the Galactic Bulge located at (17:51:40.19, −29:53:26.3) and has been observed both photometrically and astrometrically in order to measure the lens' mass. However, the nature of OB110462's lens is disputed. Sahu, Anderson, Casertano, Bond, Udalski, et al. (2022) inferred the lens to be a $M_L = 7.1 \pm 1.3 M_\odot$ dark object, making OB110462 a firm BH detection similar in mass to other known Galactic BHs in binary systems. Lam, Lu, Udalski, et al. (2022a,b) inferred a lower mass object, which depending on the modeling, led to a $M_L = 2.15^{+0.67}_{-0.54} M_\odot$ or $M_L = 3.79^{+0.62}_{-0.57} M_\odot$ dark object, implying a neutron star or low-mass BH. Both groups analyzed slightly different subsets of high-cadence ground-based photometry and high-resolution Hubble Space Telescope (*HST*) astrometry; see Mróz, Udalski, and Gould (2022) for a summary. In particular, despite analyzing the same astrometric data, both groups derived different stellar positions. In addition, they both found the microlensing parameters inferred from the ground-based photometry were in tension with the parameters inferred by their respective astrometric measurements.

Mróz, Udalski, and Gould (2022) re-analyzed the ground-based OGLE photometry of OB110462. They found systematics in the photometry resulting from imperfect image subtraction due to variations in seeing. Updated modeling using the revised data showed that the OGLE photometry could be self-consistently modeled with the astrometry of Sahu, Anderson, Casertano, Bond, Udalski, et al. (2022), and Mróz, Udalski, and Gould (2022) inferred a lens mass of $M_L = 7.88 \pm 0.82 M_\odot$.

Mereghetti et al. (2022) combined new and archival Chandra imaging to search for X-ray emission from OB110462. No X-rays were detected, and based on the detection upper limits, concluded OB110462 could be consistent with an accreting isolated BH with low radiative efficiency. A neutron star moving slowly or in a high density environment would be disfavored, but uncertainties in the velocity and environment density, as well as the accretion efficiency, did not allow stronger statements to be made on the nature of OB110462.

4.1.2 Rationale for re-analysis of OB110462

Since publication of the initial discovery and modeling papers of OB110462 in July 2022, there have been several new developments. First, as mentioned in Chapter 4.1.1, there are updated ground-based photometry data from OGLE. There are also two additional *HST* data points for OB110462. OB110462 was one of 70 targets in a *HST* snapshot program to image microlensing events (SNAP-16716; PI: K. Sahu); observations of OB110462 were taken in May 2022. In addition, the second and final epoch of a Cycle 29 program (GO-16760; PI: C. Lam) to obtain OB110462 astrometry was taken in September 2022. With regards to analysis tools, an updated version of the software used in the extraction of the astrometry from the *HST* data (`hst1pass`, Anderson 2022) was released in July 2022.

The ability to find and characterize isolated BHs is necessary to understand the evolution and death of massive stars. In turn, massive stars impact our understanding of a wide range of astrophysical problems, from the high-mass end of the stellar initial mass function, to chemical evolution, to galactic feedback. Without understanding the properties of isolated BHs, these problems cannot be solved. Thus, a re-analysis of OB110462 is a timely and worthwhile pursuit.

The remainder of this paper is outlined as follows. Chapter 4.2 lists the new and updated data used in this re-analysis of OB110462. Chapter 4.3 describes the new and updated capabilities of the `hst1pass` software and their effect on the measurement of source positions and magnitudes. Chapter 4.4 describes how these updated measurements are used to derive an updated astrometric time series, and Chapter 4.5 describes how both the updated photometry and astrometry are fit with a microlensing model. Chapter 4.6 presents the lens' properties, compares them to previous studies of OB110462, and shows that the choice of software significantly affects the astrometry and in turn the lens mass. Chapter 4.7 discusses OB110462 is the context of the known Galactic BH population and considers future searches for BHs. Chapter 4.8 provides a summary and conclusions.

4.2 Observations

4.2.1 *HST*

11 epochs of *HST* observations of OB110462 were obtained between 2011 and 2022, and are presented in Table 4.1. This includes all the data analyzed in Lam, Lu, Udalski, et al. (2022a,b) (see Table 2 in Lam, Lu, Udalski, et al. (2022b)), with several additions. First, all exposures taken on 2011-08-08 were included in this analysis (compared to Lam, Lu, Udalski, et al. (2022a,b), who excluded 3 frames that had different exposure times than the main dataset). The exposures from 2013-05-13 was also included (compared to Lam, Lu, Udalski, et al. (2022a,b), who excluded them because there were no other Spring epochs to calibrate reference frame alignment issues due to parallax; however there is now a second Spring epoch that can be used to perform this calibration). Finally, the new *HST* observations taken in 2022 have been included. Note that although the 2022-09-13 GO data was taken with the UVIS2-2K2C-SUB subarray like the previous datasets, the 2022-05-29 SNAP data was taken with the UVIS2-C1K1C-SUB subarray, which is a smaller subarray (1k×1k, vs. 2k×2k).

4.2.2 OGLE

As mentioned in Chapter 4.1, the ground-based OGLE photometry was re-reduced by Mróz, Udalski, and Gould (2022). Figure 4.1 shows the difference between the old and new light curve. In addition, Mróz, Udalski, and Gould (2022) found that data from the first half of 2010 was affected by systematics due to commissioning of a new camera, and removed this data from their analysis. They also only modeled data through 2016 as they found a potential systematic in old OGLE reductions around HJD = 2458000 (September 2017). For consistency, we also model the same subset of re-reduced OGLE data, spanning HJD = 2455376 to 2457700 (roughly July 2010 - November 2016).

4.3 Updated astrometric reductions and analysis with `hst1pass`

The software package `hst1pass` extracts precise astrometry from *HST* WFC3-UVIS imaging. It is described in Anderson and King (2006), and although it has been updated and used in many publications over the years, never formally released as Space Telescope Science Institue-supported software. Lam, Lu, Udalski, et al. (2022a,b) and Sahu, Anderson, Casertano, Bond, Udalski, et al. (2022) used one of these unofficial `hst1pass` releases to perform their astrometric analyses.

In July 2022 `hst1pass` was officially released (Anderson 2022). Most notably, this release included a tabular correction for charge transfer efficiency (CTE, Anderson, Baggett, et al. 2021) that could be used instead of a pixel-based CTE correction (Anderson, Baggett, et al. 2021), and new functionality to perform artificial star injection and recovery simulations.

Epoch (UT)	PA (deg)	Filter	T_{exp} (sec)	N_{im}
2011-08-08	270.0	F606W	75.0	3
2011-08-08	**270.0**	**F606W**	**60.0**	**1**
2011-08-08	270.0	F814W	75.0	3
2011-08-08	**270.0**	**F814W**	**60.0**	**1**
2011-08-08	**270.0**	**F814W**	**120.0**	**1**
2011-10-31	276.1	F606W	280.0	3
2011-10-31	276.1	F814W	200.0	4
2012-09-09	269.5	F606W	290.0	3
2012-09-09	269.5	F814W	190.0	4
2012-09-25	271.3	F606W	280.0	3
2012-09-25	271.3	F814W	200.0	4
2013-05-13	**99.9**	**F606W**	**280.0**	**3**
2013-05-13	**99.9**	**F814W**	**200.0**	**4**
2013-10-22	274.6	F606W	285.0	3
2013-10-22	274.6	F814W	285.0	4
2014-10-26	275.2	F606W	265.0	3
2014-10-26	275.2	F814W	265.0	4
2017-08-29	268.3	F606W	250.0	3
2017-08-29	268.3	F814W	250.0	4
2021-10-01	272.0	F606W	407.0	5
2021-10-01	272.0	F814W	307.0	6
2022-05-29	**107.9**	**F814W**	**300.0**	**2**
2022-09-13	**269.9**	**F606W**	**407.0**	**5**
2022-09-13	**269.9**	**F814W**	**307.0**	**6**

Table 4.1: *HST data analyzed.* For each epoch, the position angle (PA), *HST* WFC3-UVIS filter, exposure time T_{exp}, and number of images N_{im} are listed. *Bold text* indicates data used in this re-analysis that was not used in Lam, Lu, Udalski, et al. (2022a,b).

We note that the official release of `hst1pass` also comes with a new routine called `hst2collate` to collate the starlists of the individual frames together into a final starlist for that epoch. However, because this is a limited-use early version of `hst2collate`, we find the flexibility of the existing software routines `xym2mat` and `xym2bar` (Anderson and King 2006) to be superior. Hence, we do not use `hst2collate` in our analysis and do not discuss it further here.

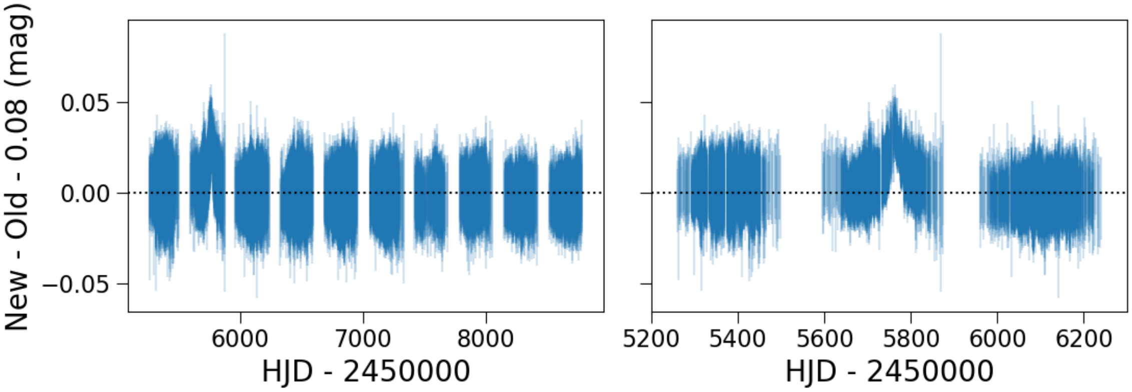

Figure 4.1: Difference between the OGLE photometry used in Mróz, Udalski, and Gould (2022) as to that used in Lam, Lu, Udalski, et al. (2022a,b) and Sahu, Anderson, Casertano, Bond, Udalski, et al. (2022). *Left:* full light curve. *Right:* light curve zoomed into the first three years (photometric peak year ± 1 year).

4.3.1 CTE correction

Lam, Lu, Udalski, et al. (2022a,b) and Sahu, Anderson, Casertano, Bond, Udalski, et al. (2022) used the CTE-corrected flat-fielded *HST* images (i.e. `flc`) for their analyses. The `flc` images were produced using Version 2.0 of a pixel-based CTE correction algorithm (Anderson, Baggett, et al. 2021). However, the pixel-based correction usually under-corrects the CTE effect on photometry (Kuhn et al. 2021).

The updated version of `hst1pass` includes a tabular correction that empirically corrects for CTE based on the brightness of the source and the sky background, which improves the extraction of photometry and astrometry (Anderson, Baggett, et al. 2021).

Both CTE correction methods alter the extracted source positions in the detector y direction, which is the parallel readout direction. At present, CTE in the detector x direction, which is the serial readout direction, is not corrected. Although there is CTE in the serial readout direction, it is negligibly small compared to CTE in the parallel readout direction (Anderson 2014).

When performing the data reduction in this work, instead of reducing the CTE pixel-corrected `flc` files, we instead reduce the flat-fielded data files (i.e. `flt`) with `hst1pass` using the tabular CTE correction. Measured positions between these two methods can differ by a tenth of a pixel and measured brightness can differ by a tenth of a magnitude (Figure 4.14 in Appendix 4.9). We then proceed with the data reduction and intra-epoch alignment process described in §4.1 of Lam, Lu, Udalski, et al. (2022b) using the tabular-CTE corrected starlists.

4.3.2 Artificial star injection and recovery tests

OB110462 is located ∼10 pixels (∼0.4 arcsec) away from an unrelated neighbor star that is 3 magnitudes brighter. This neighbor star biases the measurement of the flux and position of OB110462. Lam, Lu, Udalski, et al. (2022a,b) and Sahu, Anderson, Casertano, Bond, Udalski, et al. (2022) took different approaches to calculate this bias.

Sahu, Anderson, Casertano, Bond, Udalski, et al. (2022) used 18 nearby isolated stars with color and magnitude comparable to the neighbor to construct an "extended model" point spread function (PSF). This extended model PSF was then subtracted from each exposure to obtain an unbiased position and magnitude of OB110462. Using this method, Sahu, Anderson, Casertano, Bond, Udalski, et al. (2022) found that the typical positional bias for OB110462 was about 1.2 mas.

Lam, Lu, Udalski, et al. (2022a,b) performed injection and recovery tests to measure the bias. They injected sources around an isolated star of similar brightness to the neighbor, at the same azimuth, separation, and magnitude difference as the neighbor-OB110462 pair. Using this method, Lam, Lu, Udalski, et al. (2022b) found a smaller positional bias of around 0.3 and 0.5 mas for OB110462, in the F606W and F814W filters, respectively.

In Chapter 4.3.2.1 we describe the new `hst1pass` software used to perform source extraction for artificial stars and in Chapter 4.3.2.2, we present an updated and more extensive star-planting analysis using the new `hst1pass`.

4.3.2.1 `hst1pass` vs. `ks2` software

The version of `hst1pass` used by Lam, Lu, Udalski, et al. (2022a,b) did not have a method to generate artificial stars in the images. Thus, Lam, Lu, Udalski, et al. (2022a,b) used a different software package, called `ks2`, to perform the injection and recovery tests. `ks2` has not been formally released, but it is described in several papers, e.g., Anderson, Sarajedini, et al. (2008), Bellini, Anderson, and Grogin (2018), and Sabbi et al. (2016).

Although both `hst1pass` and `ks2` are used to extract precise astrometric measurements from *HST* imaging, they work in slightly different manners. `ks2` was specifically designed to find fainter sources than `hst1pass`. There are also certain implementation differences across the two software packages. Of relevance to the astrometry are the geometric distortion solutions used, and the specifics of the PSF fitting. With regard to the distortion solution, `ks2` has an internal geometric distortion solution that is slightly different from the standard geometric distortion correction (STDGDC) files used by `hst1pass`. With regard to the PSFs, the specific manner of fitting slightly differ, e.g., the particulars of how outlier rejection is implemented.

In Lam, Lu, Udalski, et al. (2022a,b), `hst1pass` was used instead of `ks2` for data reduction because recovery depth was not an issue and `hst1pass` had been more robustly used and tested on *HST* WFC3-UVIS data. To use `hst1pass` to obtain the positions, and then use `ks2` to calculate the bias in the position and flux of OB110462 is formally inconsistent, since the two methods of source extraction in these software differ. As a validation test,

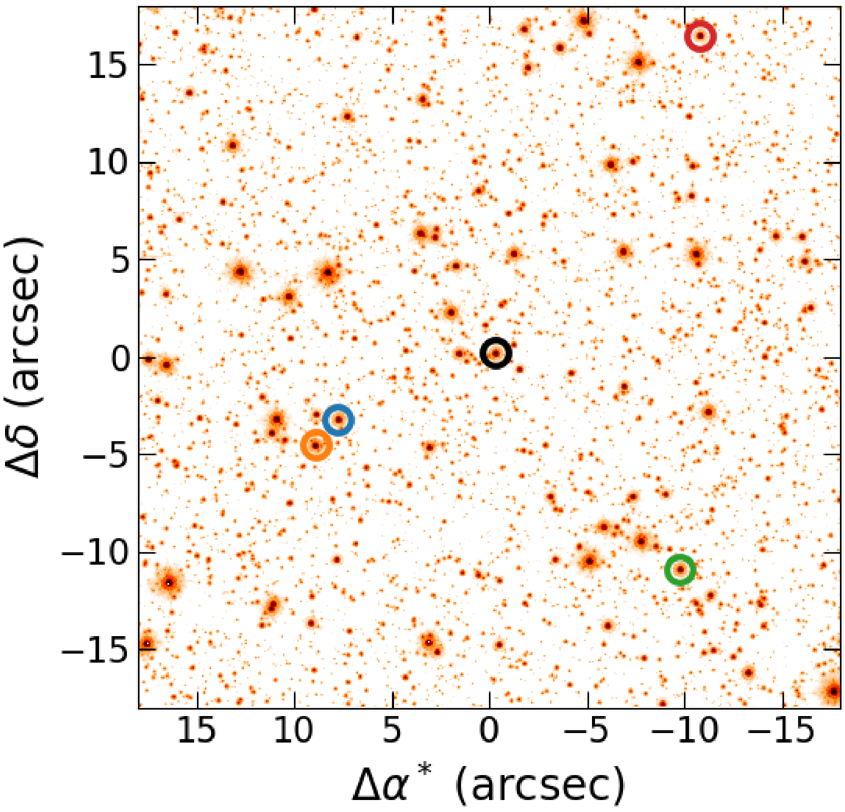

Figure 4.2: Spatial distribution of neighbor-like stars. The image shows a 36 × 36 arcsec area centered on OB110462. The black circle in the center shows the location of OB110462's bright neighbor. The four other colored circles show the location of the neighbor-like stars.

`hst1pass` and `ks2` were used to extract astrometry from the same epoch of *HST* observations and then the differences between the resultant starlists were compared. No clear trends were found to explain the differences. Since the bias correction is a relative measurement and self-consistent across one software package, it was deemed a reasonable approach to calculate the bias correction with `ks2` and then apply it to measurements made with `hst1pass`. However, now that the new version of `hst1pass` has the ability to simulate artificial stars, the injection and recovery analysis can be done in a fully self-consistent manner and this assumption can be checked.

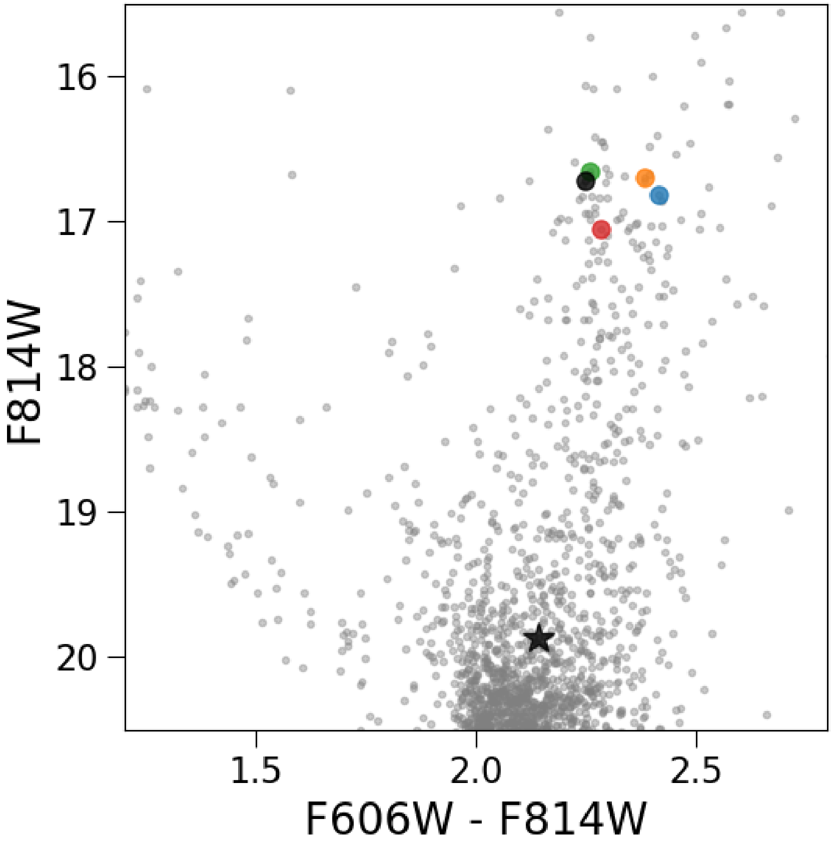

Figure 4.3: Location of neighbor-like stars on an *HST* CMD. The black circle marks OB110462's bright neighbor. The four other colored circles mark the neighbor-like stars (colors correspond to those in Figure 4.2). The black star marks OB110462 at baseline (i.e. unmagnified).

4.3.2.2 Updated methodology

Here, we update the analysis performed in Lam, Lu, Udalski, et al. (2022b). We briefly summarize the methodology here and only highlight new changes; see Appendix B of Lam, Lu, Udalski, et al. (2022b) for full details.

We calculate the bias in the position and flux of OB110462 by injecting artificial stars using `hst1pass` at the same azimuth and separation as OB110462 and its bright neighbor star, around "neighbor-like" stars. We then determine whether these injected artificial stars are recovered, and if they are, how different the recovered and injected positions and fluxes are.

The criteria for selecting nearby isolated neighbor-like stars are:

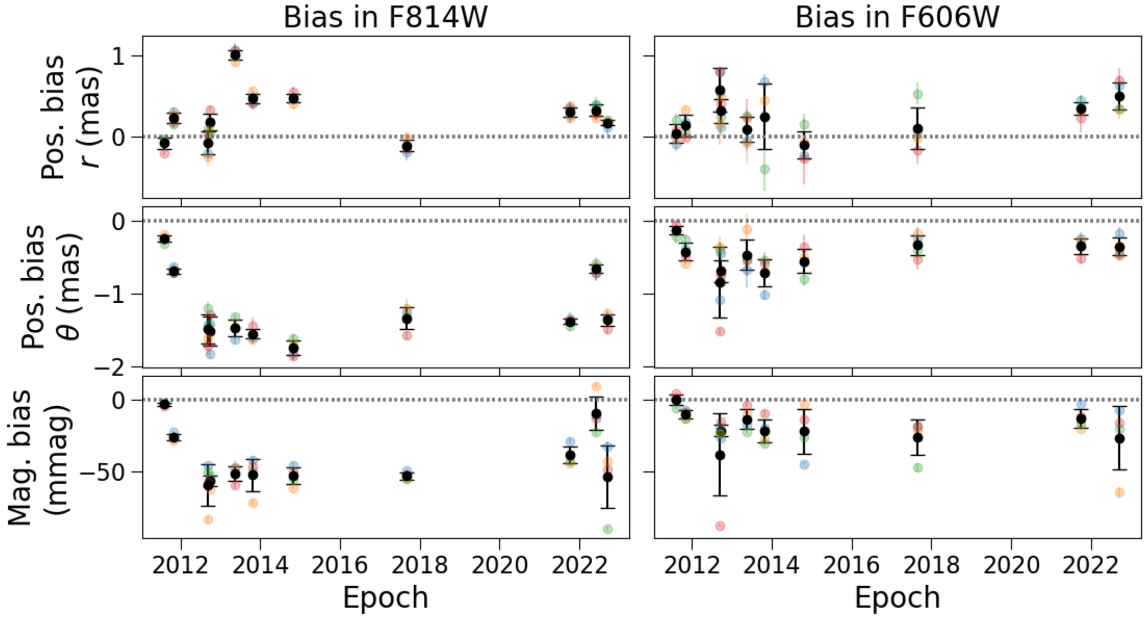

Figure 4.4: Measurement bias of a source in F814W (*left*) and F606W (*right*) due to proximity to a bright star. The bias correction is defined as the recovered minus injected value. The amount of positional bias is shown decomposed into radial r (*top row*) and azimuthal θ (*middle row*) components . The radial direction is defined by the OB110462-neighbor star separation vector, and the azimuthal direction is measured counterclockwise from the separation vector. The amount of magnitude bias is shown in the *bottom row*. The colored points show the mean and standard deviation of the measurement bias for the four different neighbor-like stars; the colors correspond to those in Figure 4.2 and Figure 4.3. The black points are the mean and standard deviation of the mean measurement bias of the four neighbor-like stars. The positional and magnitude bias in F606W is smaller than that in F814W by about a factor of two; this is not surprising since at shorter wavelength the angular resolution is higher.

- similar brightness to neighbor (within ± 0.5 mag in both F814W and F606),
- similar color to neighbor (within ± 0.25 mag in F606W − F814W),
- nearby to neighbor (within ±20 arcsec = 500 pix)
- isolated from other stars (at least 0.4 arcsec = 10 pix away from any other source detected by `hst1pass` in F814W).

There are four stars that fit all these criteria. Their positions in relation to OB110462 are shown in Figure 4.2 and on a color-magnitude diagram (CMD) in Figure 4.3.

Epoch	ΔRA (mas)	ΔDec (mas)	ΔTotal (mas)	ΔMag (mag)
F606W				
2011-08-08	-0.14 ± 0.08	0.00 ± 0.10	0.14	0.000 ± 0.004
2011-10-31	-0.46 ± 0.14	0.00 ± 0.11	0.46	-0.010 ± 0.003
2012-09-09	-0.98 ± 0.53	-0.27 ± 0.15	1.02	-0.039 ± 0.029
2012-09-25	-0.76 ± 0.17	-0.08 ± 0.12	0.76	-0.022 ± 0.004
2013-05-13	-0.48 ± 0.22	0.06 ± 0.13	0.48	-0.013 ± 0.007
2013-10-22	-0.76 ± 0.29	-0.01 ± 0.33	0.76	-0.022 ± 0.008
2014-10-26	-0.50 ± 0.20	0.27 ± 0.12	0.57	-0.022 ± 0.016
2017-08-29	-0.36 ± 0.15	0.00 ± 0.25	0.36	-0.026 ± 0.012
2021-10-01	-0.44 ± 0.08	-0.22 ± 0.10	0.49	-0.013 ± 0.007
2022-09-13	-0.50 ± 0.12	-0.36 ± 0.16	0.62	-0.027 ± 0.022
F814W				
2011-08-08	-0.21 ± 0.05	0.15 ± 0.07	0.26	-0.003 ± 0.001
2011-10-31	-0.73 ± 0.02	0.00 ± 0.07	0.73	-0.026 ± 0.002
2012-09-09	-1.39 ± 0.18	0.55 ± 0.17	1.49	-0.060 ± 0.015
2012-09-25	-1.50 ± 0.18	0.31 ± 0.13	1.53	-0.057 ± 0.003
2013-05-13	-1.72 ± 0.12	-0.47 ± 0.05	1.78	-0.052 ± 0.005
2013-10-22	-1.63 ± 0.08	0.05 ± 0.05	1.63	-0.053 ± 0.012
2014-10-26	-1.81 ± 0.10	0.11 ± 0.03	1.81	-0.053 ± 0.006
2017-08-29	-1.23 ± 0.13	0.53 ± 0.10	1.34	-0.053 ± 0.002
2021-10-01	-1.41 ± 0.05	0.15 ± 0.05	1.42	-0.039 ± 0.006
2022-05-29	-0.74 ± 0.06	-0.10 ± 0.07	0.74	-0.009 ± 0.012
2022-09-13	-1.35 ± 0.07	0.27 ± 0.04	1.37	-0.054 ± 0.022

Table 4.2: *Bias correction derived from injection and recovery.* Bias correction derived from injection/recovery around a star of comparable brightness at the same separation, azimuth, and magnitude difference as OB110462 to its bright neighbor. The bias correction is defined as the recovered minus the true injected value.

45 artificial stars are injected in a 0.2×0.2 pixel ($= 8 \times 8$ mas) area adjacent to each of the four neighbor-like stars, with a magnitude so that the artificial star has the same contrast with the neighbor-like star as OB110462 to the neighbor. The results of the injection and recovery are shown in Figures 4.4 and 4.11 (c.f. Figures 22 and 23 in Lam, Lu, Udalski, et al. (2022b)) and listed in Table 4.2 (c.f. Table 16 in Lam, Lu, Udalski, et al. (2022b)).

4.4 Updated cross-epoch alignment

We take the starlists for epoch obtained in Chapter 4.3.1 and align them onto a common reference frame, as described in §4.2 - 4.2.3 of Lam, Lu, Udalski, et al. (2022b). The photometry is calibrated as described in §4.3 of Lam, Lu, Udalski, et al. (2022b); in short, to obtain precise relative photometry, we calculate and apply a small magnitude offset that assumes the reference stars are constant brightness. One minor change in this work as compared to Lam, Lu, Udalski, et al. (2022b) is the value of the additive error added in quadrature to the positional and magnitude uncertainties. Appendix A of Lam, Lu, Udalski, et al. (2022b) describes an empirical methodology to calculate the rescaling factor, which can vary epoch to epoch. We instead simply use a constant additive error across all epochs; the value of the additive error is chosen to make the alignment residuals follow the expected χ^2 distribution. We find an additive error of 0.25 mas and 12 milli-mag added to the F606W positions and magnitudes, and 0.10 mas and 8 milli-mag in F814W, produce acceptable χ^2 distributions by eye (Figure 4.5, c.f. Figure 9 of Lam, Lu, Udalski, et al. (2022b).). Figures 4.5 and 4.6 show the 10 astrometric reference stars closest to OB110462.

The final result of the cross-epoch alignment is the *HST* photometric and astrometric time series (Figures 4.7 and 4.8). The bias correction measured in Chapter 4.3.2.2 is then applied to OB110462 to obtain its true positions and magnitudes (Table 4.3). Note that in Table 4.3 the reported uncertainties do not include the uncertainties in the transformation from a relative astrometric reference frame to the absolute Gaia reference frame, which are 0.13 mas/yr and 0.11 mas/yr in RA and Dec, respectively.

4.5 Modeling using updated data

Next, we fit the re-reduced OGLE data and updated *HST* data following the procedure outlined in Lam, Lu, Udalski, et al. (2022a,b) for their "default weight" (DW) fit. See §5 of Lam, Lu, Udalski, et al. (2022b) for details on the model parameters and modeling framework.

Simultaneously fitting the photometry and astrometry is very time-intensive, so to speed up the process, we first simultaneously fit the OGLE and *HST* photometry, accounting for correlated noise while fitting the OGLE photometry with a Gaussian Process. The joint photometric and astrometric geometric parameters are t_0, u_0, t_E, $\pi_{E,E}$, and $\pi_{E,N}$. The photometric-only parameters are $b_{SFF,O}$, $m_{base,O}$, $b_{SFF,H8}$, $m_{base,H8}$, $b_{SFF,H6}$, and $m_{base,H6}$. The astrometric-only parameters are $x_{S0,E}$, $x_{S0,N}$, π_S, $\log_{10}\theta_E$, $\mu_{S,E}$, and $\mu_{S,N}$. The Gaussian process parameters are $\log\sigma_{0,O}$, ρ_O, $\log\omega_{0,O}^4 S_{0,O}$, and $\log\omega_{0,O}$. See §3 of Lam, Lu, Udalski, et al. (2022a), and §5, §5.1 and Appendix F of Lam, Lu, Udalski, et al. (2022b) for a full description of all these parameters.

We then take the posterior distributions for t_0, u_0, t_E, $\pi_{E,E}$, and $\pi_{E,N}$ from the photometry fit, and use them as priors when fitting the *HST* astrometry. Note the correlations between the 5 parameters are preserved when using them as a prior in the astrometry fit. Our priors are listed in Table 4.8 in Appendix 4.10.

Epoch	RA (mas)	Dec (mas)	Mag (Vega)
F814W			
2022-09-13	-13.43 ± 0.19	-22.75 ± 0.19	19.965 ± 0.024
2022-05-29	-13.91 ± 1.17	-21.55 ± 0.76	19.926 ± 0.027
2021-10-01	-11.93 ± 0.17	-19.53 ± 0.17	19.921 ± 0.021
2017-08-29	-3.97 ± 0.29	-5.88 ± 0.27	19.949 ± 0.014
2014-10-26	2.11 ± 0.29	3.81 ± 0.28	19.964 ± 0.013
2013-10-22	4.32 ± 0.33	7.10 ± 0.34	19.918 ± 0.050
2013-05-13	5.62 ± 0.26	8.01 ± 0.23	19.916 ± 0.011
2012-09-25	7.04 ± 0.48	10.17 ± 0.46	19.849 ± 0.010
2012-09-09	6.83 ± 0.27	10.76 ± 0.26	19.846 ± 0.018
2011-10-31	8.47 ± 0.20	14.23 ± 0.21	18.897 ± 0.009
2011-08-08	8.87 ± 0.19	15.65 ± 0.20	17.230 ± 0.014
F606W			
2022-09-13	-13.31 ± 0.33	-22.48 ± 0.35	22.054 ± 0.028
2021-10-01	-11.63 ± 0.41	-19.63 ± 0.41	22.043 ± 0.014
2017-08-29	-4.15 ± 0.36	-5.76 ± 0.41	22.056 ± 0.025
2014-10-26	1.56 ± 0.42	3.03 ± 0.38	22.076 ± 0.019
2013-10-22	4.39 ± 0.42	6.66 ± 0.45	22.046 ± 0.018
2013-05-13	5.99 ± 0.48	8.18 ± 0.39	22.005 ± 0.012
2012-09-25	7.45 ± 0.57	10.52 ± 0.56	21.948 ± 0.011
2012-09-09	7.59 ± 0.62	10.15 ± 0.35	21.918 ± 0.057
2011-10-31	8.72 ± 0.48	14.41 ± 0.49	20.992 ± 0.012
2011-08-08	8.74 ± 0.32	16.00 ± 0.33	19.326 ± 0.015

Table 4.3: *HST calibrated data.* Relative positions and magnitudes of OB110462.

4.6 Results

The best-fit photometry and astrometry models are shown in Figures 4.7 and 4.8, and the posteriors are listed in Table 4.4. We find that that the lens of OB110462 has a mass of $M_L = 6.03^{+1.19}_{-1.04} M_\odot$, is at a distance $D_L = 1.72^{+0.32}_{-0.23}\,\mathrm{kpc}$, and has transverse velocity $v_{T,L} = 37.61^{+5.12}_{-5.13}\,\mathrm{km/s}$.

OB110462 cannot be a a high-mass star, and is thus a BH. In Lam, Lu, Udalski, et al. (2022a,b), they rule out any possibility of a luminous lens for OB110462, for a lens mass of $M_L = 3.8 M_\odot$ and source flux fractions $b_{SFF} = 0.9$ and 0.94 in F814W and F606W, respectively. Here, we find $M_L = 6.0 M_\odot$ and source flux fractions $b_{SFF} = 0.98$ in both F814W and F606W. In both Lam, Lu, Udalski, et al. (2022a,b) and this work, the lens is $D_L = 1.7\,\mathrm{kpc}$ away. In this work, the mass is significantly higher and the source flux fractions are also slightly higher. This means the constraint on a dark lens is much stronger—given

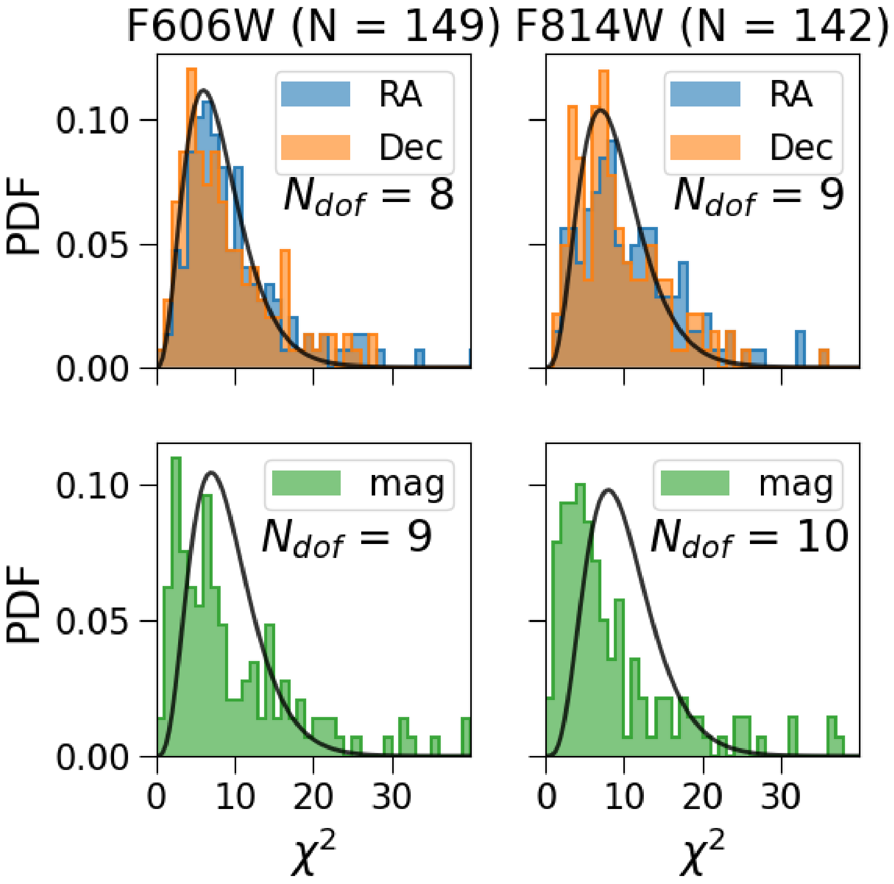

Figure 4.5: *Top:* Histogram of χ^2 residual values to linear proper motion fits (no parallax) of the reference stars. *Bottom:* Histogram of χ^2 residual values to constant magnitude vs. time fits of the reference stars. The *left* column shows the reference stars for F606W; the *right* column shows the reference stars for F814W. N denotes the number of reference stars.

the lens is at some fixed distance, a higher mass star would be much brighter, and a higher source flux fraction would mean there is less excess flux that such a star could hide in. Thus, without any shadow of a doubt, OB110462 is a BH.

In the next sections we compare these results to those of Lam, Lu, Udalski, et al. (2022a,b), Sahu, Anderson, Casertano, Bond, Udalski, et al. (2022), and Mróz, Udalski, and Gould (2022). Table 4.5 gives a short summary of the differences in the data and models used to analyze OB110462 across these works. We first compare the inferred lens properties in Chapter 4.6.1, evaluate the goodness-of-fits of the astrometric models in Chapter 4.6.2, then compare the modeled astrometric time series in Chapter 4.6.3 to understand the reasons for the differences in the inferred lens properties.

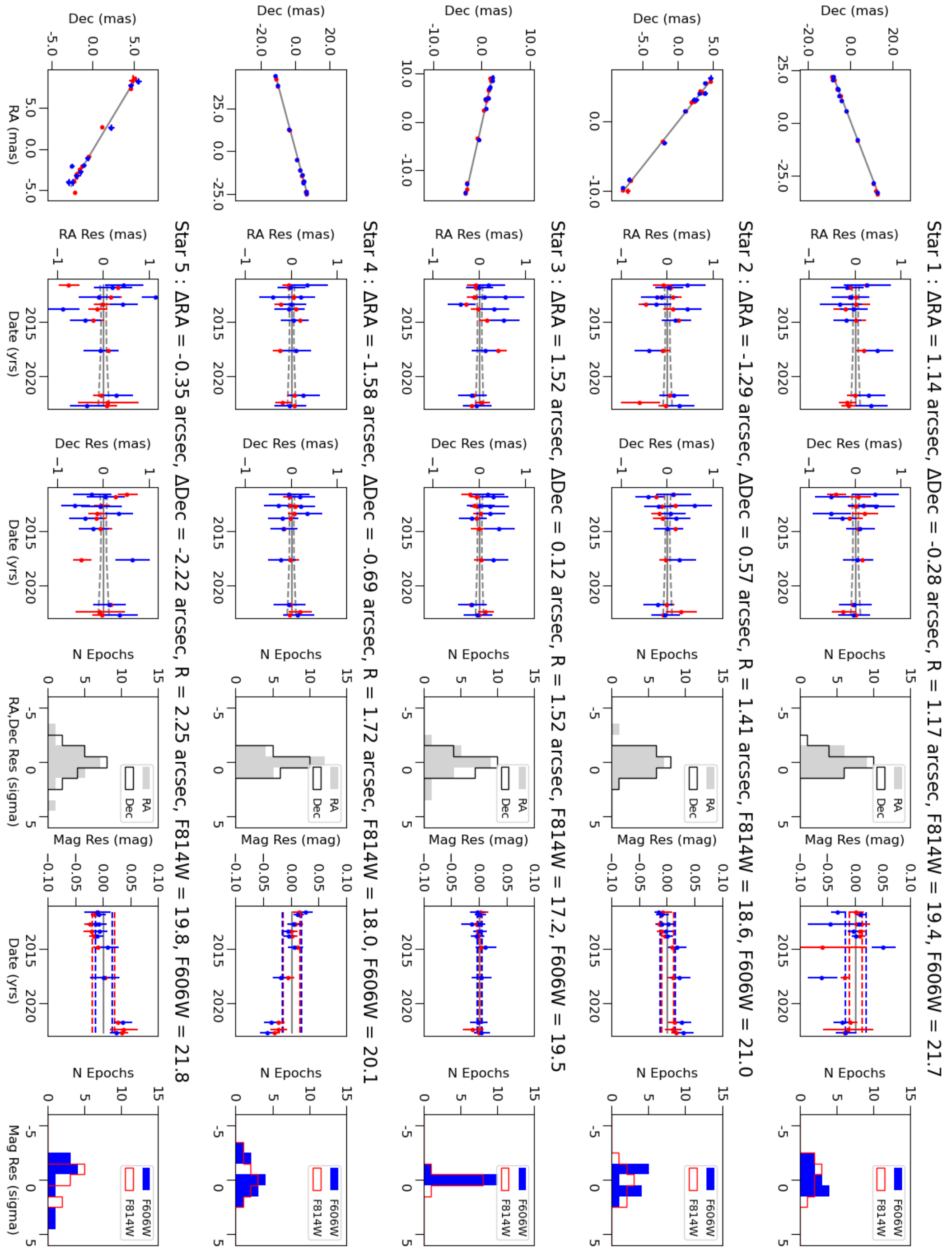
Star 1 : ΔRA = 1.14 arcsec, ΔDec = -0.28 arcsec, R = 1.17 arcsec, F814W = 19.4, F606W = 21.7

Star 2 : ΔRA = -1.29 arcsec, ΔDec = 0.57 arcsec, R = 1.41 arcsec, F814W = 18.6, F606W = 21.0

Star 3 : ΔRA = 1.52 arcsec, ΔDec = 0.12 arcsec, R = 1.52 arcsec, F814W = 17.2, F606W = 19.5

Star 4 : ΔRA = -1.58 arcsec, ΔDec = -0.69 arcsec, R = 1.72 arcsec, F814W = 18.0, F606W = 20.1

Star 5 : ΔRA = -0.35 arcsec, ΔDec = -2.22 arcsec, R = 2.25 arcsec, F814W = 19.8, F606W = 21.8

Figure 4.5: 5 reference stars nearest to OB110462. *(Caption continued on next page.)*

Figure 4.5: *(Caption continued from previous page.)* The title indicates the separation of the reference star from OB110462 in RA, Dec, and total distance, and the magnitude of the star in F814W and F606W. In the individual panels, data in the F606W (F814W) filters are shown in *blue* (*red*). *1st column:* Trajectory on sky. Note the scales across different rows vary. The positions are relative to the ΔRA and ΔDec offsets, which are relative to OB110462. The best-fit linear trajectory is shown in *gray*. Note these velocities are in a reference frame where the mean velocity of reference stars is 0, and not the Gaia reference frame. *2nd column:* Residuals to the best-fit linear trajectory in RA. The dashed lines are the 1σ uncertainties to the best-fit line. *3rd column:* Same as 2nd column, but for Dec instead of RA. *4th column:* Histogram of position residuals to the best-fit linear trajectory, in units of sigma. The solid gray is for RA; the outlined black is for Dec. *5th column:* Residuals to the best-fit constant magnitude. F814W and F606W are fit to the respective magnitudes in the title; the dashed lines show the 1σ uncertainties to the best-fit magnitude. *6th column:* Residuals to the best-fit constant magnitude, in units of sigma. The solid blue is for F606W; the outlined red is for F814W.

4.6.1 Comparison of inferred microlensing parameters

We compare the inferred lens mass, distance, transverse velocity, and proper motion of OB110462 to Lam, Lu, Udalski, et al. (2022a,b), Sahu, Anderson, Casertano, Bond, Udalski, et al. (2022), and Mróz, Udalski, and Gould (2022) in Table 4.6 and Figure 4.9. Mróz, Udalski, and Gould (2022) provides two sets of D_L and $v_{T,L}$ depending on the source distance assumed. The two solutions are consistent with each other to 1σ; here we only compare to their results using $D_S = 8.8 \pm 1.4\,\text{kpc}$. In addition, Sahu, Anderson, Casertano, Bond, Udalski, et al. (2022) do not report their uncertainties on the lens transverse velocity; we estimate it to be $\sim 5.5\,\text{km/s}$ based on the reported lens proper motion and distance uncertainties.

The lens mass of OB110462 inferred in this work $M_L = 6.03^{+1.19}_{-1.04} M_\odot$ is consistent with the measurement of Sahu, Anderson, Casertano, Bond, Udalski, et al. (2022) $M_L = 7.1 \pm 1.3 M_\odot$ to 1σ, and consistent with the Lam, Lu, Udalski, et al. (2022a,b) DW model $M_L = 3.79^{+0.62}_{-0.57} M_\odot$ and Mróz, Udalski, and Gould (2022) $M_L = 7.88 \pm 0.82 M_\odot$ measurement to 2σ (in different directions). Our uncertainties are likely larger due to using wider priors for the astrometry; Mróz, Udalski, and Gould (2022) state they use uniform priors in their modeling, but do not state the support.

The lens distance $D_L = 1.72^{+0.32}_{-0.23}\,\text{kpc}$ inferred in this work is consistent with the measurements of Lam, Lu, Udalski, et al. (2022a,b) DW model $D_L = 1.67^{+0.26}_{-0.20}\,\text{kpc}$, Sahu, Anderson, Casertano, Bond, Udalski, et al. (2022) $D_L = 1.58 \pm 0.18\,\text{kpc}$, and Mróz, Udalski, and Gould (2022) $1.62 \pm 0.15\,\text{kpc}$ to 1σ.

The lens transverse velocity $v_{T,L} = 37.61^{+5.12}_{-5.13}\,\text{km/s}$ inferred in this work is consistent with Mróz, Udalski, and Gould (2022) $v_{T,L} = 43.4 \pm 3.8\,\text{km/s}$ and Sahu, Anderson, Casertano, Bond, Udalski, et al. (2022) $v_{T,L} \sim 4.5 \pm 5.5\,\text{km/s}$ to 1σ. It is consistent with the Lam, Lu,

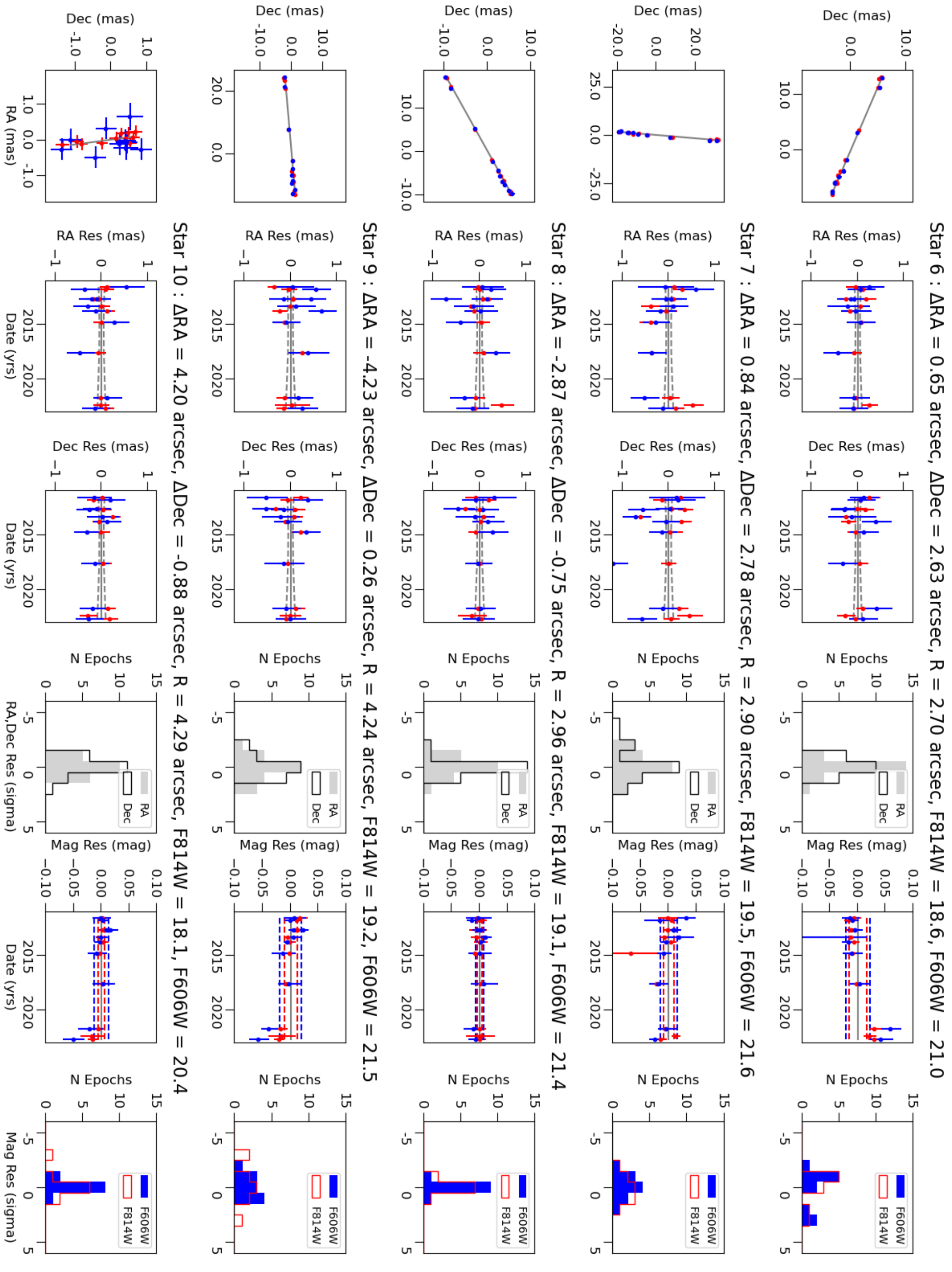

Figure 4.6: Same as Figure 4.5, but for the next 5 reference stars nearest to OB110462.

Parameter	Med$^{+1\sigma}_{-1\sigma}$	MAP	MLE
t_0 (MJD)	$55764.47^{+0.85}_{-0.93}$	55764.69	55763.84
u_0	$-0.05^{+0.007}_{-0.007}$	-0.05	-0.05
t_E (days)	$275.98^{+5.23}_{-6.01}$	267.26	287.48
$\log_{10}(\theta_E/\mathrm{mas})$	$0.68^{+0.05}_{-0.06}$	0.68	0.69
π_S (mas)	$0.11^{+0.02}_{-0.02}$	0.09	0.12
$\pi_{E,E}$	$0.03^{+0.005}_{-0.005}$	0.03	0.02
$\pi_{E,N}$	$-0.09^{+0.01}_{-0.01}$	-0.10	-0.09
$x_{S0,E}$ (mas)	$230.31^{+0.11}_{-0.11}$	230.32	230.35
$x_{S0,N}$ (mas)	$-214.76^{+0.16}_{-0.16}$	-214.90	-214.73
$\mu_{S,E}$ (mas/yr)	$-2.02^{+0.01}_{-0.01}$	-2.02	-2.02
$\mu_{S,N}$ (mas/yr)	$-3.45^{+0.02}_{-0.02}$	-3.45	-3.45
$b_{SFF,O}$	$0.05^{+0.002}_{-0.001}$	0.05	0.05
$m_{base,O}$ (mag)	$16.48^{+0.0004}_{-0.0004}$	16.49	16.49
$b_{SFF,H8}$	$0.98^{+0.03}_{-0.03}$	0.93	0.98
$m_{base,H8}$ (mag)	$19.96^{+0.005}_{-0.005}$	19.96	19.96
$b_{SFF,H6}$	$0.98^{+0.03}_{-0.03}$	0.95	0.98
$m_{base,H6}$ (mag)	$22.05^{+0.006}_{-0.006}$	22.05	22.06
M_L ($M_\odot$)	$6.03^{+1.19}_{-1.04}$	5.40	6.39
π_L (mas)	$0.58^{+0.09}_{-0.09}$	0.60	0.58
π_{rel} (mas)	$0.47^{+0.09}_{-0.09}$	0.52	0.45
$\mu_{L,E}$ (mas/yr)	$-3.80^{+0.48}_{-0.55}$	-3.84	-3.50
$\mu_{L,N}$ (mas/yr)	$2.60^{+0.83}_{-0.80}$	2.80	2.53
$\mu_{rel,E}$ (mas/yr)	$1.78^{+0.56}_{-0.48}$	1.82	1.49
$\mu_{rel,N}$ (mas/yr)	$-6.05^{+0.82}_{-0.83}$	-6.25	-5.98
θ_E (mas)	$4.79^{+1.13}_{-1.15}$	4.76	4.85
π_E	$0.10^{+0.01}_{-0.01}$	0.05	0.10
$\delta_{c,max}$ (mas)	$1.69^{+0.40}_{-0.41}$	1.68	1.72

Table 4.4: *Posterior distributions of fit parameters.* The columns list the median $\pm 1\sigma$ (68%) credible intervals, maximum a posteriori (MAP) solution, and and maximum likelihood estimator (MLE) solution for the microlensing model parameters.

Udalski, et al. (2022a,b) DW model $v_{T,L} = 23.95^{+2.95}_{-2.95}$ km/s to 2σ.

The lens proper motion $(\mu_{L,E}, \mu_{L,N}) = (-3.80^{+0.48}_{0.55}, 2.60^{+0.83}_{-0.80})$ mas/yr inferred in this work is consistent with Mróz, Udalski, and Gould (2022) $(\mu_{L,E}, \mu_{L,N}) = (-4.48 \pm 0.39, 3.29 \pm 0.5)$ mas/yr and Sahu, Anderson, Casertano, Bond, Udalski, et al. (2022) $(\mu_{L,E}, \mu_{L,N}) = (-4.36 \pm 0.22, 3.06 \pm 0.66)$ mas/yr to 1σ in RA and Dec. The proper motion inferred by the Lam, Lu, Udalski, et al. (2022a,b) DW model $(\mu_{L,E}, \mu_{L,N}) = (-2.64^{+0.18}_{-0.24}, 1.46^{+0.63}_{-0.71})$ mas/yr is discrepant to this work $\sim 3\sigma$ in RA, and consistent to this work $\sim 2\sigma$ in Dec (the

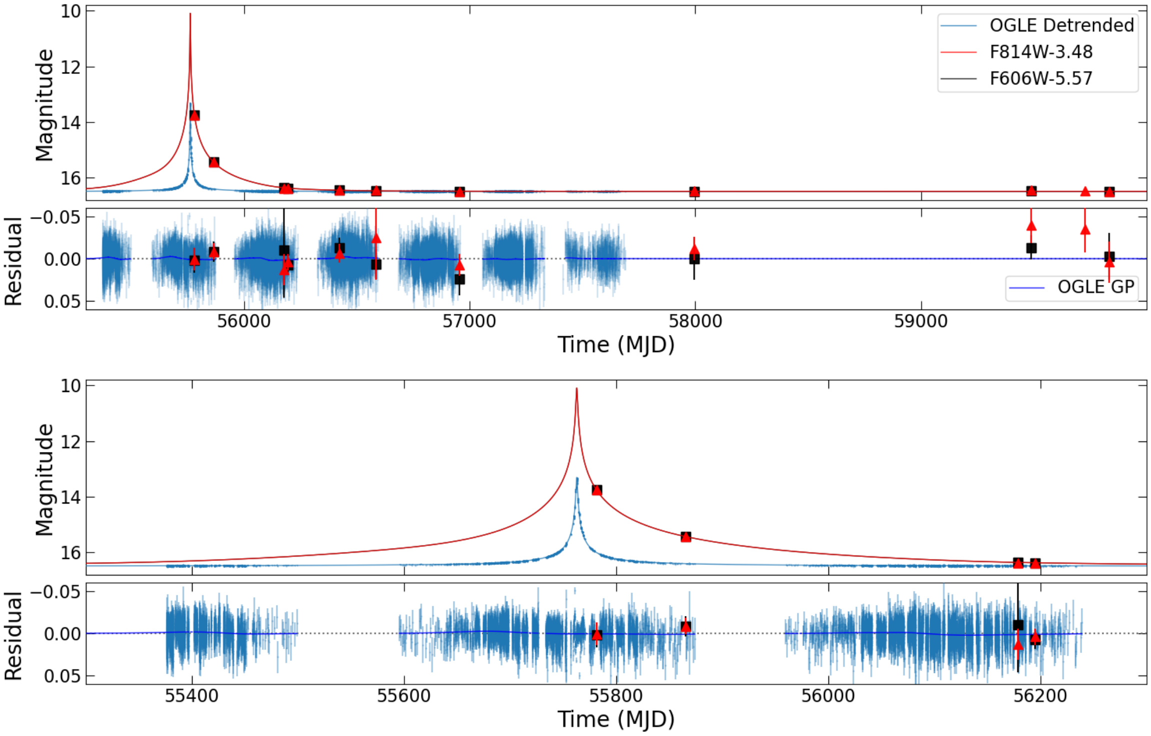

Figure 4.7: *Top panel*: *HST* F814W *red triangles*, *HST* F606W *black squares*, and detrended OGLE lighturve *blue* light curves, with the corresponding maximum likelihood model (MLE, described in Chapter 4.5) plotted over the data. *Second from top panel*: Residuals to the MLE model. The Gaussian Process (GP) model is plotted on top of the OGLE residual. *Second from bottom panel*: Same as top panel, but zoomed into the three most magnified years (2010 – 2012). *Bottom panel*: Same as second from top panel, but zoomed into the three most magnified years (2010 – 2012).

measurements in Dec have larger uncertainties than in RA).

The direction of the lens-source relative proper motion φ is not a property of the lens itself, but was an important point of comparison across previous work so we consider it here. It is defined in Sahu, Anderson, Casertano, Bond, Udalski, et al. (2022) as the position angle of the lens-source relative proper motion in equatorial coordinates. In this work, we find $\varphi = 343.75^{+4.80}_{-3.95}$ deg, consistent with the measurements of Mróz, Udalski, and Gould (2022) $\varphi = 342.5 \pm 4.9$ deg and Sahu, Anderson, Casertano, Bond, Udalski, et al. (2022) $\varphi = 342.3 \pm 3.0$ deg to 1σ. The value of Lam, Lu, Udalski, et al. (2022a,b) from the DW model $\varphi = 355.47^{+2.66}_{-2.11}$ is discrepant at $> 2\sigma$ from this work.

In general, the properties of the lens of OB110462 inferred in this work are somewhat discrepant with the Lam, Lu, Udalski, et al. (2022a,b) DW model, and in reasonable agree-

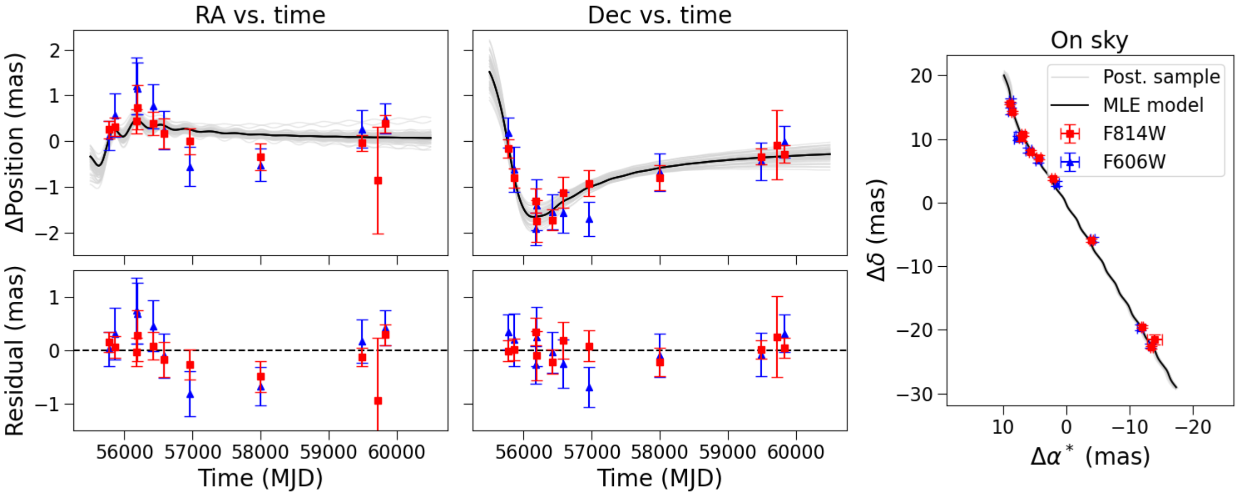

Figure 4.8: OB110462 astrometry. *Left column, top to bottom*: RA vs. time with maximum likelihood (MLE) unlensed source motion model subtracted; residuals to the MLE model for RA vs. time fit. *HST* F814W astrometry data is shown in red; *HST* F606W astrometry data is shown in blue. The MLE model is shown in black. Fifty random draws from the posterior distribution are shown in light gray. *Middle column, top to bottom*: Same as left column, except Dec instead of RA. *Right panel*: astrometry as seen on-sky, in the barycentric frame.

ment with Sahu, Anderson, Casertano, Bond, Udalski, et al. (2022) and Mróz, Udalski, and Gould (2022). We also note that they are inconsistent with the Lam, Lu, Udalski, et al. (2022a,b) EW model; the measurements of $M_L = 2.15^{+0.67}_{-0.54} M_\odot$, $D_L = 0.92^{+0.38}_{-0.22}$ kpc, $v_{T,L} = 7.26^{+4.88}_{-4.88}$ km/s, $(\mu_{L,E}, \mu_{L,N}) = (-0.69^{+0.91}_{-0.94}, 1.53^{+1.21}_{-1.12})$, and $\varphi = 18.08^{+8.60}_{-8.31}$ are discrepant $> 3\sigma$ in mass, lens-source relative proper motion, and lens proper motion in RA and $> 4\sigma$ in transverse velocity with this work.

4.6.2 Goodness-of-fits

Next, we consider the goodness-of-fits of the astrometric model to the data. As a reminder, the data and models used for each work are summarized in Table 4.5. Figure 4.10 shows the CDF of the normalized residuals of the astrometric data and models against the CDF of a standard normal distribution. For all the data sets except Sahu, Anderson, Casertano, Bond, Udalski, et al. (2022), the astrometry in F606W and F814W are separate data points; Sahu, Anderson, Casertano, Bond, Udalski, et al. (2022) averages astrometry across both F606W and F814W filters to obtain a single position.

The residuals in this work are in good agreement with that of a standard normal, as are the residuals in Mróz, Udalski, and Gould (2022) and the Lam, Lu, Udalski, et al. (2022a,b) EW model. The residuals in Lam, Lu, Udalski, et al. (2022a,b) are somewhat

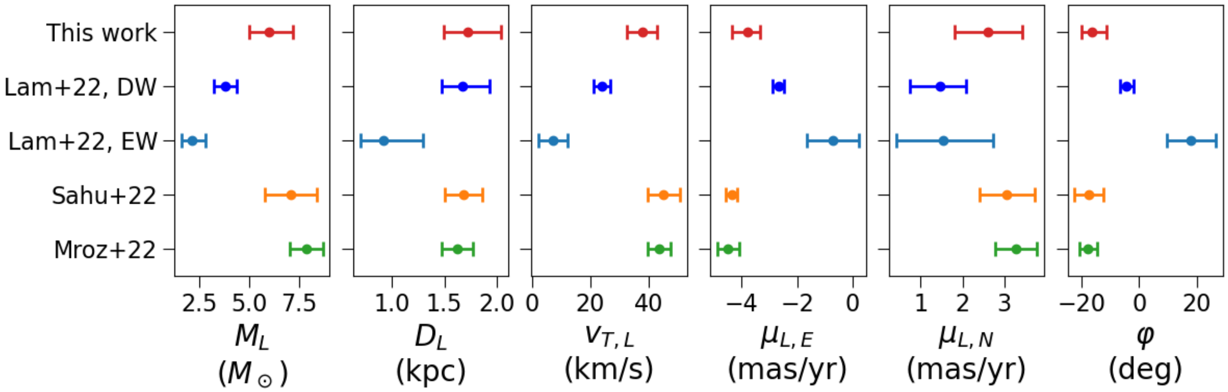

Figure 4.9: Comparison of lens mass M_L, distance D_L, transverse velocity $v_{T,L}$, proper motion vector ($\mu_{L,E}$, $\mu_{L,N}$), and lens-source relative proper motion direction φ inferred from various studies of OB110462.

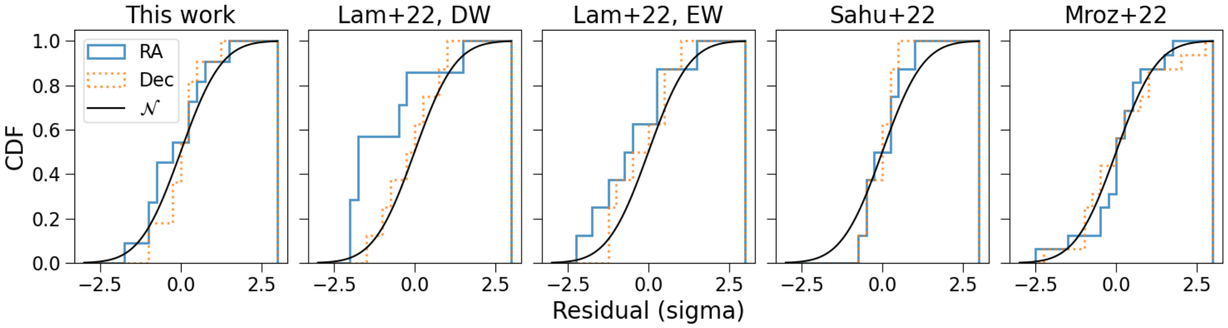

Figure 4.10: CDF of normalized residuals for astrometric models and data, as compared to the CDF of a standard normal distribution. The CDF of normalized residuals for the astrometry in RA (Dec) is shown in the blue solid (orange dotted) line. The CDF of a standard normal distribution is shown as the black curve.

Reference	OGLE data	*HST* data	Likelihood
This work	**Updated**	**2011-2022**	**DW**
Lam+22, DW	Original	2011-2021	DW
Lam+22, EW	Original	2011-2021	EW
Sahu+22	Original	2011-2017	DW
Mroz+22	Updated	2011-2017	DW

Table 4.5: *Summary of data and models in different analyses. OGLE data*: "Original" is the original OGLE reduction of OB110462 used in Lam, Lu, Udalski, et al. (2022a,b) and Sahu, Anderson, Casertano, Bond, Udalski, et al. (2022); "Updated" is the OGLE re-reduction of OB110462 presented in Mróz, Udalski, and Gould (2022). *HST data*: the timespan listed indicates the years of *HST* data used. *Likelihood*: "DW" is the likelihood used in performing the model fit that weights each data point equally; "EW" is the likelihood that weights the OGLE photometry, *HST* photometry, and *HST* astrometry equally.

Reference	$M_L (M_\odot)$	D_L (kpc)	$v_{T,L}$ (km/s)	$\mu_{L,E}$ (mas/yr)	$\mu_{L,N}$ (mas/yr)	φ (deg)
This work	$\mathbf{6.03^{+1.19}_{-1.04}}$	$\mathbf{1.72^{+0.32}_{-0.23}}$	$\mathbf{37.61^{+5.12}_{-5.13}}$	$\mathbf{-3.80^{+0.48}_{-0.55}}$	$\mathbf{2.60^{+0.83}_{-0.80}}$	$\mathbf{343.75^{+4.80}_{-3.95}}$
Lam+22, DW	$3.79^{+0.62}_{-0.57}$	$1.67^{+0.26}_{-0.20}$	$23.95^{+2.95}_{-2.95}$	$-2.64^{+0.18}_{-0.24}$	$1.46^{+0.63}_{-0.71}$	$355.47^{+2.66}_{-2.11}$
Lam+22, EW	$2.15^{+0.67}_{-0.54}$	$0.92^{+0.38}_{-0.22}$	$7.26^{+4.88}_{-4.88}$	$-0.69^{+0.91}_{-0.94}$	$1.53^{+1.21}_{-1.12}$	$18.08^{+8.60}_{-8.31}$
Sahu+22	7.1 ± 1.3	1.58 ± 0.18	$\sim 45 \pm 5.5$	-4.36 ± 0.22	3.06 ± 0.66	342.5 ± 4.9
Mroz+22	7.88 ± 0.82	1.62 ± 0.15	43.4 ± 3.8	-4.48 ± 0.39	3.29 ± 0.5	342.3 ± 3.0

Table 4.6: *Comparison of lens properties.* Comparison of lens mass M_L, distance D_L, transverse velocity $v_{T,L}$, proper motion vector ($\mu_{L,E}$, $\mu_{L,N}$), and lens-source relative proper motion direction φ inferred from various studies of OB110462.

larger than expected in RA due to the model being a poor fit to the data. The residuals in Sahu, Anderson, Casertano, Bond, Udalski, et al. (2022) are smaller than expected, possibly indicative of underestimated uncertainties.

To be more quantitative, we also perform an Anderson-Darling (AD) test to check whether the distribution of normalized residuals is consistent with a standard normal distribution. Table 4.7 lists the the AD test S-statistic, for the model fits in the RA and Dec. The critical values for significance levels of 5% and 1% are 0.709 and 0.984, respectively. Thus, all models presented are consistent with being drawn from a standard normal distribution.

4.6.3 Bias correction method

We find the main difference in the astrometry between this work and Lam, Lu, Udalski, et al. (2022a,b) stems from the bias correction. The other changes in the astrometric analysis did not significantly change the astrometry; we show this along with more detailed comparisons in Appendix 4.11.

Work	RA	Dec
This work	**0.39**	**0.24**
Lam+22, DW	0.64	0.24
Lam+22, EW	0.17	0.27
Sahu+22	0.22	0.40
Mroz+22	0.50	0.29

Table 4.7: *AD test statistic.*

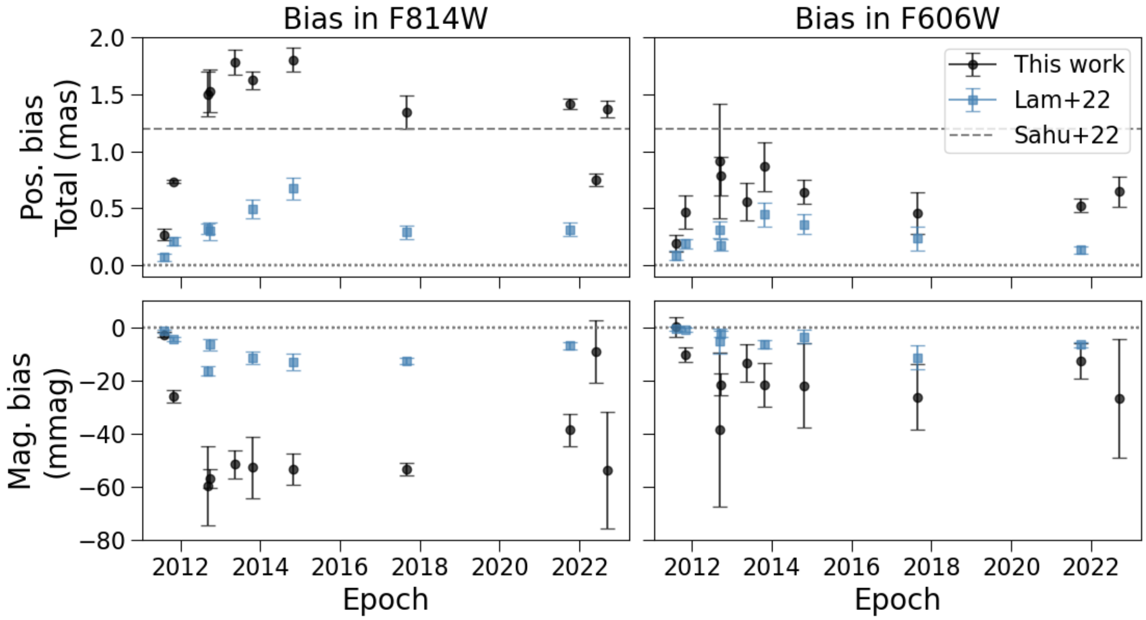

Figure 4.11: Comparison of the bias correction measured in this work to those in Lam, Lu, Udalski, et al. (2022b) and Sahu, Anderson, Casertano, Bond, Udalski, et al. (2022). The *left (right) column* shows the bias in F814W (F606W). The *top (bottom) row* shows the astrometric (photometric) bias, where the bias is defined as the recovered minus injected value. The bias measured in this work performing injection and recovery tests with `hst1pass` is shown in *black circles*. The bias measured in Lam, Lu, Udalski, et al. (2022b) performing injection and recovery tests with `ks2` is shown as *light blue squares*. The astrometric bias reported by Sahu, Anderson, Casertano, Bond, Udalski, et al. (2022) performing PSF subtraction is shown as the *dashed gray line*. Sahu, Anderson, Casertano, Bond, Udalski, et al. (2022) report a single value for the astrometric bias; we show this same value in both the F814W and F606W panels.

We compare the measured photometric and astrometric bias corrections due to the bright neighbor star in Figure 4.11. Using `hst1pass`, we find the average positional bias in non-magnified epochs is around 1.6 mas in F814W and 0.6 mas in F606W (also see Figure 4.4, Table 4.2). This is two to three times larger than the bias found by Lam, Lu, Udalski, et al. (2022b) using `ks2` (c.f. Figures 22 and 23 in Lam, Lu, Udalski, et al. (2022b), the "Neighbor-like" columns). This suggests that PSF fitting in `ks2` is more precise than `hst1pass`.

Similar to Lam, Lu, Udalski, et al. (2022b), there is minimal positional and magnitude bias in the first epoch, where OB110462 and the neighbor are of roughly equal brightness. In the third epoch onwards, the bias becomes non-negligible when OB110462 is much fainter, and the bias is primarily in the radial direction in F814W, and more mixed between radial and azimuthal in F606W. We find that the magnitude bias to be also larger in `hst1pass` than in `ks2`. The average bias in non-magnified epochs is around 15 mmag in F814, and about 5 mmag in F606W when using `ks2`, as compared to around 50 mmag in F814W and 20 mmag in F606W when using `hst1pass`. This again suggests that PSF fitting in `ks2` is more precise than `hst1pass`.

The `hst1pass` positional bias, when averaged across the two filters, is comparable to the bias of 1.2 mas[1] found by Sahu, Anderson, Casertano, Bond, Udalski, et al. (2022). This is true, even though different sets of stars were used to compute the bias (18 vs. 4) as well as different methods (PSF subtraction vs. artificial star planting tests).

The results imply combining relative measurements across `ks2` and `hst1pass` is not valid. Although the majority of the underlying source extraction algorithms are identical, the particulars of PSF fitting are different enough to significantly alter the measured positions. The two software source extraction methods cannot be combined together in a self-consistent manner. Thus, the positional bias as calculated in Lam, Lu, Udalski, et al. (2022a,b) was too small, and resulted in an incorrect set of astrometric measurements.

In addition, §4.2.5 of Lam, Lu, Udalski, et al. (2022b) noted an "astrometric color offset" between the F814W and F606W positions of OB110462 and another microlensing event called OB110037. For OB110462, the astrometry across the F814W and F606W filters were offset from each other by about 0.5 mas. This color difference was tentatively attributed to binarity. For OB110462, this color difference can mainly be attributed to the bias correction (Figure 4.12). However, the color difference in OB110037 and other stars are still unexplained.

4.7 Discussion

4.7.1 OB110462 in the context of the Galactic BH population

Before 2019, all information about Galactic BHs came from X-ray binary systems, mainly low-mass X-ray binaries (LMXBs). The observed population of BHs in LMXBs have masses tightly centered around $\sim 8 M_\odot$ (Özel, Psaltis, et al. 2010).

---

[1] Sahu, Anderson, Casertano, Bond, Udalski, et al. (2022) does not specify the bias as a function of filter; we assume that their stated bias of 1.2 mas is the average of F606W and F814W.

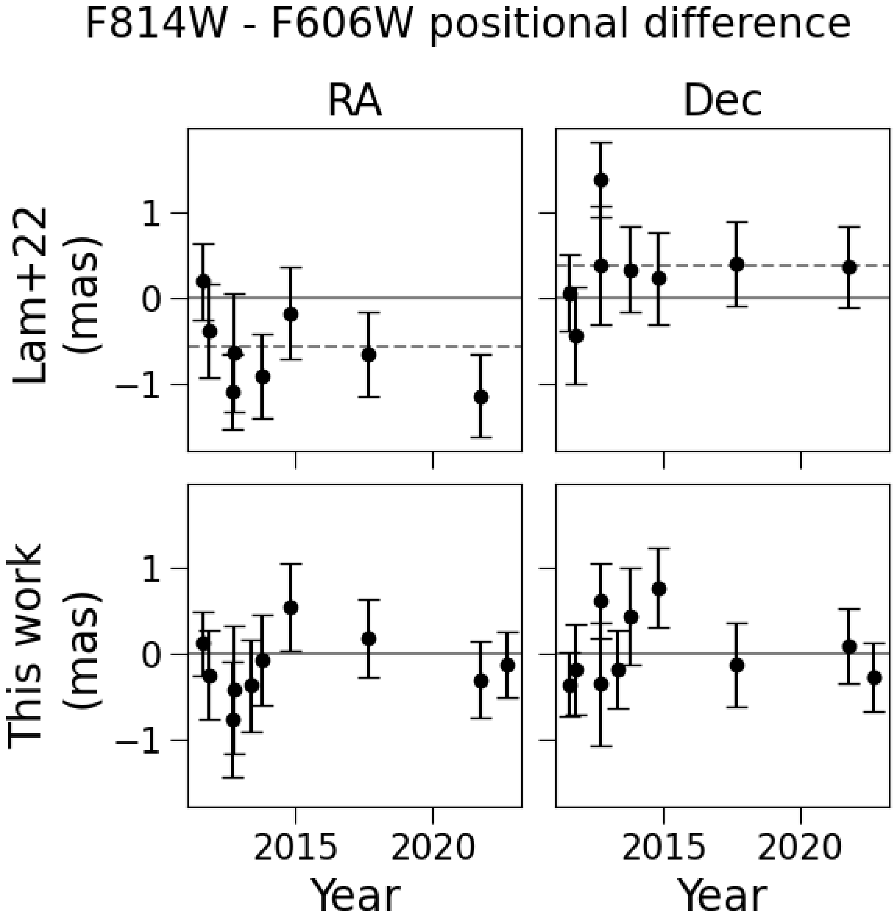

Figure 4.12: Comparison of color differences in OB110462 astrometry. The *top row* shows the difference in F606W and F814W position for OB110462 vs. time from Lam, Lu, Udalski, et al. (2022a,b). The bias correction calculated in Lam, Lu, Udalski, et al. (2022b) has been applied, but the constant positional offset between F814W and F606W is *not* included. The *dashed line* is the "empirical color offset" applied by Lam, Lu, Udalski, et al. (2022b) to get the data in the two filters to better agree with each other. There is a significant difference between the positions measured between the two filters, especially in RA. The *bottom row* shows the difference in F606W and F814W positions for OB110462 vs. time as derived in this work. The color difference has largely disappeared from the RA, and also slightly decreased in Dec.

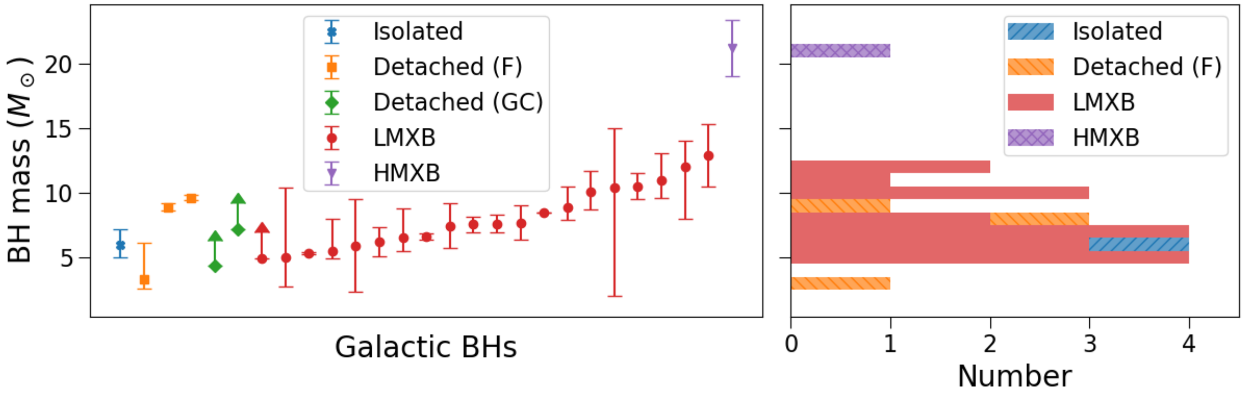

Figure 4.13: OB110462 in the context of the observed Galactic BH population. *Left:* Dynamically confirmed BHs, coded by their type (isolated, detached field binary, detached globular cluster binary, low-mass X-ray binary, high-mass X-ray binary). *Right:* Histogram of Galactic BH mass measurements, coded by type. Note that not all BHs in the left panel are included in the right panel, as some only have lower limits on the mass. Note the histogram does not account for uncertainties on measurements.

A portrait of the complete Galactic BH population is finally emerging (Figure 4.13; X-ray sources were compiled across catalogs from Aaron Geller (Northwestern)[2], Grzegorz Wiktorowicz and Chris Belcynski[3], and BlackCAT[4] (Corral-Santana et al. 2016)). Over the last 5 years, our knowledge of other types of Galactic BH systems has grown. The first BH in a non-interacting system was found to have a somewhat surprising low mass of $3M_\odot$, in the "lower mass gap" where neutron stars and BHs had not previously been observed electromagnetically (Thompson et al. 2019). Since then, two more BHs in non-interacting binary systems have been found, with masses of $9 - 10M_\odot$ (El-Badry, Rix, Cendes, et al. 2023; El-Badry, Rix, Quataert, et al. 2023; Chakrabarti et al. 2022). This is somewhat higher than the average observed BH mass in a LMXB, but falls within the typical mass range.

Now, OB110462 is the first isolated BH to have its mass measured. At $6M_\odot$, it is slightly lower than the average observed BH mass in an LMXB, although still falling within the typical mass range.

The selection effects that affect observations of BHs are important to consider if we are to understand the underlying population and BH mass function. For example, observational selection effects may cause more massive BHs in LMXBs to be undetected (Jonker et al. 2021). For BHs in detached binaries, the picture is more muddled: there is tentative evidence of a dearth of BHs below $8M_\odot$ (El-Badry, Rix, Cendes, et al. 2023) as detected from Gaia,

---

[2] `https://github.com/ageller/LIGO-Virgo-Mass-Plot_v2.0/blob/main/src/data/EMdata.json`

[3] `https://stellarcollapse.org/sites/default/files/table.pdf`

[4] `https://www.astro.puc.cl/BlackCAT/transients.php`

but ground-based RV surveys seem to not be finding these more massive BHs and have only found a single low-mass BH despite an observational bias toward higher masses (Thompson et al. 2019). For isolated BHs, there is also a selection bias towards more massive BHs as they have larger lensing cross sections; however, if there are many more low-mass BHs, those will dominate the observed sample. With one detection, no strong conclusions can be made, but there should be at least as many $6-8M_\odot$ BHs as $10M_\odot$ BHs in the Galactic BH population.

Now that detections of BHs in various types of systems have been made, understanding their selection effects are needed to quantify their population properties. This is the next research frontier that will enable us to understand the Galactic BH population as a whole.

4.7.2 Origin and formation scenarios for OB110462

With only a single isolated BH detection, tight constraints cannot be placed yet on their origins or specific formation scenarios. In addition, OB110462 does not have full 6-D kinematic information available, since microlensing does not measure the lens radial velocity. However, recent works examine possible situations that are consistent with observations of OB110462 and lay the groundwork for future studies.

Using statistical arguments and assuming OB110462 originated from a single star, Andrews et al. (2022) finds that OB110462 is kinematically consistent with the Galactic thick disk. Given the mass, distance, and transverse velocity found in this work, if OB110462 was born in the thick disk, natal kicks up to 100 km/s would be consistent with its current velocity. On the other hand, if OB110462 formed in the thin disk and received a kick to a thick disk-like orbit, the kick would have had to be around $50-100$ km/s.

Vigna-Gómez et al. (2023) study the origins of isolated BHs. They find that the majority of BHs with masses $< 10M_\odot$ originated from binary systems, while the majority of BHs with masses $> 10M_\odot$ originated as single stars. This would imply that although OB110462 is now an isolated BH, it likely originated in a stellar binary system.

With additional mass measurements of isolated BHs, these studies and their extensions will be able to place increasingly tight constraints on the formation channels and origins of isolated BHs. By performing targeted astrometric follow-up with existing facilities, it is possible to build the sample of isolated BHs to a few ($\lesssim 10$) over the next 5 to 10 years.

4.7.3 Towards a large sample of isolated BHs

Lam, Lu, Udalski, et al. (2022a,b) analyzed a sample of 5 archival BH microlensing candidates, which included OB110462. The other four candidates were not BHs. They found that after accounting for selection effects, this single BH detection was consistent with 2×10^8 isolated Galactic BHs. Although the results were consistent, they were not highly constraining due to the small sample size. The Nancy Grace Roman Space Telescope (*Roman*), NASA's next flagship mission, presents the opportunity to find and characterize hundreds of isolated

BHs with astrometric microlensing (Lam, Lu, Hosek, et al. 2020), which will expand the sample size and enable stringent constraints on the Galactic BH population.

Roman will conduct several wide-field infrared surveys to answer questions about dark energy and dark matter, and find exoplanets (Spergel et al. 2015). One of the surveys, the Galactic Bulge Time Domain Survey, nominally plans to observe $\sim 2\,\mathrm{deg}^2$ of the Galactic Bulge, finding several tens of thousands of microlensing events and a thousand exoplanets (Johnson et al. 2020; Penny, Gaudi, et al. 2019). This survey also provides an excellent opportunity to find isolated BHs with microlensing.

OB110462, in addition to being a proof-of-concept of the method, raises several technical issues that have not been previously considered, and should be examined in preparation for using microlensing to find BHs with *Roman*.

Roman's mirror is the same size as *HST* (a diameter of 2.4 m), but will be observing at longer wavelengths than the optical bands used for this and most other microlensing work. Thus the bias due to a nearby star in an event like OB110462 would be larger.

Roman will also be similarly or more undersampled than *HST*. Roman's pixel scale is 110 mas/pix; the main filter for the Galactic Bulge Time Domain Survey is nominally F146, a wide filter centered at 1.46 micron corresponding to an angular resolution of $\theta_{res} = 153\,\mathrm{mas}$ at the diffraction limit. For comparison, the *HST* WFC3-UVIS pixel scale is 40 mas/pix; the resolution at the effective wavelength of F814W = 814 nm (F606W = 606 nm) is 85 (64) mas. Thus, these PSF reconstruction and modeling methods currently required to achieve precise astrometry with *HST* will also be necessary for *Roman*.

In addition, the density of sources will be much higher in the infrared than in the (red) optical. *Roman* will observe hundreds of millions of stars down to 25th magnitude in F146, exacerbating this issue. In addition, if *Roman* chooses to observe fields closer to the Galactic plane towards $b = 0\,\mathrm{deg}$, the density of sources will also increase. Finally, Roman's field of view will be 200 times that of *HST*'s in the infrared. Events like OB110462, where a faint source of interest is near a bright one, will be common and not necessarily an ignorable edge case. A more automated or generalized way to correct the photometry and astrometry in this situation will be needed.

This also will have impact on the assumptions made in astrometry measurements. This work as well as previous studies (Lam, Lu, Udalski, et al. 2022a,b; Lu et al. 2016; Sahu, Anderson, Casertano, Bond, Udalski, et al. 2022) assume that the astrometric shift measured is completely unblended; i.e. the lens is dark, there are no unrelated neighboring stars, and the only light that makes it to the telescope aperture is from the images of the source. However, for all the reasons mentioned above, this assumption will not necessarily hold for *Roman*. Despite the resolution gain from going to space, there is expected to be a non-neglible fraction of blended microlensing events (Penny, Gaudi, et al. 2019). For dark lenses like BHs, the concern of blending would be from unrelated neighbor stars falling in Roman's aperture. This extra flux would dilute the astrometric signal. In addition, if the proper motion of the neighbor(s) was comparable to the lensing, it could affect not only the magnitude, but the shape of the astrometric shift.

Other considerations are how to best perform relative astrometry over such large fields of view. The details of detector-to-detector calibration issues will be important. Design tradeoffs in terms of observing strategy in order to attain sufficient astrometric precision should also be studied. All the statements made here are qualitative, but these issues deserves further quantitative study.

4.8 Conclusion

We reanalyze OB110462, a microlensing event due to a dark, compact-object lens. The astrometry we measure is significantly different from Lam, Lu, Udalski, et al. (2022a,b); the discrepancy is caused by a difference in the measured bias correction from a neighboring bright star. By performing both the astrometric source extraction and bias correction measurement with the new version of `hst1pass` in a self-consistent manner, we find our astrometry for OB110462 between 2011 and 2017 to be consistent with Sahu, Anderson, Casertano, Bond, Udalski, et al. (2022). Modeling the updated *HST* photometry and astrometry along with the re-reduced OGLE photometry, we find OB110462 to be a BH with a mass of $6.03^{+1.19}_{-1.04} M_{\odot}$, consistent with the measurement of Sahu, Anderson, Casertano, Bond, Udalski, et al. (2022). Thus, it appears so far that the masses of isolated Galactic BHs are similar to those in binary systems. With *Roman*, many more isolated BH systems can be characterized, and ultimately enable the measurement of the Galactic BH mass function.

4.9 Appendix: Comparison of pixel-based vs. tabular CTE correction

Here we compare the differences between the tabular and pixel-based CTE correction. The differences alone do not indicate which type of correction is better or worse, but allows us to quantify the differences in the resultant astrometry.

Specifically, the comparison is made between the starlists in Lam, Lu, Udalski, et al. (2022a,b) created using the pixel-based CTE correction (i.e. the old version of `hst1pass` run on the `flc` files) as compared to the starlists in this work created using the tabular CTE correction (i.e. the new version of `hst1pass`, run on the `flt` files). Several frames spanning 10 years of the OB110462 dataset are shown in Figure 4.14.

As a function of y detector position, there are only differences between the y position and instrumental magnitude; the differences are symmetric in x detector position. This is expected, since CTE corrections only change the y detector position and magnitude of the sources. The scatter in x-position is likely due to minor differences between the versions of `hst1pass` and differences in the choices of certain runtime parameters between the old and new reductions. The scatter in x position also allows us to see how much of the trend in y position is due to scatter, vs. the CTE correction methods themselves. As time goes on, the scatter increases greatly in the x and y position differences. The scatter also seems to increase with time for magnitude difference, although it is mostly constant after 2013 or so.

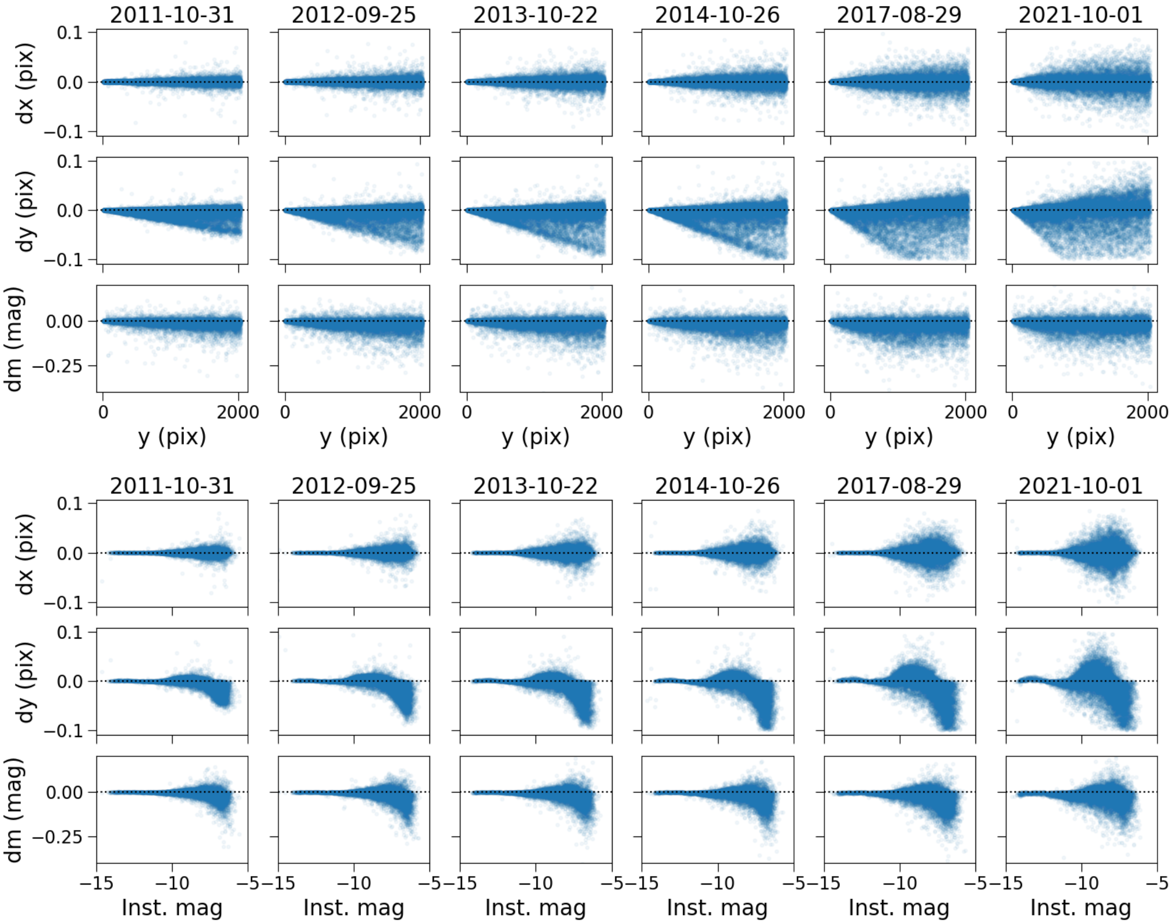

Figure 4.14: Comparison of measured positions and magnitudes using new `hst1pass` and tabular CTE correction vs. old `hst1pass` and pixel-based CTE correction. These comparisons are performed on an single exposure, i.e. on the individual `flc.xym` or `flt.XYM` files. The y-axis is the difference between the new tabular − old pixel based correction for x detector position, y detector position, and instrumental magnitude. The top (bottom) plot shows the differences as a function of y detector position (instrumental magnitude).

As a function of magnitude, the differences are again symmetric about x position, but not for y position and magnitude. In particular, for the differences in y position before 2013, the bright stars with $m < -10$ are not affected, but after 2013 there is magnitude-dependent structure.

4.10 Appendix: Priors

The priors for the fits are summarized in Table 4.8. $\mathcal{N}(\mu, \sigma)$ denotes a normal distribution with mean μ and standard deviation σ. $\mathcal{N}_T(\mu, \sigma, l_\sigma, u_\sigma)$ denotes a normal distribution with a low end truncation at $\mu + \sigma l_\sigma$ and a high end truncation at $\mu + \sigma u_\sigma$. $\mathcal{U}(a, b)$ denotes a uniform distribution from a to b. $\Gamma^{-1}(\alpha, \beta)$ is the inverse gamma distribution (Equation G1 in Lam, Lu, Udalski, et al. (2022b)).

The choice of priors is nearly identical to those in Lam, Lu, Udalski, et al. (2022a,b); see Appendix G of Lam, Lu, Udalski, et al. (2022b) for details. The only difference is for the photometric priors b_{SFF} and m_{base}. We changed the priors on m_{base} as some of the photometry was recalibrated and the baseline magnitudes were now different. We also made the priors on b_{SFF} tighter; the blending is well constrained from previous work (Lam, Lu, Udalski, et al. 2022a; Mróz, Udalski, and Gould 2022; Sahu, Anderson, Casertano, Bond, Udalski, et al. 2022). We did allow for some spread, but consider it well established that the OGLE light curve is highly blended (b_{SFF} close to 0) and the *HST* light curves are less or unaffected by blending (b_{SFF} close to 1).

Parameter	Prior
t_0 (MJD)	$\mathcal{N}(55770, 75)$
u_0	$\mathcal{N}(0, 0.5)$
t_E (days)	$\mathcal{N}_T(200, 100, -1.8, 3)$
$\pi_{E,E}$	$\mathcal{N}(-0.02, 0.12)$
$\pi_{E,N}$	$\mathcal{N}(-0.03, 0.13)$
$m_{base,O}$ (mag)	$\mathcal{N}(16.5, 0.1)$
$b_{SFF,O}$	$\mathcal{U}(0, 0.2)$
$m_{base,H8}$ (mag)	$\mathcal{N}(19.9, 0.1)$
$b_{SFF,H8}$	$\mathcal{U}(0.8, 1.1)$
$m_{base,H6}$ (mag)	$\mathcal{N}(22.0, 0.1)$
$b_{SFF,H6}$	$\mathcal{U}(0.8, 1.05)$
$\log \sigma_O$ (mag)	$\mathcal{N}(0, 5)$
ρ_O (days)	$\Gamma^{-1}(0.53, 0.31))$
$\log \omega_{0,O}^4 S_{0,O}$ (mag^2 days^{-3})	$\mathcal{N}(0.0001, 5)$
$\log \omega_{0,O}$ (days^{-1})	$\mathcal{N}(0, 5)$
θ_E (mas)	$\mathcal{N}_T(-0.2, 0.3, -4, 4)$
π_S (mas)	$\mathcal{N}_T(0.1126, 0.0213, -2.94, 90)$
$x_{S0,E}$ (arcsec)	$\mathcal{U}(0.229, 0.233)$
$x_{S0,N}$ (arcsec	$\mathcal{U}(-0.240, -0.178)$
$\mu_{S,E}$ (mas/yr)	$\mathcal{U}(-2.472, 2.515)$
$\mu_{S,N}$ (mas/yr)	$\mathcal{U}(-2.354, 4.734)$

Table 4.8: *Priors.*

4.11 Appendix: Detailed comparison to previous work

4.11.1 CTE correction method

First, we compare the pre-bias corrected astrometry presented in this work to that of Lam, Lu, Udalski, et al. (2022a,b). The differences are the number of epochs of data used, the version of the `hst1pass` software, the values of the additive error, and the method of CTE correction. Of these differences, the method of CTE correction has the largest impact on the resultant astrometry.

We find no significant difference between the two astrometric time series after cross-epoch alignment and before implementing the bias correction. While the different CTE corrections can change the measured positions of stars by several mas within a single epoch (Figure 4.14), these differences are effectively removed by the cross-epoch alignment when the starlists are transformed into a common reference frame using first and second-order polynomials.

Thus, the specific choice of CTE correction method, tabular or pixel-based, does not produce any significant change in the astrometric time series derived. It is only important that CTE be corrected in some manner; in previous work we find that if no CTE correction of any kind is applied, there are systematics in the astrometry that cannot be removed by the first or second order polynomial transformations.

4.11.2 Bias-corrected astrometric time series

Figure 4.15 directly compares the astrometry of OB110462 in Sahu, Anderson, Casertano, Bond, Udalski, et al. (2022) (their Figures 16 and 18), Lam, Lu, Udalski, et al. (2022a) (their Figure 2), and this work. We emphasize that no microlensing model is being fit in Figure 4.15. Only a constant proper motion of (RA, Dec) = (-2.263, -3.597) mas/yr has been subtracted from the positions for easier visualization. The subtracted proper motion was chosen to match the source proper motion inferred in Sahu, Anderson, Casertano, Bond, Udalski, et al. (2022) for an "apples-to-apples" comparison of the astrometry.

There is a clear discrepancy in the deflection in RA between the astrometry of Sahu, Anderson, Casertano, Bond, Udalski, et al. (2022) and Lam, Lu, Udalski, et al. (2022a,b) (*top left panel*) across the magnified epochs (2011) vs. the non-magnified epochs (after 2011). There is some minor discrepancy in Dec (*top right panel*), but the measurements are generally within $1 - 2\sigma$ of each other. The new astrometry, including the updated bias correction, presented in this work is now consistent with the measurements of Sahu, Anderson, Casertano, Bond, Udalski, et al. (2022) between 2011 and 2017. In both RA (*bottom left panel*) and Dec (*bottom right panel*, the magnified and non-magnified astrometry are now all within 1σ of each other.

The new $2021-2022$ measurements provide a more accurate source proper motion in baseline than in previous work. From Figure 4.15, the source proper motion from our updated astrometric reductions appears to be different from that of Sahu, Anderson, Casertano, Bond, Udalski, et al. (2022). For $t \gg t_0$, the slope of the proper motion-removed measurements should asymptotically approach 0. This is not the trend seen in the new 2021-2022 epochs, implying the source proper motion is different from the value inferred by Sahu, Anderson, Casertano, Bond, Udalski, et al. (2022). Although the source proper motion is not particularly interesting in and of itself, its inferred value affects the measured astrometric shift, which in turn affects the measured lens mass.

We consider whether this different proper motion could be the result of systematics in the analysis of later epochs. No systematic errors of $1-2$ mas in the $2021-2022$ astrometry were detected in the reference stars (Figures 4.5 and 4.6).

The source proper motion inferred from the fit are presented in Table 4.4. The uncertainties in the transformation from a relative astrometric reference frame to the absolute *Gaia* reference frame in which the proper motions are reported are 0.13 mas/yr and 0.11 mas/yr in RA and Dec, respectively. Sahu, Anderson, Casertano, Bond, Udalski, et al. (2022) do not state their uncertainties moving from their relative to absolute *Gaia* astrometric frame, but assuming their systematic uncertainties are comparable to ours, the source proper motion inferred in this work of $(-2.02, -3.45)$ mas/yr and Sahu, Anderson, Casertano, Bond, Udalski, et al. (2022) of $(-2.263, -3.597)$ mas/yr are consistent within $1-2\sigma$. Thus, the source proper motions across the model fits are consistent with each other. However, there appears to be a hint of correlated residuals in the later epochs from $2014-2022$ in RA (Figure 4.8).

Additional observations in the future can establish the unlensed source proper motion and confirm or reject any potential discrepancy.

4.11.3 Bias-corrected photometric time series

Figure 4.16 compares the *HST* photometry of OB110462 derived by Sahu, Anderson, Casertano, Bond, Udalski, et al. (2022) (their Figure 13), Lam, Lu, Udalski, et al. (2022b) (their Figures 7 and 8), and this work. The calibration of the photometry across the three datasets slightly differs. To calculate the difference between the zeropoint in the photometry of Lam, Lu, Udalski, et al. (2022a) and this work as compared to Sahu, Anderson, Casertano, Bond, Udalski, et al. (2022), we calculate the average magnitude difference between those datasets and the Sahu, Anderson, Casertano, Bond, Udalski, et al. (2022) photometry for the 7 common epochs between 2011 to 2017. Then to put the photometry all onto comparable footing, this constant zeropoint difference is subtracted from the photometry in Lam, Lu, Udalski, et al. (2022a) and this work.

There are minor differences between the photometry in Lam, Lu, Udalski, et al. (2022a,b) and Sahu, Anderson, Casertano, Bond, Udalski, et al. (2022) in the early $(2011-2012)$ epochs. With the updated bias correction in the photometry we derive in this work, we find the same photometry as measured by Sahu, Anderson, Casertano, Bond, Udalski, et al. (2022) within the uncertainties.

Although the astrometric bias is the main reason for the updated mass result, Figure 4.16 illustrates the photometric bias should also not be neglected. In particular, for *Roman*, with its extremely precise photometry, accounting for such systematics will be important.

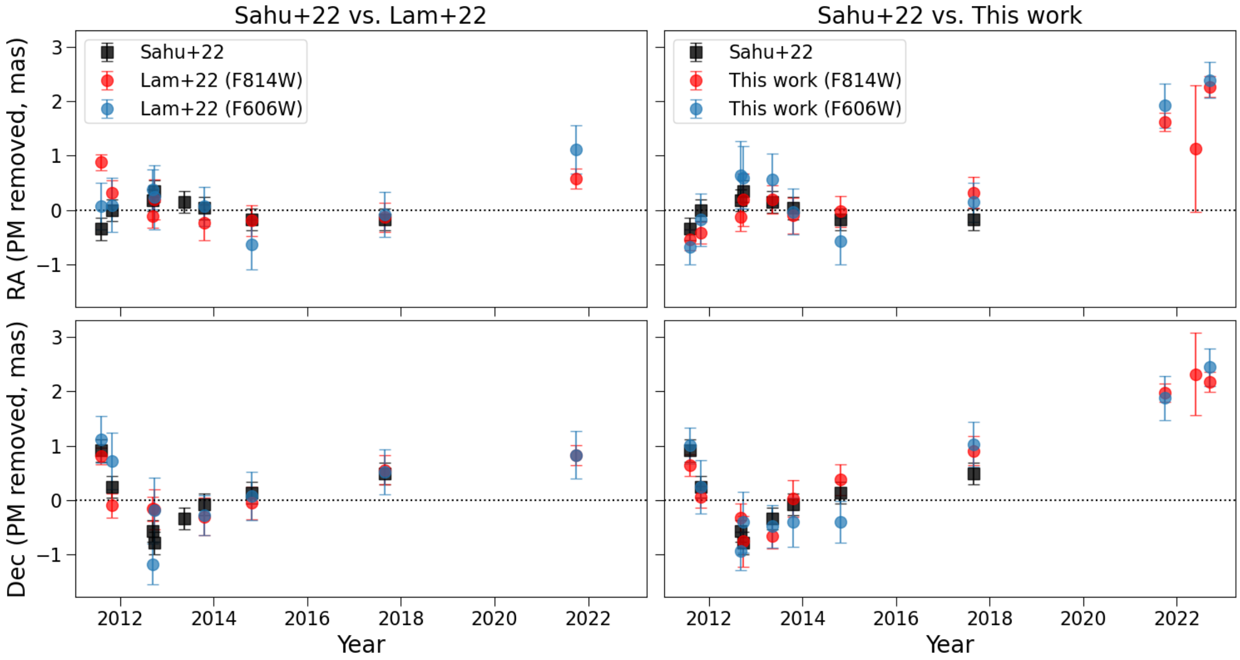

Figure 4.15: Comparison of *HST* astrometry derived by Sahu, Anderson, Casertano, Bond, Udalski, et al. (2022), Lam, Lu, Udalski, et al. (2022a,b), and this work. The *top (bottom) row* shows the astrometry in RA (Dec) vs. time, with the source proper motion reported in Sahu, Anderson, Casertano, Bond, Udalski, et al. (2022) (RA, Dec) = (−2.263, −3.597) mas/yr subtracted in order to more easily compare the astrometric deflections. The *left (right) column* compares the astrometry in Sahu, Anderson, Casertano, Bond, Udalski, et al. (2022) to Lam, Lu, Udalski, et al. (2022a,b) (this work). The positions of Sahu, Anderson, Casertano, Bond, Udalski, et al. (2022) *(black squares)* average all F814W and F606W measurements. Lam, Lu, Udalski, et al. (2022a,b) and this work keep the F814W and F606W sets separate; F814W (F606W) positions are shown in red (blue) circles.

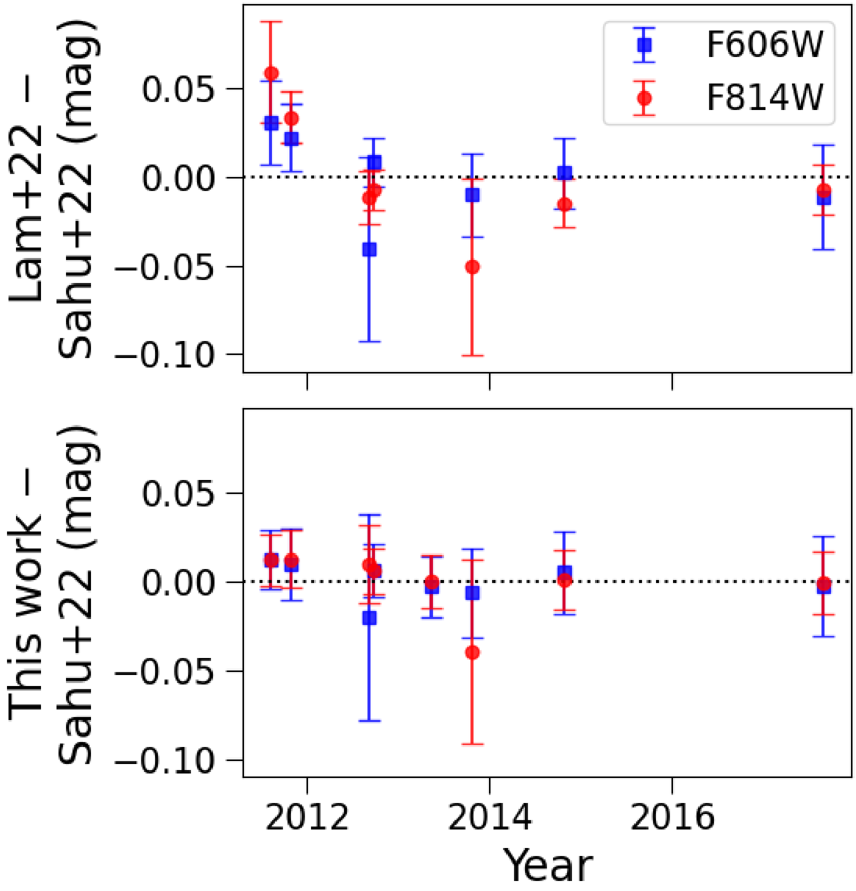

Figure 4.16: Comparison of *HST* photometry derived by Sahu, Anderson, Casertano, Bond, Udalski, et al. (2022), Lam, Lu, Udalski, et al. (2022a,b), and this work. The *top (bottom) row* compares the differences in the photometry in Sahu, Anderson, Casertano, Bond, Udalski, et al. (2022) to Lam, Lu, Udalski, et al. (2022a,b) (this work); red (blue) points denote data in the F814W (F606W) filter.

Chapter 5

Modeling microlensing light curves

5.1 Introduction

Current and upcoming time-domain surveys have the ability to find ones to thousands of microlensing events each year. The actual number of events depends on the design of the survey, which include parameters such as the observing cadence and the number and duration of observational gaps. The choices of these survey parameters also affect how precisely and accurately astrophysical parameters can be extracted from the observed microlensing events. Making accurate predictions for how well astrophysical parameters can be measured as a function of different survey designs are important for evaluating the merits and determining the final form of upcoming surveys.

In this chapter, we present a series of vignettes to explore and understand the modeling of microlensing light curves. These are not thorough investigations, but rather simple case studies that can and should be further extended in future work.

In Chapter 5.2, we study the impact of observational cadence and gaps on the inferred microlensing parameters. In Chapter 5.3 we explore the efficacy of fast Fisher matrix methods to estimate parameter uncertainties. In Chapter 5.4, we study the impact of correlated noise in microlensing light curves, and the impact of neglecting this. In Chapter 5.5 we present some applications and ways to extend this work, and conclude in Chapter 5.6.

5.2 Inferring model parameters from light curves

In this section, we consider how different sampling cadences and observational gaps in observed light curves impact the ability to infer microlensing parameters of interest.

5.2.1 Sampling cadence

First, we present a very simple and idealized example as the "best-case scenario". That is, the data are noiseless, the sampling is continuous even when the Galactic Bulge would not

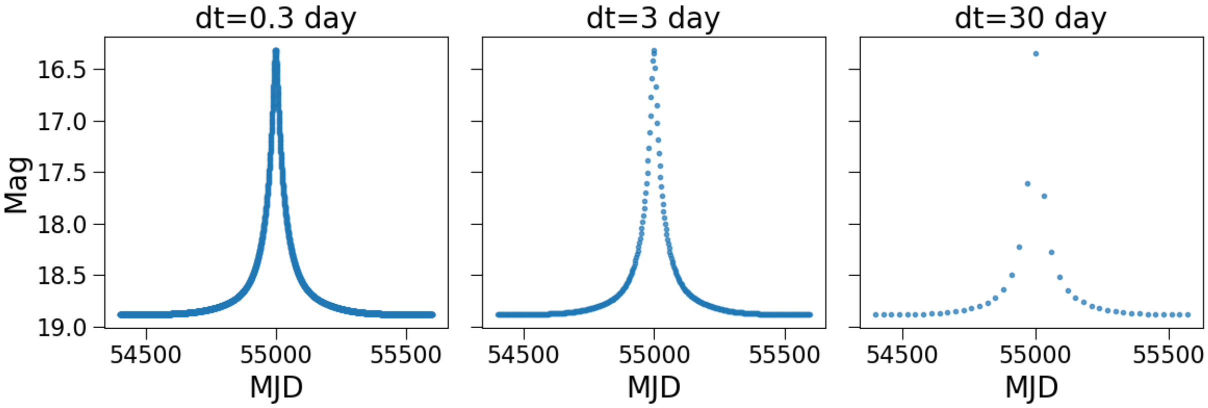

Figure 5.1: Examples of different sampling cadences.

be visible from Earth or space, and the uncertainties are very small. Several light curves sampled at different cadences are shown in Figure 5.1.

We generate light curves with black hole-like microlensing parameters listed in Table 5.1 at six different temporal samplings of $dt = 0.1$, 0.3, 1, 3, 10 and 30 days. The light curves span from 54400 to 55600 MJD (which is $t_0 \pm 5t_E$ for this event). The photometric uncertainties are 0.016 mag at baseline magnitude 19 (corresponding to an SNR=$\sqrt{4000}$). No intrinsic noise is added to these simulated light curves—the data are purely the microlensing signal, but that photometric error bars are included in the mock parameter inference via the likelihood function. We then fit these light curves using a nested sampling algorithm. The priors for the fit are also listed in Table 5.1. The fit posteriors are shown in Figure 5.2.

As expected, decreasing the sampling cadence (larger dt) means the light curve is more poorly constrained and the posteriors are wider, i.e. there is more uncertainty on the parameters. We emphasize that to constrain the properties of a light curve, it must be sampled at a cadence $dt \ll t_E$. Although t_E is the characteristic timescale of lensing, it does not correspond to the cadence at which the light curve can be sampled to infer parameters. Despite this being a long-duration event ($t_E = 120$ days) with small photometric uncertainties and no intrinsic noise, even a sampling cadence of $dt = 10$ days fails to break degeneracies in parameters like t_0 or u_0 or well-constrain physically important parameters such as the components of the microlensing parallax vector $\pi_{E,E}$ and $\pi_{E,N}$.

5.2.2 Observational gaps

Next, we consider the effect of observational gaps. For observatories on Earth, the Galactic Bulge is only observable for $9-10$ months out of the year. Thus long-duration events will generally not have their light curves fully sampled.

For the upcoming Roman Space Telescope, there will be even larger gaps. *Roman* is NASA's next flagship mission, and will conduct several wide-field infrared surveys over a

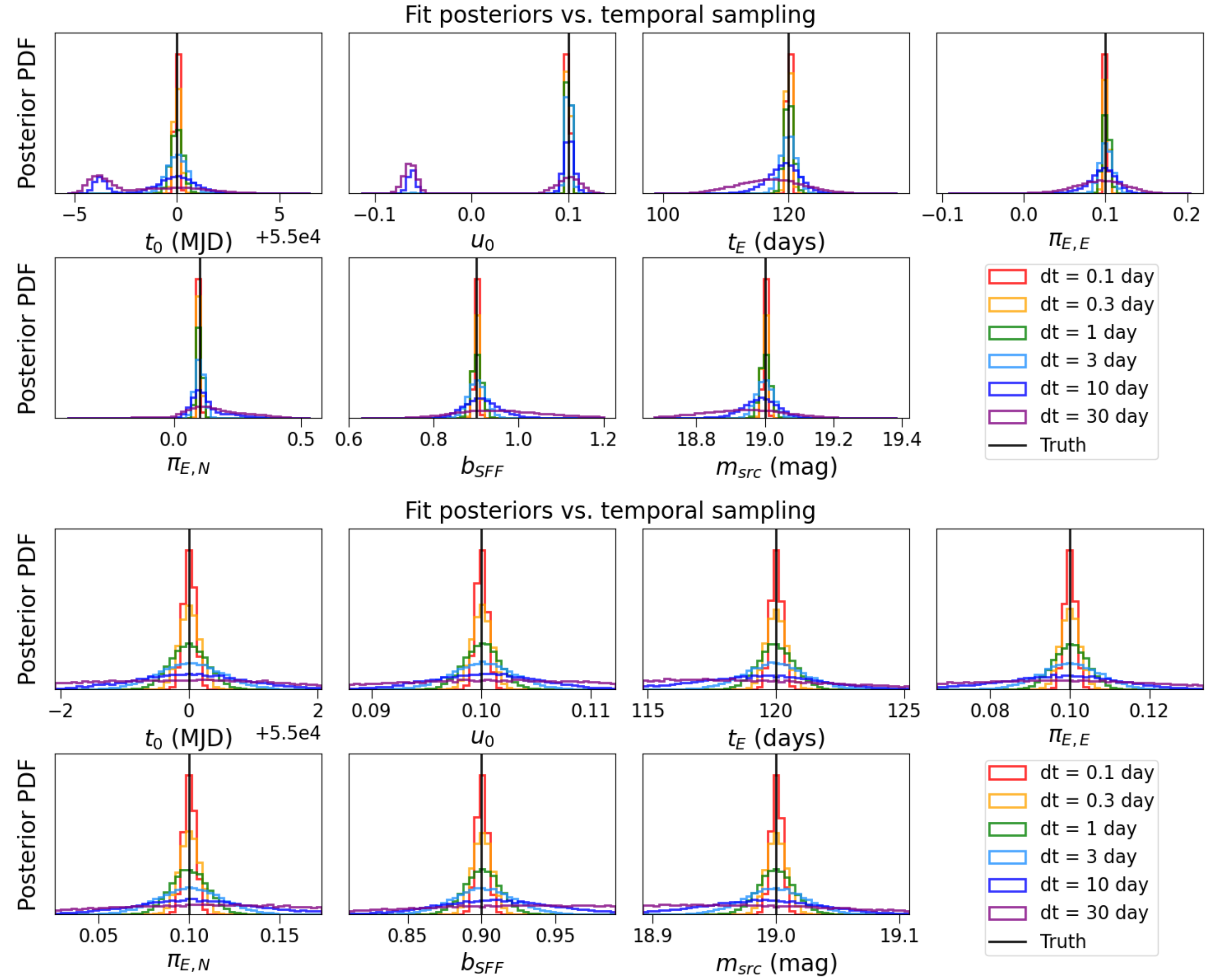

Figure 5.2: Posteriors of microlensing fits to the light curves described in Chapter 5.2.1. The posteriors are shown as a function of the light curves' sampling cadence; the black vertical line shows the true value. The bottom set of panels are zoomed-in versions of the top set of panels, to show more detail.

Parameter	Truth	Prior
t_0 (MJD)	55000	$\mathcal{U}(54975, 55025)$
u_0	0.1	$\mathcal{U}(-1, 1)$
t_E (days)	120	$\mathcal{U}(20, 500)$
$\pi_{E,E}$	0.1	$\mathcal{U}(-0.6, 0.6)$
$\pi_{E,N}$	0.1	$\mathcal{U}(-0.6, 0.6)$
b_{SFF}	0.9	$\mathcal{U}(0, 1.2)$
m_{src} (mag)	19	$\mathcal{U}(18, 23)$

Table 5.1: *Sampling cadence example.* This event is located at RA, Dec = (268, −29) deg. $\mathcal{U}(A, B)$ denotes a uniform distribution over the interval A to B.

period of 5 years (Spergel et al. 2015); one of these surveys is the Galactic Bulge Time Domain Survey (GBTDS). The GBTDS will have very large observing gaps because the Galactic Bulge is only observable in 72-day windows twice a year due to the observatory design. In addition, in the notional design of the GBTDS, only six of the 10 available Bulge seasons will be part of the GBTDS (Penny, Gaudi, et al. 2019); there is a gap of over 2 years in between the first three and last three Bulge seasons that comprise the survey.

We investigate the effect these gaps will have on characterizing long-duration events such as black holes by considering three versions of light curve coverage possible by *Roman.* V1 is the notional GBTDS design described in Penny, Gaudi, et al. (2019), with three Bulge seasons at the start and end of the 5 year survey, with observations taken every 15 minutes during those seasons. The notional GBTDS design is set by the requirement to find thousands of cold exoplanets via microlensing. Because planetary microlensing signals are very short duration, observations must be taken at a very high cadence ($\lesssim$ 15 mins). V2 is the notional GBTDS design, but during the four Bulge seasons in the middle of the *Roman* mission, sparse observations are taken. This consists of 10 short observing blocks spread evenly over each seasons 72-day Bulge window, with each observing block consisting of 10 observations at the 15 minute cadence; this corresponds to 100 observations (i.e. a full day) of observations spread over the Bulge window. V3 is the notional GBTDS design, but including all 10 Bulge seasons sampled at the 15-minute cadence continuously instead of only 6. Figure 5.3 shows what light curves look like sampled at these three cadences.

We generate light curves with the parameters listed in Table 5.2; we consider two different values of t_0 (t_0^a and t_0^b) in order to simulate microlensing events that both have and do not have observations of the peak of the microlensing light curve. The parameters were chosen from the `PopSyCLE` simulation to be representative of BH events in *Roman.* For each set of parameters, we sample them at the three cadences above; this means we have six light curves total. Following Penny, Gaudi, et al. (2019) we assume 0.01 mag precision at F146[1] = 21.15. We apply white (Gaussian) uncorrelated noise to the simulated light curves. We

---

[1] This was W149 in Penny, Gaudi, et al. (2019).

then fit these light curves using a nested sampling algorithm. The priors for the fit are also listed in Table 5.2. The fit posteriors are shown in Figure 5.4.

As the light curve coverage is improved, the posterior distributions narrow. For the event where the peak is covered in the dense sampling by the notional design (V1), additional sparse observations (V2) during the fall do not help improve the precision of the measurements. Only additional dense coverage helps (V3). However, for the event where the peak is not covered by dense sampling by the notional design (V1), having sparse observations (V2) on the fall do significantly help constrain the microlensing parameters. By having complete dense coverage (V3), there is further improvement. This also serves to illustrate that *Roman*'s dense sampling and photometric precision enable decent characterization of light curves that are not completely covered.

Finally, we note that some of the posteriors in Figure 5.4 (most notably the baseline magnitude m_{base}) are biased to the true values, even for the highly sampled V3 light curves. We discuss why this is not unexpected in Chapter 5.4.4. In short, when there is Gaussian noise present in the data, any single realization of the data is not necessarily unbiased; it is the *ensemble* of all realizations of the data that are unbiased.

Parameter	Truth	Prior
t_0^a (MJD)	61899	$\mathcal{U}(61874, 62924)$
t_0^b (MJD)	61934	$\mathcal{U}(61909, 61959)$
u_0	0.3	$\mathcal{U}(-1, 1)$
t_E (days)	130	$\mathcal{U}(20, 500)$
$\pi_{E,E}$	-0.009	$\mathcal{U}(-0.6, 0.6)$
$\pi_{E,N}$	-0.024	$\mathcal{U}(-0.6, 0.6)$
b_{SFF}	0.9	$\mathcal{U}(0, 1.2)$
m_{base} (mag)	21.89	$\mathcal{U}(18, 23)$

Table 5.2: *Observational gaps example.* Microlensing parameters for the observational gaps example. We consider two different values of t_0, which we label as t_0^a and t_0^b. For t_0^a, the peak of the light curve is sampled by the survey, while for t_0^b, the peak of the light curve is not sampled by the survey. $\mathcal{U}(A, B)$ denotes a uniform distribution over the interval A to B.

5.3 Fisher matrix comparison

Fitting microlensing models to light curves can quickly become very computationally expensive when the number of light curves becomes large. This is the case when attempting to explore a wide swath of parameter space by modeling synthetic light curves with the goal of forecasting and experimental design.

Modeling a single light curve observed in n filters with a point-source point-lens with parallax model requires $5 + 2n$ parameters. More complicated models, such as binary lenses

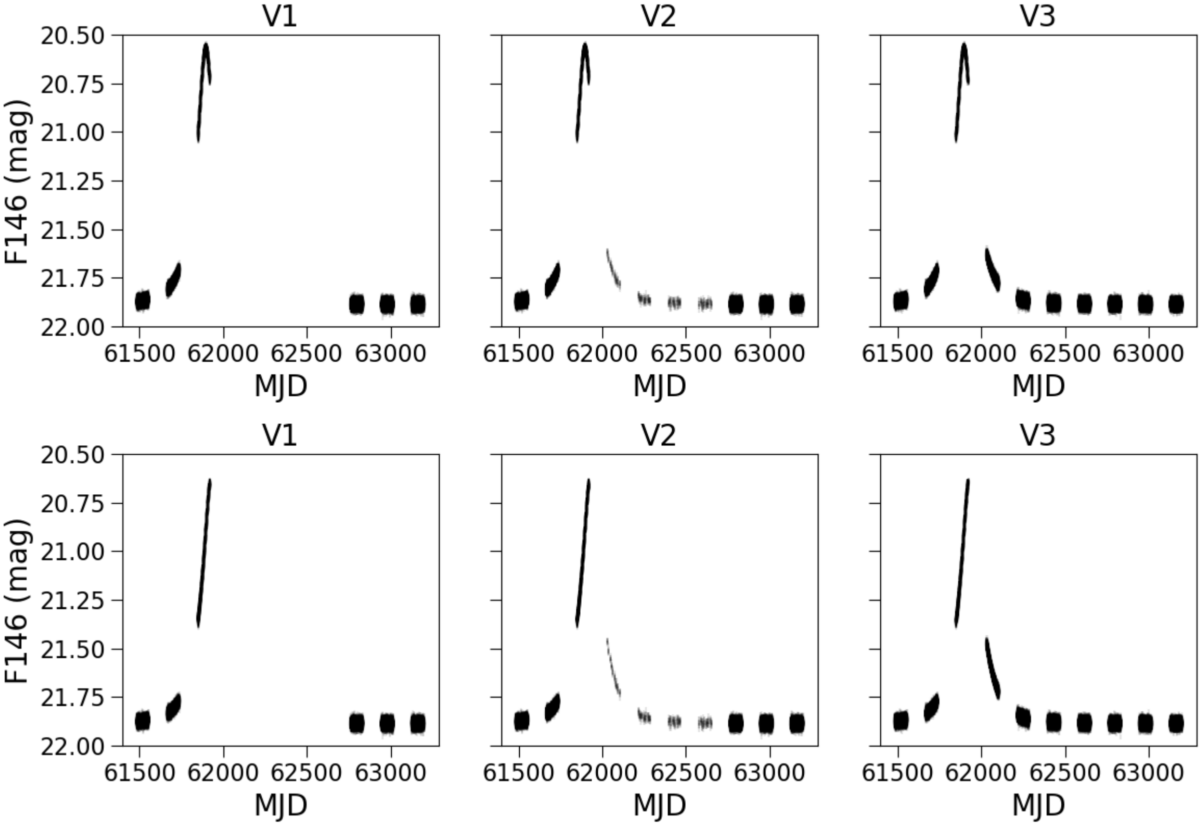

Figure 5.3: Simulated light curves with sampling at a variety of cadences. V1 is the notional GBTDS. V2 is the notional GBTDS, with additional sparse coverage in the middle 4 Bulge seasons. V3 is the notional GBTDS, expanded to contain all 10 available Bulge seasons.

with orbital motion, have even more complex parameter spaces riddled with degeneracies that make modeling even more difficult. At present, such light curves are analyzed and published one at a time, and it is intractable to do large "batch" analyses. Machine learning methods are one way around this (Zhang et al. 2021), but they still require a significant upfront cost to train the machine learning model.

The Fisher information matrix provides a way to quickly forecast the expected uncertainties on the model parameters. In astronomy, this is commonly done in cosmology (Tegmark et al. 1997). Here, we extend the method to microlensing light curves, by using Fisher matrices to forecast the uncertainties on the parameters, then comparing the results to those of Bayesian parameter inference, in order to check the validity of the estimates. We note that Karolinski et al. (2020) have used Fisher matrices in microlensing work, although their work considered the detectability of a signal using $\Delta\chi^2$ method, rather than the uncertainty in parameter estimation. We also note that Sajadian et al. (2023) has done a study making forecasts for *Roman* using Fisher matrix methods; however, they do not validate their Fisher

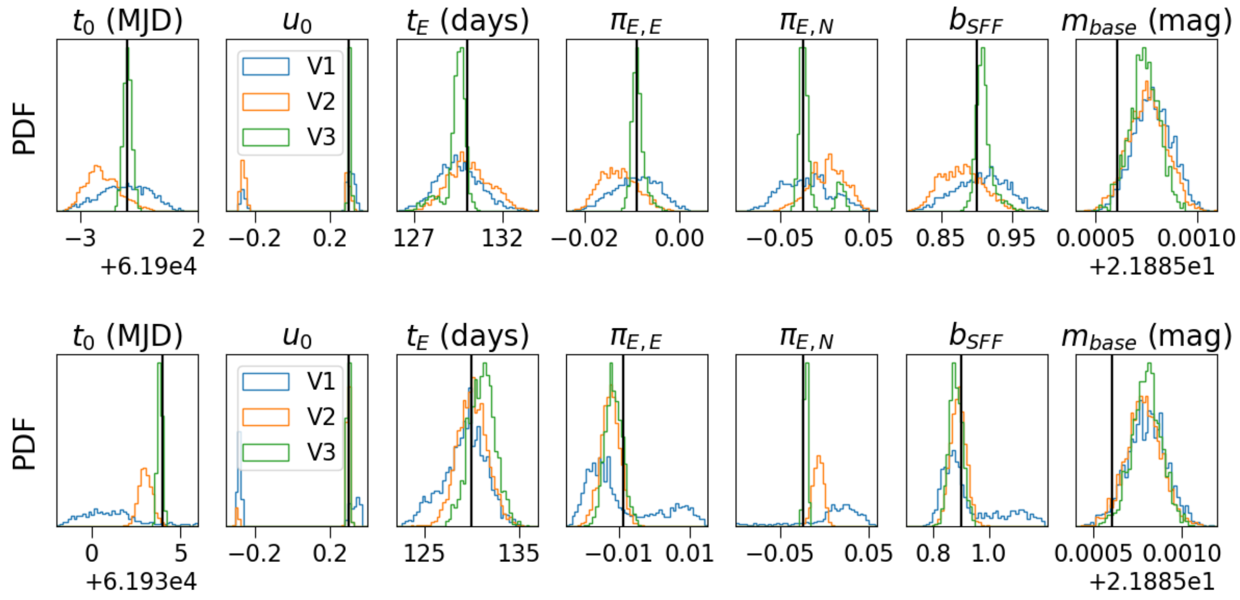

Figure 5.4: Posteriors of microlensing fits to the light curves in Figure 5.3. The top panel corresponds to the set of *Roman* light curves that cover the peak (top panel of Figure 5.3); the bottom panel corresponds to the set of *Roman* light curves without coverage of the peak (bottom panel of Figure 5.3).

matrix calculations against actual model fits.

5.3.1 Fisher matrix definition and background

The Fisher matrix $\mathcal{F}$ is an $N \times N$ matrix, where N is the number of model parameters θ that describe some function m. Suppose you have k observations at times t_k of m evaluated for some set of parameters θ_0, i.e. $m(t_k, \theta_0)$, with uncertainties $\sigma_m(t_k, \theta_0)$. Then the entries of the Fisher matrix are given by

$$\mathcal{F}_{ij} = \sum_k \frac{1}{\sigma_m^2(t_k, \theta_0)} \frac{\partial m(t_k, \theta_0)}{\partial \theta_i} \frac{\partial m(t_k, \theta_0)}{\partial \theta_j}. \tag{5.1}$$

The inverse of the Fisher matrix is the covariance matrix $\mathcal{C} = \mathcal{F}^{-1}$. The diagonal entries of $\mathcal{C}$ provide the marginalized uncertainties, where the uncertainty on the i-th parameter is $\sigma_i = \sqrt{\mathcal{C}_{ii}}$.

In words, the Fisher matrix captures the sensitivity of some function m to some model parameters θ, about the function evaluated at a specific set of model parameters $m(\theta_0)$. It provides an upper bound on how well you can estimate the parameter values of your function, as the Fisher matrix encodes the information density in a maximum-likelihood estimate. This statement is known as the Cramér-Rao bound; more formally, it states that the inverse of the Fisher information is a lower bound on the variance of an unbiased estimator, although it can be extended to biased estimators.

To calculate a Fisher matrix only requires knowing your model and your expected measurement uncertainties, which is why it is such an attractive method for forecasting. However, it operates on several assumptions. One is that the estimate are only valid if you are near the fiducial parameter set θ_0; here, we do not explicitly define "near", but statisticians labor over how to properly calculate and define such things. Another requirement is that the posterior can be approximated as a multivariate Gaussian, which means that the uncertainties are also Gaussian and that model can be linearized around the maximum likelihood solution (Hees et al. 2019).

5.3.2 Methodology

In our case, the function m in the Fisher matrix $\mathcal{F}$ is the microlensing light curve's magnitude (where m was named to suggest "magnitude"). The light curve is parameterized by 7 parameters $\theta = [t_0, u_0, t_E, \pi_{E,E}, \pi_{E,N}, b_{SFF}, m_{src}]$. To estimate the partial derivatives, we calculate the symmetric difference quotient of the light curve, where the step size of the parameter is 0.01 in its respective units.

We then compare the Fisher matrix uncertainties $\sigma_{Fisher} = \sqrt{\mathcal{F}_{ii}^{-1}}$ to the uncertainties from actually modeling the light curve σ_{fit}. We calculate σ_{fit} from the posterior distribution via $\sigma_{fit} = 0.5 \times (q_{84} - q_{16})$, where q_{84} and q_{16} are the 84th and 16th quantiles of the posterior distribution.

5.3.3 Comparison of Fisher matrix to fit uncertainties

Figure 5.5 compares the uncertainties of the Fisher matrix and the actual nested sampling fit for the light curves described in Chapter 5.2.1 (single set of microlensing parameters, change sampling cadence, small photometric uncertainties, no intrinsic noise in observations). As expected for both the Fisher matrix and nested sampling results, the sparser the sampling, the larger the uncertainty on the value of the parameter. In most cases (t_E, π_E, b_{SFF}, m_{src}), the Fisher estimate and the fit agree. For u_0, in the well-sampled regime ($\lesssim$ 10 days) the Fisher estimate and fit agree, but in the sparsely sampled regime ($\gtrsim$ 10 days) the fit uncertainty is an order of magnitude worse than Fisher. For $\pi_{E,N}$ the fit always is much worse than Fisher by an order of magnitude. Most curious is t_0, where in nearly all cases, the fit uncertainty is a factor of 2 or 3 *better* than the Fisher estimate. On the surface, this seems to violate the fact that "Fisher is the best you can do". We discuss this more in the penultimate paragraph of this section.

Figure 5.6 compares the uncertainties of the Fisher matrix and the actual nested sampling fit for the light curves described in Chapter 5.2.2 (two sets of microlensing parameters and three different amounts of light curve coverage for a total of six light curves, with small photometric uncertainties and Gaussian noise). As expected for both the Fisher matrix and nested sampling results, as the amount of light curve observational coverage increases, the smaller the uncertainty in the values of the parameters. Here, there is not good consistency between the actual fit and Fisher matrix estimates. t_0, t_E, $\pi_{E,E}$, b_{SFF} are generally within a factor of a few, and u_0 and $\pi_{E,N}$ to an order of magnitude. In several cases, the "Fisher is the best you can do" principle again seems to be violated. Most striking is how the reported uncertainties for fitting the light curve is orders of magnitude better than the Fisher prediction.

How is it that the fit can outperform the Fisher matrix estimates? We note that not all the assumptions and requirements asserted for this statement to hold are fulfilled. In particular, the microlensing parameter posteriors are definitely not well-modeled by a multivariate Gaussian. This is evident even in the 1-D posteriors shown in Figures 5.2 and 5.4. Second, we may not be near enough the fiducial model value in the fits for the estimates to hold. It might be possible to use tighter priors to enforce this condition; although not realistic for modeling real light curves, it may be acceptable for forecasting purposes.

This raises the question of the validity of the conclusions of work that uses Fisher matrices to estimate properties of microlensing parameters. We mentioned Karolinski et al. (2020) and Sajadian et al. (2023) as two examples at the beginning of this section. Karolinski et al. (2020) use Fisher matrices to argue that the microlensing parallax signal is undetectable using certain $\Delta\chi^2$ criteria. Although the specific uncertainties they derive with the Fisher matrix are probably not reliable, the conclusion still holds (that typical BH microlensing events with exisiting observations have microlensing parallaxes that are too small to constrain). Sajadian et al. (2023) use Fisher matrices to estimate the uncertainties on the measurements of lens parameters achievable with the Roman Space Telescope. It would be useful to check the validity of their results by checking several cases with actual model fits. The main results are based on the uncertainties from the covariance matrix, used to estimate precise uncertainties on physical parameters (e.g., 1%, 5%, and 10%). It is possible the assumptions of the Fisher matrix method hold in this regime, but again, checking the validity with fits is needed.

5.4 Modeling Correlated Noise with Gaussian Processes

Ignoring correlated noise when trying to model data can lead to biased results with incorrectly reported uncertainties that imply artificially high precision. Gaussian processes are a way to account for correlated noise in modeling.

Modeling correlated noise in astronomical time series using Gaussian Processes is not a new concept in astrophysics; see Aigrain et al. (2022) for a review of the method and applications. For example, it has been used to model variability in active galactic nuclei since the early 1990s. Presently, it is most commonly used in the exoplanet radial velocity and transit search communities. However, Gaussian Processes have been slow to catch on in microlensing, with only a handful of studies using them to address correlated noise in

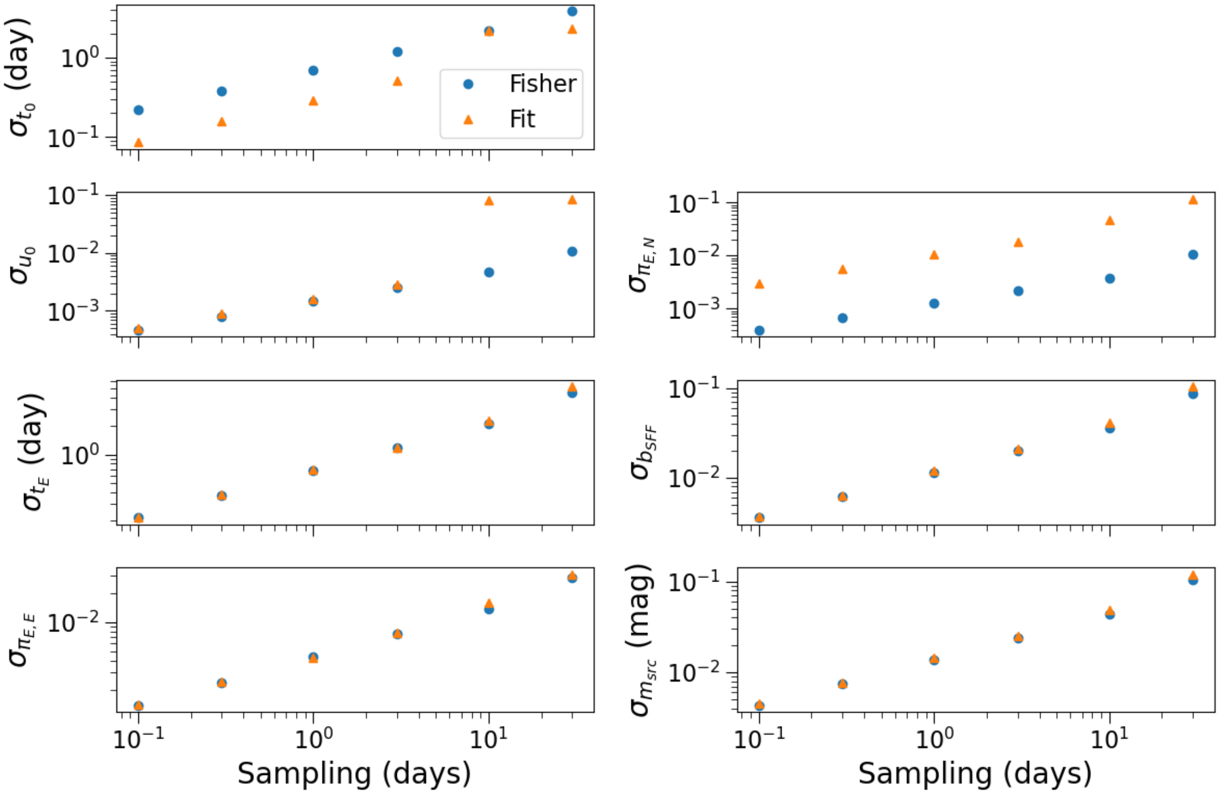

Figure 5.5: Comparison of uncertainty on inferred microlensing parameters as calculated using a Fisher matrix *(blue squares)* or performing a nested sampling fit *(orange circles)*, as a function of the sampling cadence.

modeling light curves (Golovich et al. 2022; Lam, Lu, Udalski, et al. 2022b; Li et al. 2019; Malpas et al. 2022; Medford et al. 2023).

In the previously cited works, they include Gaussian processes as part of their modeling, but as they are studying observed microlensing events, the actual ground-truth parameters of the event are unknown. Here, we generate artificial light curves, and model them in order to illustrate the difference that ignoring correlated noise can make.

5.4.1 Simulated data

We simulate two sets of photometric microlensing events, with three events in each set, for a total of six lighcurves (Figure 5.7). Each set of light curves contains a microlensing event with 1) correlated noise, 2) uncorrelated Gaussian white noise, and 3) no intrinsic noise. For each of these noise models, we inject a simulated microlensing event with the parameters listed in the "Truth" column of Table 5.3.

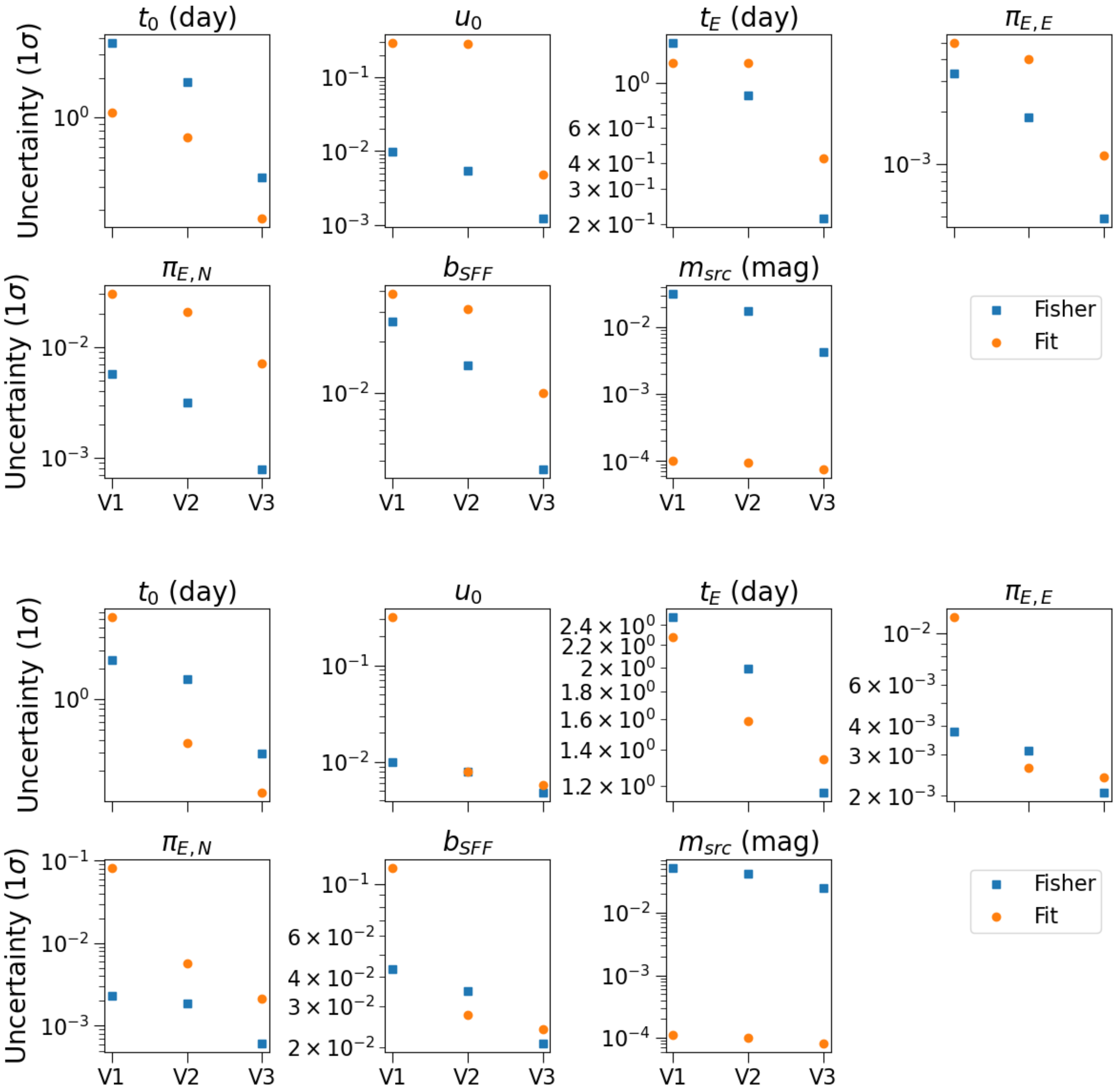

Figure 5.6: Comparison of uncertainty on inferred microlensing parameters as calculated using a Fisher matrix *(blue squares)* or performing a nested sampling fit *(orange circles)*. The top panel corresponds to the set of *Roman* light curves that cover the peak (top panel of Figure 5.3); the bottom panel corresponds to the set of *Roman* light curves without coverage of the peak (bottom panel of Figure 5.3).

To generate the synthetic light curves with correlated noise, we use data from a real microlensing light curve. We extract the baseline (unmagnified) portion of a real light curve, then subtract the average magnitude of the measurements to be left with a timeseries of correlated noise. The simulated microlensing event is then injected into this correlated noise timeseries, and the uncertainties are applied assuming Poisson noise.

To generate the synthetic light curves with uncorrelated Gaussian noise, we create a timeseries with noise drawn from a Gaussian distribution. The simulated microlensing event is then injected into the uncorrelated noise timeseries, and the uncertainties are applied assuming Poisson noise.

To generate the synthetic light curves with no intrinsic noise, we generate the simulated microlensing event, then apply the photometric uncertainties, assuming Poisson noise (this is the same procedure as described earlier in Chapter 5.2.1).

For all three light curve noise types, the photometric uncertainties and the zeropoint for the Poisson noise are taken from the real microlensing light curve.

The first set of simulated photometric microlensing events is based on the photometric properties of OGLE-2011-BLG-0037 (OB110037). The light curve at baseline is $I = 16.151$ mag with an average photometric uncertainty of 0.006 mag. There are 3516 observations over the 5 years of $2015-2019$ from which the baseline unlensed magnification is taken.

The second set of simulated photometric microlensing events is based on the photometric properties of MOA-2011-BLG-039 (MB11039). The light curve at baseline is $I = 16.161$ mag with an average photometric uncertainty of 0.011 mag. There are 11319 observations over the 5 years of $2007-2008$ and 2015-2017 from which the baseline unlensed magnification is taken.

We note that OB110037 and MB11039 are different sets of observations of the same microlensing event. The data for OB110037 was taken by the OGLE-IV collaboration at Las Campanas Observatory in Chile with a 1.3m telescope. The data for MB11039 was taken by the MOA-II collaboration at Mount John University Observatory in New Zealand with a 1.8m telescope.

5.4.2 Modeling procedure

We model our six light curves that have identical microlensing parameters but different noise properties, photometric uncertainties, and temporal samplings. We model the light curves in a Bayesian framework using the BAGLE software, which uses nested sampling to get the posterior distribution of the microlensing parameters.

First, we model all light curves in the standard way, ignoring correlated noise—that is, we only fit a microlensing model to the data. Next, we re-model the light curves with correlated noise, this time including a Gaussian process during the fitting process, as described in Chapter 3.14.

We use identical priors (the “Prior” column in Table 5.3) when modeling each light curve. We emphasize these priors are neither optimal nor realistic choices for modeling observed light curves. We are not interested here in studying the effect of the priors on the posterior distribution; we have simply roughly centered our priors on the true value (which we known in this case, but of course do not know when modeling actual microlensing events). We only ensure we are using the same set of priors when modeling the different light curves, and that the priors are sufficiently conservative such that the posterior distributions do not extend outside the prior support.

5.4.3 Results

First, we consider the model fits without Gaussian processes. The posteriors for the 7 different microlensing parameters are shown in Figure 5.8, along with the true values. Since the size of the uncertainties on all the data are equal, the *precision* of each fit is approximately the same (all the posteriors for a given parameter, across the noise models, are approximately the same width). However, the *accuracy* of the posteriors is generally poor for the OGLE and MOA noise light curves. This is because correlated noise is ignored and this is a poor assumption.

Next, we consider the model fits that did include Gaussian processes. The posteriors are shown in Figure 5.9. By including a Gaussian process, the *precision* is worse, but the *accuracy* is much better. This shows the importance of modeling correlated noise. Figure 5.10 is identical to Figure 5.9, but all in a single panel. Here, it is easily seen that the same microlensing event would have different inferred parameters because the underlying noise properties were different. In addition, the two solutions, in addition to generally being incorrect, are generally inconsistent with each other. Including Gaussian Processes in the modeling addresses both these issues.

Parameter	Truth	Prior
t_0 (MJD)	57600	$\mathcal{U}(57570, 576030)$
u_0	0.1	$\mathcal{U}(0, 0.3)$
t_E (days)	100	$\mathcal{U}(20, 500)$
$\pi_{E,E}$	0.05	$\mathcal{N}(0, 0.1)$
$\pi_{E,N}$	0.1	$\mathcal{N}(0, 0.1)$
b_{SFF}	0.8	$\mathcal{U}(0, 1)$
m_{base} (mag)	16.1506	$\mathcal{U}(16.0506, 16.2506)$
$\log \sigma$ (mag)	–	$\mathcal{N}(0, 5)$
$\log \rho$ (day)	–	$\mathcal{N}(0, 5)$
$\log \omega_0^4 S_0$ (mag^2 day^{-3})	–	$\mathcal{N}(0, 5)$
$\log \omega_0$ (day^{-1})	–	$\mathcal{N}(0, 5)$

Table 5.3: *Gaussian Process example.* $\mathcal{U}(A, B)$ denotes a uniform distribution over the interval A to B, while $\mathcal{N}(A, B)$ denotes a normal distribution with mean A and standard deviation B.

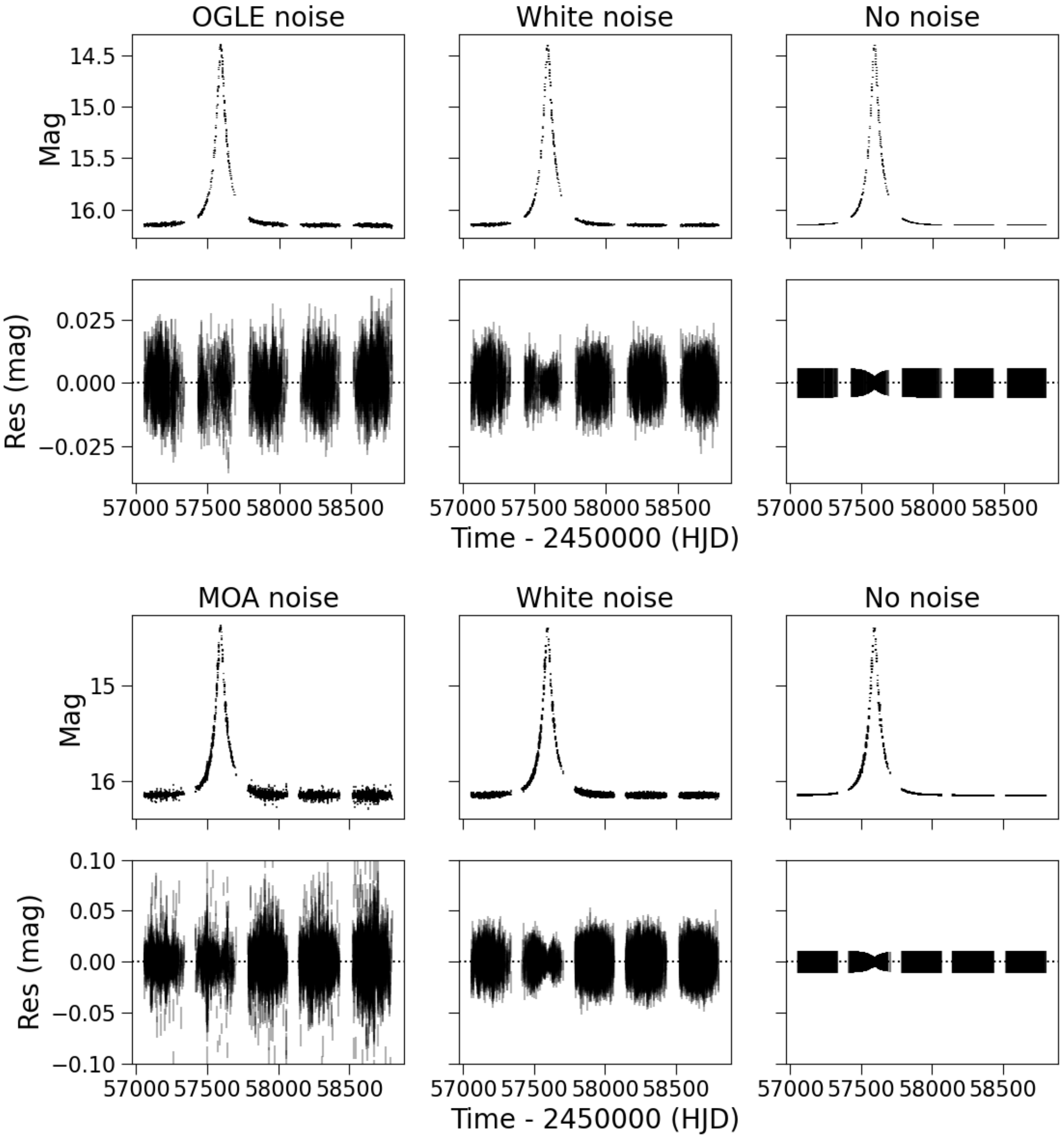

Figure 5.7: Fake light curves. The underlying microlensing parameters are identical for each light curve, they only differ in their noise properties, sampling cadences, and photometric uncertainties. The *top (bottom) panels* uses OGLE (MOA) -like sampling and uncertainties.

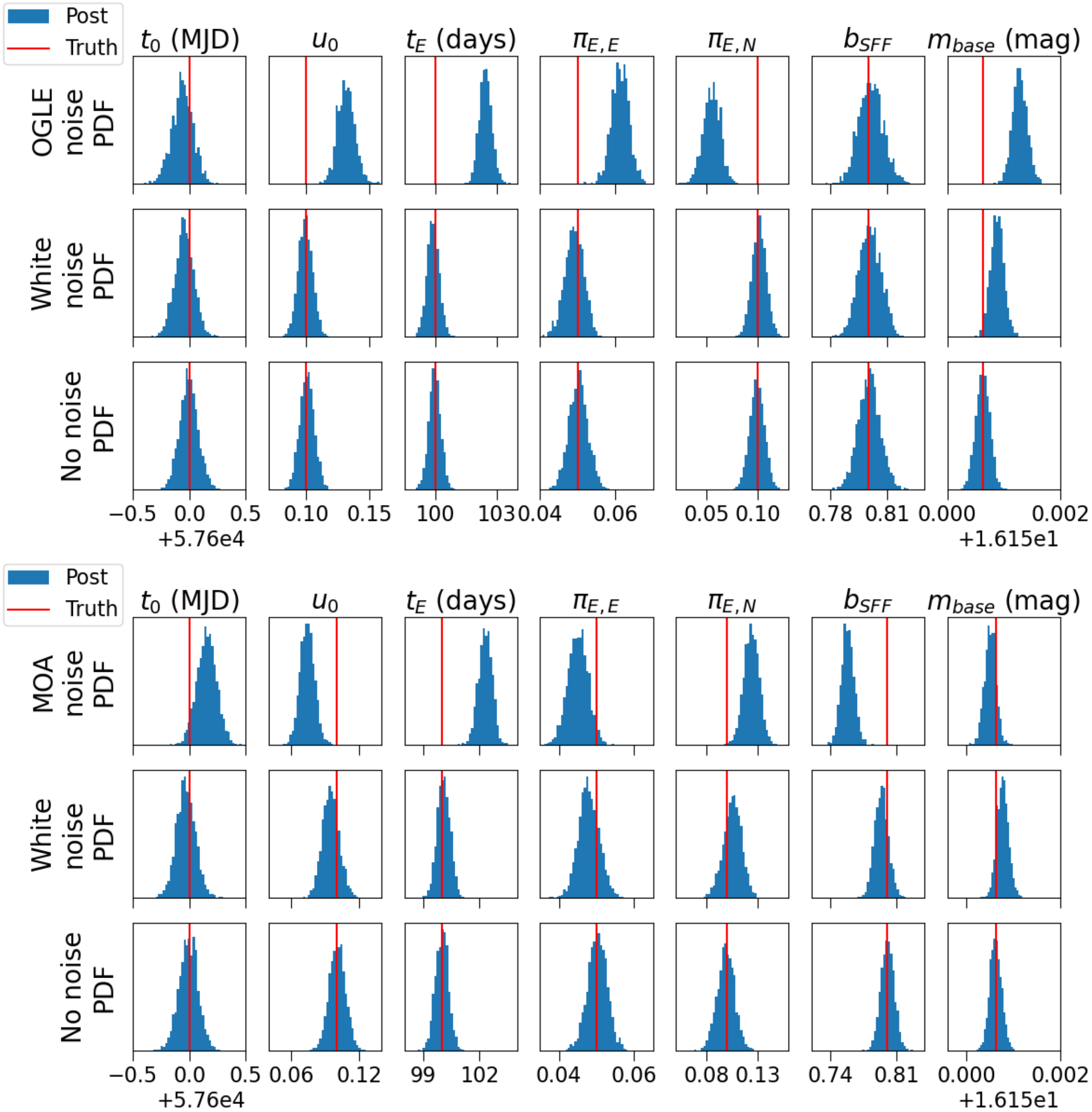

Figure 5.8: The fit posteriors for the inferred microlensing parameters from fitting the respective light curves. The priors used are identical in each case. The true value of each parameter is shown in the red line. The *top (bottom) panels* fit the light curves with OGLE (MOA) -like sampling and uncertainties. The fit light curves in the *top rows* have correlated noise, the *middle rows* have white noise, and the *bottom rows* have no intrinsic noise.

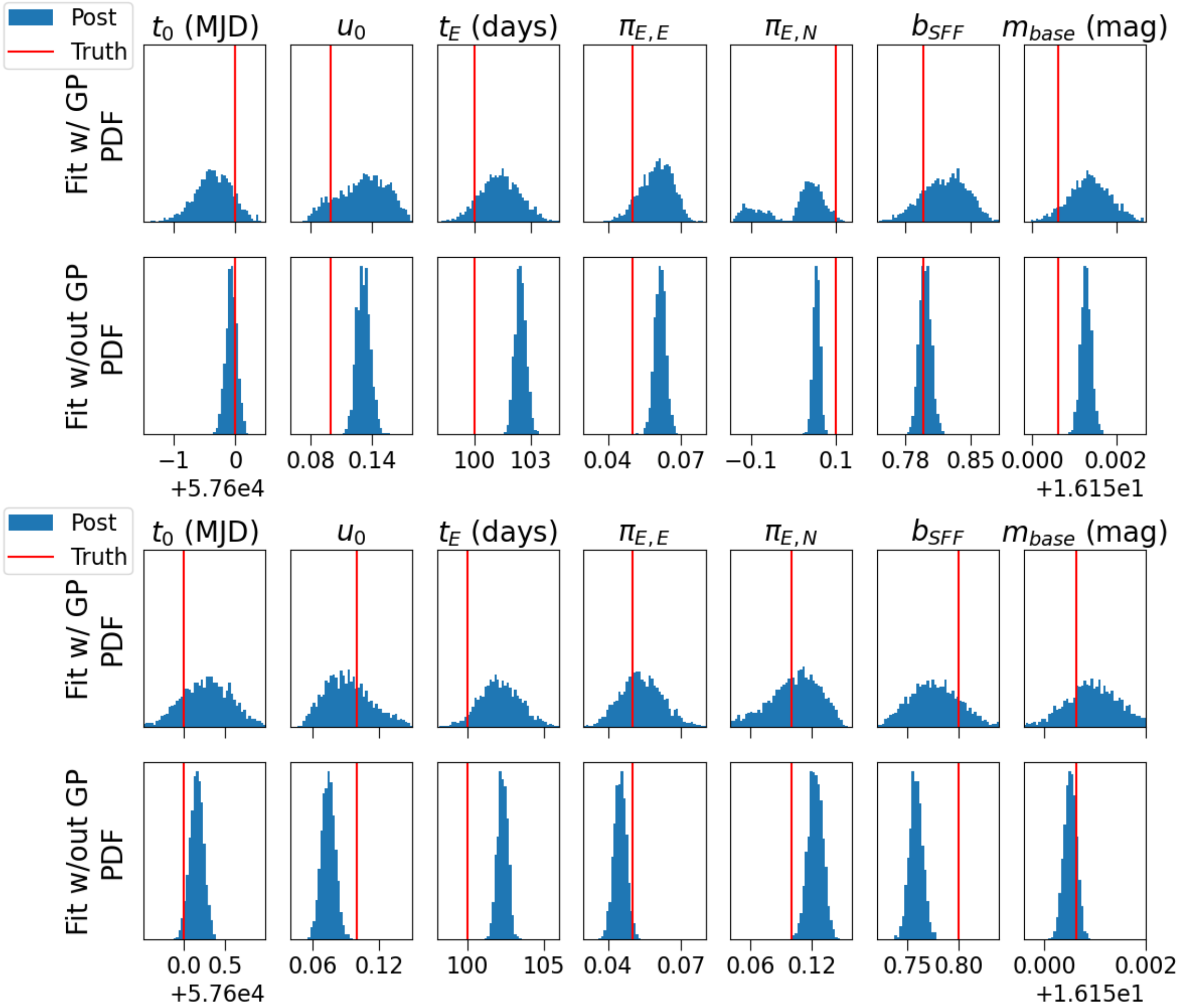

Figure 5.9: The fit posteriors for the inferred microlensing parameters, from fitting the correlated noise light curves with and without a Gaussian Process. The *top (bottom) panels* fit the light curves with OGLE (MOA) -like sampling and uncertainties. The *top row* of each panel (the fit without a Gaussian Process) is identical to the top row of each panel in Figure 5.8.

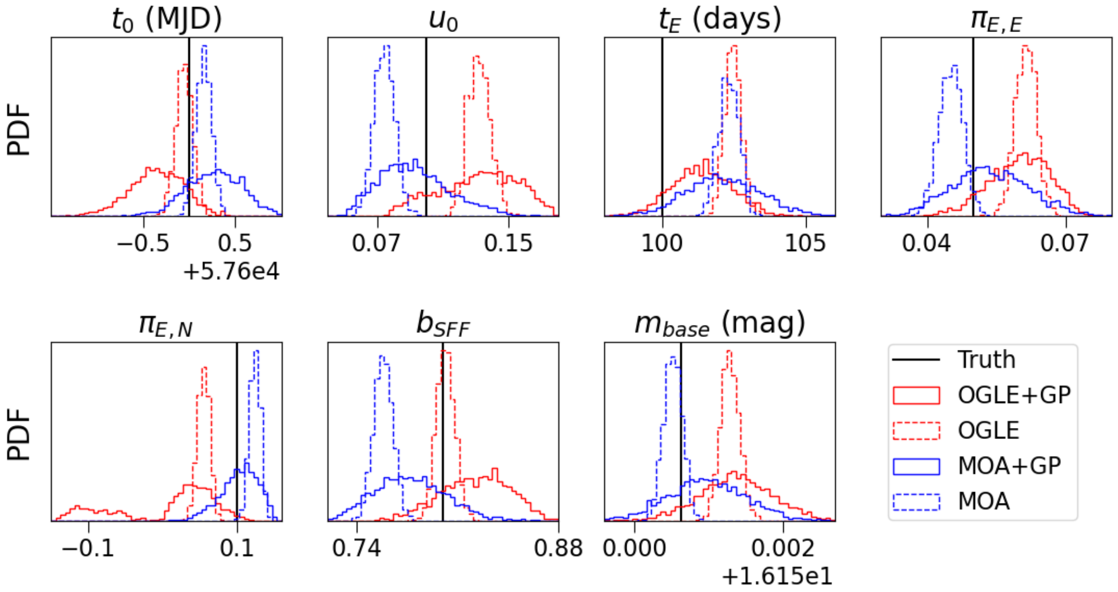

Figure 5.10: The fit posteriors for the inferred microlensing parameters, from fitting the OGLE and MOA noise light curve with and without a Gaussian Process.

5.4.4 A comment on Gaussian noise and intuition, and credible vs. confidence intervals

When developing modeling and fitting codes, before the software can be deployed to analyze real data, it needs to be validated on synthetic data to ensure it returns correct results. Sometimes, when testing our group microlensing modeling code BAGLE (Bayesian Analysis of Gravitational Lensing Events), the inferred parameters from modeling synthetic events are discrepant from the true values. This brings up whether there is an issue with the software itself, or whether this is expected. Here we investigate changing the realization of random noise on a light curve.

We generate 25 light curves with the parameters listed in Table 5.1. The light curves span 54400 to 55600 MJD, sampled at a cadence of 0.1 days with no gaps. The photometric uncertainties corresponding to SNR=$\sqrt{4000}$ at 19th magnitude (0.016 mag). We add uncorrelated Gaussian noise to the observations. For the 25 different light curves, the only difference is the specific realization of the random noise. That is, the noise properties are always the same (uncorrelated Gaussian noise), but we change the specific values of the simulated noise (i.e. changing the random seed used by `numpy` when generating a sequence of random numbers). We are effectively performing a frequentist thought experiment, where our parameters our fixed, but we repeat the experiment multiple times via generation of different realizatons of the data.

Figure 5.11 shows the fits to 25 different realizations of the light curve described in

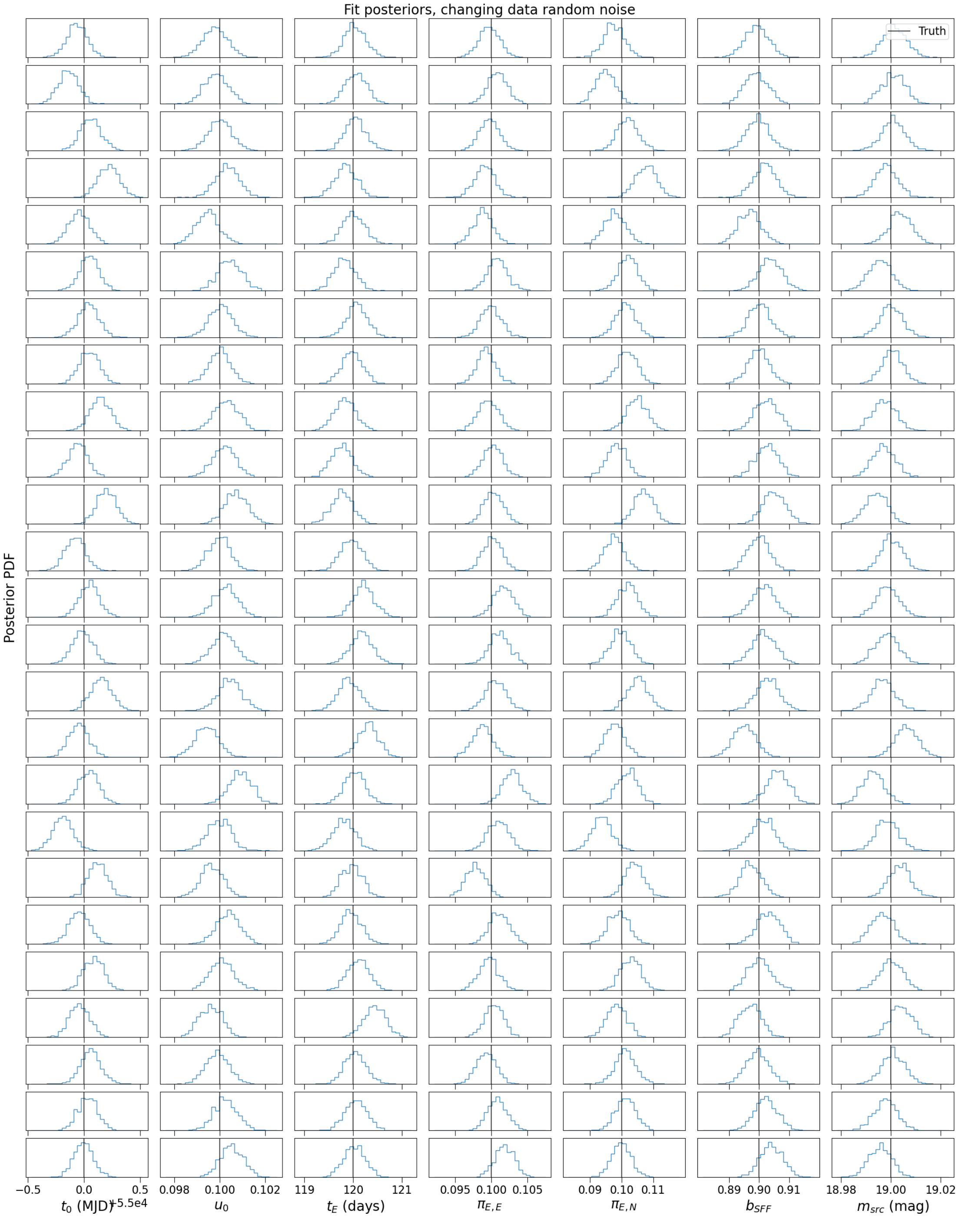

Figure 5.11: Each row is a nested sampling fit posterior to a different realization of the random noise. The model is the same, and the noise properties are the same, it is just the realization that is different. The true input value is the black vertical line.

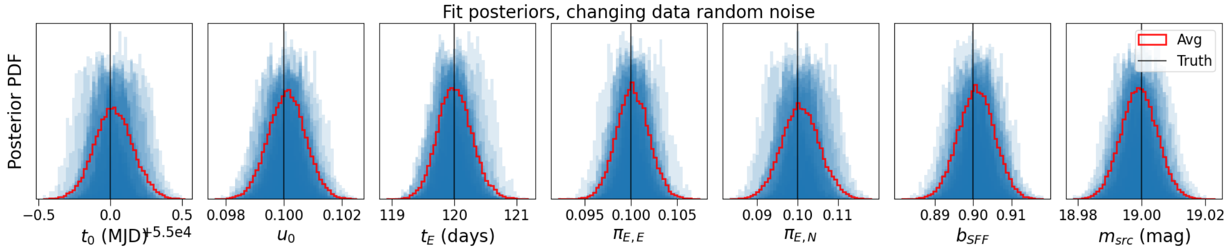

Figure 5.12: All 25 posteriors in Figure 5.11 are plotted on top of each other in blue. Average of the 25 posteriors in Figure 5.11 is shown in red line. The true value is in black.

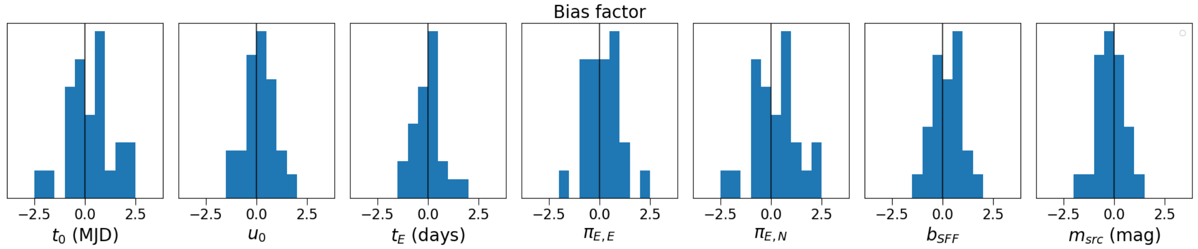

Figure 5.13: The bias factor (median − truth, divided by the standard deviation) for the 25 posteriors in Figure 5.11.

the previous paragraph. Despite the noise properties being uncorrelated and identical, in a substantial number of cases, the inferred parameters are quite biased. This seems potentially worrisome, given that in this case, the simulated light curves do not have correlated noise, only white uncorrelated noise.

Figure 5.12 shows the same posteriors in Figure 5.11, but averaged together for each model parameter. It is now evident by looking at the *average* of all the modeled realizations, that there is no bias in the parameters. The width of this averaged posterior can be interpreted as the confidence interval of frequentist statistics.

Figure 5.13 is another way to visualize the bias of the averaged posteriors. In this case, we consider a histogram of the bias factor (defined as the difference between the median of the posterior and the true value, normalized the standard deviation of the posterior (O'Neil et al. 2019)) for each realization. The histograms are symmetrically centered about zero, which is another way of saying the average of the realizations also is unbiased.

It should be expected that some of the time, there is bias in the posteriors just because of that particular realization of data, even if noise is white and uncorrelated. For synthetic data, if in doubt, check with a different realization of the noise to validate. However, this is also a caution for analyzing real data, and that sometimes, you do just get lucky (or rather, unlucky). Finally, we note that although we averaged the posteriors and provide an interpretation for them using frequentist statistics and related them to confidence intervals, each individual posterior itself was a fit from a modeling procedure in a Bayesian framework, and the individual posteriors themselves are used to generate credible intervals.

5.5 Discussion and future directions

5.5.1 Considerations for future observatories

New facilities, big and small, have come or are starting to come online to do time-domain science (e.g., Zwicky Transient Facility, Rubin Observatory's Legacy Survey of Space and Time, and the La Silla Schmidt Southern Survey). Most of these facilities are not dedicated microlensing surveys, rather spanning a wide range of science cases. For those interested in microlensing, the question is whether these facilities have surveys that are capable of performing interesting microlensing science. Many metrics are proposed to quickly assess microlensing detectability across parameter space. For example, the Einstein crossing time t_E is the most obvious and oft-used metric for the characteristic timescale of a microlensing event. From this work, we show that t_E (or even $t_E/2$) cannot be used as the timescale for sampling a light curve if the event is to be characterized with any useful precision. If microlensing is to be a science case for consideration for upcoming surveys, it is important that slightly more detailed modeling work be done, otherwise the risk is run of being overly optimistic in survey requirements.

The Roman Space Telescope is a future facility where microlensing *will* be a science driver. However, the science case is specifically exoplanetary microlensing. For finding black holes, the detection requirements will be somewhat different. From this work, we show it would be better for the six Bulge seasons of the GBTDS to be consecutive with each other. In order to obtain proper motions, inclusion of a short "outrigger" season at the end(s) of the survey could serve such a purpose.

Finally, we caution that using Fisher matrix methods to perform forecasts for microlensing modeling only hold under certain assumptions and to use them requires care and checking or calibrating against actual fits. We speculate that when using Fisher matrix methods, it may work better for a set of microlensing modeling parameters that form a more orthogonal basis set. Dominik (2009) does this for Paczynski light curves, but these lack parallax. If the basis set could be extended to include parallax, this may facilitate better results between the Fisher matrix estimates and the fit results.

5.5.2 Future work

The work in Chapter 5.2 can be extended to a larger suite of parameter space in order to better optimize and understanding how sampling cadence affects the inference of various microlensing parameters. This includes both a larger parameter space in terms of the microlensing parameters themselves (e.g., t_E, π_E) as well as observational parameter space (location on sky, brightness, SNR).

This work has solely been concerned with modeling microlensing photometry, but extending it to include microlensing astrometry also would be particularly relevant for *Roman* GBTDS.

Finally, applying the algorithm described in Hees et al. (2019) to quantify when it is most crucial to get photometric and astrometric measurements would also be useful in understanding the best way to structure the *Roman* GBTDS. For example, given a set of microlensing observations at baseline and an additional 100 observations, what is the best balance of these to capture the photometric and astrometric signals? Leave-one-out cross-validation methods may also be worth exploring.

5.6 Conclusions

We explored a variety of techniques and considerations when modeling microlensing light curves. In summary:

- Denser and more regular sampling allow light curves to be better characterized; to obtain any useful constraints light curves should be sampled at a cadence $dt \ll t_E$. For example, in the example of Chapter 5.2.1 which considers a relatively long-duration, large microlensing parallax, unblended, high magnification, and high SNR event, the sampling cadence still had to be < 10 days to obtain $< 1\%$ fractional uncertainties on $t_E = 120$ days. Future work should explore the effect of changing SNR, blending, and microlensing parallax on the required ratio of dt/t_E.

- Fisher matrices are a way to quickly forecast the uncertainties in parameter estimation from modeling microlensing light curves; however, care must be taken and results checked if the assumptions of the method do not hold.

- Modeling correlated noise is important, and Gaussian Processes can help do this without having a functional form for the noise model. Ignoring correlated noise leads to precise but inaccurate parameter estimation; by modeling this correlated noise with Gaussian Processes, the estimates are less precise but more accurate.

The light curves for OB110037 and MB11039 described in Chapter 5.4 were published in Lam, Lu, Udalski, et al. (2022b) and are publicly available at doi:10.5281/zenodo.6607578.

Chapter 6

Microlensing conversions

There are a variety of conventions for defining microlensing reference frames and coordinate systems in the literature. In this pedagogical note, we attempt to explain some of these conventions to the uninitiated, as well as provide equations to convert parameters reported using different conventions.

6.1 Introduction

6.1.1 In gravitational lensing, the observer is everything

The phenomenon of gravitational lensing depends on the positions and motions of the observer relative to the foreground lens and background source. Depending on the location of the observer, lensing may or may not be seen. For example, if the observer-lens separation vector is oriented orthogonal to the lens-source separation vector, no lensing will be observed. On the other hand, if the observer-lens-source are co-linear, lensing will be observed (Figure 1.6).

For strong gravitational lensing in the context of galaxies and galaxy clusters, lensing can be treated as a static phenomenon: the positions of the individual lensed (i.e. macro) images do not change on the timescale of a human lifetime (Chapter 1.2.1). However, for gravitational microlensing in the context of stars, planets, and compact objects in our Galaxy, the motions of the lenses and sources are key to the observed lensing phenomenon. Different observer velocities will result in different observed microlensing event durations (t_E), and an accelerating observer (e.g., an Earthly observer orbiting the Sun) will lead to observation of higher order effects like microlensing parallax (π_E). More generally, any parameter that has a dependence on time or velocity will be dependent on the observer's frame's motion.

Thus, given a microlensing geometry (location of observer relative to the lens and source), there is still the choice of the observer's motion with respect to that system, which will affect the measured microlensing parameters. In what follows, we will consider the effects of choice of reference frame in modeling microlensing events, and how to convert microlensing parameters between different frames.

6.1.2 Philosophy and justification of this note

The emphasis of this note is primarily pedagogical; algebra is evaluated in more detail than typical. However, we believe this note fills a certain hole in the existing literature.

First, as far as we know, the formulae to convert microlensing event parameters between different reference frame conventions and coordinate systems are not published in full anywhere. Different situations make certain conventions advantageous over others. However, in the end, it is necessary to be able to convert between different conventions if we want to make meaningful comparisons.

Second, most discussion of microlensing reference frames is a subsection of larger research papers, making it difficult for those unfamiliar with microlensing to find an accessible reference. This may not have been a concern in the past, when the microlensing community was relatively small and self-contained. However, the Roman Space Telescope to be launched in 2026 will change this—microlensing will become a much larger subfield of astronomy. The advent of large public time domain surveys, both present (e.g., the Zwicky Transient Facility) and upcoming (e.g., Vera Rubin Observatory's Legacy Survey of Space and Time), also provide new opportunities to do microlensing science. Thus, in order to enable newcomers to join and contribute to the field, it is important to clearly lay out conventions and explain the technical details in an approachable way. We note that these different conventions can even lead to confusion for those experienced with microlensing (e.g., see correction of Wyrzykowski and Mandel 2020 by Mróz and Wyrzykowski 2021).

This note is organized as follows. We start with the simplest possible model in Chapter 6.2 describing point-source point-lens (PSPL) microlensing in a rectilinear (non-accelerating) frame. In Chapter 6.3 we consider the effect of parallax creating non-rectilinear (accelerating) reference frames, and provide conversions between microlensing parameters reported using the heliocentric or geocentric projected formalism. In Chapter 6.4 we introduce static binary lenses, and provide conversions between microlensing parameters reported using different definitions of the binary lens coordinate origin. Chapter 6.5 describes several other conventions to watch out for; most come down to sign flips or angle differences by 180°. Chapter 6.6 describes how to convert between two microlensing coordinate systems and how it affects the sign of the parameter u_0. Chapter 6.7 provides some worked examples of going between these conversions. A brief discussion is presented in Chapter 6.8, and we conclude in Chapter 6.9.

6.2 PSPL microlensing in a rectilinear frame

First, consider microlensing in an arbitrary rectilinear frame. The Einstein radius θ_E is defined as

$$\theta_E = \sqrt{\frac{4GM\pi_{LS}}{c^2 \cdot 1\mathrm{AU}}} \tag{6.1}$$

where M is the mass of the lens, $\pi_{LS} = \pi_L - \pi_S$ is the relative parallax of the lens and source, G is the gravitational constant, and c is the speed of light. The Einstein radius sets the angular scale of gravitational lensing—when the source and lens approach within an on-sky projected separation of $\sim \theta_E$ of each other as seen by an observer, the lens will appreciably deflect the light of the source as it travels to the observer. In the case of microlensing, this deflection results in the observer seeing a transient brightening of the source (photometric microlensing) and a shift in the source's position (astrometric microlensing).

The two-dimensional angular position vector of the source $\boldsymbol{\theta_S}$ and lens $\boldsymbol{\theta_L}$ on the sky as a function of time t are given by

$$\boldsymbol{\theta_S}(t) = \boldsymbol{\theta_{S,0}} + \boldsymbol{\mu_S}(t - t_0) \tag{6.2}$$

$$\boldsymbol{\theta_L}(t) = \boldsymbol{\theta_{L,0}} + \boldsymbol{\mu_L}(t - t_0) \tag{6.3}$$

where $\boldsymbol{\theta_{S,0}}$, $\boldsymbol{\theta_{L,0}}$ are the positions of the source and lens at time t_0, and $\boldsymbol{\mu_S}$, $\boldsymbol{\mu_L}$ are the proper motions of the source and lens, as seen by the observer. The dimensionless source-lens separation vector $\boldsymbol{u}(t)$ is defined

$$\boldsymbol{u}(t) = \frac{\boldsymbol{\theta_S}(t) - \boldsymbol{\theta_L}(t)}{\theta_E} \equiv \boldsymbol{u_0} + \frac{\boldsymbol{\mu_{SL}}}{\theta_E}(t - t_0), \tag{6.4}$$

where

$$\boldsymbol{u_0} = \frac{\boldsymbol{\theta_{S,0}} - \boldsymbol{\theta_{L,0}}}{\theta_E} \tag{6.5}$$

is the source-lens minimum separation vector, and

$$\boldsymbol{\mu_{SL}} = \boldsymbol{\mu_S} - \boldsymbol{\mu_L} \tag{6.6}$$

is the source-lens relative proper motion. The Einstein crossing time t_E is defined

$$t_E = \frac{\theta_E}{\mu_{SL}} \tag{6.7}$$

so the dimensionless source-lens separation vector can also be written as

$$\boldsymbol{u}(t) = \boldsymbol{u_0} + \left(\frac{t - t_0}{t_E}\right)\boldsymbol{\hat{\mu}_{SL}}. \tag{6.8}$$

Note that by construction, $\boldsymbol{u_0} \perp \boldsymbol{\mu_{SL}}$, and hence

$$u(t) = \sqrt{u_0^2 + \left(\frac{t - t_0}{t_E}\right)^2}. \tag{6.9}$$

A photometric microlensing light curve is completely determined by the dimensionless source-lens separation $u(t)$. Thus, for a microlensing event observed in a rectilinear frame, there are three geometric parameters[1] that can be inferred from a photometric microlensing light curve: u_0, t_0, and t_E (Chapter 1.2.2).

Recall that microlensing is a purely geometric effect. This means that for different choices of rectilinear frames, the values of the geometric microlensing parameters will differ—in rectilinear frame R, the parameters describing the microlensing event are u_0, t_0, and t_E, while in a different rectilinear frame R', the parameters are u_0', t_0', and t_E'.

For example, consider an observer in a rectilinear reference frame R at rest with respect to the Sun. Directly along the observer's line of sight, a $0.5M_\odot$ star 4 kpc away happens to align with a background star 8 kpc away. The foreground lens is moving East 100 km/s relative to the Sun, while the background star is moving West 50 km/s relative to the Sun. Using Equations 6.1, 6.6, and 6.7, we find $t_E = 49$ days. Next, consider another observer in a different rectilinear reference frame R' that is moving 50 km/s East with respect to the Sun. In this case, μ_{SL}, and in turn t_E, are different, and for the observer in frame R', they measure $t_E' = 39$ days.

Being inhabitants of the Solar System, the most natural choice of rectilinear reference frame is a heliocentric frame. However, as will be discussed in Chapter 6.3, there are reasons for choosing other rectilinear frames.

6.3 PSPL microlensing in an accelerating Earthly frame

Photometric microlensing events are generally observed in a non-rectilinear frame. For example, microlensing survey telescopes are located on Earth, which is orbiting the Sun. This means Earth is an accelerating reference frame, and the description provided in Chapter 6.2 is not correct; this orbital motion must be taken into account. Here, we consider the Earth (geocentric) frame and annual microlensing parallax, but this formalism can be extended to any other accelerating reference frame. For example, for microlensing with the Roman Space Telescope, the frame will be the accelerating L2 frame.

As a historical side note, microlensing parallax (specifically, microlensing satellite parallax) was first described by Refsdal (1966). Annual microlensing parallax was first discussed by Gould (1992), and subsequently observed by the MACHO collaboration (Alcock, Allsman, Alves, Axelrod, Bennett, et al. 1995).

---

[1] Geometric parameters means excluding parameters like blending and source/baseline magnitude, which depend on the telescope, filter, and seeing; we call these *photometric* parameters.

6.3.1 The parallax vector

The Sun-Earth projected separation vector in AU, also called the parallax vector[2], is denoted $\boldsymbol{P}(t)$. In equatorial coordinates, the parallax vector can be decomposed as

$$P_\alpha(t) = R_{SE}(t)(\cos\epsilon\cos\alpha\sin\lambda_\odot(t) - \sin\alpha\cos\lambda_\odot(t)) \tag{6.10}$$

$$P_\delta(t) = R_{SE}(t)[(\sin\epsilon\cos\delta - \cos\epsilon\sin\alpha\sin\delta)\sin\lambda_\odot(t) - \cos\alpha\sin\delta\cos\lambda_\odot(t)] \tag{6.11}$$

where α is right ascension, δ is declination, $R_{SE}(t)$ is the Sun-Earth separation in units of AU, $\lambda_\odot = 360°(t + 284)/365$ is the ecliptic longitude of the Sun where t is clock time in days measured from the beginning of a year, and $\epsilon = 23°27'$ is the obliquity of the ecliptic (Hog et al. 1995; Van De Kamp 1967). These equations are mainly presented for an analytic reference; in practice, when implementing parallax in microlensing modeling or fitting software, it is preferable and more accurate to use numerical ephemerides which account for perturbations from other Solar System bodies such as Jupiter (e.g., from JPL ephemeris) rather than Equations 6.10 and 6.11.

6.3.2 Heliocentric rectilinear component

Since we are now considering a specific reference frame, we will use a superscript "hel" to indicate the (rectilinear) heliocentric reference frame, and "geo" to indicate the (accelerating, non-rectilinear) geocentric reference frame. Parallax modifies Equations 6.2 and 6.3 to

$$\boldsymbol{\theta}_{\boldsymbol{S}}^{\mathrm{geo}}(t) = \boldsymbol{\theta}_{\boldsymbol{S,0}}^{\mathrm{hel}} + \boldsymbol{\mu}_{\boldsymbol{S}}^{\mathrm{hel}}(t - t_0^{\mathrm{hel}}) + \pi_S\boldsymbol{P}(t) \tag{6.12}$$

$$\boldsymbol{\theta}_{\boldsymbol{L}}^{\mathrm{geo}}(t) = \boldsymbol{\theta}_{\boldsymbol{L,0}}^{\mathrm{hel}} + \boldsymbol{\mu}_{\boldsymbol{L}}^{\mathrm{hel}}(t - t_0^{\mathrm{hel}}) + \pi_L\boldsymbol{P}(t). \tag{6.13}$$

As before, we can calculate the source-lens separation vector

$$\boldsymbol{u}^{\mathrm{geo}}(t) = \frac{\boldsymbol{\theta}_{\boldsymbol{S}}^{\mathrm{geo}}(t) - \boldsymbol{\theta}_{\boldsymbol{L}}^{\mathrm{geo}}(t)}{\theta_E} \equiv \boldsymbol{u}_{\boldsymbol{0}}^{\mathrm{hel}} + \frac{\boldsymbol{\mu}_{\boldsymbol{SL}}^{\mathrm{hel}}}{\theta_E}(t - t_0^{\mathrm{hel}}) - \frac{\pi_{LS}}{\theta_E}\boldsymbol{P}(t). \tag{6.14}$$

Similar to t_E, we define the microlensing parallax

$$\pi_E = \frac{\pi_{LS}}{\theta_E} \tag{6.15}$$

and so the source-lens separation vector can alternatively be written

$$\boldsymbol{u}^{\mathrm{geo}}(t) = \boldsymbol{u}_0^{\mathrm{hel}} + \left(\frac{t - t_0^{\mathrm{hel}}}{t_E^{\mathrm{hel}}}\right)\hat{\boldsymbol{\mu}}_{\boldsymbol{SL}}^{\mathrm{hel}} - \pi_E\boldsymbol{P}(t). \tag{6.16}$$

We pause here to make four points.

---

[2] Note that some, e.g., Gould 2004, choose to define the parallax vector in the opposite direction, as the Earth-Sun separation.

First, it is assumed π_S and π_L are the same in both the heliocentric and geocentric frame. For typical source and lens distances ($> 1\,\mathrm{kpc}$), the parallaxes of the source and lens are independent of frame, since the change in the distance between the observer to the source and lens is negligible (1 AU/1 kpc $\sim 10^{-9}$). Through the rest of this document, we continue to use this assumption—that distances to the source and lens in any frames we choose do not change—without further mention. In addition, the mass of the lens and fundamental constants are not frame dependent quantities, hence θ_E and π_E are also the same in both the heliocentric and geocentric frames.

Second, in general $\boldsymbol{u}^{\rm geo}(t_0^{\rm hel}) \not\perp \boldsymbol{\mu}_{\boldsymbol{SL}}^{\rm hel}$. It is only $\boldsymbol{u}^{\rm hel}(t_0^{\rm hel}) = \boldsymbol{u}_{\boldsymbol{0}}^{\rm hel} \perp \boldsymbol{\mu}_{\boldsymbol{SL}}^{\rm hel}$. The quantities t_0, u_0, and t_E are defined in terms of the rectilinear frame. Hence with parallax, it is possible that the projected source-lens closest approach is smaller than u_0. See Figure 6.1 for an illustration.

Third, because the parallax vector $\boldsymbol{P}(t)$ breaks the symmetry of a microlensing event geometry by introducing a preferred direction into the system, this means the source-lens relative proper motion *direction* can be measured. However, the *magnitude* of the relative proper motion cannot be measured from a light curve alone, because the absolute scale of the microlensing event encoded in θ_E is not measureable from photometry only. Recall the light curve is only a function of the dimensionless source-lens separation, which is normalized by θ_E. In the microlensing literature, starting with Gould (2004), the direction of the relative proper motion was chosen to be encoded in the microlensing parallax $\boldsymbol{\pi}_{\boldsymbol{E}} = \pi_E \hat{\boldsymbol{\mu}}_{\boldsymbol{SL}}$. For a microlensing event with parallax, there are now five geometric parameters: u_0, t_0, and t_E from before, as well as $\boldsymbol{\pi}_{\boldsymbol{E}}$.[3]

Fourth and finally, the microlensing parallax vector is not to be confused with the parallax vector. To re-emphasize this point, the definitions of various words with “parallax” are listed here:

- $\boldsymbol{P}(t)$ is the *parallax vector.* The parallax vector is not a microlensing-specific concept; it encodes the 2-D projected Sun-Earth separation in units of AU.
- π_E is the *microlensing parallax.* It is defined as the relative parallax normalized by the Einstein radius π_{LS}/θ_E.
- $\boldsymbol{\pi}_{\boldsymbol{E}}$ is the *microlensing parallax vector.* By definition, $\boldsymbol{\pi}_{\boldsymbol{E}} \parallel \boldsymbol{\mu}_{\boldsymbol{SL}}$ and $|\boldsymbol{\pi}_{\boldsymbol{E}}| = \pi_E$.
- $\pi_E \boldsymbol{P}(t)$ is the *microlensing parallax motion vector.* Note that $\boldsymbol{\pi}_{\boldsymbol{E}} \nparallel \boldsymbol{P}(t)$ and $|\pi_E \boldsymbol{P}(t)| \neq \pi_E$.

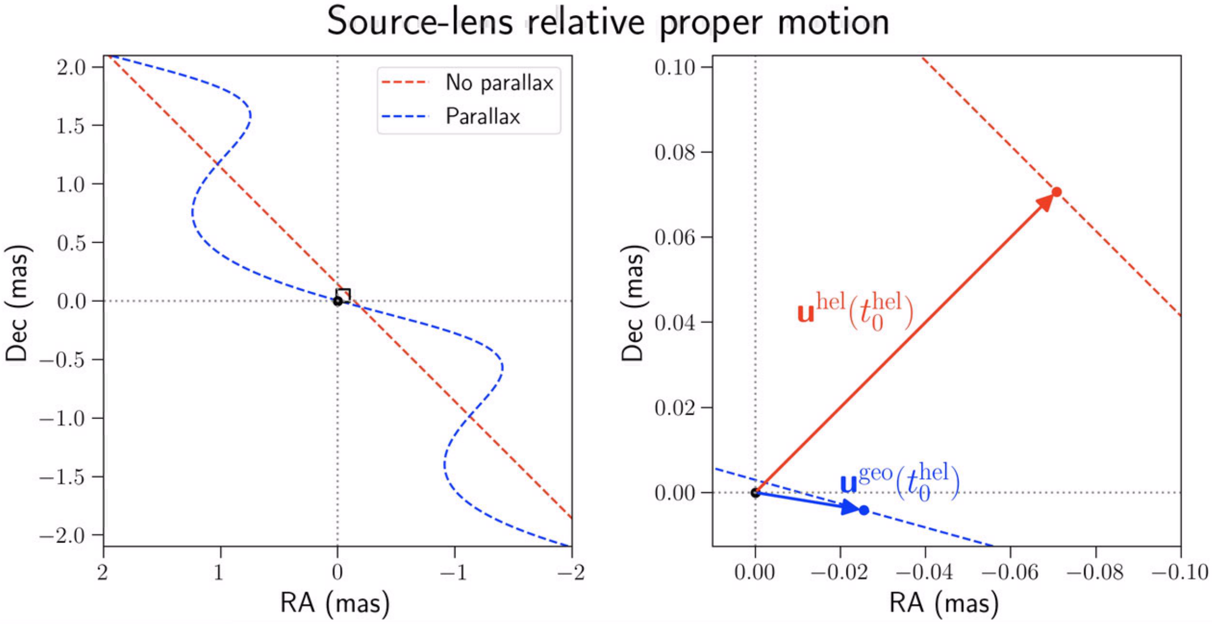

Figure 6.1: *Left panel:* source-lens trajectory in the rectilinear heliocentric (no parallax, *red dash*) and accelerating geocentric (parallax, *blue dash*) frames. The box shows a zoomed in region (*right panel*). *Right panel:* The source-lens separation vector $\boldsymbol{u}$ evaluated at the time of closest approach in the heliocentric frame t_0^{hel}. Microlensing parameters are reported as they are in the rectilinear frame, in the absence of parallax. This means the minimum lens-source separation in the geocentric frame can be smaller than the minimum in the rectilinear frame at the time when the minimum value in the latter frame is reached, i.e. $|\boldsymbol{u}^{\mathrm{geo}}(t_0^{\mathrm{hel}})| < |\boldsymbol{u}^{\mathrm{hel}}(t_0^{\mathrm{hel}})|$, where $\boldsymbol{u}_{\mathbf{0}}^{\mathrm{hel}} = \boldsymbol{u}^{\mathrm{hel}}(t_0^{\mathrm{hel}})$. This serves to emphasize that the reported parameters are defined in the rectilinear heliocentric frame. Note also that the minimum source-lens separation in the geocentric frame is even smaller and is realized at a different time than in the heliocentric frame, i.e. $|\boldsymbol{u}_{\mathbf{0}}^{\mathrm{geo}}| < |\boldsymbol{u}_{\mathbf{0}}^{\mathrm{hel}}|$, where $\boldsymbol{u}_{\mathbf{0}}^{\mathrm{geo}} = \boldsymbol{u}^{\mathrm{geo}}(t_0^{\mathrm{geo}})$ and $t_0^{\mathrm{geo}} \neq t_0^{\mathrm{hel}}$.

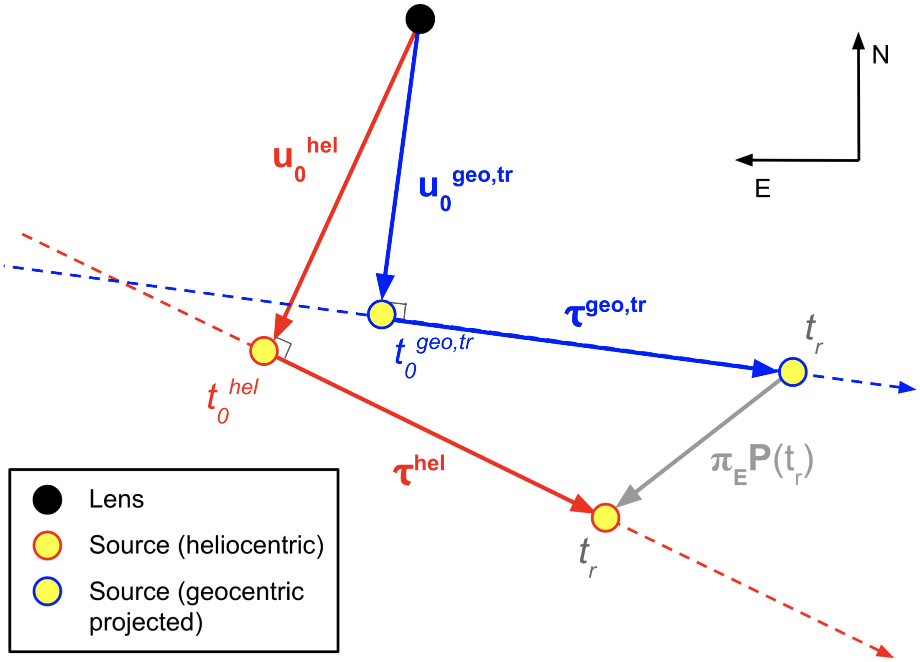

Figure 6.2: Visual interpretation of Equation 6.17. This diagram serves to show how the heliocentric and geoprojected frames are related to each other via the chosen reference time t_r, the parallax vector $\boldsymbol{P}$, and the microlensing parallax π_E. Positions are in units of θ_E. The lens is at the origin (*black circle*), i.e. the source-lens reference frame. Red lines/"hel" superscripts denote quantities in the (rectilinear) heliocentric frame, while blue lines/"geo,tr" superscripts denote quantities in the (rectilinear) geoprojected frame. The dashed lines denote the source-lens relative proper motion in the rectilinear reference frame. The yellow circles show the positions of the source at different times (labeled in *italic text*) in the different frames. The vectors pointing from the origin to the lens are the source-lens minimum separation vector $\boldsymbol{u_0}$. The vectors perpendicular to $\boldsymbol{u_0}$ are in the direction of the source-lens relative proper motion, have magnitude equal to $(t_r - t_0)/t_E$, for each frame's respective values of t_0 and t_E, and are labeled $\boldsymbol{\tau}$. The gray arrow is the microlensing parallax motion vector evaluated at the reference time $\pi_E \boldsymbol{P}(t_r)$.

6.3.3 Geocentric projected rectilinear component

In the previous section, the accelerating geocentric ("geo") frame was defined by modifying the rectilinear heliocentric ("hel") frame with parallax

$$\boldsymbol{u}^{\text{geo}}(t) = \boldsymbol{u}^{\text{hel}}(t) - \pi_E \boldsymbol{P}(t), \tag{6.17}$$

where

$$\boldsymbol{u}^{\text{hel}}(t) = \boldsymbol{u}_0^{\text{hel}} + \left(\frac{t - t_0^{\text{hel}}}{t_E^{\text{hel}}} \right) \hat{\boldsymbol{\mu}}_{\boldsymbol{SL}}^{\text{hel}} \tag{6.18}$$

is the rectilinear portion and $\pi_E \boldsymbol{P}(t)$ describes the accelerating portion.

In this section, we define a new rectilinear frame ("geo,t_r")

$$\begin{aligned}
\boldsymbol{\theta}_{\boldsymbol{S}}^{\text{geo},t_r}(t) &= \boldsymbol{\theta}_{\boldsymbol{S}}^{\text{hel}}(t) + \pi_S[\boldsymbol{P}(t_r) + (t - t_r)\dot{\boldsymbol{P}}(t_r)] && (6.19)\\
\boldsymbol{\theta}_{\boldsymbol{L}}^{\text{geo},t_r}(t) &= \boldsymbol{\theta}_{\boldsymbol{L}}^{\text{hel}}(t) + \pi_L[\boldsymbol{P}(t_r) + (t - t_r)\dot{\boldsymbol{P}}(t_r)] && (6.20)\\
\boldsymbol{u}^{\text{geo},t_r}(t) &= \boldsymbol{u}^{\text{hel}}(t) - \pi_E[\boldsymbol{P}(t_r) + (t - t_r)\dot{\boldsymbol{P}}(t_r)]. && (6.21)
\end{aligned}$$

where t_r is an arbitrarily chosen reference time.[4] At time $t = t_r$, this new rectilinear frame $\boldsymbol{u}^{\text{geo},t_r}(t)$ has the same position and velocity as the accelerating geocentric frame, i.e. $\boldsymbol{u}^{\text{geo},t_r}(t_r) = \boldsymbol{u}^{\text{geo}}(t_r)$ and $\dot{\boldsymbol{u}}^{\text{geo},t_r}(t_r) = \dot{\boldsymbol{u}}^{\text{geo}}(t_r)$. This formalism was first introduced in An et al. 2002, and popularized in Gould 2004. In the microlensing literature convention, this is commonly called the geocentric formalism, and this rectilinear frame is known as the geocentric frame. However, to avoid confusion between the true geocentric frame which is accelerating, we call this rectilinear frame the geocentric projected reference frame at time t_r ("geo, t_r"), or geoprojected frame for short.

Differentiating Equation 6.21 with respect to time, and multiplying through by θ_E yields the relationship between the source-lens relative proper motions in the heliocentric and geoprojected frames:

$$\boldsymbol{\mu}_{\boldsymbol{SL}}^{\text{geo},t_r} = \boldsymbol{\mu}_{\boldsymbol{SL}}^{\text{hel}} - \pi_{LS}\dot{\boldsymbol{P}}(t_r). \tag{6.22}$$

We can also recast the geocentric frame to use the geoprojected frame as the rectilinear reference, instead of using the heliocentric frame:

$$\begin{aligned}
\boldsymbol{u}^{\text{geo}}(t) &= \boldsymbol{u}^{\text{hel}}(t) - \pi_E \boldsymbol{P}(t) && (6.23)\\
&= \boldsymbol{u}^{\text{geo},t_r}(t) + \pi_E[\boldsymbol{P}(t_r) + (t - t_r)\dot{\boldsymbol{P}}(t_r)] - \pi_E \boldsymbol{P}(t). && (6.24)
\end{aligned}$$

There are several historical reasons for working in the geocentric projected frame instead of the heliocentric frame. For sufficiently short duration microlensing events, the geocentric

---

[3] $\boldsymbol{\pi_E}$ counts as two parameters because it has both magnitude and direction. It is also sometimes parameterized as π_E and ϕ, where ϕ is the direction of the relative proper motion.

[4] This reference time is called t_c in An et al. (2002) and t_p in Gould (2004). It is commonly denoted $t_{0,par}$ in more recent microlensing literature, where "par" is short for "parameter" (Skowron, Udalski, Gould, et al. 2011).

projected frame provides a simple way to approximate Earth's orbital motion as linear motion with higher order perturbations, such as a constant acceleration term, or a constant jerk term (An et al. 2002; Gould 2004; Smith, Mao, and Paczyński 2003). This has enabled the discovery of degeneracies between microlensing parameters, which in turn uncovered solutions to microlensing events that had initially been missed.

6.3.4 Converting between heliocentric and geoprojected photometric microlensing parameters

Suppose we have photometric microlensing parameters t_0, u_0, t_E, $\boldsymbol{\pi_E}$ calculated in the heliocentric frame that we wish to convert to parameters in the geoprojected frame.

Before diving into the formulae, consider the conceptual reason why these values will change. The source-lens relative proper motion $\boldsymbol{\mu_{SL}}$ will change, both magnitude and direction. By virtue of the point above, $\boldsymbol{\pi_E}$ will change since it encodes the direction of $\boldsymbol{\mu_{SL}}$ ($\boldsymbol{\pi_E} = \pi_E \boldsymbol{\hat{\mu}_{SL}}$) and t_E will change because it encodes the magnitude of $\boldsymbol{\mu_{SL}}$ ($t_E = \theta_E/\mu_{SL}$). Recall from Chapter 6.3.2 that π_E (the scalar quantity) does not change. Finally, the impact parameter $\boldsymbol{u_0}$ and time of closest approach t_0 will change.

First, we convert $\boldsymbol{\pi_E}$ and t_E; here we very closely follow Gould (2004). Equation 6.22 is used to convert $\boldsymbol{\pi_E}$ and t_E. With photometry alone, we cannot measure μ_{SL}. To convert into quantities we have, divide Equation 6.22 through by π_{LS}, defining

$$\tilde{\boldsymbol{v}}^{\mathrm{geo},t_r} = \tilde{\boldsymbol{v}}^{\mathrm{hel}} - \dot{\boldsymbol{P}}(t_r) \tag{6.25}$$

where

$$\tilde{\boldsymbol{v}} = \frac{\boldsymbol{\mu_{SL}}}{\pi_{LS}} = \frac{\boldsymbol{\pi_E}}{\pi_E^2}\frac{1}{t_E}. \tag{6.26}$$

Thus we have

$$\tilde{\boldsymbol{v}}^{\mathrm{hel}} = \frac{\boldsymbol{\pi_E}^{\mathrm{hel}}}{\pi_E^2}\frac{1}{t_E^{\mathrm{hel}}} \tag{6.27}$$

$$\tilde{\boldsymbol{v}}^{\mathrm{geo},t_r} = \frac{\boldsymbol{\pi_E}^{\mathrm{hel}}}{\pi_E^2}\frac{1}{t_E^{\mathrm{hel}}} - \dot{\boldsymbol{P}}(t_r). \tag{6.28}$$

Since by definition, $\boldsymbol{\pi_E} \parallel \boldsymbol{\mu_{SL}} \parallel \tilde{\boldsymbol{v}}$,

$$\boxed{\boldsymbol{\pi_E}^{\mathrm{geo},t_r} = \pi_E \frac{\tilde{\boldsymbol{v}}^{\mathrm{geo},t_r}}{|\tilde{\boldsymbol{v}}^{\mathrm{geo},t_r}|}.} \tag{6.29}$$

And since $\pi_E t_E^{\mathrm{geo},t_r} = 1/|\tilde{\boldsymbol{v}}^{\mathrm{geo},t_r}|$ and $\pi_E t_E^{\mathrm{hel}} = 1/|\tilde{\boldsymbol{v}}^{\mathrm{hel}}|$,

$$\boxed{t_E^{\mathrm{geo},t_r} = t_E^{\mathrm{hel}} \frac{|\tilde{\boldsymbol{v}}^{\mathrm{hel}}|}{|\tilde{\boldsymbol{v}}^{\mathrm{geo},t_r}|}.} \tag{6.30}$$

Next, we convert t_0 and $\boldsymbol{u}_{\mathbf{0}}$. To do this, we exploit the orthogonality definition: $\boldsymbol{u}_{\mathbf{0}}^{\mathrm{geo},t_r} \cdot \hat{\boldsymbol{\mu}}_{\boldsymbol{SL}}^{\mathrm{geo},t_r} = 0$. First, write $\boldsymbol{u}^{\mathrm{geo},t_r}(t)$ such that all the time-dependent terms are grouped together.

$$
\begin{aligned}
\boldsymbol{u}^{\mathrm{geo},t_r}(t) &= \boldsymbol{u}^{\mathrm{hel}}(t) - \pi_E[\boldsymbol{P}(t_r) + (t - t_r)\dot{\boldsymbol{P}}(t_r)] \\
&= \boldsymbol{u}_{\mathbf{0}}^{\mathrm{hel}} + \Big(\frac{t - t_0^{\mathrm{hel}}}{\theta_E}\Big)\boldsymbol{\mu}_{\boldsymbol{SL}}^{\mathrm{hel}} - \pi_E[\boldsymbol{P}(t_r) + (t - t_r)\dot{\boldsymbol{P}}(t_r)] \\
&= \boldsymbol{u}_{\mathbf{0}}^{\mathrm{hel}} + \Big(\frac{t - t_0^{\mathrm{hel}}}{\theta_E}\Big)(\boldsymbol{\mu}_{\boldsymbol{SL}}^{\mathrm{geo},t_r} + \pi_{LS}\dot{\boldsymbol{P}}(t_r)) - \pi_E[\boldsymbol{P}(t_r) + (t - t_r)\dot{\boldsymbol{P}}(t_r)] \\
&= \boldsymbol{u}_{\mathbf{0}}^{\mathrm{hel}} + \Big(\frac{t - t_0^{\mathrm{hel}}}{t_E^{\mathrm{geo},t_r}}\Big)\hat{\boldsymbol{\mu}}_{\boldsymbol{SL}}^{\mathrm{geo},t_r} - \pi_E[\boldsymbol{P}(t_r) + (t_0^{\mathrm{hel}} - t_r)\dot{\boldsymbol{P}}(t_r)].
\end{aligned}
\tag{6.31}
$$

Then dot $\boldsymbol{u}_{\mathbf{0}}^{\mathrm{geo},t_r} = \boldsymbol{u}^{\mathrm{geo},t_r}(t_0^{\mathrm{geo},t_r})$ against $\boldsymbol{\mu}_{\boldsymbol{SL}}^{\mathrm{geo},t_r}$ and impose the orthogonality condition:

$$
\begin{aligned}
\boldsymbol{u}^{\mathrm{geo},t_r}(t_0^{\mathrm{geo},t_r}) \cdot \hat{\boldsymbol{\mu}}_{\boldsymbol{SL}}^{\mathrm{geo},t_r} &= \Bigg[\boldsymbol{u}_{\mathbf{0}}^{\mathrm{hel}} + \Big(\frac{t_0^{\mathrm{geo},t_r} - t_0^{\mathrm{hel}}}{t_E^{\mathrm{geo},t_r}}\Big)\hat{\boldsymbol{\mu}}_{\boldsymbol{SL}}^{\mathrm{geo},t_r} - \pi_E[\boldsymbol{P}(t_r) + (t_0^{\mathrm{hel}} - t_r)\dot{\boldsymbol{P}}(t_r)]\Bigg] \cdot \hat{\boldsymbol{\mu}}_{\boldsymbol{SL}}^{\mathrm{geo},t_r} \\
&= \frac{t_0^{\mathrm{geo},t_r} - t_0^{\mathrm{hel}}}{t_E^{\mathrm{geo},t_r}} + \Bigg[\boldsymbol{u}_{\mathbf{0}}^{\mathrm{hel}} - \pi_E[\boldsymbol{P}(t_r) + (t_0^{\mathrm{hel}} - t_r)\dot{\boldsymbol{P}}(t_r)]\Bigg] \cdot \hat{\boldsymbol{\mu}}_{\boldsymbol{SL}}^{\mathrm{geo},t_r} \\
&= 0.
\end{aligned}
\tag{6.32}
$$

Solving for t_0^{geo,t_r} yields

$$
\boxed{t_0^{\mathrm{geo},t_r} = t_0^{\mathrm{hel}} - t_E^{\mathrm{geo},t_r}\hat{\boldsymbol{\pi}}_{\boldsymbol{E,SL}}^{\mathrm{geo},t_r} \cdot \Bigg[\boldsymbol{u}_{\mathbf{0}}^{\mathrm{hel}} - \pi_E[\boldsymbol{P}(t_r) + (t_0^{\mathrm{hel}} - t_r)\dot{\boldsymbol{P}}(t_r)]\Bigg],}
\tag{6.33}
$$

where we have used the fact that $\hat{\boldsymbol{\mu}}_{\boldsymbol{SL}}^{\mathrm{geo},t_r} = \hat{\boldsymbol{\pi}}_{\boldsymbol{E,SL}}^{\mathrm{geo},t_r}$, since by definition $\boldsymbol{\pi}_{\boldsymbol{E}} \parallel \boldsymbol{\mu}_{\boldsymbol{SL}}$.

We can then substitute t_0^{geo,t_r} into $\boldsymbol{u}^{\mathrm{geo}}(t)$ (Equation 6.31) to solve for $\boldsymbol{u}_{\mathbf{0}}^{\mathrm{geo},t_r}$:

$$
\boxed{\boldsymbol{u}_{\mathbf{0}}^{\mathrm{geo},t_r} = \boldsymbol{u}_{\mathbf{0}}^{\mathrm{hel}} + \Big(\frac{t_0^{\mathrm{geo},t_r} - t_0^{\mathrm{hel}}}{t_E^{\mathrm{geo},t_r}}\Big)\hat{\boldsymbol{\pi}}_{\boldsymbol{E,SL}}^{\mathrm{geo},t_r} - \pi_E[\boldsymbol{P}(t_r) + (t_0^{\mathrm{hel}} - t_r)\dot{\boldsymbol{P}}(t_r)].}
\tag{6.34}
$$

Alternatively, by evaluating Equation 6.17 at $t = t_r$ we can solve for $\boldsymbol{u}_{\mathbf{0}}^{\mathrm{geo},t_r}$:

$$
\boxed{\boldsymbol{u}_{\mathbf{0}}^{\mathrm{geo},t_r} = \boldsymbol{u}_{\mathbf{0}}^{\mathrm{hel}} + \Big(\frac{t_r - t_0^{\mathrm{hel}}}{t_E^{\mathrm{hel}}}\Big)\hat{\boldsymbol{\pi}}_{\boldsymbol{E,SL}}^{\mathrm{hel}} - \Big(\frac{t_r - t_0^{\mathrm{geo},t_r}}{t_E^{\mathrm{geo},t_r}}\Big)\hat{\boldsymbol{\pi}}_{\boldsymbol{E,SL}}^{\mathrm{geo},t_r} - \pi_E\boldsymbol{P}(t_r).}
\tag{6.35}
$$

Note that this equation can be “read off” from the vectors in Figure 6.2 (which serves to illustrate Equation 6.17.)

For completeness, we list the conversions from geoprojected to heliocentric microlensing parameters below. The derivations are analogous to above. Alternatively, they can be deduced from the symmetry of the equations, by making the exchange ${}^{\mathrm{hel}} \leftrightarrow {}^{\mathrm{geo},t_r}$ and changing the sign of the $\pi_E[\boldsymbol{P}(t_r) + (t_0 - t_r)\dot{\boldsymbol{P}}(t_r)]$ terms.

$$\boxed{\boldsymbol{\pi}_{\boldsymbol{E}}^{\mathrm{hel}} = \pi_E \frac{\tilde{\boldsymbol{v}}^{\mathrm{hel}}}{|\tilde{\boldsymbol{v}}^{\mathrm{hel}}|}} \tag{6.36}$$

$$\boxed{t_E^{\mathrm{hel}} = t_E^{\mathrm{geo},t_r} \frac{|\tilde{\boldsymbol{v}}^{\mathrm{geo},t_r}|}{|\tilde{\boldsymbol{v}}^{\mathrm{hel}}|}} \tag{6.37}$$

$$\boxed{t_0^{\mathrm{hel}} = t_0^{\mathrm{geo},t_r} - t_E^{\mathrm{hel}} \hat{\boldsymbol{\pi}}_{\boldsymbol{E,SL}}^{\mathrm{hel}} \cdot \left[\boldsymbol{u}_{\boldsymbol{0}}^{\mathrm{geo},t_r} + \pi_E[\boldsymbol{P}(t_r) + (t_0^{\mathrm{geo},t_r} - t_r)\dot{\boldsymbol{P}}(t_r)]\right]} \tag{6.38}$$

$$\boxed{\boldsymbol{u}_{\boldsymbol{0}}^{\mathrm{hel}} = \boldsymbol{u}_{\boldsymbol{0}}^{\mathrm{geo},t_r} + \left(\frac{t_0^{\mathrm{hel}} - t_0^{\mathrm{geo},t_r}}{t_E^{\mathrm{hel}}}\right) \hat{\boldsymbol{\pi}}_{\boldsymbol{E,SL}}^{\mathrm{hel}} + \pi_E[\boldsymbol{P}(t_r) + (t_0^{\mathrm{geo},t_r} - t_r)\dot{\boldsymbol{P}}(t_r)]} \tag{6.39}$$

$$\boxed{\boldsymbol{u}_{\boldsymbol{0}}^{\mathrm{hel}} = \boldsymbol{u}_{\boldsymbol{0}}^{\mathrm{geo},t_r} + \left(\frac{t_r - t_0^{\mathrm{geo},t_r}}{t_E^{\mathrm{geo},t_r}}\right) \hat{\boldsymbol{\pi}}_{\boldsymbol{E,SL}}^{\mathrm{geo},t_r} - \left(\frac{t_r - t_0^{\mathrm{hel}}}{t_E^{\mathrm{hel}}}\right) \hat{\boldsymbol{\pi}}_{\boldsymbol{E,SL}}^{\mathrm{hel}} + \pi_E \boldsymbol{P}(t_r)} \tag{6.40}$$

6.3.5 Converting between heliocentric and geoprojected astrometric microlensing parameters

The photometry conversions are derived in the previous section. There are six astrometry-only parameters. Here we parametrize them as θ_E, π_S, $\boldsymbol{\mu_S}$, and $\boldsymbol{\theta_{S,0}}$.

First, we consider what parameters are independent of choice of rectilinear frame. Distances (d_L, d_S, or equivalently π_L, π_S) are independent. Mass does not change with frame choice, so θ_E is also frame independent. We used these facts in the previous section's derivations.

Next, we consider which parameters are dependent on the choice of rectilinear frame. Parameters that depend on time will differ between the two frames. This includes the position at closest approach and proper motions of the source and lens.

Eqs. 6.19 and 6.20 provide the conversions to the source and lens position. By substituting t_0^{geo,t_r} (as calculated in the previous section), we can get $\boldsymbol{\theta}_{\boldsymbol{S,0}}^{\mathrm{geo},t_r}$ and $\boldsymbol{\theta}_{\boldsymbol{L,0}}^{\mathrm{geo},t_r}$:

$$\boldsymbol{\theta}_{\boldsymbol{S,0}}^{\mathrm{geo},t_r} \equiv \boldsymbol{\theta}_{\boldsymbol{S}}^{\mathrm{geo},t_r}(t_0^{\mathrm{geo},t_r}) = \boldsymbol{\theta}_{\boldsymbol{S}}^{\mathrm{hel}}(t_0^{\mathrm{geo},t_r}) + \pi_S[\boldsymbol{P}(t_r) + (t_0^{\mathrm{geo},t_r} - t_r)\dot{\boldsymbol{P}}(t_r)] \tag{6.41}$$

$$\boldsymbol{\theta}_{\boldsymbol{L,0}}^{\mathrm{geo},t_r} \equiv \boldsymbol{\theta}_{\boldsymbol{L}}^{\mathrm{geo},t_r}(t_0^{\mathrm{geo},t_r}) = \boldsymbol{\theta}_{\boldsymbol{L}}^{\mathrm{hel}}(t_0^{\mathrm{geo},t_r}) + \pi_L[\boldsymbol{P}(t_r) + (t_0^{\mathrm{geo},t_r} - t_r)\dot{\boldsymbol{P}}(t_r)]. \tag{6.42}$$

Eqs. 6.19 and 6.20 also provide the conversions to the source and lens proper motion. Differentiating with respect to time,

$$\boldsymbol{\mu_S}^{\text{geo},t_r} = \boldsymbol{\mu_S}^{\text{hel}} + \pi_S \dot{\boldsymbol{P}}(t_r) \tag{6.43}$$

$$\boldsymbol{\mu_L}^{\text{geo},t_r} = \boldsymbol{\mu_L}^{\text{hel}} + \pi_L \dot{\boldsymbol{P}}(t_r). \tag{6.44}$$

6.4 PSBL microlensing

Point-source binary-lens (PSBL) microlensing introduces three additional parameters: the mass ratio q of the lenses, the projected separation s of the lenses, and the angle between the source-lens relative proper motion and the binary axis α. We explain each of these parameters in more detail in the next paragraph. Note that this assumes a *static* binary lens; if there is orbital motion, additional parameters are needed.

We define the mass ratio as the mass of the secondary to the primary

$$q = \frac{m_2}{m_1}. \tag{6.45}$$

Note that there is no condition on the masses of the primary or secondary; the definition of primary and secondary is defined by different subfields' convention[5]. The projected separation of the lenses s is given in units of the Einstein radius θ_E, where the mass used to calculate θ_E is the total mass of the lenses $M = m_1 + m_2$. We define the binary axis to point from the secondary toward the primary. The angle that the source-lens relative proper motion $\boldsymbol{\mu_{SL}}$ makes with binary axis α is measured East of North (counterclockwise) from the binary axis.

6.4.1 Definition of source-lens minimum separation

The concept of a minimum source-lens separation is uniquely defined when the source and lens are single objects. However, it is unclear what this means when the lens is a binary system. Is it the minimum separation between the source and primary lens? binary lens center of mass? binary lens geometric center? where maximum magnification occurs?

For a photometric binary microlensing event light curve, there are eight geometric parameters of interest: t_0, u_0, t_E, $\boldsymbol{\pi_E}$, q, s, α. Of these parameters, u_0 and t_0 depend on the choice of how this minimum separation is defined. The following section explores how defining the lens position as the center of mass vs. the geometric midpoint of the lenses affects t_0 and u_0 and how to relate the two definitions. These are not the only two possibilities, but we choose to use them as a concrete example here.

---

[5] For planetary microlensing, the primary is the star and the secondary is the planet; for stellar binaries the definition is not as clear-cut; it depends on the subfield. For example, in single-lined spectroscopic binaries, primary labels the visible companion, secondary labels the unseen companion even though it may be more massive.

Let $\boldsymbol{x_{Li}} = \boldsymbol{\theta_{Li}}/\theta_E$ and m_i denote the angular position normalized by θ_E and mass of the i-th lens. Since the lens is a binary system, $i = 1, 2$.

The binary's geometric midpoint $\boldsymbol{x_{L,mid}}$ and center of mass $\boldsymbol{x_{L,com}}$ are given by

$$\boldsymbol{x_{L,mid}} = \frac{1}{2}(\boldsymbol{x_{L1}} + \boldsymbol{x_{L2}}) \tag{6.46}$$

$$\boldsymbol{x_{L,com}} = \frac{m_1\boldsymbol{x_{L1}} + m_2\boldsymbol{x_{L2}}}{m_1 + m_2}. \tag{6.47}$$

The binary separation vector points from the secondary to the primary,

$$\boldsymbol{s} = \boldsymbol{x_{L1}} - \boldsymbol{x_{L2}}. \tag{6.48}$$

Next, rewrite $\boldsymbol{x_{L1}}$ and $\boldsymbol{x_{L2}}$ in terms of $\boldsymbol{x_{L,com}}$, $\boldsymbol{s}$, and q:

$$\boldsymbol{x_{L1}} = \boldsymbol{x_{L,com}} + \frac{1}{1+q}\boldsymbol{s} \tag{6.49}$$

$$\boldsymbol{x_{L2}} = \boldsymbol{x_{L,com}} - \frac{q}{1+q}\boldsymbol{s}. \tag{6.50}$$

Do the same with $\boldsymbol{x_{L,mid}}$ (although in this case, q is irrelevant):

$$\boldsymbol{x_{L1}} = \boldsymbol{x_{L,mid}} + \frac{1}{2}\boldsymbol{s} \tag{6.51}$$

$$\boldsymbol{x_{L2}} = \boldsymbol{x_{L,mid}} - \frac{1}{2}\boldsymbol{s}. \tag{6.52}$$

Now equate the two expressions for $\boldsymbol{x_{L1}}$ (or equivalently, $\boldsymbol{x_{L2}}$) to relate $\boldsymbol{x_{L,mid}}$ and $\boldsymbol{x_{L,com}}$ via $\boldsymbol{s}$ and q. Doing so yields the relationship

$$\boldsymbol{x_{L,mid}} - \boldsymbol{x_{L,com}} = q'\boldsymbol{s}, \tag{6.53}$$

where

$$q' \equiv \frac{1-q}{2(1+q)}. \tag{6.54}$$

Figure 6.3 shows the geometry of the setup. The component of the center of mass-geometric midpoint separation parallel to the source-lens proper motion is given by $q's\cos\alpha$. The time required for the source to traverse this distance is t_E. Thus, to convert between t_0,

$$\boxed{t_{0,com} = t_{0,mid} + q'st_E\cos\alpha.} \tag{6.55}$$

The component of the center of mass-geometric midpoint separation parallel to the source-lens separation vector is given by $q's\sin\alpha$. Thus, to convert between u_0,

$$\boxed{\boldsymbol{u_{0,com}} = \boldsymbol{u_{0,mid}} + q's\sin\alpha\,\boldsymbol{\hat{u}_{0,com}}.} \tag{6.56}$$

Note that $\boldsymbol{u_{0,com}} \parallel \boldsymbol{u_{0,mid}}$, so Equation 6.56 can also be written $|\boldsymbol{u_{0,com}}| = |\boldsymbol{u_{0,mid}}| + q's\sin\alpha$.

6.4.2 Converting between heliocentric and geoprojected binary microlensing parameters

Of the three binary parameters, q and s are independent of the choice of the rectilinear frame, since mass and distances do not change with choice of frame. However, α does change, because it is defined as the angle between the source-lens relative proper motion vector and the binary axis. While the binary axis remains the same, the source-lens relative proper motion changes as discussed in Chapter 6.3.4.

First, convert the photometric parameters t_0, u_0, t_E, and $\boldsymbol{\pi_E}$ as outlined in Chapter 6.3.4. Next, calculate the angle of the relative proper motion vector (East of North)

$$\phi^{\mathrm{geo},t_r} = \arctan(\pi_{E,E}^{\mathrm{geo},t_r}/\pi_{E,N}^{\mathrm{geo},t_r}) \tag{6.57}$$

$$\phi^{\mathrm{hel}} = \arctan(\pi_{E,E}^{\mathrm{hel}}/\pi_{E,N}^{\mathrm{hel}}), \tag{6.58}$$

where $\pi_{E,E}$ and $\pi_{E,N}$ are the East and North components, respectively, of the microlensing parallax vector $\boldsymbol{\pi_E}$. α and ϕ in the two frames are related via

$$\alpha^{\mathrm{geo},t_r} = \alpha^{\mathrm{hel}} - (\phi^{\mathrm{hel}} - \phi^{\mathrm{geo},t_r}). \tag{6.59}$$

To convert the other 5 photometric parameters (or 6 astrometric parameters) in common with PSPL microlensing events, the conversions are generalized from those presented in Chapter 6.3.4 and Chapter 6.3.5. The Einstein radius is now defined as the total mass of the binary system, and the position (e.g., binary center of mass, geometric center, primary, secondary) adopted for the lens origin must be explicitly defined. Beyond that, the conversions are identical. As a final note, it is possible to choose both a different definition for the lens origin, as well as different rectilinear frame; if this occurs, both must be taken into account when performing the conversions.

6.5 Relative conventions

Microlensing is concerned with how the source and lens(es) are moving relative to each other. However, "relative" can be defined in two directions—for example, as source relative to lens, or lens relative to source. This introduces a possible point of confusion if "relative" is not defined explicitly.

6.5.1 Source-lens vs. lens-source relative proper motion

Following Gould (2004), most photometric microlensing papers since then have worked in the lens-source frame, i.e. the frame where the source is at rest. Older theoretical astrometric microlensing papers (Hog et al. 1995; Miyamoto et al. 1995; Walker 1995), and more recent observational astrometric microlensing papers (Lam, Lu, Udalski, et al. 2022a,b; Lu et al. 2016) work in the source-lens frame, i.e. the frame where the lens is at rest. This means that

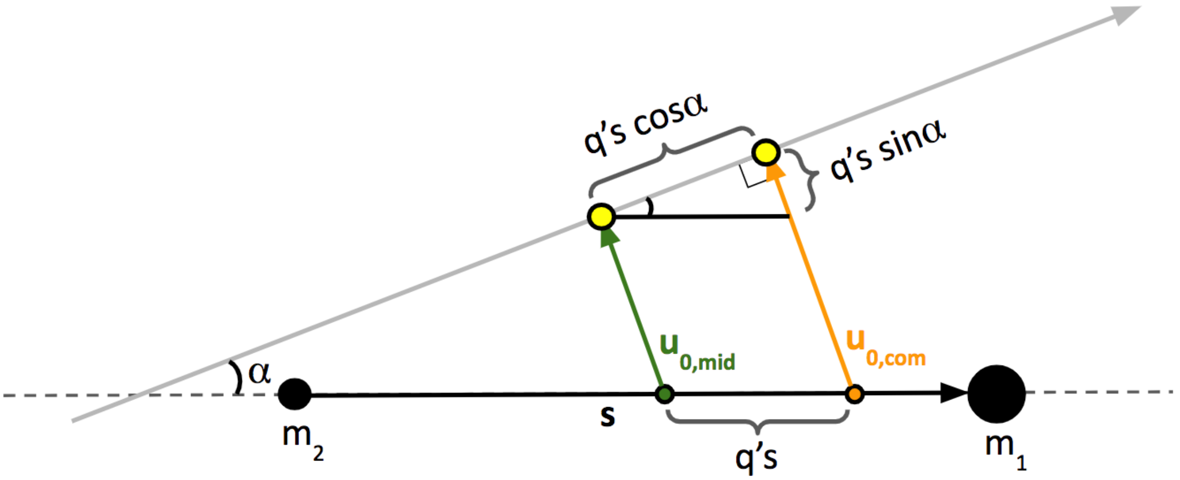

Figure 6.3: The values of t_0 and u_0 depend on whether the binary lens' center of mass or geometric midpoint is used as the lens position. The lenses are the black circles labeled m_1 and m_2. The binary projected separation vector $\boldsymbol{s}$ is the black arrow. The light gray arrow shows the direction of the source-lens relative proper motion $\boldsymbol{\mu_{SL}}$. Then angle between the separation vector and the relative proper motion is α. The position of the lens' center of mass and geometric midpoint are shown as the small orange and green circles, respectively. The minimum source-lens separation vectors using the center of mass and geometric midpoint are shown as the orange and green arrows, and labeled $\boldsymbol{u_{0,com}}$ and $\boldsymbol{u_{0,mid}}$, respectively. The yellow circles show the source position at those times. The magnitude of the difference between $\boldsymbol{u_{0,com}}$ and $\boldsymbol{u_{0,mid}}$ is $q's$, where q' is defined in Equation 6.54. The component of the difference along the direction of the relative proper motion is given by $q's\cos\alpha$, while the component along the source-lens separation vector is given by $q's\sin\alpha$.

across these two conventions, the direction of the relative proper motions, and in turn the microlensing parallax vector, will differ by a sign:

$$\boldsymbol{\mu_{SL}} = -\boldsymbol{\mu_{LS}}$$
$$\boldsymbol{\pi_E}\ (SL)\ \text{convention} = -\boldsymbol{\pi_E}\ (LS)\ \text{convention}$$

6.5.2 Angle of relative proper motion to binary lens axis

The angle between the relative proper motion and the binary lens axis α can differ by 180° depending on several convention choices. This includes the choice of which lens is primary vs. secondary, the direction of the binary axis as primary-secondary or secondary-primary, the choice of relative proper motion to be source-lens vs. lens-source, and whether the angle is measured clockwise or counterclockwise from the binary axis. For example, Skowron,

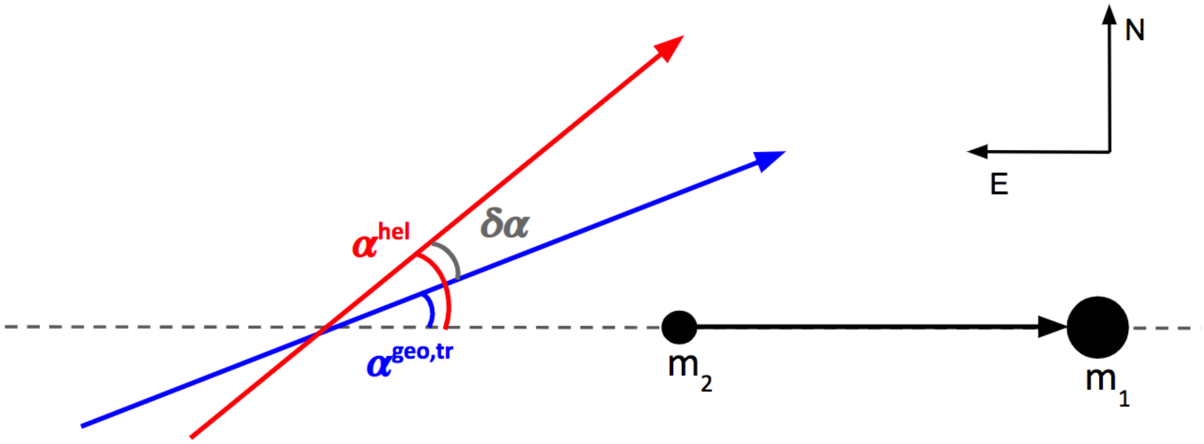

Figure 6.4: Converting α between the heliocentric and geoprojected frames. α is the angle between the binary axis and the source-lens relative proper motion. The direction of relative proper motion in the heliocentric and geoprojected frames are shown as the red and blue arrows, respectively. The binary axis is shown as the dashed line, and the binary separation vector is shown as the black arrow. α in the heliocentric and geoprojected frames are labeled. The difference between the two angles is labeled $\delta\alpha$.

Udalski, Gould, et al. 2011 and Poleski et al. 2019 differ in their conventions by 180°. Care must be taken in the various definitions that are needed to calculate α.

6.6 τ-β vs. E-N coordinate system

In physics, the impact parameter is a distance, and hence always a non-negative quantity. However, in microlensing literature convention, the impact parameter u_0 carries a sign with it for reasons we explain below.

6.6.1 Why is the impact parameter a signed quantity?

In a rectilinear reference frame, the direction of the source-lens separation vector $\boldsymbol{u_0}$ (Equation 6.5) has no impact on the appearance of a microlensing light curve[6]; only the magnitude of the separation $|\boldsymbol{u_0}|$ matters. However, once acceleration is introduced (e.g., parallax due to Earth's orbital motion around the Sun), this introduces directionality into the problem and breaks the symmetry of a rectilinear frame. Now the direction of the source-lens separation *does* matter, because the parallax vector $\boldsymbol{P}(t)$ introduces a preferred direction into

---

[6] $\boldsymbol{u_0}$ *does* have an effect on the astrometric signal, but only in terms of its absolute orientation on the sky.

the problem. Because by definition $\boldsymbol{u_0}$ is perpendicular to $\boldsymbol{\mu_{SL}}$, there are two possible orientations for $\boldsymbol{u_0}$, where the angle between $\boldsymbol{u_0}$ and $\boldsymbol{\mu_{SL}}$ is either 90° or 270°. In microlensing convention, these two possibilities are distinguished by assigning a sign to $|\boldsymbol{u_0}|$. The question now is how exactly that sign is assigned to $|\boldsymbol{u_0}|$. There exist at least two conventions in the literature on how to do this—one using a coordinate system defined with respect to the relative proper motion of the system, and one in a coordinate system defined with respect to the sky.

6.6.2 τ-β: coordinates relative to the system's proper motion

Gould (2004) works in a coordinate system with respect to the relative proper motion of the system, which we dub the "τ-β" coordinate system. Gould (2004) defines (τ, β) as the position of the lens relative to the source in units of θ_E; to make the system right-handed, it is also defined that if $u_0 > 0$, then the lens is passing the source on its right as seen from Earth. We claim that the definition above is equivalent to the following interpretation.

Define

$$\boldsymbol{\hat{\tau}} = (\tau_E, \tau_N) = \frac{1}{\pi_E}(\pi_{E,E}, \pi_{E,N}), \tag{6.60}$$

which encodes direction of the source-lens relative proper motion[7], and

$$\boldsymbol{\hat{\beta}} = (\beta_E, \beta_N) = \frac{1}{\pi_E}(-\pi_{E,N}, \pi_{E,E}), \tag{6.61}$$

which is orthogonal to $\boldsymbol{\hat{\tau}}$. By this definition, $(\boldsymbol{\tau}, \boldsymbol{\beta})$ is always right-handed. The source-lens separation is $\boldsymbol{u_0}$ (Equation 6.5). Then the sign of u_0 is assigned as follows:

$$\begin{aligned} &\text{If } \boldsymbol{u_0} \text{ is } \textit{parallel} \text{ to } \boldsymbol{\beta}\text{, then } u_0 > 0. \\ &\text{If } \boldsymbol{u_0} \text{ is } \textit{anti-parallel} \text{ to } \boldsymbol{\beta}\text{, then } u_0 < 0. \end{aligned} \tag{6.62}$$

Conversely, if the sign of u_0 is given, then $\boldsymbol{u_0}$ can be inferred from $\boldsymbol{\hat{\tau}}$ as follows:

$$\begin{aligned} &\text{If } \mathrm{sign}(u_0) > 0\text{, then } \boldsymbol{\hat{u}_0} = (\tau_N, -\tau_E). \\ &\text{If } \mathrm{sign}(u_0) < 0\text{, then } \boldsymbol{\hat{u}_0} = (-\tau_N, \tau_E). \end{aligned} \tag{6.63}$$

6.6.3 E-N: coordinates relative to the sky

On the other hand, Lu et al. (2016) defines a coordinate system East-North on the sky. The sign of u_0 is then defined as follows:

$$\begin{aligned} &\text{If } u_{0,E} > 0\text{, then } u_0 > 0. \\ &\text{If } u_{0,E} < 0\text{, then } u_0 < 0. \end{aligned} \tag{6.64}$$

---

[7] Note that $\boldsymbol{\hat{\tau}} = \boldsymbol{\hat{\mu}}_{SL}$; this equivalent definition is to keep nomenclature consistent with Gould (2004).

Conversely, if the sign of u_0 is given, then $\boldsymbol{u_0}$ can be inferred from $\hat{\boldsymbol{\tau}}$ as follows:

$$\begin{aligned}&\text{If } \mathrm{sign}(u_0 \cdot \pi_{E,N}) > 0, \text{ then } \hat{\boldsymbol{u}}_{\boldsymbol{0}} = (\tau_N, -\tau_E).\\ &\text{If } \mathrm{sign}(u_0 \cdot \pi_{E,N}) < 0, \text{ then } \hat{\boldsymbol{u}}_{\boldsymbol{0}} = (-\tau_N, \tau_E).\end{aligned} \tag{6.65}$$

6.6.4 Comments on potential points of confusion

Note that the convention of coordinate system (i.e. τ-β vs. E-N) is an independent choice from of the convention of what "relative" means (i.e. source-lens vs. lens-source). In Equations 6.60 – 6.63, we have written everything in terms of source-lens relative positions and motions in an East-North system. However, Gould 2004 prefers to use a convention of lens-source relative positions and motions in a North-East system. We note that this choice of source-lens vs. lens-source is distinct from the concept of defining the coordinate system with respect to the relative proper motion of the system. Likewise, Equations 6.64 – 6.65 are written in terms of the source-lens relative positions and motions in an East-North system, but the idea of a coordinate system with respect to the sky can also be applied to lens-source relative positions and motions. It requires careful accounting of the sign flips introduced by the different conventions. As long as self-consistency is used within any given system, it is always possible to convert between conventions.

6.7 Examples

Some public photometric microlensing modeling codes (e.g., MulensModel, pyLIMA) work using the geoprojected rectilinear frame, using the lens-source frame convention and the τ-β convention of Gould (2004). Other codes (e.g., photometric + astrometric microlensing code BAGLE) use a source-lens frame convention using the East-North convention of Lu et al. 2016. Thus, to successfully compare model parameters across these codes requires converting the parameters across different choice of rectilinear frame and coordinate system. Here we provide some concrete examples of how to apply the conversions described above in practice.

6.7.1 Changing reference frames with a fixed set of microlensing parameters

First, we show how changing the reference frame affects the photometry and astrometry for a fixed set of microlensing parameters. In this section, we follow the coordinate system convention of Lu et al. (2016).

We generate four sets of microlensing light curves and astrometry with the parameters listed in Table 6.1. We consider a heliocentric frame, and three geoprojected frames with t_r = 57000, 57050, and 57060 MJD. The light curves and astrometry are shown in Figure 6.5. The photometry and astrometry look very different, despite having the same microlensing parameters. This shows the importance of specifying the frame and/or reference time when describing a microlensing event, and that aggregating microlensing parameters across different reference frames should not be done; aggregated events need to be in the same reference frame for valid comparisons to be made.

Parameter	Value
t_0 (MJD)	57000
u_0	-0.1
t_E (days)	120
$\pi_{E,E}$	-0.5
$\pi_{E,N}$	-0.5
m_{base} (mag)	18
b_{SFF}	0.8
θ_E (mas)	5
π_S (mas)	0.125
$x_{S0,E}$ (mas)	0
$x_{S0,N}$ (mas)	0
$\mu_{S,E}$ (mas)	5
$\mu_{S,N}$ (mas)	-5

Table 6.1: Microlensing parameters for the light curve and astrometric shift in Figure 6.5. The event is located at (RA, Dec) = (259.5, −29.0).

6.7.2 PSPL photometric conversions

Here we consider the PSPL microlensing event shown in Figure 6.6. Its photometric parameters in the convention of Lu et al. (2016) (source-lens relative frame, East-North coordinate system) in both the heliocentric frame and geocentric projected frame at $t_r = 57000$ MJD are shown in Figure 6.7. Its photometric parameters in the convention of Gould (2004) (lens-source relative frame, $\tau - \beta$) in both the heliocentric frame and geocentric projected frame at $t_r = 57000$ MJD are shown in Figure 6.8. In addition, the parameter names and values needed to reproduce this light curve using the microlensing model codes BAGLE (Lu et al. (2016) convention in the heliocentric frame) and MulensModel (Gould (2004) convention in the geocentric projected frame at $t_r = 57000$ MJD) are provided in Table 6.2. We re-emphasize that these are all identical ways of parametrizing the light curve in Figure 6.6; the only differences are the choice of reference frame and coordinate system.

6.7.3 PSBL photometric conversions

Here we consider the PSBL microlensing event shown in Figure 6.9. Its photometric parameters in the convention of Lu et al. (2016) (source-lens relative frame, East-North coordinate

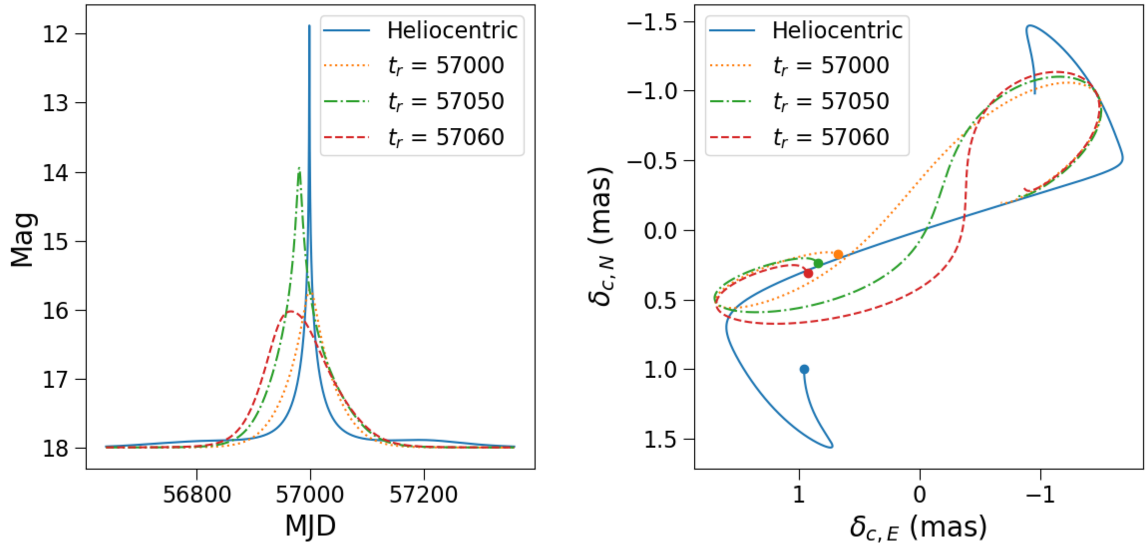

Figure 6.5: Microlensing light curve *(left)* and astrometric shift *right*. The parameters of the event are listed in Table 6.1. The reference frame and/or time is listed in the legend. The models span the time range 56640 - 57360 MJD. In the right panel, the dot shows MJD = 56640.

Name (units)	Value
t_0 (HJD)	2457317.51
t_0_par (HJD)	2457000.5
u_0	0.06
t_E (days)	659.42
pi_E_N	0.18
pi_E_E	0.13

(a) MulensModel parameters, using the Gould (2004) convention in the geocentric projected frame at $t_r = 57000$ MJD.

Name (units)	Value
t0 (MJD)	57000
u0_amp	0.5
tE (days)	300
piE_E	0.2
piE_N	−0.1

(b) BAGLE parameters, using the Lu et al. (2016) convention in the heliocentric frame.

Table 6.2: PSPL microlensing model parameters corresponding to the light curve in Figure 6.6. The event is located at (RA, Dec) = (259.0, −29.0). The source magnitude is 22 and there is no blending.

system) in both the heliocentric frame and geocentric projected frame at $t_r = 57000$ MJD are shown in Figure 6.10. Its photometric parameters in the convention of Gould (2004) (lens-source relative frame, $\tau - \beta$) in both the heliocentric frame and geocentric projected frame at $t_r = 57000$ MJD are shown in Figure 6.11. In addition, the parameter names and

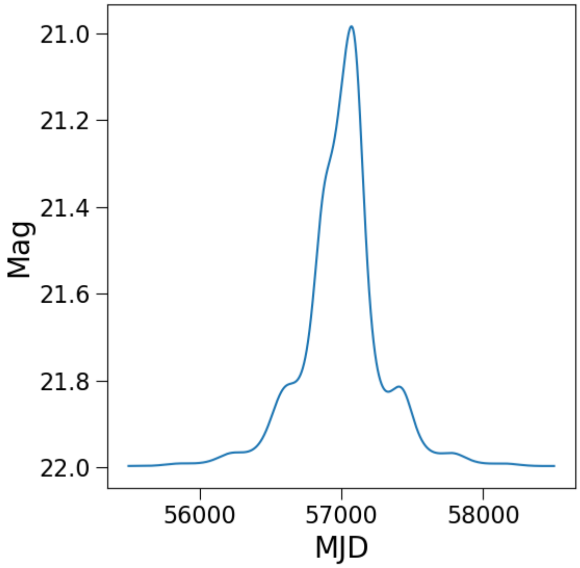

Figure 6.6: light curve for the set of microlensing parameters listed in Table 6.2. Different choices of reference frame and coordinate system will lead to different values for microlensing parameters; however, these different parameters all describe the same microlensing geometry and light curve.

values needed to reproduce this light curve using the microlensing model codes BAGLE (Lu et al. (2016) convention in the heliocentric frame) and MulensModel (Gould (2004) convention in the geocentric projected frame at $t_r = 57000$ MJD) are provided in Table 6.3. We re-emphasize that these are all identical ways of parametrizing the light curve in Figure 6.9; the only differences are the choice of reference frame and coordinate system.

6.7.4 Geoprojected with $t_r = t_{peak,phot}$

As explained in Gould (2004), by choosing t_r to equal the time of the the photometric maximum $t_{peak,phot}$, t_0 becomes uncorrelated with the other microlensing parameters. Below is an example fitting a light curve in the heliocentric formalism as well as the geoprojected formalism with $t_r = t_{peak,phot}$. The light curve is shown in Figure 6.12 with parameters listed in Table 6.4.

The fits were performed with the Bayesian microlensing modeling code BAGLE. The priors (also listed in Table 6.4) were artificially narrow and centered on the true input values for the fit to run quickly. When fitting a real microlensing event, the true parameters are obviously unknown and so this trick cannot be played; however, for the purposes of this illustration this is fine, as we are primarily interested in the correlation between parameters.

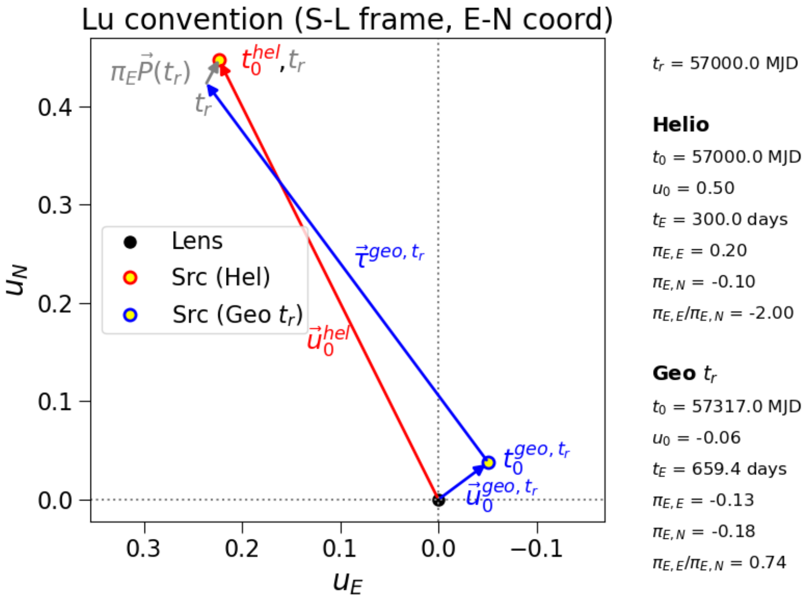

Figure 6.7: Same as Figure 6.2, but for a specific set of microlensing parameters. It lists the converted values, using the convention in Lu et al. (2016) (source-lens frame, East-North coordinate system, parallax as Sun-Earth separation). Note that because $t_r = t_0^{\text{hel}}$, $\boldsymbol{\tau}^{\text{hel}} = 0$.

Name (units)	Value
t_0 (HJD)	2456988.16
t_0_par (HJD)	2457000.5
u_0	0.24
t_E (days)	59.65
pi_E_N	−0.12
pi_E_E	−0.19
alpha (deg)	332.207
s	1.5
q	0.5

(a) MulensModel parameters, using the Gould (2004) convention in the geocentric projected frame at $t_r = 57000$ MJD.

Name (units)	Value
t0 (MJD)	57000
u0_amp	0.1
tE (days)	50
piE_E	0.2
piE_N	0.1
alpha (deg)	339
s	1.5
q	2

(b) BAGLE parameters, using the Lu et al. (2016) convention in the heliocentric frame.

Table 6.3: PSBL microlensing model parameters corresponding to the light curve in Figure 6.9. The event is located at (RA, Dec) = (259.0, −29.0). The source magnitude is 22 and there is no blending.

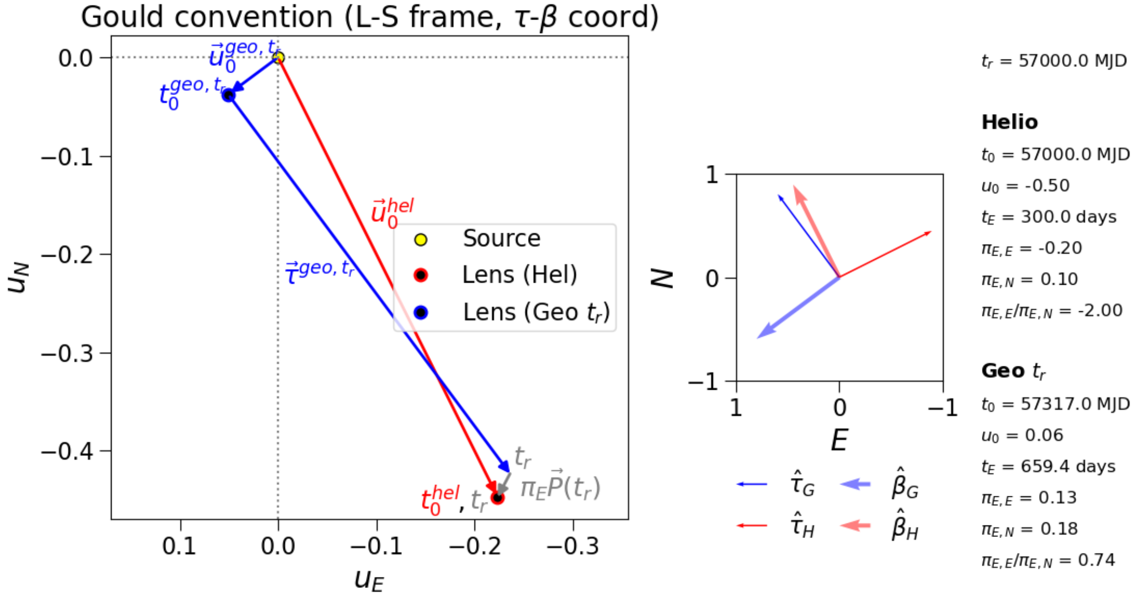

Figure 6.8: This is like Figure 6.7, but in the convention of Gould (2004) (lens-source frame, $\tau - \beta$ coordinate system, parallax as Earth-Sun separation). The small panel shows the direction of the $\hat{\boldsymbol{\tau}}$ and $\hat{\boldsymbol{\beta}}$ vectors in the heliocentric (subscript H) and geoprojected (subscript G) frames. Note that because $t_r = t_0^{\rm hel}$, $\boldsymbol{\tau}^{\rm hel} = 0$.

Figures 6.13 and 6.14 are the corresponding posteriors from the fit. As mentioned earlier, it is evident that fitting in the geoprojected formalism with $t_r = t_{peak,phot}$ results in t_0 being decorrelated with the other parameters. In the heliocentric formalism, t_0 is highly correlated with the other parameters. In addition, the posterior for t_0 is much narrower in the geoprojected formalism than the heliocentric formalism, despite the width of the prior on that parameter being the same in both fits (2 days). However, there is no "free lunch"—even if a fit is initially performed in the the geoprojected formalism, the parameters will need to be converted to the heliocentric values. In the end, the uncertainties and correlations will be the same as if the fit had just been performed in the heliocentric formalism.

6.8 Discussion

There are now several public microlensing modeling codes (e.g., MulensModel (Poleski et al. 2019), pyLIMA (Bachelet et al. 2017), VBBINARYLENSING (Bozza et al. 2018)) that mainly work in the geocentric projected formalism. This note can be used to compare the outputs to codes that work in the heliocentric formalism, such as BAGLE.

For simplicity throughout, we have said the heliocentric frame is a non-accelerating rectilinear frame. However, the Sun is actually accelerating because of Jupiter and other Solar

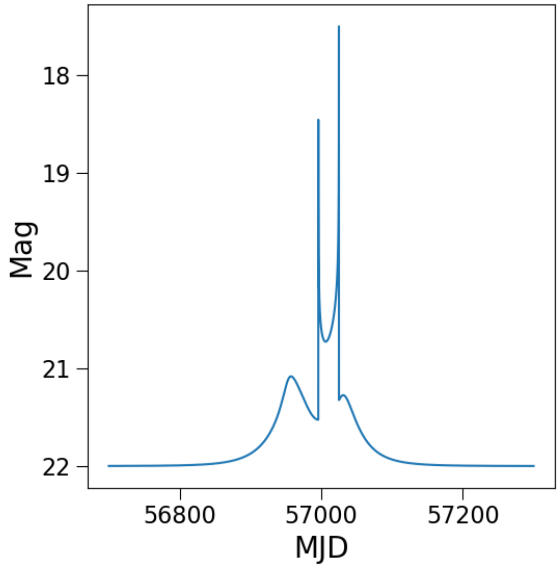

Figure 6.9: light curve for the set of microlensing parameters listed in Table 6.3. Different choices of reference frame and coordinate system will lead to different values for microlensing parameters; however, these different parameters all describe the same microlensing geometry and light curve.

Name (units)	Values (Lu et al. (2016) convention)	Values (Gould (2004) convention, $t_r = 57009.6$ MJD)	Uniform prior range
t_0 (MJD)	57000	57009.60	± 1 day
u_0	0.1	0.104	± 0.01
t_E (days)	120	128.7	± 5 days
$\pi_{E,E}$	0.1	0.004	± 0.01
$\pi_{E,N}$	0.2	−0.224	± 0.01
m_{src} (mag)	19	19	± 0.1
b_{SFF}	0.8	0.8	± 0.1

Table 6.4: Microlensing parameters corresponding to the light curve in Figure 6.12. The event is located at (RA, Dec) = (260.0, −30.0).

System bodies. The actual correct statement would be that the solar system barycenter (SSB) is the non-accelerating rectilinear frame. However, in the spirit of keeping this document pedagogical and analytic, we have used "the Sun" and "heliocentric" instead of "SSB". In practice, microlensing modeling codes use the SSB instead of the Sun as the reference.

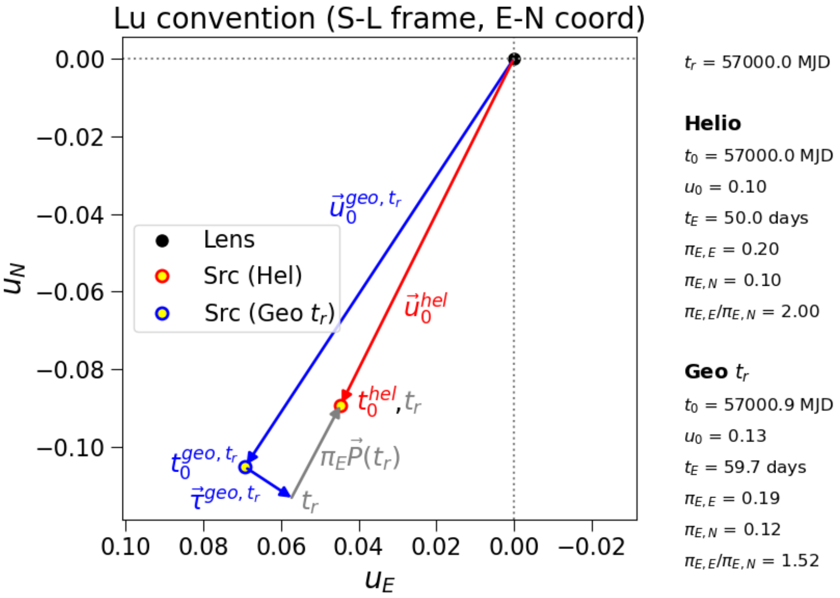

Figure 6.10: Same as Figure 6.2, but for a specific set of microlensing parameters. It lists the converted values, using the convention in Lu et al. (2016) (source-lens frame, East-North coordinate system, parallax as Sun-Earth separation). Note that because $t_r = t_0^{\text{hel}}$, $\boldsymbol{\tau}^{\text{hel}} = 0$.

6.9 Conclusions

In this pedagogical note, we have explained how to convert between several different microlensing modeling conventions. We describe different choices of rectilinear reference frame, binary lens reference positions, and coordinate system conventions. The hope is that this note can serve as a useful reference to those new to microlensing.

It is important to be careful with conversions. Especially when one is aggregating results from multiple sources, take care to note their conventions. There are many choices: coordinate system, rectilinear reference frame (for parallax), coordinate origin (for binary systems).

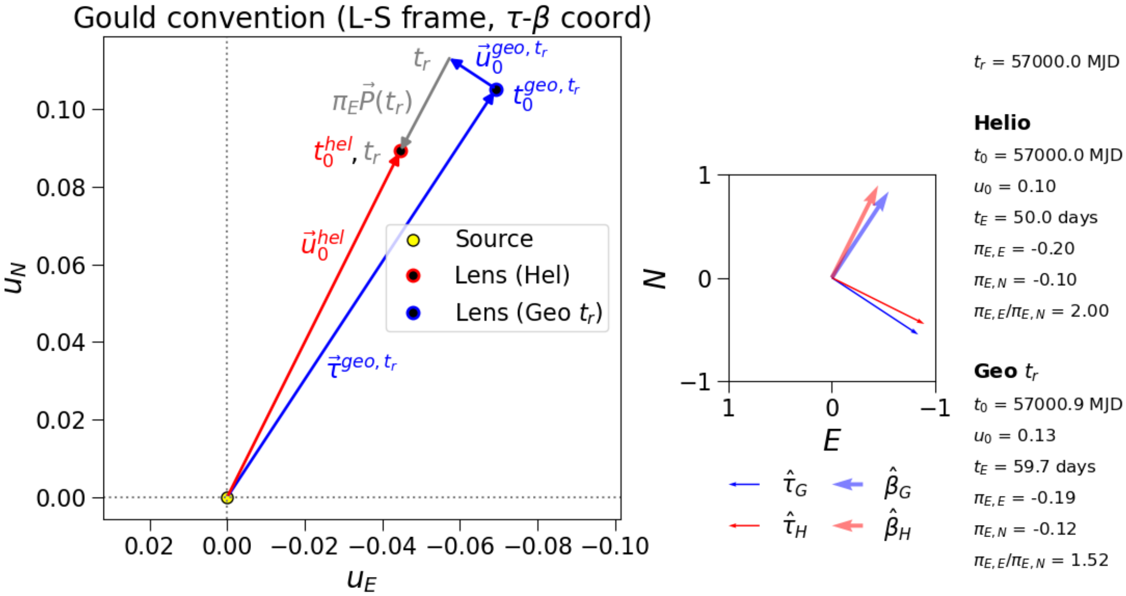

Figure 6.11: This is like Figure 6.10, but in the convention of Gould (2004) (lens-source frame, $\tau - \beta$ coordinate system, parallax as Earth-Sun separation). The small panel shows the direction of the $\hat{\boldsymbol{\tau}}$ and $\hat{\boldsymbol{\beta}}$ vectors in the heliocentric (subscript H) and geoprojected (subscript G) frames. Note that because $t_r = t_0^{\rm hel}$, $\boldsymbol{\tau}^{\rm hel} = 0$.

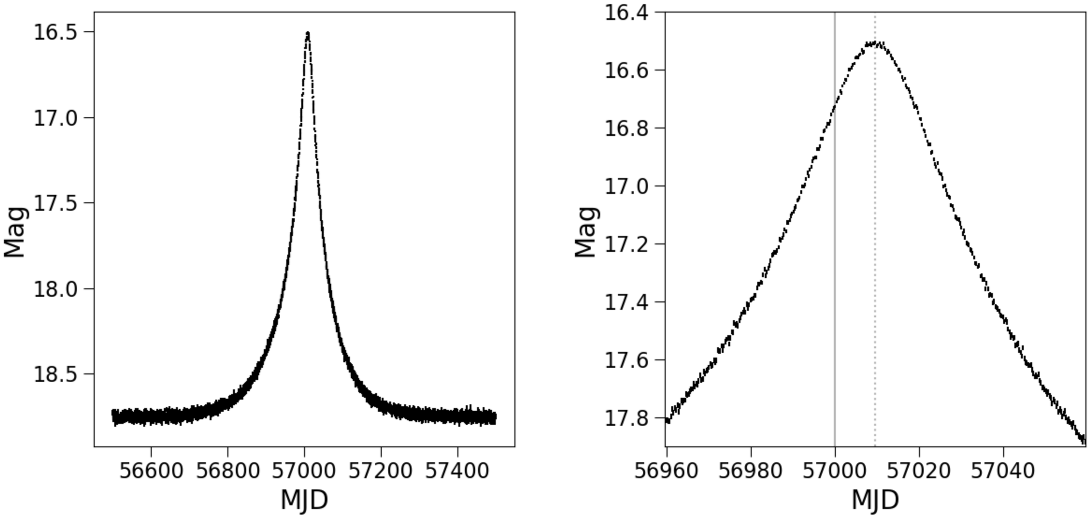

Figure 6.12: light curve with parameters listed in Table 6.4. The left panel shows the full light curve; the right panel shows a zoom-in near the peak. In the right panel, the solid gray line marks $t_0 = 57000$ MJD in the rectilinear reliocentric frame; the dashed gray line marks the photometric peak $t_{peak,phot} = 57009.6$ MJD as seen in the accelerating geocentric frame. The asymmetry of the light curve about the photometric peak can also be more readily seen in right panel. By choosing $t_r = t_{peak,phot}$, the value of t_0 in the rectilinear geoprojected frame decorrelates from the other microlensing parameters.

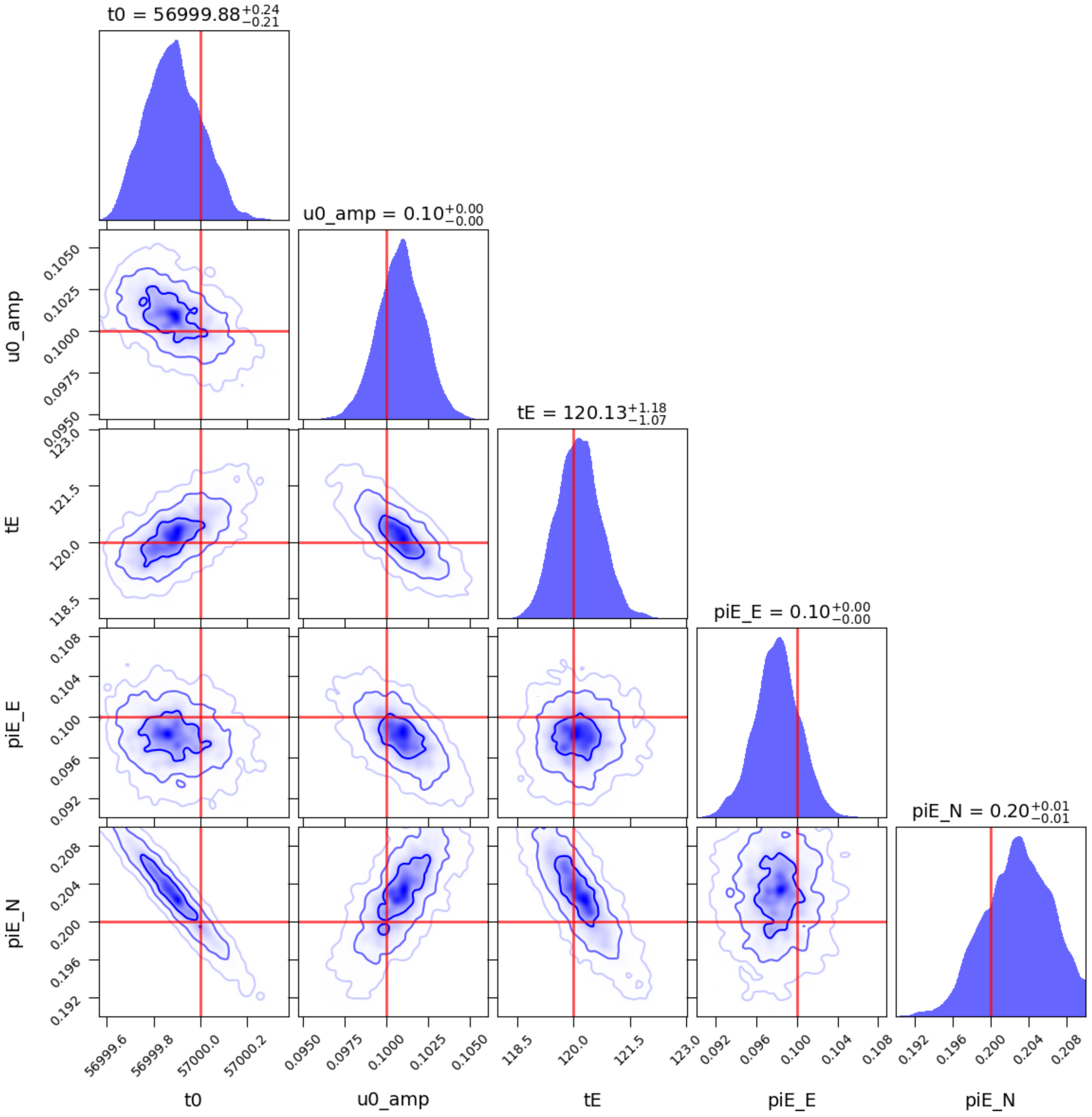

Figure 6.13: Posterior distributions of microlensing parameters from fitting the light curve in Figure 6.12 in the heliocentric reference frame. The contours denote $1-2-3\sigma$ intervals. The red lines denote the true value. Note that t_0 is highly correlated with many of the fit parameters (first column).

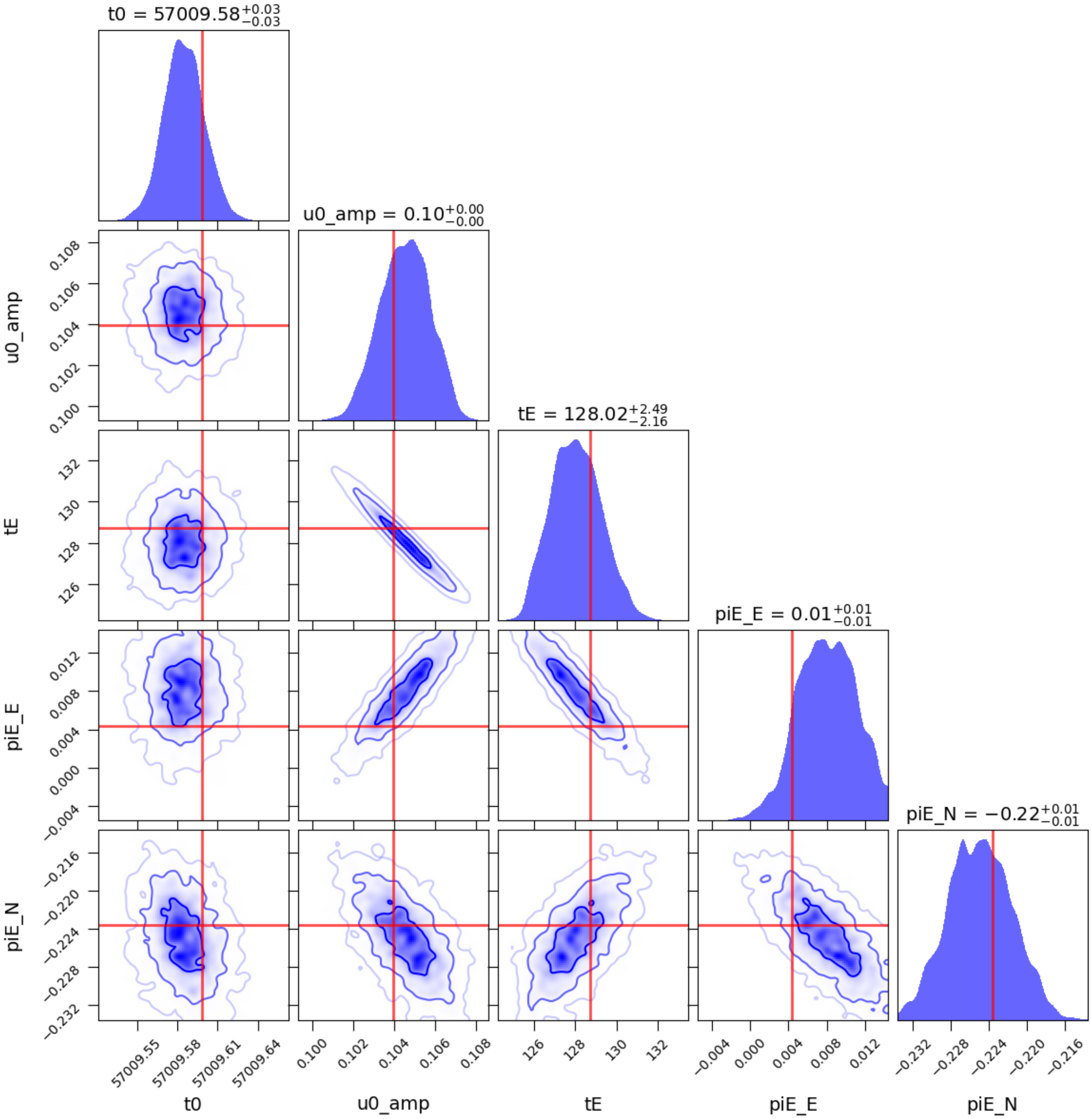

Figure 6.14: Same as Figure 6.13, but fitting in the geocentric projected coordinate system with $t_r = t_{peak,phot}$. Note here that t_0 is uncorrelated with all the other fit parameters (first column). Only the choice of $t_r = t_{peak,phot}$ results in the decorrelation.

Chapter 7

Conclusions and Future Directions

Fifty years after the discovery of the first black hole in an X-ray binary in 1972, an isolated black hole has finally been discovered. Despite being expected to comprise the majority of the Galaxy's 100 million black holes, isolated black holes are particularly elusive and difficult to find because they do not have a companion to interact with and produce either gravitational or electromagnetic radiation. Gravitational microlensing is the only practical way to uncover these elusive black holes. In particular, photometric and astrometric microlensing are both needed to characterize the masses and velocities of these isolated black holes. The technological advances required to make the first detection of an isolated black hole were numerous, including detector technology and computing power to enable time-domain surveys, as well as astrometric precision enabled by the stability of the Hubble Space Telescope and the software to analyze its data. Continuing at this level of technology, we can expect to continue finding another isolated black hole every couple years.

However, we are now are the threshold of the next great step in the study of isolated black holes, which will enable us to move from the characterization of individual systems, to the study of the population. The Nancy Grace Roman Space Telescope Spergel et al. 2015, mentioned throughout this thesis, is slated to launch in 2026. With its wide field of view, photometric and astrometric precision, and high-cadence observations, it has the ability to detect and characterize hundreds of isolated black holes over its nominal 5 year mission. *Roman* will enable the study of isolated black hole demographics, and finally allow us to measure the Galactic black hole mass function and velocity distribution. This will also provide the observations needed to constrain the outputs of massive star evolution simulations, rapid population synthesis codes, and binary interaction theories.

We re-emphasize that precise relative astrometry was crucial to making the measurements in this thesis, as photometry alone is not able to break fundamental degeneracies needed to measure lens masses with microlensing. Ensuring that the astrometric abilities of *Roman* are fully realized will be critical in making future black hole mass measurements possible.

It is customary to end talks and papers with "the future of (insert subject here) is bright". However, we will instead end here by saying that future of understanding the Galactic black hole population is dark.

Bibliography

Abbott, B. P., R. Abbott, T. D. Abbott, M. R. Abernathy, et al. (Oct. 2016). "Binary Black Hole Mergers in the First Advanced LIGO Observing Run". In: *Physical Review X* 6.4, 041015, p. 041015. DOI: `10.1103/PhysRevX.6.041015`. arXiv: `1606.04856 [gr-qc]`.

Abbott, B. P., R. Abbott, T. D. Abbott, S. Abraham, F. Acernese, K. Ackley, C. Adams, R. X. Adhikari, V. B. Adya, C. Affeldt, M. Agathos, K. Agatsuma, N. Aggarwal, O. D. Aguiar, L. Aiello, A. Ain, P. Ajith, G. Allen, A. Allocca, M. A. Aloy, P. A. Altin, A. Amato, S. Anand, et al. (Mar. 2020). "GW190425: Observation of a Compact Binary Coalescence with Total Mass $\sim 3.4\ \mathrm{M}_\odot$". In: *ApJ* 892.1, L3, p. L3. DOI: `10.3847/2041-8213/ab75f5`. arXiv: `2001.01761 [astro-ph.HE]`.

Abbott, B. P., R. Abbott, T. D. Abbott, S. Abraham, F. Acernese, K. Ackley, C. Adams, R. X. Adhikari, V. B. Adya, C. Affeldt, M. Agathos, K. Agatsuma, N. Aggarwal, O. D. Aguiar, L. Aiello, A. Ain, P. Ajith, G. Allen, A. Allocca, M. A. Aloy, P. A. Altin, A. Amato, A. Ananyeva, et al. (Sept. 2019). "GWTC-1: A Gravitational-Wave Transient Catalog of Compact Binary Mergers Observed by LIGO and Virgo during the First and Second Observing Runs". In: *Phys. Rev. X* 9 (3), p. 031040. DOI: `10.1103/PhysRevX.9.031040`. URL: `https://link.aps.org/doi/10.1103/PhysRevX.9.031040`.

Abbott, B. P., R. Abbott, T. D. Abbott, F. Acernese, et al. (Dec. 2017). "Search for Post-merger Gravitational Waves from the Remnant of the Binary Neutron Star Merger GW170817". In: *ApJ* 851.1, L16, p. L16. DOI: `10.3847/2041-8213/aa9a35`. arXiv: `1710.09320 [astro-ph.HE]`.

Abbott, R., T. D. Abbott, S. Abraham, et al. (June 2020). "GW190814: Gravitational Waves from the Coalescence of a 23 Solar Mass Black Hole with a 2.6 Solar Mass Compact Object". In: *ApJ* 896.2, L44, p. L44. DOI: `10.3847/2041-8213/ab960f`. arXiv: `2006.12611 [astro-ph.HE]`.

Abdurrahman, Fatima N., Haynes F. Stephens, and Jessica R. Lu (May 2021). "On the Possibility of Stellar Lenses in the Black Hole Candidate Microlensing Events MACHO-96-BLG-5 and MACHO-98-BLG-6". In: *ApJ* 912.2, 146, p. 146. DOI: `10.3847/1538-4357/abee83`. arXiv: `2103.09923 [astro-ph.SR]`.

Agol, Eric and Marc Kamionkowski (Aug. 2002). "X-rays from isolated black holes in the Milky Way". In: *MNRAS* 334.3, pp. 553–562. DOI: `10.1046/j.1365-8711.2002.05523.x`. arXiv: `astro-ph/0109539 [astro-ph]`.

Agol, Eric, Marc Kamionkowski, et al. (Sept. 2002). “Finding Black Holes with Microlensing”. In: *ApJ* 576.2, pp. L131–L135. DOI: `10.1086/343758`. arXiv: `astro-ph/0203257 [astro-ph]`.

Aigrain, Suzanne and Daniel Foreman-Mackey (Sept. 2022). “Gaussian Process regression for astronomical time-series”. In: *arXiv e-prints*, arXiv:2209.08940, arXiv:2209.08940. DOI: `10.48550/arXiv.2209.08940`. arXiv: `2209.08940 [astro-ph.IM]`.

Alcock, C., C. W. Akerlof, et al. (Oct. 1993). “Possible gravitational microlensing of a star in the Large Magellanic Cloud”. In: *Nature* 365, pp. 621–623. DOI: `10.1038/365621a0`. eprint: `astro-ph/9309052`.

Alcock, C., R. A. Allsman, D. Alves, T. S. Axelrod, A. C. Becker, D. P. Bennett, K. H. Cook, K. C. Freeman, K. Griest, J. Guern, et al. (Sept. 1997). “The MACHO Project Large Magellanic Cloud Microlensing Results from the First Two Years and the Nature of the Galactic Dark Halo”. In: *ApJ* 486.2, pp. 697–726. DOI: `10.1086/304535`. arXiv: `astro-ph/9606165 [astro-ph]`.

Alcock, C., R. A. Allsman, D. Alves, T. S. Axelrod, A. C. Becker, D. P. Bennett, K. H. Cook, K. C. Freeman, K. Griest, M. J. Keane, et al. (Dec. 1997). “First Detection of a Gravitational Microlensing Candidate toward the Small Magellanic Cloud”. In: *ApJ* 491.1, pp. L11–L13. DOI: `10.1086/311053`. arXiv: `astro-ph/9708190 [astro-ph]`.

Alcock, C., R. A. Allsman, D. Alves, T. S. Axelrod, D. P. Bennett, et al. (Dec. 1995). “First Observation of Parallax in a Gravitational Microlensing Event”. In: *ApJ* 454, p. L125. DOI: `10.1086/309783`. arXiv: `astro-ph/9506114 [astro-ph]`.

Alcock, C., R. A. Allsman, D. R. Alves, T. S. Axelrod, A. C. Becker, D. P. Bennett, K. H. Cook, N. Dalal, et al. (Oct. 2000). “The MACHO Project: Microlensing Results from 5.7 Years of Large Magellanic Cloud Observations”. In: *ApJ* 542.1, pp. 281–307. DOI: `10.1086/309512`. arXiv: `astro-ph/0001272 [astro-ph]`.

Alcock, C., R. A. Allsman, D. R. Alves, T. S. Axelrod, A. C. Becker, D. P. Bennett, K. H. Cook, A. J. Drake, et al. (Dec. 2001). “Direct detection of a microlens in the Milky Way”. In: *Nature* 414, pp. 617–619. DOI: `10.1038/414617a`.

An, Jin H. et al. (June 2002). “First Microlens Mass Measurement: PLANET Photometry of EROS BLG-2000-5”. In: *ApJ* 572.1, pp. 521–539. DOI: `10.1086/340191`. arXiv: `astro-ph/0110095 [astro-ph]`.

Anderson, Jay (Apr. 2014). *The Impact of x-CTE in the WFC3/UVIS detector on Astrometry.* Space Telescope WFC Instrument Science Report.

— (Mar. 2016). *Empirical Models for the WFC3/IR PSF.* Space Telescope WFC Instrument Science Report.

— (Aug. 2021). *Table-Based CTE Corrections for flt-Format WFC3/UVIS.* Space Telescope WFC Instrument Science Report.

— (July 2022). *One-Pass HST Photometry with hst1pass.* Instrument Science Report WFC3 2022-5, 55 pages.

Anderson, Jay, Sylvia Baggett, and Ben Kuhn (June 2021). *Updating the WFC3/UVIS CTE model and Mitigation Strategies.* Space Telescope WFC Instrument Science Report.

Anderson, Jay and Ivan R. King (Feb. 2006). *PSFs, Photometry, and Astronomy for the ACS/WFC*. Instrument Science Report ACS 2006-01.

Anderson, Jay, Ata Sarajedini, et al. (June 2008). "The Acs Survey of Globular Clusters. V. Generating a Comprehensive Star Catalog for each Cluster". In: *AJ* 135.6, pp. 2055–2073. DOI: `10.1088/0004-6256/135/6/2055`. arXiv: `0804.2025 [astro-ph]`.

Andrews, Jeff J. and Vicky Kalogera (May 2022). "Constraining Black Hole Natal Kicks with Astrometric Microlensing". In: *ApJ* 930.2, 159, p. 159. DOI: `10.3847/1538-4357/ac66d6`. arXiv: `2203.15156 [astro-ph.HE]`.

Aubourg, E. et al. (Oct. 1993). "Evidence for gravitational microlensing by dark objects in the Galactic halo". In: *Nature* 365, pp. 623–625. DOI: `10.1038/365623a0`.

Awiphan, S., E. Kerins, and A. C. Robin (Feb. 2016). "Besançon Galactic model analysis of MOA-II microlensing: evidence for a mass deficit in the inner bulge". In: *MNRAS* 456, pp. 1666–1680. DOI: `10.1093/mnras/stv2625`. arXiv: `1510.06347 [astro-ph.EP]`.

Bachelet, E. et al. (Nov. 2017). "pyLIMA: An Open-source Package for Microlensing Modeling. I. Presentation of the Software and Analysis of Single-lens Models". In: *AJ* 154.5, 203, p. 203. DOI: `10.3847/1538-3881/aa911c`.

El-Badry, Kareem, Hans-Walter Rix, Yvette Cendes, et al. (Feb. 2023). "A red giant orbiting a black hole". In: *arXiv e-prints*, arXiv:2302.07880, arXiv:2302.07880. DOI: `10.48550/arXiv.2302.07880`. arXiv: `2302.07880 [astro-ph.SR]`.

El-Badry, Kareem, Hans-Walter Rix, Eliot Quataert, et al. (Jan. 2023). "A Sun-like star orbiting a black hole". In: *MNRAS* 518.1, pp. 1057–1085. DOI: `10.1093/mnras/stac3140`. arXiv: `2209.06833 [astro-ph.SR]`.

El-Badry, Kareem, Rhys Seeburger, et al. (June 2022). "Unicorns and giraffes in the binary zoo: stripped giants with subgiant companions". In: *MNRAS* 512.4, pp. 5620–5641. DOI: `10.1093/mnras/stac815`. arXiv: `2203.06348 [astro-ph.SR]`.

Bailyn, Charles D. et al. (May 1998). "The Mass Distribution of Stellar Black Holes". In: *ApJ* 499.1, pp. 367–374. DOI: `10.1086/305614`. arXiv: `astro-ph/9708032 [astro-ph]`.

Baraffe, I. et al. (May 2015). "New evolutionary models for pre-main sequence and main sequence low-mass stars down to the hydrogen-burning limit". In: *A&A* 577, A42, A42. DOI: `10.1051/0004-6361/201425481`. arXiv: `1503.04107 [astro-ph.SR]`.

Bardeen, James M. and Jacobus A. Petterson (Jan. 1975). "The Lense-Thirring Effect and Accretion Disks around Kerr Black Holes". In: *ApJ* 195, p. L65. DOI: `10.1086/181711`.

Bardeen, James M., William H. Press, and Saul A. Teukolsky (Dec. 1972). "Rotating Black Holes: Locally Nonrotating Frames, Energy Extraction, and Scalar Synchrotron Radiation". In: *ApJ* 178, pp. 347–370. DOI: `10.1086/151796`.

Batista, V. et al. (Aug. 2015). "Confirmation of the OGLE-2005-BLG-169 Planet Signature and Its Characteristics with Lens-Source Proper Motion Detection". In: *ApJ* 808.2, 170, p. 170. DOI: `10.1088/0004-637X/808/2/170`. arXiv: `1507.08914 [astro-ph.EP]`.

Belczynski, K., G. Wiktorowicz, et al. (Sept. 2012). "Missing Black Holes Unveil the Supernova Explosion Mechanism". In: *ApJ* 757, 91, p. 91. DOI: `10.1088/0004-637X/757/1/91`. arXiv: `1110.1635`.

Belczynski, Krzysztof, Vassiliki Kalogera, et al. (Jan. 2008). "Compact Object Modeling with the StarTrack Population Synthesis Code". In: *The Astrophysical Journal Supplement Series* 174, pp. 223–260. DOI: `10.1086/521026`. arXiv: `astro-ph/0511811 [Astrophysics]`.

Belczynski, Krzysztof, Aleksander Sadowski, and Frederic A. Rasio (Aug. 2004). "A Comprehensive Study of Young Black Hole Populations". In: *ApJ* 611.2, pp. 1068–1079. DOI: `10.1086/422191`. arXiv: `astro-ph/0404068 [astro-ph]`.

Bellini, A., J. Anderson, and L. R. Bedin (May 2011). "Astrometry and Photometry with HST WFC3. II. Improved Geometric-Distortion Corrections for 10 Filters of the UVIS Channel". In: *PASP* 123.903, p. 622. DOI: `10.1086/659878`. arXiv: `1102.5218 [astro-ph.IM]`.

Bellini, Andrea, Jay Anderson, and Norman A. Grogin (Nov. 2018). *Focus-diverse, empirical PSF models for the ACS/WFC.* Instrument Science Report ACS 2018.

Bellini, Andrea, Mattia Libralato, et al. (Jan. 2018). "The HST Large Programme on ω Centauri. II. Internal Kinematics". In: *ApJ* 853.1, 86, p. 86. DOI: `10.3847/1538-4357/aaa3ec`. arXiv: `1801.01504 [astro-ph.GA]`.

Bennett, D. P., A. C. Becker, et al. (Nov. 2002). "Gravitational Microlensing Events Due to Stellar-Mass Black Holes". In: *ApJ* 579.2, pp. 639–659. DOI: `10.1086/342225`. arXiv: `astro-ph/0109467 [astro-ph]`.

Bennett, D. P., A. Bhattacharya, et al. (Aug. 2015). "Confirmation of the Planetary Microlensing Signal and Star and Planet Mass Determinations for Event OGLE-2005-BLG-169". In: *ApJ* 808.2, 169, p. 169. DOI: `10.1088/0004-637X/808/2/169`. arXiv: `1507.08661 [astro-ph.EP]`.

Bird, S. et al. (May 2016). "Did LIGO Detect Dark Matter?" In: *Physical Review Letters* 116.20, 201301, p. 201301. DOI: `10.1103/PhysRevLett.116.201301`. arXiv: `1603.00464`.

Blaauw, A. (May 1961). "On the origin of the O- and B-type stars with high velocities (the "run-away" stars), and some related problems". In: *Bull. Astron. Inst. Netherlands* 15, p. 265.

Bolton, C. T. (Feb. 1972). "Identification of Cygnus X-1 with HDE 226868". In: *Nature* 235.5336, pp. 271–273. DOI: `10.1038/235271b0`.

Bond, I. A., F. Abe, et al. (Nov. 2001). "Real-time difference imaging analysis of MOA Galactic bulge observations during 2000". In: *MNRAS* 327.3, pp. 868–880. DOI: `10.1046/j.1365-8711.2001.04776.x`. arXiv: `astro-ph/0102181 [astro-ph]`.

Bond, I. A., D. P. Bennett, et al. (Aug. 2017). "The lowest mass ratio planetary microlens: OGLE 2016-BLG-1195Lb". In: *MNRAS* 469.2, pp. 2434–2440. DOI: `10.1093/mnras/stx1049`. arXiv: `1703.08639 [astro-ph.EP]`.

Bovy, Jo et al. (May 2019). "Life in the fast lane: a direct view of the dynamics, formation, and evolution of the Milky Way's bar". In: *arXiv e-prints*, arXiv:1905.11404, arXiv:1905.11404. arXiv: `1905.11404 [astro-ph.GA]`.

Bozza, Valerio et al. (Oct. 2018). "VBBINARYLENSING: a public package for microlensing light-curve computation". In: *MNRAS* 479.4, pp. 5157–5167. DOI: `10.1093/mnras/sty1791`. arXiv: `1805.05653 [astro-ph.IM]`.

Bullock, J. S. and K. V. Johnston (Dec. 2005). “Tracing Galaxy Formation with Stellar Halos. I. Methods”. In: *ApJ* 635, pp. 931–949. DOI: 10.1086/497422. eprint: astro-ph/0506467.

Byrne, R. A. and M. Fraser (July 2022). “Nothing to see here: failed supernovae are faint or rare”. In: *MNRAS* 514.1, pp. 1188–1205. DOI: 10.1093/mnras/stac1308. arXiv: 2201.12187 [astro-ph.SR].

Campos, Fabıola et al. (Mar. 2016). “A comparative analysis of the observed white dwarf cooling sequence from globular clusters”. In: *MNRAS* 456, pp. 3729–3742. DOI: 10.1093/mnras/stv2911. arXiv: 1512.03114 [astro-ph.SR].

Carr, Bernard and Florian Kühnel (Oct. 2020). “Primordial Black Holes as Dark Matter: Recent Developments”. In: *Annual Review of Nuclear and Particle Science* 70, pp. 355–394. DOI: 10.1146/annurev-nucl-050520-125911. arXiv: 2006.02838 [astro-ph.CO].

Carr, Bernard, Florian Kühnel, and Marit Sandstad (Oct. 2016). “Primordial black holes as dark matter”. In: *Phys. Rev. D* 94 (8), p. 083504. DOI: 10.1103/PhysRevD.94.083504. URL: https://link.aps.org/doi/10.1103/PhysRevD.94.083504.

Castelli, F. and R. L. Kurucz (May 2004). “New Grids of ATLAS9 Model Atmospheres”. In: *ArXiv Astrophysics e-prints*. eprint: astro-ph/0405087.

Chakrabarti, Sukanya et al. (Oct. 2022). “A non-interacting Galactic black hole candidate in a binary system with a main-sequence star”. In: *arXiv e-prints*, arXiv:2210.05003, arXiv:2210.05003. DOI: 10.48550/arXiv.2210.05003. arXiv: 2210.05003 [astro-ph.GA].

Chapline, G. and J. Barbieri (2018). “MACHO Messages from the Big Bang”. In: *LHEP* 1.1, pp. 17–20. DOI: 10.31526/LHEP.1.2018.04. arXiv: 1801.07345 [gr-qc].

Choi, J. et al. (June 2016). “Mesa Isochrones and Stellar Tracks (MIST). I. Solar-scaled Models”. In: *ApJ* 823, 102, p. 102. DOI: 10.3847/0004-637X/823/2/102. arXiv: 1604.08592 [astro-ph.SR].

Clarke, Jonathan P. et al. (Nov. 2019). “The Milky Way bar/bulge in proper motions: a 3D view from VIRAC and Gaia”. In: *MNRAS* 489.3, pp. 3519–3538. DOI: 10.1093/mnras/stz2382.

Clarkson, W., K. Sahu, et al. (Sept. 2008). “Stellar Proper Motions in the Galactic Bulge from Deep Hubble Space Telescope ACS WFC Photometry”. In: *ApJ* 684, pp. 1110–1142. DOI: 10.1086/590378. arXiv: 0809.1682.

Clarkson, W. I., A. Calamida, et al. (May 2018). “Chemically Dissected Rotation Curves of the Galactic Bulge from Main-sequence Proper Motions”. In: *ApJ* 858, 46, p. 46. DOI: 10.3847/1538-4357/aaba7f. arXiv: 1804.01103.

Corral-Santana, J. M. et al. (Mar. 2016). “BlackCAT: A catalogue of stellar-mass black holes in X-ray transients”. In: *A&A* 587, A61, A61. DOI: 10.1051/0004-6361/201527130. arXiv: 1510.08869 [astro-ph.HE].

Dai, S. et al. (Apr. 2015). “Gravitational Microlensing by Neutron Stars and Radio Pulsars: Event Rates, Timescale Distributions, and Mass Measurements”. In: *ApJ* 802, 120, p. 120. DOI: 10.1088/0004-637X/802/2/120. arXiv: 1502.02776.

Damineli, A. et al. (Dec. 2016a). “Extinction law in the range 0.4-4.8 μm and the 8620 Å DIB towards the stellar cluster Westerlund 1”. In: *MNRAS* 463, pp. 2653–2666. DOI: `10.1093/mnras/stw2122`. arXiv: `1607.04639 [astro-ph.SR]`.

— (Dec. 2016b). “Extinction law in the range 0.4-4.8 μm and the 8620 Å DIB towards the stellar cluster Westerlund 1”. In: *MNRAS* 463.3, pp. 2653–2666. DOI: `10.1093/mnras/stw2122`. arXiv: `1607.04639 [astro-ph.SR]`.

Davies, Ben and Emma R. Beasor (Feb. 2018). “The initial masses of the red supergiant progenitors to Type II supernovae”. In: *MNRAS* 474.2, pp. 2116–2128. DOI: `10.1093/mnras/stx2734`. arXiv: `1709.06116 [astro-ph.SR]`.

— (July 2020a). “’On the red supergiant problem’: a rebuttal, and a consensus on the upper mass cut-off for II-P progenitors”. In: *MNRAS* 496.1, pp. L142–L146. DOI: `10.1093/mnrasl/slaa102`. arXiv: `2005.13855 [astro-ph.SR]`.

— (Mar. 2020b). “The ‘red supergiant problem’: the upper luminosity boundary of Type II supernova progenitors”. In: *MNRAS* 493.1, pp. 468–476. DOI: `10.1093/mnras/staa174`. arXiv: `2001.06020 [astro-ph.SR]`.

de Jong, J. T. A. et al. (Apr. 2004). “First microlensing candidates from the MEGA survey of M 31”. In: *A&A* 417, pp. 461–477. DOI: `10.1051/0004-6361:20031734`. arXiv: `astro-ph/0307072 [astro-ph]`.

Di Stefano, R. and A. A. Esin (July 1995). “Blending of Light in Gravitational Microlensing Events”. In: *ApJ* 448, p. L1. DOI: `10.1086/309588`. eprint: `astro-ph/9506092`.

Dominik, M. (May 1998). “Where are the binary source galactic microlensing events?” In: *A&A* 333, pp. 893–896. arXiv: `astro-ph/9801119 [astro-ph]`.

— (Mar. 2009). “Parameter degeneracies and (un)predictability of gravitational microlensing events”. In: *MNRAS* 393, pp. 816–821. DOI: `10.1111/j.1365-2966.2008.14276.x`. arXiv: `0811.4173 [astro-ph]`.

Dominik, M. and K. C. Sahu (May 2000). “Astrometric Microlensing of Stars”. In: *ApJ* 534, pp. 213–226. DOI: `10.1086/308716`.

Dong, Subo et al. (Jan. 2019). “First Resolution of Microlensed Images”. In: *ApJ* 871.1, 70, p. 70. DOI: `10.3847/1538-4357/aaeffb`. arXiv: `1809.08243 [astro-ph.SR]`.

Dotter, A. (Jan. 2016). “MESA Isochrones and Stellar Tracks (MIST) 0: Methods for the Construction of Stellar Isochrones”. In: *ApJS* 222, 8, p. 8. DOI: `10.3847/0067-0049/222/1/8`. arXiv: `1601.05144 [astro-ph.SR]`.

Drlica-Wagner, A. et al. (Feb. 2019). “Probing the Fundamental Nature of Dark Matter with the Large Synoptic Survey Telescope”. In: *arXiv e-prints*. arXiv: `1902.01055`.

Duchêne, Gaspard and Adam Kraus (Aug. 2013). “Stellar Multiplicity”. In: *ARA&A* 51.1, pp. 269–310. DOI: `10.1146/annurev-astro-081710-102602`. arXiv: `1303.3028 [astro-ph.SR]`.

Eddington, A. S. (Mar. 1919). “The total eclipse of 1919 May 29 and the influence of gravitation on light”. In: *The Observatory* 42, pp. 119–122.

Elbert, O. D., J. S. Bullock, and M. Kaplinghat (Jan. 2018). “Counting black holes: The cosmic stellar remnant population and implications for LIGO”. In: *MNRAS* 473, pp. 1186–1194. DOI: `10.1093/mnras/stx1959`. arXiv: `1703.02551`.

Ertl, T. et al. (Feb. 2016). “A Two-parameter Criterion for Classifying the Explodability of Massive Stars by the Neutrino-driven Mechanism”. In: *ApJ* 818.2, 124, p. 124. DOI: `10.3847/0004-637X/818/2/124`. arXiv: `1503.07522 [astro-ph.SR]`.

Evans, Ian N., Christopher Allen, Craig S. Anderson, Jamie A. Budynkiewicz, Douglas Burke, Judy Chen, Francesca Civano, Raffaele D’Abrusco, Stephen M. Doe, Janet D. Evans, Giuseppina Fabbiano, Danny G. Gibbs, Kenny J. Glotfelty, Dale E. Graessle, John D. Grier, Roger Hain, Diane M. Hall, Peter N. Harbo, John C. Houck, Jennifer Lauer, Omar Laurino, Nicholas P. Lee, Rafael Martinez-Galarza, et al. (Mar. 2019). “Chandra Source Catalog Release 2.0 - The State of the Art Serendipitous X-ray Source Catalog”. In: *AAS/High Energy Astrophysics Division*. Vol. 17. AAS/High Energy Astrophysics Division, 114.01, p. 114.01.

Evans, Ian N., Christopher Allen, Craig S. Anderson, Jamie A. Budynkiewicz, Douglas Burke, Judy Chen, Francesca M. Civano, Raffaele D’Abrusco, Stephen M. Doe, Janet D. Evans, Giuseppina Fabbiano, Danny G. Gibbs, Kenny J. Glotfelty, Dale E. Graessle, John D. Grier, Roger Hain, Diane M. Hall, Peter N. Harbo, John C. Houck, J. Lauer, Omar Laurino, Nicholas P. Lee, Rafael Martınez-Galarza, et al. (Jan. 2019). “Chandra Source Catalog Release 2.0 - The State of the Art Serendipitous X-ray Source Catalog”. In: *American Astronomical Society Meeting Abstracts #233*. Vol. 233. American Astronomical Society Meeting Abstracts, 379.01, p. 379.01.

Evans, P. A., K. L. Page, et al. (Apr. 2020). “2SXPS: An Improved and Expanded Swift X-Ray Telescope Point-source Catalog”. In: *ApJS* 247.2, 54, p. 54. DOI: `10.3847/1538-4365/ab7db9`. arXiv: `1911.11710 [astro-ph.IM]`.

Evans, Thomas M., Suzanne Aigrain, et al. (July 2015). “A uniform analysis of HD 209458b Spitzer/IRAC light curves with Gaussian process models”. In: *MNRAS* 451.1, pp. 680–694. DOI: `10.1093/mnras/stv910`. arXiv: `1504.05942 [astro-ph.EP]`.

Fabricius, C. et al. (May 2021). “Gaia Early Data Release 3. Catalogue validation”. In: *A&A* 649, A5, A5. DOI: `10.1051/0004-6361/202039834`. arXiv: `2012.06242 [astro-ph.GA]`.

Farr, Will M. et al. (Nov. 2011). “The Mass Distribution of Stellar-mass Black Holes”. In: *ApJ* 741.2, 103, p. 103. DOI: `10.1088/0004-637X/741/2/103`. arXiv: `1011.1459 [astro-ph.GA]`.

Fender, R. P., T. J. Maccarone, and I. Heywood (Apr. 2013). “The closest black holes”. In: *MNRAS* 430.3, pp. 1538–1547. DOI: `10.1093/mnras/sts688`. arXiv: `1301.1341 [astro-ph.HE]`.

Feroz, F., M. P. Hobson, and M. Bridges (Oct. 2009). “MULTINEST: an efficient and robust Bayesian inference tool for cosmology and particle physics”. In: *MNRAS* 398.4, pp. 1601–1614. DOI: `10.1111/j.1365-2966.2009.14548.x`. arXiv: `0809.3437 [astro-ph]`.

Foreman-Mackey, Daniel et al. (Dec. 2017). “Fast and Scalable Gaussian Process Modeling with Applications to Astronomical Time Series”. In: *AJ* 154.6, 220, p. 220. DOI: `10.3847/1538-3881/aa9332`. arXiv: `1703.09710 [astro-ph.IM]`.

Fryer, C. L. et al. (Apr. 2012). “Compact Remnant Mass Function: Dependence on the Explosion Mechanism and Metallicity”. In: *ApJ* 749, 91, p. 91. DOI: `10.1088/0004-637X/749/1/91`. arXiv: `1110.1726 [astro-ph.SR]`.

Gaia Collaboration, A. G. A. Brown, et al. (May 2021). "Gaia Early Data Release 3. Summary of the contents and survey properties". In: *A&A* 649, A1, A1. DOI: `10.1051/0004-6361/202039657`. arXiv: `2012.01533 [astro-ph.GA]`.

Gaia Collaboration, T. Prusti, et al. (Nov. 2016). "The Gaia mission". In: *A&A* 595, A1, A1. DOI: `10.1051/0004-6361/201629272`. arXiv: `1609.04153 [astro-ph.IM]`.

Gaudi, B. S. (Sept. 2012). "Microlensing Surveys for Exoplanets". In: *ARA&A* 50, pp. 411–453. DOI: `10.1146/annurev-astro-081811-125518`.

Gennaro, M. et. al. (May 2018). *WFC3 Data Handbook, Version 4.0.* Baltimore: STScI.

Gibson, N. P. et al. (Feb. 2013). "A Gemini ground-based transmission spectrum of WASP-29b: a featureless spectrum from 515 to 720 nm". In: *MNRAS* 428.4, pp. 3680–3692. DOI: `10.1093/mnras/sts307`. arXiv: `1210.7798 [astro-ph.EP]`.

Gilbertson, Christian et al. (Dec. 2020). "Toward Extremely Precise Radial Velocities. II. A Tool for Using Multivariate Gaussian Processes to Model Stellar Activity". In: *ApJ* 905.2, 155, p. 155. DOI: `10.3847/1538-4357/abc627`. arXiv: `2009.01085 [astro-ph.IM]`.

Golovich, Nathan et al. (May 2022). "A Reanalysis of Public Galactic Bulge Gravitational Microlensing Events from OGLE-III and -IV". In: *ApJS* 260.1, 2, p. 2. DOI: `10.3847/1538-4365/ac5969`.

Gould, Andrew (June 1992). "Extending the MACHO Search to approximately 10 6 M sub sun". In: *ApJ* 392, p. 442. DOI: `10.1086/171443`.

— (June 2000). "Measuring the Remnant Mass Function of the Galactic Bulge". In: *ApJ* 535.2, pp. 928–931. DOI: `10.1086/308865`. arXiv: `astro-ph/9906472 [astro-ph]`.

— (May 2004). "Resolution of the MACHO-LMC-5 Puzzle: The Jerk-Parallax Microlens Degeneracy". In: *ApJ* 606.1, pp. 319–325. DOI: `10.1086/382782`. arXiv: `astro-ph/0311548 [astro-ph]`.

Green, Gregory M. (June 2018). "dustmaps: A Python interface for maps of interstellar dust". In: *The Journal of Open Source Software* 3.26, p. 695. DOI: `10.21105/joss.00695`.

Griest, Kim et al. (May 1991). "Gravitational Microlensing as a Method of Detecting Disk Dark Matter and Faint Disk Stars". In: *ApJ* 372, p. L79. DOI: `10.1086/186028`.

Groh, Jose H. et al. (Sept. 2020). "Massive Black Holes Regulated by Luminous Blue Variable Mass Loss and Magnetic Fields". In: *ApJ* 900.2, 98, p. 98. DOI: `10.3847/1538-4357/aba2c8`. arXiv: `1912.00994 [astro-ph.SR]`.

Groth, E. J. (May 1986). "A pattern-matching algorithm for two-dimensional coordinate lists". In: *AJ* 91, pp. 1244–1248. DOI: `10.1086/114099`.

Han, C. (Oct. 1999). "Analytic relations between the observed gravitational microlensing parameters with and without the effect of blending". In: *MNRAS* 309, pp. 373–378. DOI: `10.1046/j.1365-8711.1999.02832.x`. eprint: `astro-ph/9810401`.

Han, C. and A. Gould (July 2003). "Stellar Contribution to the Galactic Bulge Microlensing Optical Depth". In: *ApJ* 592, pp. 172–175. DOI: `10.1086/375706`. eprint: `astro-ph/0303309`.

Han, Cheongho and Youngjin Jeong (Nov. 1998). "Where are the binary source gravitational microlensing events? II". In: *MNRAS* 301.1, pp. 231–234. DOI: `10.1046/j.1365-8711.1998.02023.x`. arXiv: `astro-ph/9804273 [astro-ph]`.

Hawking, Stephen (Jan. 1971). “Gravitationally collapsed objects of very low mass”. In: *MNRAS* 152, p. 75. DOI: `10.1093/mnras/152.1.75`.

Hearnshaw, J. B. et al. (Jan. 2006). “The MOA 1.8-metre alt-az Wide-field Survey Telescope and the MOA Project”. In: *The 9th Asian-Pacific Regional IAU Meeting*. Ed. by W. Sutantyo et al., p. 272. arXiv: `astro-ph/0509420 [astro-ph]`.

Hees, A. et al. (Aug. 2019). “An Adaptive Scheduling Tool to Optimize Measurements to Reach a Scientific Objective: Methodology and Application to Measurements of Stellar Orbits in the Galactic Center”. In: *ApJ* 880.2, 87, p. 87. DOI: `10.3847/1538-4357/ab2ae0`. arXiv: `1906.03099 [astro-ph.IM]`.

Heger, A. et al. (July 2003). “How Massive Single Stars End Their Life”. In: *ApJ* 591, pp. 288–300. DOI: `10.1086/375341`. eprint: `astro-ph/0212469`.

Hog, E., I. D. Novikov, and A. G. Polnarev (Feb. 1995). “MACHO photometry and astrometry.” In: *A&A* 294, pp. 287–294.

Hosek Matthew W., Jr., Jessica R. Lu, Jay Anderson, Francisco Najarro, et al. (Jan. 2019). “The Unusual Initial Mass Function of the Arches Cluster”. In: *ApJ* 870, 44, p. 44. DOI: `10.3847/1538-4357/aaef90`. arXiv: `1808.02577 [astro-ph.GA]`.

Hosek Matthew W., Jr., Jessica R. Lu, Casey Y. Lam, et al. (Sept. 2020). “SPISEA: A Python-based Simple Stellar Population Synthesis Code for Star Clusters”. In: *AJ* 160.3, 143, p. 143. DOI: `10.3847/1538-3881/aba533`. arXiv: `2006.06691 [astro-ph.SR]`.

Hosek Jr., M. W., J. R. Lu, J. Anderson, A. M. Ghez, et al. (Nov. 2015). “The Arches Cluster: Extended Structure and Tidal Radius”. In: *ApJ* 813, 27, p. 27. DOI: `10.1088/0004-637X/813/1/27`. arXiv: `1509.04716 [astro-ph.SR]`.

Howard, C. D., R. M. Rich, W. Clarkson, et al. (Sept. 2009). “Kinematics at the Edge of the Galactic Bulge: Evidence for Cylindrical Rotation”. In: *ApJ* 702, pp. L153–L157. DOI: `10.1088/0004-637X/702/2/L153`. arXiv: `0908.1109 [astro-ph.GA]`.

Howard, C. D., R. M. Rich, D. B. Reitzel, et al. (Dec. 2008). “The Bulge Radial Velocity Assay (BRAVA). I. Sample Selection and a Rotation Curve”. In: *ApJ* 688, pp. 1060–1077. DOI: `10.1086/592106`. arXiv: `0807.3967`.

Husser, T.-O. et al. (May 2013). “A new extensive library of PHOENIX stellar atmospheres and synthetic spectra”. In: *A&A* 553, A6, A6. DOI: `10.1051/0004-6361/201219058`. arXiv: `1303.5632 [astro-ph.SR]`.

Janka, H.-T. (Nov. 2012). “Explosion Mechanisms of Core-Collapse Supernovae”. In: *Annual Review of Nuclear and Particle Science* 62, pp. 407–451. DOI: `10.1146/annurev-nucl-102711-094901`. arXiv: `1206.2503 [astro-ph.SR]`.

Janka, Hans-Thomas (July 2013). “Natal kicks of stellar mass black holes by asymmetric mass ejection in fallback supernovae”. In: *Monthly Notices of the Royal Astronomical Society* 434.2, pp. 1355–1361. ISSN: 0035-8711. DOI: `10.1093/mnras/stt1106`. eprint: `http://oup.prod.sis.lan/mnras/article-pdf/434/2/1355/18497202/stt1106.pdf`. URL: `https://doi.org/10.1093/mnras/stt1106`.

Johnson, Samson A. et al. (Sept. 2020). “Predictions of the Nancy Grace Roman Space Telescope Galactic Exoplanet Survey. II. Free-floating Planet Detection Rates”. In: *AJ* 160.3, 123, p. 123. DOI: `10.3847/1538-3881/aba75b`. arXiv: `2006.10760 [astro-ph.EP]`.

Jonker, Peter G. et al. (Nov. 2021). "The Observed Mass Distribution of Galactic Black Hole LMXBs Is Biased against Massive Black Holes". In: *ApJ* 921.2, 131, p. 131. DOI: `10.3847/1538-4357/ac2839`. arXiv: `2104.03596 [astro-ph.HE]`.

Kains, N. et al. (July 2017). "Microlensing Constraints on the Mass of Single Stars from HST Astrometric Measurements". In: *ApJ* 843.2, 145, p. 145. DOI: `10.3847/1538-4357/aa78eb`. arXiv: `1706.04196 [astro-ph.SR]`.

Kalirai, J. S. et al. (Mar. 2008). "The Initial-Final Mass Relation: Direct Constraints at the Low-Mass End". In: *ApJ* 676, 594-609, pp. 594–609. DOI: `10.1086/527028`. arXiv: `0706.3894`.

Karolinski, Numa and Wei Zhu (Nov. 2020). "Detecting isolated stellar-mass black holes in the absence of microlensing parallax effect". In: *MNRAS* 498.1, pp. L25–L30. DOI: `10.1093/mnrasl/slaa121`. arXiv: `2006.02441 [astro-ph.SR]`.

Kerins, E., A. C. Robin, and D. J. Marshall (June 2009). "Synthetic microlensing maps of the Galactic bulge". In: *MNRAS* 396, pp. 1202–1210. DOI: `10.1111/j.1365-2966.2009.14791.x`. arXiv: `0805.4626`.

Kerr, Roy P. (Sept. 1963). "Gravitational Field of a Spinning Mass as an Example of Algebraically Special Metrics". In: *Phys. Rev. Lett.* 11.5, pp. 237–238. DOI: `10.1103/PhysRevLett.11.237`.

Kim, Seung-Lee et al. (Feb. 2016). "KMTNET: A Network of 1.6 m Wide-Field Optical Telescopes Installed at Three Southern Observatories". In: *Journal of Korean Astronomical Society* 49.1, pp. 37–44. DOI: `10.5303/JKAS.2016.49.1.037`.

Kochanek, C. S. (Apr. 2020). "On the red supergiant problem". In: *MNRAS* 493.4, pp. 4945–4949. DOI: `10.1093/mnras/staa605`. arXiv: `2001.07216 [astro-ph.SR]`.

Kochanek, Christopher S. et al. (Sept. 2008). "A Survey About Nothing: Monitoring a Million Supergiants for Failed Supernovae". In: *ApJ* 684.2, pp. 1336–1342. DOI: `10.1086/590053`. arXiv: `0802.0456 [astro-ph]`.

Koester, D. (Jan. 2010). "White dwarf spectra and atmosphere models". In: *Mem. Soc. Astron. Italiana* 81, pp. 921–931.

Kreidberg, Laura et al. (Sept. 2012). "Mass Measurements of Black Holes in X-Ray Transients: Is There a Mass Gap?" In: *ApJ* 757.1, 36, p. 36. DOI: `10.1088/0004-637X/757/1/36`. arXiv: `1205.1805 [astro-ph.HE]`.

Kroupa, P. (Apr. 2001). "On the variation of the initial mass function". In: *MNRAS* 322, pp. 231–246. DOI: `10.1046/j.1365-8711.2001.04022.x`. eprint: `astro-ph/0009005`.

Kuhn, Benjamin and Jay Anderson (June 2021). *WFC3/UVIS: New FLC External CTE Monitoring 2009-2020*. Space Telescope WFC Instrument Science Report.

Lai, D. (2001). "Neutron Star Kicks and Asymmetric Supernovae". In: *Physics of Neutron Star Interiors*. Ed. by D. Blaschke, N. K. Glendenning, and A. Sedrakian. Vol. 578. Lecture Notes in Physics, Berlin Springer Verlag, p. 424. eprint: `astro-ph/0012049`.

Lam, Casey and Jessica Ryan Lu (June 2021). *First detection of an isolated stellar mass black hole with astrometric microlensing*. HST Proposal.

Lam, Casey Y., Jessica R. Lu, Jr. Hosek Matthew W., et al. (Jan. 2020). “PopSyCLE: A New Population Synthesis Code for Compact Object Microlensing Events”. In: *ApJ* 889.1, 31, p. 31. DOI: `10.3847/1538-4357/ab5fd3`. arXiv: `1912.04510 [astro-ph.SR]`.

Lam, Casey Y., Jessica R. Lu, Andrzej Udalski, et al. (July 2022a). “An Isolated Mass-gap Black Hole or Neutron Star Detected with Astrometric Microlensing”. In: *ApJ* 933.1, L23, p. L23. DOI: `10.3847/2041-8213/ac7442`. arXiv: `2202.01903 [astro-ph.GA]`.

— (June 2022b). “Supplement: “An Isolated Mass-gap Black Hole or Neutron Star Detected with Astrometric Microlensing” (2022, ApJL, 933, L23)”. In: *ApJS* 260.2, 55, p. 55. DOI: `10.3847/1538-4365/ac7441`.

Laplace, Pierre Simon (July 1799). “Beweis des Satzes, dass die anziehende Kraft bey einem Weltkörper so groß seyn könne, dass das Licht davon nicht ausströmen kann”. In: *Allgemeine Geographische Ephemeriden* 4.1, pp. 1–6.

Li, S. -S. et al. (Sept. 2019). “OGLE-2017-BLG-1186: first application of asteroseismology and Gaussian processes to microlensing”. In: *MNRAS* 488.3, pp. 3308–3323. DOI: `10.1093/mnras/stz1873`. arXiv: `1904.07718 [astro-ph.SR]`.

Libralato, Mattia et al. (June 2023). “JWST-TST Proper Motions. I. High-precision NIRISS Calibration and Large Magellanic Cloud Kinematics”. In: *ApJ* 950.2, 101, p. 101. DOI: `10.3847/1538-4357/acd04f`. arXiv: `2303.00009 [astro-ph.GA]`.

Lindegren, L., U. Bastian, et al. (May 2021). “Gaia Early Data Release 3. Parallax bias versus magnitude, colour, and position”. In: *A&A* 649, A4, A4. DOI: `10.1051/0004-6361/202039653`. arXiv: `2012.01742 [astro-ph.IM]`.

Lindegren, L., S. A. Klioner, et al. (May 2021). “Gaia Early Data Release 3. The astrometric solution”. In: *A&A* 649, A2, A2. DOI: `10.1051/0004-6361/202039709`. arXiv: `2012.03380 [astro-ph.IM]`.

Lu, J. R. et al. (Oct. 2016). “A Search for Stellar-Mass Black Holes via Astrometric Microlensing”. In: *ApJ* 830. DOI: `10.3847/0004-637X/830/1/41`. arXiv: `1607.08284`.

Luri, X. et al. (Aug. 2018). “Gaia Data Release 2. Using Gaia parallaxes”. In: *A&A* 616, A9, A9. DOI: `10.1051/0004-6361/201832964`. arXiv: `1804.09376 [astro-ph.IM]`.

Lynden-Bell, D. (Aug. 1969). “Galactic Nuclei as Collapsed Old Quasars”. In: *Nature* 223.5207, pp. 690–694. DOI: `10.1038/223690a0`.

Maeda, Yoshitomo et al. (Sept. 2005). “A Search for X-Rays from the Long-Duration Microlensing Event MACHO-96-BLG-5”. In: *ApJ* 631.1, pp. L65–L68. DOI: `10.1086/491698`.

Malpas, Amber et al. (Sept. 2022). “OGLE-2017-BLG-1038: A Possible Brown-dwarf Binary Revealed by Spitzer Microlensing Parallax”. In: *AJ* 164.3, 102, p. 102. DOI: `10.3847/1538-3881/ac7d4c`. arXiv: `2302.07497 [astro-ph.SR]`.

Manchester, R. N. et al. (Apr. 2005). “The Australia Telescope National Facility Pulsar Catalogue”. In: *AJ* 129.4, pp. 1993–2006. DOI: `10.1086/428488`. arXiv: `astro-ph/0412641 [astro-ph]`.

Mao, Shude and Bohdan Paczynski (June 1991). “Gravitational Microlensing by Double Stars and Planetary Systems”. In: *ApJ* 374, p. L37. DOI: `10.1086/186066`.

Mao, Shude, Martin C. Smith, et al. (Jan. 2002). “Optical Gravitational Lensing Experiment OGLE-1999-BUL-32: the longest ever microlensing event - evidence for a stellar mass black hole?” In: *MNRAS* 329.2, pp. 349–354. DOI: `10.1046/j.1365-8711.2002.04986.x`. arXiv: `astro-ph/0108312 [astro-ph]`.

Margalit, B. and B. D. Metzger (Dec. 2017). “Constraining the Maximum Mass of Neutron Stars from Multi-messenger Observations of GW170817”. In: *ApJ* 850, L19, p. L19. DOI: `10.3847/2041-8213/aa991c`. arXiv: `1710.05938 [astro-ph.HE]`.

Marshall, D. J. et al. (July 2006). “Modelling the Galactic interstellar extinction distribution in three dimensions”. In: *A&A* 453.2, pp. 635–651. DOI: `10.1051/0004-6361:20053842`. arXiv: `astro-ph/0604427 [astro-ph]`.

Mashian, N. and A. Loeb (Sept. 2017). “Hunting black holes with Gaia”. In: *MNRAS* 470, pp. 2611–2616. DOI: `10.1093/mnras/stx1410`. arXiv: `1704.03455 [astro-ph.HE]`.

McGill, Peter et al. (Nov. 2020). “Predictions of Gaia’s prize microlensing events are flawed”. In: *MNRAS* 498.1, pp. L6–L10. DOI: `10.1093/mnrasl/slaa118`. arXiv: `2006.13958 [astro-ph.SR]`.

Medford, Michael S. et al. (Apr. 2023). “60 Microlensing Events from the Three Years of Zwicky Transient Facility Phase One”. In: *ApJ* 947.1, 24, p. 24. DOI: `10.3847/1538-4357/acba8f`. arXiv: `2201.08335 [astro-ph.GA]`.

Mereghetti, S. et al. (July 2022). “X-Ray Observations of the Isolated Black Hole Candidate OGLE-2011-BLG-0462 and Other Collapsed Objects Discovered through Gravitational Microlensing”. In: *ApJ* 934.1, 62, p. 62. DOI: `10.3847/1538-4357/ac7965`. arXiv: `2206.07480 [astro-ph.HE]`.

Michell, John (Jan. 1784). “On the Means of Discovering the Distance, Magnitude, &c. of the Fixed Stars, in Consequence of the Diminution of the Velocity of Their Light, in Case Such a Diminution Should be Found to Take Place in any of Them, and Such Other Data Should be Procured from Observations, as Would be Farther Necessary for That Purpose. By the Rev. John Michell, B. D. F. R. S. In a Letter to Henry Cavendish, Esq. F. R. S. and A. S.” In: *Philosophical Transactions of the Royal Society of London Series I* 74, pp. 35–57.

Miyamoto, M. and Y. Yoshii (Sept. 1995). “Astrometry for Determining the MACHO Mass and Trajectory”. In: *AJ* 110, p. 1427. DOI: `10.1086/117616`.

Mróz, P., A. Udalski, J. Skowron, R. Poleski, et al. (Aug. 2017). “No large population of unbound or wide-orbit Jupiter-mass planets”. In: *Nature* 548, pp. 183–186. DOI: `10.1038/nature23276`. arXiv: `1707.07634 [astro-ph.EP]`.

Mróz, P. and Ł. Wyrzykowski (June 2021). “Measuring the Mass Function of Isolated Stellar Remnants with Gravitational Microlensing I. Revisiting the OGLE-III Dark Lens Candidates”. In: *Acta Astron.* 71.2, pp. 89–102. DOI: `10.32023/0001-5237/71.2.1`. arXiv: `2107.13701 [astro-ph.SR]`.

Mróz, Przemek, Andrzej Udalski, and Andrew Gould (Oct. 2022). “Systematic Errors as a Source of Mass Discrepancy in Black Hole Microlensing Event OGLE-2011-BLG-0462”. In: *ApJ* 937.2, L24, p. L24. DOI: `10.3847/2041-8213/ac90bb`. arXiv: `2207.10729 [astro-ph.SR]`.

Mróz, Przemek, Andrzej Udalski, Jan Skowron, Michał K. Szymański, et al. (Oct. 2019a). "Microlensing Optical Depth and Event Rate toward the Galactic Bulge from 8 yr of OGLE-IV Observations". In: *ApJS* 244.2, 29, p. 29. DOI: `10.3847/1538-4365/ab426b`. arXiv: `1906.02210 [astro-ph.SR]`.

— (Oct. 2019b). "Microlensing Optical Depth and Event Rate toward the Galactic Bulge from 8 yr of OGLE-IV Observations". In: *ApJS* 244.2, 29, p. 29. DOI: `10.3847/1538-4365/ab426b`. arXiv: `1906.02210 [astro-ph.SR]`.

Muraki, Y. et al. (Jan. 1999). "Search for Machos by the MOA Collaboration". In: *Progress of Theoretical Physics Supplement* 133, pp. 233–246. DOI: `10.1143/PTPS.133.233`.

Nataf, David M. et al. (June 2013). "Reddening and Extinction toward the Galactic Bulge from OGLE-III: The Inner Milky Way's R_V ~2.5 Extinction Curve". In: *ApJ* 769.2, 88, p. 88. DOI: `10.1088/0004-637X/769/2/88`. arXiv: `1208.1263 [astro-ph.GA]`.

Nucita, A. A., F. De Paolis, G. Ingrosso, D. Elia, et al. (Nov. 2006). "An XMM-Newton Search for X-Ray Emission from the Microlensing Event MACHO-96-BLG-5". In: *ApJ* 651.2, pp. 1092–1097. DOI: `10.1086/507784`.

Nucita, A. A., F. De Paolis, G. Ingrosso, M. Giordano, et al. (June 2016). "Parallax and Orbital Effects in Astrometric Microlensing with Binary Sources". In: *ApJ* 823.2, 120, p. 120. DOI: `10.3847/0004-637X/823/2/120`. arXiv: `1606.02062 [astro-ph.SR]`.

O'Connor, Evan and Christian D. Ott (Apr. 2011). "Black Hole Formation in Failing Core-Collapse Supernovae". In: *ApJ* 730.2, 70, p. 70. DOI: `10.1088/0004-637X/730/2/70`. arXiv: `1010.5550 [astro-ph.HE]`.

O'Neil, K. Kosmo et al. (July 2019). "Improving Orbit Estimates for Incomplete Orbits with a New Approach to Priors: with Applications from Black Holes to Planets". In: *AJ* 158.1, 4, p. 4. DOI: `10.3847/1538-3881/ab1d66`. arXiv: `1809.05490 [astro-ph.EP]`.

Olejak, A. et al. (June 2020). "Synthetic catalog of black holes in the Milky Way". In: *A&A* 638, A94, A94. DOI: `10.1051/0004-6361/201936557`. arXiv: `1908.08775 [astro-ph.SR]`.

Osłowski, S. et al. (Feb. 2008). "Gravitational lensing as a probe of compact object populations in the Galaxy". In: *A&A* 478, pp. 429–434. DOI: `10.1051/0004-6361:20066802`. eprint: `astro-ph/0611736`.

Özel, F. and P. Freire (Sept. 2016). "Masses, Radii, and the Equation of State of Neutron Stars". In: *ARA&A* 54, pp. 401–440. DOI: `10.1146/annurev-astro-081915-023322`. arXiv: `1603.02698 [astro-ph.HE]`.

Özel, Feryal, Dimitrios Psaltis, et al. (Dec. 2010). "The Black Hole Mass Distribution in the Galaxy". In: *ApJ* 725.2, pp. 1918–1927. DOI: `10.1088/0004-637X/725/2/1918`. arXiv: `1006.2834 [astro-ph.GA]`.

Paczynski, B. (May 1986a). "Gravitational Microlensing by the Galactic Halo". In: *ApJ* 304, p. 1. DOI: `10.1086/164140`.

— (May 1986b). "Gravitational microlensing by the galactic halo". In: *ApJ* 304, pp. 1–5. DOI: `10.1086/164140`.

— (Apr. 1991). "Gravitational Microlensing of the Galactic Bulge Stars". In: *ApJ* 371, p. L63. DOI: `10.1086/186003`.

Palanque-Delabrouille, N. et al. (Apr. 1998). “Microlensing towards the Small Magellanic Cloud EROS 2 first year survey”. In: *A&A* 332, pp. 1–9. DOI: `10.48550/arXiv.astro-ph/9710194`. arXiv: `astro-ph/9710194 [astro-ph]`.

Park, B. -G. et al. (July 2004). “MOA 2003-BLG-37: A Bulge Jerk-Parallax Microlens Degeneracy”. In: *ApJ* 609.1, pp. 166–172. DOI: `10.1086/420926`. arXiv: `astro-ph/0401250 [astro-ph]`.

Paulin-Henriksson, S. et al. (July 2003). “The POINT-AGAPE survey: 4 high signal-to-noise microlensing candidates detected towards M 31”. In: *A&A* 405, pp. 15–21. DOI: `10.1051/0004-6361:20030519`. arXiv: `astro-ph/0207025 [astro-ph]`.

Paxton, B., L. Bildsten, et al. (Jan. 2011). “Modules for Experiments in Stellar Astrophysics (MESA)”. In: *ApJS* 192, 3, p. 3. DOI: `10.1088/0067-0049/192/1/3`. arXiv: `1009.1622 [astro-ph.SR]`.

Paxton, B., M. Cantiello, et al. (Sept. 2013). “Modules for Experiments in Stellar Astrophysics (MESA): Planets, Oscillations, Rotation, and Massive Stars”. In: *ApJS* 208, 4, p. 4. DOI: `10.1088/0067-0049/208/1/4`. arXiv: `1301.0319 [astro-ph.SR]`.

Paxton, B., P. Marchant, et al. (Sept. 2015). “Modules for Experiments in Stellar Astrophysics (MESA): Binaries, Pulsations, and Explosions”. In: *ApJS* 220, 15, p. 15. DOI: `10.1088/0067-0049/220/1/15`. arXiv: `1506.03146 [astro-ph.SR]`.

Peebles, P. J. E. (June 1972). “Gravitational collapse and related phenomena from an empirical point of view, or, black holes are where you find them.” In: *General Relativity and Gravitation* 3.1-2, pp. 63–82. DOI: `10.1007/BF00755923`.

Penny, M. T., E. Kerins, et al. (Sept. 2013). “ExELS: an exoplanet legacy science proposal for the ESA Euclid mission - I. Cold exoplanets”. In: *MNRAS* 434, pp. 2–22. DOI: `10.1093/mnras/stt927`. arXiv: `1206.5296 [astro-ph.EP]`.

Penny, Matthew T., B. Scott Gaudi, et al. (Mar. 2019). “Predictions of the WFIRST Microlensing Survey. I. Bound Planet Detection Rates”. In: *ApJS* 241.1, 3, p. 3. DOI: `10.3847/1538-4365/aafb69`. arXiv: `1808.02490 [astro-ph.EP]`.

Petit, V. et al. (Apr. 2017). “Magnetic massive stars as progenitors of ‘heavy’ stellar-mass black holes”. In: *MNRAS* 466.1, pp. 1052–1060. DOI: `10.1093/mnras/stw3126`. arXiv: `1611.08964 [astro-ph.SR]`.

Pflamm-Altenburg, J. and P. Kroupa (Nov. 2006). “A highly abnormal massive star mass function in the Orion Nebula cluster and the dynamical decay of trapezium systems”. In: *MNRAS* 373, pp. 295–304. DOI: `10.1111/j.1365-2966.2006.11028.x`. eprint: `astro-ph/0610230`.

Poindexter, Shawn et al. (Nov. 2005). “Systematic Analysis of 22 Microlensing Parallax Candidates”. In: *ApJ* 633.2, pp. 914–930. DOI: `10.1086/468182`. arXiv: `astro-ph/0506183 [astro-ph]`.

Poleski, R. and J. C. Yee (Jan. 2019). “Modeling microlensing events with MulensModel”. In: *Astronomy and Computing* 26, 35, p. 35. DOI: `10.1016/j.ascom.2018.11.001`. arXiv: `1803.01003 [astro-ph.IM]`.

Portail, Matthieu et al. (Feb. 2017). “Dynamical modelling of the galactic bulge and bar: the Milky Way’s pattern speed, stellar and dark matter mass distribution”. In:

MNRAS 465.2, pp. 1621–1644. DOI: `10.1093/mnras/stw2819`. arXiv: `1608.07954 [astro-ph.GA]`.

Raithel, C. A., T. Sukhbold, and F. Özel (Mar. 2018). "Confronting Models of Massive Star Evolution and Explosions with Remnant Mass Measurements". In: *ApJ* 856, 35, p. 35. DOI: `10.3847/1538-4357/aab09b`. arXiv: `1712.00021 [astro-ph.HE]`.

Rasmussen, Carl Edward and Christopher K. I. Williams (2006). *Gaussian Processes for Machine Learning.*

Refsdal, S. (Jan. 1966). "On the possibility of determining the distances and masses of stars from the gravitational lens effect". In: *MNRAS* 134, p. 315. DOI: `10.1093/mnras/134.3.315`.

Remillard, R. A. and J. E. McClintock (Sept. 2006). "X-Ray Properties of Black-Hole Binaries". In: *ARA&A* 44, pp. 49–92. DOI: `10.1146/annurev.astro.44.051905.092532`. eprint: `astro-ph/0606352`.

Repetto, S., M. B. Davies, and S. Sigurdsson (Oct. 2012). "Investigating stellar-mass black hole kicks". In: *MNRAS* 425, pp. 2799–2809. DOI: `10.1111/j.1365-2966.2012.21549.x`. arXiv: `1203.3077 [astro-ph.GA]`.

Repetto, Serena, Andrei P. Igoshev, and Gijs Nelemans (May 2017). "The Galactic distribution of X-ray binaries and its implications for compact object formation and natal kicks". In: *MNRAS* 467.1, pp. 298–310. DOI: `10.1093/mnras/stx027`. arXiv: `1701.01347 [astro-ph.HE]`.

Robin, A. C., D. J. Marshall, et al. (Feb. 2012). "Stellar populations in the Milky Way bulge region: towards solving the Galactic bulge and bar shapes using 2MASS data". In: *A&A* 538, A106, A106. DOI: `10.1051/0004-6361/201116512`. arXiv: `1111.5744 [astro-ph.GA]`.

Robin, A. C., C. Reylé, et al. (Oct. 2003). "A synthetic view on structure and evolution of the Milky Way". In: *A&A* 409, pp. 523–540. DOI: `10.1051/0004-6361:20031117`.

Rowan, D. M. et al. (Oct. 2021). "High tide: a systematic search for ellipsoidal variables in ASAS-SN". In: *MNRAS* 507.1, pp. 104–115. DOI: `10.1093/mnras/stab2126`. arXiv: `2105.02242 [astro-ph.SR]`.

Rybicki, Krzysztof A. et al. (May 2018). "On the accuracy of mass measurement for microlensing black holes as seen by Gaia and OGLE". In: *MNRAS* 476.2, pp. 2013–2028. DOI: `10.1093/mnras/sty356`. arXiv: `1802.03258 [astro-ph.SR]`.

Rybizki, Jan et al. (Feb. 2022). "A classifier for spurious astrometric solutions in Gaia eDR3". In: *MNRAS* 510.2, pp. 2597–2616. DOI: `10.1093/mnras/stab3588`. arXiv: `2101.11641 [astro-ph.IM]`.

Sabbi, E. et al. (Jan. 2016). "Hubble Tarantula Treasury Project. III. Photometric Catalog and Resulting Constraints on the Progression of Star Formation in the 30 Doradus Region". In: *ApJS* 222.1, 11, p. 11. DOI: `10.3847/0067-0049/222/1/11`. arXiv: `1511.06021 [astro-ph.GA]`.

Sahu, Kailash (July 2009). *Detecting Isolated Black Holes through Astrometric Microlensing.* HST Proposal.

Sahu, Kailash (Oct. 2012). *Detecting Isolated Black Holes through Astrometric Microlensing.* HST Proposal.

Sahu, Kailash C., Jay Anderson, Stefano Casertano, Howard E. Bond, Pierre Bergeron, et al. (June 2017). "Relativistic deflection of background starlight measures the mass of a nearby white dwarf star". In: *Science* 356.6342, pp. 1046–1050. DOI: `10.1126/science.aal2879`. arXiv: `1706.02037 [astro-ph.SR]`.

Sahu, Kailash C., Jay Anderson, Stefano Casertano, Howard E. Bond, Andrzej Udalski, et al. (Jan. 2022). "An Isolated Stellar-Mass Black Hole Detected Through Astrometric Microlensing". In: *arXiv e-prints*, arXiv:2201.13296, arXiv:2201.13296. arXiv: `2201.13296 [astro-ph.SR]`.

Sajadian, Sedighe and Kailash C. Sahu (Mar. 2023). "Detecting Isolated Stellar-mass Black Holes with the Roman Telescope". In: *AJ* 165.3, 96, p. 96. DOI: `10.3847/1538-3881/acb20f`. arXiv: `2301.03812 [astro-ph.GA]`.

Samland, M. (Mar. 1998). "Modeling the Evolution of Disk Galaxies. II. Yields of Massive Stars". In: *ApJ* 496.1, pp. 155–171. DOI: `10.1086/305368`.

Sana, H. et al. (July 2012). "Binary Interaction Dominates the Evolution of Massive Stars". In: *Science* 337.6093, p. 444. DOI: `10.1126/science.1223344`. arXiv: `1207.6397 [astro-ph.SR]`.

Sana, Hugues (Nov. 2017). "The multiplicity of massive stars: a 2016 view". In: *The Lives and Death-Throes of Massive Stars*. Ed. by J. J. Eldridge et al. Vol. 329, pp. 110–117. DOI: `10.1017/S1743921317003209`. arXiv: `1703.01608 [astro-ph.SR]`.

Sanders, Jason L., Leigh Smith, and N. Wyn Evans (July 2019). "The pattern speed of the Milky Way bar from transverse velocities". In: *MNRAS*, p. 1855. DOI: `10.1093/mnras/stz1827`. arXiv: `1903.02009 [astro-ph.GA]`.

Sarmiento, Marıa H. et al. (Oct. 2019). "XMM-Newton Science Archive (XSA)". In: *Astronomical Data Analysis Software and Systems XXVI*. Ed. by Marco Molinaro, Keith Shortridge, and Fabio Pasian. Vol. 521. Astronomical Society of the Pacific Conference Series, p. 104.

Sartore, N. and A. Treves (Nov. 2010). "Probing isolated compact remnants with microlensing". In: *A&A* 523, A33, A33. DOI: `10.1051/0004-6361/201015060`. arXiv: `1009.0005 [astro-ph.GA]`.

Sasaki, M. et al. (Aug. 2016). "Primordial Black Hole Scenario for the Gravitational-Wave Event GW150914". In: *Physical Review Letters* 117.6, 061101, p. 061101. DOI: `10.1103/PhysRevLett.117.061101`. arXiv: `1603.08338`.

Schlegel, D. J., D. P. Finkbeiner, and M. Davis (June 1998). "Maps of Dust Infrared Emission for Use in Estimation of Reddening and Cosmic Microwave Background Radiation Foregrounds". In: *ApJ* 500, pp. 525–553. DOI: `10.1086/305772`. eprint: `astro-ph/9710327`.

Schneider, Peter, Jürgen Ehlers, and Emilio E. Falco (1992). *Gravitational Lenses.* DOI: `10.1007/978-3-662-03758-4`.

Schwarzschild, Karl (Jan. 1916). "Über das Gravitationsfeld eines Massenpunktes nach der Einsteinschen Theorie". In: *Sitzungsberichte der Königlich Preussischen Akademie der Wissenschaften*, pp. 189–196.

Shapiro, Stuart L. and Saul A. Teukolsky (1983). *Black holes, white dwarfs, and neutron stars : the physics of compact objects.*

Sharma, S. et al. (Mar. 2011). "Galaxia: A Code to Generate a Synthetic Survey of the Milky Way". In: *ApJ* 730, 3, p. 3. DOI: `10.1088/0004-637X/730/1/3`. arXiv: `1101.3561`.

Shemmer, O. et al. (Oct. 2004). "Near-Infrared Spectroscopy of High-Redshift Active Galactic Nuclei. I. A Metallicity-Accretion Rate Relationship". In: *ApJ* 614.2, pp. 547–557. DOI: `10.1086/423607`. arXiv: `astro-ph/0406559 [astro-ph]`.

Shu, F. H. (Nov. 1969). "Models of Partially Relaxed Stellar Disks". In: *ApJ* 158, p. 505. DOI: `10.1086/150214`.

Skilling, John (Nov. 2004). "Nested Sampling". In: *Bayesian Inference and Maximum Entropy Methods in Science and Engineering: 24th International Workshop on Bayesian Inference and Maximum Entropy Methods in Science and Engineering.* Ed. by Rainer Fischer, Roland Preuss, and Udo Von Toussaint. Vol. 735. American Institute of Physics Conference Series, pp. 395–405. DOI: `10.1063/1.1835238`.

Skowron, J., A. Udalski, A. Gould, et al. (Sept. 2011). "Binary Microlensing Event OGLE-2009-BLG-020 Gives Verifiable Mass, Distance, and Orbit Predictions". In: *ApJ* 738.1, 87, p. 87. DOI: `10.1088/0004-637X/738/1/87`. arXiv: `1101.3312 [astro-ph.SR]`.

Skowron, J., A. Udalski, S. Kozłowski, et al. (Jan. 2016). "Analysis of Photometric Uncertainties in the OGLE-IV Galactic Bulge Microlensing Survey Data". In: *Acta Astron.* 66.1, pp. 1–14. arXiv: `1604.01966 [astro-ph.IM]`.

Smartt, S. J. et al. (May 2009). "The death of massive stars - I. Observational constraints on the progenitors of Type II-P supernovae". In: *MNRAS* 395.3, pp. 1409–1437. DOI: `10.1111/j.1365-2966.2009.14506.x`. arXiv: `0809.0403 [astro-ph]`.

Smartt, Stephen J. (Sept. 2009). "Progenitors of Core-Collapse Supernovae". In: *ARA&A* 47.1, pp. 63–106. DOI: `10.1146/annurev-astro-082708-101737`. arXiv: `0908.0700 [astro-ph.SR]`.

Smith, Martin C., Shude Mao, and Bohdan Paczyński (Mar. 2003). "Acceleration and parallax effects in gravitational microlensing". In: *MNRAS* 339.4, pp. 925–936. DOI: `10.1046/j.1365-8711.2003.06183.x`.

Smith, Martin C., Shude Mao, P. Woźniak, et al. (Oct. 2002). "Optical gravitational lensing experiment: OGLE-1999-BUL-19 - the first multipeak parallax event". In: *MNRAS* 336.2, pp. 670–684. DOI: `10.1046/j.1365-8711.2002.05811.x`. arXiv: `astro-ph/0206503 [astro-ph]`.

Spera, Mario, Michela Mapelli, and Alessandro Bressan (Aug. 2015). "The mass spectrum of compact remnants from the PARSEC stellar evolution tracks". In: *MNRAS* 451, pp. 4086–4103. DOI: `10.1093/mnras/stv1161`.

Spergel, D. et al. (Mar. 2015). "Wide-Field InfrarRed Survey Telescope-Astrophysics Focused Telescope Assets WFIRST-AFTA 2015 Report". In: *arXiv e-prints*, arXiv:1503.03757, arXiv:1503.03757. arXiv: `1503.03757 [astro-ph.IM]`.

Sukhbold, T., T. Ertl, et al. (Apr. 2016). "Core-collapse Supernovae from 9 to 120 Solar Masses Based on Neutrino-powered Explosions". In: *ApJ* 821, 38, p. 38. DOI: `10.3847/0004-637X/821/1/38`. arXiv: `1510.04643 [astro-ph.HE]`.

Sukhbold, T., S. E. Woosley, and A. Heger (June 2018). "A High-resolution Study of Presupernova Core Structure". In: *ApJ* 860, 93, p. 93. DOI: `10.3847/1538-4357/aac2da`. arXiv: `1710.03243 [astro-ph.HE]`.

Sumi, T. (Jan. 2008). "MOA-II microlensing survey". In: *Manchester Microlensing Conference*. Ed. by E. Kerins et al., 25, p. 25.

Sumi, T., D. P. Bennett, et al. (Dec. 2013). "The Microlensing Event Rate and Optical Depth toward the Galactic Bulge from MOA-II". In: *ApJ* 778, 150, p. 150. DOI: `10.1088/0004-637X/778/2/150`. arXiv: `1305.0186 [astro-ph.GA]`.

Sumi, T., K. Kamiya, et al. (May 2011). "Unbound or distant planetary mass population detected by gravitational microlensing". In: *Nature* 473, pp. 349–352. DOI: `10.1038/nature10092`. arXiv: `1105.3544 [astro-ph.EP]`.

Sumi, T. and M. T. Penny (Aug. 2016). "Possible Solution of the Long-standing Discrepancy in the Microlensing Optical Depth toward the Galactic Bulge by Correcting the Stellar Number Count". In: *ApJ* 827, 139, p. 139. DOI: `10.3847/0004-637X/827/2/139`. arXiv: `1603.05797 [astro-ph.GA]`.

Tegmark, Max, Andy N. Taylor, and Alan F. Heavens (May 1997). "Karhunen-Loève Eigenvalue Problems in Cosmology: How Should We Tackle Large Data Sets?" In: *ApJ* 480.1, pp. 22–35. DOI: `10.1086/303939`. arXiv: `astro-ph/9603021 [astro-ph]`.

The LIGO Scientific Collaboration et al. (Nov. 2018). "Binary Black Hole Population Properties Inferred from the First and Second Observing Runs of Advanced LIGO and Advanced Virgo". In: *arXiv e-prints*, arXiv:1811.12940, arXiv:1811.12940. arXiv: `1811.12940 [astro-ph.HE]`.

Thompson, Todd A. et al. (Nov. 2019). "A noninteracting low-mass black hole-giant star binary system". In: *Science* 366.6465, pp. 637–640. DOI: `10.1126/science.aau4005`. arXiv: `1806.02751 [astro-ph.HE]`.

Timmes, F. X., S. E. Woosley, and Thomas A. Weaver (Feb. 1996). "The Neutron Star and Black Hole Initial Mass Function". In: *ApJ* 457, p. 834. DOI: `10.1086/176778`. arXiv: `astro-ph/9510136 [astro-ph]`.

Tisserand, P. et al. (July 2007). "Limits on the Macho content of the Galactic Halo from the EROS-2 Survey of the Magellanic Clouds". In: *A&A* 469.2, pp. 387–404. DOI: `10.1051/0004-6361:20066017`. arXiv: `astro-ph/0607207 [astro-ph]`.

Trimble, Virginia L. and Kip S. Thorne (June 1969). "Spectroscopic Binaries and Collapsed Stars". In: *ApJ* 156, p. 1013. DOI: `10.1086/150032`.

Tsang, Benny T. -H., David Vartanyan, and Adam Burrows (Sept. 2022). "Applications of Machine Learning to Predicting Core-collapse Supernova Explosion Outcomes". In: *ApJ* 937.1, L15, p. L15. DOI: `10.3847/2041-8213/ac8f4b`. arXiv: `2208.01661 [astro-ph.SR]`.

Tsuna, Daichi, Norita Kawanaka, and Tomonori Totani (June 2018). "X-ray detectability of accreting isolated black holes in our Galaxy". In: *MNRAS* 477.1, pp. 791–801. DOI: `10.1093/mnras/sty699`. arXiv: `1801.04667 [astro-ph.HE]`.

Udalski, A., M. Szymanski, J. Kaluzny, M. Kubiak, and M. Mateo (1992). "The Optical Gravitational Lensing Experiment". In: *Acta Astron.* 42, pp. 253–284.

Udalski, A., M. Szymanski, J. Kaluzny, M. Kubiak, M. Mateo, et al. (July 1994). "The Optical Gravitational Lensing Experiment. The Early Warning System: Real Time Microlensing". In: *Acta Astron.* 44, pp. 227–234. arXiv: `astro-ph/9408026 [astro-ph]`.

Udalski, A., M. K. Szymański, and G. Szymański (Mar. 2015). "OGLE-IV: Fourth Phase of the Optical Gravitational Lensing Experiment". In: *Acta Astron.* 65.1, pp. 1–38. arXiv: `1504.05966 [astro-ph.SR]`.

Uglesich, Robert R. et al. (Sept. 2004). "Evidence of Halo Microlensing in M31". In: *ApJ* 612.2, pp. 877–893. DOI: `10.1086/422131`. arXiv: `astro-ph/0403248 [astro-ph]`.

Van De Kamp, P. (1967). *Principles of astrometry.*

van Leeuwen, F. et al. (Mar. 2021). *Gaia EDR3 documentation.* Gaia EDR3 documentation.

Vigna-Gómez, Alejandro and Enrico Ramirez-Ruiz (Mar. 2023). "A Binary Origin for the First Isolated Stellar-mass Black Hole Detected with Astrometric Microlensing". In: *ApJ* 946.1, L2, p. L2. DOI: `10.3847/2041-8213/acc076`. arXiv: `2203.08478 [astro-ph.GA]`.

Walker, Mark A. (Nov. 1995). "Microlensed Image Motions". In: *ApJ* 453, p. 37. DOI: `10.1086/176367`.

Wang, Y. H. (1993). "ON THE NUMBER OF SUCCESSES IN INDEPENDENT TRIALS". In: *Statistica Sinica* 3.2, pp. 295–312. ISSN: 10170405, 19968507. URL: `http://www.jstor.org/stable/24304959`.

Webster, B. Louise and Paul Murdin (Jan. 1972). "Cygnus X-1-a Spectroscopic Binary with a Heavy Companion ?" In: *Nature* 235.5332, pp. 37–38. DOI: `10.1038/235037a0`.

Wegg, Christopher and Ortwin Gerhard (Nov. 2013). "Mapping the three-dimensional density of the Galactic bulge with VVV red clump stars". In: *MNRAS* 435.3, pp. 1874–1887. DOI: `10.1093/mnras/stt1376`. arXiv: `1308.0593 [astro-ph.GA]`.

Wegg, Christopher, Ortwin Gerhard, and Matthieu Portail (July 2015). "The structure of the Milky Way's bar outside the bulge". In: *MNRAS* 450.4, pp. 4050–4069. DOI: `10.1093/mnras/stv745`. arXiv: `1504.01401 [astro-ph.GA]`.

WFIRST Astrometry Working Group et al. (Oct. 2019). "Astrometry with the Wide-Field Infrared Space Telescope". In: *Journal of Astronomical Telescopes, Instruments, and Systems* 5, 044005, p. 044005. DOI: `10.1117/1.JATIS.5.4.044005`. arXiv: `1712.05420 [astro-ph.IM]`.

Wiktorowicz, Grzegorz, Youjun Lu, et al. (Dec. 2020). "Noninteracting Black Hole Binaries with Gaia and LAMOST". In: *ApJ* 905.2, 134, p. 134. DOI: `10.3847/1538-4357/abc699`. arXiv: `2006.08317 [astro-ph.HE]`.

Wiktorowicz, Grzegorz, Łukasz Wyrzykowski, et al. (Nov. 2019). "Populations of Stellar-mass Black Holes from Binary Systems". In: *ApJ* 885.1, 1, p. 1. DOI: `10.3847/1538-4357/ab45e6`. arXiv: `1907.11431 [astro-ph.HE]`.

Wolfe, A. M. and G. R. Burbidge (Aug. 1970). "Black Holes in Elliptical Galaxies". In: *ApJ* 161, p. 419. DOI: `10.1086/150549`.

Wood, A. and S. Mao (Sept. 2005). "Optical depths and time-scale distributions in Galactic microlensing". In: *MNRAS* 362, pp. 945–951. DOI: `10.1111/j.1365-2966.2005.09357.x`. eprint: `astro-ph/0507210`.

Wozniak, P. R. (Dec. 2000). “Difference Image Analysis of the OGLE-II Bulge Data. I. The Method”. In: *Acta Astron.* 50, pp. 421–450. arXiv: `astro-ph/0012143 [astro-ph]`.

Woźniak, P. and B. Paczyński (Sept. 1997). “Microlensing of Blended Stellar Images”. In: *ApJ* 487, pp. 55–60. DOI: `10.1086/304607`. eprint: `astro-ph/9702194`.

Wyrzykowski, Ł., Z. Kostrzewa-Rutkowska, et al. (May 2016). “Black hole, neutron star and white dwarf candidates from microlensing with OGLE-III”. In: *MNRAS* 458.3, pp. 3012–3026. DOI: `10.1093/mnras/stw426`. arXiv: `1509.04899 [astro-ph.SR]`.

Wyrzykowski, Ł., A. E. Rynkiewicz, et al. (Jan. 2015). “OGLE-III Microlensing Events and the Structure of the Galactic Bulge”. In: *ApJS* 216, 12, p. 12. DOI: `10.1088/0067-0049/216/1/12`. arXiv: `1405.3134 [astro-ph.SR]`.

Wyrzykowski, L., J. Skowron, et al. (Oct. 2011). “The OGLE view of microlensing towards the Magellanic Clouds - IV. OGLE-III SMC data and final conclusions on MACHOs”. In: *MNRAS* 416.4, pp. 2949–2961. DOI: `10.1111/j.1365-2966.2011.19243.x`. arXiv: `1106.2925 [astro-ph.GA]`.

Wyrzykowski, Łukasz and Ilya Mandel (Apr. 2019). “Constraining the masses of microlensing black holes and the mass gap with Gaia DR2”. In: *arXiv e-prints*, arXiv:1904.07789, arXiv:1904.07789. arXiv: `1904.07789 [astro-ph.SR]`.

— (Apr. 2020). “Constraining the masses of microlensing black holes and the mass gap with Gaia DR2”. In: *A&A* 636, A20, A20. DOI: `10.1051/0004-6361/201935842`. arXiv: `1904.07789 [astro-ph.SR]`.

Yalinewich, Almog et al. (Nov. 2018). “Dark passengers in stellar surveys”. In: *MNRAS* 481.1, pp. 930–937. DOI: `10.1093/mnras/sty2327`. arXiv: `1807.00835 [astro-ph.SR]`.

Yamaguchi, Masaki S. et al. (July 2018). “Detecting Black Hole Binaries by Gaia”. In: *ApJ* 861.1, 21, p. 21. DOI: `10.3847/1538-4357/aac5ec`. arXiv: `1710.09839 [astro-ph.SR]`.

Zel’dovich, Ya. B. and I. D. Novikov (Jan. 1966). “The Hypothesis of Cores Retarded during Expansion and the Hot Cosmological Model”. In: *AZh* 43, p. 758.

Zeldovich, Ya. B. and O. H. Guseynov (May 1966). “Collapsed Stars in Binaries”. In: *ApJ* 144, p. 840. DOI: `10.1086/148672`.

Zhang, Keming et al. (June 2021). “Real-time Likelihood-free Inference of Roman Binary Microlensing Events with Amortized Neural Posterior Estimation”. In: *AJ* 161.6, 262, p. 262. DOI: `10.3847/1538-3881/abf42e`. arXiv: `2102.05673 [astro-ph.IM]`.

Zurlo, A. et al. (Oct. 2018). “The gravitational mass of Proxima Centauri measured with SPHERE from a microlensing event”. In: *MNRAS* 480.1, pp. 236–244. DOI: `10.1093/mnras/sty1805`. arXiv: `1807.01318 [astro-ph.SR]`.